Dynamic Response of TLPs During Tether Installation

by

Alwyn McLeary B.Eng.

Submitted for the degree of Doctor of Philosophy (Ph.D.)

University of Glasgow

Department of Naval Architecture and Ocean Engineering

 August 1998

ProQuest LLC.
789 East Eisenhower Parkway
P.O. Box 1346
Ann Arbor, MI 48106 – 1346

DEDICATION

To Lynda.

DECLARATION

Unless otherwise referenced, the research detailed in this Thesis is believed by the Author to be original.

ACKNOWLEDGEMENT

The research study detailed within this thesis was conducted under the support of the Department of Naval Architecture and Ocean Engineering at the University of Glasgow.

The author would like to thank the following:

Professor Atilla Incecik for his excellent supervision throughout the research study.

Professors Nigel Barltrop and Douglas Faulkner for there support as heads of department.

Mr. Stephane Cornut and Dr. Peter Gorf of BP Exploration Operating Company for there excellent support during the CASE studentship.

Mr. Richard Snell of BP Exploration Operating Company for granting CASE funding support from BP.

Dr. Oguz Yilmaz for his time and efforts during many technical discussion at the laboratory.

The late Mr. R. Christison and all the technicians at the Glasgow University laboratory for their support during my experimental work.

The University of Newcastle, Marine Technology Department and the towing/wave tank technicians for there excellent support during experimental work conducted in their towing/wave tank.

The Engineering and Physical Sciences Research Council (EPSRC) for financial support to conduct this research study.

CONTENTS

ABSTRACT

A research study has been conducted into the *dynamic response of TLPs during tether installation.*

The aims of this research study were to investigate tether dynamics due to coupled tether/TLP system response. In particular, to focus on low pretension conditions to include tether system behaviour during slacking (Ref. Chapter 1).

To facilitate this research study numerical prediction tools were developed and validated by means of comparison with experimental measurements.

The prediction tools developed to predict the dynamic response of the coupled tether/TLP systems during installation utilise the time-domain simulation technique. 2No. forms of coupled tether/TLP model were developed: a Phase 1 model where the tether system was represented by a rotating axial spring system; a Phase 2 model where the tether system was represented by an assembly of 3D beam-column finite-elements (Ref. Chapter 4).

In addition to this software, a closed-form solution to the diffraction solution for an array of circular cylinders was also implemented into software (Ref. Chapter 2).

Software validation consisted of comparisons with experimental work conducted at the Universities of Glasgow and Newcastle on a case study TLP geometry (Heidrun TLP). The experiments at Glasgow University consisted of measurements of wave excitation and hydrodynamic reaction force components (Ref. Chapter 3). The Newcastle experiments consisted of measurements of TLP system motion and tether tension dynamic response (Ref. Chapter 5).

A Case Study result data base was generated for 3No. TLP systems representative of a spectrum of TLP systems (Ref. Chapter 6 and Appendix A).

Comparisons were made between the Phase 1 and Phase 2 simulation models and the experimental data. Following these comparisons, and with reference to simulation and experimental data, conclusions were drawn regarding the response mechanisms governing the TLP/tether system response at low pretensions (Ref. Chapter 7).

The research study undertaken is represented in the following flowchart:

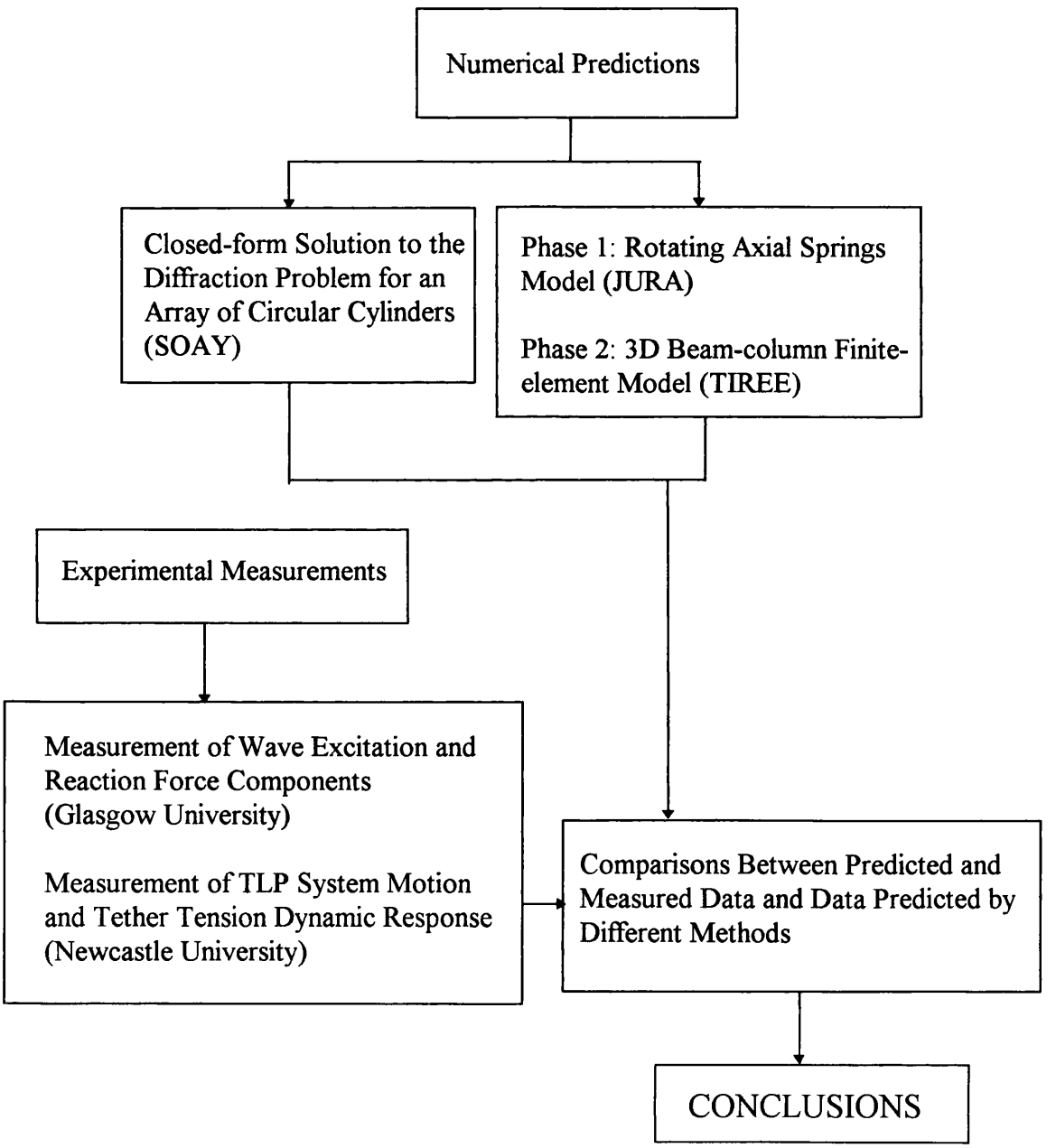

A primary conclusion drawn from this study is the significance of the coupled TLP/tether system dynamics on the tether system motion and tension dynamic response during low pretension conditions.

CHAPTER 1

INTRODUCTION

1.1 Research Overview

A programme of research to investigate the *Dynamic Response of TLPs during Tether Installation* has been conducted. This research programme followed the form: literature survey; establishment of physical models; derivation of mathematical models; software development; experimental validation and case study generation.

Objectives

The objectives of this research study were to develop a prediction method and analysis tools based on this method to predict the behaviour of deep water TLP tether systems during installation. The tools developed enable the designer to determine the installation weather window for a given TLP geometry and metocean parameters. Tools developed were validated by experimental work.

Deliverables

1) Validated tools to predict the behaviour of deep water TLP tether systems.

2) Case study results based on geometrical and metocean data provided by BP illustrating the loading and response of TLP mooring components during installation.

Physical Models

The pretensioning installation stage consists of the following stages:

a) Tugs position the TLP hull over the foundation templates.

b) The pre-installed tethers are latched into the TLP hull tether balconies.

c) Ballast is discharged therefore reducing the mass of the hull.

d) The tethers take up the excess buoyancy force and pretension is developed.

e) Ballast continues to be discharged until static pretension is reached.

During the initial stages of the pretensioning operation the tethers undergo an alternating slacking and tensioning sequence which is a function of the hydrostatic mooring stiffness characteristics of the TLP hull and the prevailing metocean parameters.

During this transient stage snatch type loads can occur due to the instantaneous nature of the heave, roll and pitch tether stiffness components.

To control this all TLP installations to date have incorporated motion compensation mechanisms.

Mathematical Models

(Phase 1)

In order to simulate the lock-off operation a mathematical model has been developed and implemented into software.

Key aspects incorporated are as follows:

1) Dynamic nature of response.

2) Coupled time-dependent characteristics of tether mooring system.

3) Installation metocean conditions.

4) Deballasting operation.

To model the dynamic nature of the TLP/tether response a time-domain solution to the system of 2nd order differential equations (6DOF) governing the TLP motion response is utilised.

$$[M + m_{avm}]\{\ddot{X}\} + [C_1]\{\dot{X}\} + [K_m]\{X\} = \{F\} \qquad \text{(6DOF)} \qquad (1)$$

The above system of equations are solved in the time-domain using the Runge-Kutta method.

The coupled time-dependent characteristics of the tether mooring system are incorporated by the derivation of a (6DOF) tether mooring stiffness matrix $[K_m]$ which includes the hull hydrostatic components.

This mooring stiffness $[K_m]$ is based on modeling the tether system as a group of rotating axial springs and incorporating hull hydrostatic stiffness by assuming small angle stability theory.

Frequency-domain 1st order wave excitation forces/moments {F} and hydrodynamic reaction force components m_{avm} and b_v are utilised.

Deballasting is simulated by a heave ramp function superimposed with the 1st order wave excitation force in heave.

(Phase 2)

To model TLP installation operations incorporating tether wave excitation and hydrodynamic reaction force components a finite-element tether model has been developed.

This model consists of 3D beam-column elements (Chen & Atsuta, 1977) with a Morison excitation loading formulation for randomly orientated cylinders (Chakrabarti *et al*, 1975) and strip-theory hydrodynamic reaction force components.

This model consists of 2No. Schemes:

1) Coupled tether/TLP finite-element model consisting of global system matrices representing the finite-element model of the tether bundle system and the TLP rigid-body system.

2) Finite-element tether bundle model incorporating an external applied force vector. The external applied force vector can consist of translation force components derived by a coupled tether/TLP analysis or representative installation loads (due to tow-out, upending, etc).

The 2nd order differential equation system governing the finite-element model is as follows:

$$[M + m_{svm}]\{\ddot{X}\} + [C_{nl}]\{\dot{X}\}\{\dot{X}\} + [C_l]\{\dot{X}\} + [K_m]\{X\} = \{F\} \quad (2)$$

The governing equation system is solved in the time-domain utilising the ISML solver routine DIVPAG based on the Gear BDF method (5th order) for stiff systems.

The above governing equation system is a large DOF system (e.g. Scheme 1, 10 No. elements/tether bundle=206DOF, Scheme 2, 10 No. elements/tether bundle=55DOF).

1.2 TLP Technology Historical Development

The future of offshore oil development requires the recovery of deep water (300m+, 1000ft+) reserves. Conventional fixed jacket structures are uneconomical/unfeasible for these deep water developments. The future developments therefore will rely on floating production systems. One such system is the TLP system. There are other possible floating systems e.g.: floating production storage and off-loading systems, SPAR Buoy, guyed tower.

A full discussion of the advantages/disadvantages of each system is beyond the scope of this research study, however, key features of the TLP system will be noted:

Advantages

- Good motion response characteristics (low down-time)
- Dry valve trees
- Drilling possible from platform
- Easy well intervention
- Low water depth sensitivity (as the field is delineated the optimum platform position may change-TLP systems can accommodate this)
- No theoretical limit to water depth suitability (except shallow water <100m)

Disadvantages

- Relatively expensive (due to "one off" nature of design at present)
- No storage capability (requires pipeline infrastructure, therefore not suitable for undeveloped regions)
- Low payload capability (requires frequent supply boat trips)
- Weather sensitive installation operations (investigated in this research study)

TLP Design

The principal design parameters of insitu TLPs consist of the following:

Column and Pontoon Geometry: The selection of column and pontoon geometry is based on hydrodynamic considerations. Ratios based on optimising hydrodynamic characteristics for TLPs have been published by Horton (1992). These are principally that the preferred ratio of column displacement to total displacement is ~0.7, with, therefore the optimum pontoon ratio of ~0.3.

All TLPs to date have adopted circular cylinders with pontoons either circular (Jolliet TLWP) or rectangular with/without the corners rounded for all the other TLPs to date. Higher pontoon to total displacement ratios lead higher heave forces/motions at low wave frequencies and lower at higher frequencies. This is beneficial with regard to extreme tether tensions. Lower pontoon to total displacement rations lead to lower heave forces/motions for low wave frequencies and higher for high frequencies. This is beneficial for tether fatigue life.

Number of Columns: Most TLPs installed to date with the exception of the trial TLP TLP-X1 (3No. columns) and Hutton (6No. columns) have utilised 4No. columns. The principle effect of the number of columns is an impact on the ratio a hull steel weight between the deck structure and column/pontoon structure. By increasing the number of columns the deck structure spans reduce and therefore the structural steel weight reduces. However this leads to and increase in column/pontoon structural steel weight. One possibility for significant cost savings could be the use of a multi column concrete hull, therefore reducing the deck structure cost at the expense of the lower cost concrete structure. The disadvantage of this is the significant increase in displacement that a concrete hull entails (as is illustrated with Heidrun TLP at 289000Tonne).

Tether Pretension Level: The main criteria for the selection of pretension level is provide adequate motion response characteristics for the TLP system and ensure tether slacking snatch loads do not occur. The minimum pretension criteria is also depended on the type of bottom connectors utilised as some with fallout and disconnect if pretension reduces to zero. The tether behaviour at low pretensions is a complex problem as (as has been investigate during the course of this research study). Present TLP system developed generally have a pretension to displacement ratio of ~0.25, with the exception of Heidrun which is considerably lower at ~0.13.

All the above criteria are assessed from an insitu perspective and not optimised for installation.

TLPs in Service

TLP-X1

the first TLP in the world was installed off of Catalina Island (offshore southern California) in 1974. This platform consisted of a three column structure installed in 58m of water for a three month period. The funding for this trial installation was provided by a consortium of 17 oil companies with the development conducted by Deep Oil Technology.

Hutton TLP

Hutton TLP was installed in 1983 in the northern North Sea in 150m water depth and is operated by Conoco. Hutton consists of a six column semi-submersible type hull structure. The tether system on Hutton consists of multi-part thick wall thickness drilling string pipe. The tethers were installed from inside the corner columns of the TLP hull structure.

Jolliet TLWP

The Jolliet Tension Leg Wellhead Platform (TLWP) was installed in 1989 in 540m of water in the Gulf of Mexico. The tether system on Jolliet consist of twelve (three/column) one piece buoyant thin walled pipe.

Snorre TLP

Snorre TLP was installed by for Saga Petroleum 1992 in the Norwegian sector of the northern North Sea in 310m water depth. The tether system of Snorre is similar to that of Hutton consisting of pipe lengths installed through the four columns (four tether/column) of the hull structure. Unlike Hutton the tethers on Snorre are thin wall neutrally buoyant pipe.

Auger TLP

The Auger TLP was installed in 1994 for Shell in 870m in the Gulf of Mexico. Auger consists of a four column hull structure with rectangular pontoons. The tethers on Auger consist of three one piece thin walled pipe/column.

Heidrun TLP

The Heidrun is the only reinforced concrete TLP in the world and is also the largest at an installed displacement of 289300tonne. The tether system on Heidrun consists of sixteen thin walled pipes (four/column). The platform was installed in 1995 in 350m water depth.

New Shell TLPs in the Gulf of Mexico

Shell has recently installed three TLPs in the Gulf of Mexico: Mars, Ram-Powell and Ursa. Unfortunately there is very little public domain literature detailing these developments.

Literature Survey

TLP Technology

Pioneering research work on the development of TLP systems has been reported by Mercier (1982) and Mercier *et al* (1991) detailing the historical development of TLP technology, TLP system design requirements and methodologies and existing TLP principal particulars. During the course of the research undertaken and reported within this thesis extensive use has been made of the time-domain simulation technique. A fundamental paper detailing the application of this technique to Semi-submersible and TLP systems was published by Paulling (1977). A review of TLP motion response analysis was presented by Natvig *et al* (1992). Due to the nature of the tether mooring system TLPs are sensitive to resonant responses in the heave, roll and pitch modes.

These resonant responses are considered to consist of two distinct types of response: springing; a steady state response excited by the sum-frequency forces acting on the TLP hull; ringing; a transient response excited by steep wave non-linearities and also considered to be a function of the tether system dynamics. Natvig and Vogel (1991) published a design methodology to incorporate sum-frequency effects in both fatigue and extreme tether response predictions. In 1994 Natvig published a TLP ringing prediction methodology. A detailed account of analysis methodologies applicable to floating systems was presented by Patel & Witz (1991).

Sea Loads

The above published work is relevant to the design/analysis of insitu TLP systems. An input to the techniques detailed in the above papers is a hull specific hydrodynamic database. Research on the topic of fluid loading on column (cylinder) based geometries has taken place over many years from the initial work by Morison *et al* (1950) and Keulegan & Carpenter (1958) on fluid loading on slender cylinders (w.r.t. wave lenght). A detailed account of the fundamentals underlying hydrodynamics was presented by Lighthill in 1979. As TLP hull structures consist of large diameter cylinders (typically >20m) the diffraction/radiation effects of the individual cylinders and the interaction between the array of cylinders must be taken into account. In a paper in 1954 MacCamy & Fuchs presented an analytical method for the solution of the diffraction problem for a single bottom mounted cylinder (surge/sway and roll/pitch DOF). Solution in closed form to the diffraction interactions between arrays of bottom mounted cylinders in waves was presented by Linton & Evans (1990) with further advancement to include the solution for truncated cylinders and the radiation problem by Kim (1993); surge, sway, roll, pitch and yaw DOF (with both papers referring to earlier work by Spring & Monkmeyer, 1974). An analytical solution to the heave (and surge/sway, roll/pitch) diffraction problem for a single cylinder in finite water depth was presented by Garrett (1971). In 1988 Williams and Demirbilek presented a methodology for the closed form solution to the heave diffraction problem for an array of truncated cylinders. A review of efficient methods of computing sea loads on TLP hull type geometries was presented by Kim *et al* (1993).

Although not considered within the scope of this research study detailed works on the solution of the 2nd order diffraction problem has been presented by Kim & Yue (1988, 1989 and 1990). Huang and Eatock Taylor (1997) presented a semi-analytical methodology to determine the Quadratic Transfer Functions (QTFs) on an array of truncated cylinders. A comparative study on steady drift forces acting on a cylinder due to viscous and potential origins was presented by Chakrabarti (1984). Detailed accounts of sea load prediction have been published by Faltinsen (1990) and Sarpkaya & Isaacson (1981).

Tether Tensions

With respect to the estimation of TLP tether tensions a detailed review of the "state-of-practice" within the oil industry was presented by Hodges *et al* in 1992. Natvig (1996) presented a paper detailing a methodology for the estimation of installation transient loads (this paper was published after the drafting of the Software Specification document drafted by the author and utilised during the development of simulation programs applied within this research programme). In this paper a rotating axial springs type model was utilised to represent the tether system. The principal conclusions of this research study were that installation transient tether tension, for installation type sea-states, did not exceed the static pretension level for the TLP geometry investigated. Also, the effects of tether dynamics in the form of a catenary type sagging of the tethers at low pretension levels may be import and required further investigation. The conclusions of this research are consistent with the conclusion drawn by the Author. With reference to time-domain simulations detailed in Chapter 6 and experimental measurements detailed in Chapter 5, the tether transients were generally lower than the installed static pretension. With reference to Chapter 7, the effects of tether dynamics at low pretensions is concluded to be significant. The approach employed during the development of the coupled tether/TLP model utilises a finite-element model of the tether system to accurately capture the tether system dynamics. This approach is more closely associated with riser and mooring line dynamics and reference was made to the work of McIver & Lunn (1983). A detailed description of the application of the finite-element method to model mooring lie system was presented by Webster (1975). Another application of the finite-element method

applied to dynamic analysis of riser type systems was presented by Gardner & Kotch (1976) and a detailed account of the finite-element method applied to space-frame structures was published by Chen & Atsuta (1977).

Numerical Methods

During the development of prediction software undertaken during the course of this research study extensive use was made of numerical methods for the solution of systems of differential equations.

Newmark (1959) published a solution methodology for systems of 2^{nd} order differential equations (implicit Newmark-β, unconditional stable for $\beta=0.25$). Use was also made of the Runge-Kutta explicit method (ref. Thomson 1988).

A detailed account of numerical methods in finite-element analysis was published by Bathe & Wilson in 1976. There exists many different established methods for solution of systems of differential equations. For applications to engineering systems these generally take the form of direct integration methods, i.e. that the equations are integrated directly without transformation of the original equations. Direct integration methods are based on 2No. principals: that an adequate solution to the system of differential equations can be achieved by solution at a discrete number of points separated by a time-step δt; and that a form of variation of the accelerations, velocities and displacement between these discrete time-steps can be assumed. The main methods in use are as follows:

- Central Difference Method (conditionally stable explicit method)
- Houbolt Method (unconditionally stable implicit method)
- Newmark-β Method (for $\beta=0.25$ unconditionally stable implicit method)
- Wilson-θ Method (for $\theta \geq 1.37$ unconditionally stable implicit method)
- Runge-Kutta (conditionally stable explicit method)
- Gear Stiff Methods

An explicit method is one where a solution is reached at time $t+\delta t$ based on equilibrium at time t, with an implicit method solution is reached at time $t+\delta t$ based on equilibrium at time $t+\delta t$.

A conditionally stable method is one where solution can only be reached by utilising a time-step below a certain threshold, which is dependent on the nature of the differential equation system. An unconditionally stable method returns a solution for any time-step. However care must be exercised to ensure the returned solution is not erroneous.

The nature of the finite-element assemble modeling the tether system yields a stiff system of differential equations which required the use of a Gear (1971) stiff solving algorithm.

1.3 TLP Installation

1.3.1 Introduction

For the purpose of this study the TLP installation procedure was decomposed into 6 No. stages:

1) Tether float-out.

2) Tether upending.

3) Tether latch to foundation.

4) Vertical tethers unconnected to TLP hull.

5) Tether pretensioning to "lock-off".

6) Insitu TLP.

The pretensioning installation stage (Stage 5="lock-off") was modeled as the following stages:

a) Tugs position the TLP hull over the foundation templates.

b) The pre-installed tethers are latched into the TLP hull tether balconies.

c) Ballast is discharged therefore reducing the mass of the hull.

d) The tethers take up the excess buoyancy force and pretension is developed.

e) Ballast continues to be discharged until static pretension is reached.

During the initial stages of the pretensioning operation the tethers undergo an alternating "slacking" and tensioning sequence which is a function of the hydrostatic mooring stiffness characteristics of the TLP hull and the prevailing metocean parameters.

During this transient stage "snatch" type loads can occur due to the instantaneous nature of the heave, roll and pitch tether stiffness components.

To control this all TLP installations to date have incorporated motion compensation mechanisms.

1.3.2 Marine Operations

The process of towing and installing structures offshore is termed marine operations which is an area of expertise involving the interaction of naval architecture and offshore engineering with sea-going knowledge and experience.

A fundamental part of marine operations involves marine warranty appraisal. This is the formal approval procedure, typically conducted by a Classification Society, to assess the marine operation procedures. This approval procedure work scope includes

items such as: survey of work units, ensure vessels are in Class, etc; metocean assessment for weather window; survey of sea fastenings/tow motion assessment, etc and on station survey and approval of installation.

1.4 Thesis Synopsis

A programme of research to investigate the *Dynamic Response of TLPs during Tether Installation* has been conducted. This research programme followed the form: literature survey; establishment of physical models; derivation of mathematical models; software development; experimental validation and case study generation.

Chapter 1 contains an introduction to the research programme. Marine operations are briefly described and a Thesis synopsis is given.

Chapter 2 details theoretical loading calculations for sea loads on TLP based geometrys. Results are presented for program SOAY (analytical solution to the diffraction problem for an array of circular cylinders, based on theoretical developed by Linton and Evans, 1989) and SEIL (diffraction solution for heave loading acting on an array of circular cylinders) developed by the author. In addition, results are presented for the diffraction/radiation solution by numerical methods computed by the AQWA (Atkins Quantitative Wave Analysis) suite of software.

SOAY: This program calculates the diffraction solution for an array of truncated circular cylinders. The method utilised is that published by Linton & Evans, 1989 (Ref. Chapter 2 for theory). The 1st order wave excitation forces/moments in surge, sway, roll, pitch and yaw are calculated. This program was implemented in FORTRAN 90. The principal advantage of this closed form method is the fast solution (50 incident wave frequencies are solved in ~ 10 seconds, compared to hours for a d/r code analyser). The principal disadvantage is the heave DOF is not solved and the method is not generalised with respect to geometry. This prevents the pontoon loading and pontoon/column interaction being included in the solutions.

SEIL: This program calculates the diffraction solution for the heave DOF for an array of circular cylinders. The method adopted is detailed in Chapter 2. The diffraction solution for a single cylinder is assembled with appropriate phase effects incorporated to that of an array of cylinders. The method does not capture in interact effects between the adjacent cylinders.

Full diffraction/radiation results were generated for a case study TLP hull geometry (with and without the pontoons meshed) using the AQWA suite of programs.

The interaction between the above approaches was by comparison of results for a case study TLP hull geometry.

Chapter 3 details experimental work conducted in the University of Glasgow towing/wave tank. This work involved the design, construction and testing of scale case study TLP model (Heidrun ~1:100). Wave excitation and hydrodynamic reaction forces measured in extreme waves and currents are detailed.

Chapter 4 describes theoretical modeling of TLP system response during installation. 2No. time-domain programs were developed by the author: JURA, 6DOF time-domain program based frequency-dependent added mass, damping and excitation force vector, with the mooring system characteristics modeled via a time-dependent rotating linear-elastic spring system.; TIREE, a finite-element based program consisting of 2No. schemes; a fully coupled TLP/tether system model with the NDOF system solved at each time-step (NDOF=number of tether nodes x 5DOF/node + 6DOF for platform); a finite-element model of a single tether/tether bundle with an applied force vector defined with loadings at each element node.

JURA: This program simulates a coupled tether/TLP system response either installed or at low pretension (and during lock-off) in the time-domain. A platform tether system geometry and hull hydrodynamic database is input. The tether system is represented by a rotating axial springs model (Ref. to Chapter 4 for theory).

TIREE: This program simulates a coupled tether/TLP system response either installed or a low pretension in the time-domain. As above, a platform tether system geometry and hull hydrodynamic database is input. The tether system is represented by an assembly of 3D beam-column elements. This allows the capture of tether dynamics.

By comparison of results from the above methods the effect of tether dynamics were investigated (Ref. to Chapter 4 for theory).

By comparison of results from the above time-domain simulations and those derived from experiments an investigation of the mechanisms governing tether dynamics and coupled tether/TLP system response was investigated.

The above time-domain models are represented in the figures below:

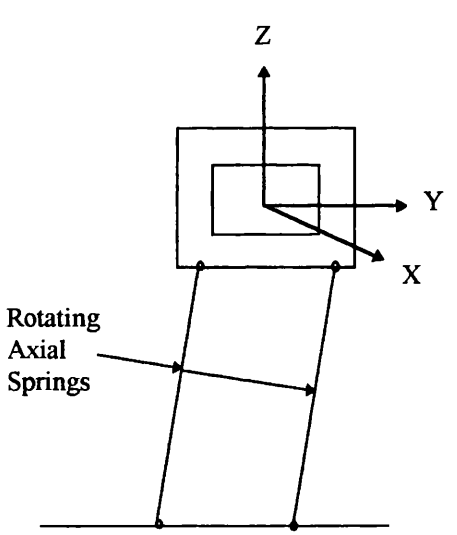

Phase 1 (JURA) Model

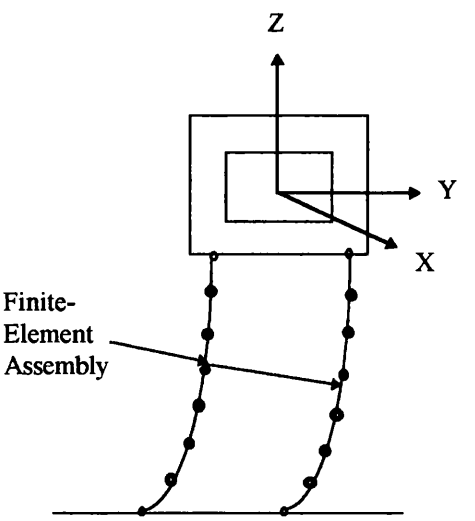

Phase 2 (TIREE) Model

Chapter 5 reports the experimental programme investigating the tether tension and platform motion response. This experimental work consisted of the design, construction and testing of a scale model of a case study TLP system (Heidrun TLP). This experimental work was conducted at the University of Newcastle towing/wave tank and involved sampling tether tensions and platform motions for moored system at low pretension levels.

Chapter 6 details the results of the case study numerical simulation work. 3No. case study TLP systems (AA TLP, Heidrun TLP and Snorre TLP) were investigated with the aid of the time-domain prediction tools developed by the author and reported in Chapter 4.

Chapter 7 details and discusses the results and conclusions of the research study undertaken.

1.5 References

Bathe K. J. & Wilson E. L. (1976) **Numerical Methods in Finite Element Analysis,** Prentice-Hall, INC, ISBN 0-13-627190-1.

Chakrabarti S.K. (1984) Steady Drift Forces on Vertical Cylinder-Viscous v's Potential, **Journal of Applied Ocean Research,** Vol. 6, No. 2, pp. 73-82.

Chakrabarti S.K., Tam W.A. and Wolbert A.L. (1975) Wave Forces on a Randomly Orientated Tube, **Proceedings of the 7th Offshore Technology Conference OTC'75,** OTC2190, pp 433-447.

Chen W.F. and Atsuta T. (1977) **Theory of Beam-columns, Volume 2: Space Frame Behaviour and Design,** McGraw-Hill International Book Company.

Faltinsen O.M. (1990) **Sea Loads on Ships and Offshore Structures,** Cambridge University Press.

Gardner T. N. & Kotch M. A. (1976) Dynamic Analysis of Risers and Caissons by the Finite Element Method, **Proceedings of the 8th Offshore Technology Conference OTC'76,** OTC2651, pp 403-413.

Garrett C.J. (1971) Wave Forces on a Circular Dock, **Journal of Fluid Mechanics,** Vol. 46, Part 1, pp. 129-139.

Gear C.W. (1971) The Automatic Integration of Ordinary Differential Equations, **Numerical Mathematics,** Vol. 14, pp. 176-190.

Hodges S. B., Chiu H. & Kan W. C. (1992) A Comparison of Methods for Predicting Extreme TLP Tendon Tensions, **Proceedings of the 24th Offshore Technology Conference OTC'92,** OTC, pp 129-137.

Horton E. (1992) Development Configuration, Session 4, **TLP Design Technology Seminar**, OMAE and Petroleum Division of ASME.

Huang J.B. and Eatock Taylor R. (1997) Evaluation of Second-Order Forces on an Array of Truncated Cylinders by a Semi-Analytical Method, **Proceedings of the 16th International Conference on Offshore Mechanics and Arctic Engineering OMAE'97**, Vol. 1-A, pp. 401-408.

Keulegan G.H. and Carpenter L.H. (1958) Forces on Cylinders and Plates in an Oscillating Fluid. **Journal of Research of the National Bureau of Standards**, Research Paper No. 2857, pp 420-440.

Kim M.H. (1993) Interaction of waves with N Vertical Circular Cylinders, **Journal of Waterway, Port, Coastal and Ocean Engineering**, Vol. 119, No. 6, pp. 671-689.

Kim M. H., Mercier R. S., Gu G., Wu C. & Botelho D. (1993) PC-Based Wave Load Computation for Large Volume Multi-Column Structures, **Proceedings of the 3rd International Offshore and Polar Engineering Conference, ISOPE'93**, Vol. III, pp. 200-206.

Kim M.H. and Yue D. K. P. (1990), The Complete Second-Order Diffraction Solution for an Axisymmetric Body, Part 2, Bichromatic Incident Waves and Body Motions, **Journal of Applied Ocean Research**, Vol. 211, pp. 557-593.

Kim M.H. and Yue D. K. P. (1989) The Complete Second-Order Diffraction Solution for an Axisymmetric Body, Part 1, Monochromatic Waves, **Journal of Fluid Mechanics**, Vol. 200, pp. 235-264.

Kim M.H. and Yue D. K. P. (1988) The Nonlinear Sum-Frequency Wave Excitation and response of a Tension-Leg Platform, **Proceedings of Behaviour of Offshore Structures BOSS'88**, Vol. 2, pp. 687-703.

Lighthill J. (1979) Waves and Hydrodynamic Loading, **Proceedings of Behaviour of Offshore Structures BOSS'79**, Opening Address, pp. 1-40.

Linton C.M. and Evans D.V. (1990) The Interaction of Waves with Arrays of vertical Circular Cylinders, **Journal of Fluid Mechanics**, Vol. 215, pp 549-569.

MacCamy R.C. and Fuchs R.A. (1954) Wave Forces on Piles a Diffraction Theory, **Technical Memorandum No. 69, Beach Erosion Board Corps of Engineers**.

McIver D. B. & Lunn T. S. (1983) Improvements to Frequency Domain Riser Programs, **Proceedings of the 15th Offshore Technology Conference OTC'83**, OTC4559.

Mercier J. A., Birell N. D., Chivvis J. C. & Hunter A. F. (1991) Tension Leg Platforms-Progress and Prospects, **SNAME Transactions**, Vol. 99, pp 249-279.

Mercier J. A. (1982) Evolution of Tension Leg Platform Technology, **Proceedings of the Behaviour of ships and Offshore Structures 1982 BOSS'92**.

Morison J.R., O'Brien M.P., Johnson J.W. and Schaaf S.A. (1950) The Wave Forces Exerted by Surface Waves on Piles, **Journal of Petroleum Technology, American Institute of Mining Engineers**, Vol. 189, pp. 149-154.

Natvig B. J. (1996) TLP Installation without Motion Compensation, **Proceedings of the 6th International Offshore and Polar Engineering Conference, ISOPE'96,** Vol. I, pp 228-233.

Natvig B. J. (1994) A Proposed Ringing Analysis Model for Higher Order Tether Response, **Proceedings of the 4th International Offshore and Polar Engineering Conference, ISOPE'94,** Vol. I, pp 40-51.

Natvig B. J., Vogel H. S. & Johnsen O. (1992) TLP Global Motion Performance Analysis Procedures, **Proceedings of the 24th Offshore Technology Conference OTC'92**.

Natvig B. J. & Vogel H. (1991) Sum-Frequency Excitations in TLP Design, **Proceedings of the 1st International Offshore and Polar Engineering Conference, ISOPE'91,** Vol. I, pp 93-99.

Newmark (1959) A Method of Computation for Structural Dynamics, **Journal of the Engineering Mechanics Division, proceedings of the American Society of Civil Engineers (ASCE)** , Paper 2094, Vol. 85, No. EM3.

Patel M. H. & Witz J. A. (1991) **Compliant Offshore Structures**, Butterworth-Heinemann, ISBN 0 7506 1070 0.

Paulling J.R. (1977) Time Domain Simulation of Semisubmersible Platform Motion with Application to the Tension-Leg Platform, **The Society of Naval Architects and Marine Engineers**, Proceedings of the Spring Meeting/Star Symposium, pp. 303-314.

Sarpkaya T. and Isaacson M. (1981) Mechanics of wave Forces on Offshore Structures, **Van Nostrand Reinhold**.

Spring B. H. & Monkmeyer P. L. (1974) Interaction of Plane Waves with Vertical Cylinders, **Proceedings of the 14th Conference on Coastal Engineering**, No. 107.

Thomson W.T. (1988) **Theory of Vibration**. Unwin Hyman.

Webster R. L. (1975) Nonlinear Static and Dynamic Response of Underwater Cable Structures Using the Finite Element Method, **Proceedings of the 7th Offshore Technology Conference OTC'75**, OTC2322, pp 753-763.

Williams A.N. and Demirbilek (1988) Hydrodynamic Interactions in Floating Cylinder Arrays-I. Wave Scattering, **Journal of Ocean Engineering**, Vol. 15, No. 6, pp. 549-583.

CHAPTER 2

THEORETICAL DERIVATION OF FORCES ACTING ON TLPs

2.1 Introduction to Forces Acting on TLPs

The objectives of this chapter were: to review the prediction techniques available to calculate the forces acting on TLP systems; to calculate the loads for a Case Study TLP geometry; make comparisons between different methods; discuss sensitivity of loads to geometric parameters and make comparisons against experimental and loading data from other sources (Ref. Chapter 7).

The forces acting on TLPs are composed of 3No. primary components:

1) Excitation Forces

2) Reaction Forces

3) Restoring Forces

These primary force components can be further decomposed into forces due to: sea loads and wind (excitation forces); added mass and damping (reaction forces); hydrostatic stiffness and mooring system stiffness (restoring forces). This Chapter details prediction methodology suitable for the estimation of excitation and reaction forces (Chapter 4 details prediction methodology for the estimation of restoring forces). Simulated data representative of loading components applicable to the Heidrun TLP are detailed.

2.2 Excitation Forces Acting on TLPs

2.2.1 Introduction

The excitation forces acting on TLPs consist of components due to sea loads and wind effects:

1) Hull Steady Wind Forces (Superstructure)

2) Hull Dynamic Wind Forces (Superstructure)

3) Hull Steady Current Forces

4) Hull Wave Frequency (1st order) Forces

5) Hull Steady Drift (2nd Order) Forces

6) Hull Sum and Difference Frequency (2nd order) Forces

7) Tether Excitation Forces (Wave and Current)

2.2.2 Hull Wind Forces

To estimate the excitation forces due to wind a design wind speed (steady wind forces) and design wind spectrum (dynamic wind forces) are assumed. These assumed values represent the likely wind conditions at the location of interest and are usually specified in a return period manner. Once the design wind speed, wind spectrum and direction has been established the wind loading is calculated based on the exposed area of hull/superstructure.

It was assumed that due to offshore personnel safety reasons TLP installation activities would generally not take place during moderate-high wind conditions and as such wind loading was not incorporated in this research study.

It is acknowledged that wind loading would be important when considering the analysis of installed TLP systems. In particular the effects of dynamic wind gusting would have to be investigated due to the compliant nature of TLPs.

2.2.3 Hull Steady Current Forces

Hull steady current loading can be calculated based on a Morison (Morison, 1950) drag formulation. A design current velocity, profile and incident direction is assumed and an immersed area of structure perpendicular to the incident current is estimated. Applying the drag component of the Morison equation (2-1) the steady current excitation loads can be computed.

$$\overline{F}_{Current} = \frac{1}{2}\rho C_d A_p \dot{U}|\dot{U}| \qquad (2\text{-}1)$$

Where,

$\overline{F}_{Current}$ =the steady drag loading due to current

C_d =the drag coefficient

ρ =the density of sea water (assumed 1.025Tonne/m^3)

A_p =projected area of immersed structure perpendicular to the incident current

$\dot{U}$=current velocity at a given water depth

When determining the appropriate drag coefficient to apply reference should be made to published data detailing the drag coefficient vs Reynolds number (R_n) dependency (e.g. Sarpkaya and Isaacson, 1981).

For the purpose of this research study current loading utilised was supplied by the CASE sponsor (BP). This data took the form of global steady current loading acting on the Case Study TLP hull geometry for a range of current velocities and incident headings.

2.2.4 Hull Wave Frequency (1st order) Forces

2.2.4.1 Introduction

When calculating wave frequency loads there are 2No. levels of analysis that can be adopted:

- Morison loading model (small body theory)
- diffraction loading model (large body theory)

When the ratio of the body diameter/length to incident wave length is small the presence of the body has negligible effect on the flow field. For this loading regime the use of a Morison equation based model is applicable.

When the dimensions of the body are large and hence the ratio of the body diameter/length to incident wave length is large the effect of the body on the incident flow field is significant and must be incorporated.

The effects of a large body on the incident wave and hence the loading regime are termed diffraction effects and are estimated utilising potential theory.

Due to the large diameters of TLP columns and the generally close spacing of adjacent columns the computation of wave frequency loads must incorporate these diffraction effects.

Wave frequency forces acting on the case study TLP geometries considered where estimated utilising a closed form analytical solution to the diffraction problem for arrays of circular cylinders developed by Linton and Evans (1989) and extended by Kim (1993).

2.2.4.2 Synopsis of Potential Theory

A brief synopsis of potential theory applied to loading on TLPs is given below, however for a full description reference should be made to the thorough review and discussion presented by Lighthill (1979).

For any irrotational flow within an incompressible, inviscid and homogenous fluid there exists a velocity potential $\phi(x,y,z,t)$ which is a continuous scalar function the partial derivatives of which describe the fluid velocities w.r.t. the Cartesian coordinate system.

$$u = \frac{\partial \phi}{\partial x},\ v = \frac{\partial \phi}{\partial y} \text{ and } w = \frac{\partial \phi}{\partial z} \tag{2-2}$$

Where,

u =fluid velocity in the x-direction

v =fluid velocity in the y-direction

w =fluid velocity in the z-direction

Assuming that the fluid is incompressible requires that this velocity potential satisfies the continuity equation:

$$\nabla . q = \frac{\partial u}{\partial x} + \frac{\partial v}{\partial y} + \frac{\partial w}{\partial z} = 0 \tag{2-3}$$

Where,

$\nabla = \frac{\partial}{\partial x}\vec{i} + \frac{\partial}{\partial y}\vec{j} + \frac{\partial}{\partial z}\vec{k}$ is the vector differential operator (Nabla)

$q = \vec{i}u + \vec{j}v + \vec{k}w$ is the velocity vector

And,

$\vec{i}$, $\vec{j}$ and $\vec{k}$ are unit vectors in the x, y and z coordinates of a right-handed Cartesian coordinate system

Assuming that the flow is irrotational requires that all components of the rotation vector are zero:

$$\frac{\partial w}{\partial y}-\frac{\partial v}{\partial z}=0,\ \frac{\partial u}{\partial z}-\frac{\partial w}{\partial x}=0 \text{ and } \frac{\partial v}{\partial x}-\frac{\partial u}{\partial y}=0 \qquad (2\text{-}4)$$

Which equations (2-2) satisfy and therefore by substitution of equations (2-2) into the continuity equation (2-3) a 2nd order differential equation is derived:

$$\nabla^2\phi=\frac{\partial^2\phi}{\partial x^2}+\frac{\partial^2\phi}{\partial y^2}+\frac{\partial^2\phi}{\partial z^2}=0 \text{ (Laplace equation)} \qquad (2\text{-}5)$$

This equation (2-5) is known as the Laplace equation and therefore a velocity potential must satisfy equation (2-5) for an incompressible fluid and an irrotational flow.

For the solution of the velocity potential describing the flow regime around a body boundary conditions must be imposed which the potential must also satisfy.

Irrotational flow represent the instantaneous description of the fluid which is independent of the previous fluid flow and therefore the boundary conditions are fundamental to the solution.

These boundary conditions are required to represent the physical model and consist of the following:

- $\frac{\partial\phi}{\partial n}=0$ body boundary condition

- $\frac{\partial \phi}{\partial z} = \frac{\partial \eta}{\partial t} + u\frac{\partial \eta}{\partial x} + v\frac{\partial \eta}{\partial y}$ kinematic free-surface condition, at $z = \eta$
- $\frac{\partial \phi}{\partial t} + \frac{1}{2}q^2 + g\eta = F(t)$ dynamic free-surface condition, at $z = \eta$

Where,

n =direction normal to body surface

$z = \eta(x,y,t)$ represents the free-surface

$q^2 = u^2 + v^2 + w^2$

F(t) =arbitrary function dependent on time

The physical interpretation of the above boundary conditions are: fluid cannot pass through the body surface; fluid particles on the free-surface will not leave the surface and fluid pressure at the free-surface must equal atmospheric pressure.

Once a velocity potential satisfying the Laplace equation (2-5) and all the boundary conditions has been established the pressure in the fluid can be computed by application of the Bernoulli equation:

$$p = -\rho\frac{\partial \phi}{\partial t} - \frac{\rho}{2}\nabla\phi.\nabla\phi - \rho gz \qquad (2\text{-}6)$$

Where,

p =pressure in the fluid

ρ =density of fluid

g=acceleration due to gravity (9.81m/s)

For wave frequency diffraction pressures acting on an arbitrary geometry the velocity potential consists of components due to the incident waves, diffracted waves and radiation waves.

$$\phi_{Total} = \phi_{Incident} + \phi_{Diffraction} + \phi_{Radiation} \tag{2-7}$$

With the physical meaning as follows: incident potential represents the undisturbed incident wave; diffraction potential represents the modification to the incident wave due to the presence of the body and the radiation potential represent waves generated by motions of the body.

When calculating the wave frequency pressure it is sufficient to ignore terms which are 2^{nd} w.r.t. wave amplitude. In addition to this a linearised form of the Bernoulli equation is utilised:

$$p = -\rho\frac{\partial\phi}{\partial t} \tag{2-8}$$

Once the wave frequency pressure has be established this is then integrated over the body surface to determine the wave frequency forces/moments. As the pressure calculated will be dependent on the location on the body surface and the geometry of the body surface a boundary element method is employed were the arbitrary body surface is meshed with elements and velocity potentials and hence pressures are estimated for the mid-point of these elements. These element pressures are then integrated with their corresponding position vectors to yield the global wave frequency forces/moments.

$$\begin{Bmatrix} \vec{F} \\ \vec{M} \end{Bmatrix} = -i\rho\omega\int\int_{S_b}\frac{\partial\phi}{\partial t}\begin{Bmatrix} \vec{n} \\ \vec{r}\times\vec{n} \end{Bmatrix}ds \tag{2-9}$$

Where,

$\vec{F}$ =wave frequency force vector

$\vec{M}$ =wave frequency moment vector

$i = \sqrt{-1}$

ω =wave frequency

S_b =mean body surface

$\vec{n} = (n_1, n_2, n_3)$ =unit normal vector

$\vec{r} = (x, y, z)$ =position vector

ds=body surface element

Assumptions

- flow is assumed incompressible, irrotational and inviscid, i.e. satisfying Laplace equation
- body motions are assumed to be small
- body surface corresponds to immersed surface to SWL
- computed forces/moments are linear
- body motions are linear

In practice the above procedure is a very time consuming and numerically demanding one.

There exist closed form semi-analytical solutions to the diffraction and radiation problem which were utilised in this study.

2.2.4.3 Analytical Solution to 1st Diffraction Problem for Circular Cylinders

An analytical solution to the 1st order diffraction problem for arrays of circular cylinders developed by Linton and Evans (1990) and extended by Kim (1993) was utilised to calculate the wave frequency loading for a Case Study TLP.

Assuming an incompressible, irrotational and inviscid flow regime represented by an incident wave velocity potential:

$$\phi_{Incident} = Re\left\{-\frac{ig\xi_a}{\omega} f(z) e^{ikr\cos(\theta-\beta)}\right\} \qquad (2\text{-}10)$$

Where,

ξ_a =incident wave amplitude

$$f(z) = \frac{\cosh k(z+h)}{\cosh kh} \text{ (depth function)} \qquad (2\text{-}11)$$

With,

k =wave number, calculated from the Dispersion relationship,

$$\frac{\omega^2}{g} = k \tanh kh \text{ (Dispersion relationship)} \qquad (2\text{-}12)$$

h =water depth

z =vertical coordinate (measured +ve upwards from the SWL)

And,

r,θ =polar coordinates of a point in the flow model

β =incident wave angle with the x-axis

For N number of circular cylinders there are N+1 coordinate systems (i.e. for a four column TLP there are five coordinate systems utilised): (r,θ) are polar coordinates in the X-Y plane centred at the origin with a series of further polar coordinate systems (r_j,θ_j) centred on the centre of j^{th} column.

The incident wave velocity potential (Eqn. 2-10) can be written in terms of the local coordinate system of the j^{th} cylinder:

$$\phi_{Incident} = -\frac{ig\xi_a}{\omega} f(z) I_j e^{ikr_j \cos(\theta_j - \beta)} \qquad (2\text{-}13)$$

Where,

$$I_j = e^{ik(x_j \cos\beta + y_j \sin\beta)} \text{ (phase factor of } j^{th} \text{ cylinder)} \qquad (2\text{-}14)$$

And,

x_j, y_j =the coordinates of the centre of the j^{th} cylinder

The diffraction wave potential may be described by:

$$\phi^j_{Diffraction} = -\frac{ig\xi_a}{\omega} f(z) \sum_{n=-\infty}^{\infty} A^j_n Z^j_n H^{(1)}_n(kr_j) e^{in\theta_j} \qquad (2\text{-}15)$$

Where,

A^j_n =coefficient to be solved for

$$Z_n^j \equiv Z_{-n}^j = \frac{J_n'(ka_j)}{H_n^{(1)'}(ka_j)} \tag{2-16}$$

$$H_n^{(1)}(ka_j) \equiv J_n(ka_j) + iY_n(ka_j) \text{ (Hankel function, 1st kind)} \tag{2-17}$$

With,

J_n =n^{th} order Bessel function of the 1st kind

Y_n =n^{th} order Bessel function of the 2nd kind

And,

a_j =radius of the j^{th} cylinder

Where,

J_n' =derivative of the n^{th} order Bessel function of the 1st kind

(ref. Handbook of Mathematical Functions, 1965)

$$J_n'(ka_j) = \frac{J_{n-1}(ka_j) - J_{n+1}(ka_j)}{2} \tag{2-18}$$

$H_n^{(1)'}$ =derivative of the n^{th} order Hankel function, 1st kind

(ref. Handbook of Mathematical Function, 1965)

$$H_N^{(1)'}(ka_j) = J_n'(ka_j) + iY_n'(ka_j) \tag{2-19}$$

Where,

$$Y_n'(ka_j) = \frac{Y_{n-1}(ka_j) - Y_{n+1}(ka_j)}{2} \tag{2-20}$$

Assuming a scattering velocity potential consisting of the sum of the incident and diffraction wave potential thus:

$$\phi_{Scattering} = \phi_{Incident} + \phi_{Diffraction} \tag{2-21}$$

Therefore,

$$\phi_{Scattering} = \phi_{Incident} + \sum_{j=1}^{N} \phi^{j}_{Diffraction} \tag{2-22}$$

Thus,

$$\phi_{Scattering} = -\frac{ig\xi_a}{\omega} f(z)\left\{ I_j e^{ikr\cos(\theta-\beta)} + \sum_{j=1}^{N}\sum_{n=-\infty}^{\infty} A_n^j Z_n^j H_n(kr_j) e^{in\theta_j} \right\} \tag{2-23}$$

By application of Graf's addition theorem (ref. Linton & Evans paper) and the appropriate boundary conditions:

$$\frac{\partial \phi_{Diffraction}}{\partial r_j} = 0 \text{ for } r_j = a_j \text{ and } j = 1,...,N \tag{2-24}$$

Eqn. (2-23) may be expressed in terms of the polar coordinates of the adjacent cylinder thus:

$$A_m^k + \sum_{\substack{j=1 \\ \neq k}}^{N}\sum_{n=-\infty}^{\infty} A_n^j Z_n^j e^{i(n-m)\alpha_{ik}} H_{n-m}(kR_{jk}) = -I_k e^{im(\frac{\pi}{2}-\beta)} \tag{2-25}$$

$k = 1,...,N$ and $-\infty < m < \infty$

Where,

α_{jk} =angle between the X-axis of the j^{th} and k^{th} cylinders (+ve anti-clockwise)

R_{jk} =distance between the centre of the j^{th} and k^{th} cylinders

To determine the unknown coefficients A_n^j the infinite system of Eqn. (2-25) is truncated to a linear finite system of N(2M+1) with N(2M+1) unknowns, i.e.:

$$A_m^k + \sum_{\substack{j=1 \\ \neq k}}^{N} \sum_{n=-M}^{M} A_n^j Z_n^j e^{i(n-m)\alpha_{jk}} H_{n-m}(kR_{jk}) = -I_k e^{im(\frac{\pi}{2}-\beta)} \qquad (2\text{-}26)$$

$k = 1,...,N$ and $m = -M,...,M$

With acceptable accuracy achieved with M=6.

Once the unknown coefficients A_n^j have been determined an expression for the scattering velocity potential on the k^{th} can be determined by application of the Wronskian formula to Eqn. (2-25), ref. Linton & Evans paper.

$$\phi_{Scattering} = -\frac{2g\xi_a}{\pi\omega k a_k} f(z) \sum_{n=-\infty}^{\infty} \frac{A_n^k}{H_n'(ka_k)} e^{in\theta_k} \qquad (2\text{-}27)$$

By application of Eqn. (2-9) the wave forces/moments on each cylinder may be calculated.

The surge and sway wave forces on the j^{th} truncated circular cylinder of deep draft can be calculated by:

$$\begin{Bmatrix} F_x^j \\ F_y^j \end{Bmatrix} = -\begin{Bmatrix} i \\ 1 \end{Bmatrix} \frac{2\rho g\xi_a}{k^2 H_1'(ka_j)} \frac{[\sinh kh - \sinh k(h-D)]}{\cosh kh} \left\{A_{-1}^j \pm A_1^j\right\} \qquad (2\text{-}28)$$

Where,

D=draft of columns

The roll and pitch by:

$$\begin{Bmatrix} M_x^j \\ M_y^j \end{Bmatrix} = -\begin{Bmatrix} i \\ 1 \end{Bmatrix} \frac{2\rho g \xi_a}{k^3 H_1'(ka_j)} \frac{\left[kD\sinh k(h-D) - \cosh kh + \cosh k(h-D)\right]}{\cosh kh} \left\{A_{-1}^j \pm A_1^j\right\} \tag{2-29}$$

With the yaw:

$$M_z^j = -Y_j F_x^j + X_j F_y^j \tag{2-30}$$

Applying Eqns. (2-28), (2-29) and (2-30) to a TLP geometry and summing the individual cylinder solution in complex form the total wave forces/moments acting can be calculated:

$$F_{\text{Surge/Sway}} = \sum_{i=1}^{N} (2-28) \tag{2-31}$$

$$M_{\text{Roll/Pitch}} = \sum_{i=1}^{N} (2-29) \tag{2-32}$$

$$M_{\text{Yaw}} = \sum_{i=1}^{N} (2-30) \tag{2-33}$$

The above solution does not incorporate pontoon effects in the surge, sway, roll, pitch and yaw wave frequency forces/moments calculations.

The above solution methodology does not yield the heave wave forces.

Refer to section (2.5.2) for results of the above computations.

2.2.4.4 Simplified Analytical Solution to Wave Heave Forces on a TLP Geometry

To calculate the heave wave forces a simplified method consisting of an analytical solution for the Froude-Krylov forces acting on a circular cylinder was utilised. This method estimates the Froude-Krylov forces for a single cylinder which is then assembled to the solution for an array of cylinders by summing the single cylinder solutions in complex form incorporating the phase factors. The diffraction effects due to: the cylinder and adjacent cylinders were not solved. Closed-form solutions to this problem have been developed by Garrett (1971) and Williams & Demirbilek (1988) however due to time restriction these methods were not utilised in this study.

Assuming an incident wave velocity potential of the form:

$$\phi_{\text{Incident}} = \text{Re}\left\{-\frac{ig\xi_a}{\omega} f(z) e^{ikr\cos(\theta-\beta)}\right\} \qquad (3\text{-}34a)$$

Which can be expressed in Cartesian coordinate form without the depth function thus,

$$\phi_{\text{Incident}} = \text{Re}\left\{-\frac{ig\xi_a}{\omega} e^{kz+ikx-i\omega t}\right\} \qquad (2\text{-}34b)$$

Where,

x, z=local Cartesian coordinates of the column base, origin at the centre of the j^{th} column at the SWL

By application of the linearised Bernoulli equation (Eqn. 2-8) and incorporating only the incident wave velocity potential (Eqn. 2-34) the Froude-Krylov pressure can be calculated:

$$p_{F-K} = \rho g \xi_a e^{kz+ikx-\omega t} \qquad (2\text{-}35)$$

Where,

p_{F-K}=Froude-Krylov pressure

For the base of the j^{th} TLP column the Froude-Krylov force in the heave mode can be calculated by:

$$F_{F-K(Heave)_j} = I_j \iint_{S_b} p_{F-K} n_z ds \qquad (2\text{-}36)$$

Where,

$F_{F-K(Heave)_j}$=Froude-Krylov force in the heave mode for j^{th} column

n_z=normal to the column base (+ve into the fluid)

And the phase factor is calculated with reference to the origin of the global coordinate system of the array of cylinders.

By substitution of Eqn. (2-35) in Eqn. (2-36),

$$F_{F-K(Heave)_j} = \rho g \xi_a I_j \int_{-a_j}^{a_j} \int_{-\sqrt{a_j^2-x_j^2}}^{\sqrt{a_j^2-x_j^2}} e^{-kD+ikx_j} dxdy \qquad (2\text{-}37)$$

Which can be expressed,

$$F_{F-K(Heave)_j} = 2\rho g \xi_a e^{-kD} a_j^2 I_j \int_0^{\pi} \sin^2\phi e^{ika_j\cos\phi} d\phi \qquad (2\text{-}38)$$

Where,

ϕ =angle between cylinder radius and local X-axis

Eqn. (2-38) can be evaluated to:

$$F_{F-K(Heave)_j} = 2\rho g \xi_a e^{-kD} a_j^2 \frac{1}{2}\left(\int_0^{\pi} e^{ika_j \cos\phi} d\phi - \int_0^{\pi} e^{ika_j \cos\phi} \cos 2\phi d\phi\right) \quad (2\text{-}39)$$

As,

$$\int_0^{\pi} e^{ika_j \cos\phi} d\phi = \pi J_0(ka_j) \quad (2\text{-}40)$$

And,

$$\int_0^{\pi} e^{ika_j \cos\phi} \cos 2\phi d\phi = -\pi J_2(ka_j) \quad (2\text{-}41)$$

Where,

J_0 =0th order Bessel function of the 1st kind

J_2 =2nd order Bessel function of the 1st kind

Therefore Eqn. (2-38) can be simplified to:

$$F_{F-K(Heave)_j} = \rho g \xi_a e^{-kD} a_j^2 I_j(\pi J_o(ka_j) + \pi J_2(ka_j)) \quad (2\text{-}42)$$

To incorporate the effects on the pontoons in heave a Morison model with linear wave theory was assumed (drag effects ignored).

For deep water the water particle acceleration in the Z-axis is given by (linear wave theory),

$$\ddot{w} = -\omega^2 \xi_a e^{kz} \cos(kx - \omega t) \qquad (2\text{-}43)$$

Where,

$\ddot{w}$ =water particle acceleration in the Z-axis

For NP number of pontoons sub-divide into NS number of strips and incorporating Eqn. (2-43) the global heave force of all pontoons is given by:

$$FP_{(Heave)} = \sum_{j=1}^{NP} \sum_{k=1}^{NS} -\omega^2 \xi_a e^{-kD_p} I_{j,k} C_m \rho P_w P_d \delta \qquad (2\text{-}44)$$

Where,

D_p =depth to centre of pontoons

$I_{j,k}$ =phase factor for pontoon elements (see Eqn. 2-14)

C_m =inertia coefficient (assumed 2.5)

P_w =pontoon width

P_d =pontoon depth

δ =pontoon strip length

The above method does not incorporate the column/pontoon junction interaction effects.

For results of the above analysis reference should be made to section (2.5.2).

2.2.4.5 Alternative Analytical Solution to Diffraction Problem for Circular Cylinders

To quantify the cylinder interaction effects computed in 2.2.4.3 an alternative approach to the solution of the diffraction problem for circular cylinders was utilised based on that developed by M^{ac}Camy & Fuchs (1954).

This method details an analytical solution to the diffraction problem for a single circular cylinder.

Assuming an incident wave potential of the form,

$$\phi_{\text{Incident}} = \text{Re}\left\{-\frac{ig\xi_a}{\omega} f(z) e^{ikr\cos(\theta-\beta)}\right\} \qquad (2\text{-}45)$$

Expressing (2-45) in terms of local polar coordinates for head sea incident wave heading and expanding yields,

$$\phi_{\text{Incident}} = -\frac{ig\xi_a}{\omega}\frac{\cosh k(d+z)}{\cosh kd}\left\{J_0(kr) - \sum_{m=1}^{\infty} 2i^m \cos m\theta J_m(kr) e^{-i\omega t}\right\} \qquad (2\text{-}46)$$

It is assumed that the diffracted wave can be expressed by a similar expansion for $\phi(-\theta) = \phi(\theta)$ giving,

$$\phi_{\text{Diffraction}_n} = A_n \cos n\theta + \left\{J_n(kr) + iY_n(kr)\right\} e^{-i\omega t} \qquad (2\text{-}47)$$

Eqn. (2-47) represents for large values of cylinder radius a periodic wave moving outward in the radial direction and vanishing at $r = \infty$.

The scattering velocity potential ($\phi_{Incident} + \phi_{Diffraction}$) is determined by the superposition of the velocity potentials with the coefficients A_n determined by setting the water particle velocity normal to the cylinder equal to zero (ref. body-boundary condition 2.4.2.2).

The above procedure yields,

$$\phi_{Scattering} = \frac{g\xi_a}{\omega} e^{-i\omega t} \frac{\cosh k(d+z)}{\cosh kd} \left\{ \begin{array}{l} J_0(kr) - \frac{J_0'(ka)}{H^{(2)\prime}(ka)} H^{(2)}(kr) + \\ 2\sum_{n=1}^{\infty} i^n \left(J_n(kr) - \frac{J_n(ka)}{H_n^{(2)}(ka) H_n^{(2)}} (kr) \cos n\theta \right. \end{array} \right\} \quad (2\text{-}48)$$

Where,

$$H_n^{(2)}(ka) = J_n - i(ka)Y_n(ka) \text{ is the Hankel function, } 2^{nd} \text{ kind} \quad (2\text{-}49)$$

By application of the linearised Bernoulli equation (Eqn. 2-8) the horizontal component of force can be calculated from,

$$F_{X-axis/unit} = \frac{4\rho g\xi_a}{k} \frac{\cosh k(d+z)}{\cosh kd} A(ka)\cos(\omega t - \alpha) \quad (2\text{-}50)$$

Where,

$F_{X-axis/unit}$ =force in the X-axis/unit length at depth z

$$\tan\alpha = \frac{J_1'(ka)}{Y_1'(ka)} \quad (2\text{-}51)$$

And,

$$A(ka) = \frac{1}{\sqrt{J_1'^2(ka) + Y_1'^2(ka)}} \qquad (2\text{-}52)$$

Eqn. (2-50) yields the wave frequency (linear) horizontal force acting on a single bottom mounted circular cylinder in regular waves.

To determine the global surge wave frequency forces acting on a TLP geometry the local surge forces acting on an array of circular cylinders are summed in complex form with the appropriate phase factor (Eqn. 2-14).

This procedure results in an expression of the form:

$$F_{Surge} = \sum_{j=1}^{N} I_j \frac{4\rho g \xi_a}{k} \frac{\cosh k(d+z)}{\cosh kd} A(ka_j)\cos(\omega t - \alpha) \qquad (2\text{-}53)$$

The above solution of the global surge wave forces acting on a TLP geometry takes no account of pontoon and column interaction effects. With reference to Chapter 7, Figure 7.1, the effect of the pontoons and the column/pontoon junctions on the global surge wave force is low, this is illustrated by comparing the AQWA-Line CO (Column only model) with the AQWA-line CM (complete model).

Results of the above prediction method are given in (2.5.2).

2.2.5 Hull Steady Drift (2nd Order) Forces

In both regular and irregular sea-states there exist steady drift forces. These forces can be due to both potential and viscous effects.

Potential origin drift forces in a regular sea-state are in part due to the alternating wetting of the body surface as the wave crests and troughs pass the body. If the body is large diameter and the body modifies the wave form then these effects are increased. In an irregular sea-state steady drift forces are also created by the combination of discrete wave frequencies constituting the irregular sea spectrum (ref. 2.2.6).

When potential origin drift forces are small, viscous origin drift forces can dominate. Viscous origin drift are third order forces w.r.t. wave amplitude (ref. Faltinsen, 1990) and therefore become increasingly important as incident wave amplitude increases.

An investigation covering both potential and viscous origin steady drift forces by Chakrabarti (1984) details a qualitative assessment of the predominance of potential or viscous steady drift forces for a fixed vertical circular cylinder in deep water.

As this study covers installation sea-states which have in the past been defined as a significant wave height of 2.5m it was assumed that for typical TLP hull column diameters that the potential origin steady drift forces would dominate.

Steady drift forces utilised in this study are of potential origin and were calculated utilising the method detailed by Linton & Evans (1990).

Steady drift force coefficients were provided by the CASE sponsor (BP) for the case study TLP geometries. These steady drift force coefficients were then utilised in the Case Study time-domain analyses performed and detailed in Chapter 6. For comparison/validation, steady drift force coefficients were computed during the diffraction/radiation code analysis for one of the Case Study TLP hull geometries (2.4, 2.5.2) and compared with those provided by the CASE sponsor. The agreement show was good (Ref. Chapter 7, Figure 7.4).

2.2.6 Hull Sum and Difference Frequency (2nd order) Forces

In an irregular sea-state there exist sum and difference frequency forces, where sum refers to forces at the frequency of the sum of two discrete regular wave frequencies $(\omega_i + \omega_j)$ and difference frequency refers to forces at the frequency of the difference of two discrete wave frequencies $(\omega_i - \omega_j)$. Faltinsen (1990) has detailed a simple way to describe the origins of these nonlinear wave forces as follows:

Taking the quadratic velocity term of the Bernoulli equation thus:

$$-\frac{\rho}{2}\nabla\phi.\nabla\phi = -\frac{\rho}{2}(u^2 + v^2 + w^2) \tag{2-54}$$

Assuming an irregular sea-state consisting of two wave components where the horizontal water particle velocity can be represented as:

$$u = \xi_{a_i}\cos(\omega_i t + \beta_i) + \xi_{a_j}\cos(\omega_j t + \beta_j) \tag{2-55}$$

Expanding Eqn. (2-54) for the horizontal water particle velocity only yields:

$$-\frac{\rho}{2}u^2 = -\frac{\rho}{2}\left[\begin{array}{l}\dfrac{\xi_{a_i}^2}{2} + \dfrac{\xi_{a_j}^2}{2} + \dfrac{\xi_{a_i}^2}{2}\cos(2\omega_i t + 2\beta_i) + \dfrac{\xi_{a_j}^2}{2}\cos(2\omega_j t + 2\beta_j) + \\ \xi_{a_i}\xi_{a_j}\cos\left\{\left(\omega_i - \omega_j\right)t + \beta_i - \beta_j\right\} + \\ \cos\left\{\left(\omega_i + \omega_j\right)t + \beta_i + \beta_j\right\}\end{array}\right] \tag{2-56}$$

By inspection of Eqn. (2-56) force components that are mean, sum and difference are illustrated.

It is acknowledged that the above serves as an illustration of the presence of sum and difference frequency forces and is not a methodology for the estimation of these 2nd order forces.

For details on the computation of these forces reference can be made in the first instance to papers by Kim (1992) for difference frequency forces, Kim & Yue (1989) for sum frequency forces and also Kim & Yue (1988) for sum frequency forces and response of TLPs. With further work in this field reported by Huang & Eatock Taylor (1997).

Due to the time limitations of this study a detailed investigation of the sum and difference frequency forces applicable to TLPs was not undertaken.

It is acknowledged that there exist other mechanisms governing the exists of sum frequency forces including the full integration of pressure up to the instantaneous free-surface level and wave amplitude enhancement due to run-up (ref. Arnott *et al*, 1997).

2.2.7 Tether Excitation Forces (Wave and Current)

To compute the wave and current excitation forces acting on the tethers a Morison (Morison *et al*, 1950) was utilised.

The method employed was a generalised form of the Morison equation applicable to randomly orientated cylinders developed by Chakrabarti *et al*, 1975.

The well known Morison equation for a vertical cylinder is of the form,

$$f_{Horizontal} = \frac{1}{2}\rho C_d D\dot{U}|\dot{U}| + C_m \rho \frac{\pi D}{4}\ddot{U} \qquad (2\text{-}57)$$

Where,

$f_{Horizontal}$ =force in the horizontal axis/unit length at a defined depth in the fluid

C_d =drag coefficient

C_m =inertia coefficient

$\dot{U}, \ddot{U}$ =water particle horizontal velocity and acceleration (normal to cylinder) respectively

For a inclined cylinder the generalised form of the Morison equation is of the form,

$$\vec{f}_{Normal} = \frac{1}{2}\rho C_d D \vec{\dot{W}}\left|\vec{\dot{W}}\right| + C_m \rho \frac{\pi D}{4}\vec{\ddot{W}} \qquad (2\text{-}58)$$

Where,

$\vec{f}_{Normal}$ =force vector normal to the cylinder/unit length at a defined depth in the fluid

$\vec{\dot{W}}, \vec{\ddot{W}}$ =the water particle velocity and acceleration vectors normal to the cylinder

The tangential component of velocity and accelerations is ignored, as is the assumption in the vertical cylinder case (cross flow assumption).

Assuming a unit vector along the cylinder long axis thus,

$$\vec{C} = C_x\vec{i} + C_y\vec{j} + C_z\vec{k} \qquad (2\text{-}59)$$

Where $\vec{i}, \vec{j}$ and $\vec{k}$ are unit vectors in the x, y and z-axis of a Cartesian coordinate system.

The normal velocity vector may be expressed as the cross product:

$$\dot{\vec{W}} = \vec{C} \times \left\{ \left(u\vec{i} + w\vec{j} \right) \times \vec{C} \right\} \tag{2-60}$$

With the magnitude of the normal velocity vector defined as,

$$\left| \dot{\vec{W}} \right| = \left(\dot{\vec{W}} \cdot \dot{\vec{W}} \right)^{\frac{1}{2}} = \left\{ u^2 + w^2 - \left(C_x u + C_y w \right)^2 \right\}^{\frac{1}{2}} \tag{2-61}$$

By application of spherical coordinates,

$$C_x = \sin\varepsilon \cos\tau \tag{2-62}$$

$$C_y = \cos\varepsilon \tag{2-63}$$

$$C_z = \sin\varepsilon \sin\tau \tag{2-64}$$

Where ,

ε =angle of the inclined cylinder to the space fixed Z-axis

τ =angle of the inclined cylinder to the space fixed X-axis

Expressing the normal velocity and acceleration vectors in Cartesian coordinates thus:

$$\begin{pmatrix} \dot{\vec{W}} \\ \ddot{\vec{W}} \end{pmatrix} = \begin{pmatrix} \dot{u}_x \\ \ddot{u}_x \end{pmatrix} \vec{i} + \begin{pmatrix} \dot{u}_y \\ \ddot{u}_y \end{pmatrix} \vec{j} + \begin{pmatrix} \dot{u}_z \\ \ddot{u}_z \end{pmatrix} \vec{k} \tag{2-65}$$

Where,

$$\dot{u}_x = u - C_x (C_x u + C_y w) \tag{2-66}$$

$$\dot{u}_y = w - C_y (C_x u + C_y w) \tag{2-67}$$

$$\dot{u}_z = -C_z(C_x u + C_y w) \tag{2-68}$$

By substitution of Eqn. (2-65) into (2-58) the force vector acting on a randomly inclined circular cylinder may be written,

$$\begin{pmatrix} \vec{f}_x \\ \vec{f}_y \\ \vec{f}_z \end{pmatrix} = \frac{1}{2}\rho C_d D \begin{pmatrix} \dot{u}_x \\ \dot{u}_y \\ \dot{u}_z \end{pmatrix} \left|\vec{W}\right| + C_m \rho \frac{\pi D}{4} \begin{pmatrix} \ddot{u}_x \\ \ddot{u}_y \\ \ddot{u}_z \end{pmatrix} \tag{2-69}$$

To incorporate current effects a linear superposition of the current velocity and incident wave kinematic velocity was applied. Linear wave theory was used to calculate the incident wave kinematics

The above calculation procedure was utilised in time-domain simulations of the coupled TLP/tether system (Chapter 4). The procedure was applied in a nonlinear method where at each time-step the tether excitation force vector was reassembled based on the previous time-step orientation.

2.3 Reaction Forces Acting on TLPs

2.3.1 Introduction

When a body floating in a fluid undergoes forced rigid-body oscillations there are generated waves that radiate away from the body. This in turn leads to oscillating pressures acting on the body surface which may be integrated over the body surface to yield the hydrodynamic reaction force components of added mass and damping.

The added mass and damping reaction force components are described by the following equation (ref. Faltinsen, 1990),

$$F_k = -A_{kj}\frac{d^2\eta_j}{dt^2} - B_{kj}\frac{d\eta_j}{dt} \qquad (2\text{-}70)$$

Where,

F_k =total force acting on the body in the k^{th} mode

A_{kj}=added mass coefficient in the k^{th} mode due to motions in the j^{th} mode

B_{kj}= radiation damping coefficient in the k^{th} mode due to motions in the j^{th} mode

And,

$\frac{d^2\eta_j}{dt^2}$ and $\frac{d\eta_j}{dt}$ =rigid-body acceleration and velocity respectively in the j^{th} mode

A potential theory approach is employed allowing a velocity potential to be calculated satisfying the various boundary conditions and the Laplace equation Eqn. (2-5).

The approach employed is similar to that outlined in section 2.2.4.2, with an additional radiation boundary condition required at infinity and the body surface boundary modified to:

$\frac{\partial\phi}{\partial n} = \frac{d\eta}{dt}$ body boundary condition

With the physical meaning that the fluid particle velocity at the body surface must be equal to the body velocity.

Once a velocity potential satisfy all the boundary conditions has been determined then the pressures can be estimated by application of the linearised Bernoulli equation (Eqn. 2-8). Then by application of Eqn. (2-9) the total reaction forces/moments acting on the body can be estimated.

In addition to the above potential origin damping forces there also exist damping forces due to viscous drag force effects within the fluid. This form of damping is significant only for small dimension bodies or in modes where there is very low radiation damping. Viscous damping effects acting on the TLP hull are low and may be ignored. The viscous damping effects acting on the tether system are higher and were included in the Phase 2 coupled tether/TLP finite element model (Ref. Chapter 4, section 4.3).

2.3.2 Hull Reaction Forces

The hydrodynamic reaction force components of added mass and radiation damping were calculated for the Case Study TLP hull geometry utilising analytical solutions to the radiation problem developed by Kim (1993).

Added mass and radiation damping data was provided by the CASE sponsor (BP) and used during the Case Study time-domain simulations. For comparison/validation purposes, values of added mass and radiation damping were computed with the aid of a diffraction/radiation analysis performed for one the Case Study TLP hull geometries and compared with the CASE sponsor supplied data (Ref. Chapter 7, Figure 7.6).

For results of the TLP hull reaction force computation refer to section 2.5.3.

Comparisons and discussions between experimental and prediction data are given in Chapter 7.

A significant form of damping not investigated as part of this research study is wave drift damping. By experimental investigation Wichers (1988) demonstrated that this damping is 2nd order in origin w.r.t. wave amplitude and can be obtained experimentally by added resistance towing tests.

This source of damping is of particular importance when determining the low frequency large amplitude surge/sway motions of an installed TLP geometry. These motions are of significance when determining the design air-gap and risers system characteristics for a given TLP geometry.

As it was assumed that there would be station keeping assistance, in the form of tugs, during TLP installation activities preventing surge/sway resonance type behaviour occurring this form of damping was not investigated.

2.3.3 Tether Reaction Forces

2.3.3.1 Introduction

For a TLP system there exist hydrodynamic reaction force components applicable to the hull and tether system motions. Section 2.3.2 outlined the approach employed when determining the hull reaction force components.

Additional reaction forces are generated by hull induced motions of the tether system through the fluid environment.

A Strip theory approach was utilised to predict added mass and drag viscous damping generated by tether motions.

2.3.3.2 Tether Added Mass

The tether added mass was calculated by application of the added mass coefficients detailed by Sarpkaya & Isaacson (1981).

Assuming that the tethers can be represented by a number of finite-elements, the added mass for each finite-element can be calculated by,

$$\rho\frac{\pi D^2}{4}L_{Element} \tag{2-71}$$

This finite-element added mass was lumped to each node in the form,

$$m_{avm(Node)} = \rho\frac{\pi D^2}{4}\frac{L_{Element}}{2} \tag{2-73}$$

Where,

$m_{avm(Node)}$ =lumped to node tether finite-element added mass

Further details of the method employed are given in Chapter 4.

2.3.3.3 Tether Damping

Tether drag damping was calculated by application of a Morison type quadratic drag model. Again assuming the tether represented by an assembly of finite-elements, the drag damping coefficient applicable to each finite-element was given by:

$$\frac{1}{2}\rho C_d D L_{Element} \tag{2-74}$$

With the damping also lumped to the element nodes,

$$C_{NL(Node)} = \frac{1}{2}\rho C_d D\frac{L_{Element}}{2} \tag{2-75}$$

Where,

$C_{NL(Node)}$ =lumped to node tether finite-element drag damping (nonlinear)

Refer to Chapter 4 for further details.

Other sources of damping in addition to the fluid damping detailed above are material/structural damping and foundation soil interaction damping.

The material/structural damping was incorporated by use of a viscous Coulomb damping model.

Assuming a stress-strain relationship for the tether material thus:

$$\sigma = E\varepsilon + \kappa \frac{d\varepsilon}{dt} \qquad (2\text{-}76)$$

Where,

σ =stress in the material

E =Young's modulus of the material

ε =strain in the material

κ =coefficient of viscosity of the material

$\frac{d\varepsilon}{dt}$ =rate of change of strain

For the purpose of this study the Young's modulus and coefficient of viscosity of the tether material were assumed to be $2.07 \times 10^5 N/mm^2$ and $58.65 Ns/mm^2$ (mild steel values) respectively.

This material damping was superimposed with the linear radiation damping in the heave mode as follows:

$$F = \left(E\varepsilon + \kappa \frac{d\varepsilon}{dt} \right) A_{Tether} \qquad (2\text{-}77)$$

Where the second term represents the material damping reaction force.

$$C_{Material(Linear)} = \frac{\kappa A_{Tether}}{L} \qquad (2\text{-}78)$$

Where,

$C_{Material(Linear)}$ =material damping coefficient

Foundation/soil interaction may be a significant source of damping for an installed TLP system. Unfortunately there is little quantitative data available in this area and therefore this effect could not be incorporated. Recent research activities (Narasimha Rao, 1997) has highlighted the possibility of the use of suction type anchors for TLPs. The use of such anchor system would require the mechanisms of soil/foundation damping to be investigated and included in the coupled TLP/tether system analysis.

2.4 Diffraction/Radiation Code Analysis of a TLP Geometry

2.4.1 Introduction

A diffraction/radiation analysis of the Case Study TLP geometry was conducted utilising the AQWA (LINE) code. AQWA (LINE) is one element of the AQWA suite of software developed by W S Atkins. 2No. models were analysed consisting of the Case Study TLP represented by columns only (2260 elements, Figure 2.1) and by columns plus pontoons (3620 elements, complete hull model, Figure 2.2).

The AQWA (LINE) program is a diffraction/radiation program based on the boundary element method (ref. Faltinsen, 1993 and AQWA (LINE) User Manual (1997)).

The basic stages of this analysis are:

- Discretisation of the body immersed surface (meshing)
- Distribution of sources/sinks over the body surface
- Generation of element velocity potentials satisfying the various boundary conditions
- Application of the linearised Bernoulli equation to determine pressures
- Numerical integration of the element pressure over the body immersed surface yielding forces and moments

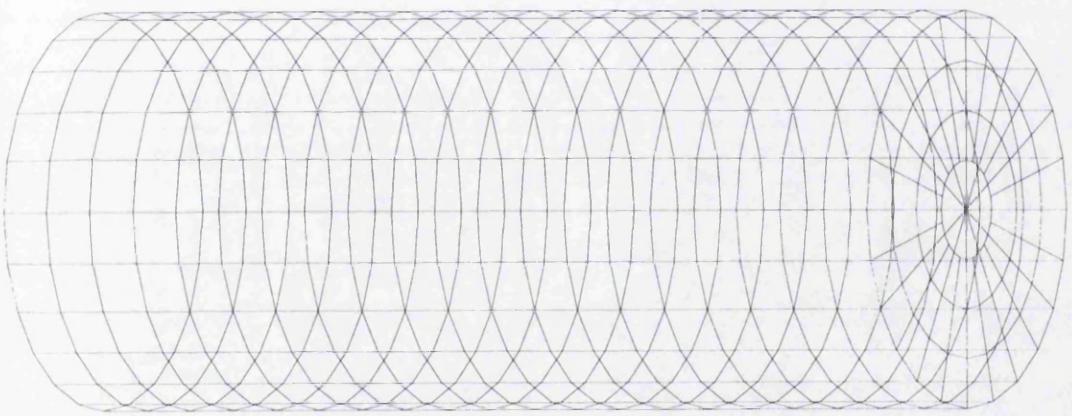

PLOT TITLE- RUN 0008
RUN TITLE- HEIDRUN D/R ANALYSIS (COLUMNS ONLY, 1/4 MESH)

Figure 2.1: Case Study TLP Diffraction/Radiation Model

(Columns Only)

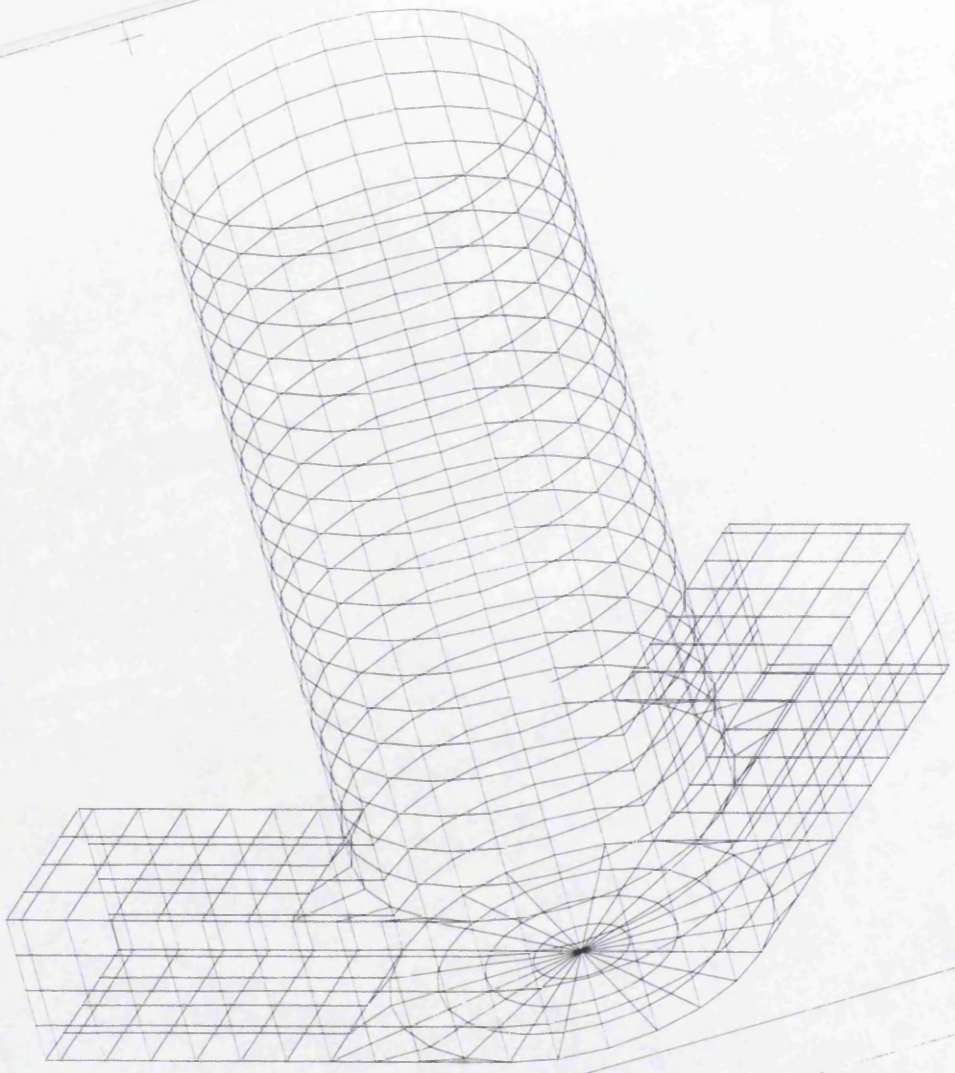

Figure 2.2: Case Study TLP Diffraction/Radiation Model
(Complete Hull)

2.4.2 Hull Mesh Generation

The user input to this process is the definition of the mesh modeling the immersed body surface. This is a crucial part of the analysis procedure. One important consideration before attempting to mesh the body is due to the generation of element velocity potentials at the element mid-points, a fine mesh should be employed in regions of large pressure gradients. There are other theoretical and computational meshing rules applicable to the use of AQWA (LINE) as follows:

- elements must cover all the mean wetted surface (without gaps)
- plate length $< \frac{\lambda}{7}$
- element side dimensions < local radius of curvature
- element normal must point into the fluid
- element sizes must vary gradually
- element aspect ratio $> \frac{1}{3}$

Where,

$$\text{aspect ratio} = \frac{\text{area}}{L^2} C \quad \text{with,} \quad C = \frac{4}{n \tan(90 - \frac{360}{2n})}, \quad n = \text{No. elements}$$

- element centres to be at least an equivalent facet radius apart, r_c

Where,

$$r_c = \sqrt{\frac{\text{area}}{\pi}}$$

- centre of all diffraction elements must be, z_s, below SWL (analysis position)

Where,

$z_s = 0.000273h$ and $z_s = 0.0000132\lambda$

- centre of all diffraction elements must be $> \frac{r_c}{2}$ above sea-bed
- adjacent diffraction elements should have an area ratio $> \frac{1}{3}$

Where,

$$\text{adjacent area ratio=minimum of } \frac{i^{th} \text{ area}}{j^{th} \text{ area}} \text{ and } \frac{j^{th} \text{ area}}{i^{th} \text{ area}}$$

- maximum number of diffraction elements that can be defined is 1500 with 6000 the maximum number of all elements with SYMX and SYMY
- SYMX and SYMY is only applicable to plate elements

With the above limitations in mind a grid work of nodes is define covering the body immersed surface. With plate elements then defined by a number of nodes.

The results of this diffraction/radiation study of the Case Study TLP hull are given in section 2.5 with comparisons between prediction and experimental data given in Chapter 7.

2.5 Results of TLP Theoretical Force Investigation

2.5.1 Introduction

Result plots are detailed for the Case Study TLP. These results have been collated into excitation and reaction force sections. For comparison with experimentally derived data refer to Chapter 7.

2.5.2 Excitation Forces

The predicted excitation forces (sea loads) for the Case Study TLP hull geometry are given in Figures 2.3-2.19.

Figures 2.3-2.5 detail the wave excitation forces acting on the Case Study TLP geometry for head sea regular waves of unit wave amplitude (solution by analytical method).

Figures 2.6-2.10 detail the wave excitation forces acting on the Case Study TLP geometry for quartering sea regular waves of unit wave amplitude (solution by analytical method).

Figures 2.11-2.13 detail the wave excitation forces acting on the Case Study TLP geometry for head sea regular waves of unit wave amplitude (diffraction/radiation code solution, 2No. models).

Figures 2.14-2.18 detail the wave excitation forces acting on the Case Study TLP geometry for quartering sea regular waves of unit wave amplitude (diffraction/radiation code solution, 2No. models).

Figures 2.19 and 2.20 detail the surge wave drift forces acting on the Case Study TLP geometry for head and quartering sea regular waves of unit wave amplitude (diffraction/radiation code solution, 2No. models).

By inspection of Figures 2.11-2.13, 2.19 and Figures 2.14-2.18, 2.20 (head and quartering sea incident wave heading respectively) the effects of the pontoons on the global wave excitation and steady drift forces can be deduced.

Figure 2.11-2.13 detail the Case Study TLP hull surge, heave and pitch wave excitation forces/moments respectively (with/without pontoons modeled) for the head sea incident wave heading. For all three modes the pontoon effects were observed to be significant for low frequency/long waves.

This is consistent with the slower decay w.r.t. depth from the free-surface of the fluid kinematics for longer waves. In the heave and pitch modes the loading contribution of the pontoons was approximately 50% of the total force/moment predicted with a trend towards zero in the long wave limit for the pitch excitation moment (as with the surge wave excitation force). For the surge mode the pontoon loading consists of approximately 10% of the total force (in the low frequency range at ~0.2rad/s).

Figure 19 details the wave drift force for the head sea condition and indicates no pontoon effects are present for the wave drift forces in surge. This illustrates the dependency of wave drift forces on the wave making characteristics on the body which is a function of the water plane area for the surge mode.

Figures 2.14-2.18, 2.20 detail the Case Study TLP hull surge, sway, heave, roll and pitch wave excitation forces/moments respectively (with/without pontoons modeled) for the quartering sea heading. Similar trends to those discussed for the head sea condition were observed for the surge, heave and pitch modes. In addition to this, comparisons between the sway and roll wave frequency force/moment revealed an approximately 10% load contribution due to pontoons in sway and ~50% in roll, both in the low frequency range.

For all comparisons the predicted forces/moments with and without the pontoons modeled converge as the wave frequency increases. This is consistent with the rapid decay of fluid kinematics w.r.t. water depth for short wave lengths, with due consideration of the deep draft of the Case Study TLP pontoons (64.3m).

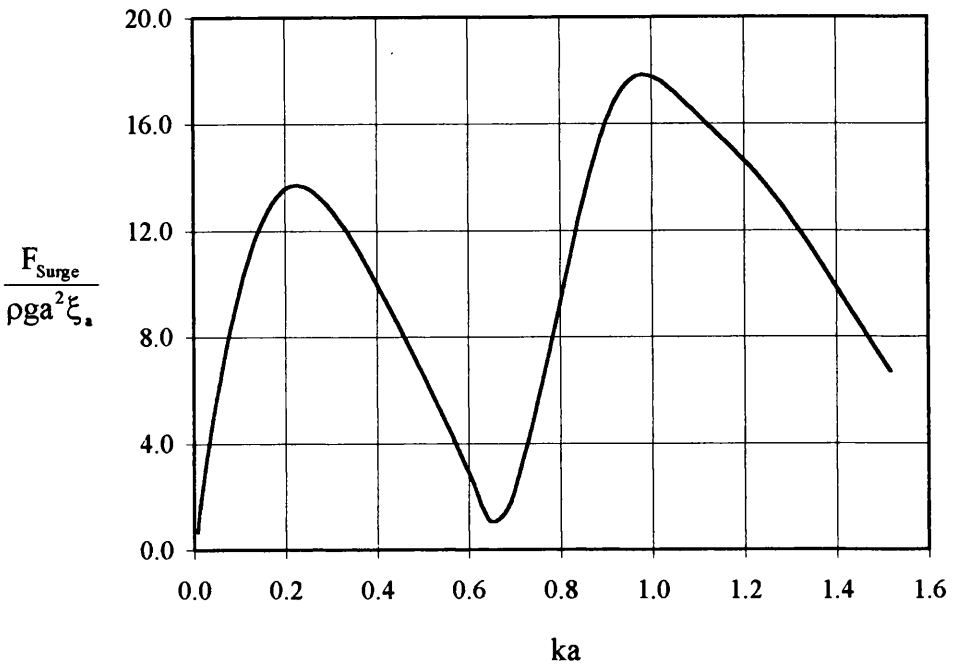

Figure 2.3: Case Study TLP Surge Force $\beta = 0$

(Analytical Method)

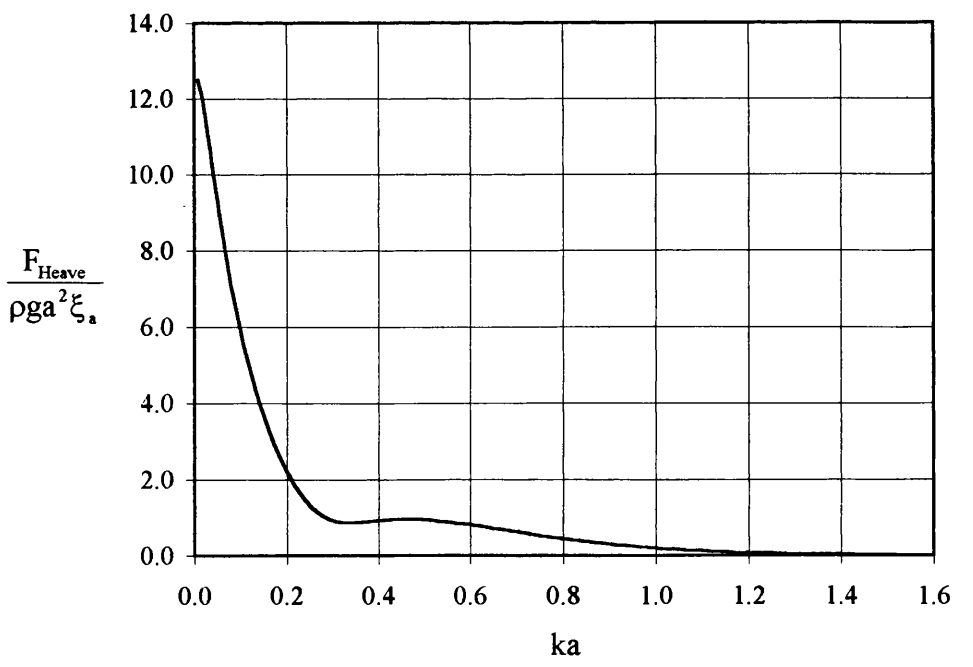

Figure 2.4: Case Study TLP Heave Force $\beta = 0$

(Analytical Method)

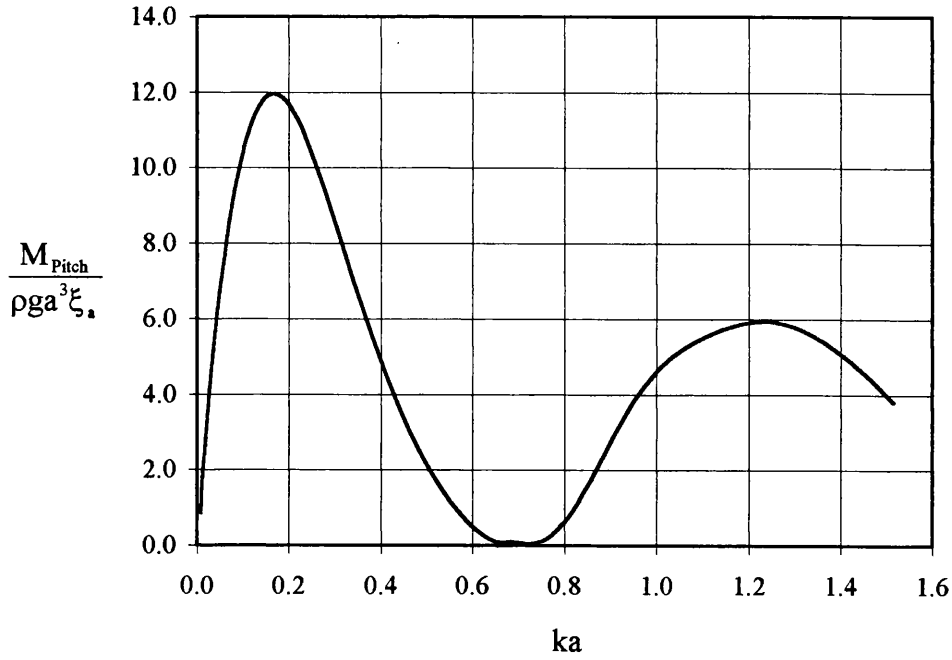

Figure 2.5: Case Study TLP Pitch Moment $\beta = 0$

(Analytical Method)

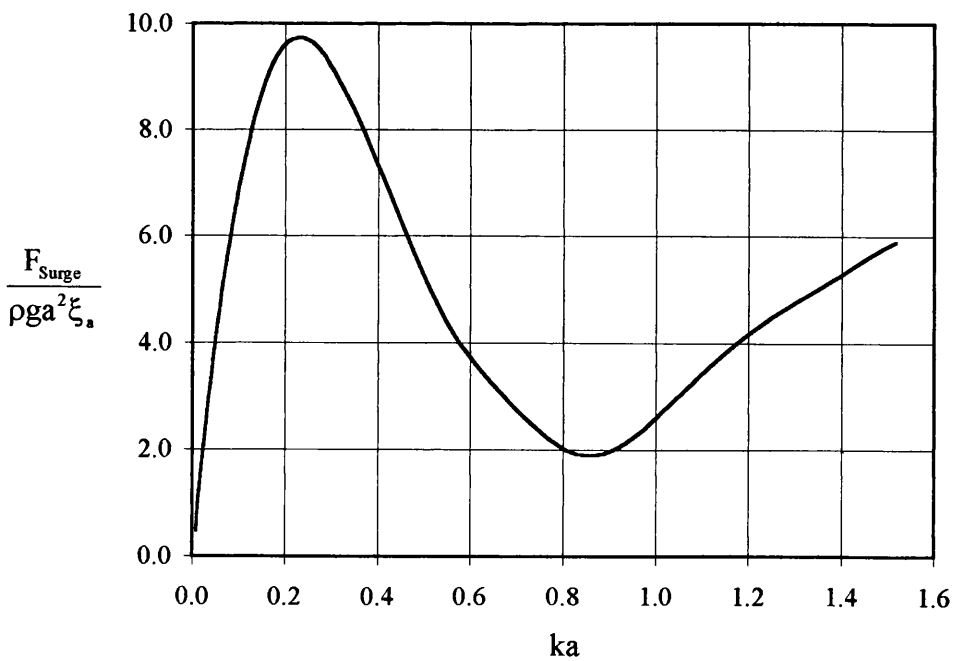

Figure 2.6: Case Study TLP Surge Force $\beta = \frac{\pi}{4}$

(Analytical Method)

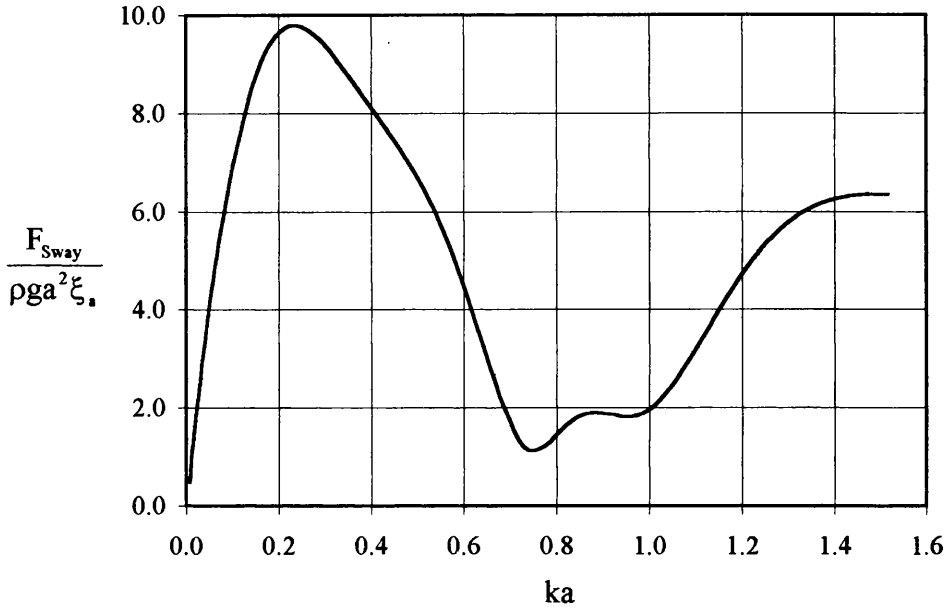

Figure 2.7: Case Study TLP Sway Force $\beta = \frac{\pi}{4}$

(Analytical Method)

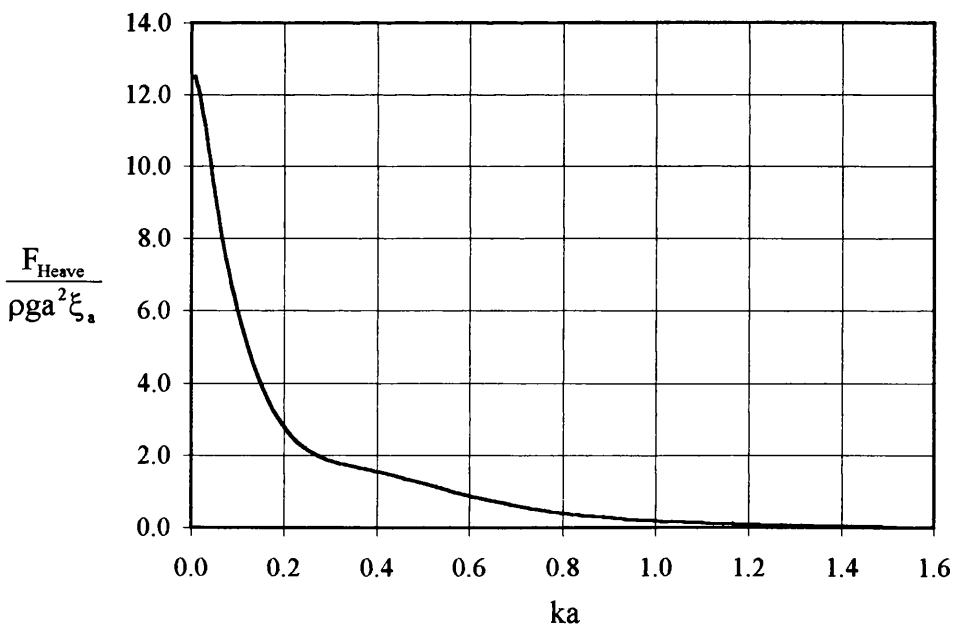

Figure 2.8: Case Study TLP Heave Force $\beta = \frac{\pi}{4}$

(Analytical Method)

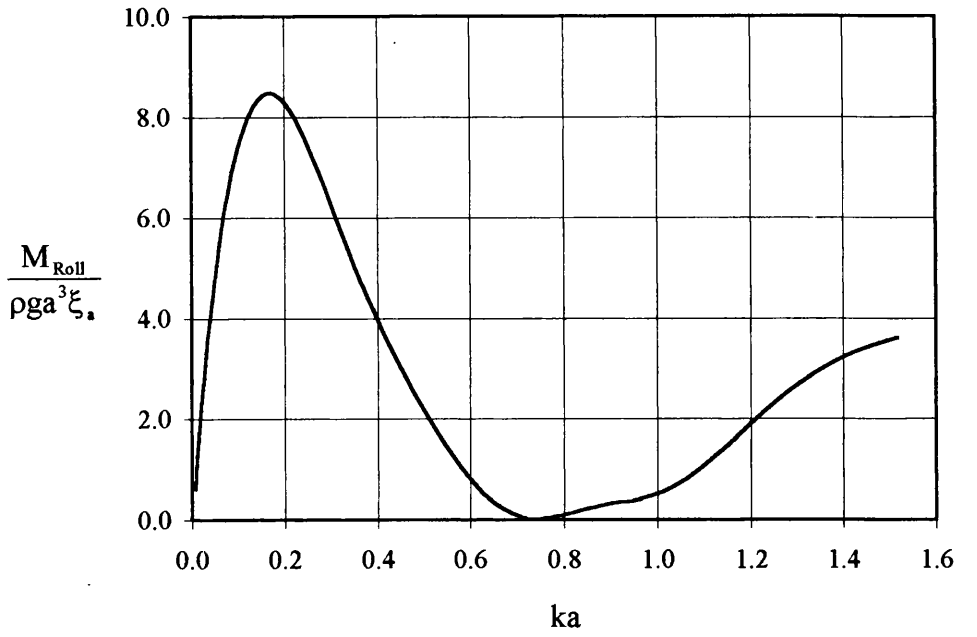

Figure 2.9: Case Study TLP Roll Moment $\beta = \frac{\pi}{4}$

(Analytical Method)

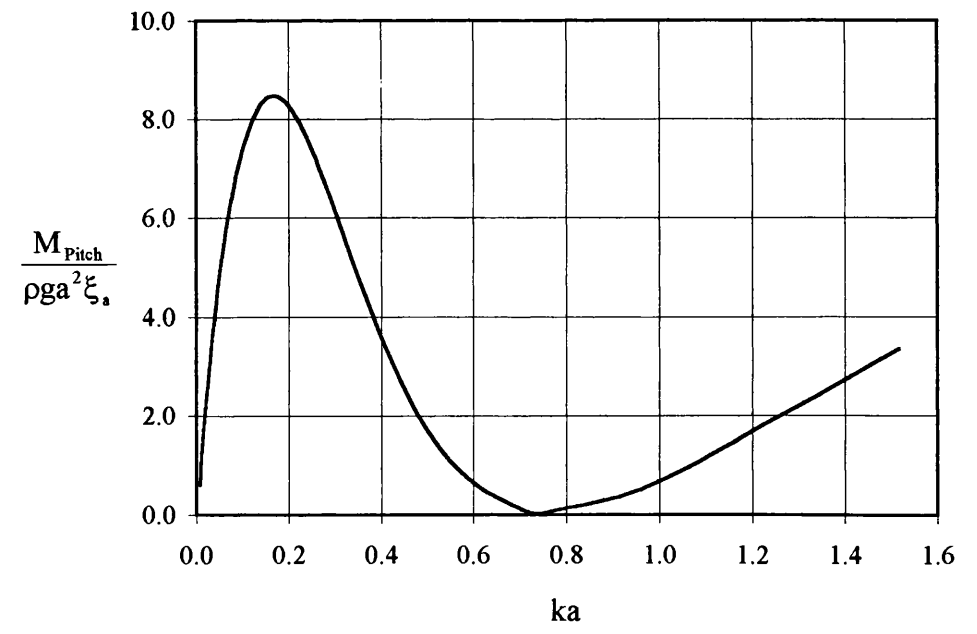

Figure 2.10: Case Study TLP Pitch Moment $\beta = \frac{\pi}{4}$

(Analytical Method)

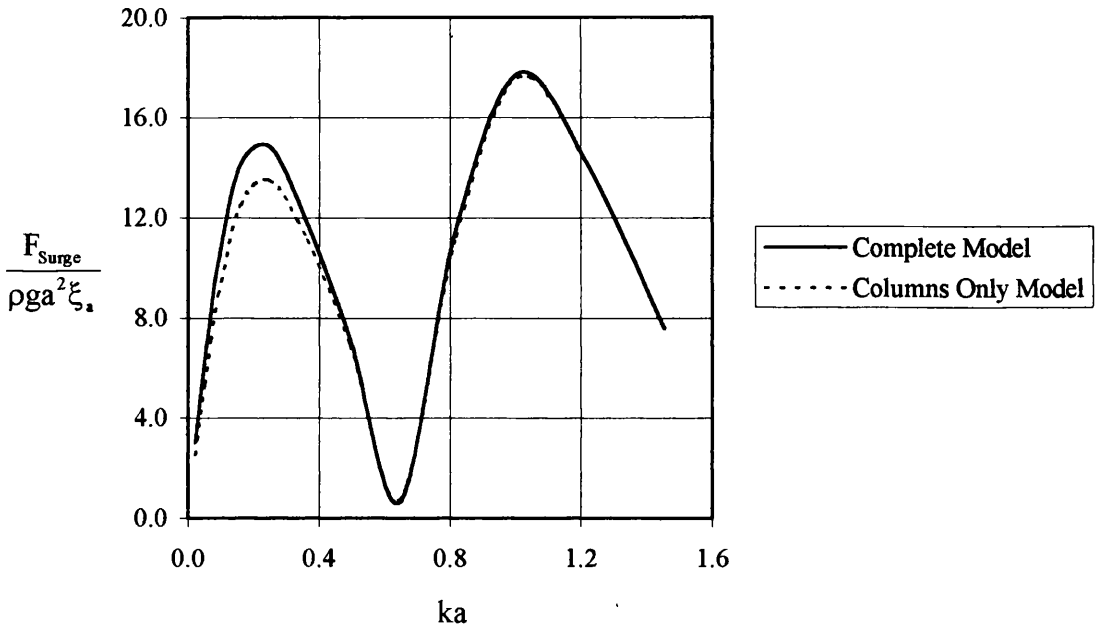

Figure 2.11: Case Study TLP Surge Force $\beta = 0$

(Diffraction/Radiation Code)

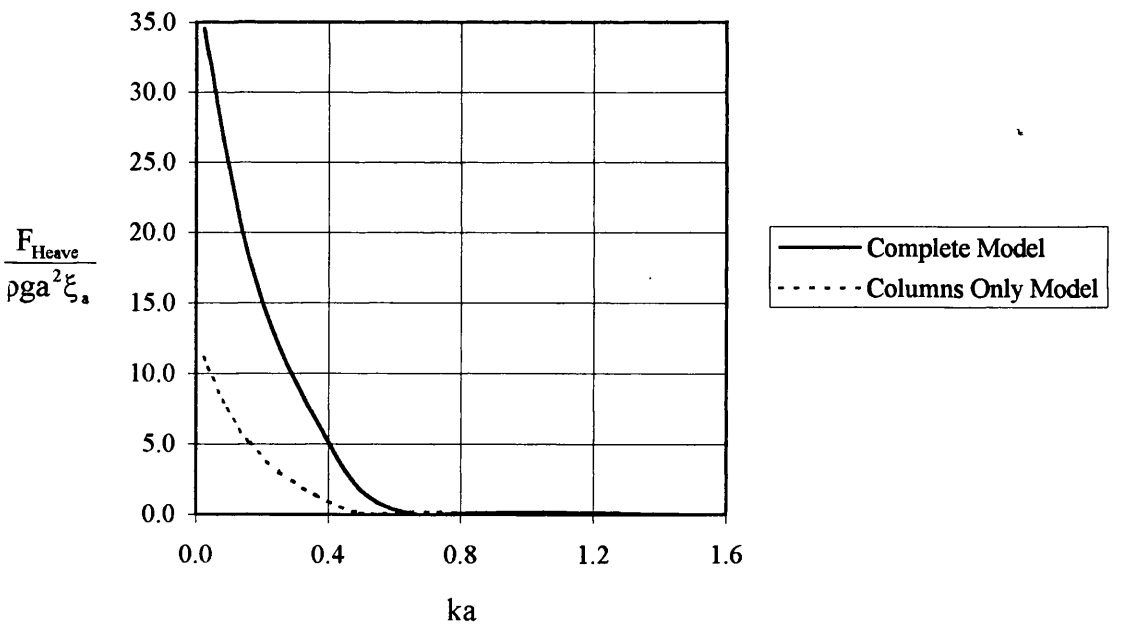

Figure 2.12: Case Study TLP Heave Force $\beta = 0$

(Diffraction/Radiation Code)

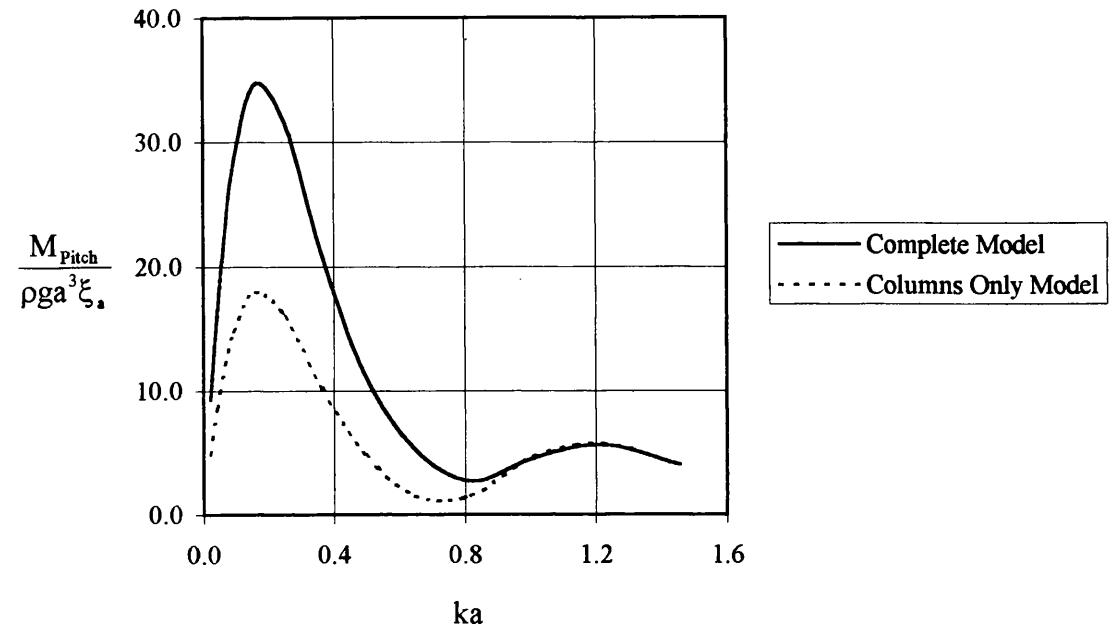

Figure 2.13 Case Study TLP Pitch Moment $\beta = 0$

(Diffraction/Radiation Code)

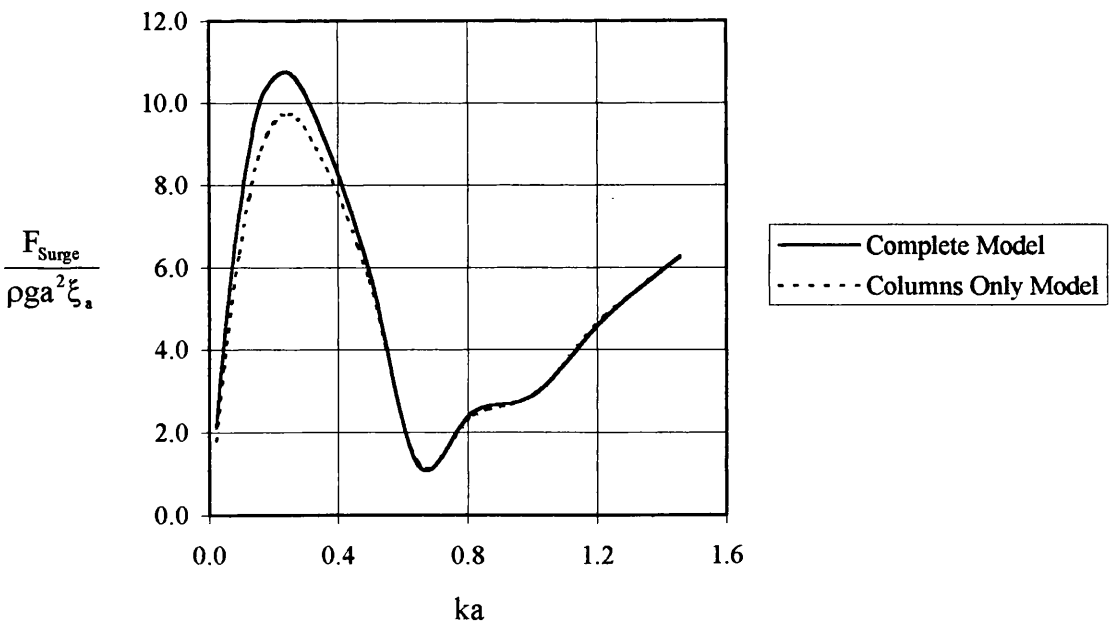

Figure 2.14 Case Study TLP Surge Force $\beta = \frac{\pi}{4}$

(Diffraction/Radiation Code)

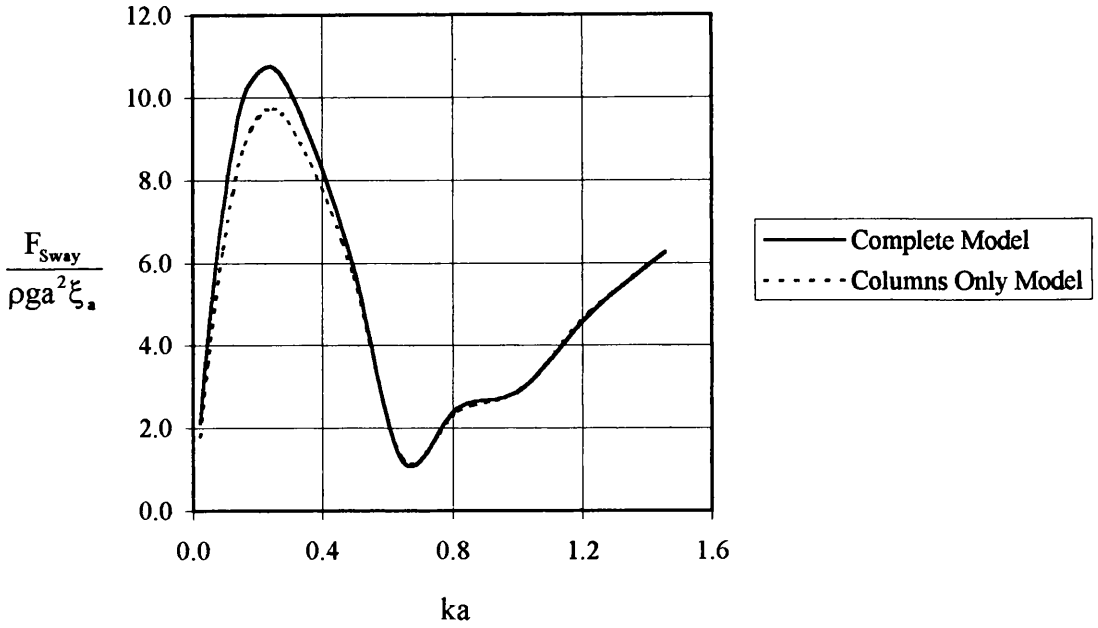

Figure 2.15 Case Study TLP Sway Force $\beta = \frac{\pi}{4}$

(Diffraction/Radiation Code)

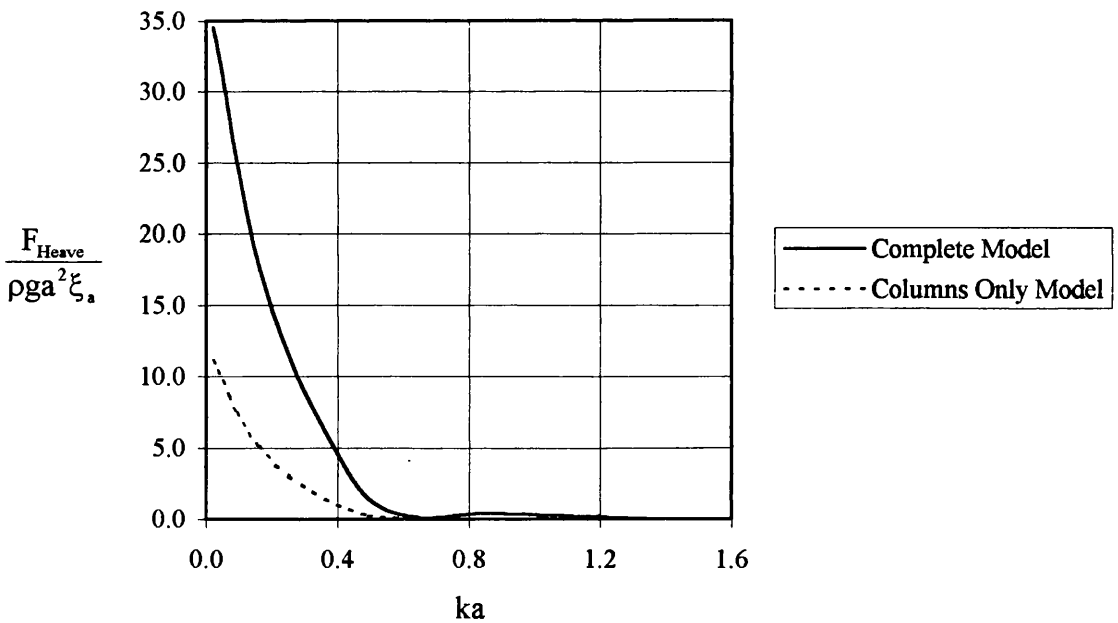

Figure 2.16 Case Study TLP Heave Force $\beta = \frac{\pi}{4}$

(Diffraction/Radiation Code)

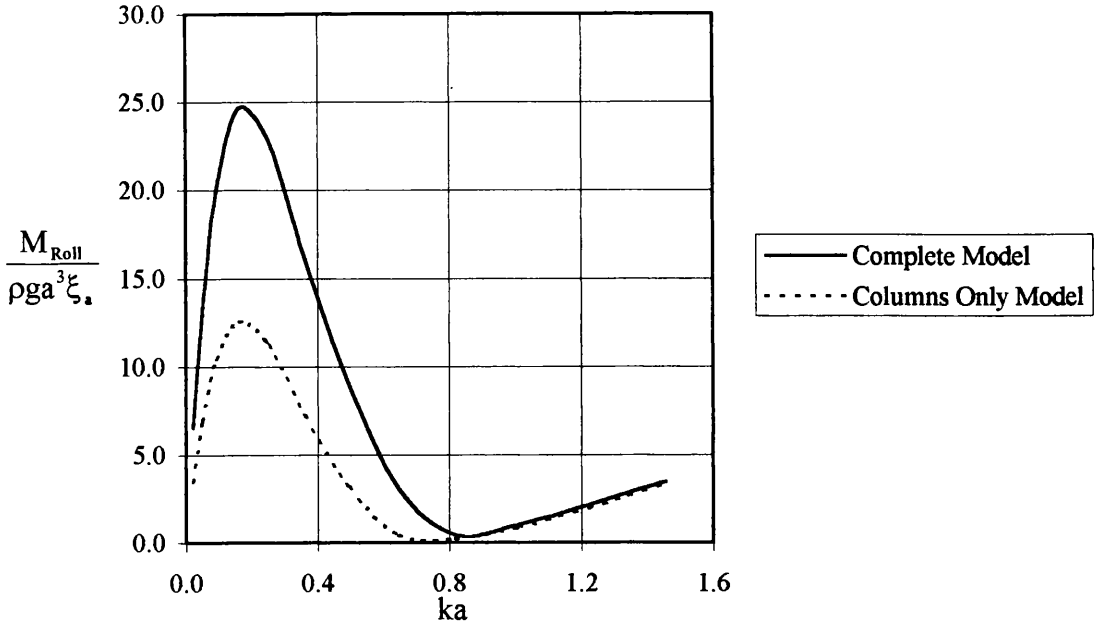

Figure 2.17 Case Study TLP Roll Moment $\beta = \frac{\pi}{4}$

(Diffraction/Radiation Code)

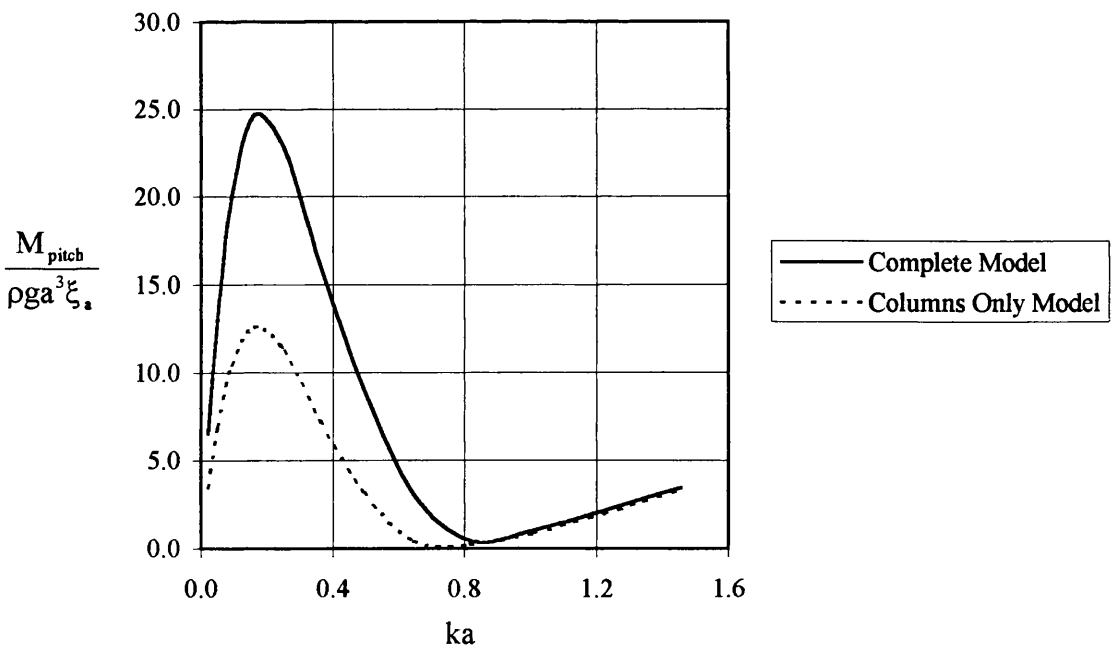

Figure 2.18 Case Study TLP Pitch Moment $\beta = \frac{\pi}{4}$

(Diffraction/Radiation Code)

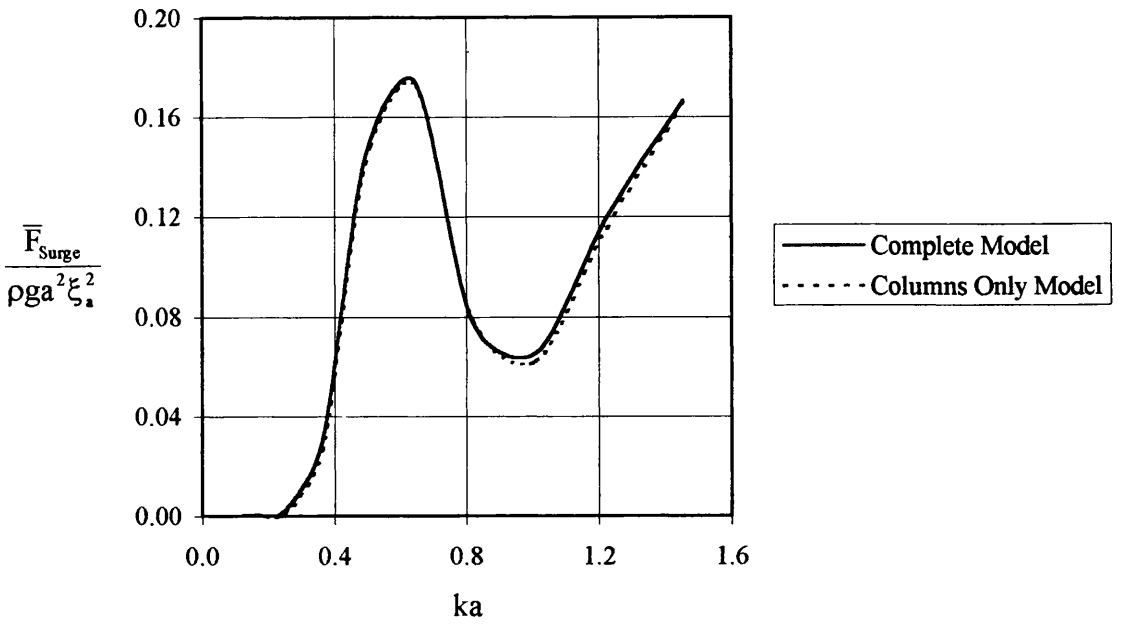

Figure 2.19 Case Study TLP Surge Wave Drift Force $\beta = 0$

(Diffraction/Radiation Code)

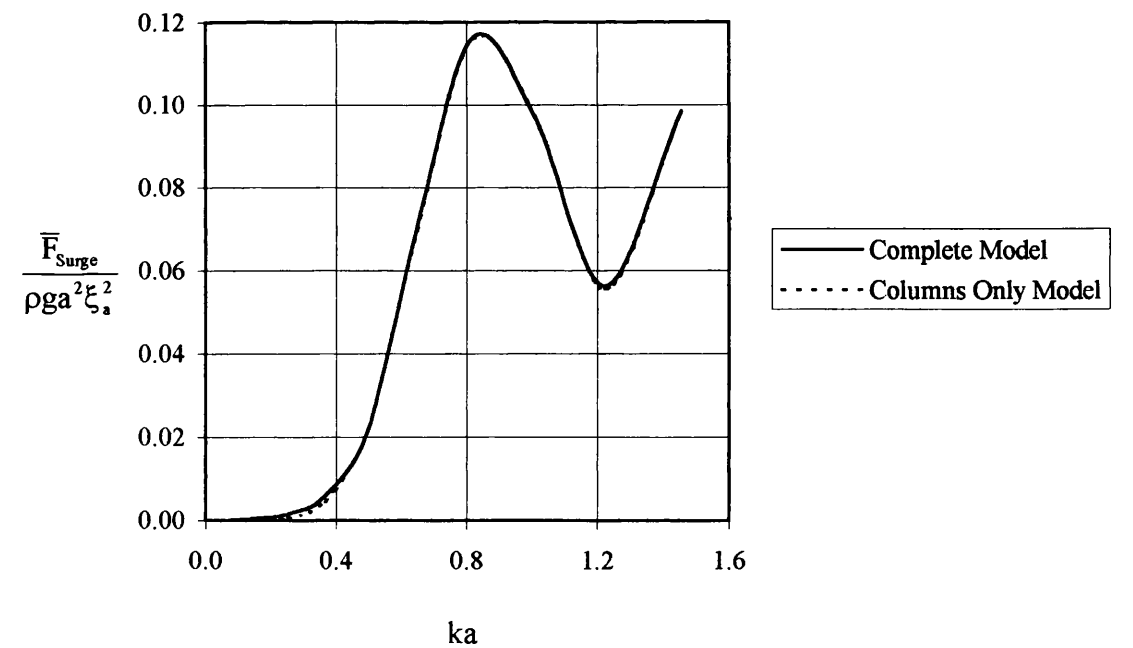

Figure 2.20 Case Study TLP Surge Wave Drift Force $\beta = \frac{\pi}{4}$

(Diffraction/Radiation Code)

2.5.3 Reaction Forces

The predicted reaction forces (potential origin) for the Case Study TLP geometry are given in Figures 2.21-2.32.

Figures 2.21-2.26 details the Case Study TLP geometry added mass (diffraction/radiation code solution, 2No. models).

Figures 2.27-2.32 detail the Case Study TLP geometry radiation damping (diffraction/radiation code solution, 2No. models).

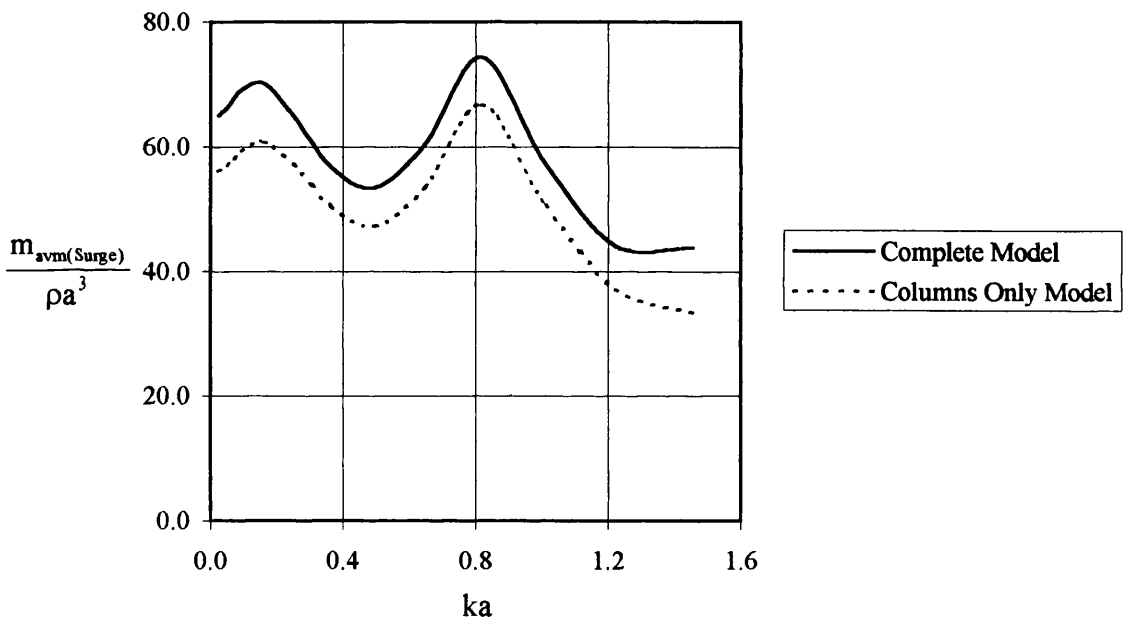

Figure 2.21 Case Study TLP Surge Added Mass
(Diffraction/Radiation Code)

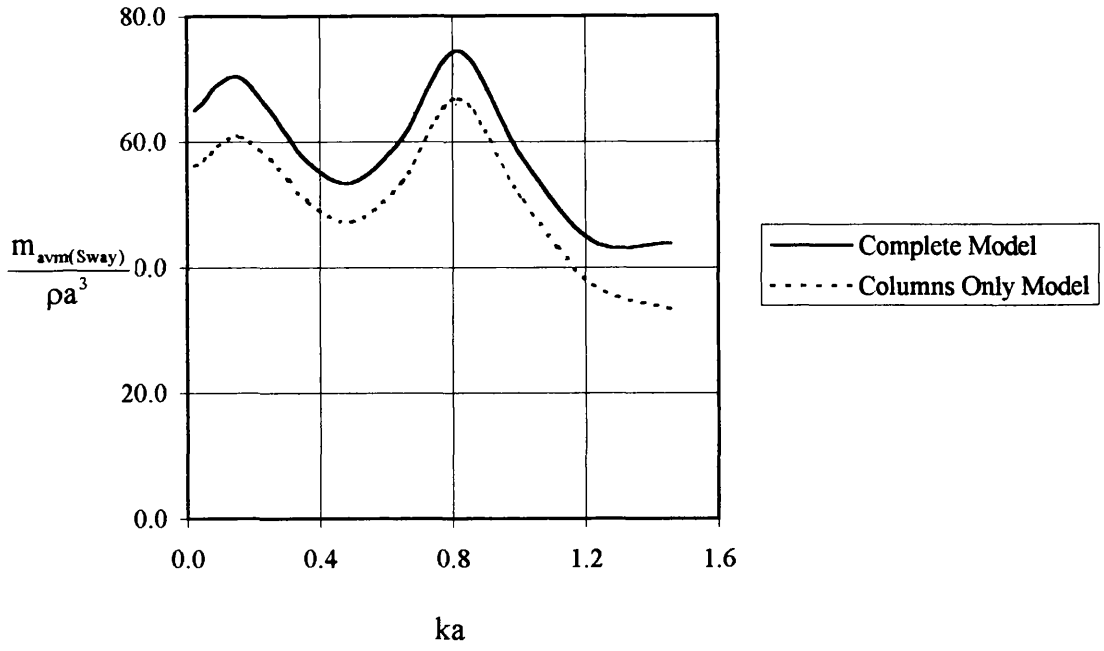

Figure 2.22 Case Study TLP Sway Added Mass

(Diffraction/Radiation Code)

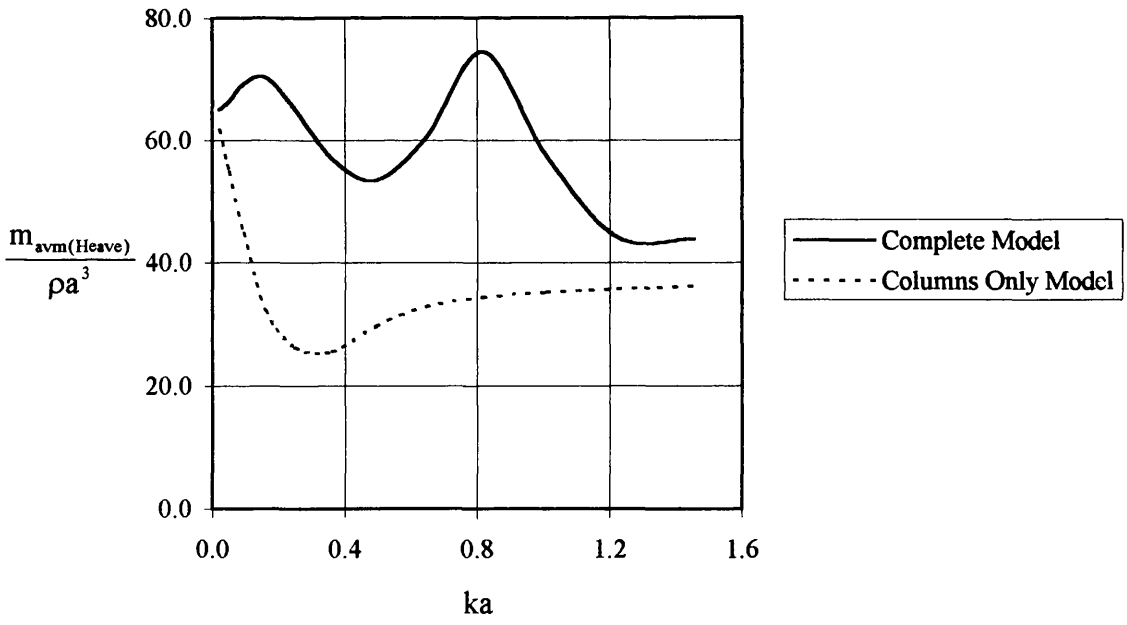

Figure 2.23 Case Study TLP Heave Added Mass

(Diffraction/Radiation Code)

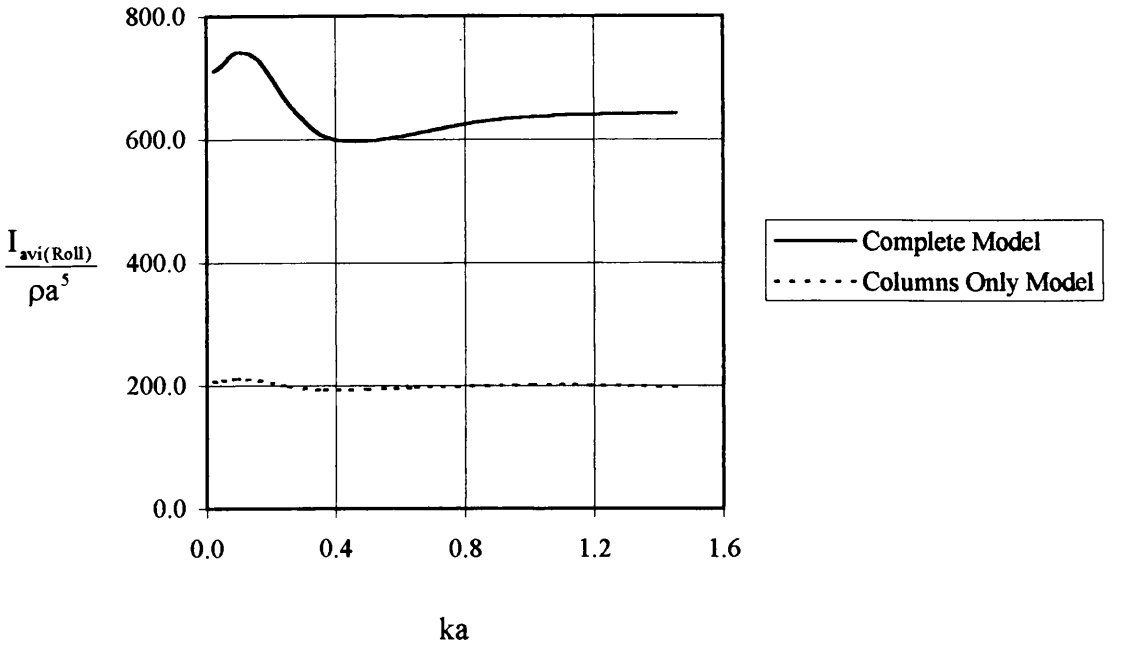

Figure 2.24 Case Study TLP Roll Added Moment of Inertia

(Diffraction/Radiation Code)

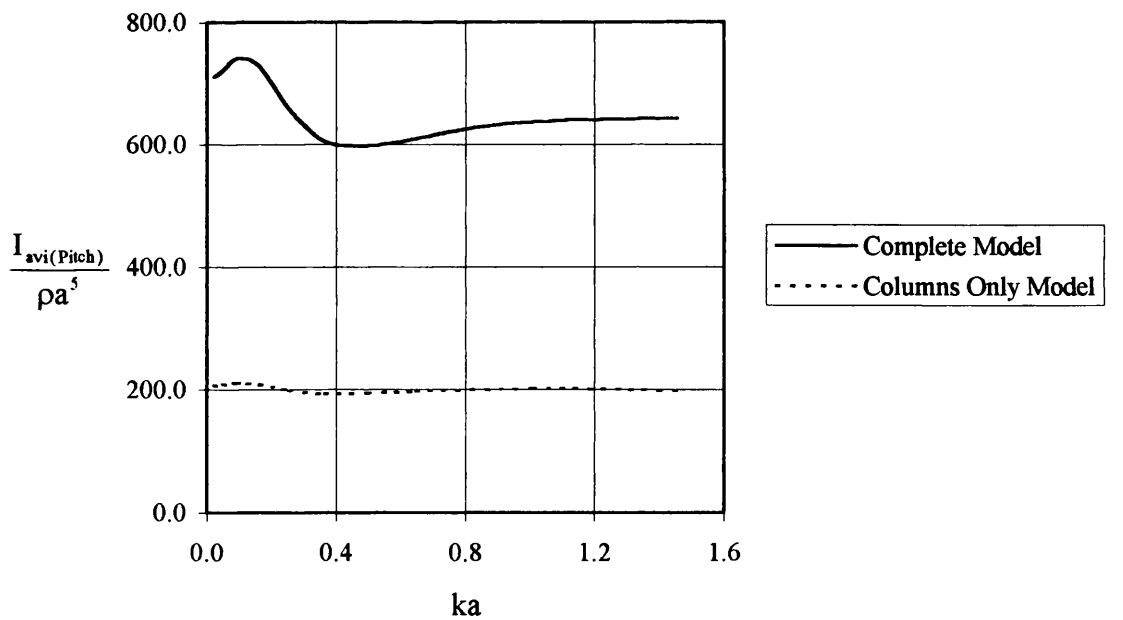

Figure 2.25 Case Study TLP Pitch Added Moment of Inertia

(Diffraction/Radiation Code)

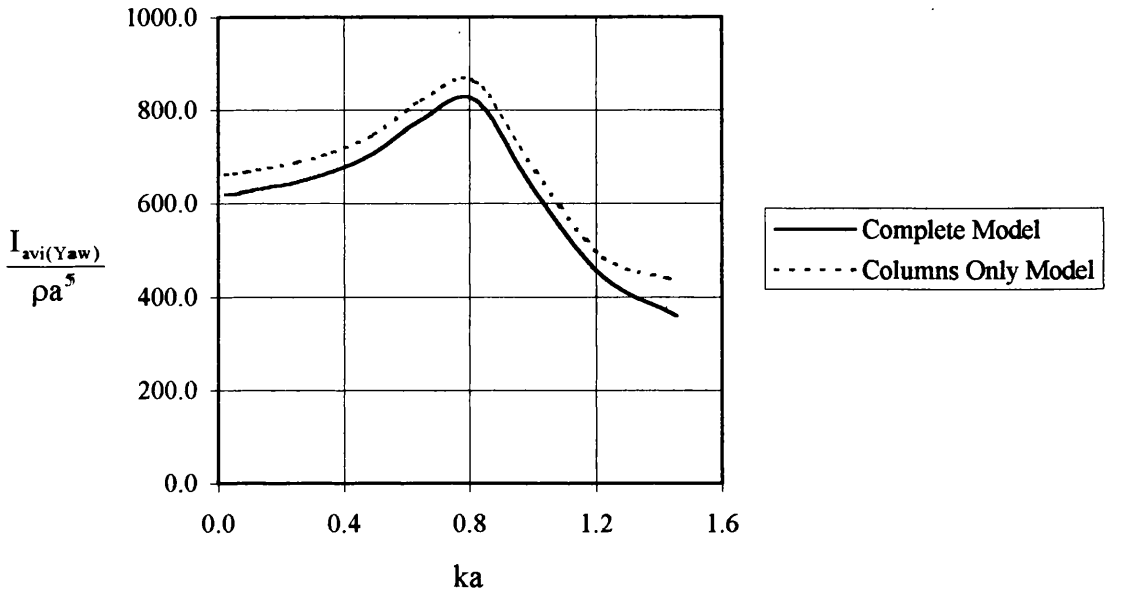

Figure 2.26 Case Study TLP Yaw Added Moment of Inertia

(Diffraction/Radiation Code)

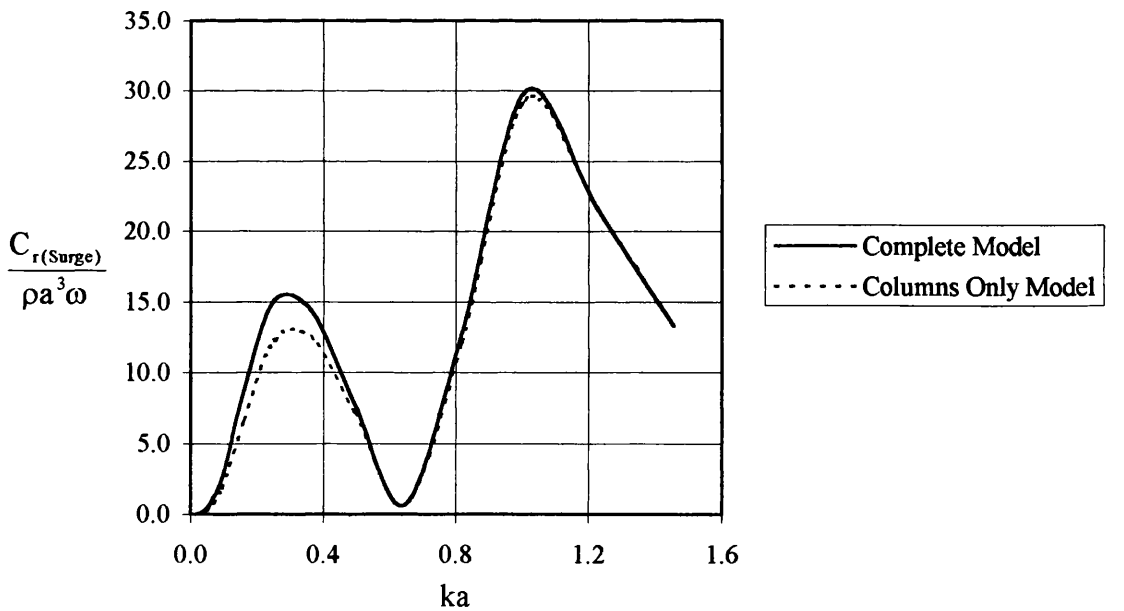

Figure 2.27 Case Study TLP Surge Radiation Damping

(Diffraction/Radiation Code)

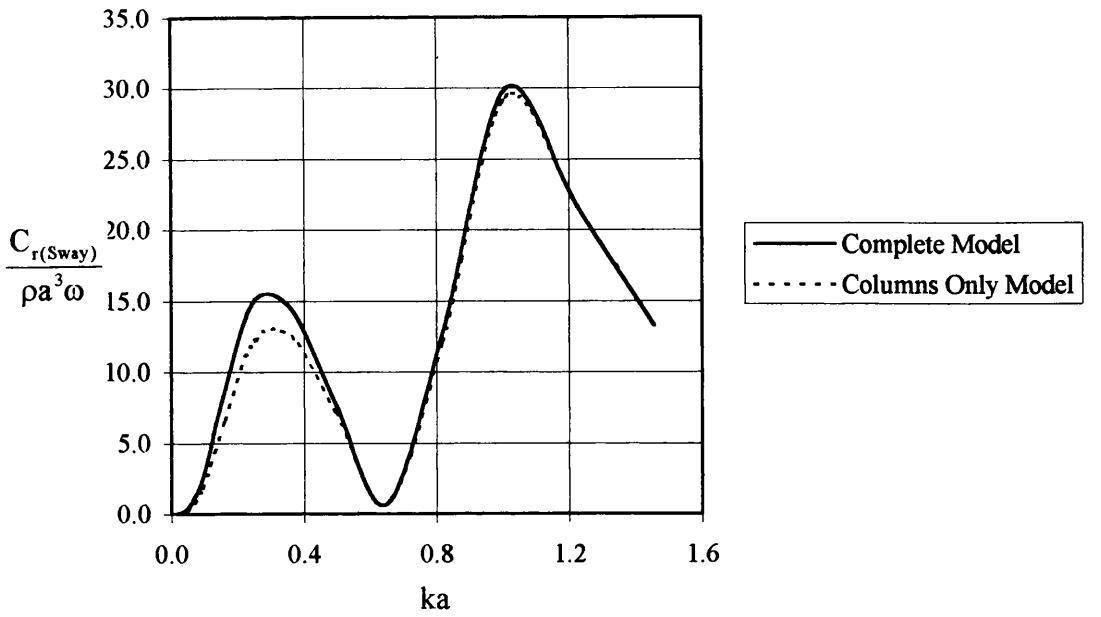

Figure 2.28 Case Study TLP Sway Radiation Damping

(Diffraction/Radiation Code)

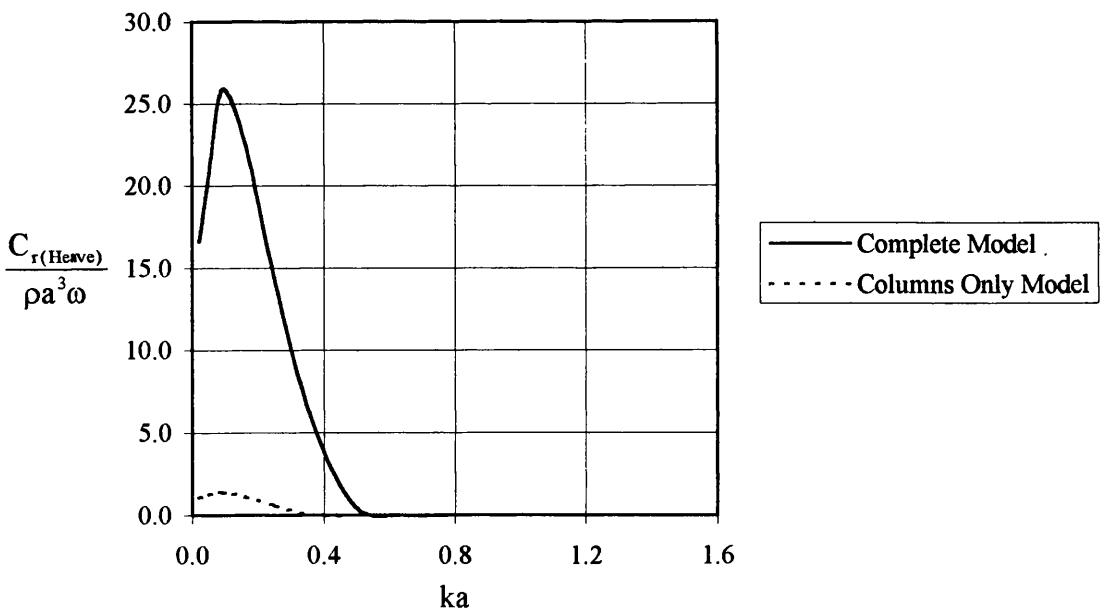

Figure 2.29 Case Study TLP Heave Radiation Damping

(Diffraction/Radiation Code)

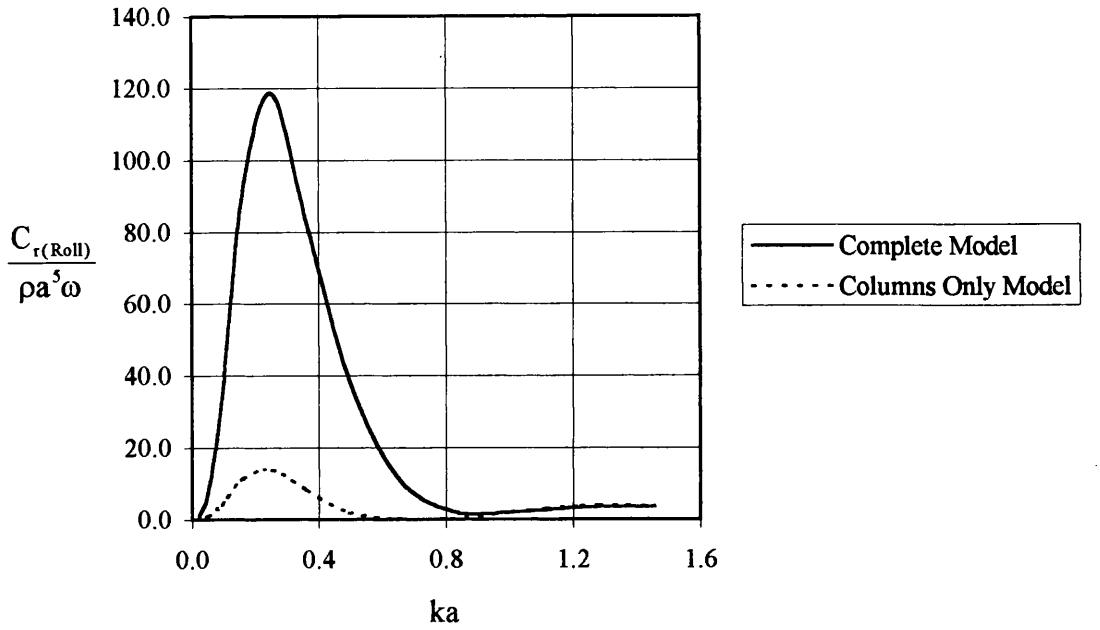

Figure 2.30 Case Study TLP Roll Radiation Damping

(Diffraction/Radiation Code)

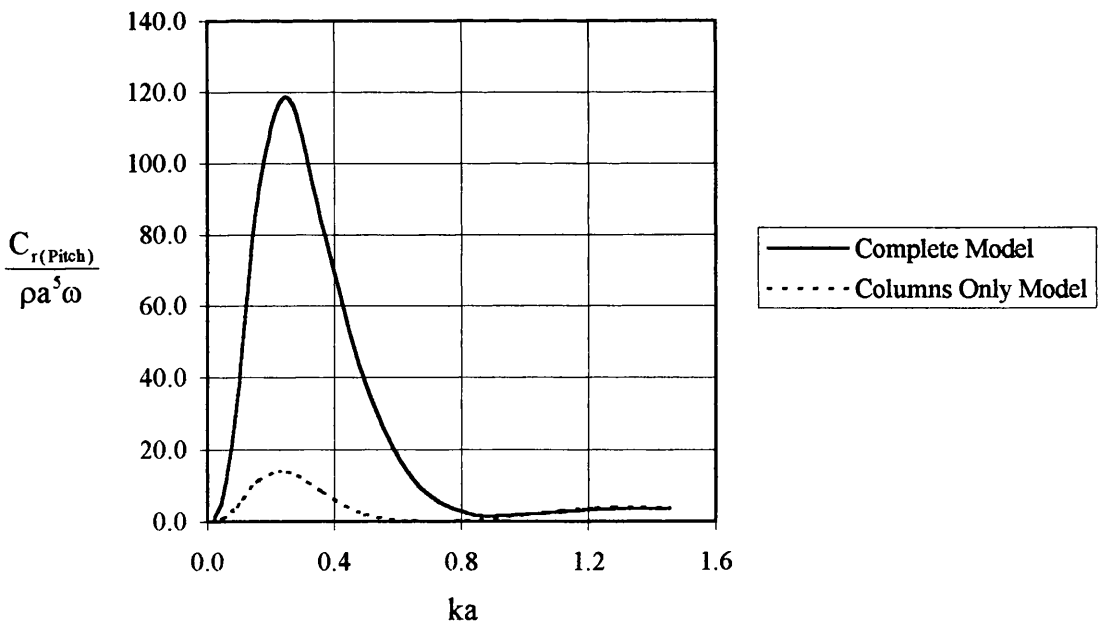

Figure 2.31 Case Study TLP Pitch Radiation Damping

(Diffraction/Radiation Code)

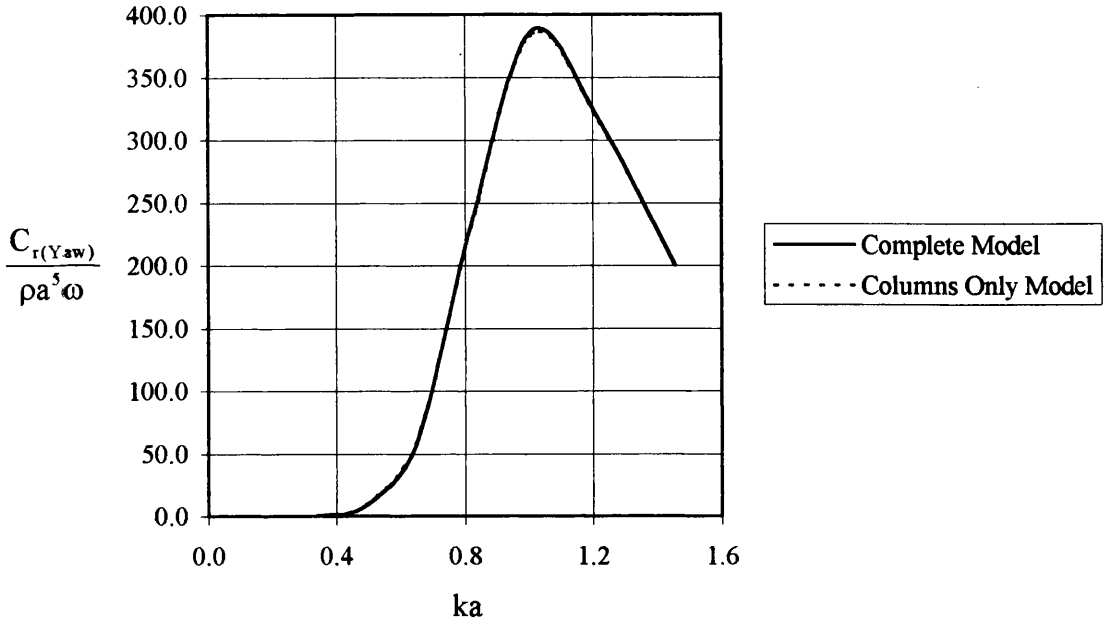

Figure 2.32 Case Study TLP Yaw Radiation Damping

(Diffraction/Radiation Code)

2.6 References

Atkins Quantitative Wave Analysis (AQWA), AQWA (LINE) Users Manual (1997), **WS Atkins**.

Abramowitz M. and Stegun I.A. (1964) Handbook of Mathematical Functions with Formulas, Graphs and Mathematical Tables, **National Bureau of Standards**.

Arnott A.D., Greated C.A., Incecik A. and M^{c}Leary A. (1997) An Investigation of Extreme Wave Behaviour Around a Model TLP, **Proceedings of the 7th International Offshore and Polar Engineering Conference OMAE'97**, Vol. 1, pp. 185-192.

Chakrabarti S.K. (1984) Steady Drift Forces on Vertical Cylinder-Viscous v's Potential, **Journal of Applied Ocean Research**, Vol. 6, No. 2, pp. 73-82.

Chakrabarti S.K., Tam W.A. and Wolbert A.L. (1975) Wave Forces on a Randomly Orientated Tube, **Proceedings of the 7th Offshore Technology Conference OTC'75**, OTC2190, pp. 433-447.

Faltinsen O.M. (1990) **Sea Loads on Ships and Offshore Structures**, Cambridge University Press.

Garrett C.J. (1971) Wave Forces on a Circular Dock, **Journal of Fluid Mechanics**, Vol. 46, Part 1, pp. 129-139.

Huang J.B. and Eatock Taylor R. (1997) Evaluation of Second-Order Forces on an Array of Truncated Cylinders by a Semi-Analytical Method, **Proceedings of the 16th International Conference on Offshore Mechanics and Arctic Engineering OMAE'97**, Vol. 1-A, pp. 401-408.

Kim M.H. (1993) Interaction of waves with N Vertical Circular Cylinders, **Journal of Waterway, Port, Coastal and Ocean Engineering**, Vol. 119, No. 6, pp. 671-689.

Kim M.H. (1993) Second-harmonic Vertical Wave Loads on Arrays of Deep-Draft Circular Cylinders in Monochromatic Uni-and-Multi-Diurectional Waves, **Journal of Applied Ocean Research**, Vol.15, pp. 245-262.

Kim M.H. and Yue D.K.P. (1989) The Complete Second-Order Diffraction Solution for an Axisymmetric Body, Part 1, Monochromatic Waves, **Journal of Fluid Mechanics**, Vol. 200, pp. 235-264.

Kim M.H. and Yue D.K.P. (1988) The Nonlinear Sum-Frequency Wave Excitation and response of a Tension-Leg Platform, **Proceedings of Behaviour of Offshore Structures BOSS'88**, Vol. 2, pp. 687-703.

Lighthill J. (1979) Waves and Hydrodynamic Loading, **Proceedings of Behaviour of Offshore Structures BOSS'79**, Opening Address, pp. 1-40.

Linton C.M. and Evans D.V. (1990) The Interaction of Waves with Arrays of Vertical Circular Cylinders, **Journal of Fluid Mechanics**, Vol. 215, pp. 549-569.

MacCamy R.C. and Fuchs R.A. (1954) Wave Forces on Piles a Diffraction Theory, **Technical Memorandum No. 69, Beach Erosion Board Corps of Engineers**.

Morison J.R., O'Brien M.P., Johnson J.W. and Schaaf S.A. (1950) The Wave Forces Exerted by Surface Waves on Piles, **Journal of Petroleum Technology, American Institute of Mining Engineers**, Vol. 189, pp. 149-154.

Narasimha Rao S., Ravi R. and Ganapathy C. (1997) Behaviour of Suction Anchors in marine Clays Under TLP Loading, **Proceedings of the 16th International Conference on Offshore Mechanics and Arctic Engineering OMAE'97**, Vol. 1-B, pp. 151-155.

Sarpkaya T. and Isaacson M. (1981) Mechanics of wave Forces on Offshore Structures, **Van Nostrand Reinhold**.

Williams A.N. and Demirbilek (1988) Hydrodynamic Interactions in Floating Cylinder Arrays-I. Wave Scattering, **Journal of Ocean Engineering**, Vol. 15, No. 6, pp. 549-583.

CHAPTER 3

EXPERIMENTAL INVESTIGATION OF HYDRODYNAMIC EXCITATION/REACTION FORCES ACTING ON TLPs

3.1 Introduction to Hydrodynamic Force Experimental Investigation

To determine the dynamic response characteristics of a TLP the wave excitation and hydrodynamic reaction forces must be determined accurately.

The study described in this chapter aims to investigate experimentally the wave excitation and hydrodynamic reaction forces acting on a case study TLP geometry.

The approach followed is one of design/construction and testing of a ~1.100 scale model of the case study TLP geometry (Heidrun TLP, see Figure 3.1 and Table 3.2) enabling both global and local excitation and reaction forces to be measured for a range of experimental conditions (Table 3.1).

The experimental wave excitation and hydrodynamic reaction force data will be utilised to validate the prediction methods employed in Chapter 2, Ref. 3.6 Conclusions.

3.2 Hydrodynamic Force Experimental Programme

3.2.1 Introduction

To investigate the hydrodynamic forces acting on the case study TLP geometry an experimental programme was developed. This programme involved measuring wave excitation forces in the presence of regular waves and hydrodynamic reaction force components during forced oscillations (calm water). The programme of experiments conducted is detailed in the Matrix of Experiments (Excitation/Reaction Forces) given in Table 3.1. The global wave force measurements in surge and heave were utilised for comparisons with numerical predictions detailed in Chapters 2 and 7. The local force measurements were utilised to make comparisons between wave forces acting on FWD and AFT hull members.

Test/ Heading	Wave Force Tests	Forced Oscillation Tests	Decay Tests[1]
Head Sea	Waves, 0.19-0.63rad/s incs. 0.06rad/s, max. wave-maker height available	Oscillations, 0.23, 0.29, 0.33, 0.38 and 0.4rad/s, amp.=13.127m, without/with current=0.99 and 1.98m/s	Calm water, (Surge DOF only)
Quartering Sea	Waves, 0.19-0.63rad/s incs. 0.06rad/s, max. wave-maker height available		

Table 3.1: Matrix of Experiments

(Excitation/Reaction Force Experiments)

3.2.2 Measurement of Wave Excitation Forces

Wave forces were sampled for a range of wave frequencies and heights with the model held stationary (head and quartering sea orientation) in the Glasgow University Towing/wave Tank. Wave probe, global and local wave excitation force time-series were all sampled simultaneously.

3.2.3 Measurement of Hydrodynamic Reaction Forces

Hydrodynamic reaction force components were sampled for a range of Forced Oscillation tests and Decay tests[1] in the Glasgow University Towing/wave Tank. Wave probe, global and local hydrodynamic reaction force time-series were all sampled simultaneously.

[1] Tests conducted with a 1.281.8 scale model of the case study TLP geometry (Heidrun) in the University of Newcastle Towing/wave Tank, see Chapter 5.

3.3 Hydrodynamic Force Experimental Setup

3.3.1 Introduction

The experimental investigation of the wave excitation and hydrodynamic reaction forces acting on the case study TLP geometry was conducted in the Glasgow University Towing/wave Tank (77x4.6x2.4m), Ref. Figure 3.1. The Glasgow Tank is equipped with an electro-hydraulic wave-maker at one end with a passive wave absorbing beach at the other. A towing carriage spans the tank providing adequate space to mount the experimental setup and data acquisition systems.

The experimental setup used in the Glasgow Tank consists of 4No. main components:

1) Data Acquisition System

2) Instrumentation System

3) Case Study TLP Model

4) Oscillator System

3.3.2 Data Acquisition System

Force time-series were sampled at 1000/s for 20s. Data was sampled with the aid of a *Macintosh* IIci computer and *Labview* 2.21 software. Data was then transferred to a *Digital* DEC 3000/400 AXP workstation operating Virtual Memory System (VMS) for analysis. All channels were filtered for 50Hz cut-off. This data acquisition system has been used extensively at the Glasgow Tank and has proved reliable. Surface video footage was also obtained via a Camcorder.

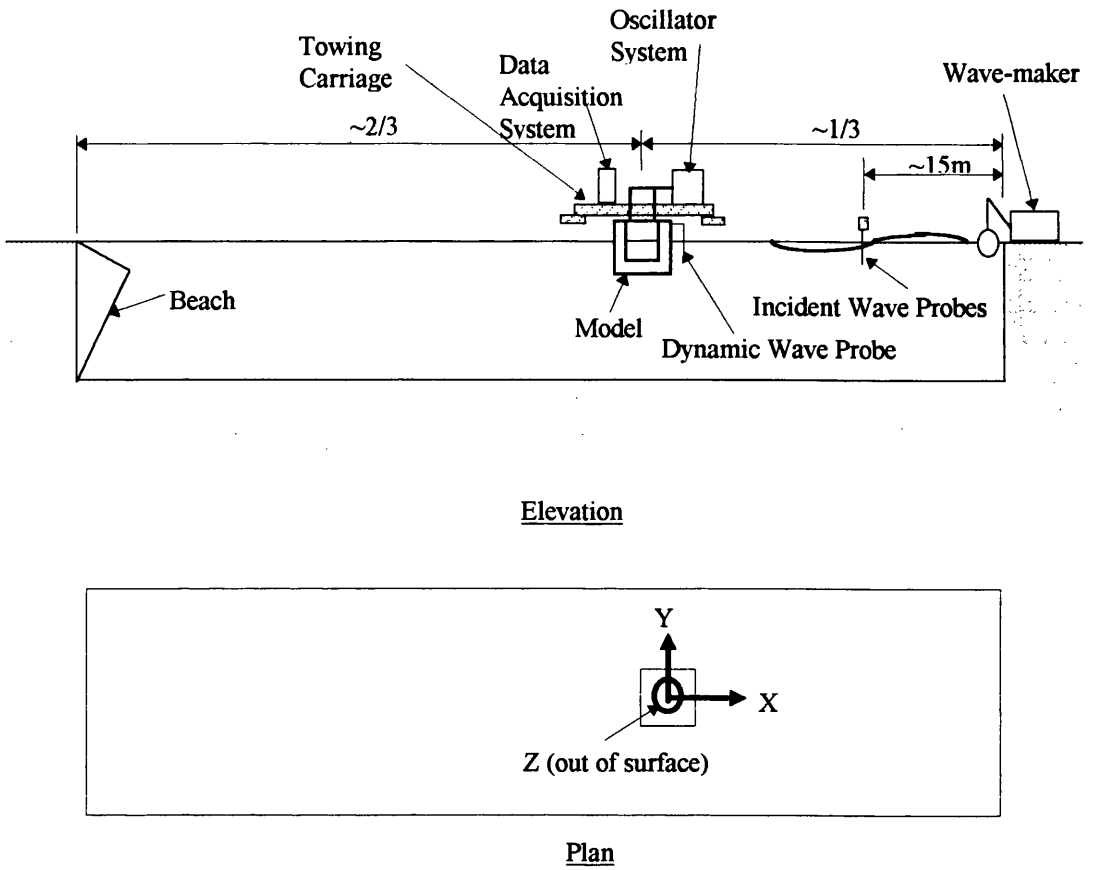

Figure 3.1: Experimental Setup

3.3.3 Instrumentation System

The selection of the measuring instrumentation was carefully considered and chosen to suit the form, magnitude and frequency of the parameter under investigation.

For incident wave amplitude/frequency measurement 3No. resistance type static wave probes were used (b/2, b/3 and b/4, ~15m from wave-maker). For encounter wave amplitude and frequency measurement a resistance type dynamic wave probe was used (mounted on the deck of the TLP model). This probe being aligned on the centre of the FWD columns of the TLP model a measured distance from the 3No. static wave probes. By time-base calibration of the dynamic and static signals (phase) wave length was measured. Utilising the measured wave amplitude and length wave steepness was derived.

Strain-gauges fitted to accurately machined bars facilitated the measurement of global wave excitation and hydrodynamic reaction forces. The dimensions of these bars were chosen to ensure adequate stiffness to prevent resonance of the model system but still permit a reasonable magnitude of response. The desired response being a function of the amplifier gain and the required sample resolution.

Novatech F225 25Kg load cells were installed in 100mm working sections (Table 3.3) for local hydrodynamic force measurements. The model and all working sections were sealed against water penetration. Preliminary tests were conducted on the working section configurations to establish the response characteristics.

A *LED-Selspot* optical displacement measuring system was used to obtain global displacement time-series of the model during the Forced Oscillation tests. This system consists of a camera incorporating a photosensitive detector surface focused on a Light Emitting Diode (LED). The photo current detected on the surface due to infrared light is linearly related to the 2D coordinates of the LED.

3.3.4 Case Study TLP Model

The case study TLP model that was used in this experimental programme was a 1:98.4 scale model of Heidrun TLP (Figures 3.1 and 3.2), principle dimension listed in Table 3.2.

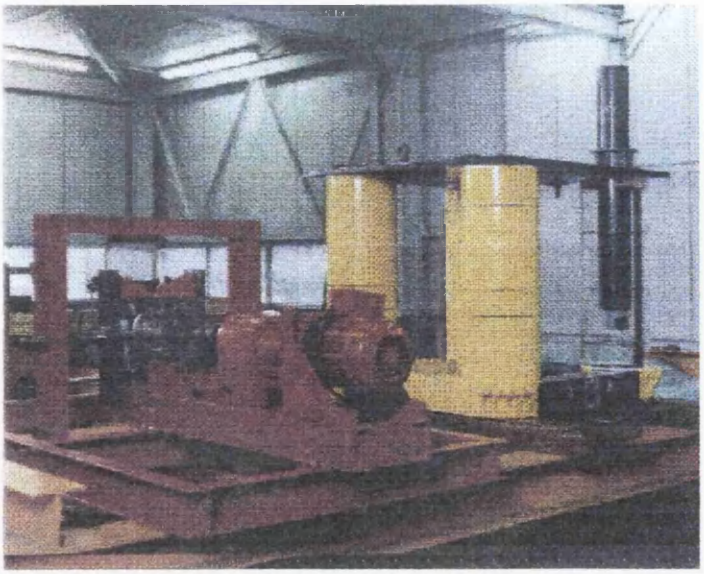

Figure 3.2: Case Study TLP Model and Oscillator System

(1:98.4, Heidrun)

Dimension	Heidrun	Model (1:98.4)
Displacement	289300Tonne	303.6Kg
Column Diameter	31m	0.315m
Column Spacing	80m	0.813m
Pontoon Depth	13m	0.132m
Pontoon Width	15.95m	0.162m

Table 3.2: Case Study TLP Principal Dimensions

The model was constructed primarily from Poly-Vinyl Chloride (PVC) sections welded together with a 1" (25.4mm) mild steel square hollow section (SHS) internal support frame stiffening the model structure.

To facilitate the generation of a light sheet to perform Particle Image Velocimetry (PIV) measurements undertaken by researchers at the University of Edinburgh, Fluid Dynamics Unit, the FWD port column was fabricated from transparent Acrylic with the adjacent pontoons constructed from transparent PVC.

Loadcell	Position	Mode
1	FWD Starboard Column (-0.325m below SWL)	Surge
2	AFT Starboard Column (-0.325m below SWL)	Surge
3	FWD Pontoon (-0.717m below SWL)	Surge
4	AFT Pontoon (-0.717m below SWL)	Surge
5	FWD Pontoon (-0.717m below SWL)	Heave
6	AFT Pontoon (-0.717m below SWL)	Heave
7	FWD Starboard Column (SWL)	Surge

Table 3.3: Position of Novatech F225 Loadcells

During the case study model design stage loading estimates were obtained utilising the Morison equation (Morison *et al*, 1950) and Stokes 2nd order wave theory (Stokes, 1847) to conduct an assessment of both the global and local structural requirements. These estimates were also used to size experimental load measuring devices to ensure adequate resolution.

3.3.5 Oscillator System

To conduct Forced Oscillation tests at a range of frequencies/amplitudes (see Table 3.1) an oscillator driving system was designed and fabricated (Figure 3.1). This system consisted of an existing *Stemens Sphuckert* variable speed oscillator motor (3KW) and a *Eurodrive* gearbox unit (reduction ratio 7.84:1) modified to facilitate vertical and horizontal motions (independently). The output from the oscillator unit was connected via a stiff model support frame, consisting of 127x76 RSC section, to the strain gauged bars and subsequently to the deck of the case study TLP model.

3.3.6 Calibration Techniques

The calibration technique used for the global and local force measurement devices was an adapted form of a standard calibration method used extensively at the laboratory. The case study TLP model was calibrated insitu.

In the heave mode this consisted of loading the deck of the model with a known mass (40 and 80kg) and calibrating the global heave strain gauges. In the surge mode the method used consisted of wire, dial-gauge and bottle screw adjustment. Loading of 20, 40 and 60kg was applied via the AFT columns and both FWD and AFT sets of global surge strain gauges were calibrated.

For the local calibration of the column and pontoon test sections a wire, frictionless pulley and suspended mass technique was utilised. FWD starboard column local surge force calibrations involved the use of a wire/bar arrangement to prevent the calibration wire fouling the AFT starboard column.

3.4 Hydrodynamic Force Analysis Techniques

3.4.1 Introduction

Quantitative analysis techniques were developed and programmed in *FORTRAN 77* and run on a *Digital* DEC 3000/400 AXP workstation operating VMS. *NAG* routines, *NAG* (1990), were utilised along with *SIMPLEPLOT* (*BUSS*, 1991) for graphical presentation of data and results.

Before analysis of the force time-series a Fast Fourier Transform (FFT) was carried out (*NAG* routine G13 CBF, 1990), and where appropriate, raw time-series data was low-pass filtered (digitally) to remove noise and any spurious irregularities. The filter technique utilised was one developed by Bozic (1979) and has been previously used successfully within the activities at the laboratory, Helvacioglu (1990). This filter is a non-recursive digital filter with a Hamming window and can be expressed as follows:

$$y_m = \frac{T\omega_c}{\pi} \sum_{n=-N}^{N} W_h \frac{\sin nT\omega_c}{nT\omega_c} x_{m-n} \qquad \textbf{(3-1)}$$

Where,

y_m =output filtered signal at m^{th} time-step

T =sampling rate

ω_c =cut-off frequency

N =number of samples

n =span of Hamming Window

W_h =Hamming Window

x_m =input signal at m^{th} time-step

With,

$$W_n = 0.54 + 0.46\cos\frac{n\pi}{N} \qquad \textbf{(3-2)}$$

3.4.2 Analysis of Wave Tests

The measurement of the wave excitation forces acting on the case study TLP geometry in the Heave and Surge DOF was conducted to allow validation of prediction methods utilised in Chapter 2.

The analysis routines employed for this group of experiments are *NAG* G13 CBF (*NAG*, 1990) for higher order force components and an adapted form of that developed by Keulegan and Carpenter (1958) for coefficients.

Assuming for regular waves,

$$F_e = F_a \sin(\omega t + \beta) \qquad \textbf{(3-3)}$$

Where,

F_e =hydrodynamic excitation force

F_a =force amplitude

Which can be linearised,

$$F_e = F_i \sin\omega t + F_d \cos\omega t \qquad \textbf{(3-4)}$$

Where,

F_i =inertia force component

F_d =drag force component

To obtain the inertia and drag force components of the measured force time-series a Fourier analysis technique was employed:

$$F_i = \frac{1}{n\pi} \int_0^{2n\pi} F_e \sin\omega t \qquad \textbf{(3-5)}$$

$$F_d = \frac{1}{n\pi} \int_0^{2n\pi} F_e \cos\omega t \qquad \textbf{(3-6)}$$

Inertia C_m and drag C_d coefficients (Fourier averaged) can then be derived for components of the case study TLP geometry thus:

$$C_m = -\frac{F_i}{\rho A_s \ddot{U}} \tag{3-7}$$

$$C_d = -\frac{F_d}{\frac{1}{2}\rho A_p \dot{U}|\dot{U}|} \tag{3-8}$$

Where,

ρ =density of water in the testing tank (1000Kg/m^3)

A_s =volume of test section

$\ddot{U}$ =water particle acceleration

A_p =projected area of test component (perpendicular to kinematics)

$\dot{U}$ =water particle velocity

3.4.3 Analysis of Forced Oscillation Tests

To measure the hydrodynamic reaction force components of added mass and viscous damping for the case study TLP geometry Forced Oscillation tests were conducted.

The analysis method utilised for this group of experiments was that described by Hooft (1972).

Assuming the 2nd differential equation describing oscillating body motion thus:

$$(M + m_{avm})\ddot{X} + C_v\dot{X} + KX = F_r \sin(\omega t + \beta) \quad \textbf{(3-9)}$$

Where,

M =physical mass

m_{avm} =added mass

$\ddot{X}$ =rigid-body acceleration

C_v =viscous damping coefficient

$\dot{X}$ =rigid-body velocity

K =stiffness coefficient

X =rigid-body displacement

F_r =hydrodynamic reaction force

Where the hydrodynamic reaction force acting on the body can be linearised as follows:

$$F_r = F_{in} \sin\omega t + F_{out} \cos\omega t \quad \textbf{(3-10)}$$

With,

F_{in} =the force in-phase with the body displacement

F_{out} =the force out-of-phase with the body displacement

To obtain the in-phase and out-of-phase components of the measured time-series a Fourier analysis technique similar to that outlined in the wave force measurement analysis was used. Then rearranging the assumed differential equation yields global added mass m_{avm} and viscous damping C_v (Fourier averaged) for the case study TLP geometry.

$$m_{avm} = -\frac{F_{in}}{\omega^2 x_a} - M \qquad \textbf{(3-11)}$$

$$C_v = \frac{F_{out}}{\omega x_a} \qquad \textbf{(3-12)}$$

Where,

ω =rigid-body oscillation frequency

x_a =rigid-body oscillation displacement amplitude

3.4.4 Analysis of Decay Tests

Decay tests were performed with the case study TLP model to provide comparison measurements of the viscous damping.

The analysis procedure detailed by Thomson (1988) was adopted based on the determination of the logarithmic decrement. It can be shown (see Thomson, 1988) that the logarithmic decrement can be determined from the ratio of any two successive motion decay amplitudes.

$$\delta = \ln \frac{x_1}{x_2} \qquad \textbf{(3-13)}$$

Where,

δ =logarithmic decrement

With the definition of x_1 and x_2 as illustrated in Figure 3.3.

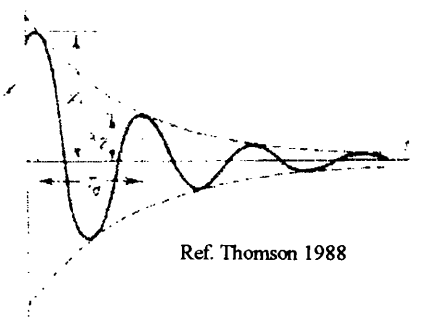

Ref. Thomson 1988

Figure 3.3: Motion Decay Curve

With,

$$\delta = \frac{2\pi\zeta}{\sqrt{1-\zeta^2}} \qquad \textbf{(3-14)}$$

Where,

ζ =damping factor= $\frac{C}{C_c}$

With,

C =damping

C_c =critical damping coefficient= $2M\omega_n$

And,

ω_n =undamped natural frequency

Where for small ζ, $\sqrt{1-\zeta^2} \approx 1$ and therefore:

$$\delta \approx 2\pi\zeta \qquad \textbf{(3-15)}$$

By performing Decay tests in calm water the viscous damping at the Surge natural frequency was obtained.

3.5 Results of Experimental Force Investigation

3.5.1 Introduction

Global and local wave excitation and hydrodynamic reaction forces are given for the case study TLP geometry. All results are given in the **prototype** scale unless otherwise noted.

For comparisons between the experimental and simulated data see Section 3.6 (3.6.2 Excitation Forces and 3.6.3 Reaction Forces).

The coordinate system utilised for the experimental programme is as given in Figure 3.1, with the X-axis (Surge) orientated perpendicular to the wave-maker (wave propagation towards the model), with +ve Surge displacement towards the wave-maker.

The forward speed/current was measured along the Surge axis with +ve forward speed towards the wave-maker and +ve current measured in the -ve Surge direction.

For the quartering sea (incident wave heading=45^0) the coordinate system was as noted above with the model rotated by 45^0 in the +ve Yaw direction.

The experimental wave parameters are given in Figures 3.4 and 3.5. Figure 3.4 details the wave frequencies and corresponding nominal wave amplitudes generated at the Glasgow University Towing/wave tank. Figure 3.5 describes the associated wave steepness for each regular wave.

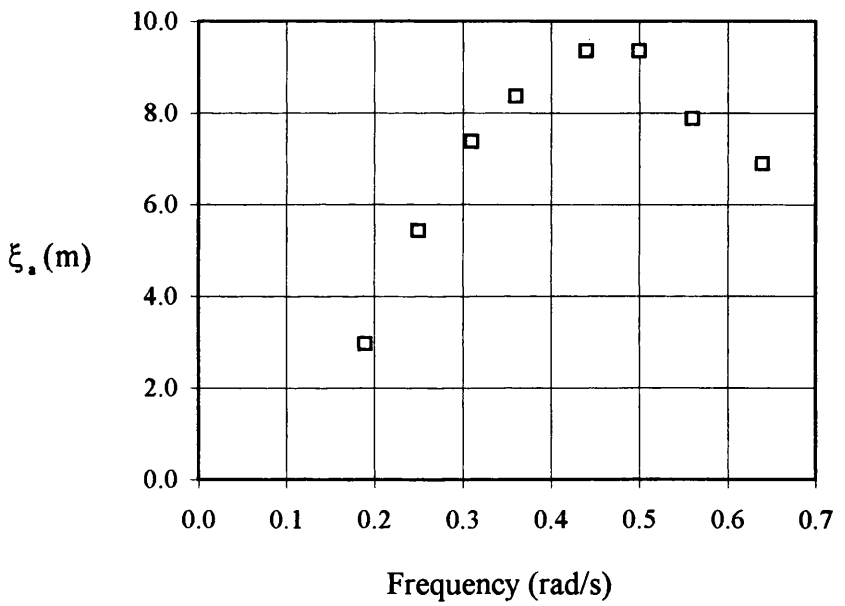

Figure 3.4: Experimental Wave Amplitude (Nominal)

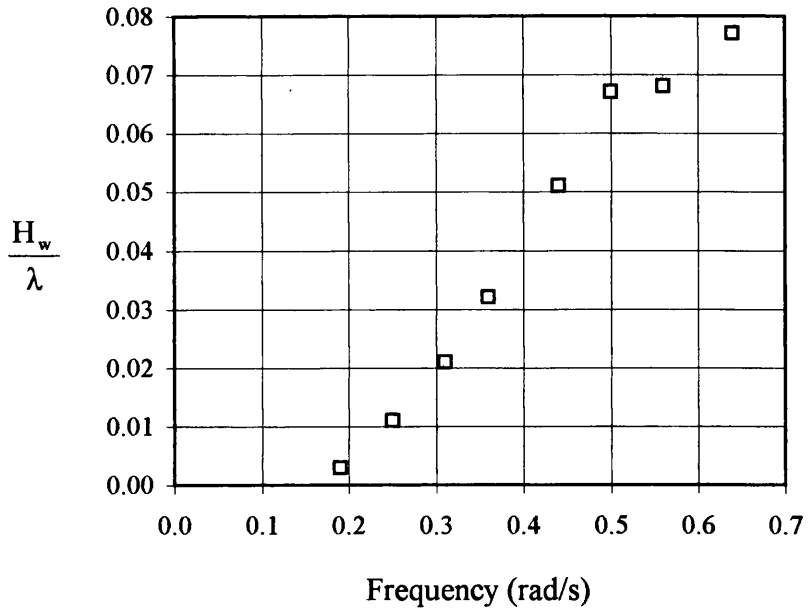

Figure 3.5: Experimental Wave Steepness

(Nominal)

3.5.2 Hull Wave Frequency Forces

The wave frequency (1st order) global Heave and Surge excitation forces acting on the case study TLP in regular waves (head and quartering sea) are given in Figures 3.6 and 3.7.

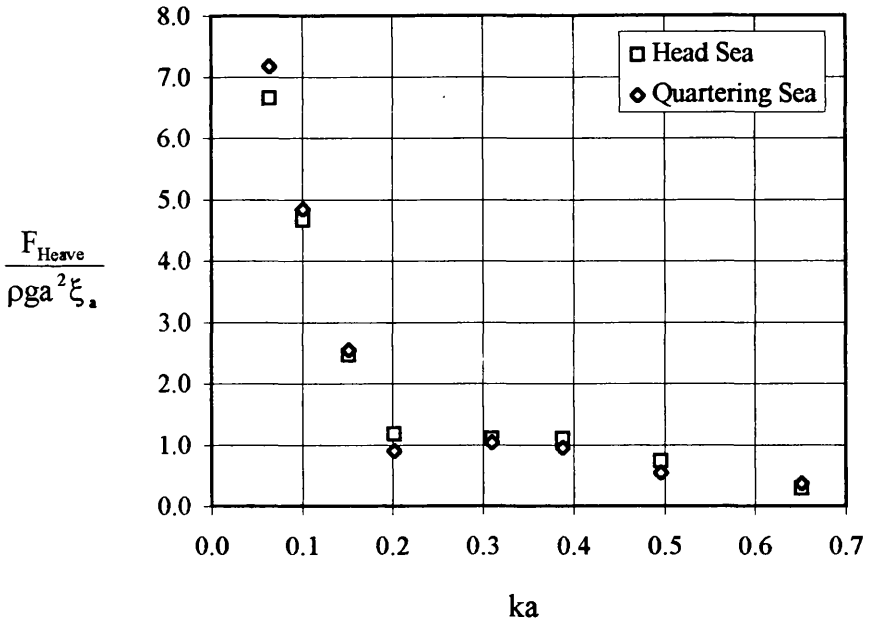

Figure 3.6: Experimental Global Heave Force

(1^{st} order)

Where,

k =wave number

a =cylinder radius

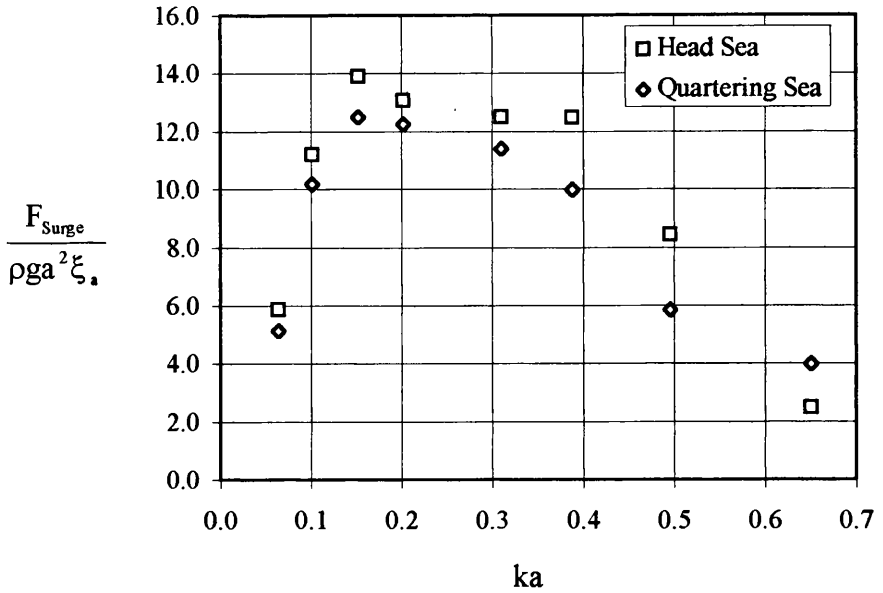

Figure 3.7: Experimental Global Surge Force

(1^{st} order)

Local wave excitation forces acting on the test sections in the columns and pontoons (Table 3.3) for the head sea condition are given in Figures 3.8-3.10. Figure 3.8 details the local wave excitation force in Surge acting on loadcells Nos. 1 and 2 (FWD and AFT, starboard columns), Figure 3.9 and 3.10 detail the local wave excitation forces acting on the pontoons in the Surge (FWD and AFT pontoons, b =pontoon breadth) and Heave (FWD only) DOF respectively.

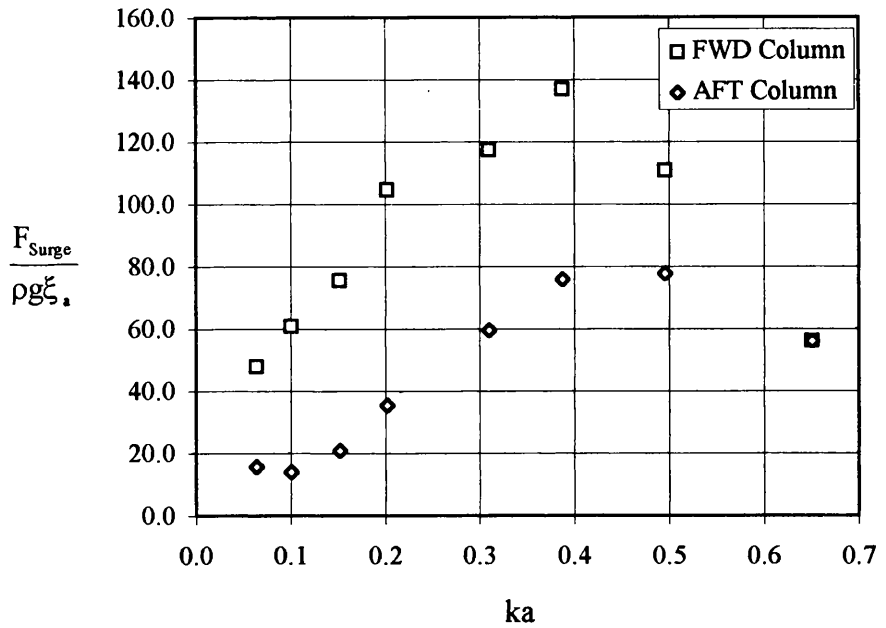

Figure 3.8: Experimental Local Surge Force (Column)

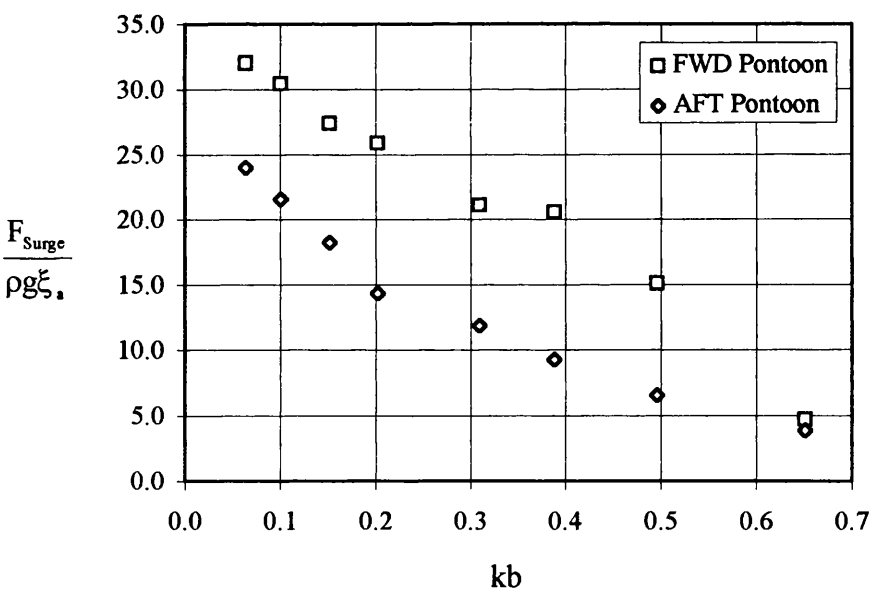

Figure 3.9: Experimental Local Surge Force (Pontoons)

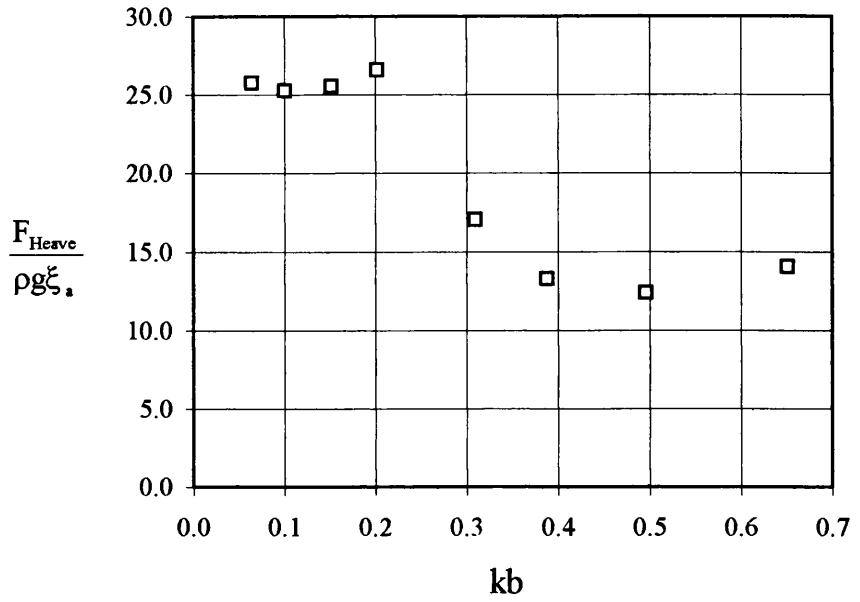

Figure 3.10: Experimental Local Heave Force

(FWD Pontoon)

Unfortunately Loadcell No. 6 was damaged during the experiments preventing local wave excitation Heave forces acting on the AFT pontoon from being measured.

In addition to obtaining the global and local hydrodynamic excitation forces acting on the case study TLP geometry a Fourier analysis was performed to extract the inertia force component applicable to the force time-series (Surge) measured on the FWD column local test section. From the inertia force components the inertia coefficients (Fourier averaged) were obtained.

It had been proposed to derive the drag force components in a similar manner and determine the Fourier averaged drag coefficients. In practice this was not achieved due to the low amplitude of the drag forces being masked by noise in the signals.

Finite depth linear wave theory was used to estimate the appropriate water particle accelerations to calculate the inertia coefficients.

The inertia coefficients derived experimentally for the head sea condition applicable to the FWD column local test section are detailed in Figure 3.11.

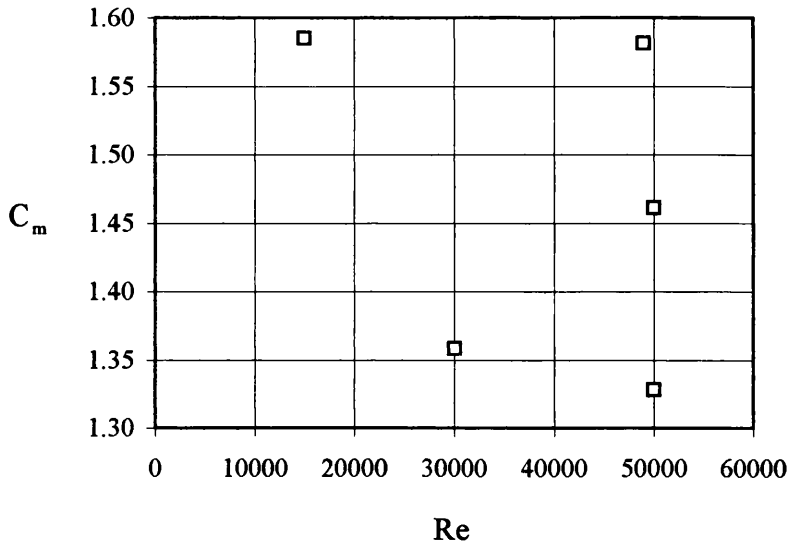

Figure 3.11: FWD Column Inertia Coefficient
(Head Sea)

3.5.3 Higher Order Hydrodynamic Excitation Forces

During the FFT analysis of the global and local wave excitation force time-series data, force components at multiples of the incident wave frequencies were observed. These multiple incident wave frequency components (2nd and 3rd order components) have been extracted from the time-series data and plotted.

Figures 3.12-3.15 detail the sampled excitation force time-series (in the **model** scale) for global Heave and Surge in the quartering sea condition with the corresponding FFT force amplitude spectrums for an example regular wave.

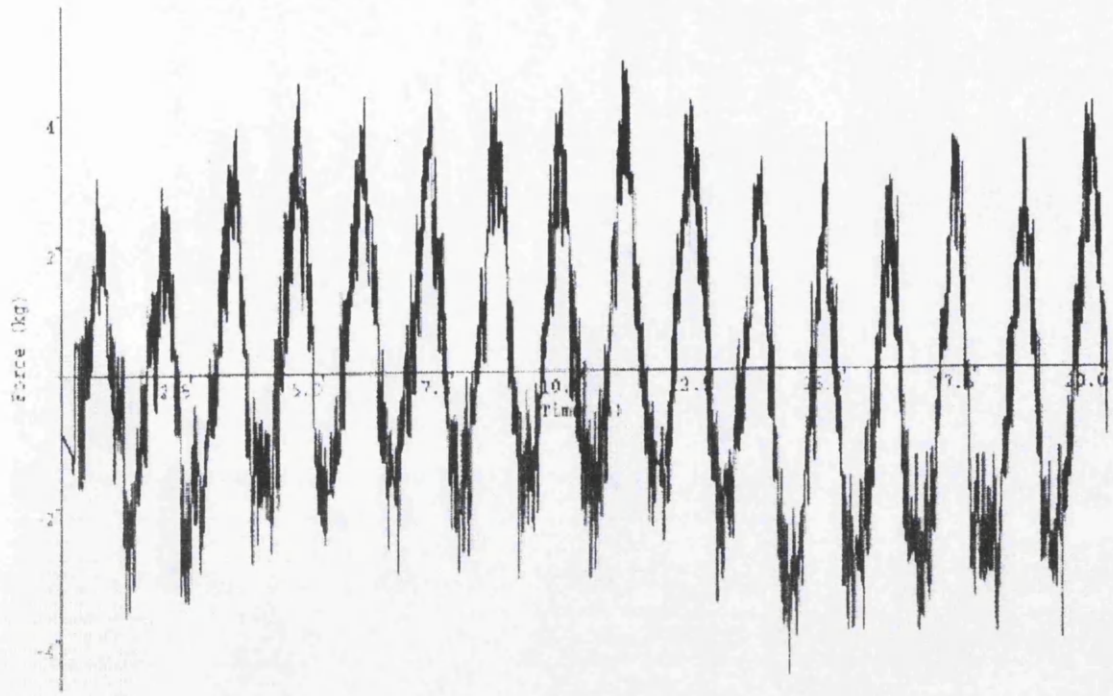

Figure 3.12: Experimental Global Heave Force Time-series

(ω =5.0rad/s, ξ_a =0.097m)

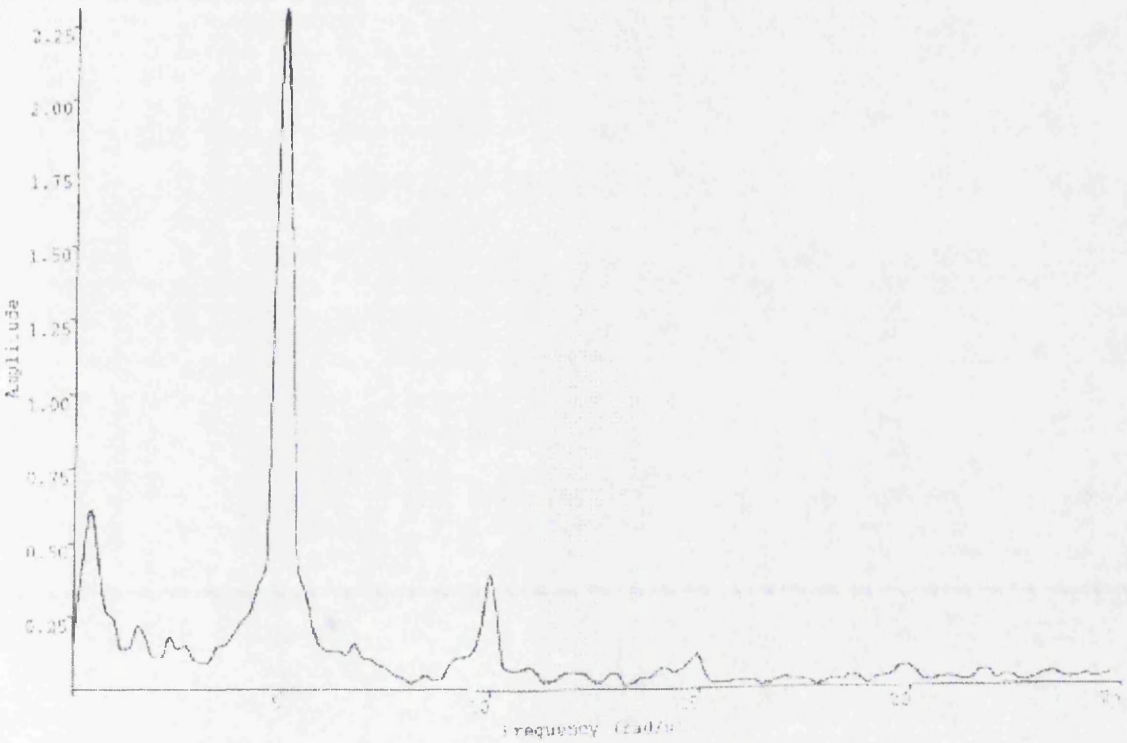

Figure 3.13: Experimental Global Heave Force Spectrum

(ω =5.0rad/s, ξ_a =0.097m)

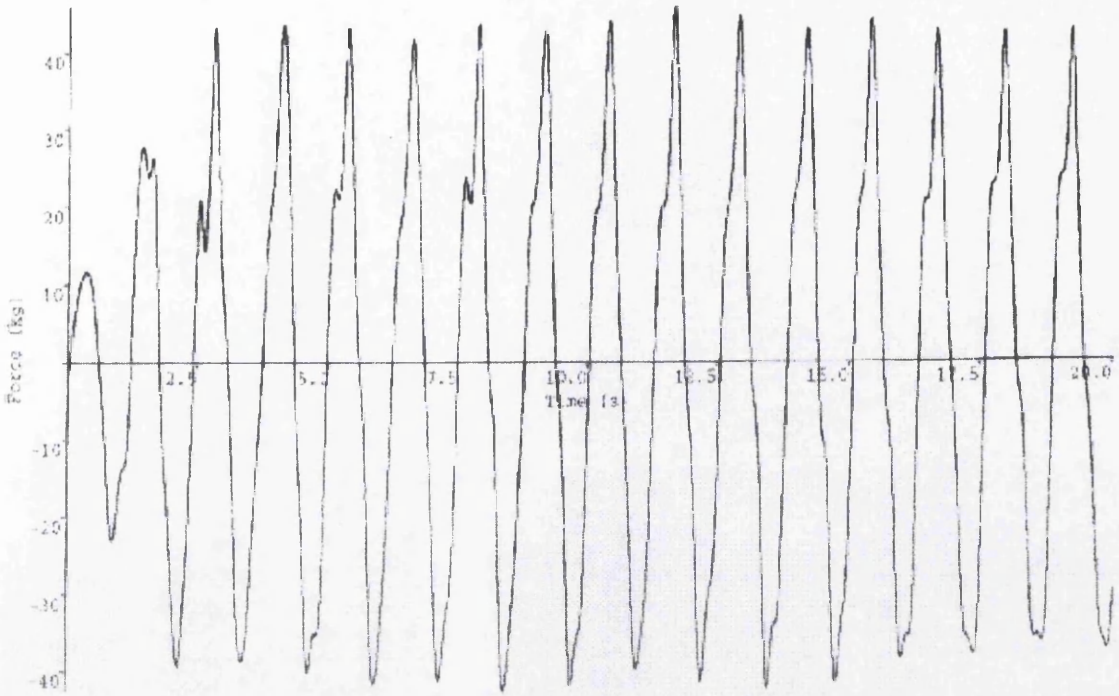

Figure 3.14: Experimental Global Surge Force Time-series

(ω =5.0rad/s, ξ_a =0.097m)

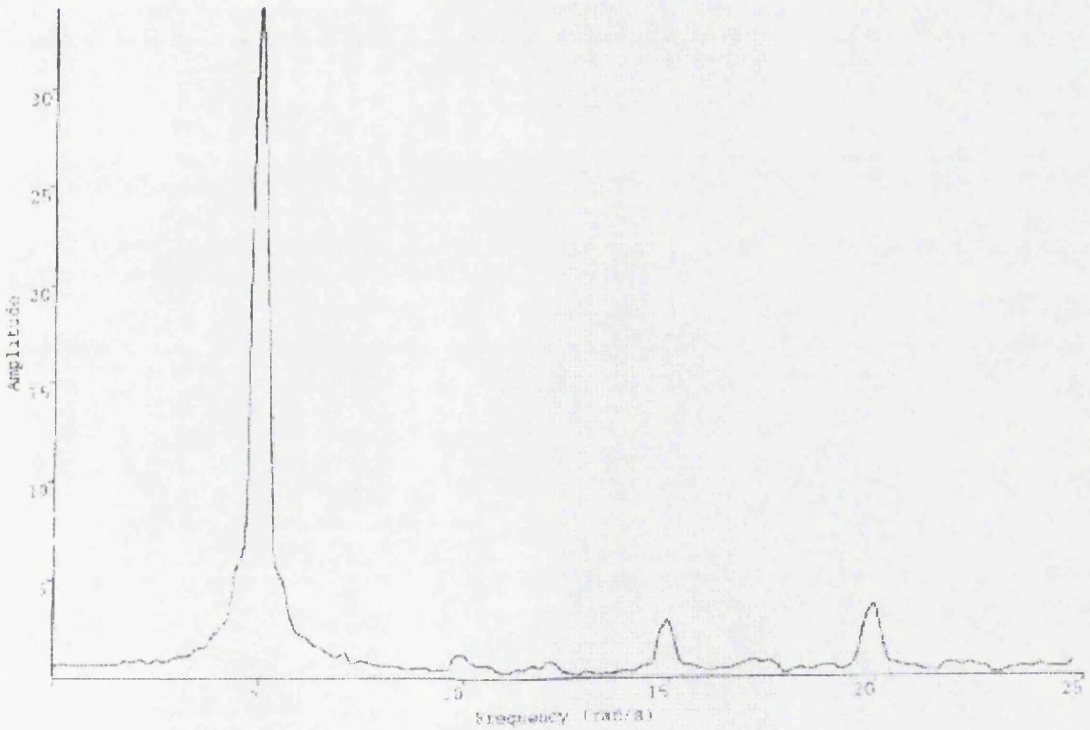

Figure 3.15: Experimental Global Surge Force Spectrum

(ω =5.0rad/s, ξ_a =0.097m)

The experimental 2nd order global Heave force in the head and quartering wave condition for a range of regular waves are given in Figure 3.16, with the 2nd order global Surge force detailed in Figure 3.17.

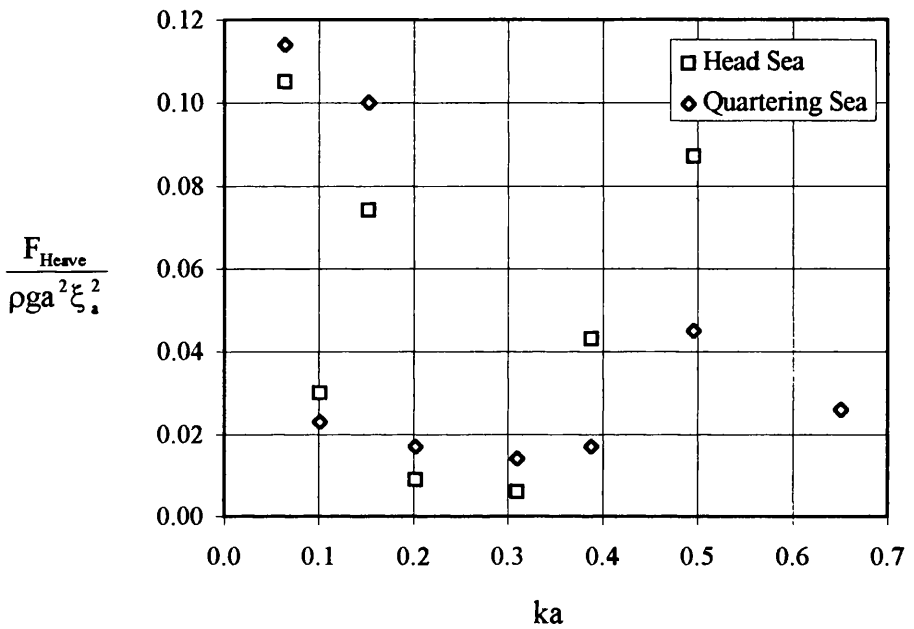

Figure 3.16: Experimental Global Heave Force (2^{nd} order)

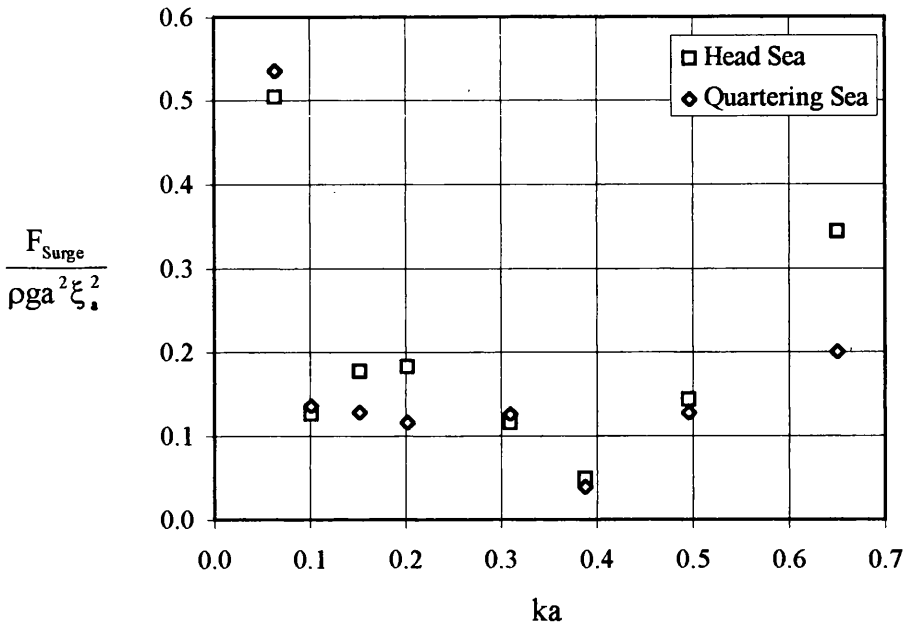

Figure 3.17: Experimental Global Surge Force

(2^{nd} order)

Experimental 3rd order global Heave force in the head and quartering wave condition are given in Figure 3.18, with the 3rd order global Surge force detailed in Figure 3.19.

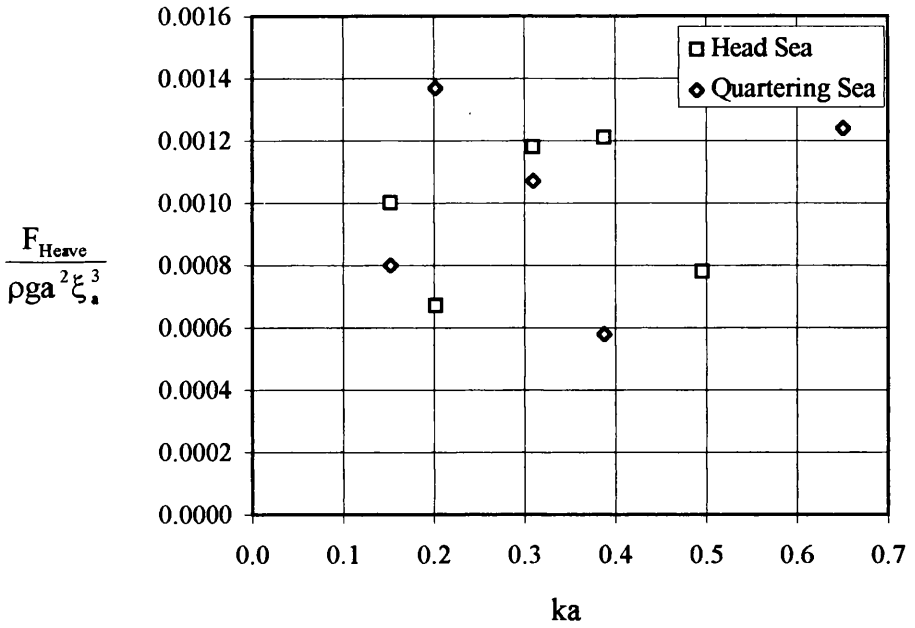

Figure 3.18: Experimental Global Heave Force

(3^{rd} order)

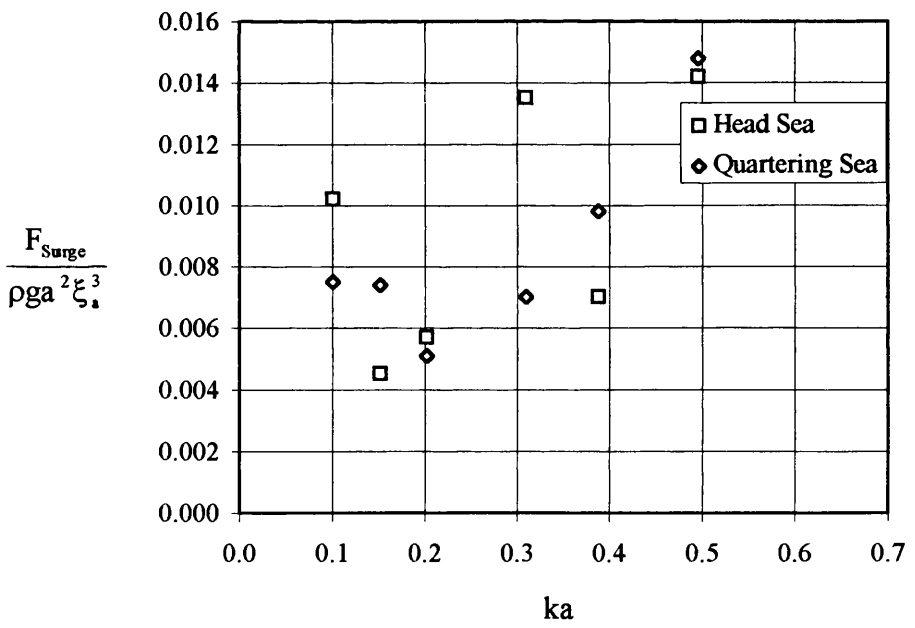

Figure 3.19: Experimental Global Surge Force

(3^{rd} order)

3.5.4 Hull Hydrodynamic Reaction Forces

3.5.4.1 Calm Water Tests

Calm water forced oscillation tests were conducted for a range of frequencies in the surge mode (see Table 3.1). After filtering to remove spurious irregularities the analysis technique detailed in 3.4.3 was applied and the Fourier averaged global surge added mass and linear viscous damping calculated.

The global Surge added mass and viscous damping for the head sea condition are given in Figures 3.20 and 3.21.

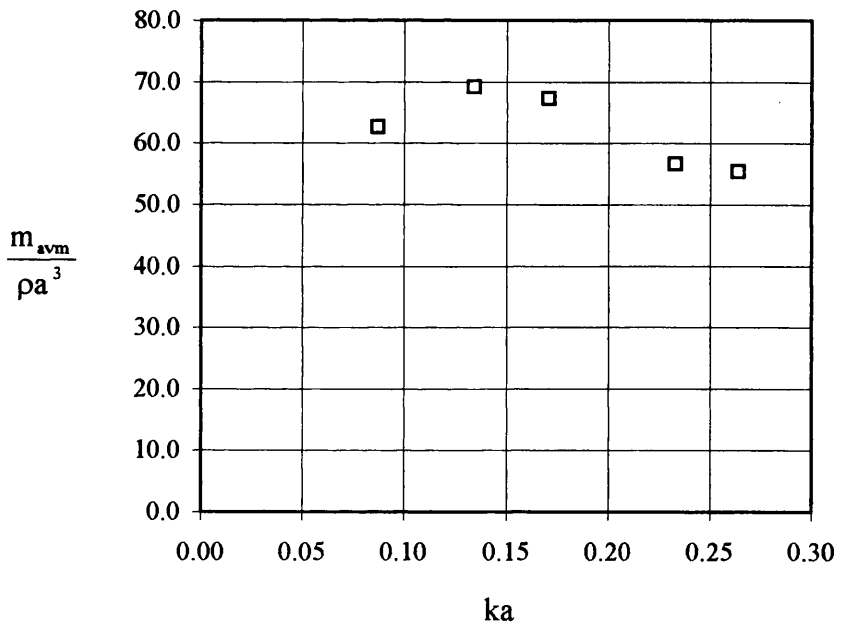

Figure 3.20: Global Surge Added Mass

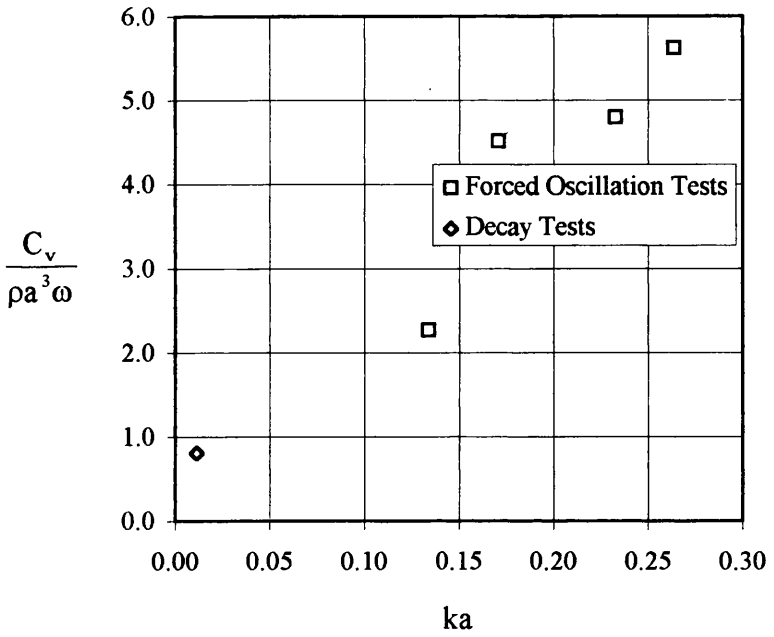

Figure 3.21: Global Surge Viscous Damping

3.5.4.2 Hydrodynamic Reaction Forces with Current Effects

To investigate the effects of current on the hydrodynamic reaction force components forced oscillation tests were undertaken in the presence of forward speed. For the purpose of this experimental programme it was assumed that towing the model and therefore modeling forward speed would yield a physically comparable test case to that of current acting on the hull (ref. Chapter 7 for discussion of limitations).

Figures 3.22-3.23 detail global surge added mass and viscous damping for the Case Study TLP hull in the head sea condition.

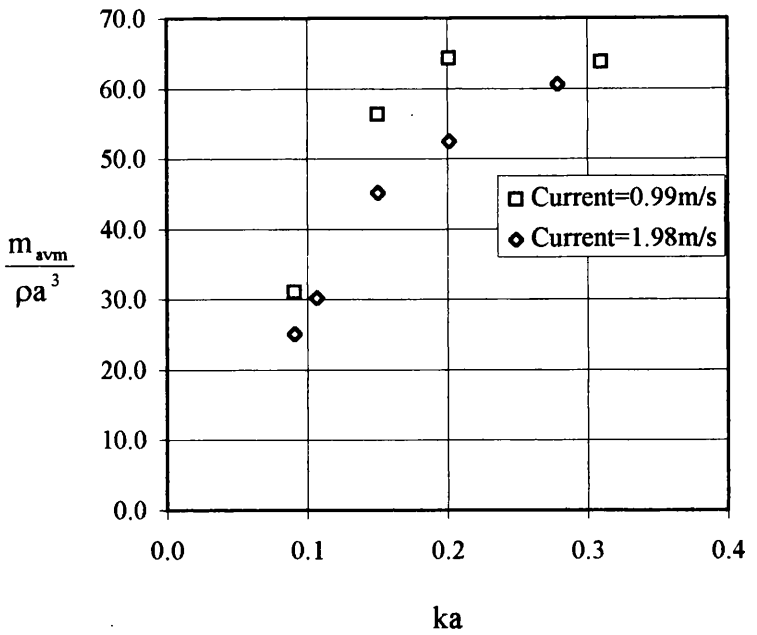

Figure 3.22: Global Surge Added Mass

(With Current Effects)

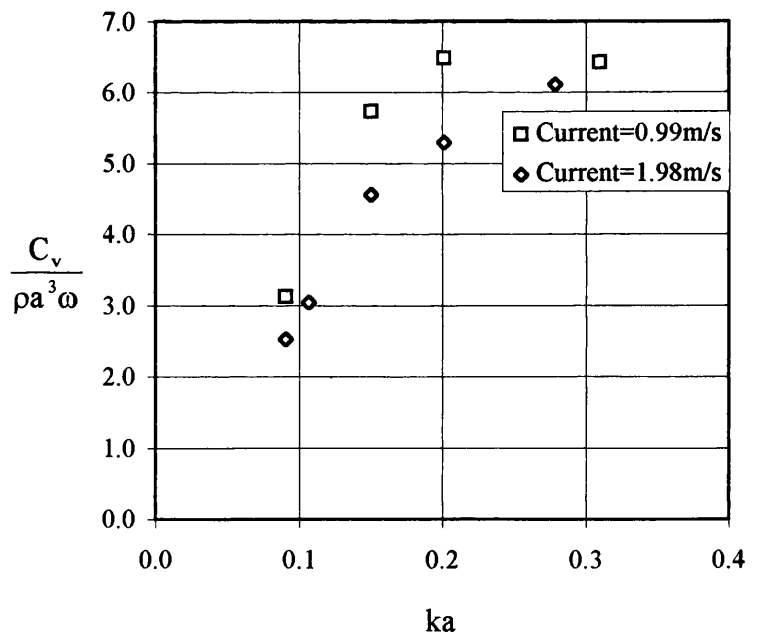

Figure 3.23: Global Surge Viscous Damping

(With Current Effects)

3.5.4.3 Hydrodynamic Reaction Forces with Waves Present

To investigate the effects of waves on the hydrodynamic reaction force components forced oscillation tests were undertaken in the presence of waves.

Figure 3.24 details the hydrodynamic reaction force components obtained during forced oscillation tests in the presence of regular waves.

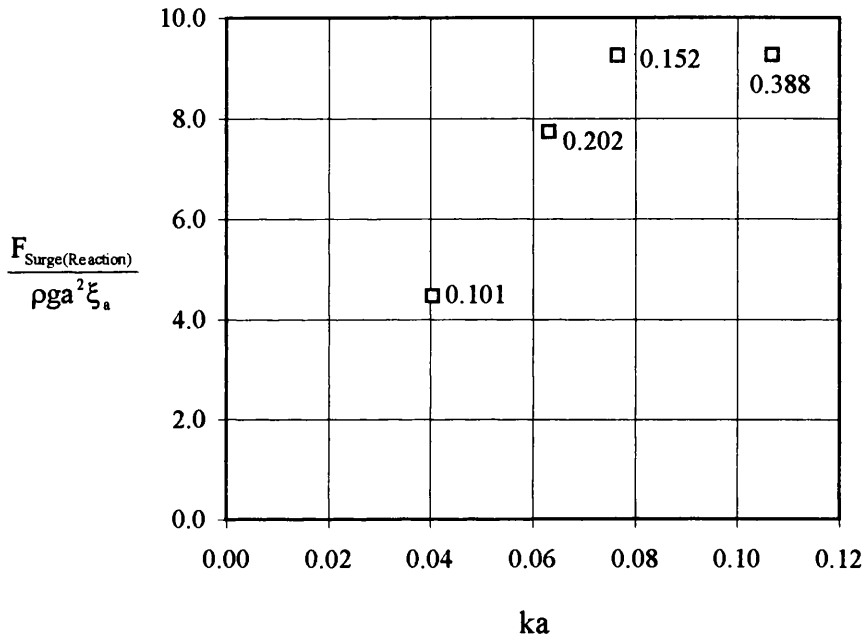

Figure 3.24: Global Surge Hydrodynamic Reaction Forces
(With Wave Effects)

The definition of hydrodynamic reaction force component is force component derived by Fourier Transform occurring at the forced rigid-body oscillation frequency. The X-axis of Figure 3.24 corresponds to the forced rigid-body oscillation frequency and the data values correspond to the incident regular wave frequency.

3.6 Discussion and Conclusions

3.6.1 Introduction

The experimentally determined global surge and heave wave forces were compared the predicted data (Ref. Chapter 2) and discussed. Conclusions on the reliability of the prediction techniques detailed in Chapter 2 were then drawn.

3.6.2 Wave Forces

Comparisons between analytical and numerical diffraction methods as well as the experimental data for the wave surge and heave forces for head sea (180^0) incident regular waves are detailed in Figures 3.25-3.26.

Figure 3.25 details the comparison of the wave excitation force in surge. AQWA-Line (CO) denotes the numerical d/r solution for a columns only model. SOAY (CO) denotes the analytical solution for a column only model. AQWA-Line (CM) denotes the numerical d/r solution for the complete model. Experimental (CM) denotes the experimental results for the complete model.

The comparison between the AQWA-Line (CO) and SOAY (CO) results show very good agreement. The comparison between the AQWA-Line (CM) and the Experimental (CM) results show acceptable agreement, with slight discrepancy occurring around the 1st loading peak. The column only and complete model results converge as incident wave frequency increases (wave lenght reduces). This is consistent with the effects of the pontoons reducing as the wave length reduces. The pontoon effects are most pronounced at the lower incident wave frequencies with ~10% additional load at the 1st loading peak (~0.4rad/s).

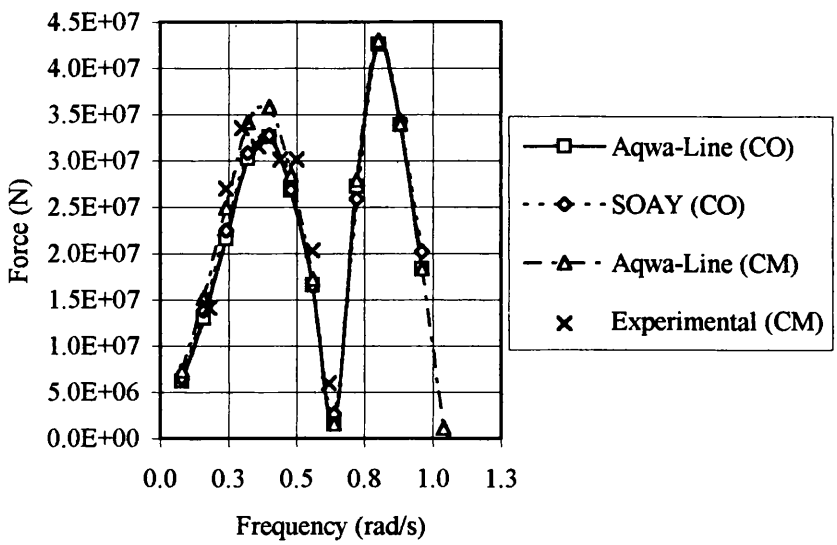

Figure 3.25: Surge Wave Force Comparison

Figure 3.26 details the comparison of the wave excitation force in heave. The curves are as those detailed above. Considerable scatter exists with all predictions for the low frequencies, with convergence to ~zero for all results in the high frequencies. The trend to zero as the incident wave frequency increases is consistent with the rapid decay w.r.t. water depth position of the wave kinematics. The comparison between the experimental and predicted values show some anomalies. When considering this it should be noted that the experimental data was derived from model testing of the complete TLP model in extreme waves. Therefore, effects due to: wave non-linearity; forces up to the free-surface (the AQWA-Line (CO), SEIL (CO) and AQWA-Line (CM) results are valid to SWL only) and drag forces are all present. By comparison of the AQWA-Line (CO) and (CM) data the effects of pontoons in heave is illustrated (pontoons contribute ~50% of the total wave heave force at low frequencies). Comparison between the AQWA-Line (CO) and SEIL (CO) data illustrates the diffraction effects between the array of cylinders (the SEIL (CO) results are for columns only, with the diffraction solution for a single column calculated and then assembled to the global solution with appropriate phase accounted for, but without the diffraction between the array of cylinders modeled).

By inspection the diffraction effects between the cylinder array in heave is low at low incident wave frequency increasing to a maximum of ~50% of the total heave force at ~0.45rad/s for the Heidrun TLP geometry and then converging to ~zero as incident wave frequency continues to increase.

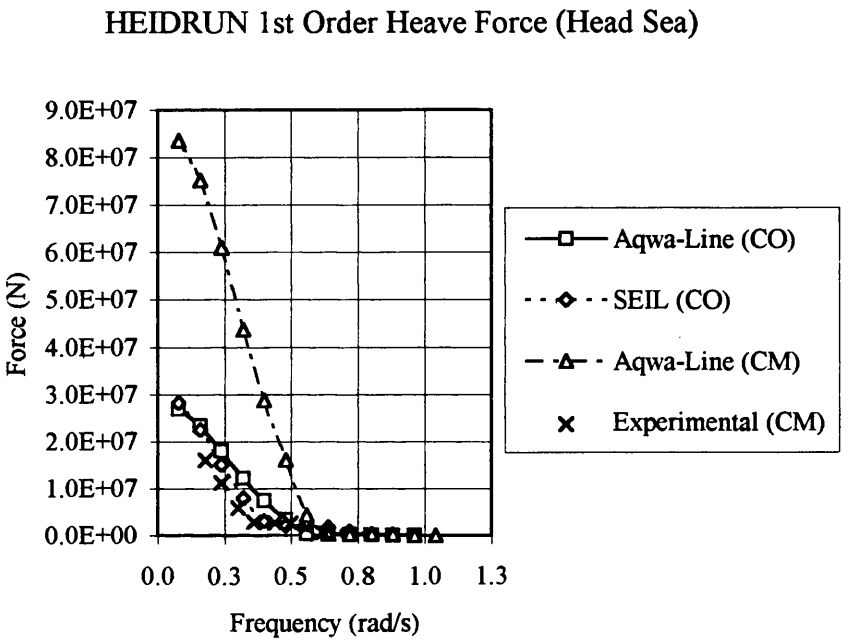

Figure 3.26: Heave Wave Force Comparison

3.6.3 Reaction Forces

Comparison between diffraction and experimental data for the surge added mass for head sea (180^0) incident regular waves is detailed in Figure 3.27.

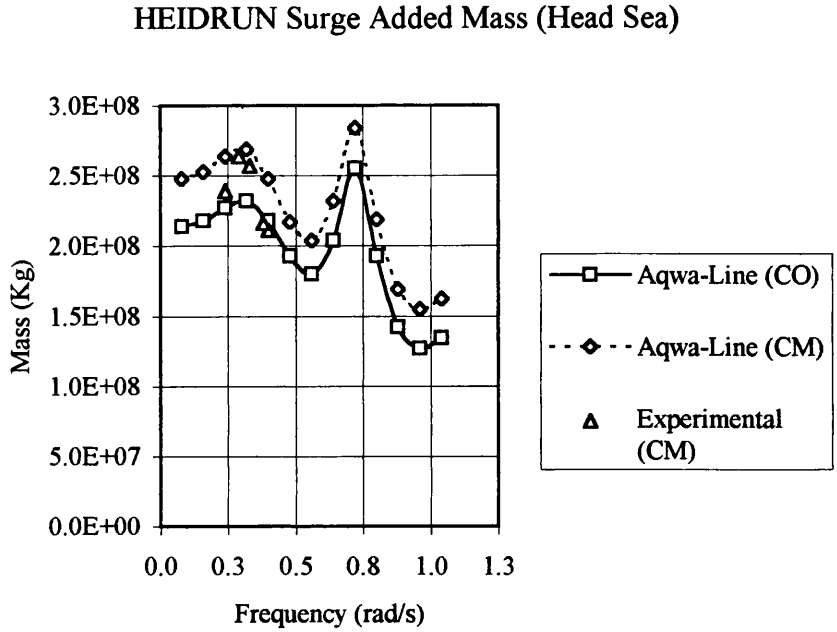

Figure 3.27: Surge Added Mass Comparison

Figure 3.27 details the surge added mass comparisons. By comparison between the AQWA-Line (CO) and AQWA-Line (CM) data the pontoon contribution of ~ 10% is illustrated. The experimentally derived data for the complete TLP hull is also plotted (Experimental (CM)).

In conclusion, the numerical prediction tools utilised and developed as detailed in Chapter 2 have been demonstrated to be reliable for wave excitation and reaction force prediction. There exists some uncertainty regarding the accuracy of heave wave force prediction. This would require further investigation before use in detailed design work. A 1st stage investigation would involve a re-meshing of the case Study TLP hull and re-analysis with the d/r code.

3.7 References

Bozic S.A. (1979) ***Digital and Kalman Filtering***. Edward Arnold.

Buss (1991) SIMPLEPLOT. ***Bradford University Software Services (BUSS) Ltd,*** Bradford University.

Helvacioglu I.H. (1990) ***Dynamic Analysis of Coupled Articulated Tower and Floating Production Systems***. Ph.D. thesis, University of Glasgow.

Hooft J.P. (1972) ***Hydrodynamic Aspects of Semi-Submersible Platforms***. Ph.D. thesis, Delft University of Technology, The Netherlands, Publication No. 400.

Keulegan G.H. and Carpenter L.H. (1958) Forces on Cylinders and Plates in an Oscillating Fluid. ***Journal of Research of the National Bureau of Standards***, Research Paper No. 2857, pp 420-440.

Morison J.R., O'Brien M.P., Johnson J.W. and Schaaf S.A. (1950) The Force Exerted by Surface Waves on Piles. ***Petroleum Transactions, American Institute of Mining Engineers***, Vol. 189, pp 149-154.

NAG (1990) The NAG FORTRAN Library Manual, Mark 14. ***The Numerical Algorithms Group (NAG) Ltd***, Oxford.

Stokes G.G. (1847) On the Theory of Oscillatory Waves. ***Transactions Cambridge Phil. Soc.***, Vol. 8, pp 441-455.

Thomson W.T. (1988) ***Theory of Vibration***. Unwin Hyman.

CHAPTER 4

SIMULATION OF TLP DYNAMIC RESPONSE DURING TETHER INSTALLATION

4.1 Introduction to TLP Installation Simulation

The dynamic response of coupled tether/TLP systems during pretensioning operations leading to lock-off has been investigated in the time-domain (6DOF). Attention focused on determining the maximum tether bundle loads during the transient period between the free-floating and pretensioned steady-states.

This investigation was composed of a Phase 1 (Rigid-body) and Phase 2 (Finite-element) models.

4.2 Mathematical Model (Phase 1, Rigid-body Approach, JURA)

4.2.1 Introduction

The Phase investigation focused on the determination of the TLP motion and tether axial force response during "lock-off" operations.

Frequency-dependent 1^{st} order wave excitation forces/moments and reaction components are utilised in conjunction with a time-dependent nonlinear mooring stiffness matrix to develop the system of coupled 2^{nd} order differential equations modeling the tether/TLP system.

Physical Models

The pretensioning installation stage lock-off consists of the following stages:

- Tugs position the TLP hull over the foundation templates
- The pre-installed tethers are latched into the TLP hull tether balconies
- Ballast is discharged therefore reducing the mass of the hull

- The tethers take up the excess buoyancy force and pretension is developed

- Ballast continues to be discharged until static pretension is reached

During the initial stages of the pretensioning operation the tethers undergo an alternating slacking and tensioning sequence which is a function of the hydrostatic mooring stiffness characteristics of the TLP hull and the prevailing metocean parameters.

To control any snatch loading all TLP installations to date have incorporated motion compensation mechanisms.

Mathematical Models

In order to simulate the lock-off operation a mathematical model was developed based on the physical model outlined above and implemented into software.

Key aspects incorporated are as follows:

- Dynamic nature of response

- Coupled time-dependent characteristics of tether mooring system

- Installation metocean conditions

- Low pretension

To model the dynamic nature of the TLP/tether response a time-domain solution to the system of 2nd order differential equations (6DOF) governing the TLP motion response is utilised.

$$[M + m_{avm}(\omega)]\{\ddot{X}\} + [C(\omega)]\{\dot{X}\} + [K(t)]\{X\} = \{F(\omega,t)\} \qquad \text{(6DOF)} \quad (4\text{-}1)$$

Where,

M =platform actual+tether effective actual mass

m_{avm} =platform added mass (frequency dependent)

C =linear damping (platform potential, frequency dependent+% critical in heave)

K =mooring system (time dependent)+platform hydrostatic restoring stiffness

F =excitation force/moment vector (frequency and time dependent)

$\{\ddot{X}\}$, $\{\dot{X}\}$ and $\{X\}$ =space-fixed acceleration, velocity and displacement vectors

4.2.2 Excitation Forces

Frequency-dependent 1st order wave excitation forces/moments and wave drift components were computed for the Case Study TLP hull geometry (refer to Chapter 2). The hydrodynamic data utilised during the motion response simulations was that provided by the CASE Sponsor (this was due to the order in which the research activities were conducted). This data was generated by the CASE Sponsor with the aid of LoROCS (Cornut, 1995). During the course of this research (in parallel with the motion response simulations) study the author undertook the development of hydrodynamic loading prediction tools as detailed in Chapter 2. Comparisons are detailed in Chapters 3 and 7.

Harmonic forcing functions were then generated utilising these frequency-domain results as follows:

$$F_{Surge}(t) = \xi_a A_{Surge} \cos(\omega t + \beta_{Surge}) \qquad (4\text{-}2)$$

$$F_{Sway}(t) = \xi_a A_{Sway} \cos(\omega t + \beta_{Sway}) \quad (4\text{-}3)$$

$$F_{Heave}(t) = \xi_a A_{Heave} \cos(\omega t + \beta_{Heave}) \quad (4\text{-}4)$$

$$M_{Roll}(t) = \xi_a A_{Roll} \cos(\omega t + \beta_{Roll}) \quad (4\text{-}5)$$

$$M_{Pitch}(t) = \xi_a A_{Pitch} \cos(\omega t + \beta_{Pitch}) \quad (4\text{-}6)$$

$$M_{Yaw}(t) = \xi_a A_{Yaw} \cos(\omega t + \beta_{Yaw}) \quad (4\text{-}7)$$

Where,

$F_*(t) / M_*(t)$ =harmonic excitation force/moment functions

ξ_a =incident wave amplitude

A_* =frequency-domain force/moment amplitudes for each mode

β_* =frequency-domain phase angles for each mode

The 6No. harmonic forcing functions were represented in vector form thus:

$$\begin{Bmatrix} F_{Surge}(t) \\ F_{Sway}(t) \\ F_{Heave}(t) \\ M_{Roll}(t) \\ M_{Pitch}(t) \\ M_{Yaw}(t) \end{Bmatrix} = \{F(\omega, t)\} \quad (4\text{-}8)$$

4.2.3 Reaction Forces

Frequency-dependent hydrodynamic reaction force components utilised were those provided by the CASE Sponsor (BP) for the Case Study TLP hull geometry (again, due to the timetable of research activities). The author also undertook the prediction of these components (as detailed in Chapter 2) at a later stage. Comparisons are detailed in Chapter 7.

These reaction force components consisted of added mass and radiation damping data.

This data was incorporated into the motion simulations in matrix form thus:

$$\begin{bmatrix} m_{avm(1,1)} & 0 & 0 & 0 & m_{avm(1,5)} & 0 \\ 0 & m_{avm(2,2)} & 0 & m_{avm(2,4)} & 0 & 0 \\ 0 & 0 & m_{avm(3,3)} & 0 & 0 & 0 \\ 0 & I_{avm(4,2)} & 0 & I_{avm(4,4)} & 0 & 0 \\ I_{avm(5,1)} & 0 & 0 & 0 & I_{avm(5,5)} & 0 \\ 0 & 0 & 0 & 0 & 0 & I_{avm(6,6)} \end{bmatrix} \quad (4\text{-}9)$$

And,

$$\begin{bmatrix} C_{(1,1)} & 0 & 0 & 0 & C_{(1,5)} & 0 \\ 0 & C_{(2,2)} & 0 & C_{(2,4)} & 0 & 0 \\ 0 & 0 & C_{(3,3)} & 0 & 0 & 0 \\ 0 & C_{(4,2)} & 0 & C_{(4,4)} & 0 & 0 \\ C_{(5,1)} & 0 & 0 & 0 & C_{(5,5)} & 0 \\ 0 & 0 & 0 & 0 & 0 & C_{(6,6)} \end{bmatrix} \quad (4\text{-}10)$$

Where,

$m_{avm(*,*)}$=added mass

$I_{avm(*,*)}$=added inertia

$C_{(*,*)}$=linear damping

The linear damping components consisted of hull radiation damping and a percentage of the heave mode critical damping (calculation based on installed value) representing viscous effects and tether material damping. The strategy employed to determine the % critical damping employed was to select a large value initially and then conduct a number of simulations with gradual reduction of the % critical damping applied until integration failure or intuitively erroneous results occurred. The value selected was 2.5%.

4.2.4 Restoring Forces

The mooring stiffness used was based on modeling the tether system as a group of rotating axial springs and incorporates the hull hydrostatic stiffness by assuming small angle stability theory.

$$[K] = [K_{hydro}] + [K_{moor}] \tag{4-11}$$

Hydrostatic stiffness exists in the heave, roll and pitch modes defined thus:

$$K_{hydro(heave)} = \rho g A_{wp} \tag{4-12}$$

$$K_{hydro(roll)} = \rho g \nabla \overline{GM}_T \tag{4-13}$$

$$K_{hydro(pitch)} = \rho g \nabla \overline{GM}_L \tag{4-14}$$

Where,

ρ =density of sea water (assumed, 1.025tonne/m^3)

A_{wp} =water plane area

∇=displaced volume

$\overline{GM}_T$, $\overline{GM}_L$=transverse/longitudinal metacentric height

The tether stiffness matrix utilised incorporated the TLP 6DOF motions taking account of coupling between modes.

Modeling a tether as a cylinder of length L_i, with end coordinates (X_{i2}, Y_{i2}, Z_{i2}), hull connection and (X_{i1}, Y_{i1}, Z_{i1}), foundation template connection.

With direction cosines defined thus,

$$\cos\alpha = \frac{X_{i2} - X_{i2}}{L_i}, \quad \cos\beta = \frac{Y_{i2} - Y_{i1}}{L_i}, \quad \cos\gamma = \frac{Z_{i2} - Z_{i1}}{L_i} \tag{4-15}$$

Assuming that for translational displacement of the platform in the X, Y and Z modes the corresponding change in tether length δL_i of the i^{th} tether may be represented:

$$\delta L_i = \cos\alpha_i \delta_X, \quad \delta L_i = \cos\beta_i \delta_Y, \quad \delta L_i = \cos\gamma_i \delta_Z \tag{4-16}$$

Then from the geometry of the displaced tether after platform displacement in the X, Y, Z, θ_1, θ_2 and θ_3 modes (surge, sway, heave, roll, pitch and yaw) the restoring forces/moments can be derived.

Assuming the length of a tether may be represented thus:

$$L_i = \sqrt{(X_{i2} - X_{i1})^2 + (Y_{i2} - Y_{i1})^2 + (Z_{i2} - Z_{i1})^2} \tag{4-17}$$

And the change in tether length δL_i,

$$\delta L_i = \cos\alpha_i \delta_X + \cos\beta_i \delta_Y + \cos\gamma_i \delta_Z \tag{4-18}$$

The considering the geometry of a tether after undergoing surge, sway and heave displacement:

By resolving the restoring force acting on the platform by the tether due to tension in the tether at the geometry,

$$F_{iX} = F\cos\alpha_i = (T + \delta T_i)\cos\alpha_i \quad (4\text{-}19)$$

$$F_{iY} = F\cos\beta_i = (T + \delta T_i)\cos\beta_i \quad (4\text{-}20)$$

$$F_{iZ} = F\cos\gamma_i = (T + \delta T_i)\cos\gamma_i \quad (4\text{-}21)$$

Where,

F_{iX}, F_{iY} and F_{iZ} =resolved force component acting in the surge, sway and heave directions respectively

T_i =initial pretension acting on the tether

δT_i =change in pretension due to the displacements in the surge, sway and heave directions

Due to the assumption of linear elastic tether behaviour,

$$\delta T_i = \frac{EA}{L_{i(t-1)}}\delta L_i \quad (4\text{-}22)$$

Where,

E =Young's modulus of the tether material (assumed, $2.07 \times 10^5 N/mm^2$)

A =cross sectional area of the tether

$L_{i(t-1)}$ =length of the tether at the previous time-step

Substituting (4-19), (4-18) and (4-22) yields,

$$F_{iX} = (T_i + \frac{EA}{L_{i(t+1)}} \cos\alpha_i \delta_X + \cos\beta_i \delta_Y + \cos\gamma_i \delta_Z)) \cos\alpha_i \qquad (4\text{-}23)$$

Expanding,

$$\frac{F_{iX}}{\delta_X} = \frac{T_i \cos\alpha_i}{\delta_X} + \frac{EA}{L_{i(t+1)}} \cos^2\alpha_i + \frac{EA}{L_{i(t+1)}} \cos\alpha_i \cos\beta_i \frac{\delta_Y}{\delta_X} + \frac{EA}{L_{i(t+1)}} \cos\alpha_i \cos\gamma_i \frac{\delta_Z}{\delta_X} \qquad (4\text{-}24)$$

Assuming δ_X, δ_Y and δ_Z are unit displacements and the tether is initially vertical,

$$k_{iX} = (\frac{T_i}{L_{i(t+1)}} + \frac{EA}{L_{i(t+1)}} \cos^2\alpha_i) + \frac{EA}{L_{i(t+1)}} \cos\alpha_i \cos\beta_i + \frac{EA}{L_{i(t+1)}} \cos\alpha_i \cos\gamma_i \qquad (4\text{-}25)$$

By a similar method the sway and heave stiffness components can be derived,

$$k_{iY} = \frac{EA}{L_{i(t+1)}} \cos\alpha_i \cos\beta_i + (\frac{T_i}{L_{i(t+1)}} + \frac{EA}{L_{i(t+1)}} \cos^2\beta_i) + \frac{EA}{L_{i(t+1)}} \cos\beta_i \cos\gamma_i \qquad (4\text{-}26)$$

$$k_{iZ} = \frac{EA}{L_{i(t+1)}} \cos\alpha_i \cos\gamma_i + \frac{EA}{L_{i(t+1)}} \cos\beta_i \cos\gamma_i + (\frac{T_i}{L_{i(t+1)}} + \frac{EA}{L_{i(t+1)}} \cos^2\gamma_i) \qquad (4\text{-}27)$$

Assuming the rotational displacements in roll, pitch and yaw are small and neglecting products of sine, then the rotational restoring moments can be expressed as a product of rotational and translational displacement and translational stiffness.

With roll stiffness defined,

$$k_{roll} = k_{\theta 1} = k_{heave} Y_i' \tag{4-28}$$

Where k_{heave} as defined in (4-27) is function of surge, sway and heave components and Y_i' in the TLP body-fixed coordinate of the i^{th} tether/hull connection in the Y-axis.

Substituting (4-27) into (4-28),

$$k_{i\theta 1} = \left(\frac{EA}{L_{i(t+1)}} \cos\alpha_i \cos\gamma_i + \frac{EA}{L_{i(t+1)}} \cos\beta_i \cos\gamma_i + \left(\frac{T_i}{L_{i(t+1)}} + \frac{EA}{L_{i(t+1)}} \cos^2\gamma_i\right)\right) Y_i' \tag{4-29}$$

By a similar method the stiffness components in pitch and yaw can be defined:

$$k_{i\theta 2} = \left(\frac{EA}{L_{i(t+1)}} \cos\alpha_i \cos\gamma_i + \frac{EA}{L_{i(t+1)}} \cos\beta_i \cos\gamma_i + \left(\frac{T_i}{L_{i(t+1)}} + \frac{EA}{L_{i(t+1)}} \cos^2\gamma_i\right)\right) X_i' \tag{4-30}$$

$$k_{i\theta 3} = \left(\left(\frac{T_i}{L_{i(t+1)}} + \frac{EA}{L_{i(t+1)}} \cos^2\alpha_i\right) + \frac{EA}{L_{i(t+1)}} \cos\alpha_i \cos\beta_i + \frac{EA}{L_{i(t+1)}} \cos\alpha_i \cos\gamma_i\right) \sqrt{X_i'^2 + Y_i'^2} \tag{4-31}$$

Rearranging the above ((4-25), (4-26), (4-27), (4-29), (4-30) and (4-31)) in matrix form yields the stiffness matrix $[K_{tether}]$ for a single tether element,

$$[K_{Tether}] = \begin{bmatrix} \frac{T_i}{L_i} + \frac{EA}{L_i}\cos^2\alpha_i & & & & & \\ \frac{EA}{L_i}\cos\alpha_i\cos\beta_i & \frac{T_i}{L_i} + \frac{EA}{L_i}\cos^2\beta_i & & \text{sym.} & & \\ \frac{EA}{L_i}\cos\alpha_i\cos\gamma_i & \frac{EA}{L_i}\cos\beta_i\cos\gamma_i & \frac{T_i}{L_i} + \frac{EA}{L_i}\cos^2\gamma_i & & & \\ 0 & 0 & 0 & (k_{31}+k_{32}+k_{33})Y_i' & & \\ 0 & 0 & 0 & 0 & (k_{31}+k_{32}+k_{33})X_i' & \\ 0 & 0 & 0 & 0 & 0 & (k_{31}+k_{32}+k_{33})\sqrt{X_i'^2+Y_i'^2} \end{bmatrix} \quad (4\text{-}32)$$

With the mooring system stiffness matrix $[K_{moor}]$ consisting of a summation of the individual tether element stiffness matrices,

$$[K_{Tether}] = \sum_{i=1}^{n_T} \begin{bmatrix} \frac{T_i}{L_i} + \frac{EA}{L_i}\cos^2\alpha_i & & & & & \\ \frac{EA}{L_i}\cos\alpha_i\cos\beta_i & \frac{T_i}{L_i} + \frac{EA}{L_i}\cos^2\beta_i & & \text{sym.} & & \\ \frac{EA}{L_i}\cos\alpha_i\cos\gamma_i & \frac{EA}{L_i}\cos\beta_i\cos\gamma_i & \frac{T_i}{L_i} + \frac{EA}{L_i}\cos^2\gamma_i & & & \\ 0 & 0 & 0 & (k_{31}+k_{32}+k_{33})Y_i' & & \\ 0 & 0 & 0 & 0 & (k_{31}+k_{32}+k_{33})X_i' & \\ 0 & 0 & 0 & 0 & 0 & (k_{31}+k_{32}+k_{33})\sqrt{X_i'^2+Y_i'^2} \end{bmatrix} \quad (4\text{-}33)$$

To incorporate the time-dependent nonlinearity of the above mooring stiffness derivation the matrix is reassembled at each time-step.

4.2.5 Time-domain Simulation of Coupled Tether/TLP System (Nonlinear 6DOF Stiffness Matrix)

To model the dynamic nature of the TLP/tether response a time-domain solution to the system of 2nd order differential equations (6DOF) governing the TLP motion response is utilised (4-1).

The above coupled system of equations was solved in the time-domain. To investigate the sensitivity to solving algorithm both the Runge-Kutta (4-34), **explicit**, and Newmark-β (4-35) (Newmark, 1959), **implicit**, methods were utilised:

$$\vec{X}_{n+1} = \vec{X}_n + \frac{\delta t}{6}\left[\dot{\vec{X}}_n + 2\left(\dot{\vec{X}}_n + \vec{f}_1\frac{\delta t}{2}\right) + 2\left(\dot{\vec{X}}_n + \vec{f}_2\frac{\delta t}{2}\right) + \left(\dot{\vec{X}}_n + \vec{f}_3\delta t\right)\right] \quad (4\text{-}34)$$

$$\vec{X}_{n+1} = \vec{X}_n + \dot{\vec{X}}_n\delta t + \left(\frac{1}{2} - \beta\right)\ddot{\vec{X}}_n\delta t^2 + \beta\ddot{\vec{X}}_{n+1}\delta t^2 \quad (4\text{-}35)$$

Where,

$\vec{X}_{n+1}$ =displacement vector at time $n+1$, i.e. next time-step

$\vec{X}_n$ =displacement vector at time n, i.e. $n\delta t$ =position in time

δt =time-step

$\dot{\vec{X}}_n$ =velocity vector at time n

$$\vec{f}_1 = f\left(T_1, \vec{X}_1, \dot{\vec{X}}_1\right)$$

$$\vec{f}_2 = f\left(T_2, \vec{X}_2, \dot{\vec{X}}_2\right)$$

$$\vec{f}_3 = f\left(T_3, \vec{X}_3, \dot{\vec{X}}_3\right)$$

$$\vec{f}_4 = f\left(T_4, \vec{X}_4, \dot{\vec{X}}_4\right)$$

Where, $\vec{f}_{1,2,3\text{and}4}(*)$ represents accelerations based on the 2nd order d.e.s,

And,

$T_1 = t_i$ =initial time

$\vec{X}_1 = \vec{X}_i$ =initial displacement vector

$\dot{\vec{X}}_1 = \dot{\vec{X}}_i$ =initial velocity vector

$$T_2 = t_i + \frac{\delta t}{2} = T_3$$

$$\vec{X}_2 = \vec{X}_i + \dot{\vec{X}}_1 \frac{\delta t}{2}$$

$$\dot{\vec{X}}_2 = \dot{\vec{X}}_i + \vec{f}_1 \frac{\delta t}{2}$$

$$\vec{X}_3 = \vec{X}_i + \dot{\vec{X}}_2 \frac{\delta t}{2}$$

$$\dot{\vec{X}}_3 = \dot{\vec{X}}_i + \vec{f}_2 \frac{\delta t}{2}$$

$$T_4 = t_i + \delta t$$

$$\vec{X}_4 = \vec{X}_i + \dot{\vec{X}}_3 \delta t$$

$$\dot{\vec{X}}_4 = \dot{\vec{X}}_i + \vec{f}_3 \delta t$$

β=Newmark's β parameter (0.25 for unconditionally stable)

$\ddot{\vec{X}}_{n+1}$=acceleration vector at time $n+1$

The added mass and damping matrices are linear frequency-domain data with the excitation force vector consisting of time-dependent linear harmonic excitation functions.

The mass matrix consists of platform and tether effective actual mass, and hull added mass. The tether effective mass was incorporated as a lumped mass. The effective tether mass in the surge/sway and heave modes was as defined below.

To derive the effective mass of the tethers acting on the tether/hull connections ($m_{avm(eff,x,y,z)}$) the following analytical approach was utilised.

Surge/Sway (x,y)

Consider in the horizontal direction the sum about the tether/foundation template connection. Taking moments about the foundation connection leads to an equilibrium equation thus (Ref. Figure 4.1),

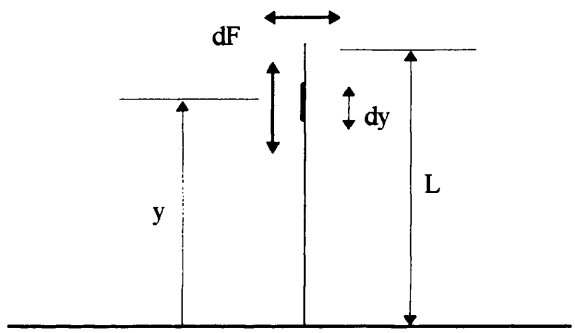

Figure 4.1

$$dFL = mdyy\frac{y}{L}ä \tag{4-36}$$

Where ä is the horizontal acceleration at the tether top connector and m is the mass/unit length.

By integration over the length of the tether L,

$$FL = \frac{mä}{L}\int_{o}^{L} y^2 dy \tag{4-37}$$

Yielding by application of Newton's 2nd law,

$$m_{eff(x,y)} = \frac{mL}{3} \tag{4-38}$$

Heave (z)

Consider in the vertical direction the integral of the incremental force dF over the tether length L.

$$dF = mdy\frac{\ddot{a}}{L}y \tag{4-39}$$

Where ä is the vertical acceleration at the tether top connector. Therefore it is assumed that the heave acceleration varies linearly from the maximum value at the tether top connector to zero at the foundation connection.

Therefore by integrating over the length L yields,

$$F = \frac{m\ddot{a}}{L}\int_0^L ydy \tag{4-40}$$

Again by application of Newton's 2nd law the effective mass in the vertical mode is given by,

$$m_{eff(z)} = \frac{mL}{2} \tag{4-41}$$

The stiffness is a nonlinear, time-dependent matrix which is reassembled at each time-step correct for the actual platform position/orientation. The coupled time-dependent characteristics of the tether mooring system were incorporated by the derivation of a (6DOF) tether mooring stiffness matrix which includes the hull hydrostatic components (refer to 4.2.4).

4.3 Mathematical Model (Phase 2, Finite-element Approach, TIREE)

4.3.1 Introduction

To model TLP installation operations incorporating tether wave excitation and hydrodynamic reaction force components a finite-element tether model was developed.

In addition to the Phase 1 (4.2) "lock-off" process the Phase 2 model was developed to incorporate the modeling of float-out and positioning of the tethers:

1) Tether float-out.

2) Tether upending.

3) Tether latch to foundation.

4) Vertical tethers unconnected to TLP hull.

6) Insitu TLP.

4.3.2 Phase 2 Finite-element System Model

This model consists of 3D beam-column elements (Chen & Atsuta, 1977) with a Morison excitation loading formulation for randomly orientated cylinders (Chakrabarti *et al*, 1975) and Strip-theory hydrodynamic reaction force components.

This model consists of 2No. Schemes:

1) Coupled tether/TLP finite-element model consisting of global system matrices representing the finite-element model of the tether bundle system and the TLP rigid-body system.

2) Finite-element tether bundle model incorporating an external applied force vector. The external applied force vector can consist of translation force components derived by a coupled tether/TLP analysis or representative installation loads (due to tow-out, upending, etc).

The 2nd order differential equation system governing the tether Finite-element/TLP model is as follows:

$$[M + m_{avm}]\{\ddot{X}\} + [C_{nl}]\{\dot{X}\}\{\dot{X}\} + [C_l]\{\dot{X}\} + [K_m]\{X\} = \{F\} \qquad (4\text{-}42)$$

Where,

$[M + m_{avm}]$=the actual mass+added mass matrix of the coupled tether/TLP system

$[C_{nl}]$=the nonlinear damping matrix of the coupled tether/TLP system

$[C_l]$=the linear damping matrix of the coupled tether/TLP system

$[K_m]$=the stiffness matrix of the coupled tether/TLP system

$\{F\}$=the excitation force vector of the coupled tether/TLP system

$\{\ddot{X}\}$, $\{\dot{X}\}$ and $\{X\}$=the acceleration, velocity and displacement vectors respectively of the coupled tether/TLP system

The governing equation system is solved in the Time-domain utilising the ISML solver routine DIVPAG based on the Gear BDF method (5th order) for stiff systems (Microsoft FORTRAN Powerstation, 1987).

The above governing equation system is a large DOF system (e.g. Scheme 1, 10 No. elements/tether bundle=206DOF, Scheme 2, 10 No. elements/tether bundle=55DOF).

The coupling of the tether/TLP system is achieved by solving at each time-step the Global System matrices. The Global System matrices consist of the Tether Group Finite-element System matrices and the TLP System matrices.

When modeling the uncoupled tethers the TLP System matrix elements are omitted.

4.3.3 Global System Matrices

4.3.3.1 Mass Matrix

The Global System Mass matrix $[M + m_{avm}]$ is time-independent and consists of: TLP actual mass+TLP added mass (frequency-domain data)+tether system actual mass (consistent mass)+tether system added mass (strip-theory).

$$[M + m_{avm}] = [M_{TLP_{actual}}] + [M_{TLP_{avm}}] + [M_{Tether_{actual}}] + [M_{Tether_{avm}}] \qquad (4\text{-}43)$$

Where,

$$[M_{TLP_{actual}}] = \begin{bmatrix} m & & & & & \\ 0 & m & & & \text{sym.} & \\ 0 & 0 & m & & & \\ 0 & 0 & 0 & I_{roll} & & \\ 0 & 0 & 0 & 0 & I_{pitch} & \\ 0 & 0 & 0 & 0 & 0 & I_{yaw} \end{bmatrix} \qquad (4\text{-}44)$$

$$[M_{TLP_{avm}}] = \begin{bmatrix} m_{avm(surge)} & & & & & \\ 0 & m_{avm(sway)} & & & \text{sym.} & \\ 0 & 0 & m_{avm(heave)} & & & \\ 0 & 0 & 0 & I_{avi(roll)} & & \\ 0 & 0 & 0 & 0 & I_{avi(pitch)} & \\ 0 & 0 & 0 & 0 & 0 & I_{avi(yaw)} \end{bmatrix} \qquad (4\text{-}45)$$

And for the individual tether finite-elements (10DOF/element),

$$\left[M_{Tether_{end}}\right]=\frac{mL}{420}\begin{bmatrix} 156 & & & & & & & & & \\ 0 & 156 & & & & & & & \text{sym.} & \\ 0 & 0 & 140 & & & & & & & \\ 0 & 22L & 0 & 4L^2 & & & & & & \\ 22L & 0 & 0 & 0 & 4L^2 & & & & & \\ 54 & 0 & 0 & 0 & 13L & 156 & & & & \\ 0 & 54 & 0 & 13L & 0 & 0 & 156 & & & \\ 0 & 0 & 70 & 0 & 0 & 0 & 0 & 140 & & \\ 0 & -13L & 0 & -3L^2 & 0 & 0 & -22L & 0 & 4L^2 & \\ -13L & 0 & 0 & 0 & -3L^2 & -22L & 0 & 0 & 0 & 4L^2 \end{bmatrix} \tag{4-46}$$

With,

m=mass/unit length of tether finite-element

L=length of tether finite-element

$$\left[M_{Tether_{mid}}\right]=\begin{bmatrix} \frac{\rho\pi D^2L}{8} & & & & & & & & & \\ 0 & \frac{\rho\pi D^2L}{8} & & & & & & & \text{sym.} & \\ 0 & 0 & 0 & & & & & & & \\ 0 & 0 & 0 & 0 & & & & & & \\ 0 & 0 & 0 & 0 & 0 & & & & & \\ \frac{\rho\pi D^2L}{8} & 0 & 0 & 0 & 0 & \frac{\rho\pi D^2L}{8} & & & & \\ 0 & \frac{\rho\pi D^2L}{8} & 0 & 0 & 0 & 0 & \frac{\rho\pi D^2L}{8} & & & \\ 0 & 0 & 0 & 0 & 0 & 0 & 0 & 0 & & \\ 0 & 0 & 0 & 0 & 0 & 0 & 0 & 0 & 0 & \\ 0 & 0 & 0 & 0 & & 0 & 0 & 0 & 0 & 0 \end{bmatrix} \tag{4-47}$$

With,

D=tether finite-element diameter

4.3.3.2 Nonlinear Damping Matrix

The Global System Nonlinear Damping matrix $[C_{nl}]$ is time-independent and consists of tether system viscous damping (strip-theory).

$$[C_{nl}] = [C_{nl(tether)}] \tag{4-48}$$

Where,

$$[C_{nl(tether)}] = \frac{1}{2}\rho C_d D \begin{bmatrix} \frac{L}{2} & & & & & & & & & \\ 0 & \frac{L}{2} & & & & & & & \text{sym.} & \\ 0 & 0 & 0 & & & & & & & \\ 0 & 0 & 0 & 0 & & & & & & \\ 0 & 0 & 0 & 0 & 0 & & & & & \\ \frac{L}{2} & 0 & 0 & 0 & 0 & \frac{L}{2} & & & & \\ 0 & \frac{L}{2} & 0 & 0 & 0 & 0 & \frac{L}{2} & & & \\ 0 & 0 & 0 & 0 & 0 & 0 & 0 & 0 & & \\ 0 & 0 & 0 & 0 & 0 & 0 & 0 & 0 & 0 & \\ 0 & 0 & 0 & 0 & & 0 & 0 & 0 & 0 & 0 \end{bmatrix} \tag{4-49}$$

With,

C_d =tether finite-element drag coefficient

4.3.3.3 Linear Damping Matrix

The Global System Linear Damping matrix $[C_l]$ is time-independent and consists of: TLP potential damping (frequency-domain data)+any other linear damping to be considered, e.g., tether structural damping, foundation/soil interaction damping, etc.

$$[C_l] = [C_{l(TLP)}] + [C_{l(other)}] \tag{4-50}$$

Where,

$$\left[C_{l(TLP)}\right]=\begin{bmatrix} C_{l(surge)} & & & & & \\ 0 & C_{l(sway)} & & & \text{sym.} & \\ 0 & 0 & C_{l(heave)} & & & \\ 0 & 0 & 0 & C_{l(roll)} & & \\ 0 & 0 & 0 & 0 & C_{l(pitch)} & \\ 0 & 0 & 0 & 0 & 0 & C_{l(yaw)} \end{bmatrix} \quad (4\text{-}51)$$

Where,

$C_{l(*)}$=TLP hull radiation damping

Details of the tether system structural damping applied are given in Chapter 2.

4.3.3.4 Stiffness Matrix

The Global System Stiffness matrix $\left[K_m\right]$ is time-dependent consisting of: TLP hydrostatic stiffness (time-independent)+tether system stiffness (flexural stiffness+incremental stiffness, applied to the TLP at the tether/TLP hull nodes).

$$\left[K_m\right]=\left[K_{TLP_{hydrostatic}}\right]+\left[K_{tether_{flexural}}\right]+\left[K_{tether_{incremental}}\right] \quad (4\text{-}52)$$

Where,

$$\left[K_{tether_{forward}}\right]=\begin{bmatrix}
\frac{12EI}{L^2} & & & & & & & & & \\
0 & \frac{12EI}{L^2} & & & & & & & \text{sym.} & \\
0 & 0 & \frac{EA}{L} & & & & & & & \\
0 & -\frac{6EI}{L^2} & 0 & \frac{4EI}{L} & & & & & & \\
-\frac{6EI}{L^2} & 0 & 0 & 0 & \frac{4EI}{L} & & & & & \\
-\frac{12EI}{L^2} & 0 & 0 & 0 & -\frac{6EI}{L^2} & \frac{12EI}{L^2} & & & & \\
0 & -\frac{12EI}{L^2} & 0 & \frac{6EI}{L^2} & 0 & 0 & \frac{12EI}{L^2} & & & \\
0 & 0 & -\frac{EA}{L} & 0 & 0 & 0 & 0 & \frac{EA}{L} & & \\
0 & -\frac{6EI}{L^2} & 0 & \frac{2EI}{L} & 0 & 0 & \frac{6EI}{L^2} & 0 & \frac{4EI}{L} & \\
-\frac{6EI}{L^2} & 0 & 0 & 0 & \frac{2EI}{L} & \frac{6EI}{L^2} & 0 & 0 & 0 & \frac{4EI}{L}
\end{bmatrix} \tag{4-53}$$

$$\left[K_{tether_{incremental}}\right]=\frac{-P}{10L}\begin{bmatrix}
12 & & & & & & & & & \\
0 & 12 & & & & & & & \text{sym.} & \\
0 & 0 & 0 & & & & & & & \\
0 & 0 & 0 & \frac{4L^3}{3} & & & & & & \\
0 & -L & 0 & 0 & \frac{4L^3}{3} & & & & & \\
-L & 0 & 0 & 0 & L & 12 & & & & \\
-12 & 0 & 0 & L & 0 & 0 & 12 & & & \\
0 & -12 & 0 & 0 & 0 & 0 & 0 & 0 & & \\
0 & -L & 0 & -\frac{L^2}{3} & 0 & 0 & L & 0 & \frac{4L^3}{3} & \\
-L & 0 & 0 & 0 & -\frac{L^3}{3} & L & 0 & 0 & 0 & \frac{4L^3}{3}
\end{bmatrix} \tag{4-54}$$

The above stiffness matrix is only valid for low-moderate axial tensions.

The TLP hull hydrostatic stiffness applied was that detailed in (4-12), (4-13) and (4-14).

4.3.3.5 Excitation Force Vector

The Global System Excitation Force vector $\{F\}$ is time-dependent consisting of: TLP hydrodynamic excitation force/moment vector (frequency-domain LoROCS data)+tether system hydrodynamic excitation force vector (3D Morison equation based model (with current superimposed)).

$$\{F\} = \begin{Bmatrix} F_{surge}(t) \\ F_{sway}(t) \\ F_{heave}(t) \\ M_{roll}(t) \\ M_{pitch}(t) \\ M_{yaw}(t) \\ F_{node1,x}(t) \\ F_{node1,y}(t) \\ F_{node1,z}(t) \\ 0 \\ 0 \\ F_{node2,x}(t) \\ F_{node2,y}(t) \\ F_{node2,z}(t) \\ 0 \\ 0... \end{Bmatrix} \tag{4-54}$$

The above vector is a partial form of the Scheme 2 coupled tether/TLP system. The Scheme 1 vector consisted of only the tether finite-element system.

4.3.3.6 Response Vectors

The Global System Response vectors $\{\ddot{X}\}$, $\{\dot{X}\}$ and $\{X\}$ are determined at each time-step yielding the TLP and tether system response.

$$\{X\} = \begin{Bmatrix} X_{surge} \\ X_{sway} \\ X_{heave} \\ X_{roll} \\ X_{pitch} \\ X_{yaw} \\ X_{node1,x} \\ X_{node1,y} \\ X_{node1,z} \\ X_{node1,\theta 1} \\ X_{node1,\theta 2} \\ X_{node2,x} \\ X_{node2,y} \\ X_{node2,z} \\ X_{node2,\theta 1} \\ X_{node2,\theta 2} \cdots \end{Bmatrix}, \text{ with velocity and acceleration similar} \qquad (4\text{-}55)$$

4.3.4 Phase 2 Model Algorithm

The Phase 2 Finite-element model can be decomposed into 7No. main stages:

CONSTRUCTOR: Constructs the tether Finite-element mass, damping and stiffness matrices (local coordinate system).

RESOLVER: Resolves the tether Finite-element mass, damping and stiffness matrices from the local to the global (space-fixed) coordinate system.

The tether/TLP Global System matrices are solved in the space-fixed coordinate system (ref. Chapter 1) yielding displacement, velocity and acceleration vectors in the space-fixed system. To facilitate this the tether finite-element matrices are resolved form the element body-fixed coordinate system to the space-fixed coordinate system by use of transformation matrices.

$$\{\overline{X}\} = [T]\{X\} \qquad (4\text{-}56)$$

Where,

$[\overline{X}]$=local displacement vector

$[T]$ =transformation matrix

$[X]$=global displacement vector

Where,

$$[T]=\begin{bmatrix} \cos\alpha & 0 & -\sin\alpha & 0 & 0 \\ \sin\beta\sin\alpha & \cos\beta & \sin\beta\cos\alpha & 0 & 0 \\ \cos\beta\sin\alpha & -\sin\beta & \cos\beta\cos\alpha & 0 & 0 \\ 0 & 0 & 0 & 1 & 0 \\ 0 & 0 & 0 & 0 & 1 \end{bmatrix} \tag{4-57}$$

Therefore,

$$\{X\}=[T]^{-1}\{\overline{X}\} \tag{4-58}$$

And as,

$$F=[T]^{-1}\overline{F} \tag{4-59}$$

And for example,

$$\overline{F}=[\overline{K}]\overline{X} \tag{4-60}$$

Therefore,

$$[M]=[T]^{-1}[\overline{M}][T] \tag{4-61}$$

$$[C]=[T]^{-1}[\overline{C}][T] \tag{4-62}$$

$$[K] = [T]^{-1}[\overline{K}][T] \qquad (4\text{-}63)$$

ASSEMBLER: Assembles the tether Finite-element mass, damping and stiffness matrices (global coordinate system) to form the Tether "Bundle" Finite-element System matrices.

The assembly procedure involves building the finite-element matrices around the common nodes to yield the Tether "Bundle" Finite-element System matrices (ref. Thomson, 1988). A partial example is detailed in Figure 4.1 for the coupled tether/TLP system (Scheme 2).

FORCER: Computes the wave/current excitation forces acting on the Tether Group Finite-element System in the global coordinate system (lumped to nodes).

Details of the calculation procedure adopted in this routine are presented in Chapter 2 (2.2.7).

GLOBAL: Processes the Tether Group Finite-element System (the sum of the Tether "Bundle" Finite-element System matrices) and TLP System matrices to form the Global System matrices and inputs to SOLVER.

SOLVER: Solves the Global System matrices in the form of equation (4-42) utilising an *implicit multistep backward differentiation formula Gear's stiff method* (IVPAG, *Microsoft* IMSL Libraries).

All the above routines are time-dependent and are therefore recalled at each time-step.

Chapter 7 details a discussion regarding the numerical issues of solving the coupled tether/TLP system of equations.

TIREE: Main program, controls the input/output processing, time-step, etc.

The Global System matrices are the sum of the Tether Group Finite-element System matrices and the TLP System matrices. A partial expression for the Global System Stiffness matrix is given over:

Figure 4.2: Partial Global System Stiffness Matrix

4.4 Results

4.4.1 Introduction

Numerical simulation work was conducted utilising the Phase 1 and Phase 2 methods outlined above to predict the tether/TLP system response for a range of metocean parameters.

Results of these simulations consisted of time-domain data detailing the tether/TLP system response as well as the tether bundle tension time-series.

This time-domain data for both Phase 1 and Phase 2 models is presented in Chapter 6 and Appendix A (Case Studies) for 3No. TLP geometries representative of the spectrum of TLP systems and for a range of metocean parameters.

Discussion of time-domain simulation results and comparisons between Phase 1 and Phase 2 methods and experimental data is given in Chapter 7.

4.5 References

Chakrabarti S.K., Tam W.A. and Wolbert A.L. (1975) Wave Forces on a Randomly Oriented Tube, **Proceedings of the 7th Offshore Technology Conference OTC'75**, OTC2190, pp. 433-447.

Chen W.F. & Astuta T. (1977) **Theory of Beam-Columns, Volume 2: Space Behaviour and Design**, Mcgraw-Hill International Book Company.

Cornut S. (1995) **An Analytical Model to Predict the Environmental Forces on a Tension Leg Platform and Time-domain Response Analysis**, M.Sc. Thesis, University of Glasgow.

Kim M.H. (1993) Interaction of waves with N Vertical Circular Cylinders, **Journal of Waterway, Port, Coastal and ocean Engineering**, Vol. 119, No. 6, pp. 671-689.

Microsoft IMSL, Visual Numerics Inc.

Microsoft FORTRAN Powerstation (1997) Microsoft Corporation.

Newmark (1959) A Method of Computation for Structural Dynamics, **Journal of the Engineering Mechanics Division, proceedings of the American Society of Civil Engineers (ASCE)** , Paper 2094, Vol. 85, No. EM3.

CHAPTER 5

EXPERIMENTAL INVESTIGATION OF TETHER TRANSIENT RESPONSE DURING PRETENSIONING OPERATIONS

5.1 Introduction to TLP Installation Experimental Investigation

This research aims to investigate experimentally the dynamic response of a case study TLP geometry during "lock-off" and low pretension conditions.

This experimental validation work was conducted in the University of Newcastle Towing/wave Tank.

This experimental investigation consisted of testing a ~1:300 scale model of the case study TLP geometry (Heidrun TLP, see Figure 5.1 and Table 5.2) at zero/low pretension conditions sampling tether "bundle" force time-series as well as the platform translational displacement time-series (3DOF) for a range of experimental conditions (Table 5.1)

The experimental tether "bundle" force and platform translational displacement time-series data will be utilised to validate the prediction methods employed in Chapter 4.

5.2 TLP Installation Experimental Programme

5.2.1 Introduction

To investigate the dynamic response of a case study TLP geometry during "lock-off" and low pretension condition an experimental programme was developed. This programme involved measuring tether "bundle" force and platform translational displacement time-series in the presence of regular waves. The programme of experiments conducted is detailed in the Matrix of Experiments (TLP Installation) given in Table 5.1.

5.2.2 Experimental Programme

The Matrix of Experiments (TLP Installation) is as follows:

Test/ Heading	PT=0N	PT=0N, Current Effects Included	PT=1/6th Installed
Head Sea	Waves, 0.31, 0.34, 0.37, 0.42, 0.47, 0.53 and 0.62rad/s, amp.=3.5m	Wave, 0.31rad/s, amp.=3.5m, Current=4.1m/s	Wave, 0.31rad/s, amp.=14.1m
Quartering Sea	Waves, 0.31, 0.34, 0.37, 0.42, 0.47, 0.53 and 0.62rad/s, amp.=3.5m		

Table 5.1: Matrix of Experiments
(TLP Installation)

5.3 Experimental Setup to Investigate TLP Installation

5.3.1 Introduction

The experimental programme was conducted in the University of Newcastle Towing/wave Tank (40x3.75x1.25m). The Towing/wave Tank is equipped with a *Seasim* Rolling Seal Absorbing Wavemaker at one end with a passive beach at the other.

5.3.2 Data Acquisition System

The data acquisition system at the University of Newcastle Towing/wave Tank consists of carriage mounted radio link to a 486 PC computer running *Labview* experimental data processing/storage software.

5.3.3 Instrumentation System

Quantitative experimental data was sampled at 50 samples/second for 20 seconds via:

1) 1No. *Novatech* F225 25Kg submersible loadcell (tether "bundle" force time-series).

2) *Selspot* optical/electronic displacement measuring system (TLP translational displacement time-series, 3DOF).

3) 2No. "resistance type" wave probes (Incident and Dynamic (encounter) wave elevation time-series).

The sampled data was transferred via a radio link to the data acquisition PC.

Qualitative experimental data consisting of underwater video footage of the tether/tether-hull node behaviour was recorded with the aid of a submersible *Elmo* CCD camera and VCR.

5.3.4 Tether System/TLP Model

The case study geometry tested was a scale model of Heidrun TLP (1:281.8) constructed from PVC.

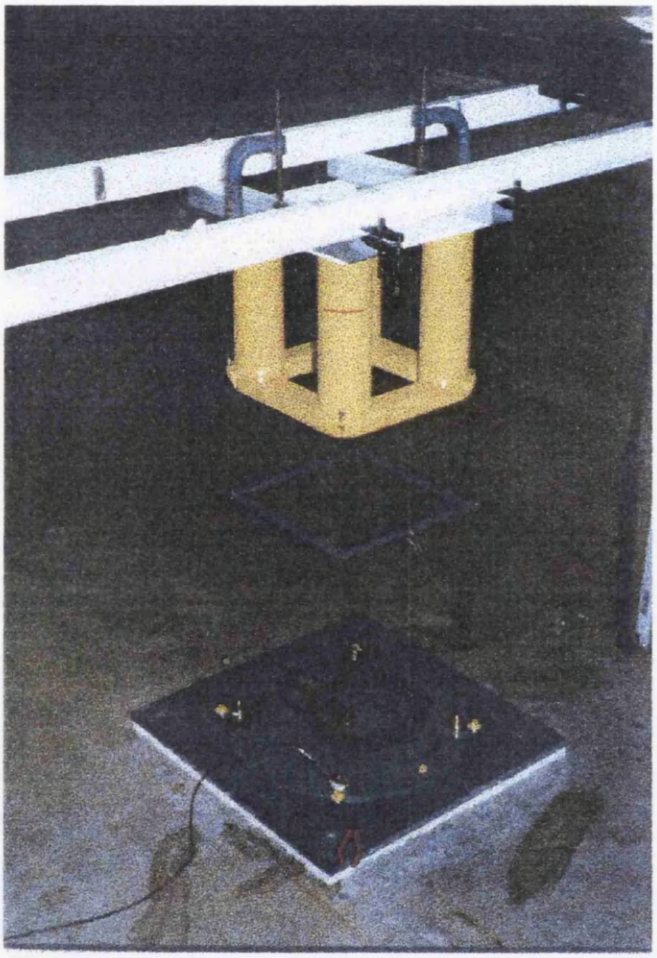

Figure 5.1: Heidrun Model (1:281.8)
During setup in the Newcastle Towing/wave Tank
(Model c.g. positioned 12.85m from face of Wavemaker)

Dimension	Heidrun	Model (1:281.8)
Displacement	289300Tonne	12.928Kg
Column Diameter	31m	0.11m
Column Spacing	80m	0.284m
Pontoon Depth	13m	0.046m
Pontoon Width	15.95m	0.057m

Table 5.2: Case Study TLP Principal Dimensions

Due to practical limitations it was not possible to match exactly the tether system properties in the model scale. In addition to this, the tether system was represented by "equivalent" tether "bundles", where each tether "bundle" represents a group of individual tethers.

Prior to the experimental runs the natural periods of the model setup were established for the installed[1] case (Table 5.3). These were determined by decay tests performed on the installed model setup in all 6DOF and are as follows:

DOF	Model (Prototype Scale)	Heidrun[2]
Surge	107.1s	131s
Sway	112.5s	131s
Heave	1s	2.97s
Roll	2.1s	3.38s
Pitch	1.7s	3.28s
Yaw	31.9s	-

Table 5.3: Natural Period Data

To incorporate the investigation of current effects on the tether transient response during "lock off" operations a mass/pulley system was developed.

The method proposed was a mass/pulley arrangement whereby a mass (force) representing a steady lateral force was applied to the tether/TLP system (Figure 5.2).

[1] Model installed pretension was greater than Heidrun installed (96.593×10^6N compared to 90.75×10^6N).
[2] Source: Norwegian Contractors.

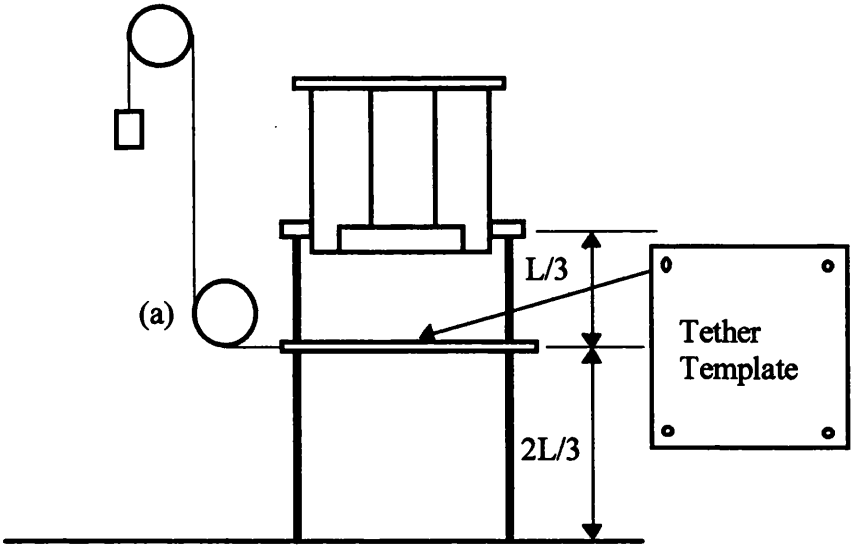

Figure 5.2: Mass/Pulley General Arrangement

(a) Mass/pulley setup to incorporate a steady lateral force representing current. A practical mass (force) was utilised with application to the tethers via a "Tether Template". The "Tether Template" consisted of a PVC sheet spacing the tethers and distributing the applied current load evenly to all 4No. tethers "bundles" (idealized tethers).

5.3.5 Calibration Techniques

Calibration was conducted both insitu and in the workshop:

The *Novatech* F225 25Kg submersible loadcell was calibrated in the workshop prior to installation in the Newcastle Towing/wave Tank.

The *Selspot* optical/electronic displacement measuring system (TLP translational displacement time-series, 3DOF) was calibrated in the workshop and then the LEDs were fitted to the deck of the TLP model.

The 2No. "resistance type" wave probes (Incident; positioned 9.5m from the face of the Wavemaker aligned on the Towing/wave Tank center-line and Dynamic (encounter); aligned 54mm in the +ve X-axis from the face of the FWD Starboard column) were calibrated insitu.

5.4 Results of TLP Installation Experimental Investigation

5.4.1 Introduction

TLP and tether installation dynamic response in regular waves are given for the case study TLP geometry. All results are given in the **prototype** scale unless otherwise noted.

For comparisons between the experimental and simulated data see Chapter 7 (7.4 TLP Dynamic Response During Installation and 7.5 Tether Dynamic Response During Installation).

The coordinate system utilised for the experimental programme is as given in Chapter 1 (Figure 1.2), with the X-axis (Surge) orientated perpendicular to the wave-maker (wave propagation towards the model), with +ve Surge displacement towards the wave-maker. The current force was represented along the Surge axis with +ve current force in the -ve Surge direction (i.e. in the direction of wave propagation).

For the quartering sea (incident wave heading=45^0) the coordinate system was as noted above with the model rotated by 45^0 in the -ve Yaw direction.

5.4.2 TLP Installation Dynamic Response (Head Sea)

The case study TLP translational DOF displacement installation dynamic response during regular waves for the Head Sea condition are given in Figures 5.3-5.20.

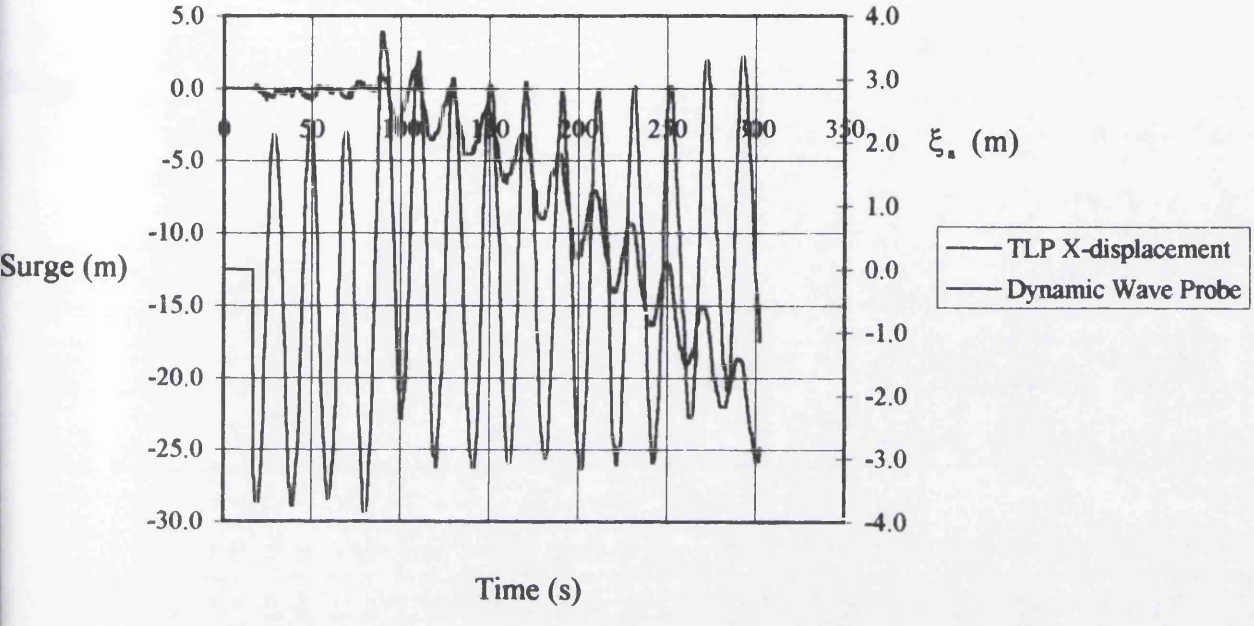

Figure 5.3: TLP X-displacement

(Head Sea, PT=0N, ω =0.31rad/s, ξ_a =3.5m)

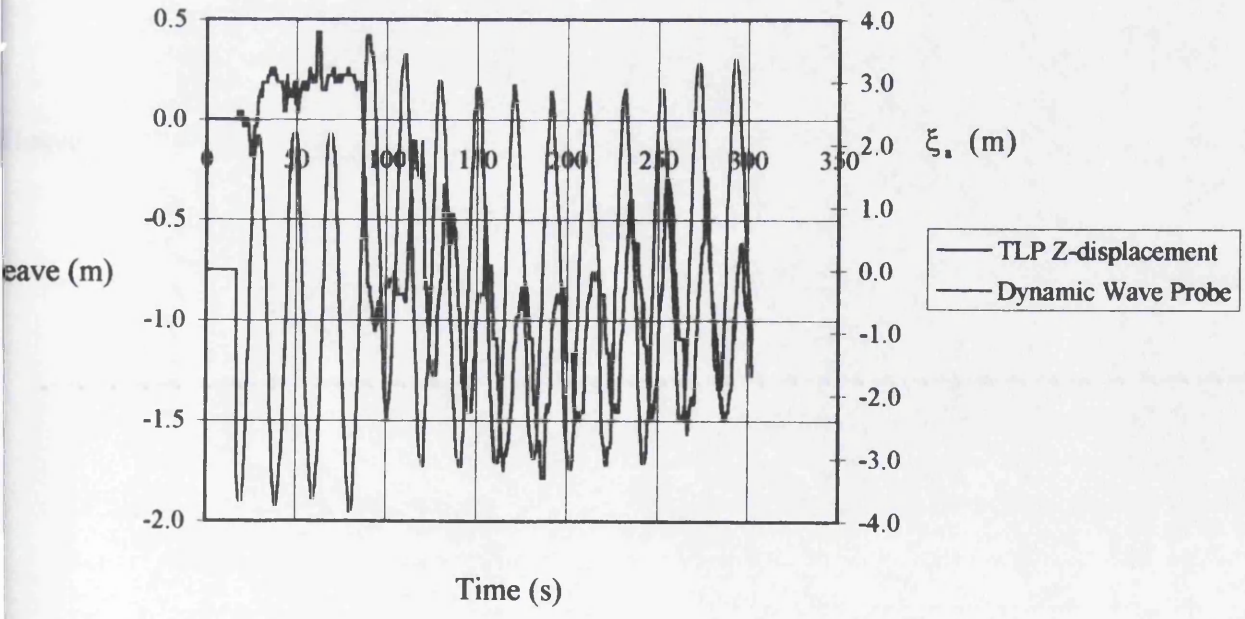

Figure 5.4: TLP Z-displacement

(Head Sea, PT=0N, ω =0.31rad/s, ξ_a =3.5m)

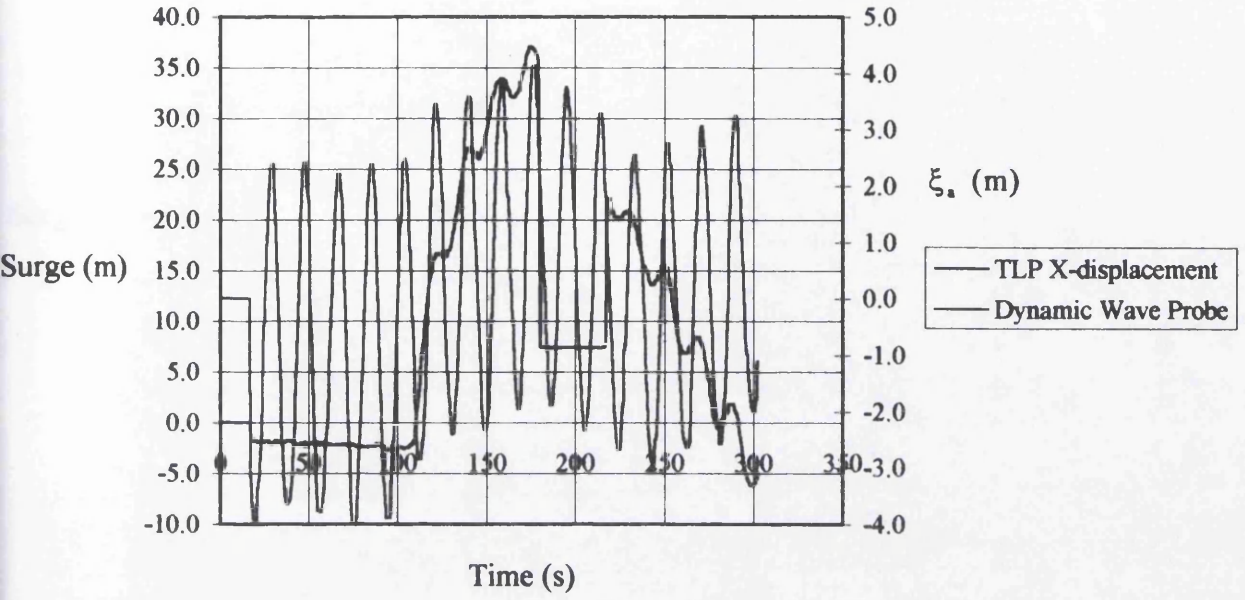

Figure 5.5: TLP X-displacement

(Head Sea, PT=0N, ω =0.34rad/s, ξ_a =3.5m)

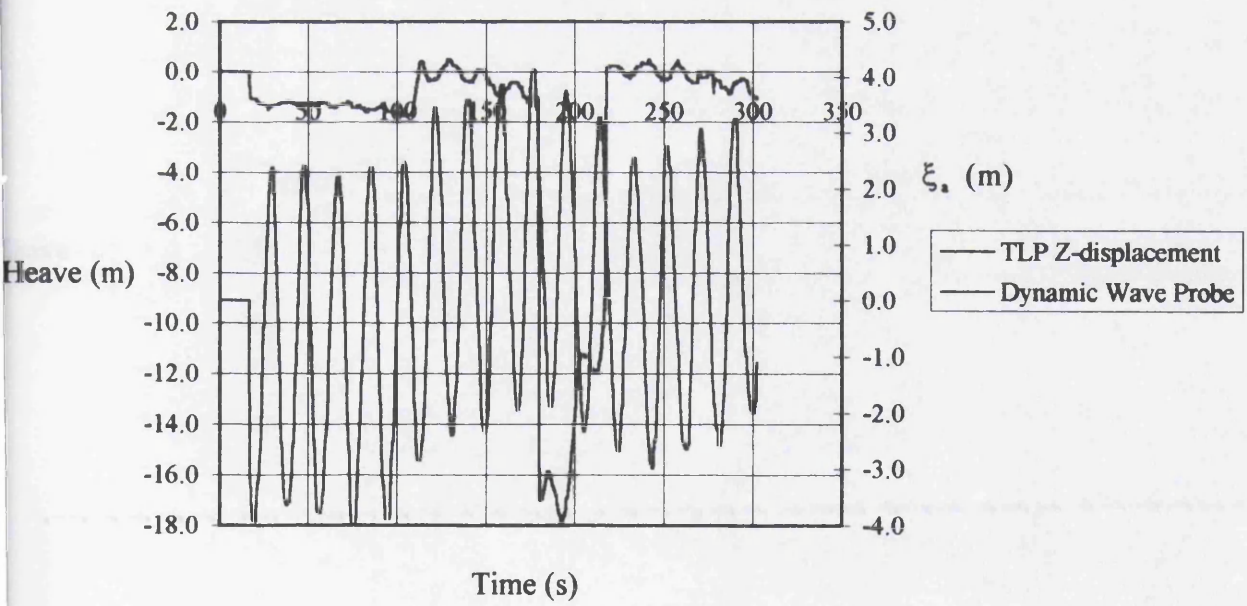

Figure 5.6: TLP Z-displacement

(Head Sea, PT=0N, ω =0.34rad/s, ξ_a =3.5m)

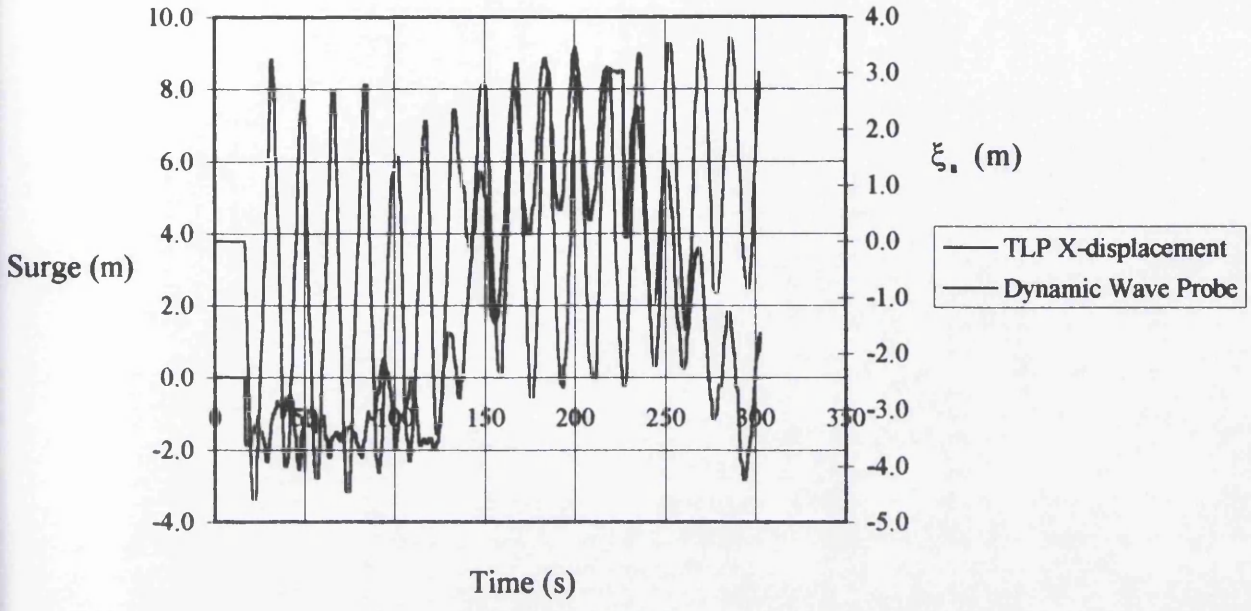

Figure 5.7: TLP X-displacement

(Head Sea, PT=0N, ω =0.37rad/s, ξ_a =3.5m)

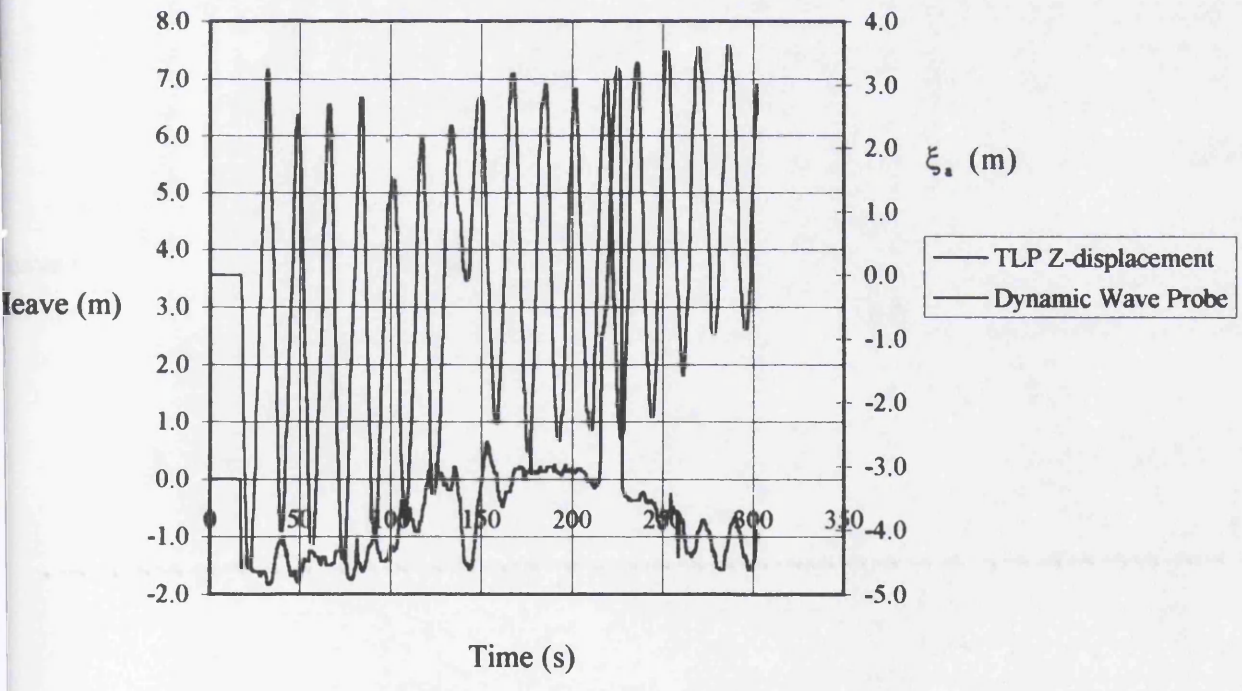

Figure 5.8: TLP Z-displacement

(Head Sea, PT=0N, ω =0.37rad/s, ξ_a =3.5m)

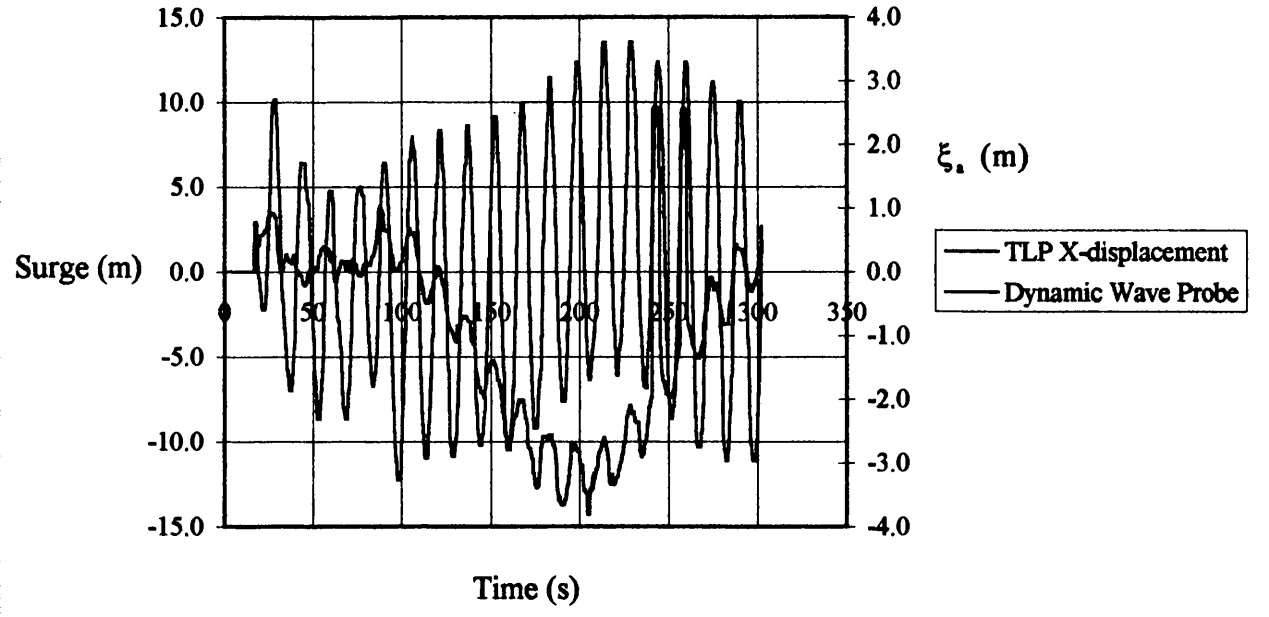

Figure 5.9: TLP X-displacement

(Head Sea, PT=0N, ω =0.42rad/s, ξ_a =3.5m)

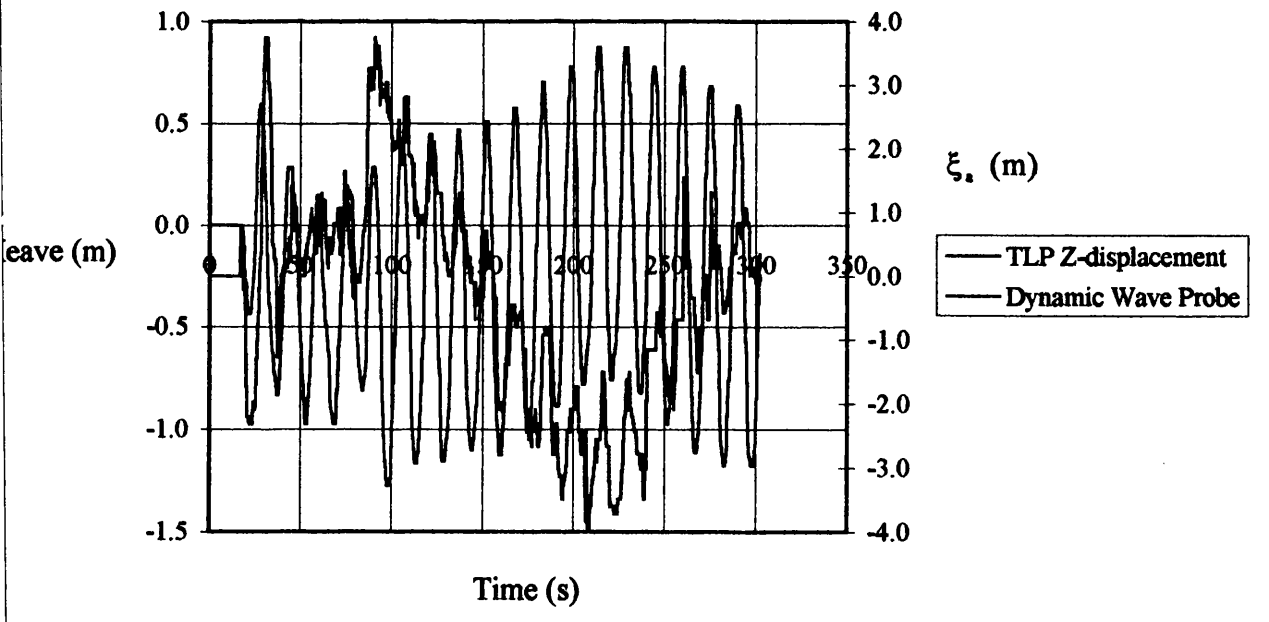

Figure 5.10: TLP Z-displacement

(Head Sea, PT=0N, ω =0.42rad/s, ξ_a =3.5m)

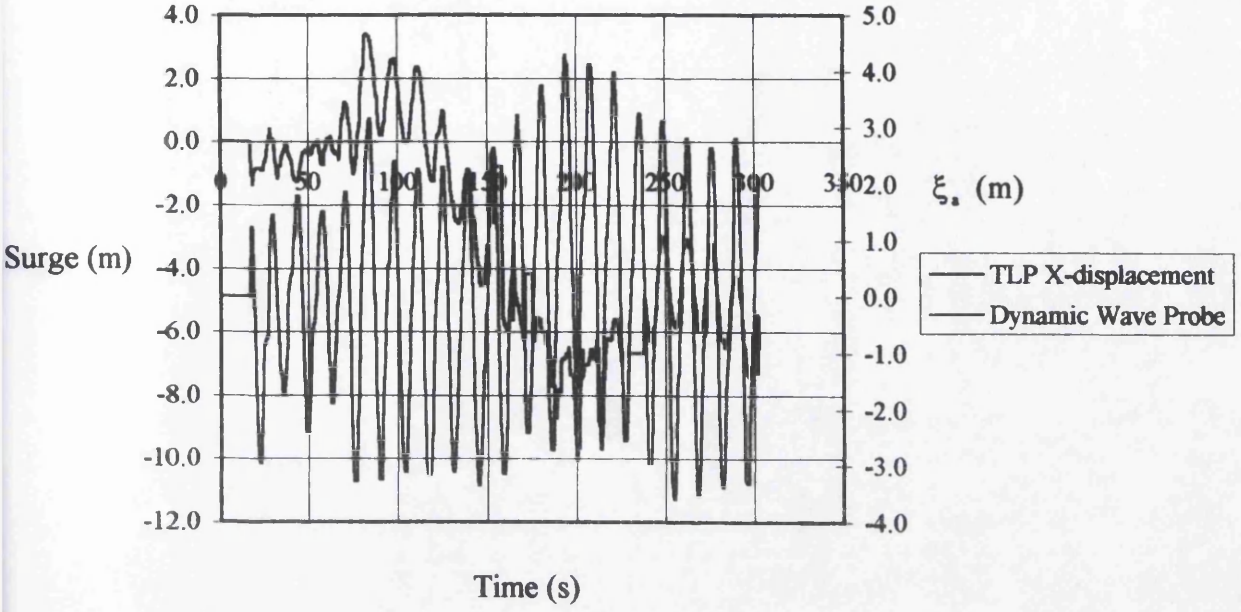

Figure 5.11: TLP X-displacement

(Head Sea, PT=0N, ω =0.47rad/s, ξ_a =3.5m)

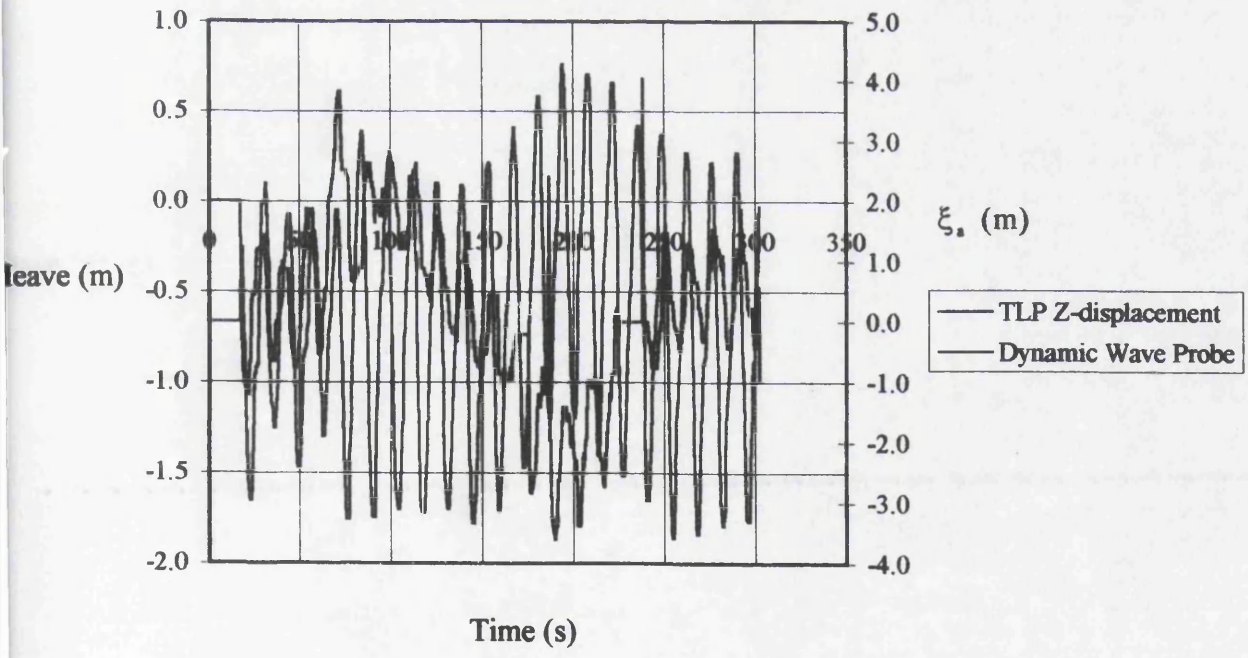

Figure 5.12: TLP Z-displacement

(Head Sea, PT=0N, ω =0.47rad/s, ξ_a =3.5m)

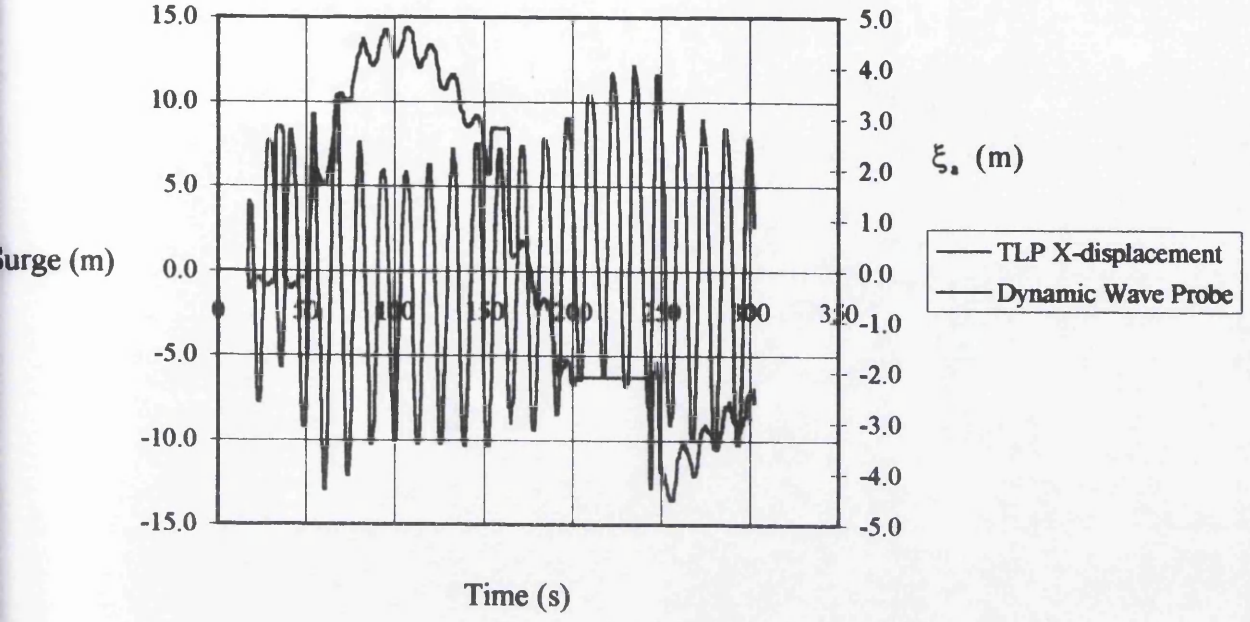

Figure 5.13: TLP X-displacement

(Head Sea, PT=0N, ω =0.53rad/s, ξ_a=3.5m)

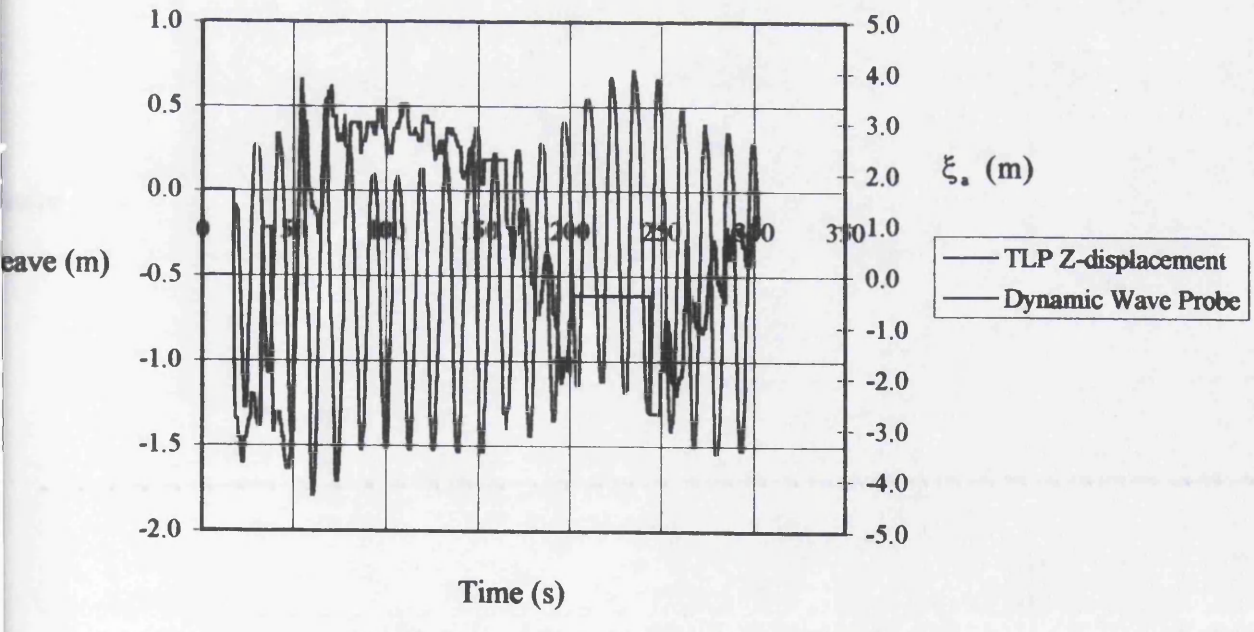

Figure 5.14: TLP Z-displacement

(Head Sea, PT=0N, ω =0.53rad/s, ξ_a=3.5m)

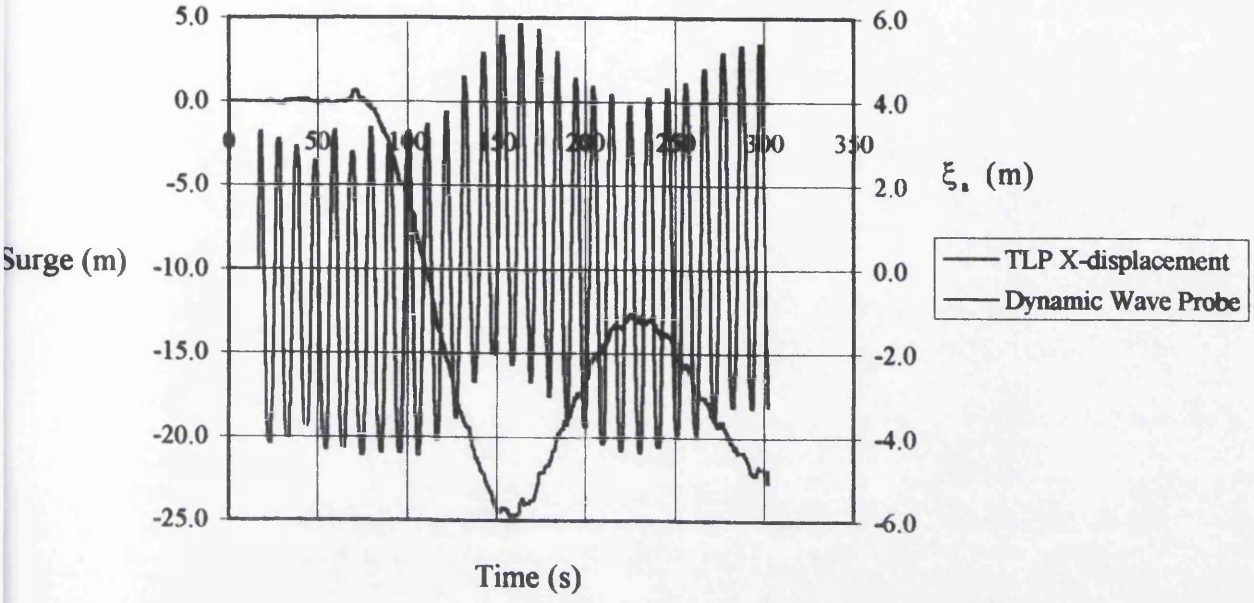

Figure 5.15: TLP X-displacement

(Head Sea, PT=0N, ω =0.62rad/s, ξ_a =3.5m)

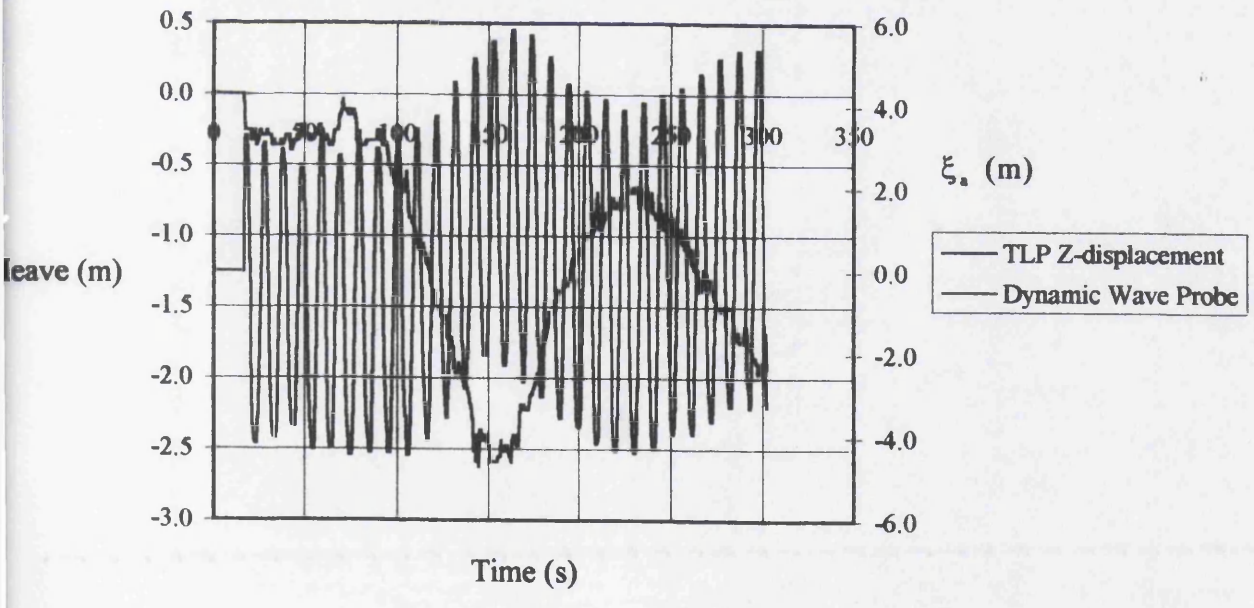

Figure 5.16: TLP Z-displacement

(Head Sea, PT=0N, ω =0.62rad/s, ξ_a =3.5m)

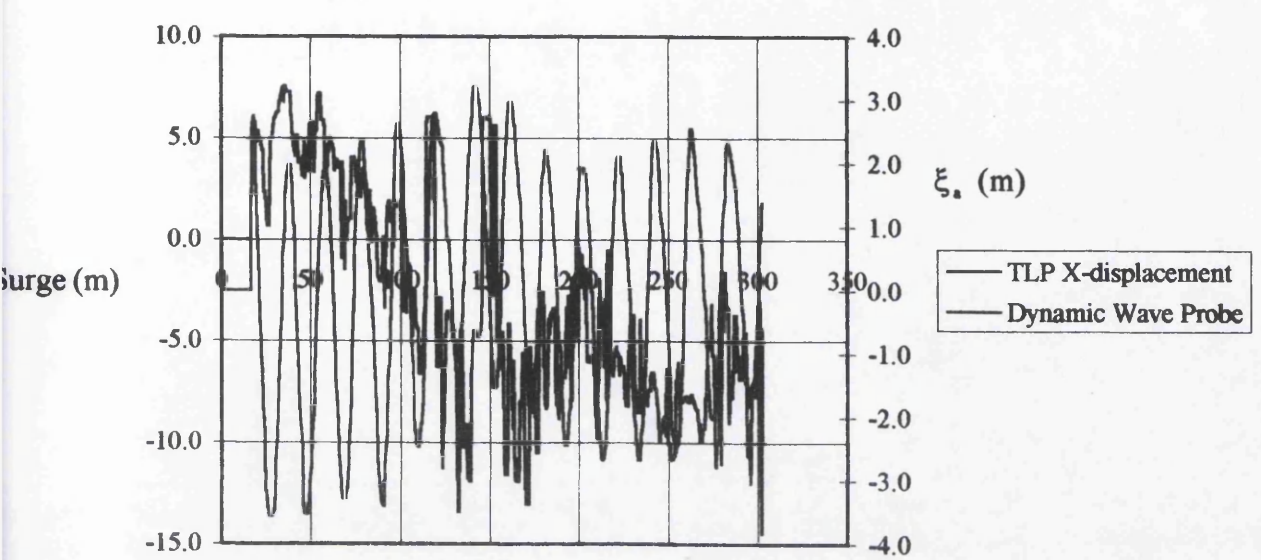

Figure 5.17: TLP X-displacement

(Head Sea, PT=0N, ω =0.31rad/s, ξ_a =3.5m, Current=4.1m/s)

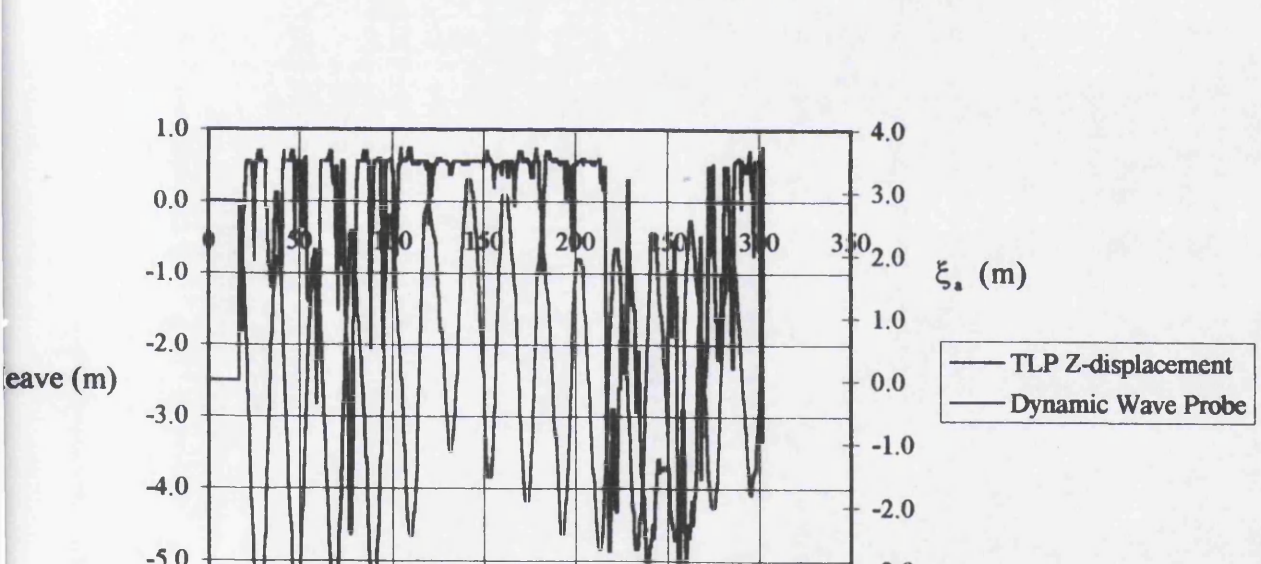

Figure 5.18: TLP Z-displacement

(Head Sea, PT=0N, ω =0.31rad/s, ξ_a =3.5m, Current=4.1m/s)

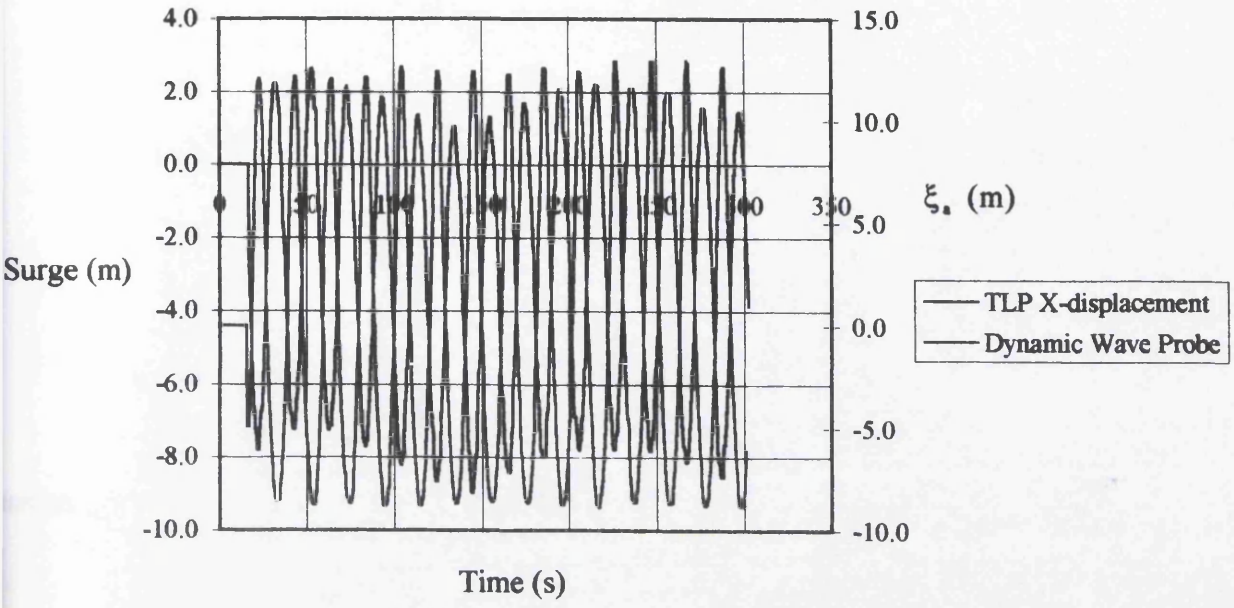

Figure 5.19: TLP X-displacement

(Head Sea, PT=15.148x10^{6}N, ω =0.31rad/s, ξ_a =14.1m)

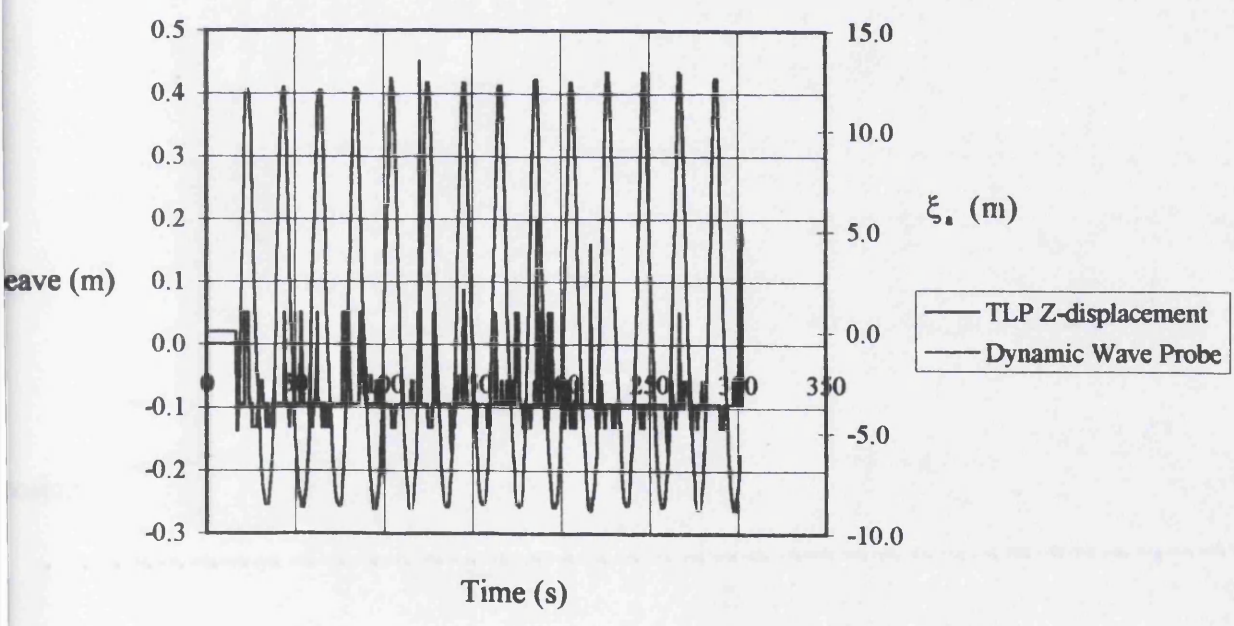

Figure 5.20: TLP Z-displacement

(Head Sea, PT=15.148x10^{6}N, ω =0.31rad/s, ξ_a =14.1m)

5.4.3 Tether Installation Dynamic Response (Head Sea)

The case study tether "bundle' axial force time-series installation dynamic response during regular waves for the Head Sea condition are given in Figures 5.21-5.29.

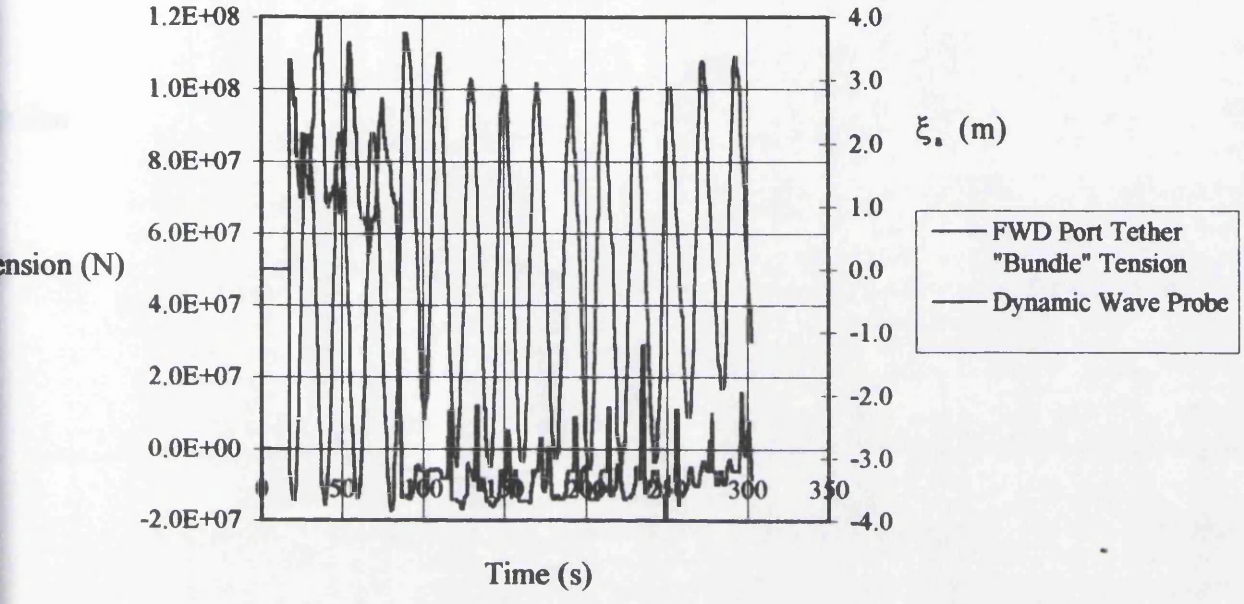

Figure 5.21: FWD Port Tether "Bundle" Tension

(Head Sea, PT=0N, ω =0.31rad/s, ξ_a=3.5m)

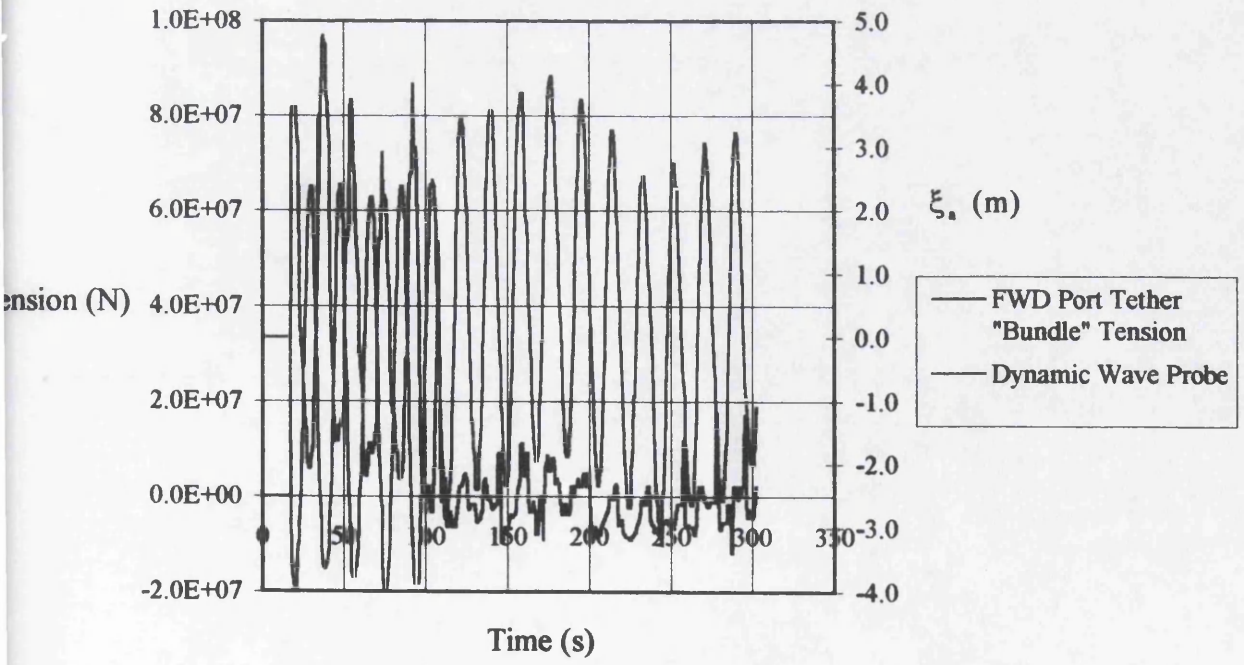

Figure 5.22: FWD Port Tether "Bundle" Tension

(Head Sea, PT=0N, ω =0.34rad/s, ξ_a=3.5m)

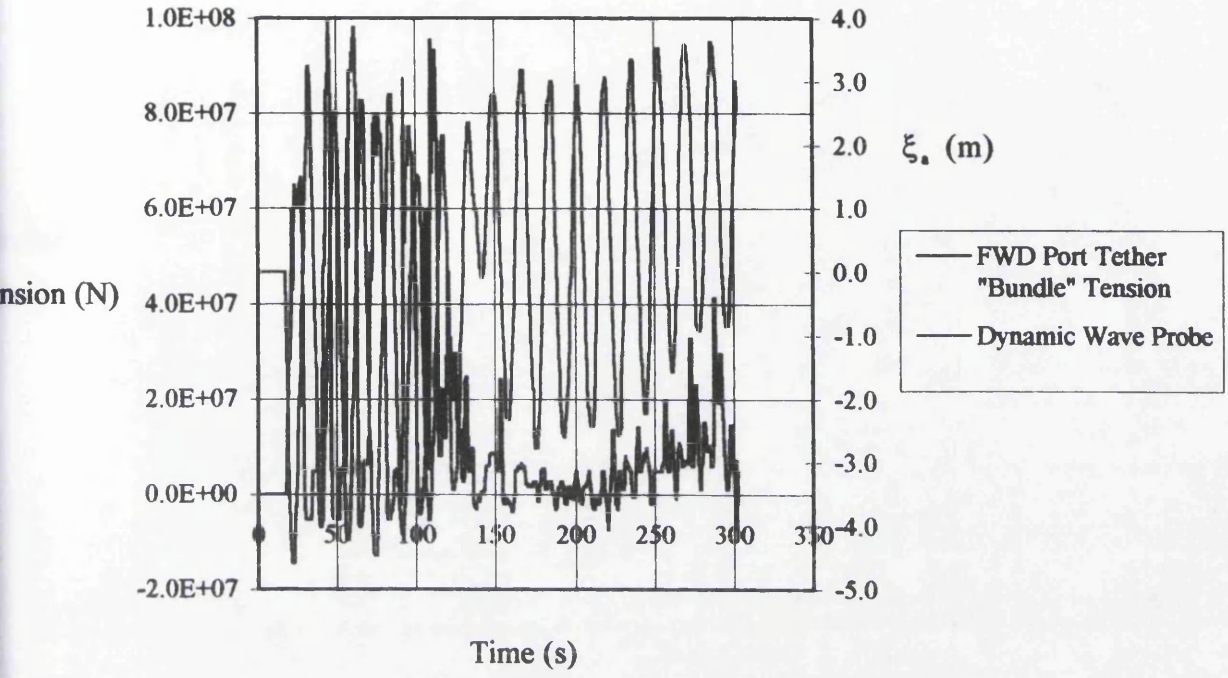

Figure 5.23: FWD Port Tether "Bundle" Tension

(Head Sea, PT=0N, ω =0.37rad/s, ξ_a =3.5m)

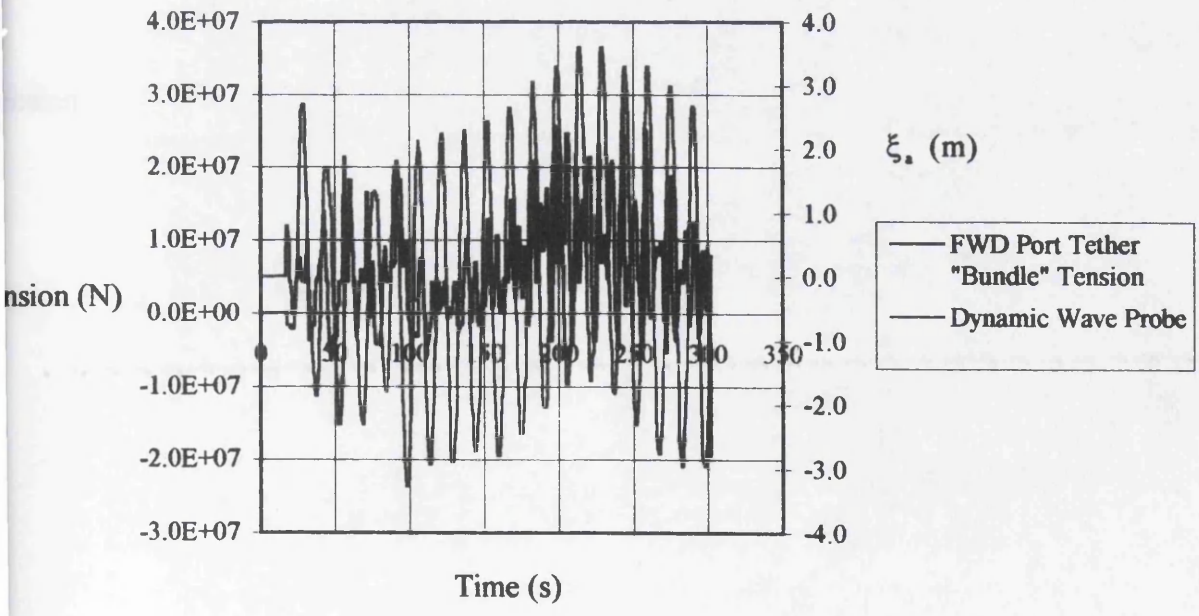

Figure 5.24: FWD Port Tether "Bundle" Tension

(Head Sea, PT=0N, ω =0.42rad/s, ξ_a =3.5m)

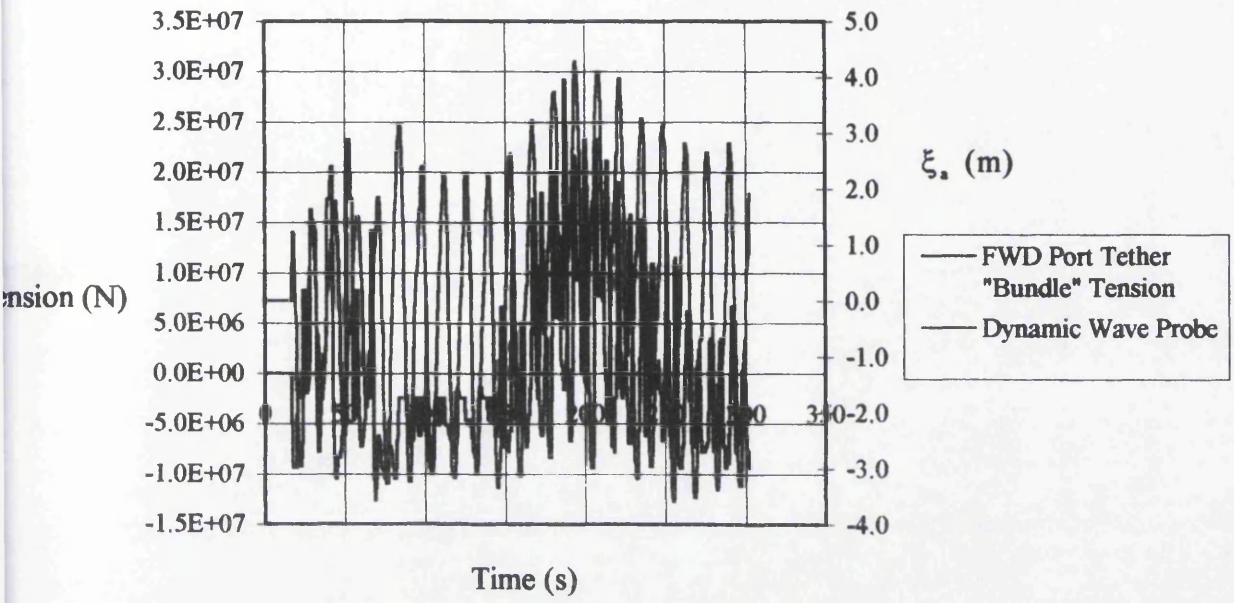

Figure 5.25: FWD Port Tether "Bundle" Tension

(Head Sea, PT=0N, ω =0.47rad/s, ξ_a =3.5m)

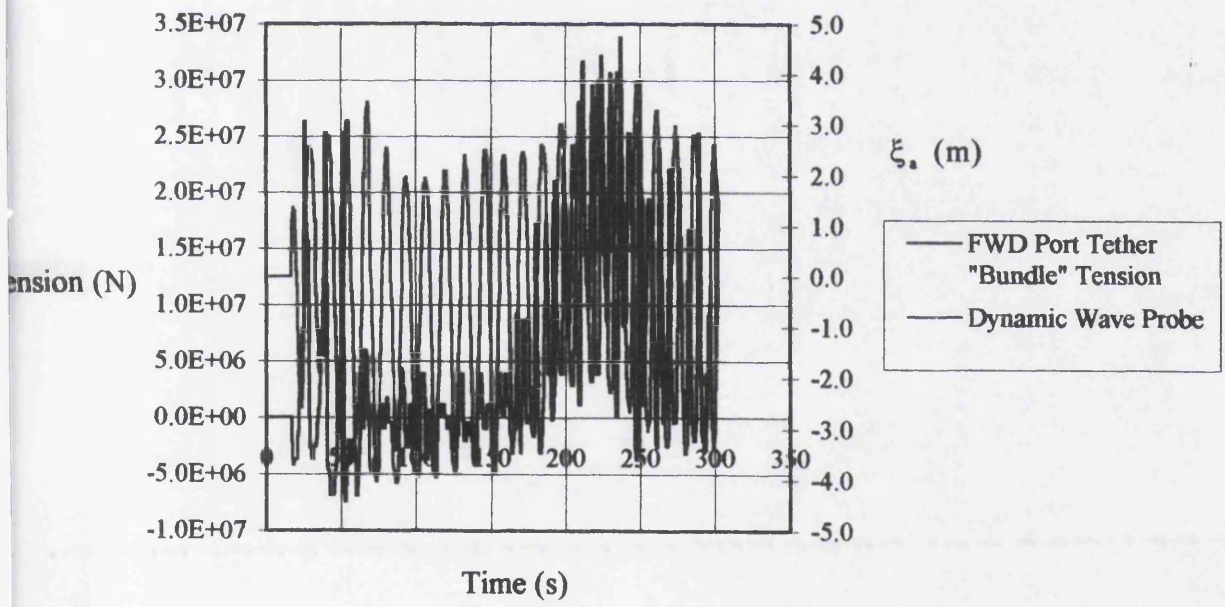

Figure 5.26: FWD Port Tether "Bundle" Tension

(Head Sea, PT=0N, ω =0.53rad/s, ξ_a =3.5m)

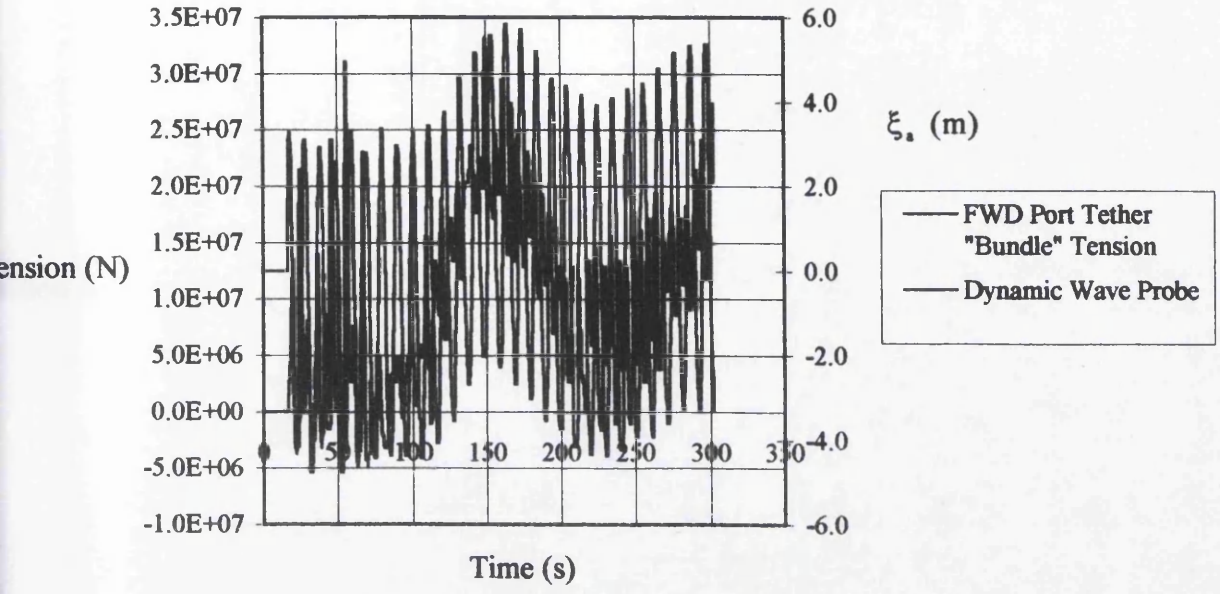

Figure 5.27: FWD Port Tether "Bundle" Tension

(Head Sea, PT=0N, ω =0.62rad/s, ξ_a =3.5m)

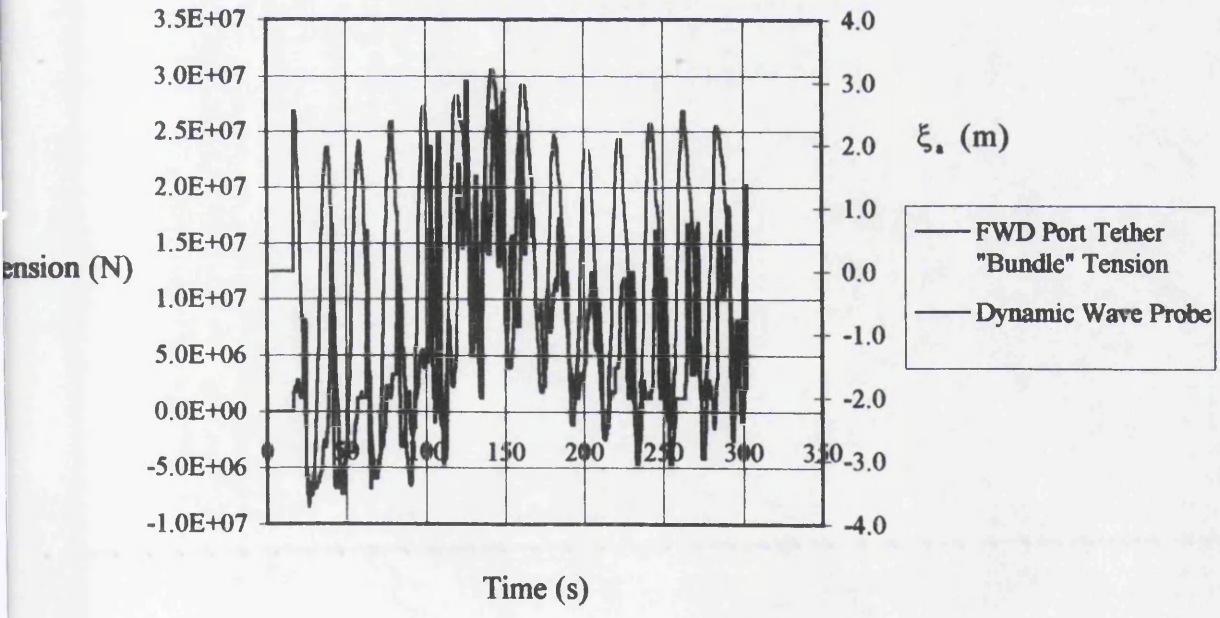

Figure 5.28: FWD Port Tether "Bundle" Tension

(Head Sea, PT=0N, ω =0.31rad/s, ξ_a =3.5m, Current=4.1m/s)

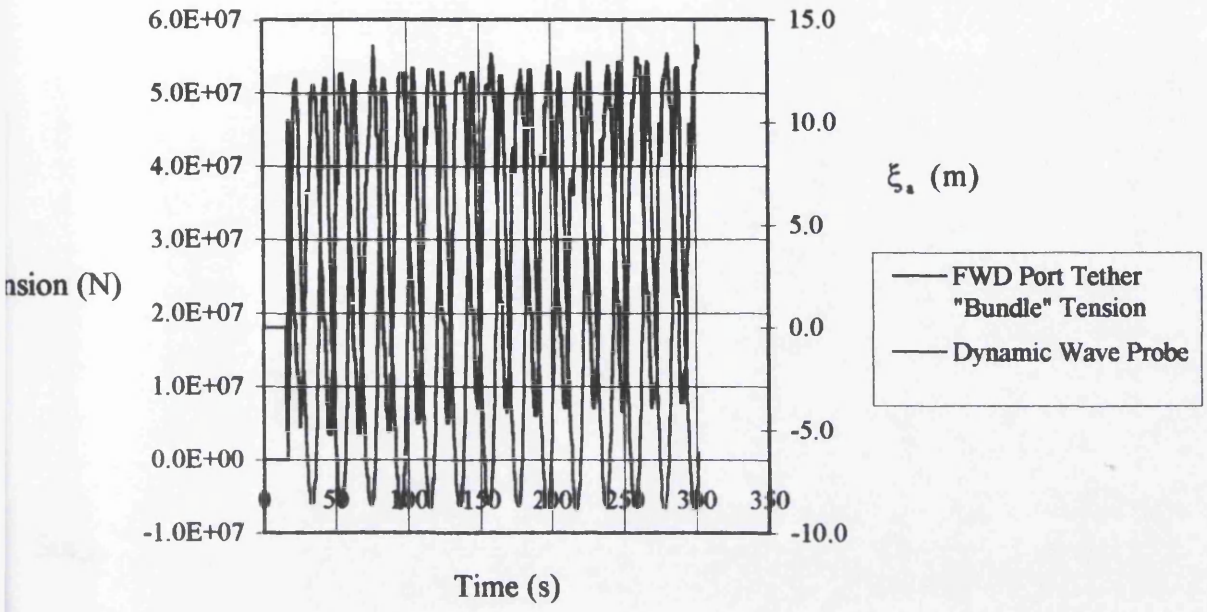

Figure 5.29: FWD Port Tether "Bundle" Tension

(Head Sea, PT=15.148x10^{6}N, ω =0.31rad/s, ξ_a =14.1m)

5.4.4 TLP Installation Dynamic Response (Quartering Sea)

The case study TLP translational DOF displacement installation dynamic response during regular waves for the Quartering Sea condition are given in Figures 5.30-5.35.

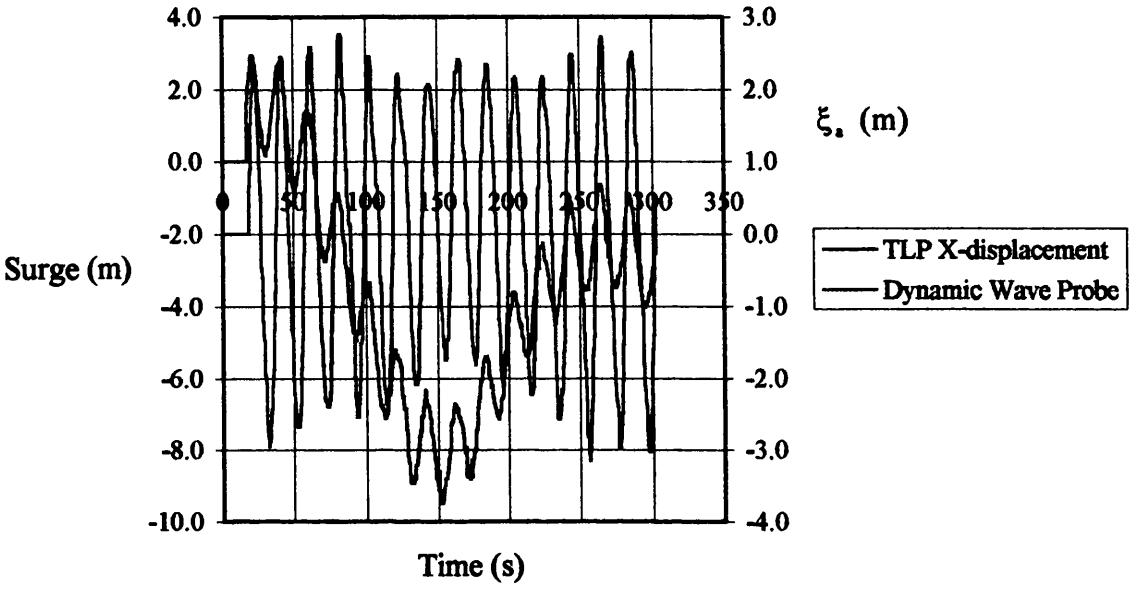

Figure 5.30: TLP X-displacement

(Quartering Sea, PT=0N, ω =0.31rad/s, ξ_a =3.5m)

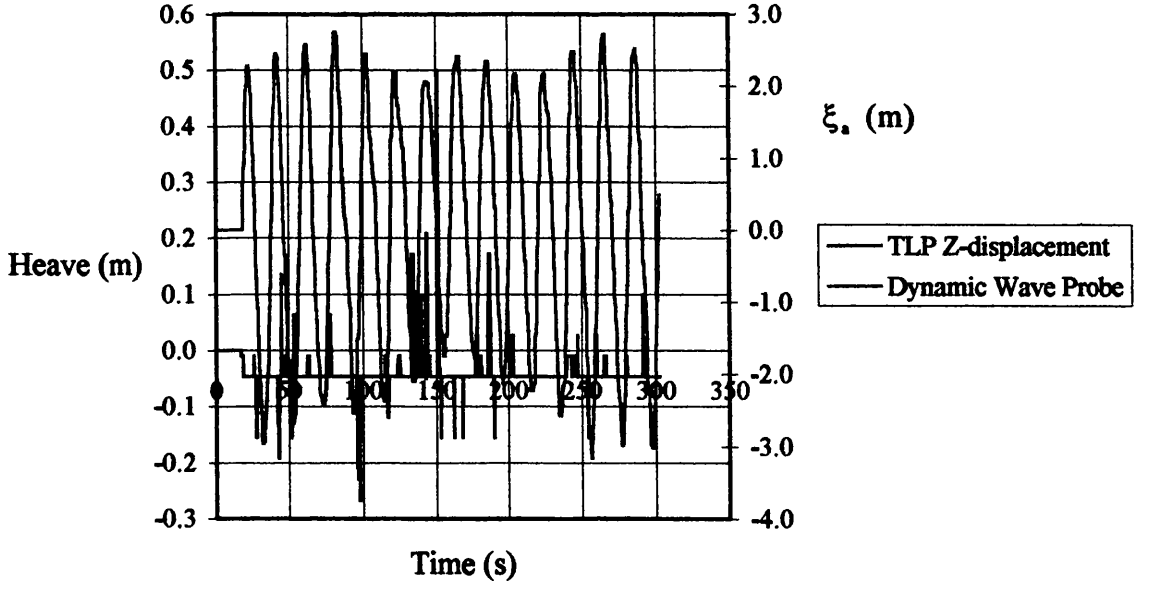

Figure 5.31: TLP Z-displacement

(Quartering Sea, PT=0N, ω =0.31rad/s, ξ_a =3.5m)

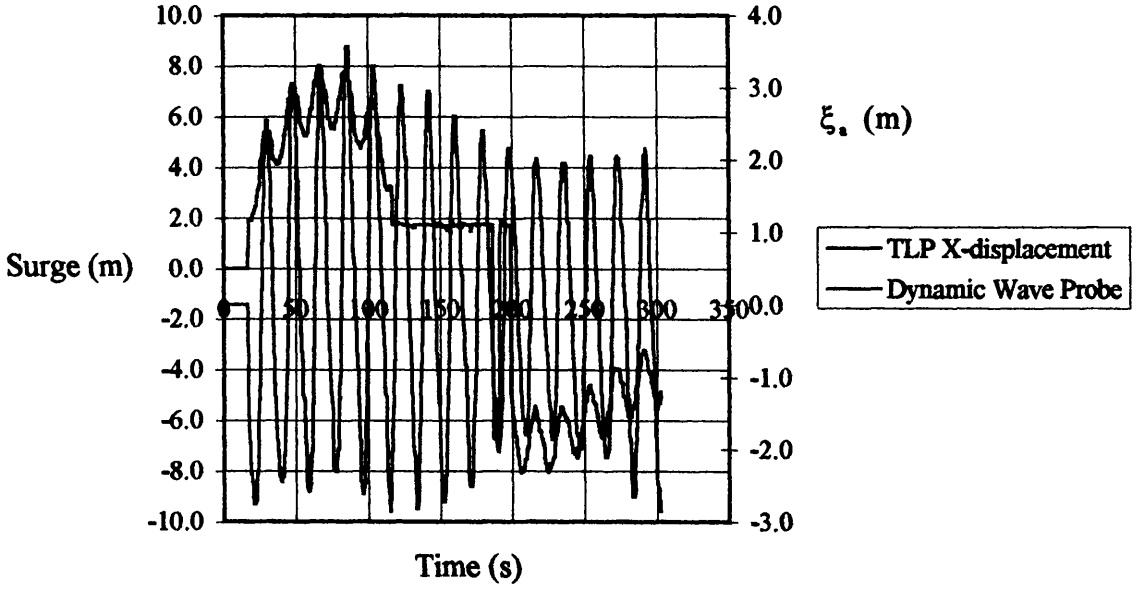

Figure 5.32: TLP X-displacement

(Quartering Sea, PT=0N, ω =0.34rad/s, ξ_a =3.5m)

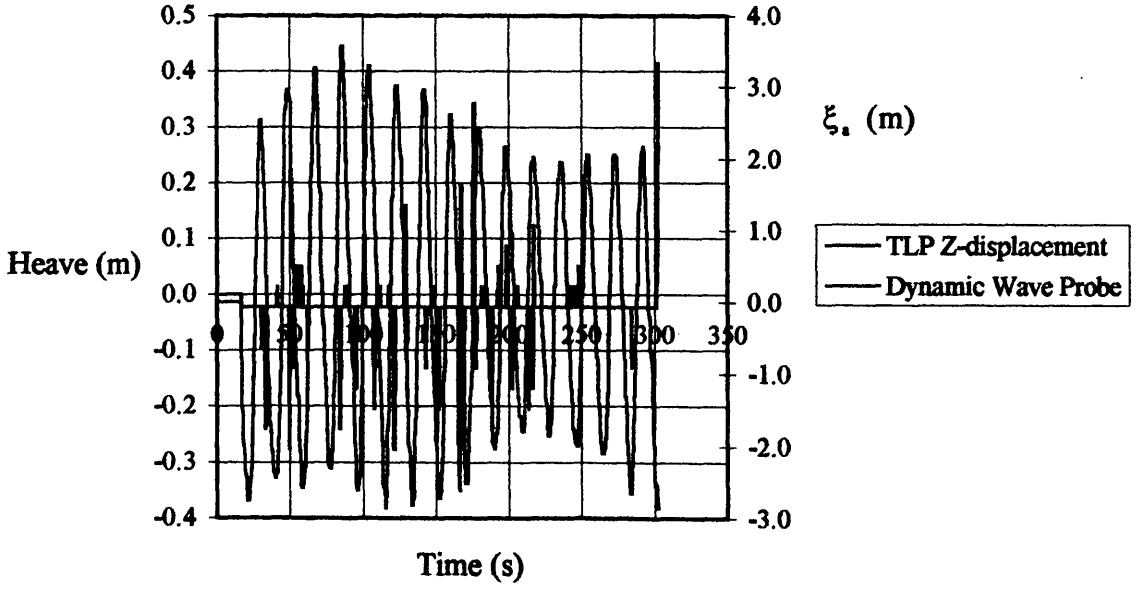

Figure 5.33: TLP Z-displacement

(Quartering Sea, PT=0N, ω =0.34rad/s, ξ_a =3.5m)

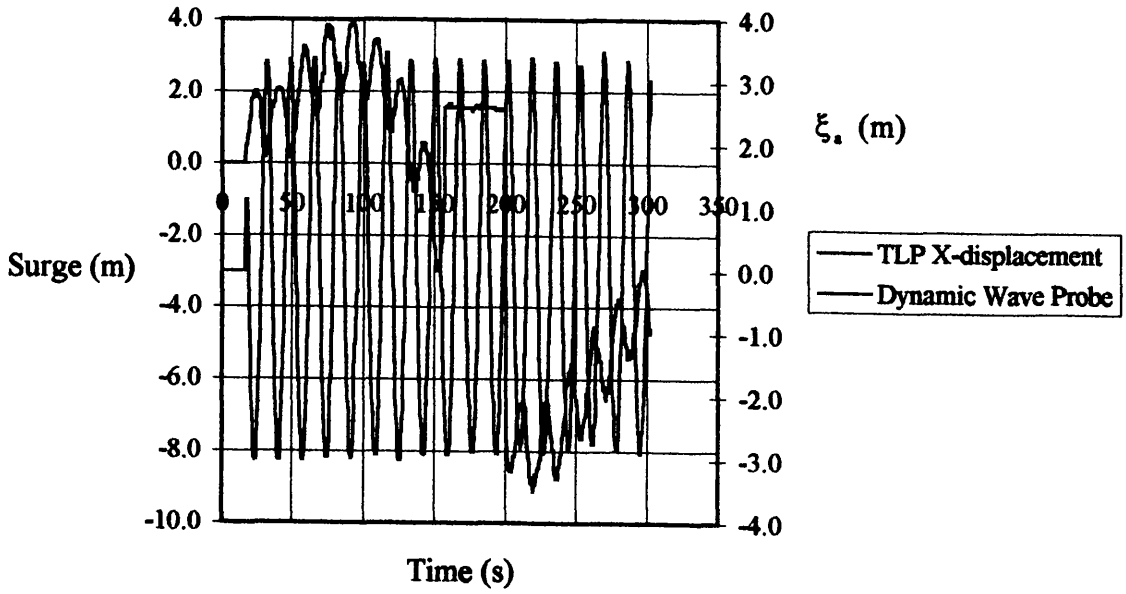

Figure 5.34: TLP X-displacement

(Quartering Sea, PT=0N, ω =0.37rad/s, ξ_a =3.5m)

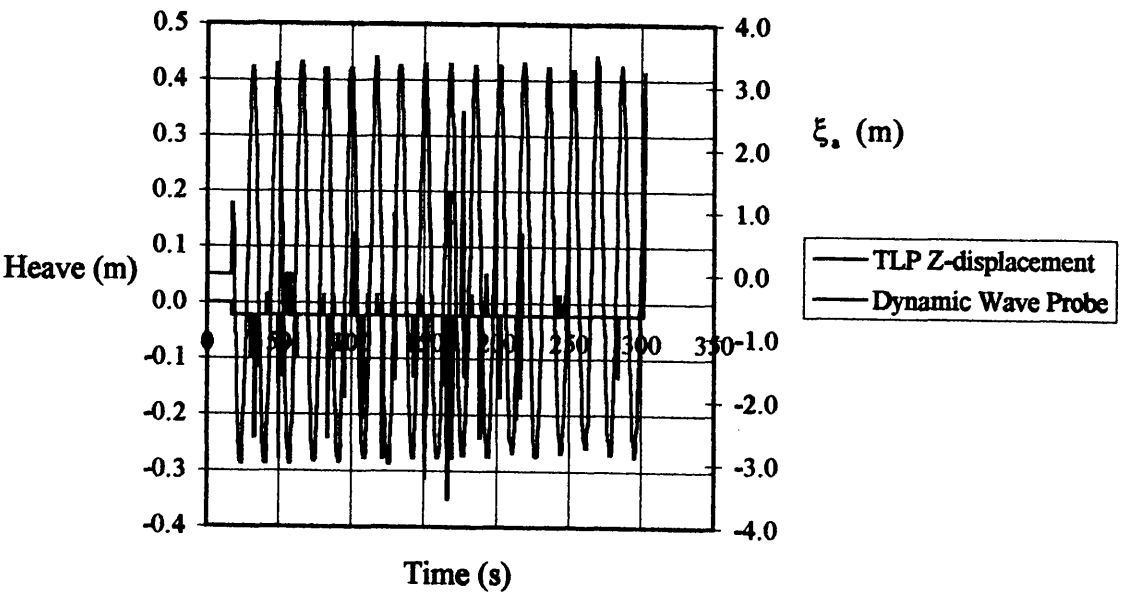

Figure 5.35: TLP Z-displacement

(Quartering Sea, PT=0N, ω =0.37rad/s, ξ_a =3.5m)

5.4.4 TLP Installation Dynamic Response (Quartering Sea)

The case study TLP translational DOF displacement installation dynamic response during regular waves for the Quartering Sea condition are given in Figures 5.36-5.38.

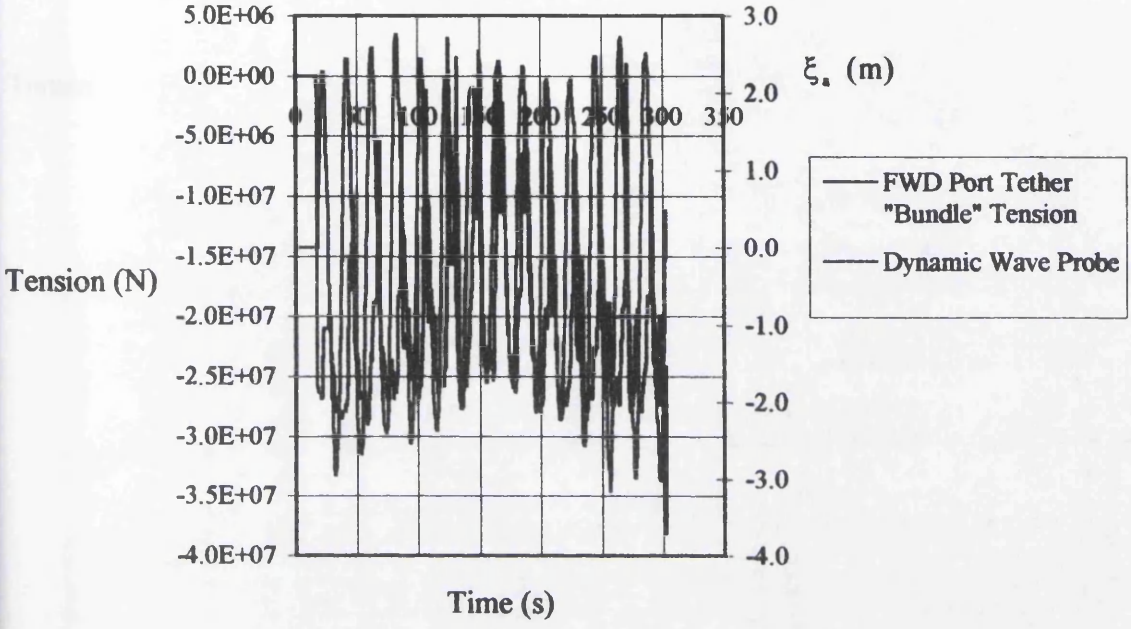

Figure 5.36: FWD Port Tether "Bundle" Tension

(Quartering Sea, PT=0N, ω =0.31rad/s, ξ_a =3.5m)

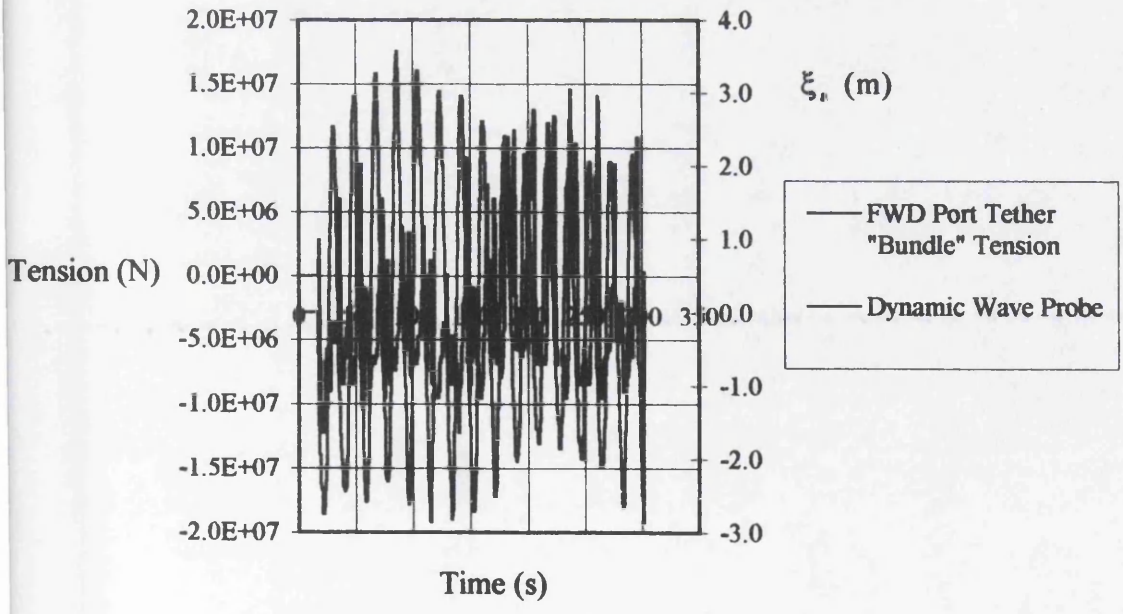

Figure 5.37: FWD Port Tether "Bundle" Tension

(Quartering Sea, PT=0N, ω =0.37rad/s, ξ_a =3.5m)

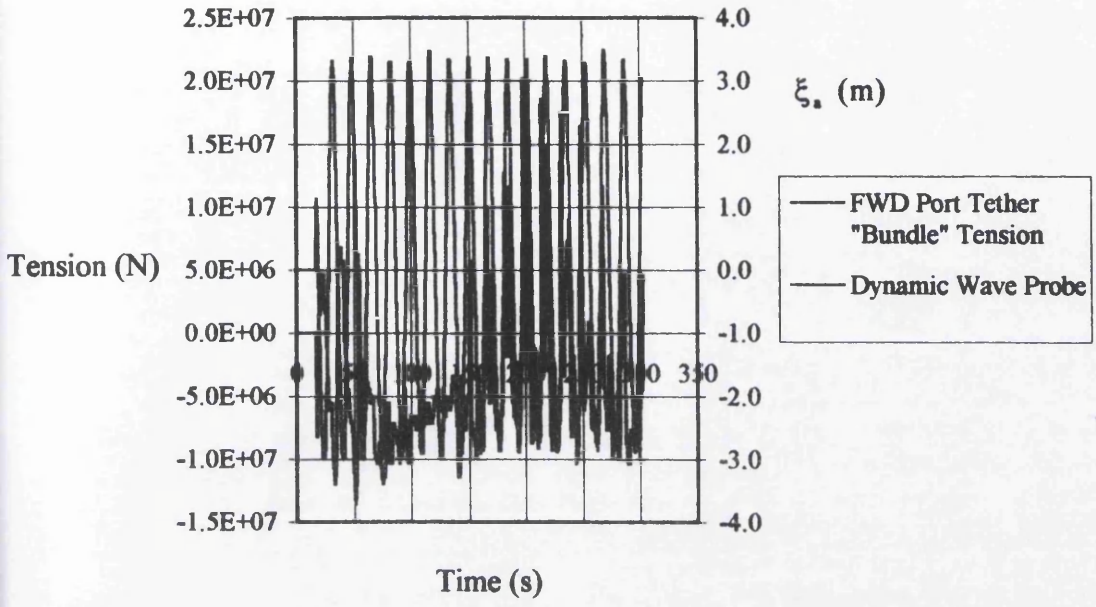

Figure 5.38: FWD Port Tether "Bundle" Tension

(Quartering Sea, PT=0N, ω =0.37rad/s, ξ_a =3.5m)

5.5 Comparisons

5.5.1 Comparisons Between Experimental and Predicted Data

Selected results are given in Figure 5.39-5.50 detailing comparisons between the experimental data (red curves) and the simulated data (blue curves). Refer to Chapter 4 for details of simulations (Phase 1 JURA model).

The procedure adopted during the experimental runs was as follows: the model was held restrained in surge/sway and yaw but free in heave roll and pitch; the wave-maker was stated and the waves generated; once the waves had developed and were passing the model it was released; the data acquisition system was stared a few seconds before releasing the model.

The above procedure results in trends evident in the experimentally sampled time-series: an initial transient region whilst the model is restrained in surge/sway and yaw, but free in heave, roll and pitch; then a sharp reduction in tension levels as drift develops and the transient cease to occur. It was observed that during the initial transient region the tension oscillations occurred around a non-zero mean. This is considered to have been due to: tether system dynamics and friction in the restraining system used during the experiments.

Tether System Modeling

The tethers used in the experimental investigation consisted of 4No. 0.9mm dia. wires (each modeling a tether bundle). The Young's modulus (E) of a specimen section of wire was established by non destructive testing prior to the experimental programme. Due to practical limitations it was not possible to match the prototype tether axial stiffness in the model scale (due to the constant E value, this would require a wire dia. of 0.2mm for mild steel).

The option of low E materials was considered but rejected due to uncertainty regarding the linearity of the response. The dia. and material chosen for the experimental setup led to a heave natural period ~1/3 of the prototype value.

The end fixings on the tether bundle wires consisted of: a soldered collar with the wire free to slide vertically (when compression develops) through a clearance hole in a mounting block at the hull/tether connection; and a mounting block fixed to the *Novatech* load cell with the tether bundle wire held in a clearance hole with a grub screw at the tether/foundation connection.

The numerical simulations for the Heidrun TLP for comparison with the experimental data were conducted for the same mooring system characteristics as that represented in the model tests. This therefore allows a valid comparisons between experimental and simulation data to be made. The shorter heave natural period would reduce the occurrence of tether/TLP system heave resonance response. The possible effect of this on the tether transient response could only be accurately investigated by further experimental work with the actual heave natural period more closely matched.

To avoid numerical instability additional damping in the heave DOF was applied. This additional damping consisted of 0.25% of the installed critical damping in Heave ($C_{cr(Heave)}$, based on the scaled to prototype model decay test results).

Figures 5.39-5.42 detail comparisons between the experimental data and the simulated data for the head sea condition, ω =0.32rad/s, ξ_a=3.523m, PT=0N.

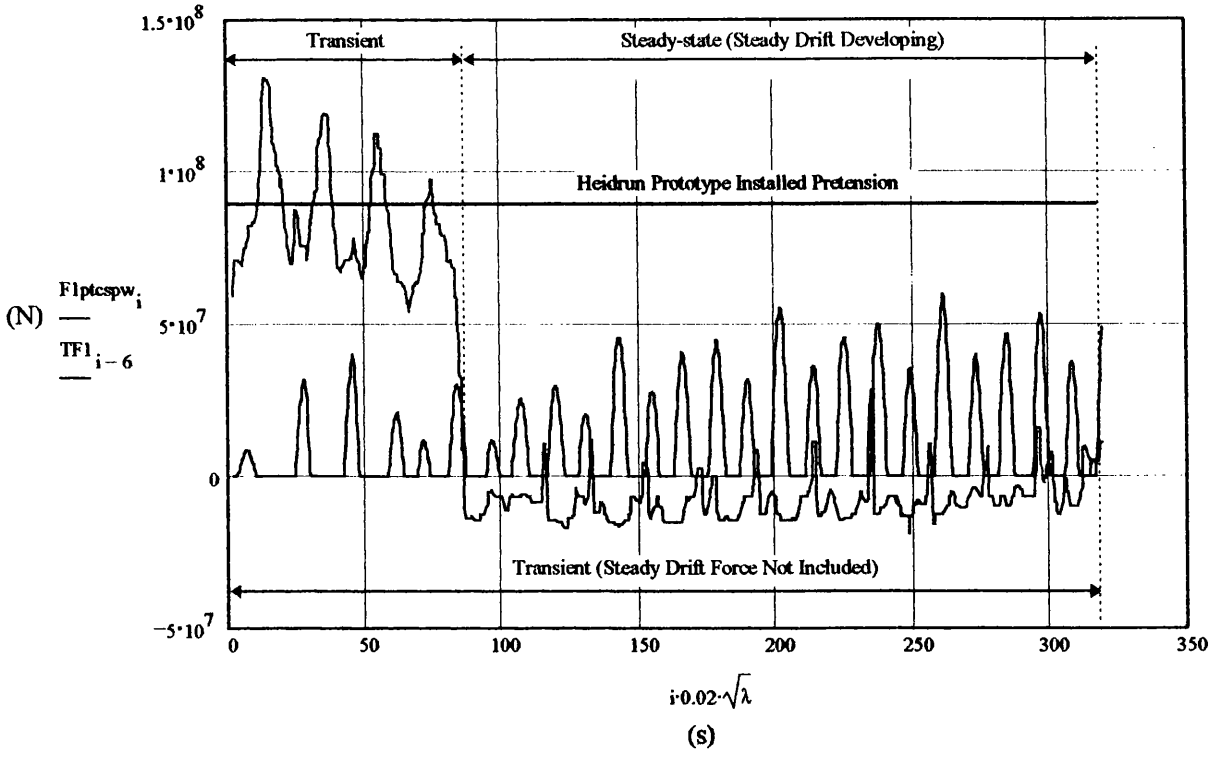

Figure 5.39: Tether Bundle Force Time-series Comparison (FWD Port)

(HS, ω =0.32rad/s, ξ_a=3.523m)

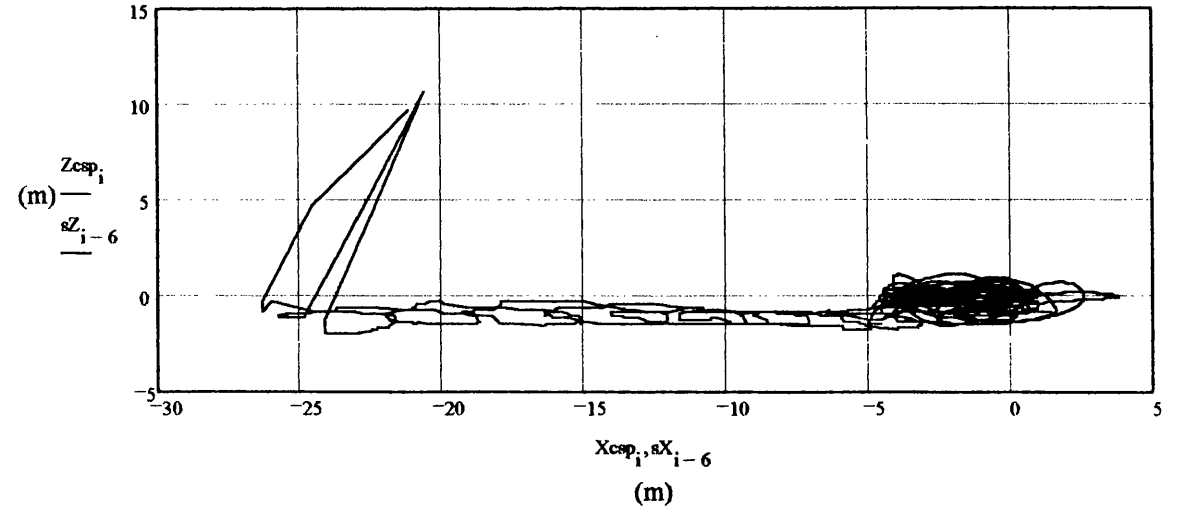

Figure 5.40: Heave v Surge Plane Comparison

(HS, ω =0.32rad/s, ξ_a=3.523m)

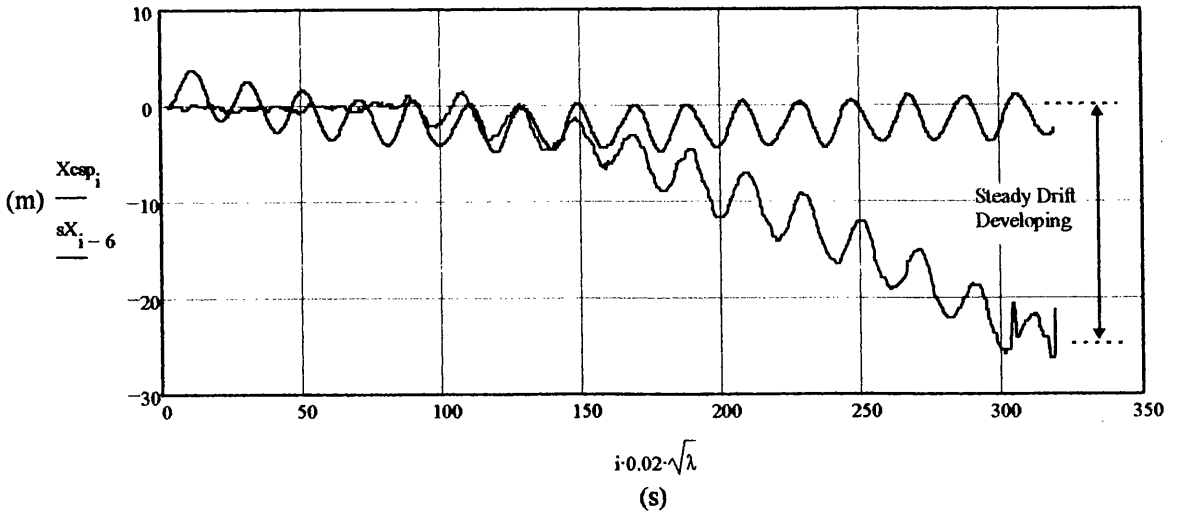

Figure 5.41: Surge Displacement Time-series Comparison

(HS, ω =0.32rad/s, ξ_a=3.523m)

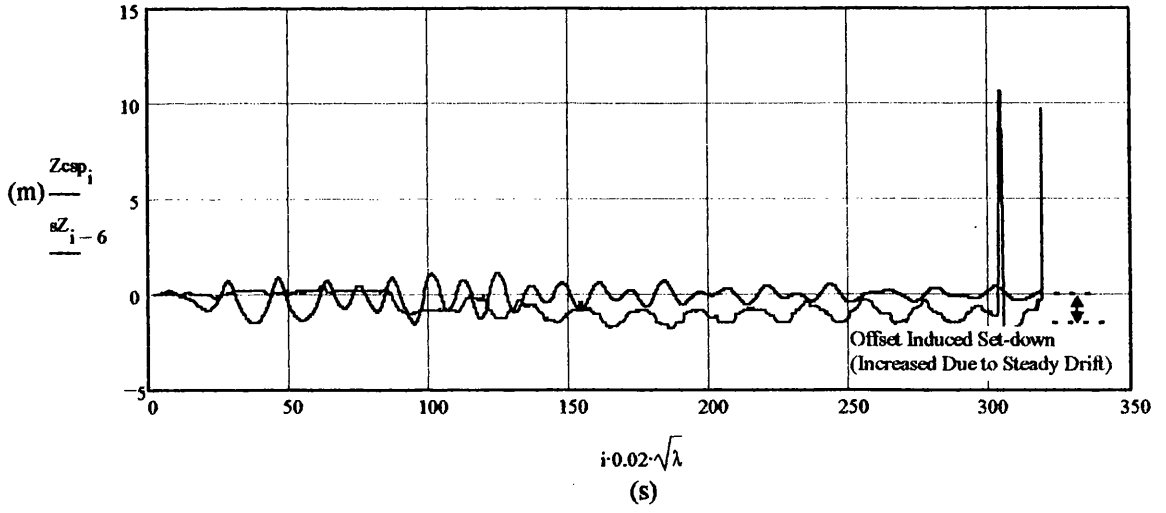

Figure 5.42: Heave Displacement Time-series Comparison

(HS, ω =0.32rad/s, ξ_a=3.523m)

Figures 5.43-5.46 detail comparisons between the experimental data and the simulated data for the head sea condition, ω =0.32rad/s, ξ_a=3.523m. The pretension ramp function applied was as follows (below):

$$F_{Pretension} = \begin{cases} \left[\frac{0.125\left(\sum_{n=1}^{NT} PT_n\right)}{0.25Nstep}\right](t-(0.25Nstep)) \text{ if } 0.25Nstep \le t \le 0.5Nstep \\ \left[0.125\left(\sum_{n=1}^{NT} PT_n\right)\right] + \left[\frac{0.375\left(\sum_{n=1}^{NT} PT_n\right)}{0.25Nstep}\right](t-(0.5Nstep)) \text{ if } 0.5Nstep \le t \le 0.75Nstep \\ 0.125\left(\sum_{n=1}^{NT} PT_n\right) + 0.375\left(\sum_{n=1}^{NT} PT_n\right) + \left[\frac{0.5\left(\sum_{n=1}^{NT} PT_n\right)}{0.25Nstep}\right](t-(0.75Nstep)) \text{ if } 0.75Nstep \le t \le Nstep \\ 0 \text{ otherwise} \end{cases} \quad (5\text{-}1)$$

The total excitation force in heave at a given time-step being the resultant of the superposition of the force due to pretension and the 1st order wave force. The limit of the pretension ramp function was 22.688×10^6N which is equivalent to one quarter of the installed Heidrun value.

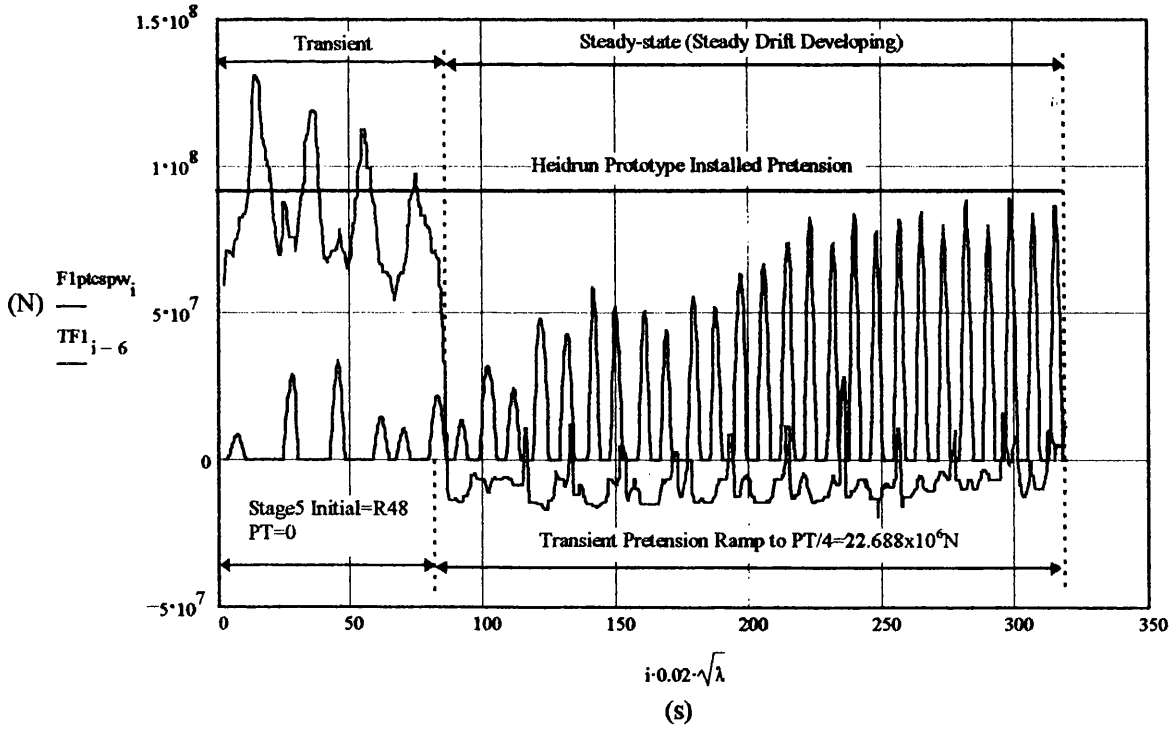

Figure 5.43: Tether Bundle Force Time-series Comparison (FWD Port)

(HS, ω =0.32rad/s, ξ_a=3.523m)

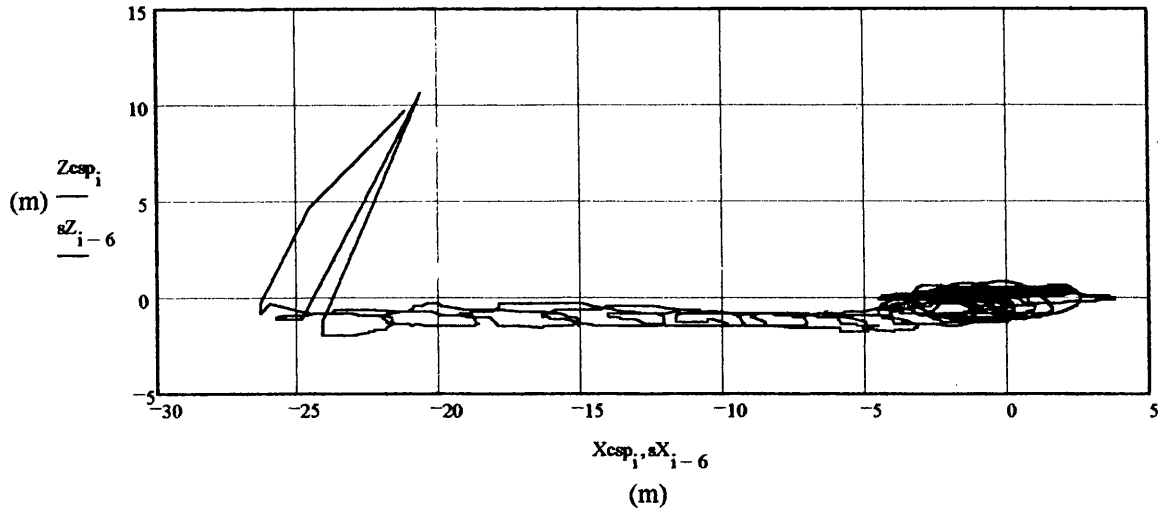

Figure 5.44: Heave v Surge Plane Comparison

(HS, ω =0.32rad/s, ξ_a=3.523m)

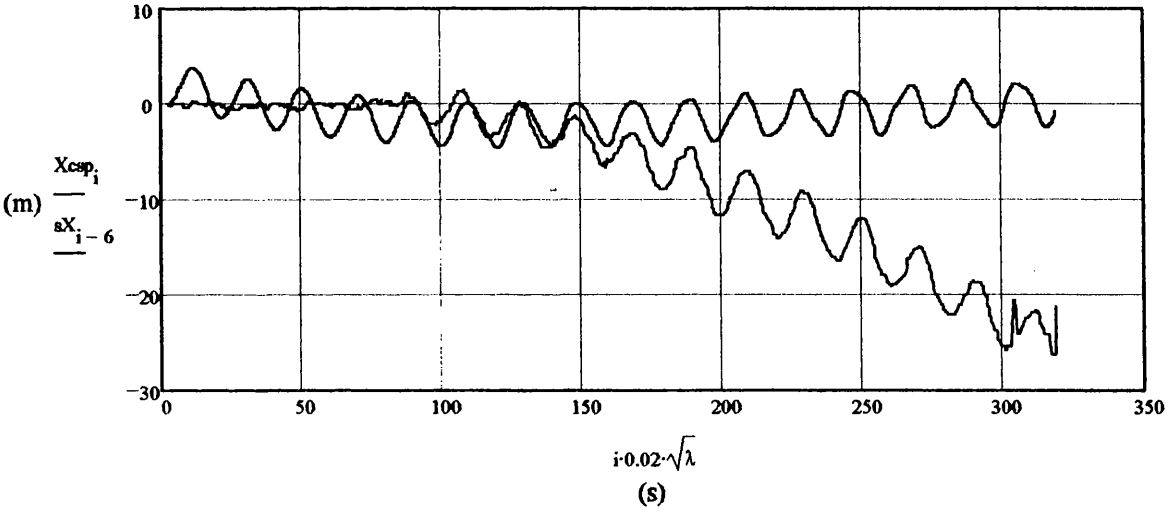

Figure 5.45: Surge Displacement Time-series Comparison

(HS, ω =0.32rad/s, ξ_a=3.523m)

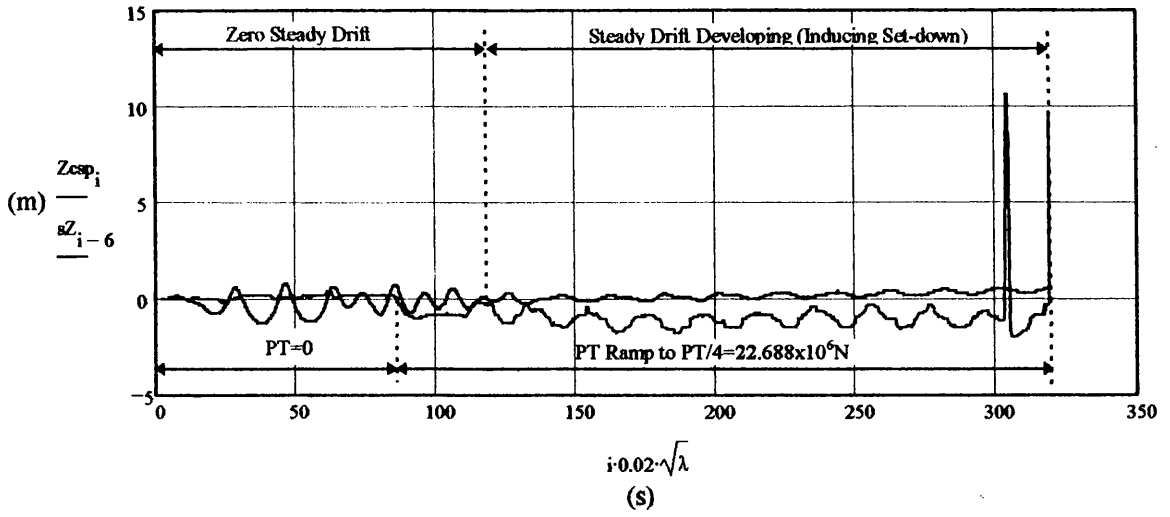

Figure 5.46: Heave Displacement Time-series Comparison

(HS, ω =0.32rad/s, ξ_a=3.523m)

Figure 5.47 compares experimental data for without and with current effects for the Head Sea condition, ω =0.32rad/s, ξ_a=3.523m, PT=0N. The current simulated represents an extreme ~8knot current (UDL) prototype scale (this unrealistic extreme value due to physical modeling limitations). The solid red curve is the without current time-series with the dotted the with current time-series.

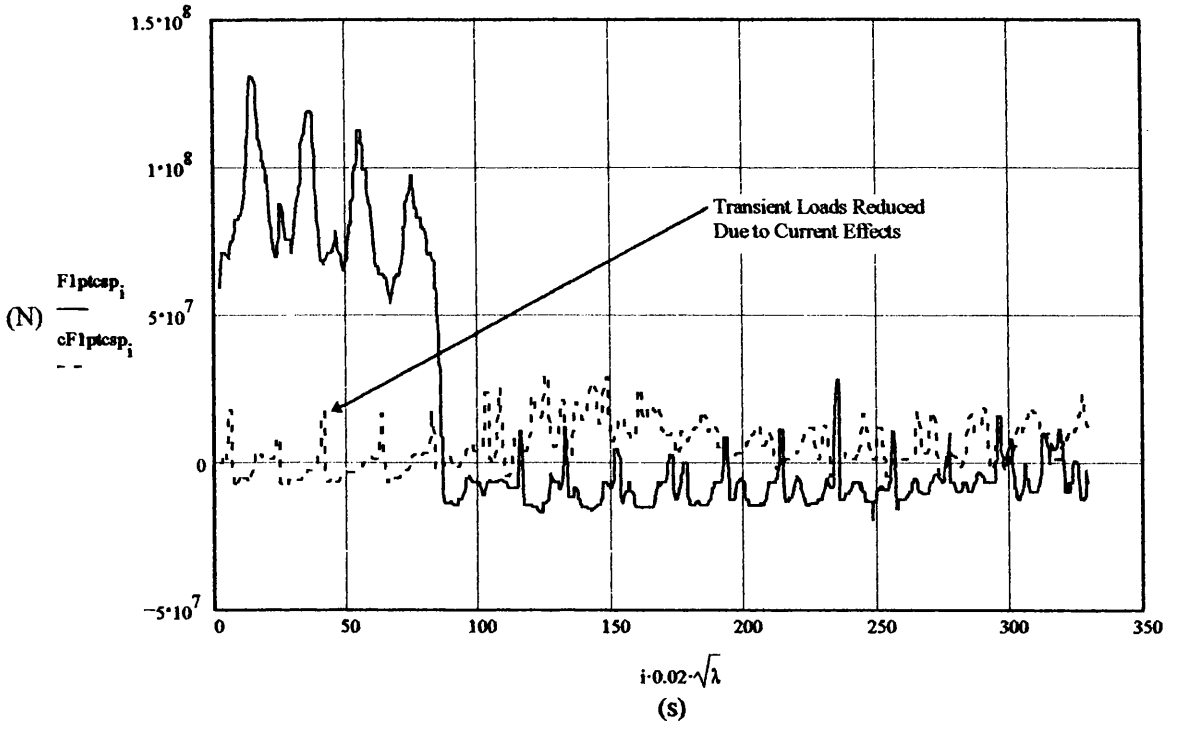

Figure 5.47: Tether Bundle Force Time-series Comparison (FWD Port)

(HS, ω =0.32rad/s, ξ_a=3.523m, Without/with Current)

Figure 5.48 compares the experimental data and the simulated data for the quartering sea condition, ω =0.62rad/s, ξ_a=3.523m, PT=0N.

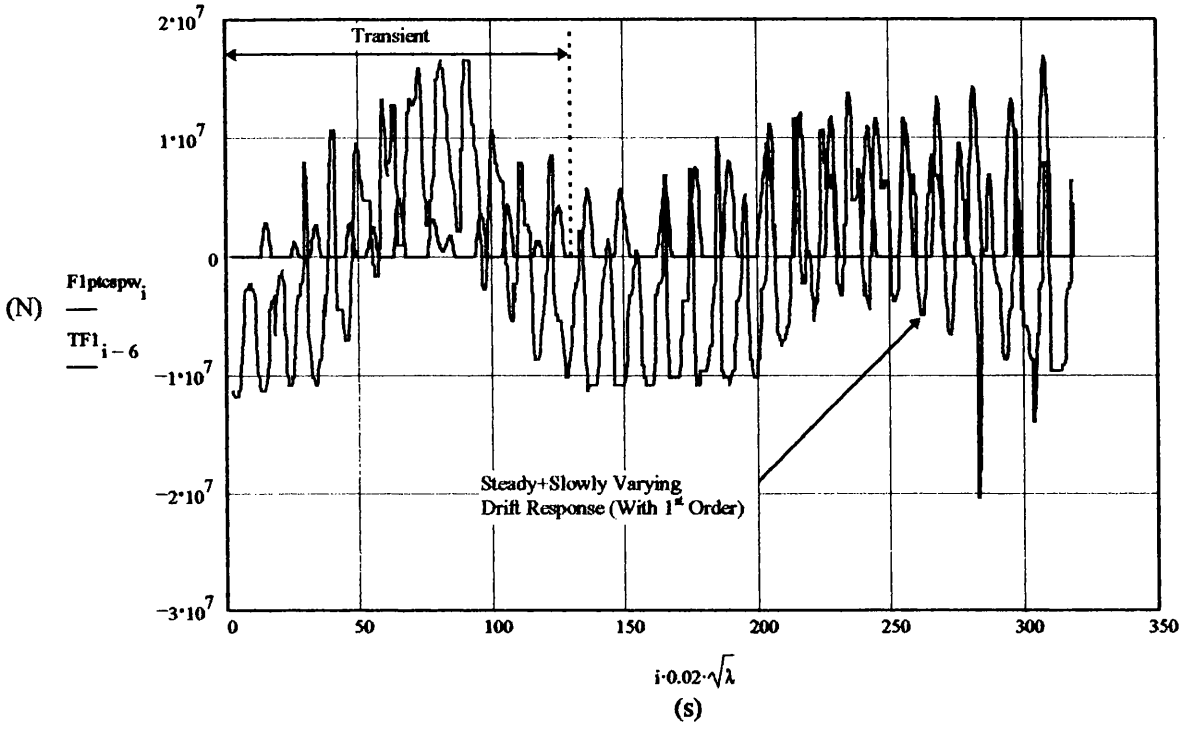

Figure 5.48: Tether Bundle Force Time-series Comparison (FWD Port)

(QS, ω =0.62rad/s, ξ_a=3.523m)

Figure 5.49 compares experimental data for without and with current effects for the quartering sea condition, ω =0.62rad/s, ξ_a=3.523m, PT=0N.

Figure 5.50 compares experimental data for without and with initial Surge offset (7m) for the quartering sea condition, ω =0.62rad/s, ξ_a=3.523m, PT=0N. The solid red curve is the without offset time-series with the dotted the with offset time-series.

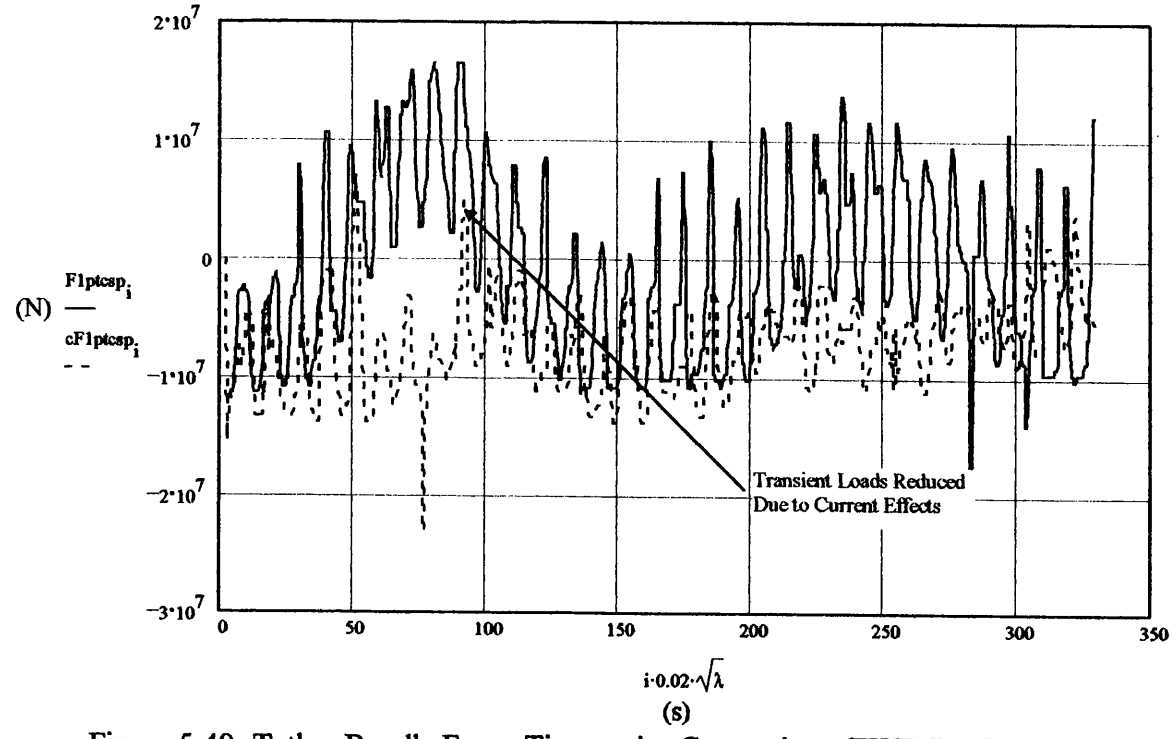

Figure 5.49: Tether Bundle Force Time-series Comparison (FWD Port)
(QS, ω =0.62rad/s, ξ_a=3.523m, Without/with Current)

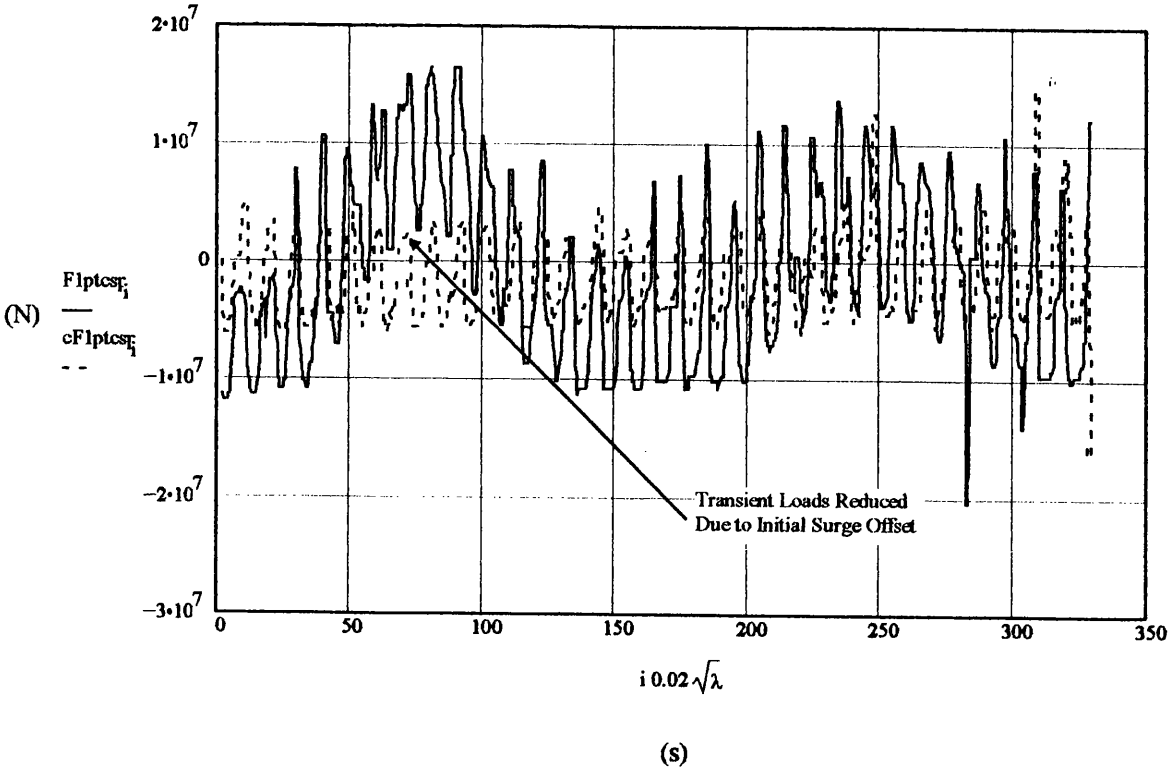

Figure 5.50: Tether Bundle Force Time-series Comparison (FWD Port)
(QS, ω =0.62rad/s, ξ_a=3.523m, Without/with Initial Surge Offset)

5.5.2 Discussion of Comparisons

An experimental investigation into the coupled tether/TLP response at low pretension has been successfully completed. The experimental data was been utilised to perform validation studies on the Phase 1 simulation software developed under the BP-EPSRC Case Studentship. Comparisons have been made between the experimental and simulation data for installed and zero pretension conditions.

For the head sea condition (installed) the Phase 1 software simulation yields a maximum FWD Port Tether "Bundle" axial tension of 6.18×10^7N and a minimum of 1.799×10^6N for an incident regular wave of $\omega = 0.32$rad/s and $\xi_a = 14.09$m. These wave parameters were considered to represent an extreme wave event and would include considerable nonlinear effects. The experimentally sampled time-series for the same extreme wave event yield a maximum FWD Port Tether "Bundle" axial tension of 5.652×10^7N and a minimum of 4.541×10^6N. It is considered that this overprediction of the maximum and underprediction of the minimum tensions are a function of tether dynamic effects due to fluid excitation and reaction forces acting on the tether system. During the course of the experimental programme considerable tether dynamics were observed via the CCD underwater video camera; especially at low pretension levels. At low pretension (during a wave cycle) the tether system developed a fluid loading/self weight induced sagging which maintained positive pretension prevented the tethers slacking.

Figure 5.39, details the comparison between the simulated and experimental data for the head sea condition (FWD Port tether "bundle" time-series), $\omega = 0.32$rad/s, $\xi_a = 3.523$m, PT=0N. A significant under-prediction is present for the transient region of the time-series (0-80s): simulated maximum transient axial tension=4.015×10^7N; experimental maximum transient axial tension=1.308×10^8N.

Subsequent investigation of the model mean heave position (before experimental run) for the head sea runs revealed an initial displacement of ~1m (model scale=3.4mm).

This indicates that the tethers had zero pretension and were "slack", i.e., the tether length was greater than the vertical distance between the tether/hull node and the foundation node. This "slack" (which was not included in the simulation) allowed higher accelerations to develop in the heave and pitch modes and contributed to the higher experimentally derived transient axial tension.

Figure 5.40, compares the surge displacement for the experimental and simulation data ω=0.32rad/s, ξ_a=3.523m, PT=0N. A large offset develops in the experimental case due to drift forces and the tether "slack" allowing increased offset before sufficient offset induced pretension occurs to equate the steady drift force. It is understood the effect of steady drift in regular waves is more pronounced than that of irregular waves due the "mean" nature of the drift forces developed in irregular sea-states. In irregular sea-states this "mean" being representative of all the wave frequencies and amplitude present in the sea-state. The simulation data does not include steady drift and therefore does not match the experimental measurements with respect to this trend. However examination of the 1st order surge displacement components present in both the simulated and experimental data do compare well. Considering this Figure in conjunction with the Figure 5.39 reveals the significant reduction effect that the steady drift produces on the tether "bundle" time-series transient response.

Figure 5.41, details the comparison between the simulated and experimental data for the head sea condition (FWD Port tether "bundle" time-series), ω=0.32rad/s, ξ_a=3.523m, with pretension ramp function as defined by equation (5-1). The under-prediction present in Figure 5.39 is subsequently reduced for the transient region of the time-series (0-80s): simulation maximum transient axial tension=8.88x10^{7}N. This increase in the maximum simulated transient axial tension being due to an increased heave force, representing the deballast operations, resulting in higher heave accelerations.

Figure 5.42, compares the experimental data sampled for the head sea condition (FWD Port tether "bundle" time-series), ω =0.32rad/s, ξ_a=3.523m, PT=0N, both without and with current effects present. The overall effect of the applied current loading is to reduce the maximum transient axial tension developed ($1.803x10^7$N compared to $1.308x10^8$N). With reference to the underwater video footage of the tether/tether-hull node behaviour for this condition, a "sagging nature" to the tether system is observed in the initial condition (before wave generation). It is considered that this sagging geometry leads to a softening of the tether mooring system response (especially in the heave, roll and pitch modes). In addition to this, the lateral load (the current loading) acting on the tether system must be overcome as the tether "bundles" are straightened. This process then leads to energy dissipation contributing to the measured reduction in the maximum transient axial tensions.

Figure 5.43, details the comparison between the simulated and experimental data for the quartering sea condition (FWD Port tether "bundle" time-series), ω =0.62rad/s, ξ_a=3.523m, PT=0N. There is good agreement for this case (simulated maximum=$1.92x10^7$N, experimental maximum (for transient region, 0-~120s)=$1.646x10^7$N). Unlike the head sea runs initial mean heave displacements measured before wave generation commenced indicated negligible tether "slack". Significant slowly varying drift force response can be observed. Steady and slowly varying drift effects were not included in the simulation. This is considered justified to permit comparison of the simulation transient response (response without drift effects) with experimental transient response (response sampled before the development of a drift force induced offset leading to the generation of pretension and a steady-state type response).

Figure 5.44, compares the experimental data sampled for the quartering sea condition (FWD Port tether "bundle" time-series), ω =0.62rad/s, ξ_a=3.523m, PT=0N, both without and with current effects present. This comparison illustrates a significant reduction in the maximum transient axial tensions ($7.493x10^6$N compared to $1.646x10^7$N).

The mechanisms governing this reduction are considered to be the same as those described in Figure 5.42.

Figure 5.45, compares the experimental data sampled for the Quartering Sea condition (FWD Port tether "bundle" time-series), ω=0.62rad/s, ξ_a=3.523m, PT=0N, both without and with initial Surge offset present. The overall effect of the Surge offset for this test case and offset magnitude (-7m[1]) is to reduce the maximum transient axial tension measured (9.891×10^6N compared to 1.646×10^7N). However the repeatability of this result is in doubt due to the physical difficulty in maintaining an induced mean offset to the TLP whilst not restraining the 6DOF of the model. It is also worth noting that increasing the induced mean offset to -15.5m leads to an increase in the maximum transient axial tension measured (1.09×10^7N compared to the -7m mean offset value of 9.891×10^6N).

[1] Initial induced Surge offset defined in the Head Sea space-fixed coordinate system, i.e., the Surge displacement is defined perpendicular to the wave-maker with -ve in the direction of wave propagation.

CHAPTER 6

CASE STUDIES

6.1 Introduction to Case Study Objectives

The objectives of the Case Study work was to generate results utilising the completed Phase 1 and Phase 2 software defining areas of possible tether/TLP installation cost reduction. Results from the Case Study simulations were compared where possible with the experimentally derived data (Ref. Chapter 5 and Chapter 7).

Results take the form of time-domain data detailing the TLP motion response (6DOF) and the corresponding tether "bundle" force time-series.

Platform c.g. response in both vertical and horizontal planes were also generated.

6.2 TLP Case Study Data Set

6.2.1 Introduction

3No. TLP geometries representative of the spectrum of TLP hull forms were investigated in anticipated installation metocean conditions with/without motion compensation during pretensioning and in the installed condition:

Case Study TLPs

Parameter	AA	Heidrun	Snorre
Water Depth	375m	345m	345m
Number of Columns	3	4	4
Number of Pontoons	3	4	4
Pontoon Breadth	14m	15.95m	11.5m
Pontoon Depth	14m	13m	11.5m
Column Diameter	28m	31m	25m
Draft	45m	77.3m	37.5m
Mass	95214Tonne	252000Tonne	80000Tonne
VCG	44.3m	58.3m	38.5m
r_{xx}	45.9m	45.5m	42.9m
r_{yy}	47.2m	45.5m	42.9m
r_{zz}	44.9m	56.6m	53.4m
Tether Length	322m	268.6m	310m
Total Pretension	19980Tonne	37000Tonne	22936Tonne
Total Tether Area	$1.55m^2$	$1.063m^2$	$1.157m^2$
Tether Youngs Modulus	$2.07x10^{11}N/m^2$	$2.07x10^{11}N/m^2$	$2.07x10^{11}N/m^2$
K_{surge}	$0.608x10^6N/m$	$1.351x10^6N/m$	$0.726x10^6N/m$
K_{sway}	"	"	"
K_{heave}	$1.015x10^9N/m$	$1.62x10^9N/m$	$0.792x10^9N/m$
K_{roll}	$1.616x10^{12}Nm/rad$	$2.567x10^{12}Nm/rad$	$1.126x10^{12}Nm/rad$
K_{pitch}	$2.476x10^{12}Nm/rad$	"	"
K_{yaw}	$2.309x10^9Nm/rad$	$4.325x10^9Nm/rad$	$2.096x10^9Nm/rad$
T_{surge}	93.3s	108.4s	83.1s
T_{sway}	"	"	"
T_{heave}	2.3s	2.9s	2.6s
T_{roll}	2.6s	3.5s	3.1s
T_{pitch}	2.2s	"	"
T_{yaw}	70.3s	71.5s	73.9s

Table 6.1: Case Study TLP Particulars

For TLP hydrostatic stiffness in roll and pitch metacentric heights of $\overline{GML}$ and $\overline{GMT}$=4.5m were assumed. Initial temporary mooring stiffness of 8.5KN/m was assumed in all cases for surge, sway and the calculation of initial yaw stiffness.

6.2.2 Phase 1

6.2.2.1 Introduction

To investigate the tether/TLP transient response during pretensioning operations numerical simulations were conducted utilising the Phase 1 methodology detailed in Chapter 4.

In the Phase 1 investigation the mass matrix [M] consists of the tether "bundle" effective actual mass+TLP actual mass+TLP frequency dependent added mass.

The linear damping matrix [D] consists of TLP potential damping (frequency-domain) +% of mode critical damping (installed).

The stiffness matrix [K] consists of nonlinear tether mooring stiffness+TLP hydrostatic stiffness in Heave, Roll and Pitch modes.

The excitation force/moment vector is time dependent calculated using frequency-domain amplitudes and phase angles and is defined for the TLP only.

Further details of the Phase 1 algorithm and data is presented in Chapter 4.

The inclusion of a % of mode critical damping (heave, roll and pitch modes) was applied to account for viscous effects and tether damping. These effects will be shown to have a high significance on peak tether 'bundle' loads.

The coupled motion equations detailed in were solved in the time-domain using the Runge-Kutta method. Simulations have also been conducted applying the Newmark-β method with good agreement shown (Chapter 7).

At each time-step the TLP c.g. space-fixed acceleration, velocity, displacement and tether/hull node coordinates are determined and the corresponding tether length/loading calculated. Tethers are assumed linear elastic.

The deballast operation is modeled as a series of linear heave force ramps added to the 1^{st} order heave force.

Motion compensation is modeled as a Vibration Isolator system consisting of a linear spring and damper. In the absence of the characteristics of industry accepted systems it was assumed that a natural frequency an order of magnitude lower than the excitation frequency with 25% critical damping (heave, roll and pitch modes compensated) could be achieved.

6.2.2.2 Metocean Parameters

The industry accepted installation sea-state adopted was H_s=2.5m, with (for West of Shetland (WoS)) T_p=10.5s. To generate tether 'bundle' RAOs these parameters were input to a Pierson Moskowitz wave spectrum:

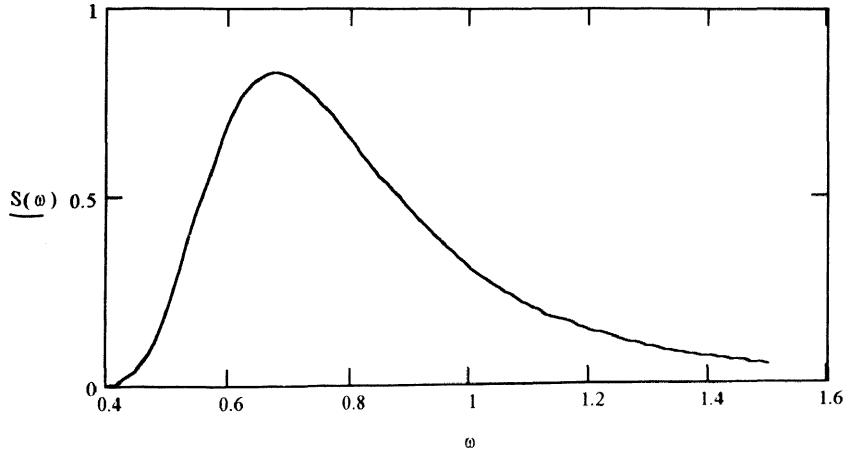

Figure 6.1: Pierson Moskowitz Wave Spectrum H_s=2.5m, T_p=10.5s (m^2s)

For the AA TLP, tether 'bundle' RAOs were calculated for a range of frequencies covering the energy spread of the spectrum. For the Heidrun and Snorre TLPs time-domain results were generated for regular waves of ξ_a=1.25m, ω=0.6rad/s (due to time constraints-1000s simulation=3hours run-time).

Incident wave directions applied were:

60^0 AA

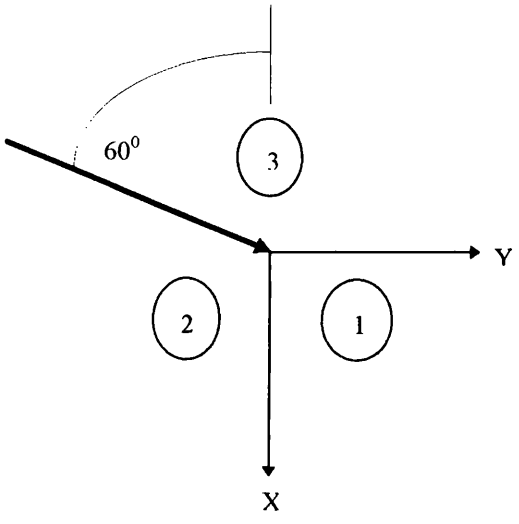

45^0 (225^0) Heidrun

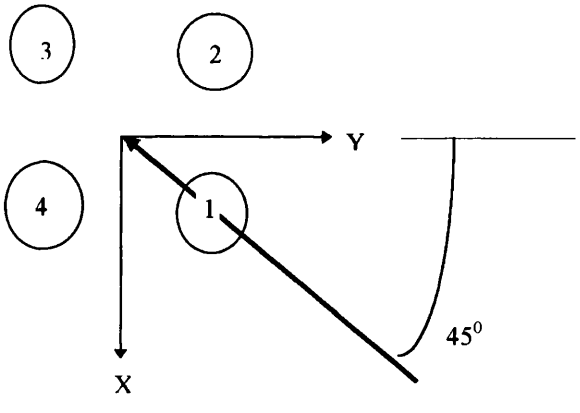

45^0 (225^0) Snorre

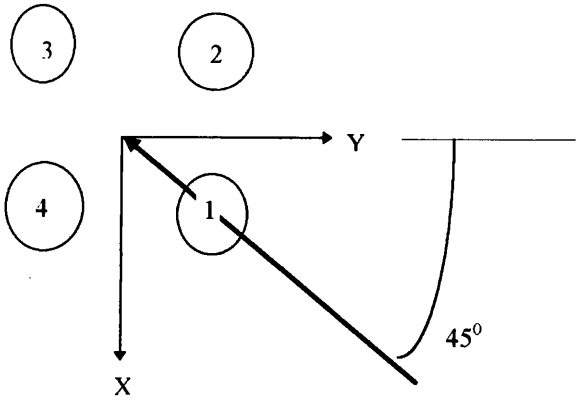

6.2.2.3 Installation Sequence

For all 3No. TLPs results were generated for pretensioning operations with/without motion compensation and for the installed condition. 4No. deballasting rates were used to represent the pretensioning operation corresponding to zero deballasting for the 1st $\frac{1}{4}$ of the simulation duration, $\frac{1}{32}$ of total pretension over the 2nd $\frac{1}{4}$ of the simulation, $\frac{3}{32}$ of total pretension over the 3rd $\frac{1}{4}$ of the simulation and $\frac{1}{8}$ of total pretension over the 4th $\frac{1}{4}$ of the simulation. Therefore at the end of the simulation $\frac{1}{4}$ of total pretension is present.

It is considered unnecessary to continue simulations beyond this level as at this stage there is sufficient acting pretension to prevent tether slacking occurring during normal installation sea-states.

The wave parameters utilised for the simulations of the installed condition were ξ_a=9m and ω=0.36rad/s representing a design extreme event.

6.2.3 Phase 2

6.2.3.1 Introduction

To investigate the coupled tether/TLP system effects including tether hydrodynamic forces (line dynamics) numerical simulation work was conducted utilising the Phase 2 methodology detailed in Chapter 4.

This numerical simulation work was conducted utilising the Heidrun TLP data set for a range of regular wave frequencies (head sea incident waves).

Selected results are presented in Figures 6.2-6.196, with further results detailed in Appendix A.

6.3 TLP Case Study Results

6.3.1 Phase 1

6.3.1.1 Introduction

Results generated take the form of time-domain data detailing the TLP motion response (6DOF) and the corresponding tether 'bundle' force time-series.

Platform motion response curves in both the vertical and horizontal planes have also been plotted.

Comparisons and discussion of numerical and experimental results are detailed in Chapter 7.

6.3.1.2 AA TLP

Figures 6.2-6.18 detail the time-domain simulation results for the AA Case Study TLP for an incident regular wave of ω =0.52rad/s (ξ_a =1m) with a heading angle of 60^0.

Figures 6.2-6.7 detail the surge, sway, heave, roll, pitch and yaw DOF response respectively.

Figure 6.8 details the tether 'bundle' tension time-series response.

Figures 6.9-6.18 detail the platform vertical/horizontal and cross-planer response.

For results for the AA Case Study TLP for incident regular waves of ω =0.6, 0.72, 0.8, 0.92, 0.1 and 1.12rad/s (ξ_a=1m) with a heading angle of 60^0 please refer to Appendix A.

TLP Global Dynamic Response in Time-domain (6*DOF*):

(Space-fixed coordinate system)

DISPLACEMENT

Surge

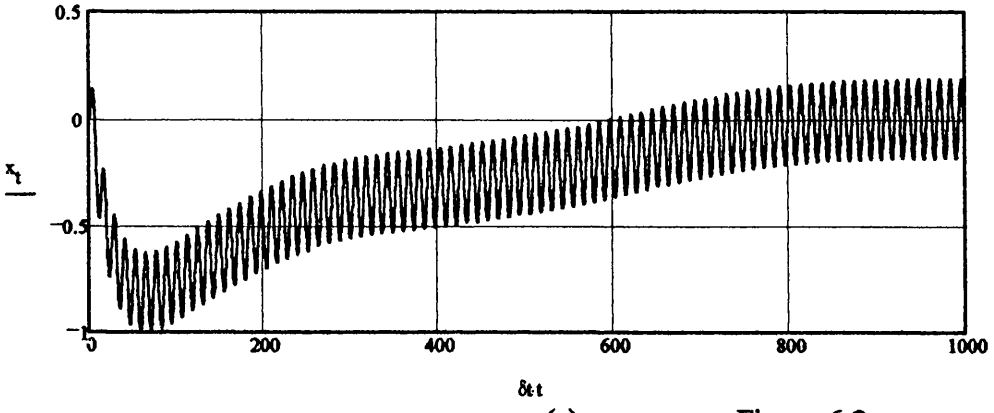

(m)

Figure 6.2

Sway

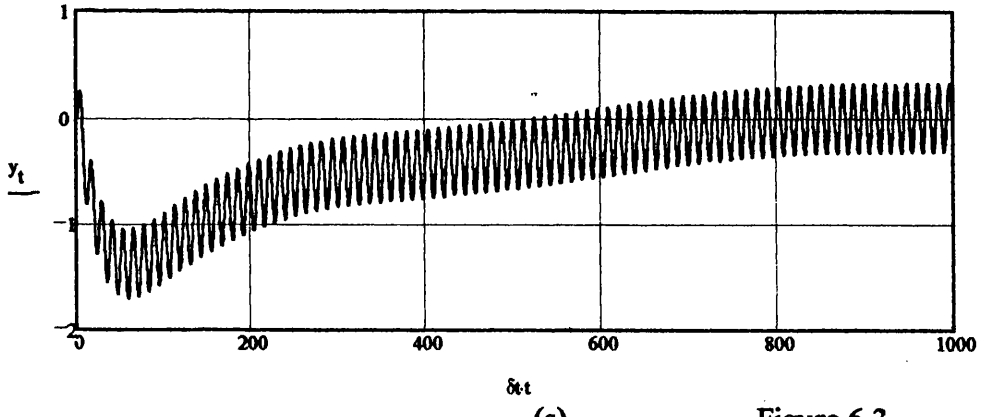

(m)

Figure 6.3

Heave

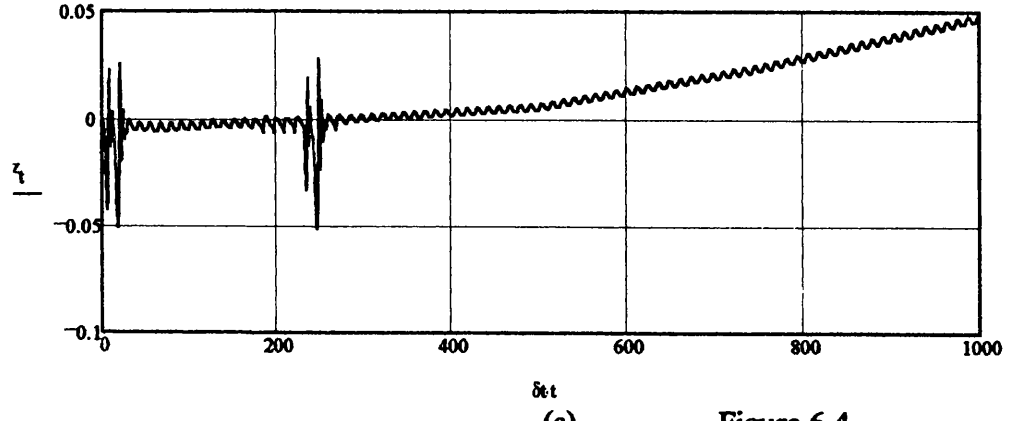

(m)

Figure 6.4

Roll

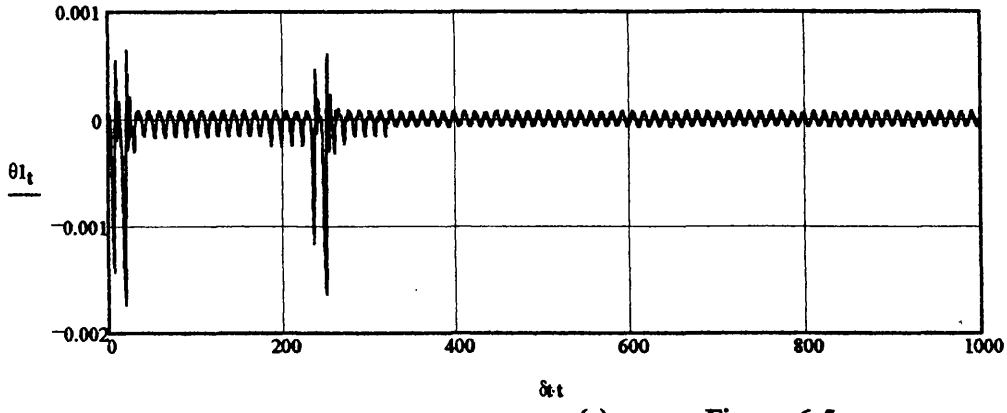

(rad)

Figure 6.5

Pitch

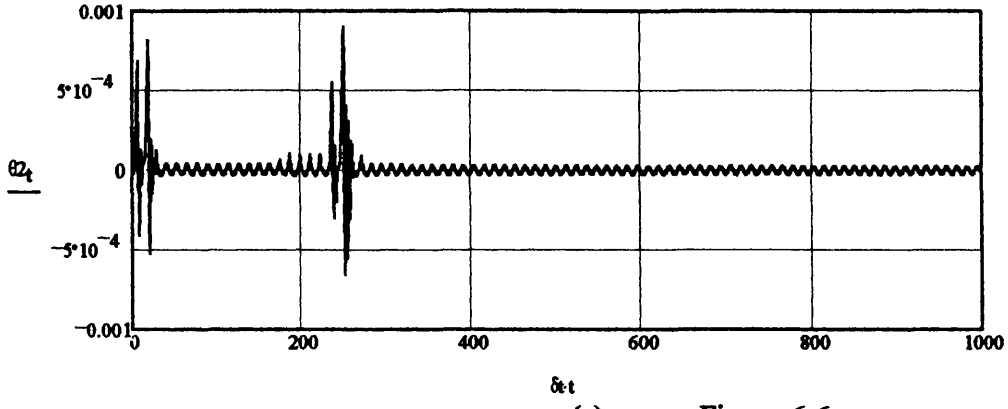

(rad)

Figure 6.6

Yaw

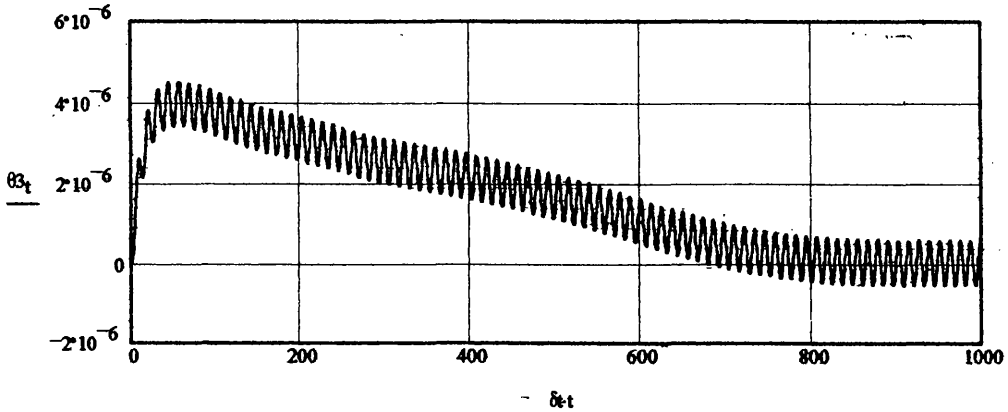

(rad)

Figure 6.7

Tether Force Time-series

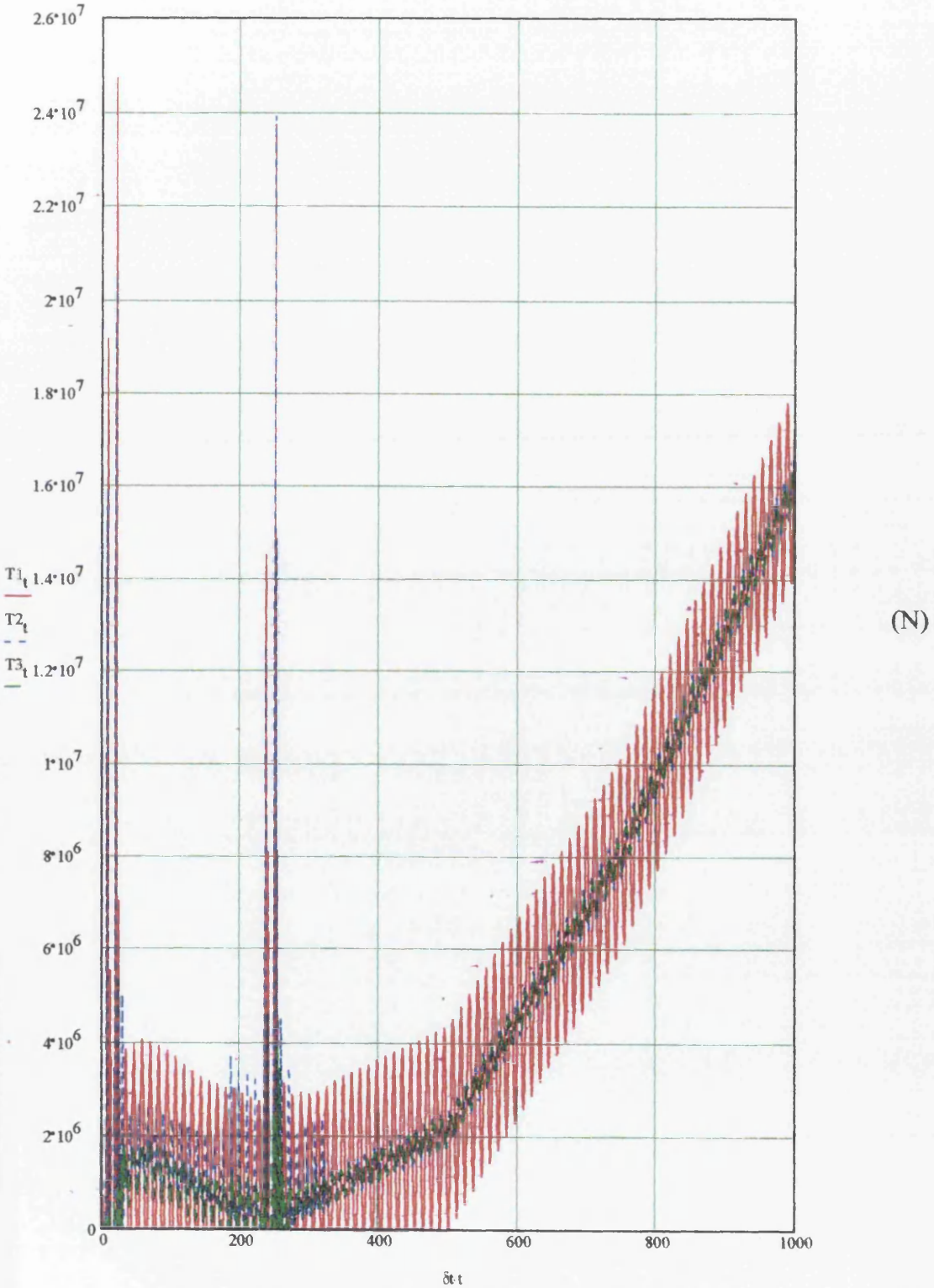

Figure 6.8

2D *TLP* c.g. Motion Response (Heave v Surge)

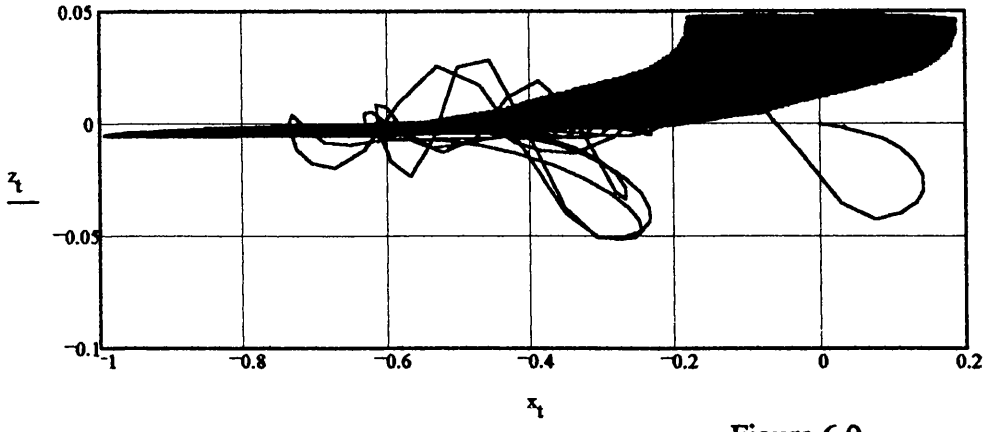

(m)

(m)

Figure 6.9

2D *TLP* c.g. Motion Response (Heave v Sway)

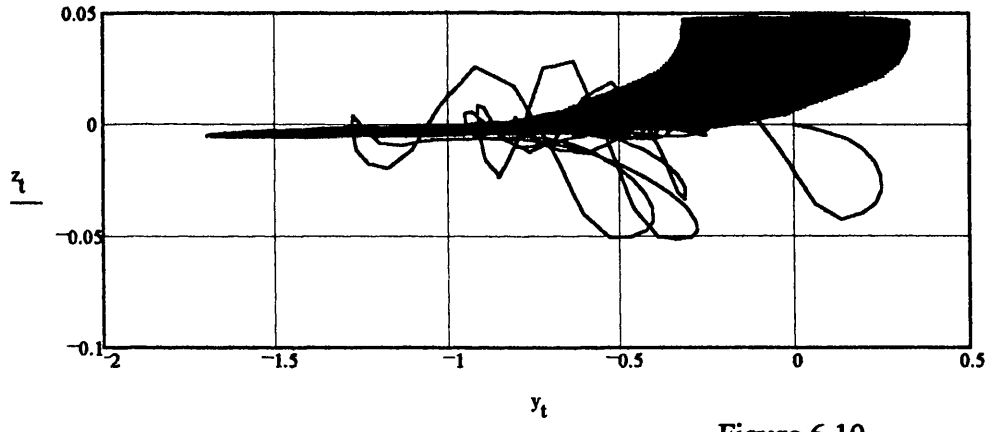

(m)

(m)

Figure 6.10

2D *TLP* c.g. Motion Response (Heave v Roll)

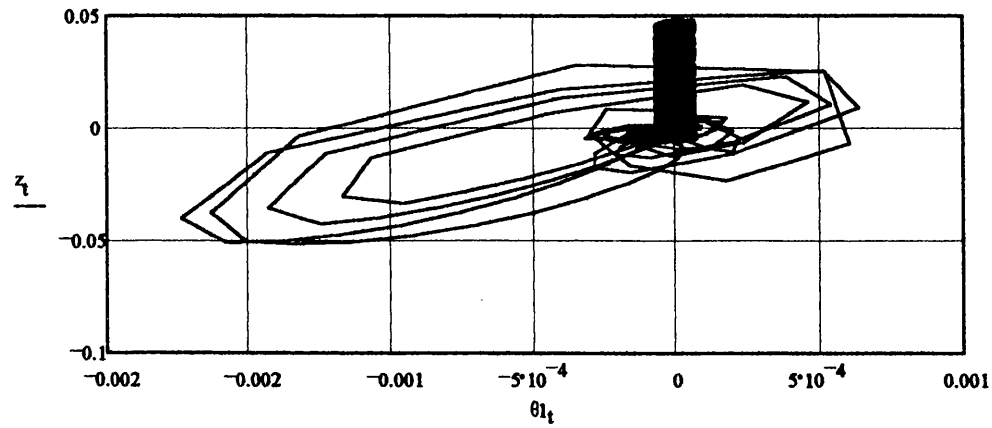

(m)

(rad)

Figure 6.11

2D *TLP* c.g. Motion Response (Heave v Pitch)

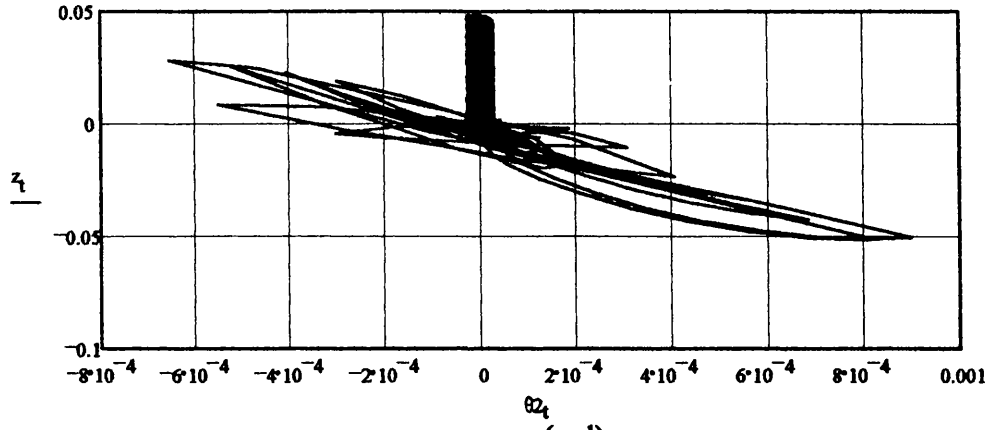

(m)

(rad)

Figure 6.12

2D *TLP* c.g. Motion Response (Heave v Yaw)

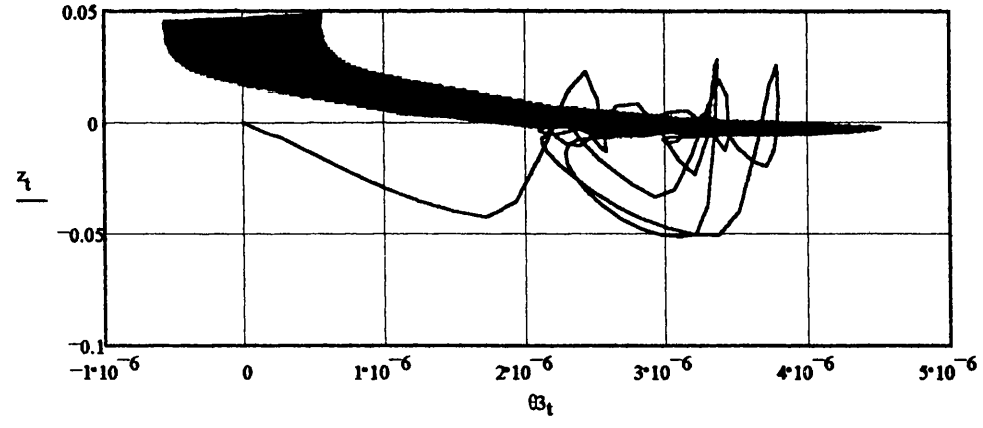

(m)

(rad)

Figure 6.13

2D *TLP* c.g. Motion Response (Surge v Sway)

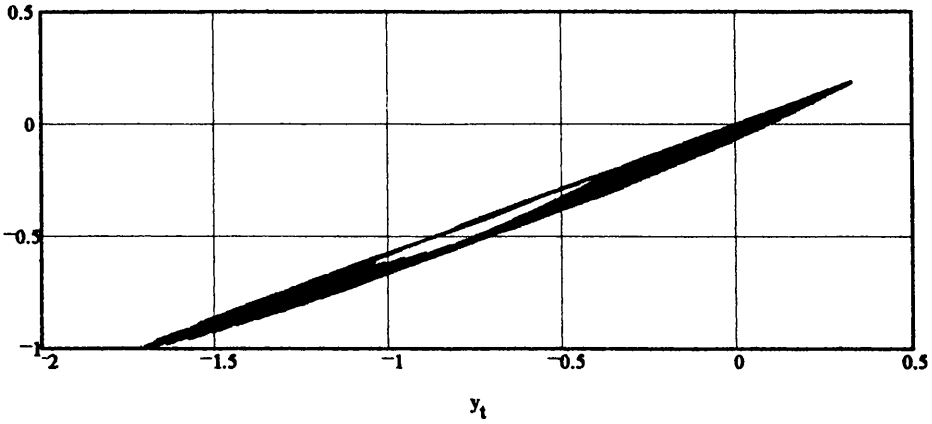

(m)

(m)

Figure 6.14

2D *TLP* c.g. Motion Response (Surge v Heave)

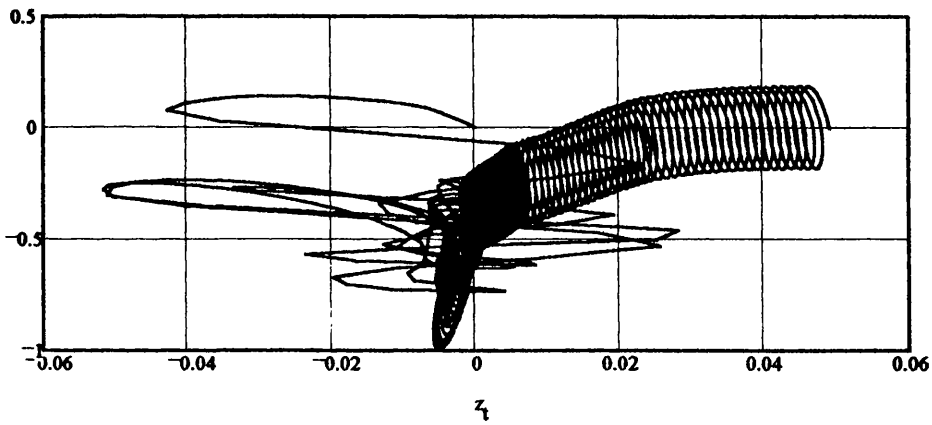

(m)

(m)

Figure 6.15

2D *TLP* c.g. Motion Response (Surge v Roll)

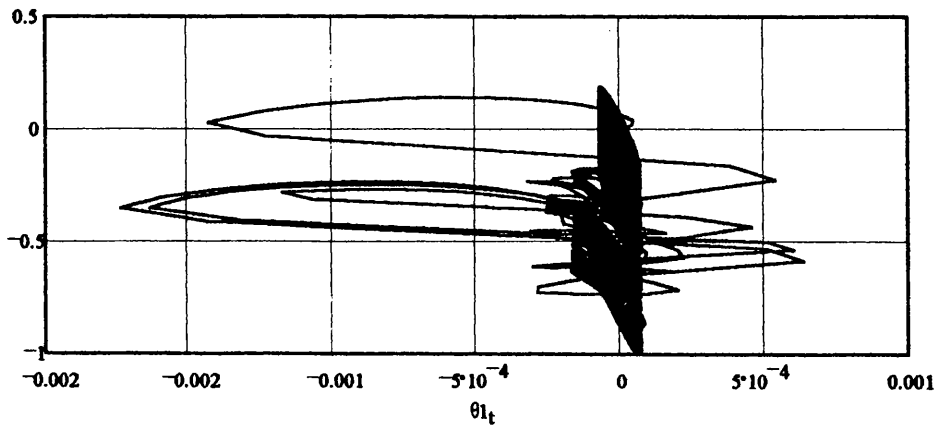

(m)

(rad)

Figure 6.16

2D *TLP* c.g. Motion Response (Surge v Pitch)

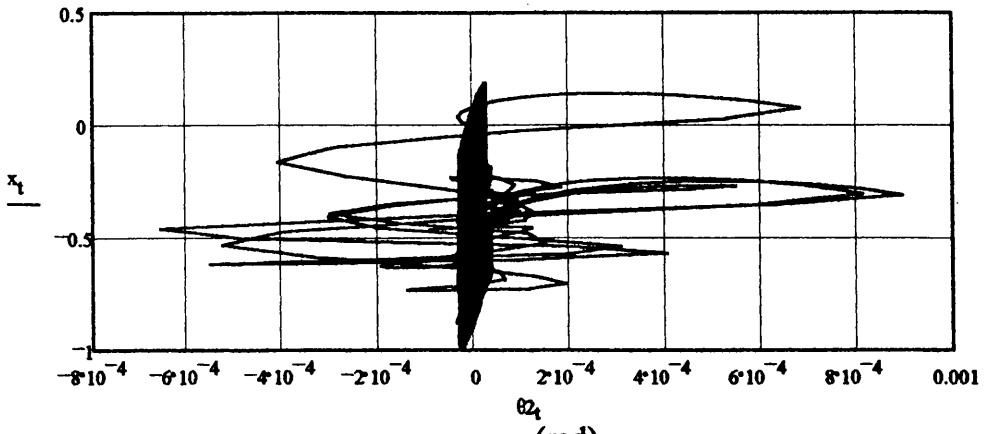

Figure 6.17

2D *TLP* c.g. Motion Response (Surge v Yaw)

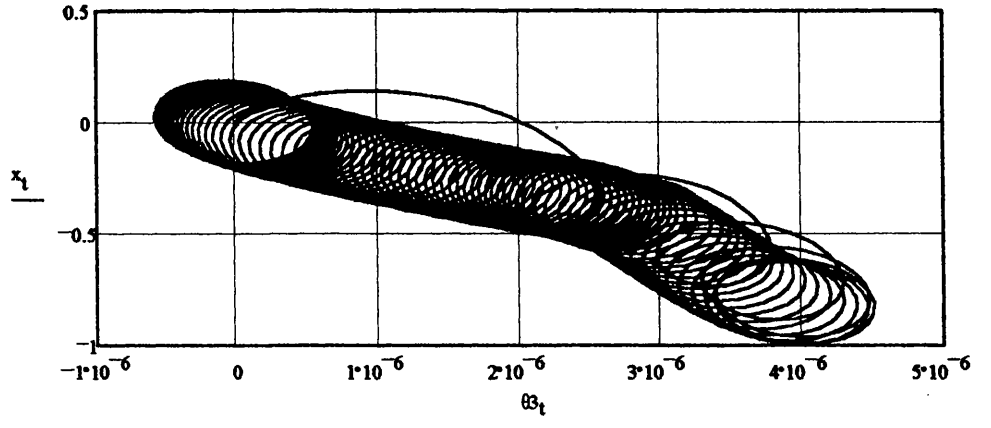

Figure 6.18

Tether 'bundle' RAOs derived from the above simulations (and those detailed in Appendix A) are given in Figure 6.19 for the AA Case Study TLP. These RAOs are derived for the pretensioning operation up to $\frac{1}{4}$ of full pretension (16.333MN). These results are calculated with 2.5% C_c (installed) applied in the Heave, Roll and Pitch modes.

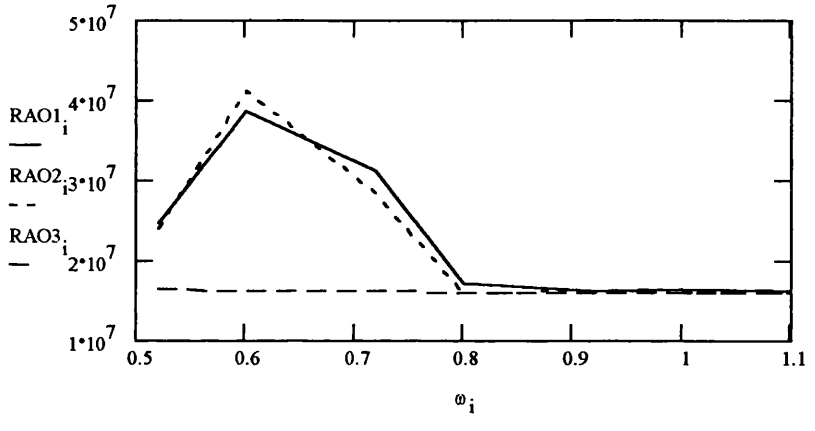

Figure 6.19: AA TLP Tether "Bundle" RAOs (N/m)

It is acknowledged that the tether 'bundle' installation transient response is nonlinear and therefore the above spectral approach is not strictly valid, however as the installation sea-states are low, with wave amplitudes rarely above 1-1.5m, it is considered that the above approach will yield acceptable accuracy.

Therefore by application of the above RAOs and a representative sea-state spectrum the irregular sea response could be derived.

To investigate the effect of motion compensation systems further simulation runs were performed for a representative installation sea-state of ω =0.6rad/s and ξ_a =1.25m.

Motion compensation was modeled as a Vibration Isolator system consisting of a linear spring and damper. In the absence of the characteristics of industry accepted systems it was assumed that a natural frequency an order of magnitude lower than the excitation frequency with 25% critical damping (Heave, Roll and Pitch modes compensated) could be achieved.

Figures 6.20-6.36 detail the time-domain simulation results for the AA Case Study TLP for an incident regular wave of ω =0.6rad/s (ξ_a =1.25m) with a heading angle of 60^0 (without motion compensation).

Figures 6.20-6.25 detail the surge, sway, heave, roll, pitch and yaw DOF response respectively.

Figure 6.26 details the tether 'bundle' tension time-series response.

Figures 6.27-6.36 detail the platform vertical/horizontal and cross-planer response.

TLP Global Dynamic Response in Time-domain (*6DOF*):

(Space-fixed coordinate system)

DISPLACEMENT

Surge

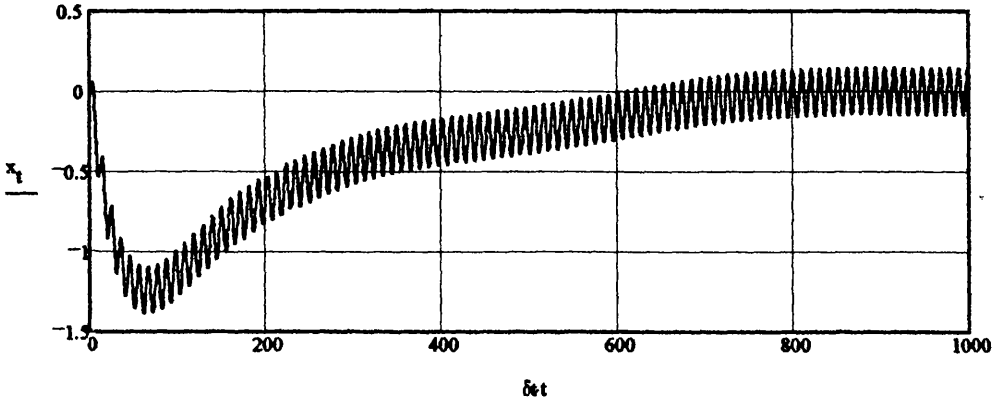

(m)

(s) Figure 6.20

Sway

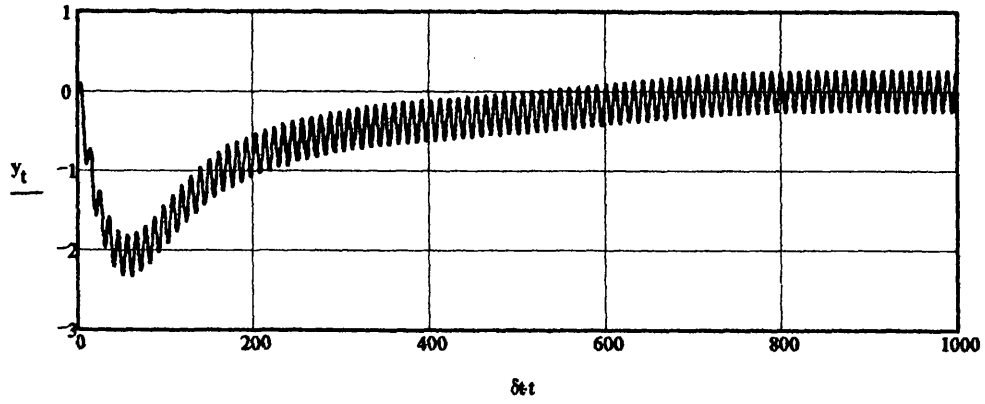

(m)

(s) Figure 6.21

Heave

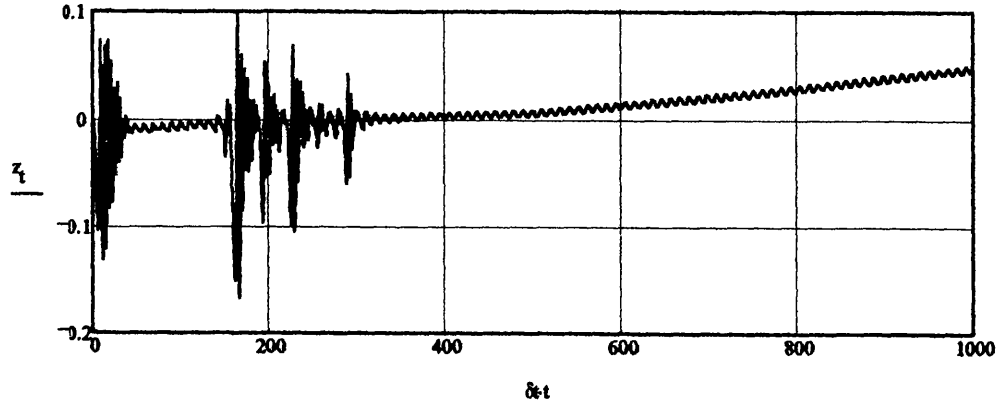

(m)

(s) Figure 6.22

Roll

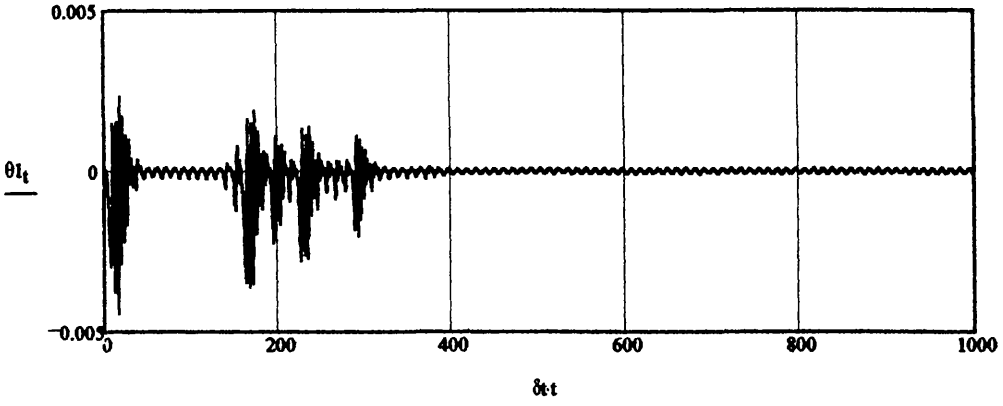

(rad)

Figure 6.23

Pitch

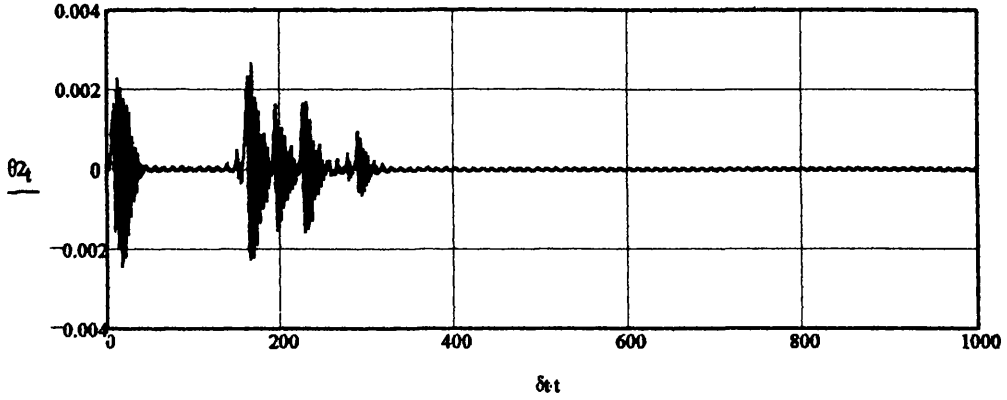

(rad)

Figure 6.24

Yaw

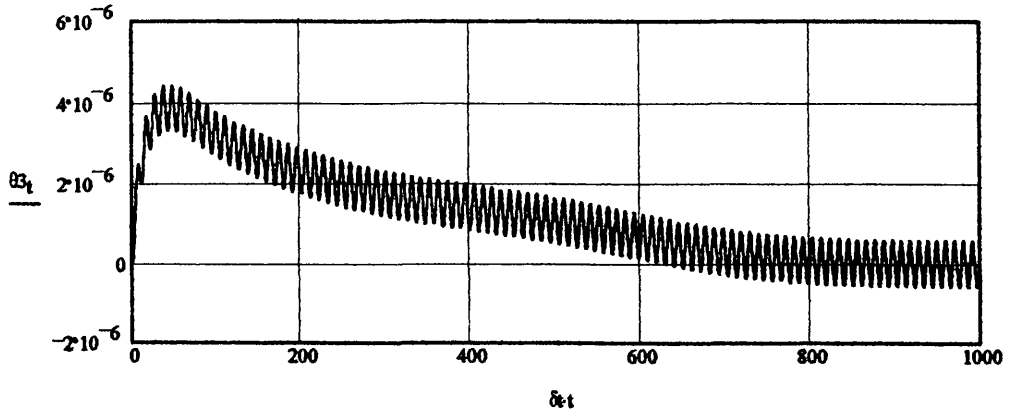

(rad)

Figure 6.25

Tether Force Time-series

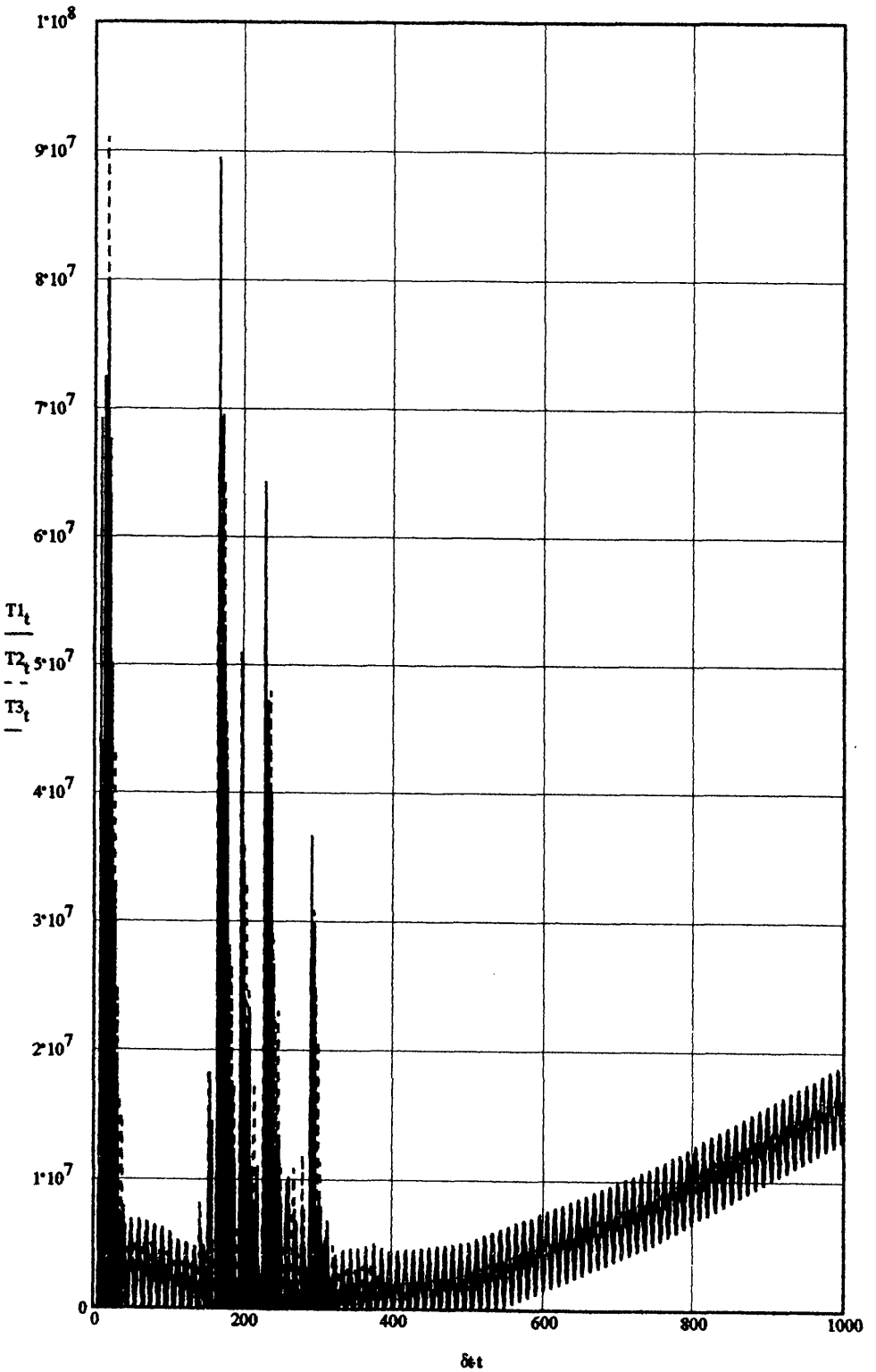

(N)

(s)

Figure 6. 16

2D *TLP* c.g. Motion Response (Heave v Surge)

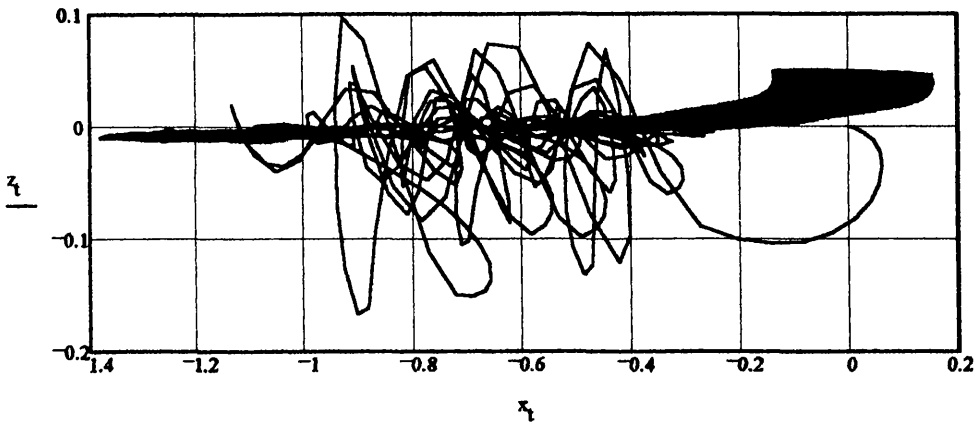

(m)

(m)

Figure 6.27

2D *TLP* c.g. Motion Response (Heave v Sway)

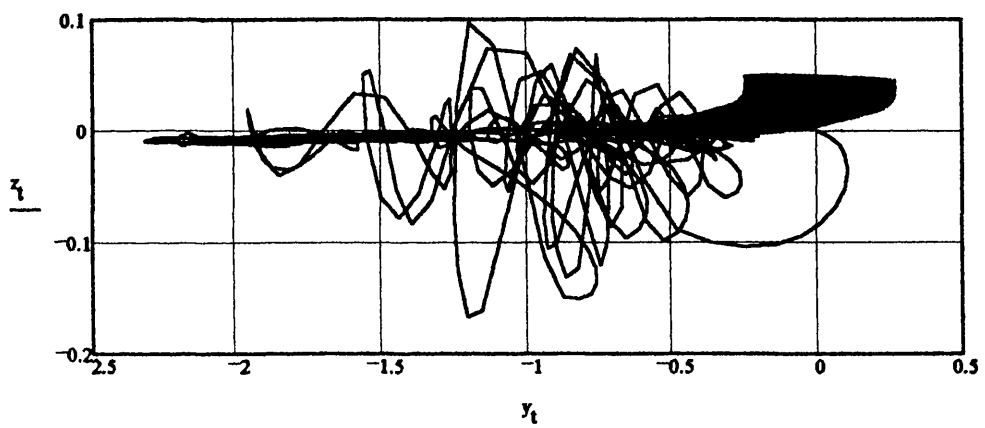

(m)

(m)

Figure 6.28

2D *TLP* c.g. Motion Response (Heave v Roll)

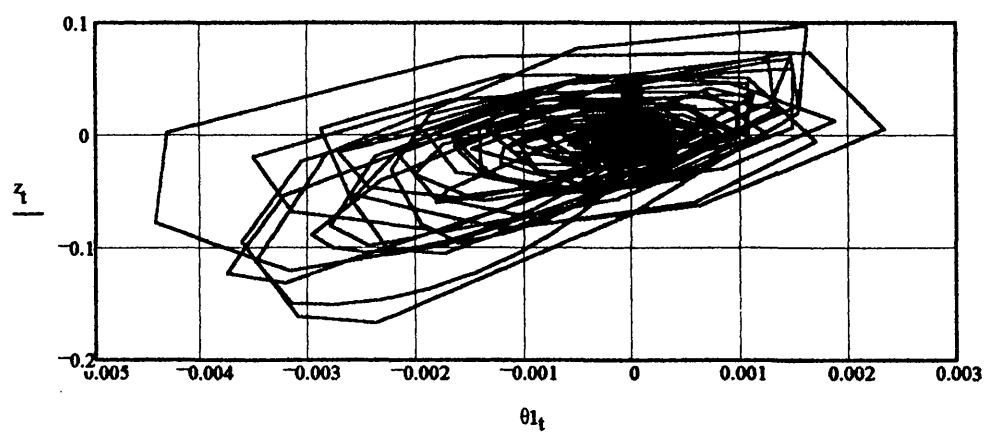

(m)

(rad)

Figure 6.29

2D *TLP* c.g. Motion Response (Heave v Pitch)

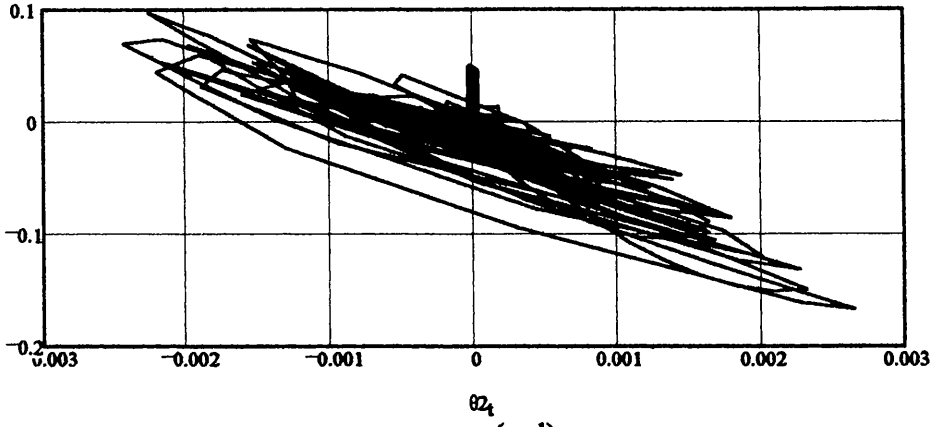

(m)

(rad)

Figure 6.30

2D *TLP* c.g. Motion Response (Heave v Yaw)

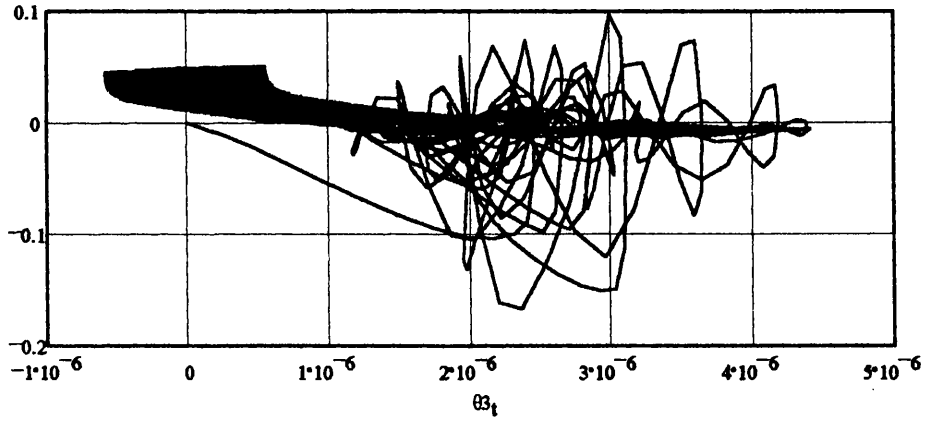

(m)

(rad)

Figure 6.31

2D *TLP* c.g. Motion Response (Surge v Sway)

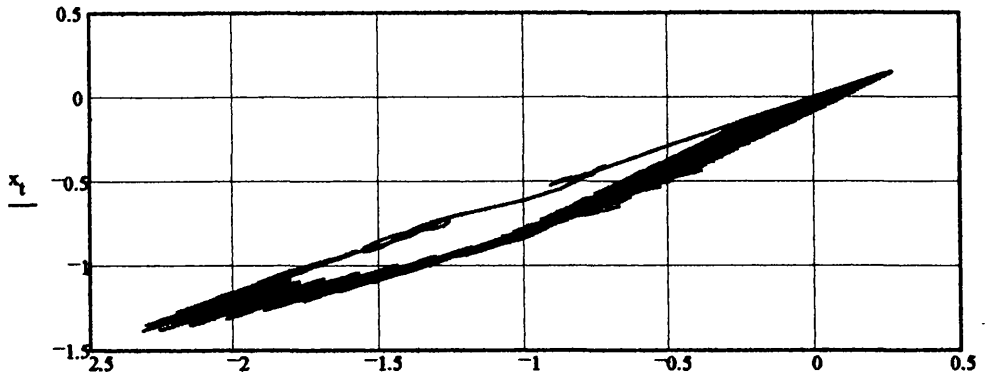

(m)

Figure 6.32

2D *TLP* c.g. Motion Response (Surge v Heave)

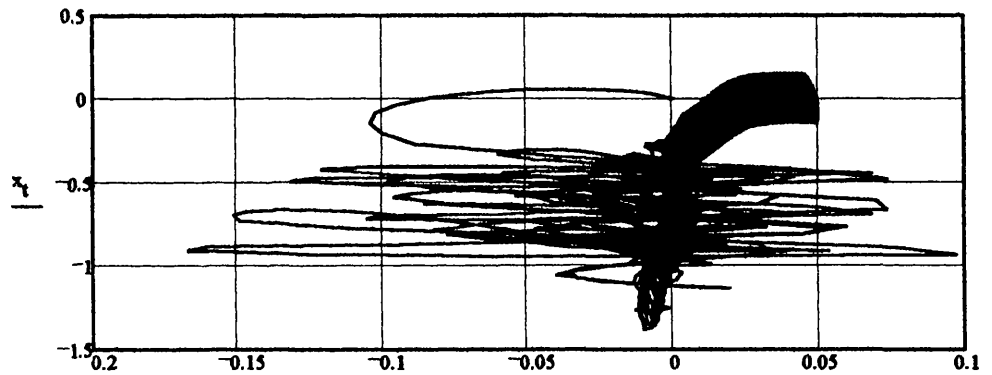

(m)

Figure 6.33

2D *TLP* c.g. Motion Response (Surge v Roll)

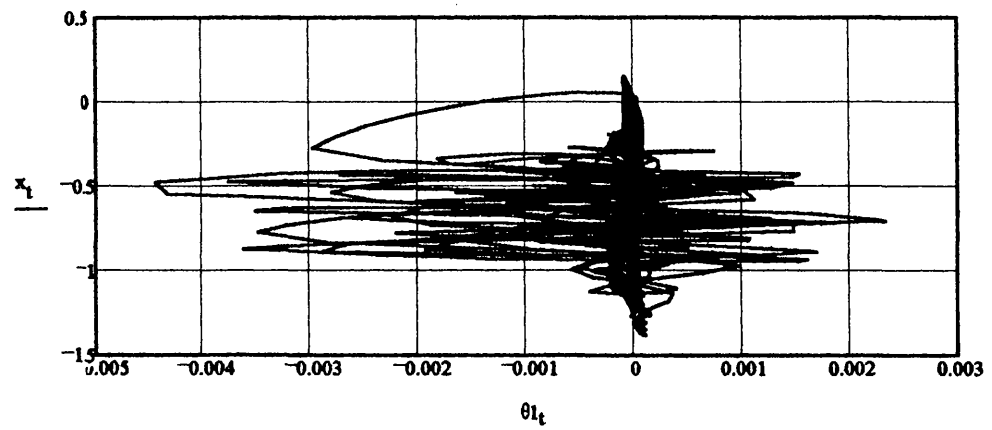

(m)

Figure 6.34

2D *TLP* c.g. Motion Response (Surge v Pitch)

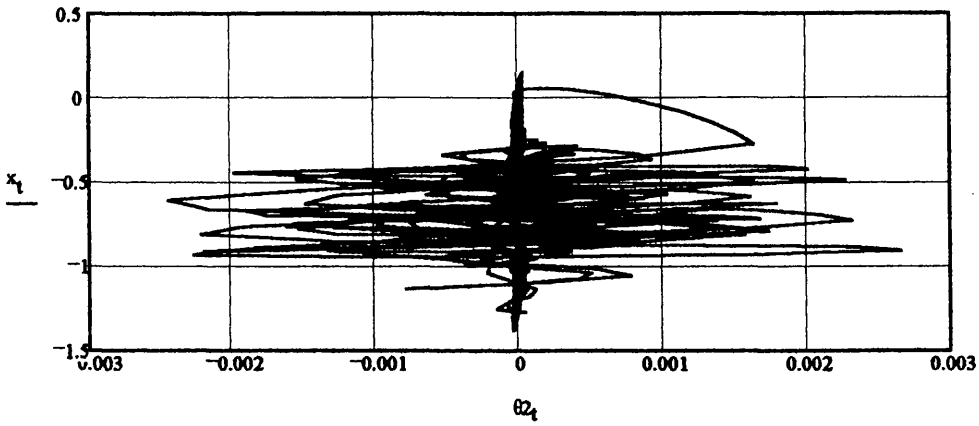

(m)

(rad)

Figure 6. 35

2D *TLP* c.g. Motion Response (Surge v Yaw)

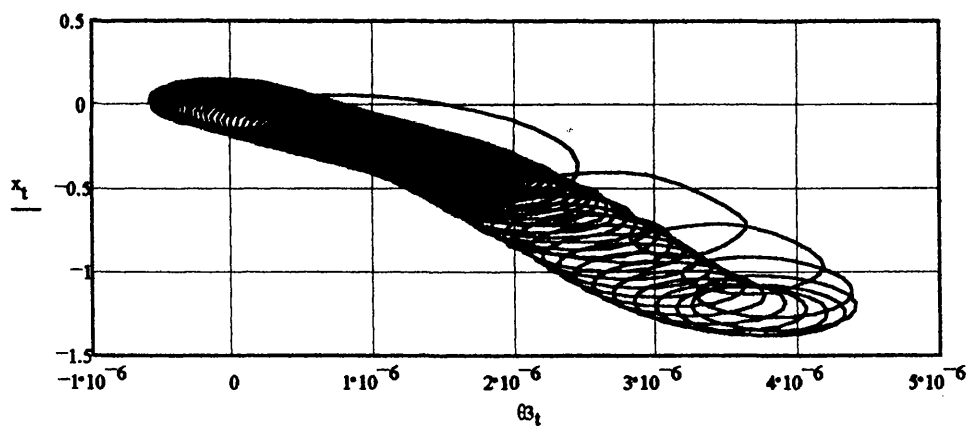

(m)

Figure 6. 36

(rad)

Figures 6.37-6.53 detail the time-domain simulation results for the AA Case Study TLP for an incident regular wave of ω =0.6rad/s (ξ_a =1.25m) with a heading angle of 60^0 (with motion compensation).

Figures 6.37-6.42 detail the surge, sway, heave, roll, pitch and yaw DOF response respectively.

Figure 6.43 details the tether 'bundle' tension time-series response.

Figures 6.44-6.53 detail the platform vertical/horizontal and cross-planer response.

TLP Global Dynamic Response in Time-domain (*6DOF*):

(Space-fixed coordinate system)

DISPLACEMENT

Surge

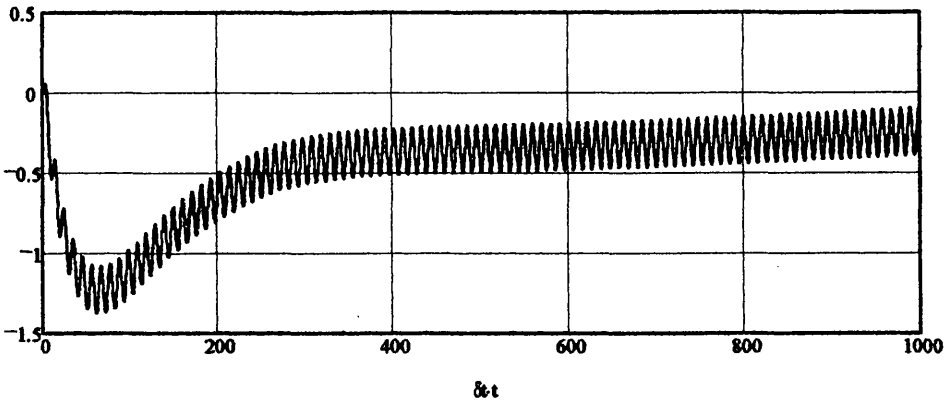

(m)

Figure 6.37

Sway

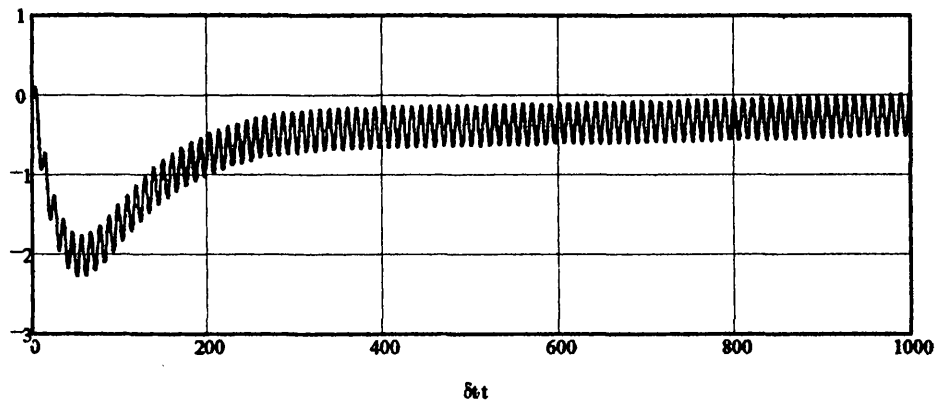

(m)

Figure 6.38

Heave

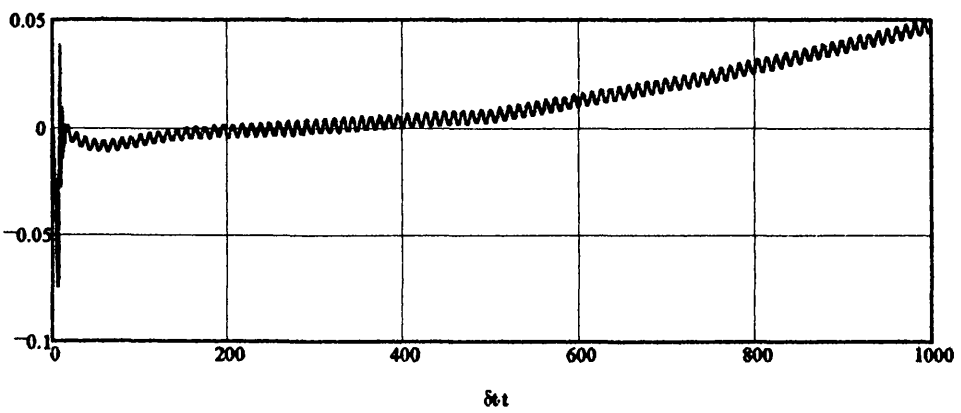

(m)

Figure 6.39

Roll

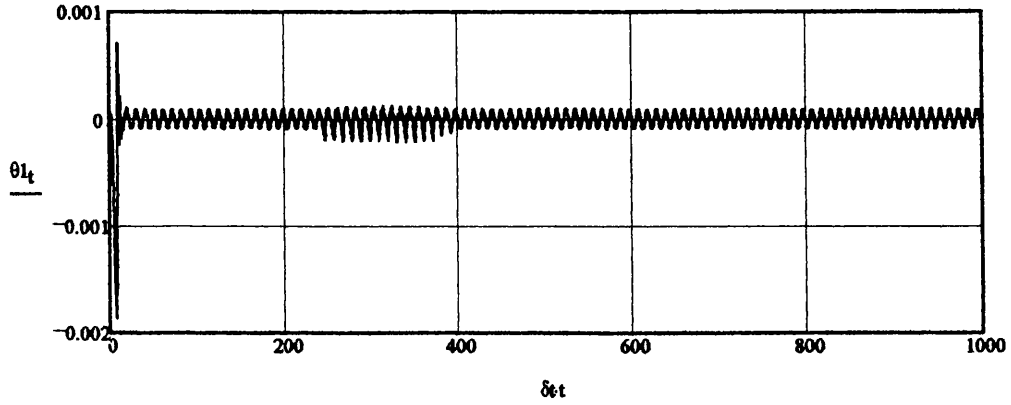

(rad)

Figure 6.40

Pitch

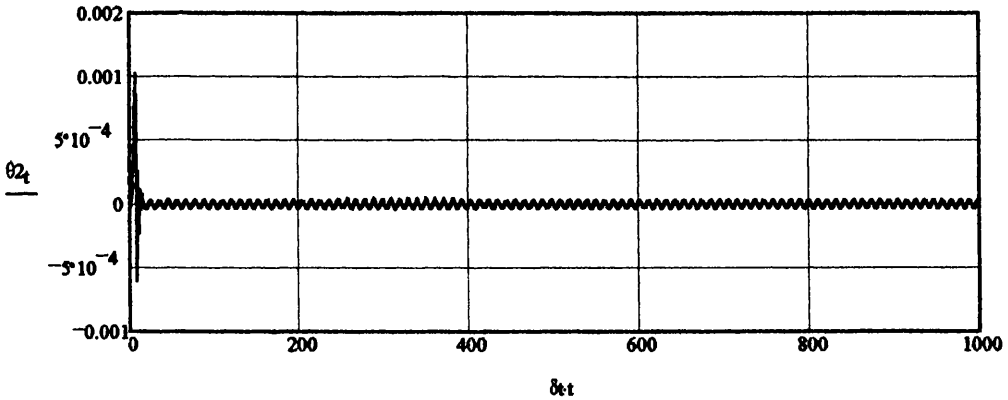

(rad)

Figure 6.41

Yaw

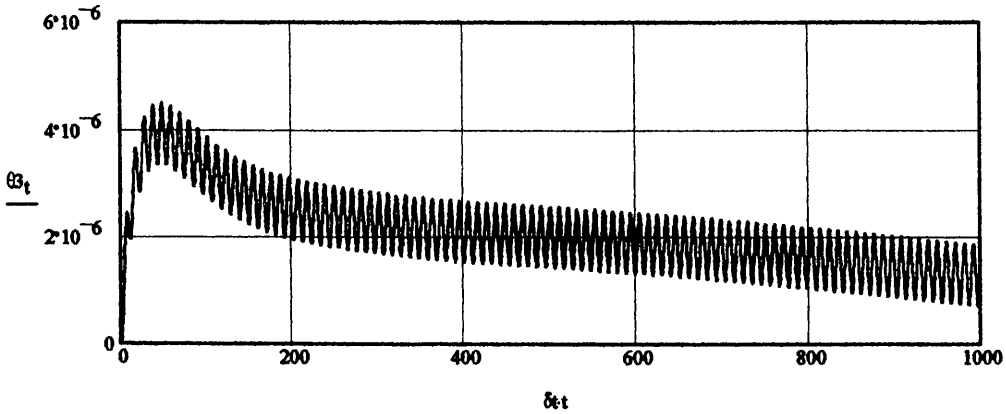

(rad)

Figure 6.42

Tether Force Time-series

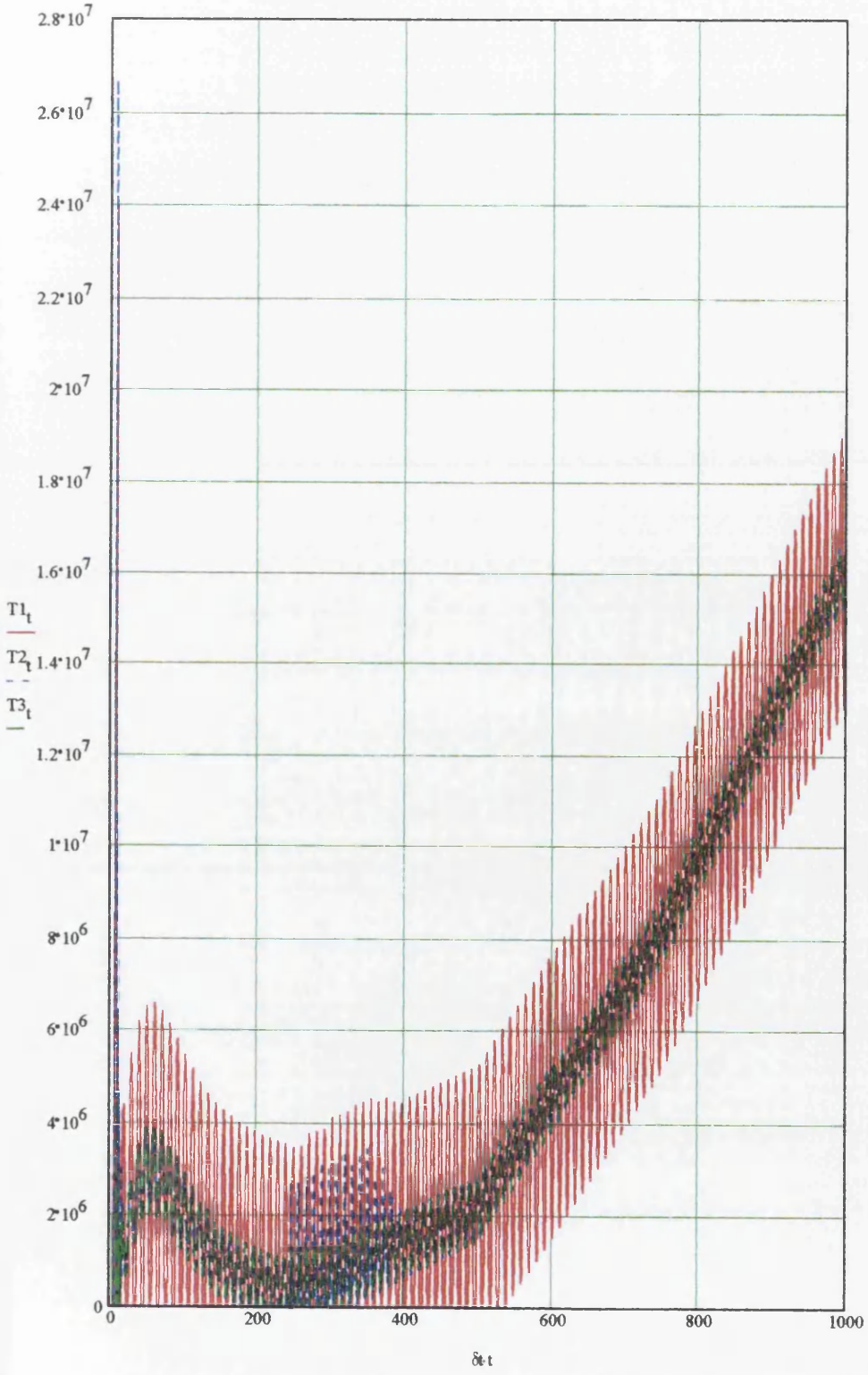

(N)

(s)

Figure 6. 43

2D *TLP* c.g. Motion Response (Heave v Surge)

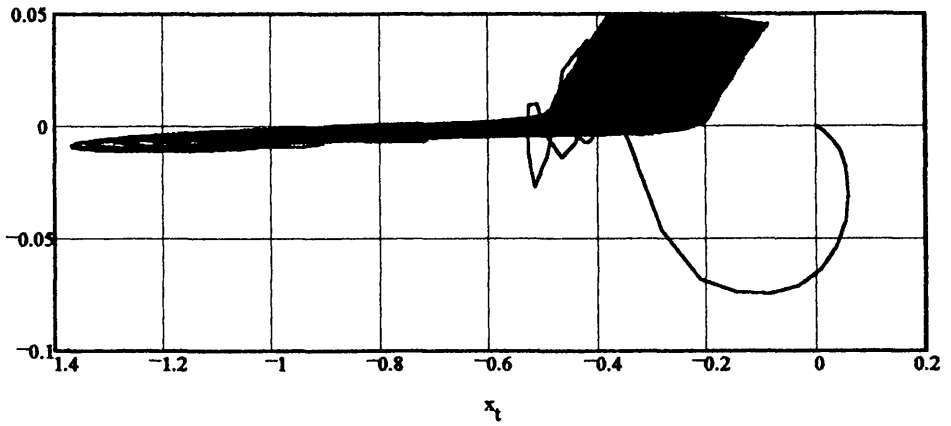

Figure 6.44

2D *TLP* c.g. Motion Response (Heave v Sway)

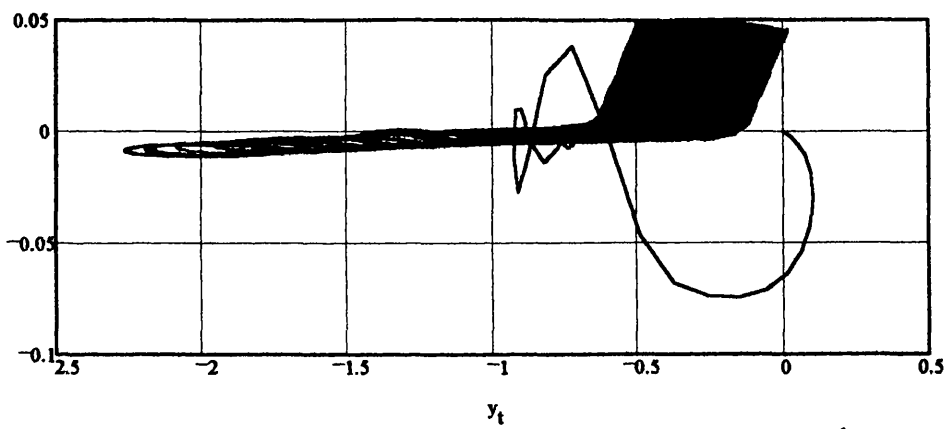

Figure 6.45

2D *TLP* c.g. Motion Response (Heave v Roll)

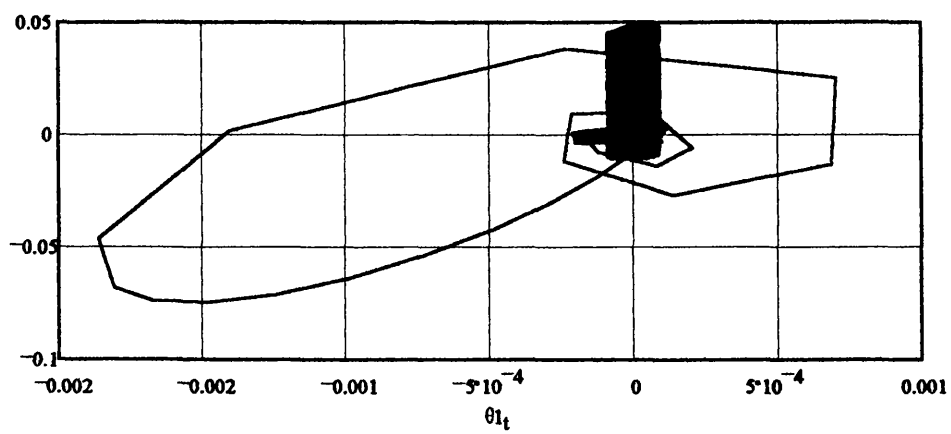

Figure 6.46

2D *TLP* c.g. Motion Response (Heave v Pitch)

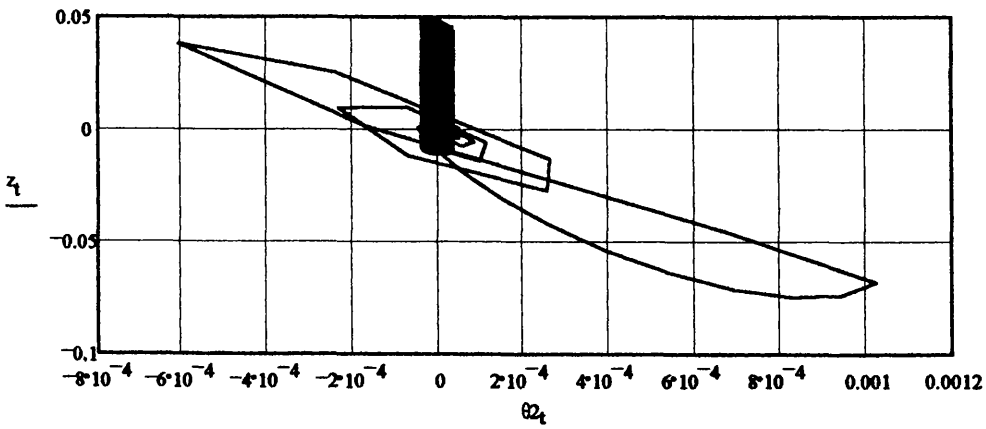

(m)

(rad)

Figure 6.47

2D *TLP* c.g. Motion Response (Heave v Yaw)

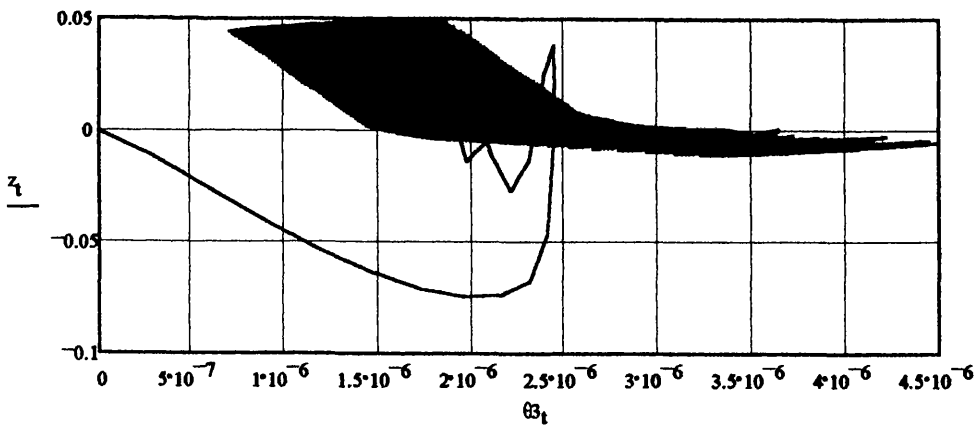

(m)

(rad)

Figure 6.48

2D *TLP* c.g. Motion Response (Surge v Sway)

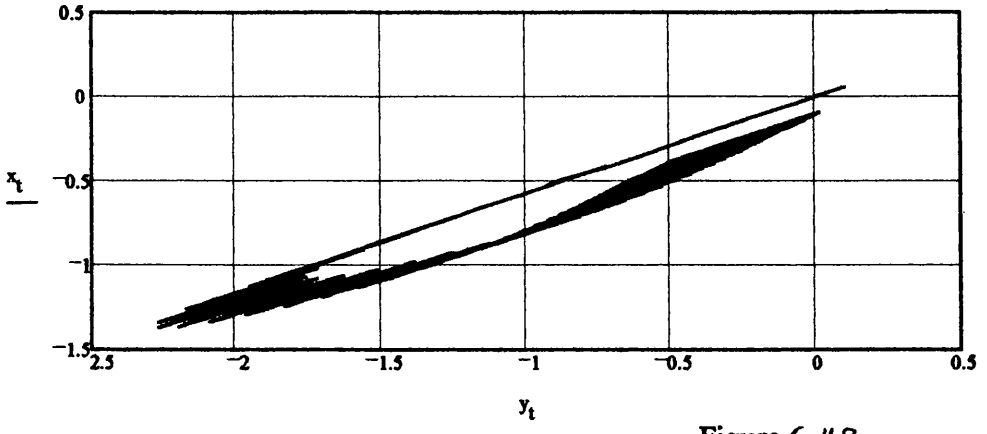

(m)

(m)

Figure 6.49

2D *TLP* c.g. Motion Response (Surge v Heave)

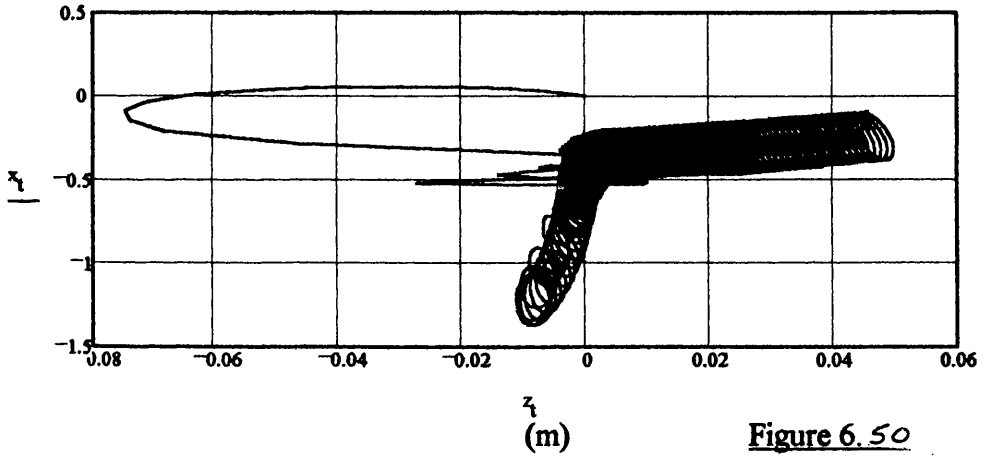

(m)

(m)

Figure 6.50

2D *TLP* c.g. Motion Response (Surge v Roll)

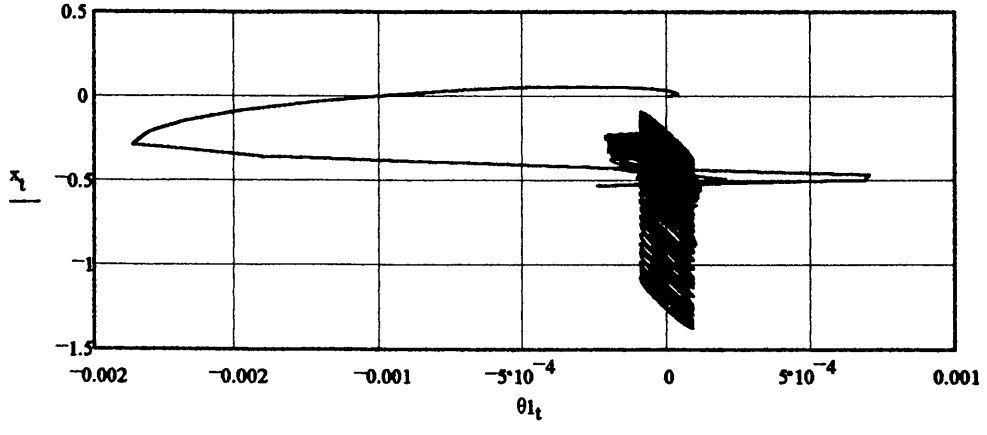

(m)

(rad)

Figure 6.51

2D *TLP* c.g. Motion Response (Surge v Pitch)

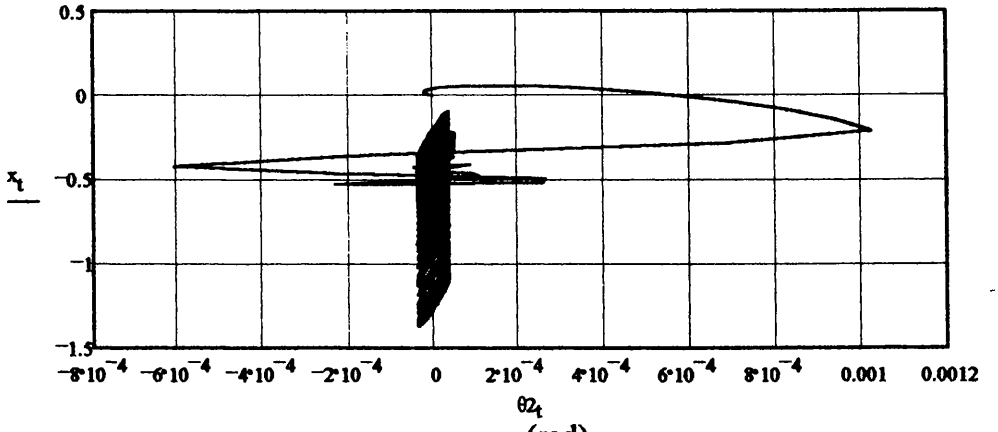

(m)

(rad)

Figure 6.52

2D *TLP* c.g. Motion Response (Surge v Yaw)

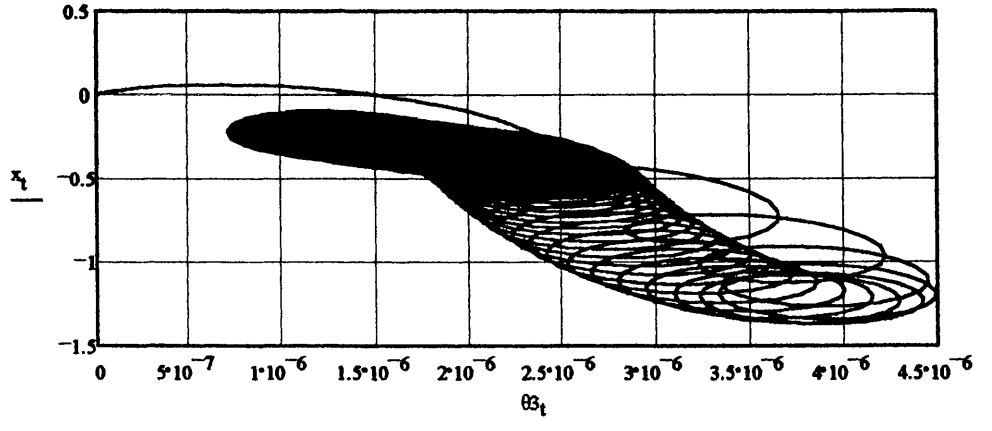

(m)

Figure 6.53

(rad)

To investigate the sensitivity of the tether 'bundle' loading to initial TLP hydrostatic stability, simulations were generated for an initial $\overline{GML}$ and $\overline{GMT}$ of 1m. Figures 6.54-6.70 detail the time-domain simulation results for the AA Case Study TLP for an incident regular wave of ω =0.6rad/s (ξ_a=1.25m) with a heading angle of 60^0 (with $\overline{GML}$ and $\overline{GMT}$=1m).

Figures 6.54-6.59 detail the surge, sway, heave, roll, pitch and yaw DOF response respectively.

Figure 6.60 details the tether 'bundle' tension time-series response.

Figures 6.61-6.70 detail the platform vertical/horizontal and cross-planer response.

TLP Global Dynamic Response in Time-domain (*6DOF*):

(Space-fixed coordinate system)

DISPLACEMENT

Surge

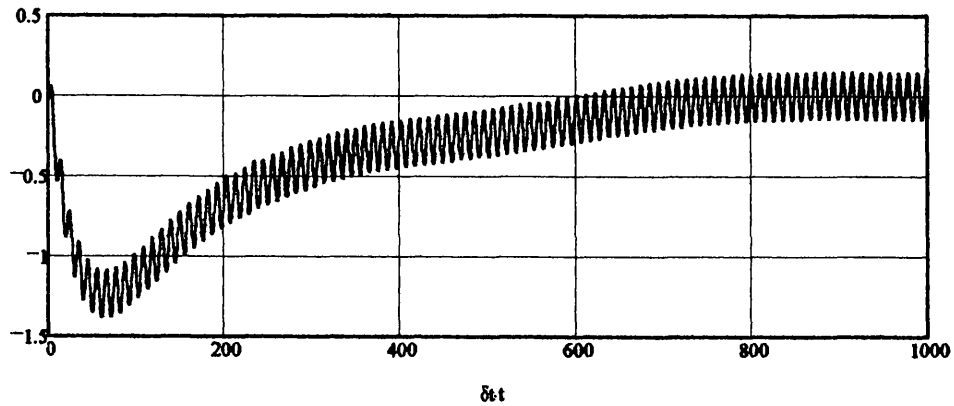

(m)

Figure 6.54

Sway

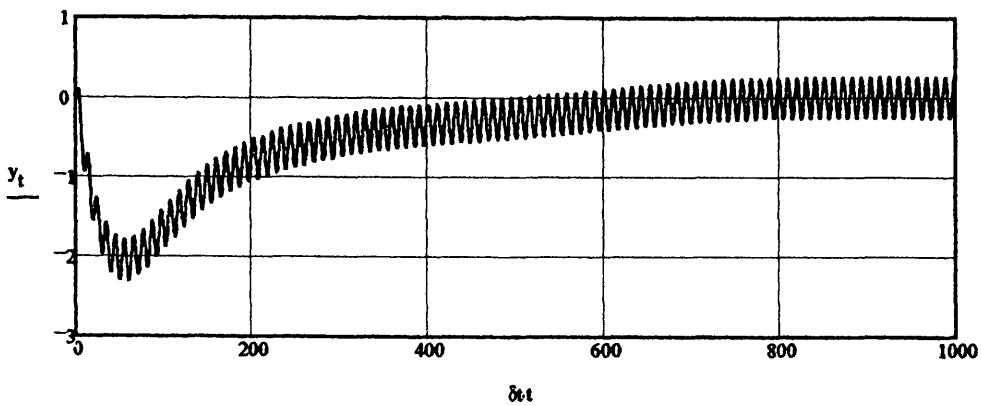

(m)

Figure 6.55

Heave

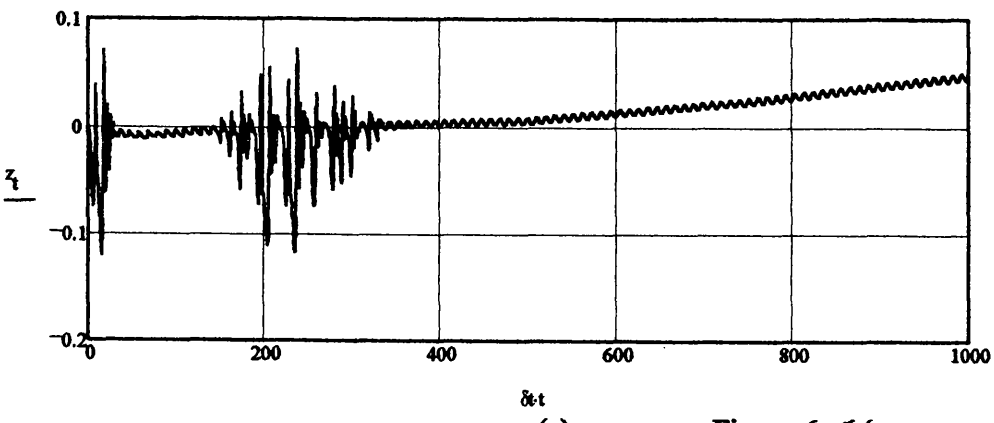

(m)

Figure 6.56

Roll

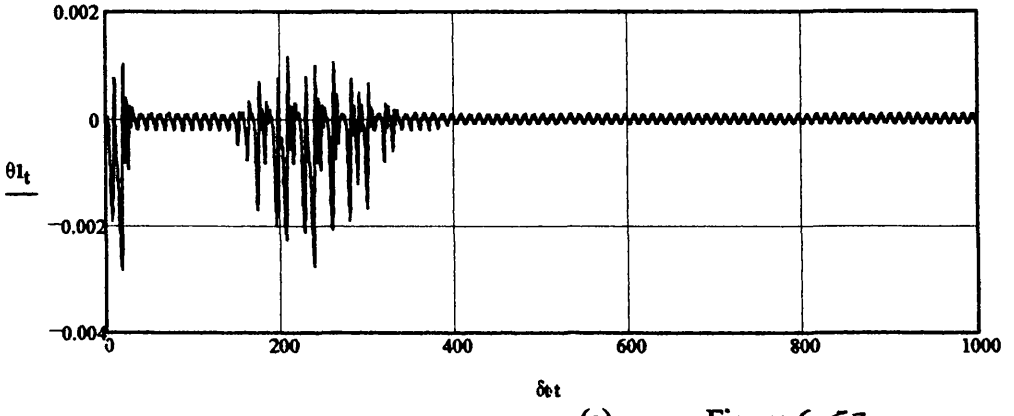

(rad)

Figure 6.57

Pitch

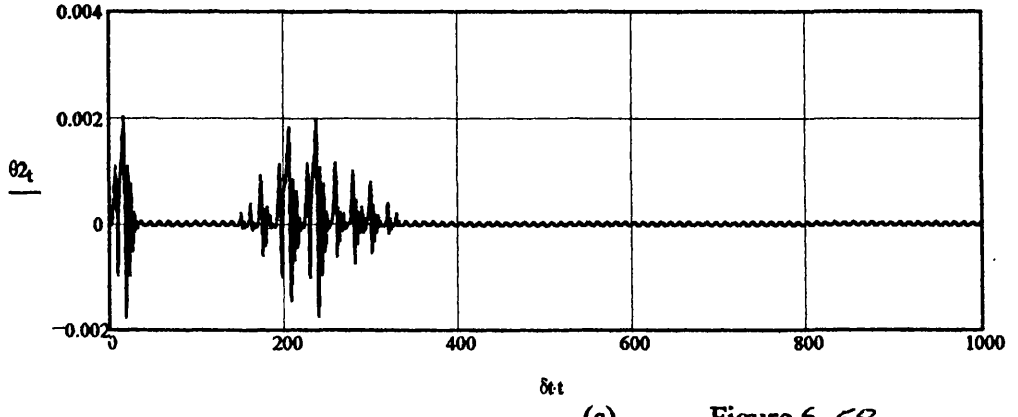

(rad)

Figure 6.58

Yaw

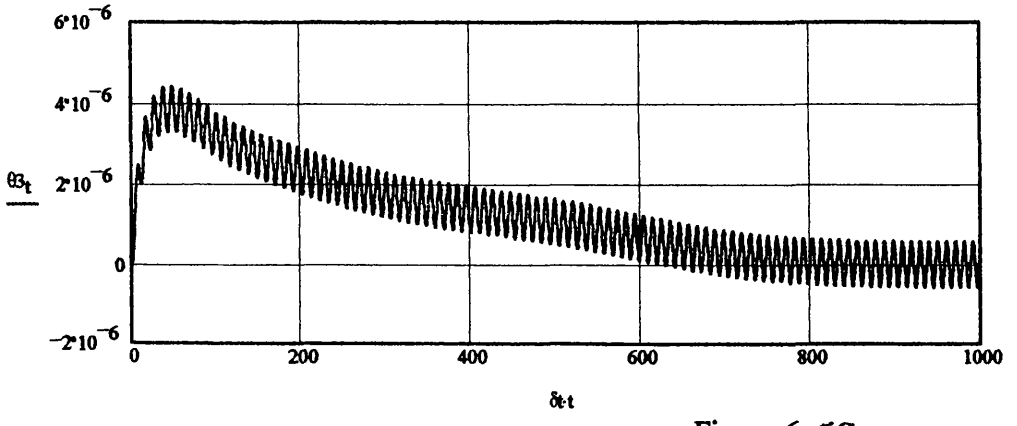

(rad)

Figure 6.59

Tether Force Time-series

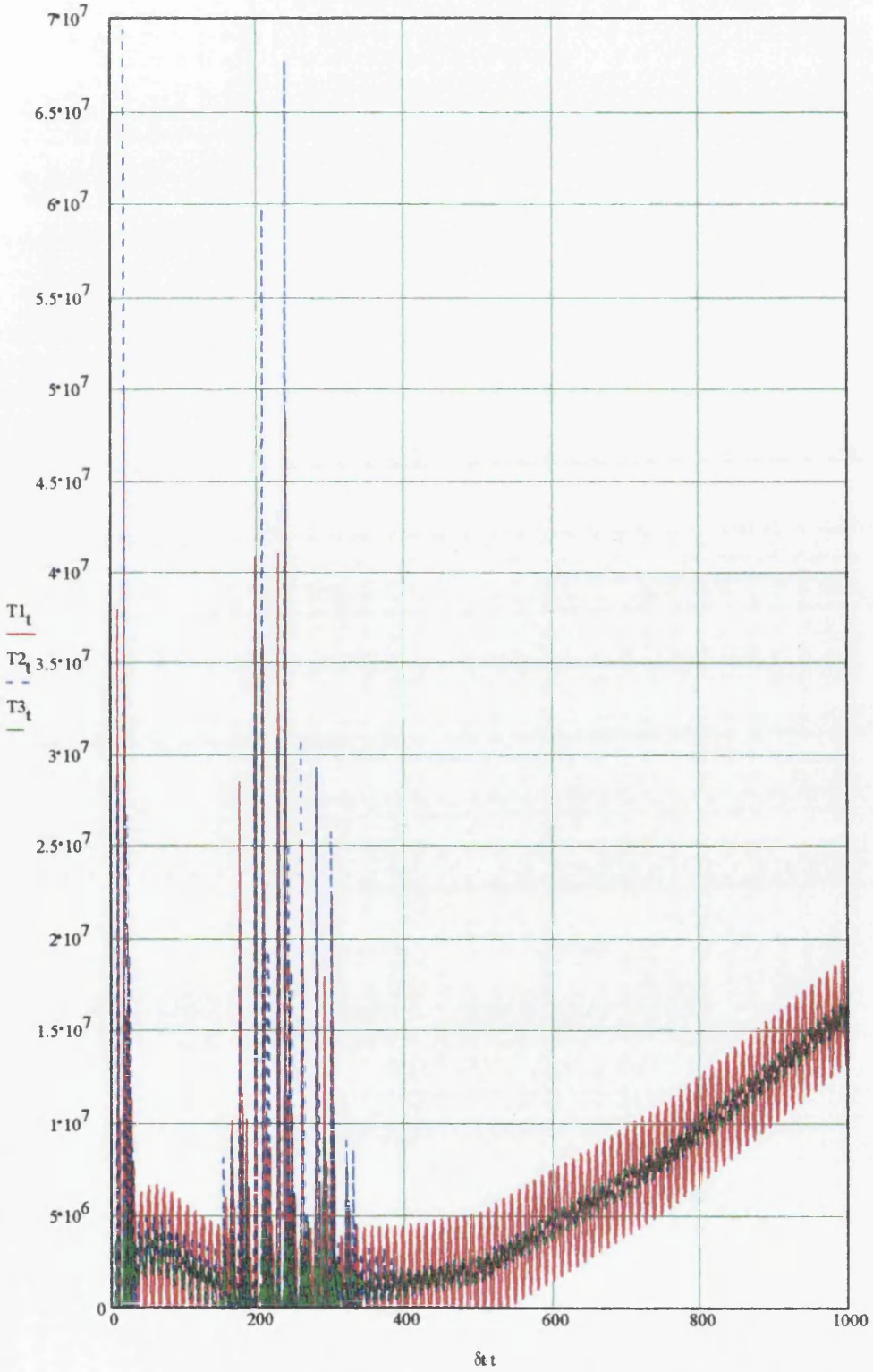

(N)

(s)

Figure 6. 60

2D *TLP* c.g. Motion Response (Heave v Surge)

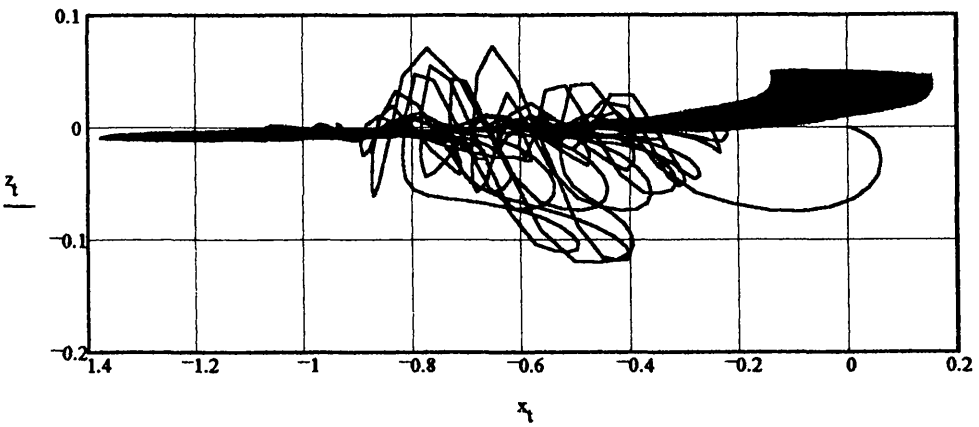

(m)

(m)

Figure 6.61

2D *TLP* c.g. Motion Response (Heave v Sway)

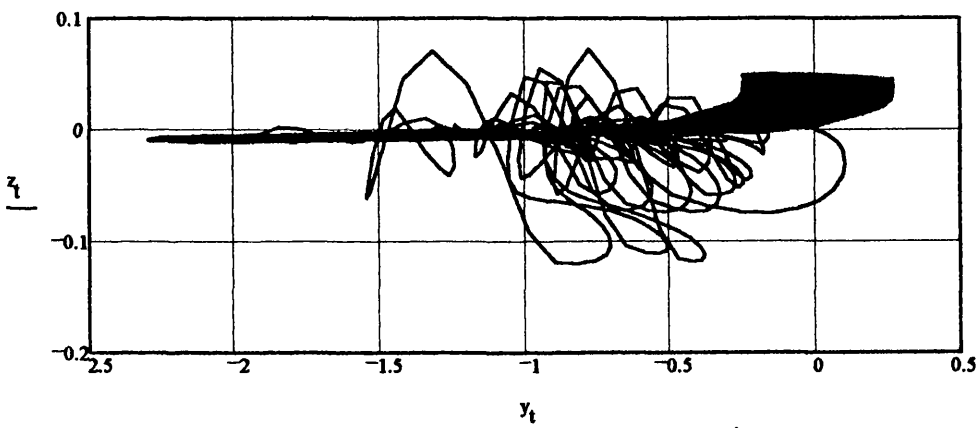

(m)

(m)

Figure 6.62

2D *TLP* c.g. Motion Response (Heave v Roll)

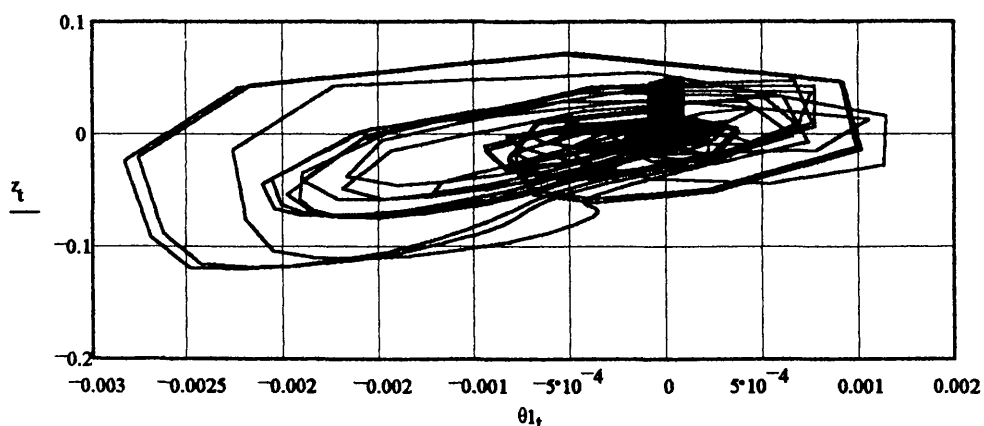

(m)

(rad)

Figure 6.63

2D *TLP* c.g. Motion Response (Heave v Pitch)

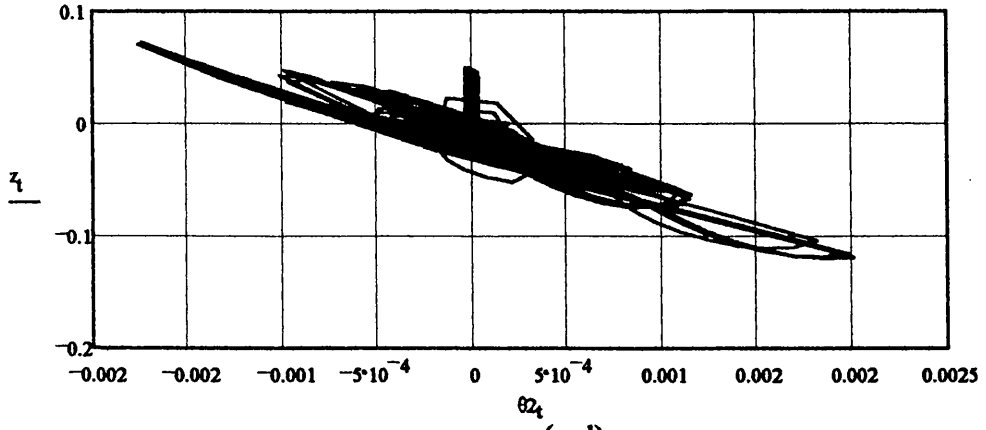

(m)

(rad)

Figure 6.64

2D *TLP* c.g. Motion Response (Heave v Yaw)

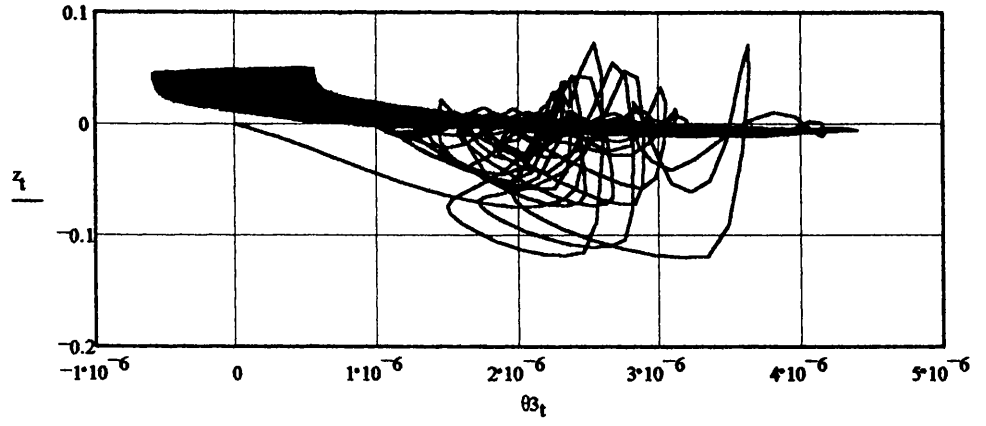

(m)

(rad)

Figure 6.65

2D *TLP* c.g. Motion Response (Surge v Sway)

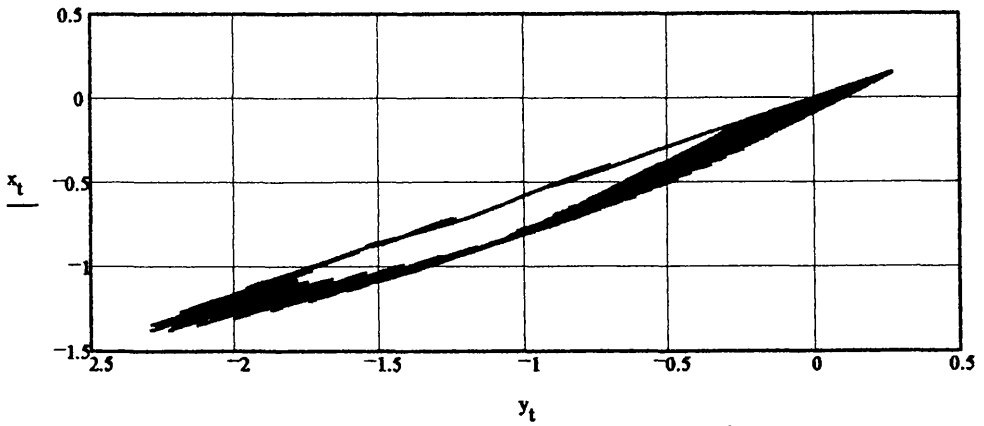

(m)

(m)

Figure 6.66

2D *TLP* c.g. Motion Response (Surge v Heave)

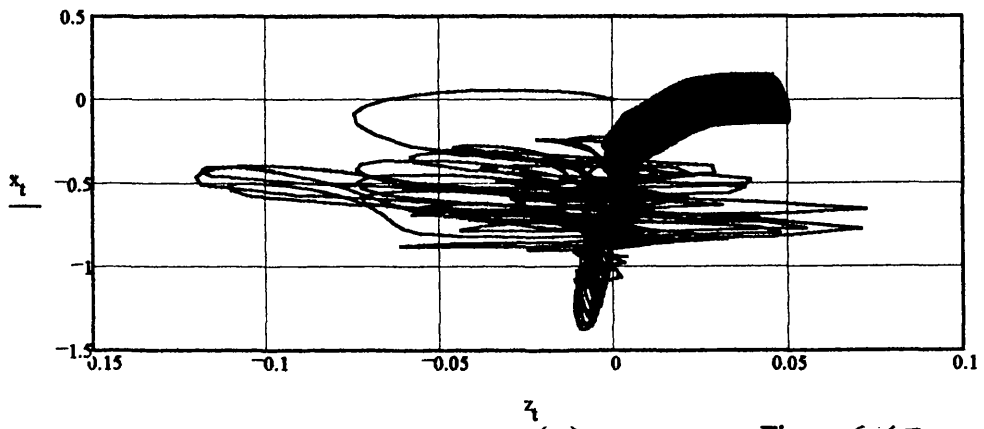

(m)

(m)

Figure 6.67

2D *TLP* c.g. Motion Response (Surge v Roll)

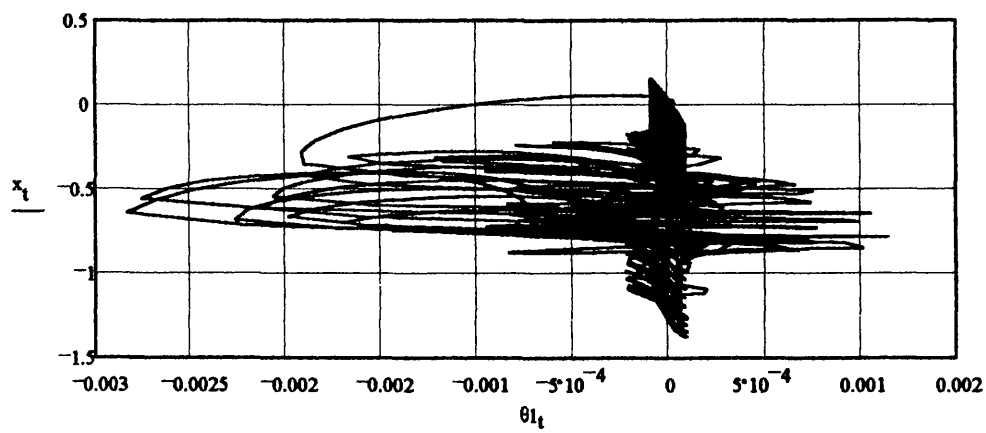

(m)

(rad)

Figure 6.68

2D *TLP* c.g. Motion Response (Surge v Pitch)

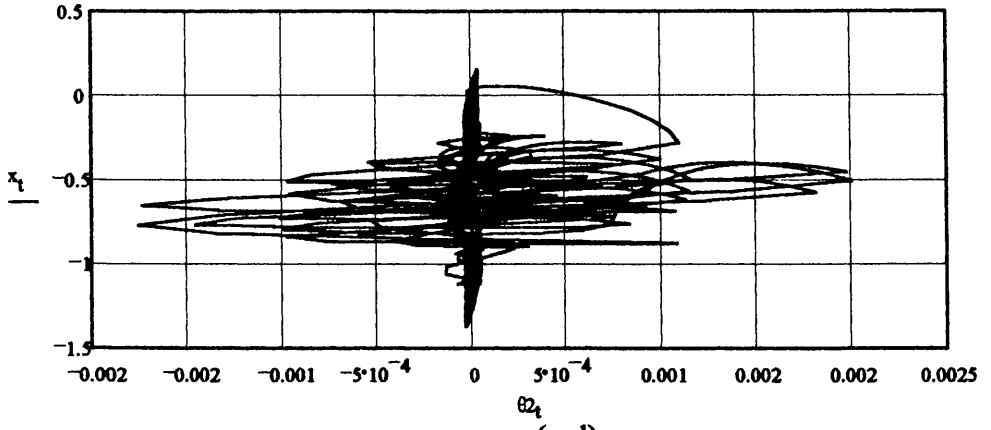

(m)

(rad)

Figure 6.69

2D *TLP* c.g. Motion Response (Surge v Yaw)

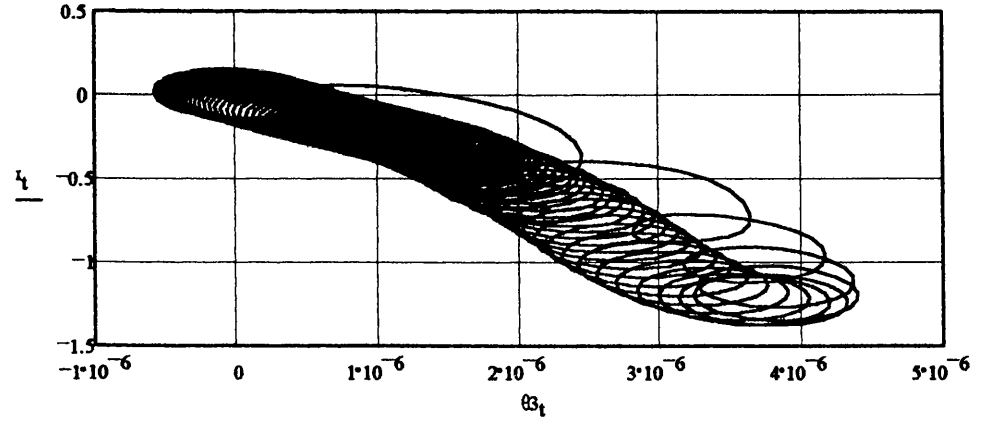

(m)

Figure 6.70

(rad)

Figures 6.71-6.87 detail the time-domain simulation results for the AA Case Study TLP for an incident regular wave of ω =0.6rad/s (ξ_a =9m) with a heading angle of 60^0.

Figures 6.71-6.76 detail the surge, sway, heave, roll, pitch and yaw DOF response respectively.

Figure 6.77 details the tether 'bundle' tension time-series response.

Figures 6.78-6.87 detail the platform vertical/horizontal and cross-planer response.

TLP Global Dynamic Response in Time-domain (*6DOF*):

(Space-fixed coordinate system)

DISPLACEMENT

Surge

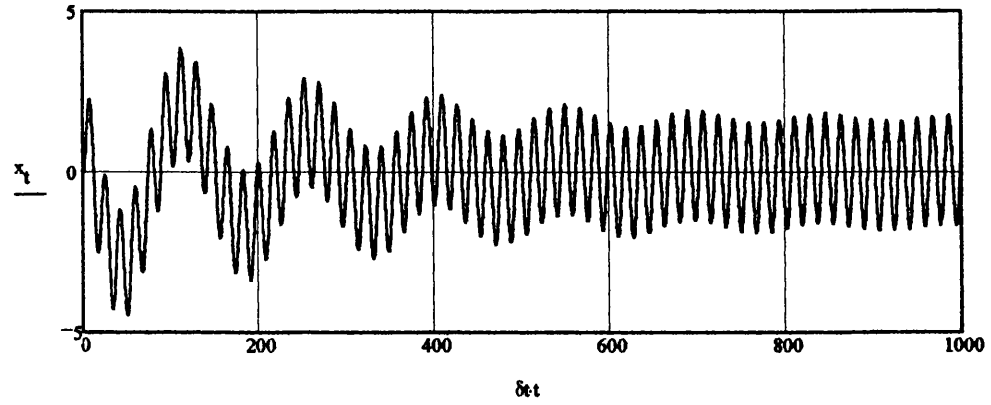

(m)

Figure 6.71

Sway

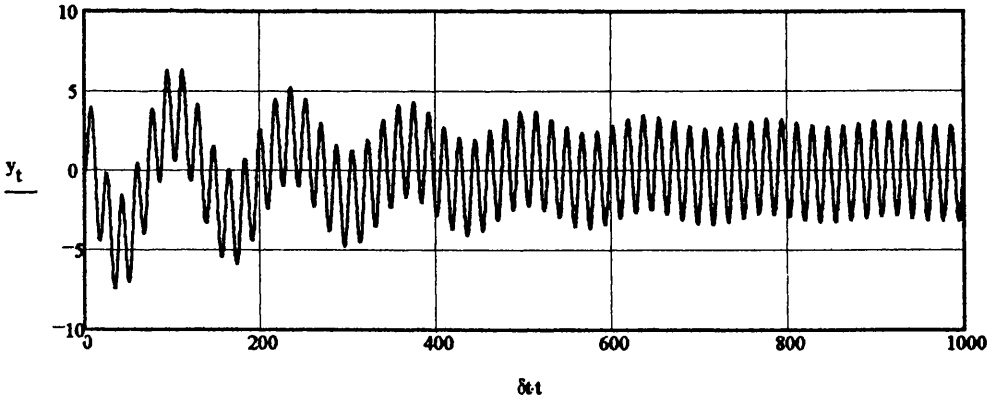

(m)

Figure 6.72

Heave

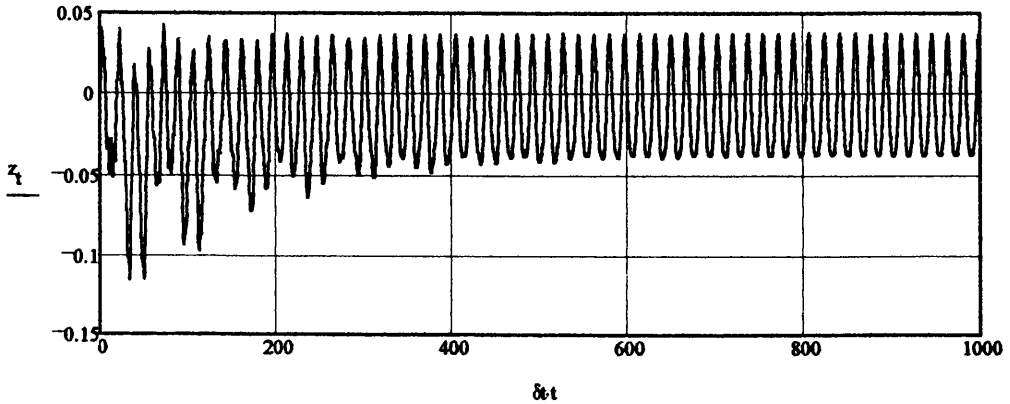

(m)

Figure 6.73

Roll

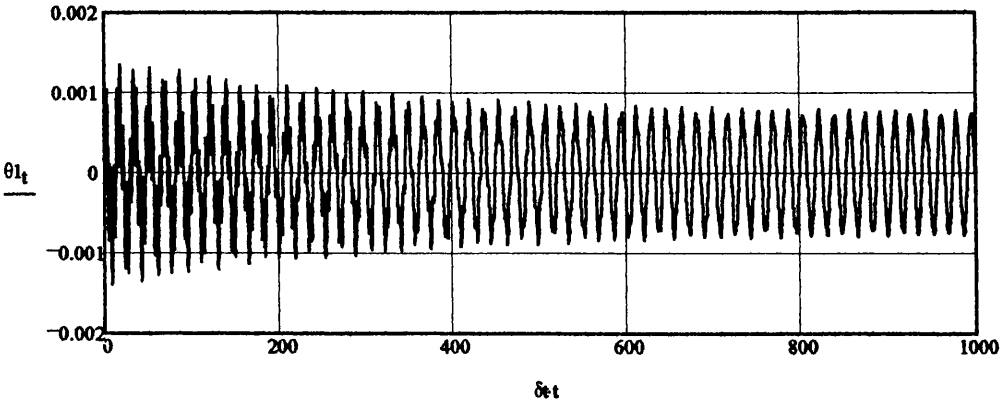

(rad)

(s)

Figure 6.74

Pitch

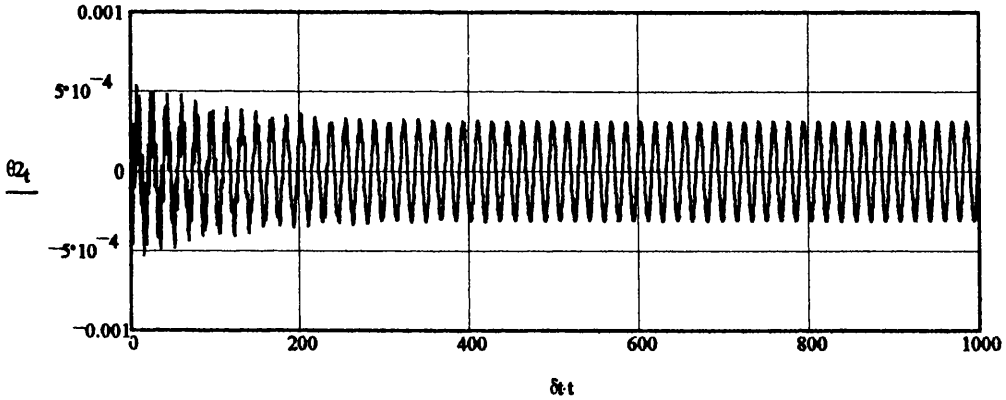

(rad)

(s)

Figure 6.75

Yaw

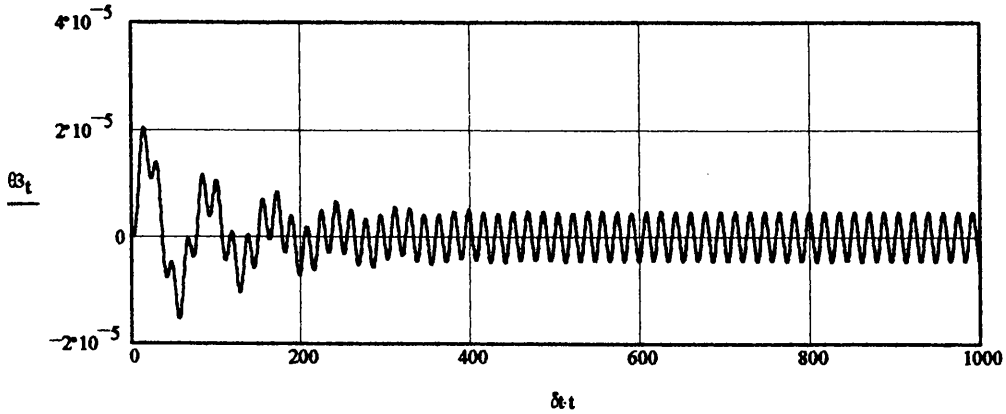

(rad)

(s)

Figure 6.76

Tether Force Time-series

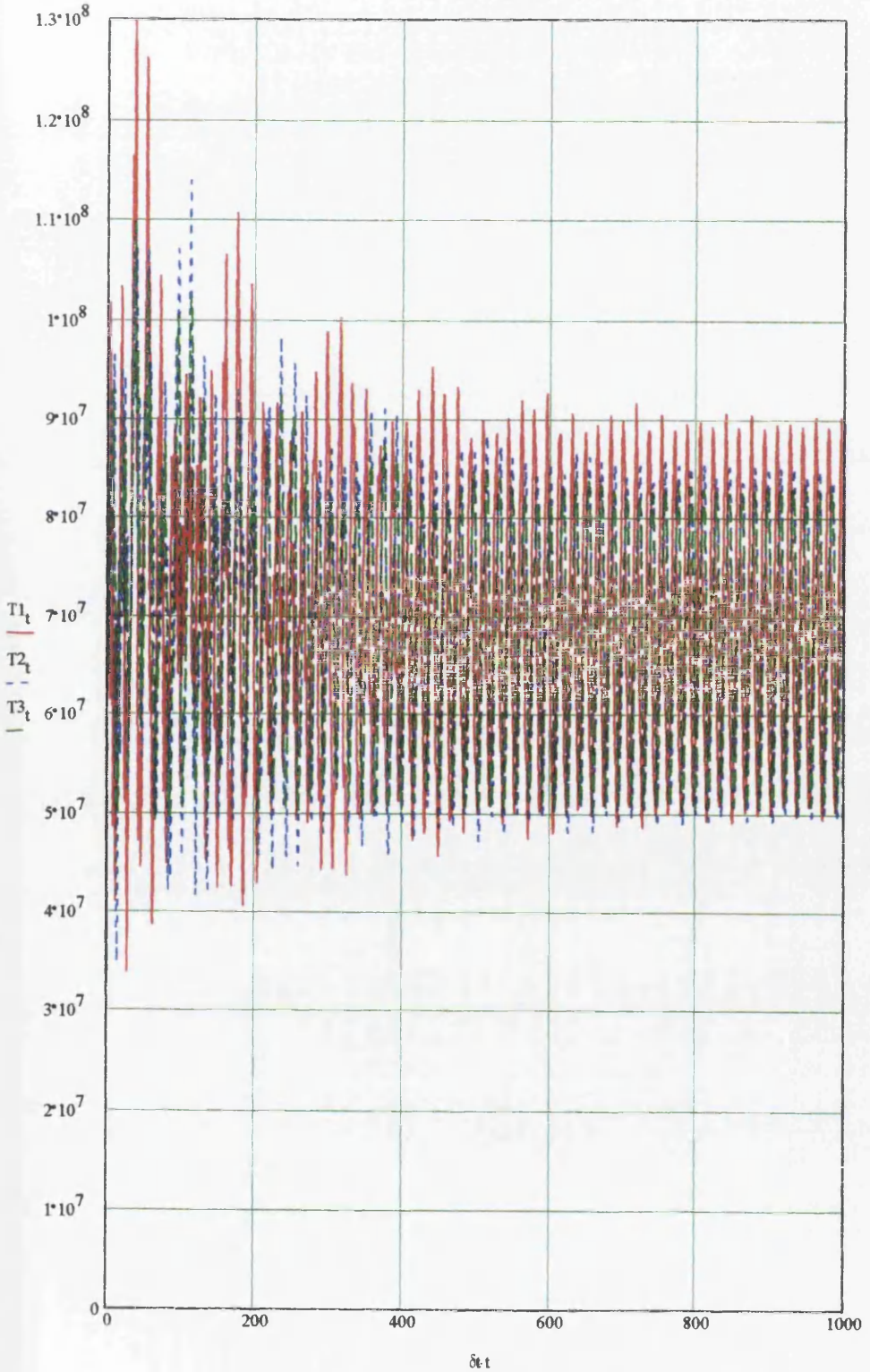

(N)

Figure 6.77

2D *TLP* c.g. Motion Response (Heave v Surge)

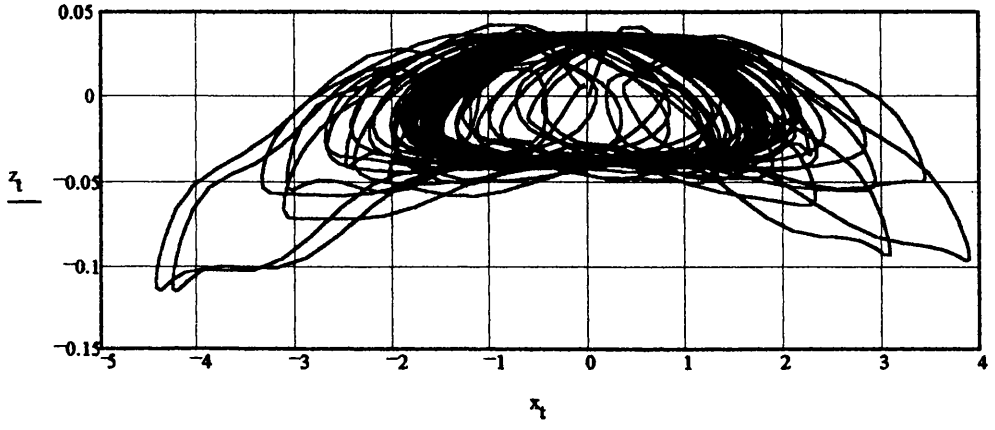

(m)

(m)

Figure 6.78

2D *TLP* c.g. Motion Response (Heave v Sway)

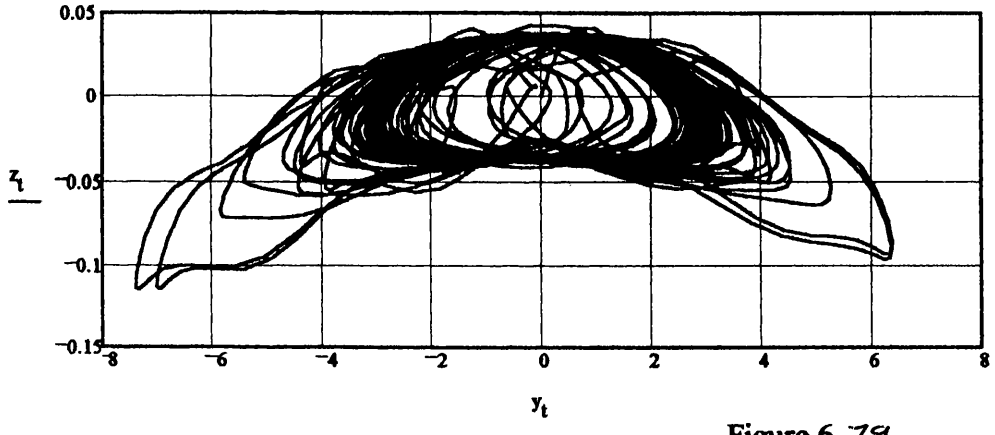

(m)

(m)

Figure 6.79

2D *TLP* c.g. Motion Response (Heave v Roll)

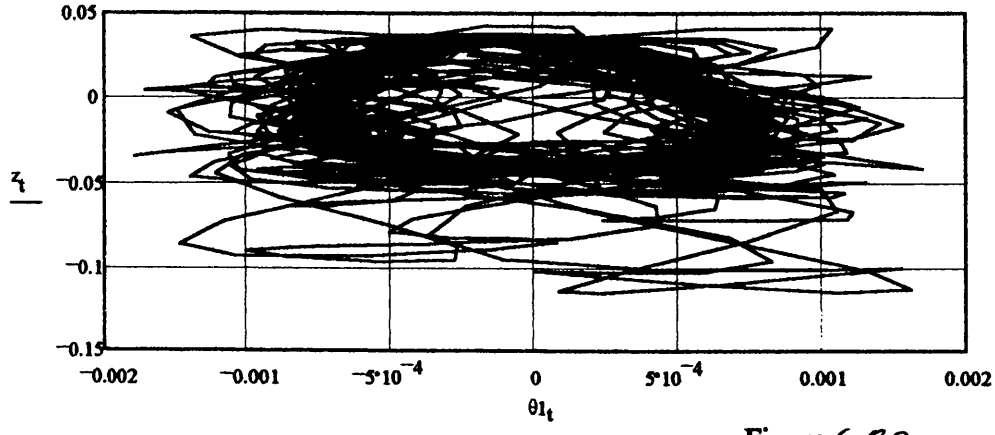

(m)

(rad)

Figure 6.80

2D *TLP* c.g. Motion Response (Heave v Pitch)

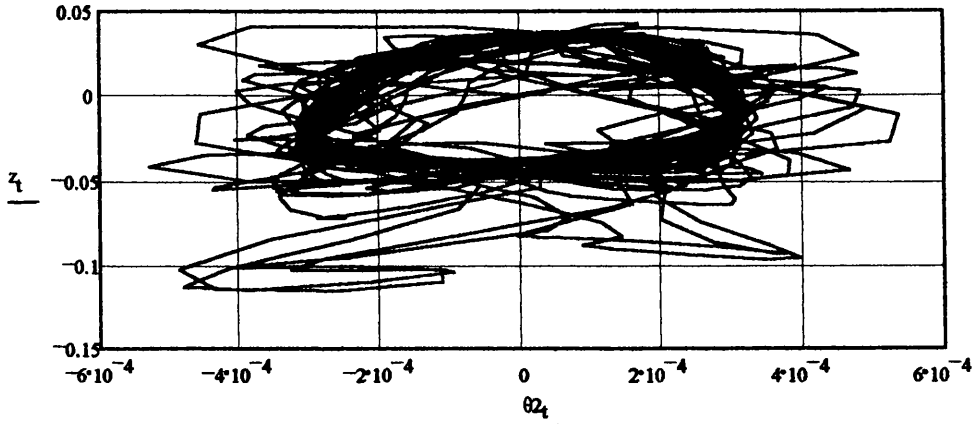

(m)

(rad)

Figure 6.81

2D *TLP* c.g. Motion Response (Heave v Yaw)

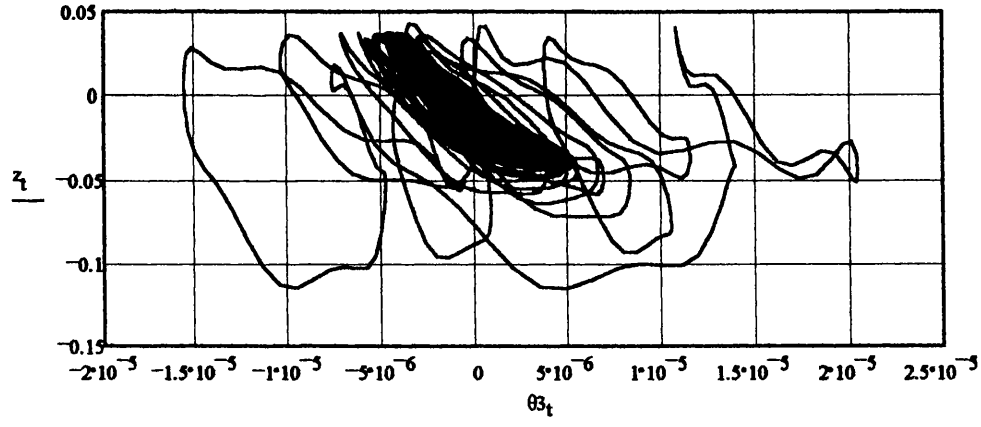

(m)

(rad)

Figure 6.82

2D *TLP* c.g. Motion Response (Surge v Sway)

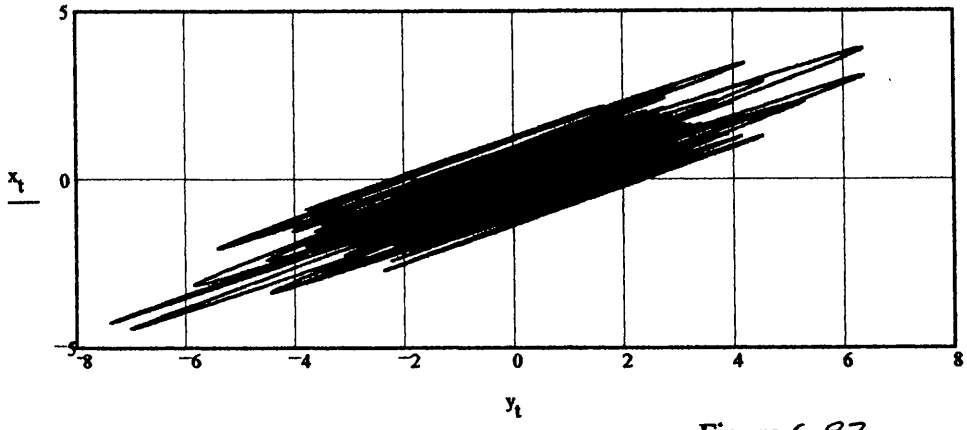

Figure 6. 83

2D *TLP* c.g. Motion Response (Surge v Heave)

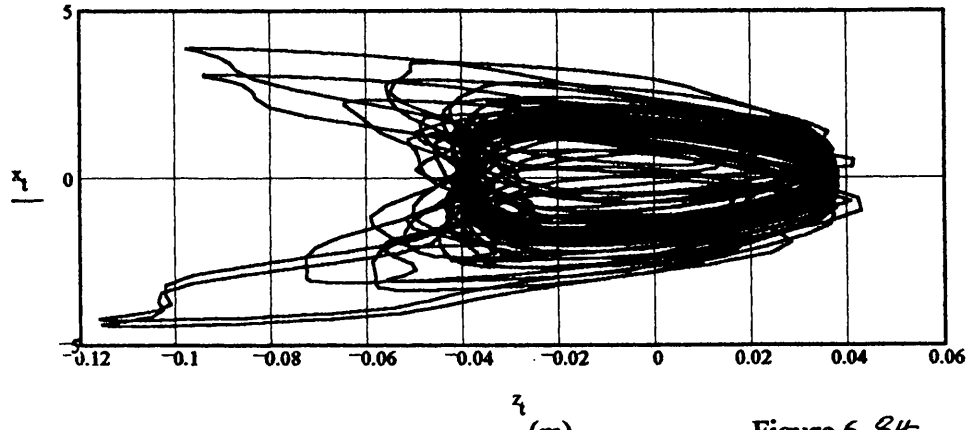

Figure 6. 84

2D *TLP* c.g. Motion Response (Surge v Roll)

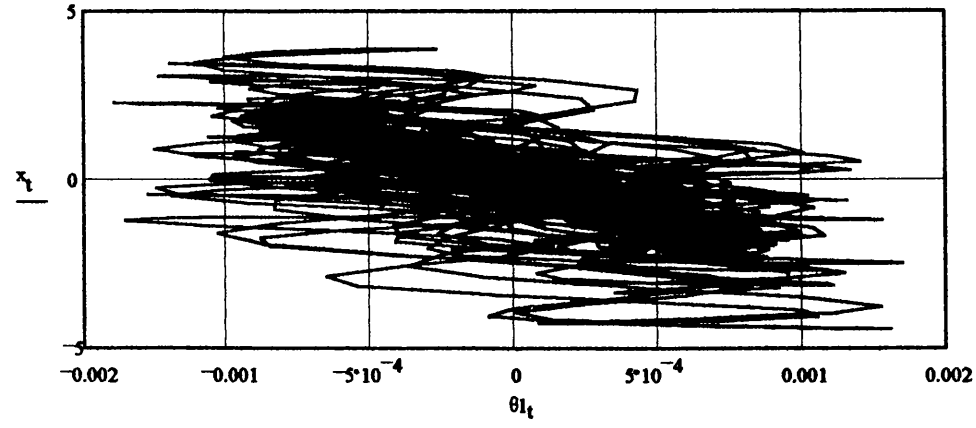

Figure 6. 85

2D *TLP* c.g. Motion Response (Surge v Pitch)

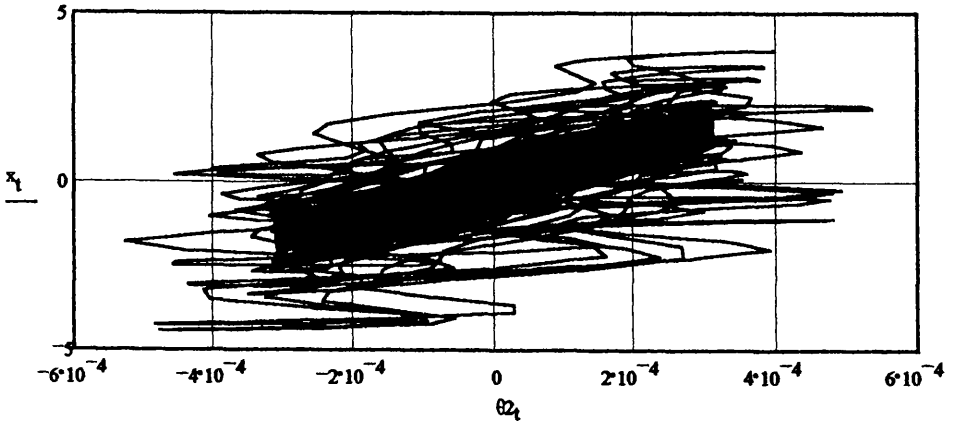

(m)

(rad)

Figure 6. 86

2D *TLP* c.g. Motion Response (Surge v Yaw)

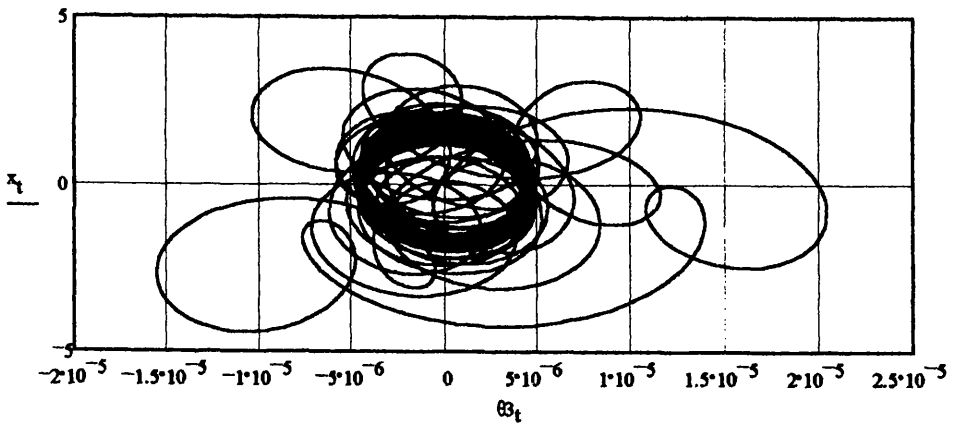

(m)

Figure 6. 87

(rad)

6.3.1.3 Heidrun TLP

Figures 6.99-6.104 detail the time-domain simulation results for the Heidrun Case Study TLP for an incident regular wave of ω =0.6rad/s (ξ_a =1.25m) with a heading angle of 45^0 (225^0) (without motion compensation).

Figures 6.88-6.93 detail the surge, sway, heave, roll, pitch and yaw DOF response respectively.

Figure 6.94 details the tether 'bundle' tension time-series response.

Figures 6.95-6.104 detail the platform vertical/horizontal and cross-planer response.

TLP Global Dynamic Response in Time-domain (6*DOF*):

(Space-fixed coordinate system)

DISPLACEMENT

Surge

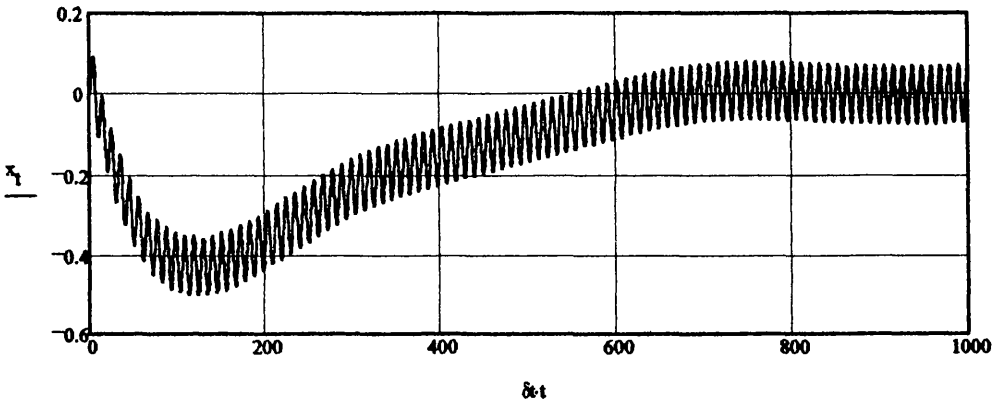

(m)

Figure 6.88

Sway

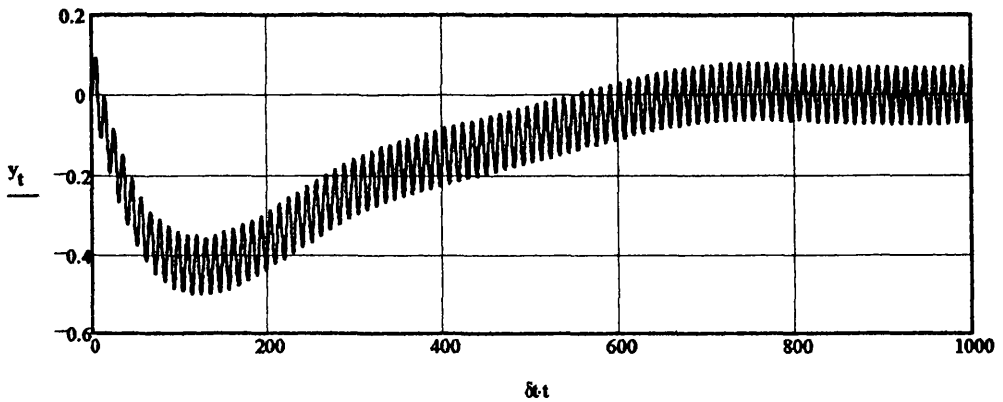

(m)

Figure 6.89.

Heave

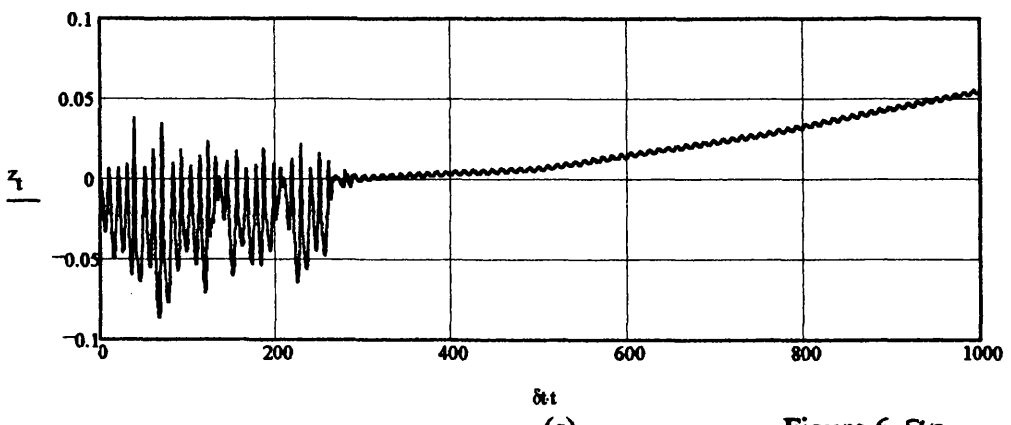

(m)

Figure 6.90

Roll

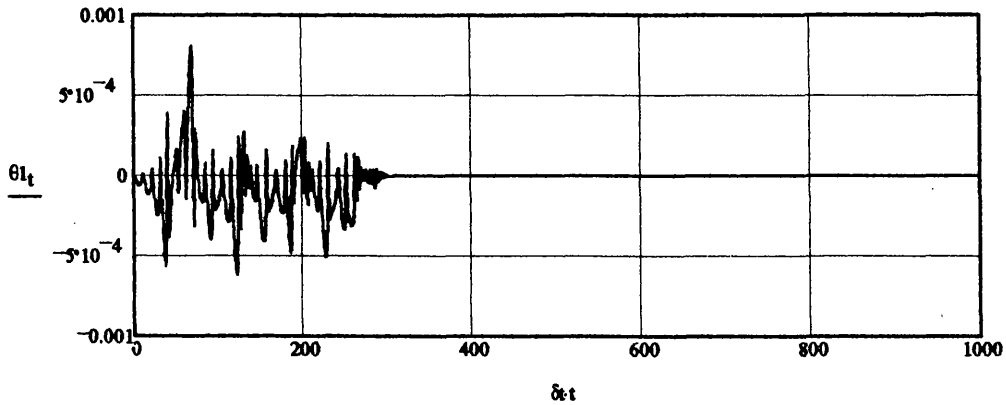

(rad)

Figure 6.91

Pitch

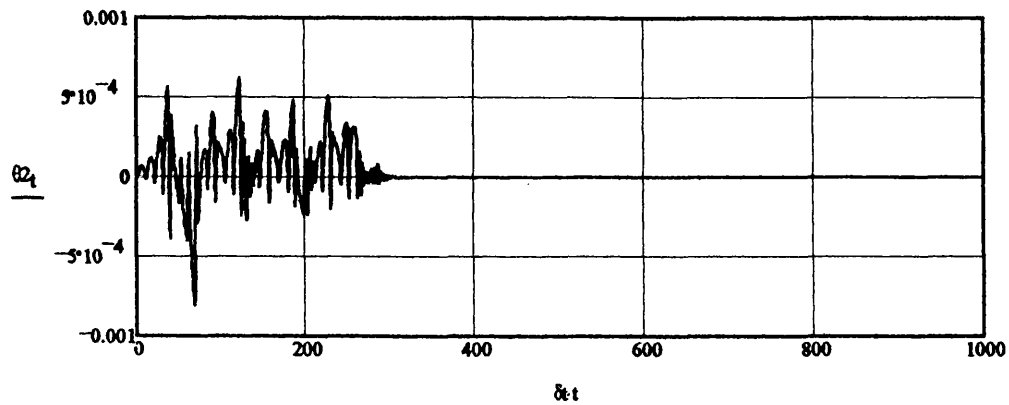

(rad)

Figure 6.92

Yaw

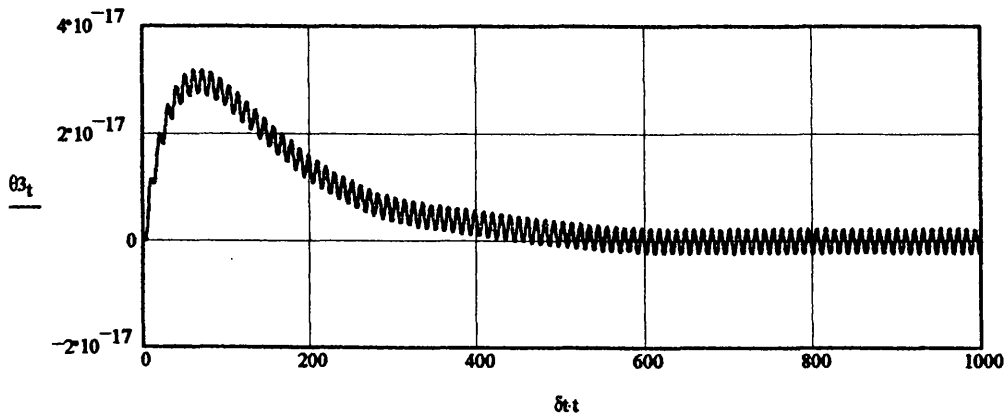

(rad)

Figure 6.93

Tether Force Time-series

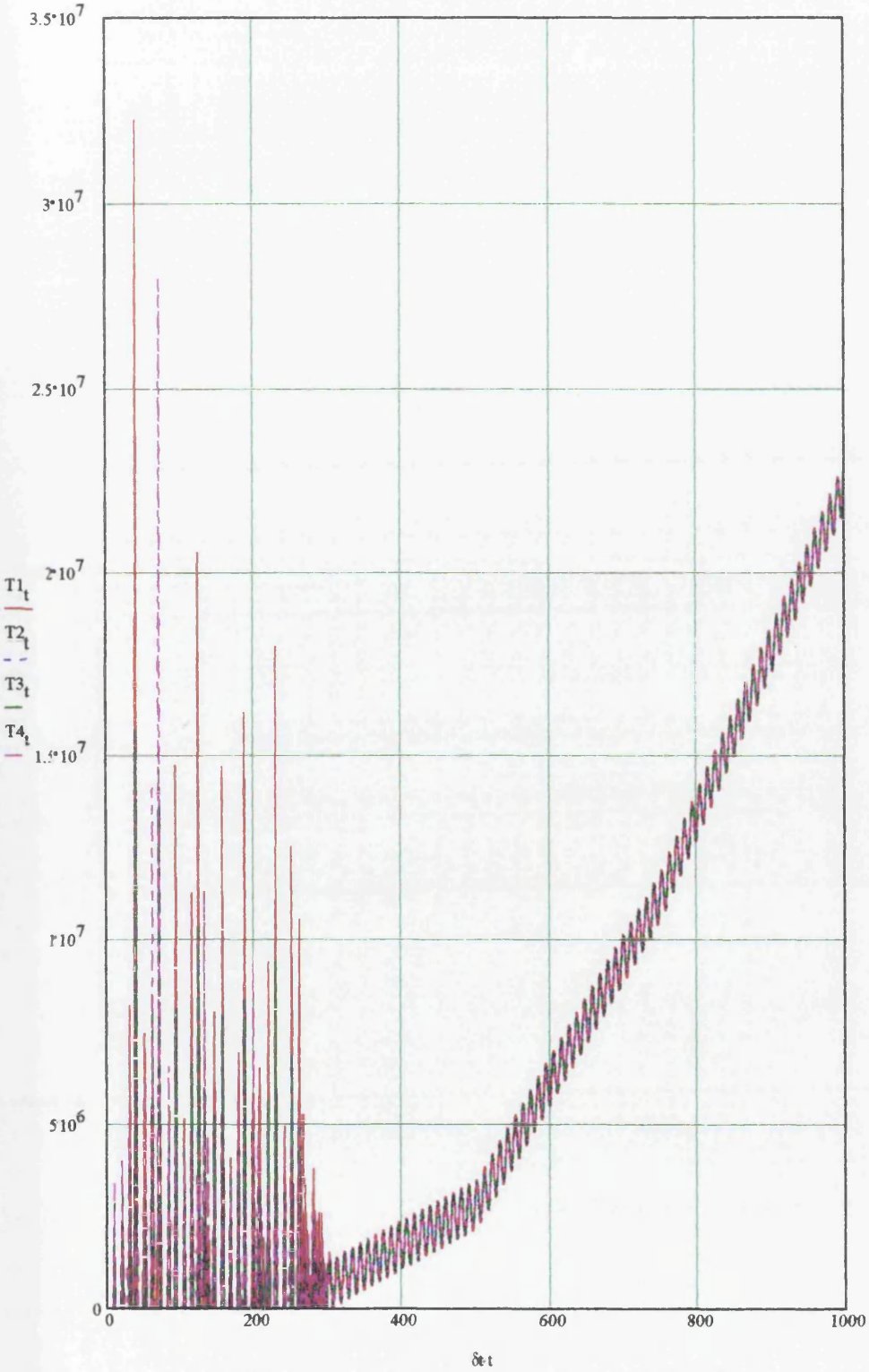

Figure 6. 94

2D *TLP* c.g. Motion Response (Heave v Surge)

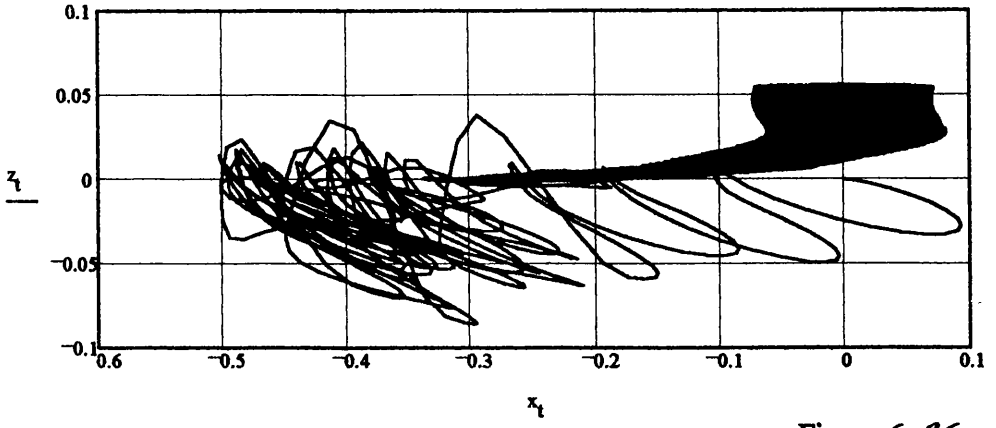

Figure 6. 95

2D *TLP* c.g. Motion Response (Heave v Sway)

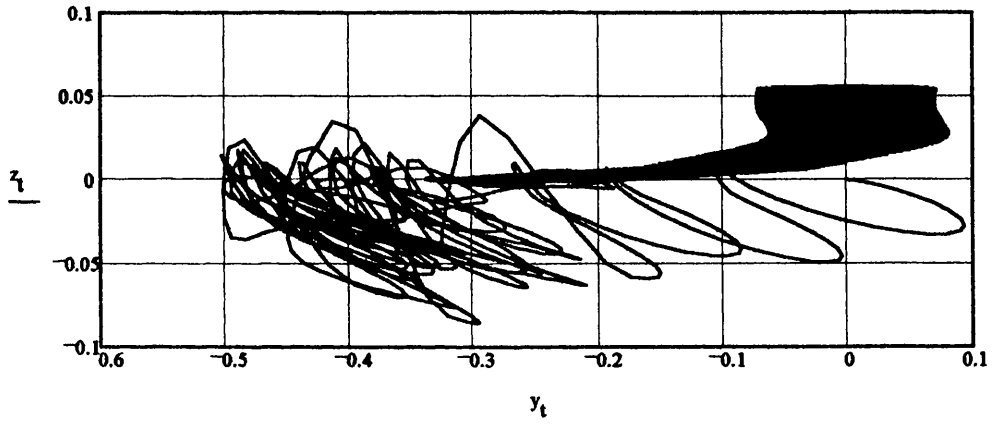

Figure 6. 96

2D *TLP* c.g. Motion Response (Heave v Roll)

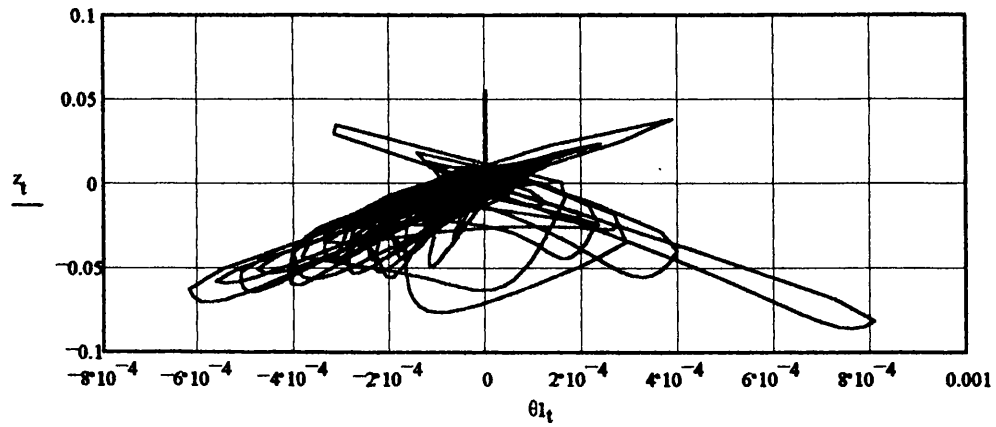

Figure 6. 97

2D *TLP* c.g. Motion Response (Heave v Pitch)

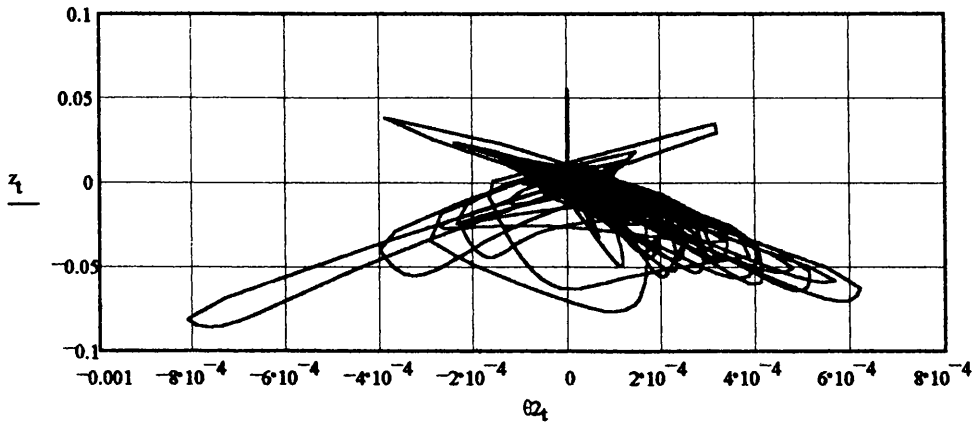

(m)

(rad)

Figure 6. 98

2D *TLP* c.g. Motion Response (Heave v Yaw)

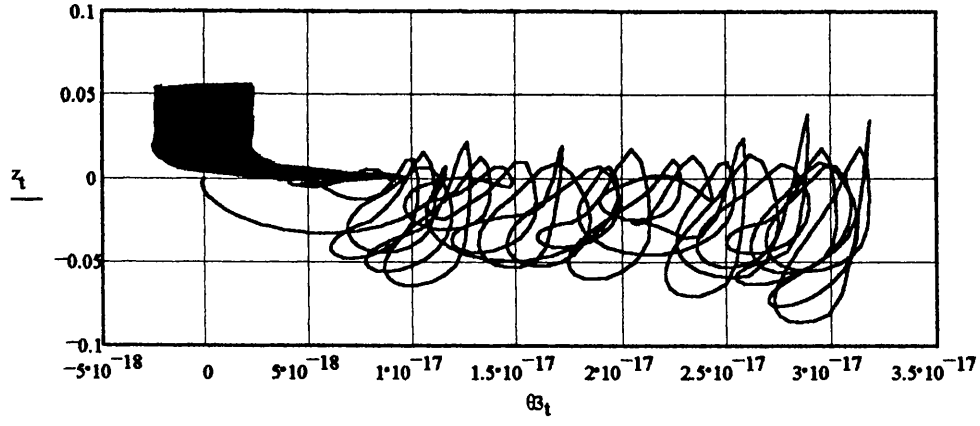

(m)

(rad)

Figure 6. 99

2D *TLP* c.g. Motion Response (Surge v Sway)

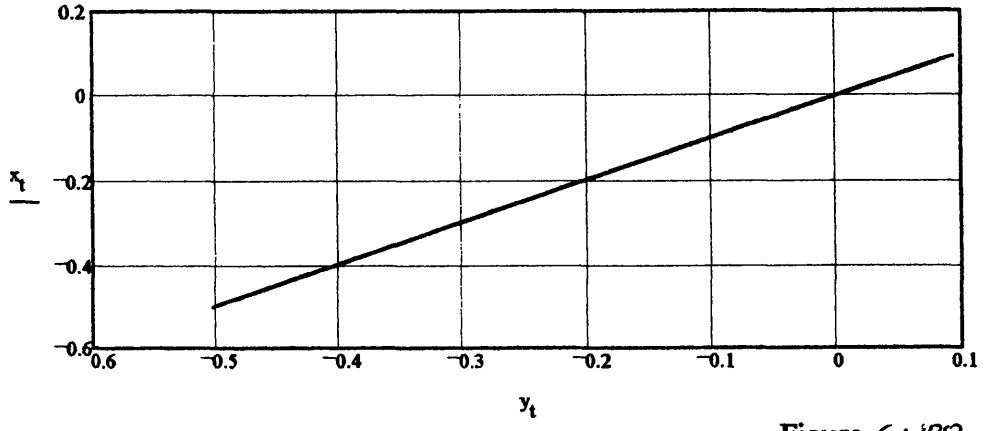

(m)

(m)

Figure 6·100

2D *TLP* c.g. Motion Response (Surge v Heave)

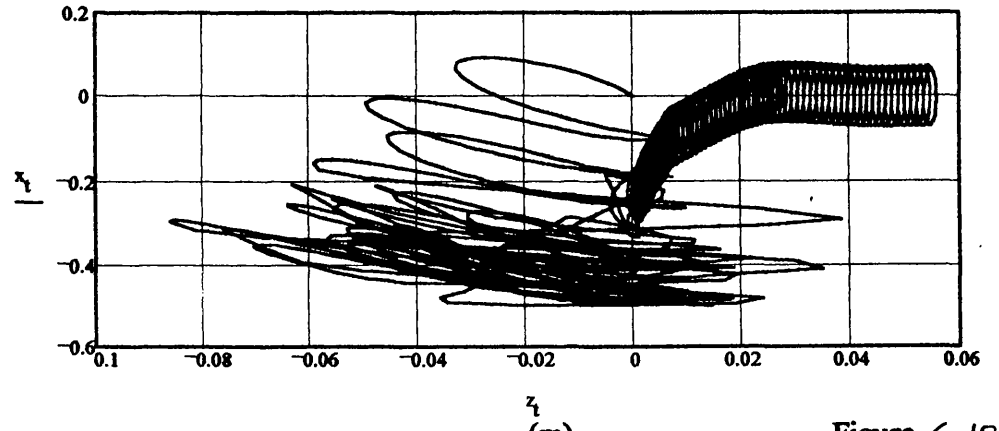

(m)

(m)

Figure 6·101

2D *TLP* c.g. Motion Response (Surge v Roll)

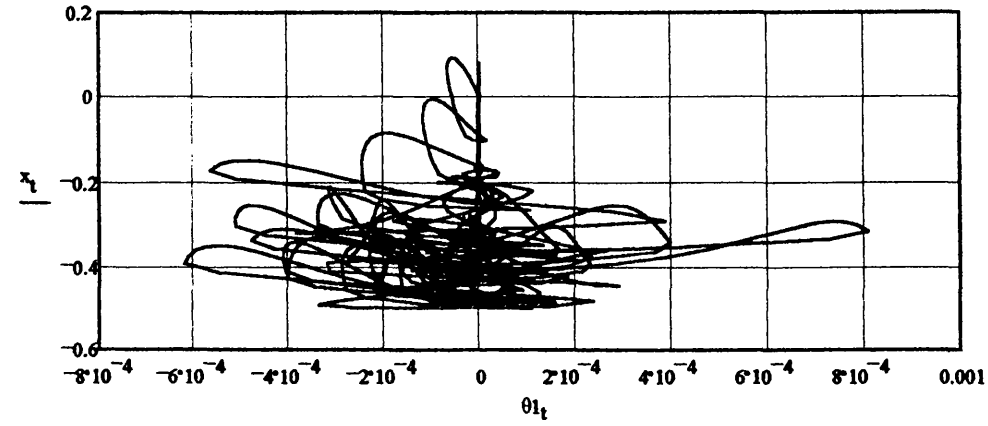

(m)

(rad)

Figure 6·102

2D *TLP* c.g. Motion Response (Surge v Pitch)

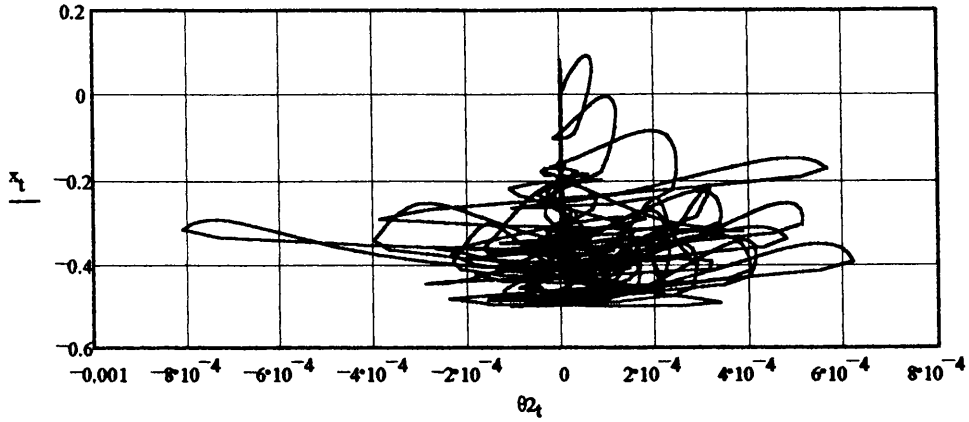

(m)

(rad)

Figure 6.103

2D *TLP* c.g. Motion Response (Surge v Yaw)

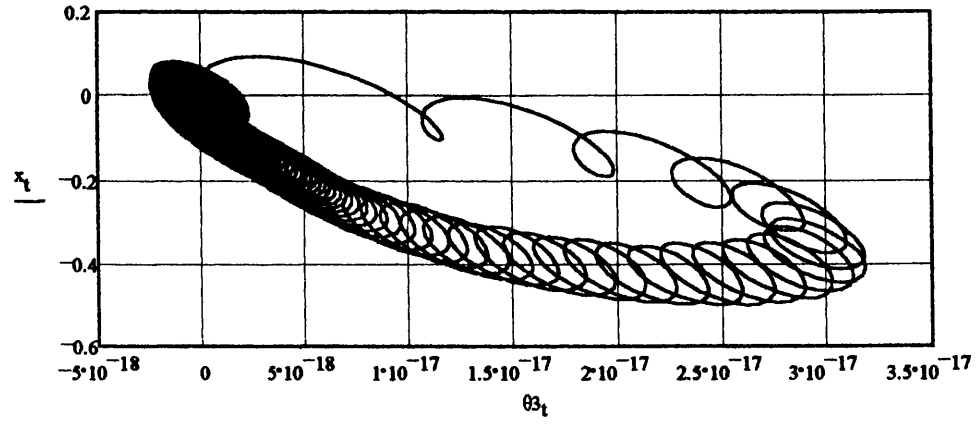

(m)

(rad)

Figure 6.104

Figures 6.105-6.121 detail the time-domain simulation results for the Heidrun Case Study TLP for an incident regular wave of ω =0.6rad/s (ξ_a =1.25m) with a heading angle of 45^0 (225^0) (with motion compensation).

Figures 6.105-6.110 detail the surge, sway, heave, roll, pitch and yaw DOF response respectively.

Figure 6.111 details the tether 'bundle' tension time-series response.

Figures 6.112-6.121 detail the platform vertical/horizontal and cross-planer response.

TLP Global Dynamic Response in Time-domain (*6DOF*):

(Space-fixed coordinate system)

DISPLACEMENT

Surge

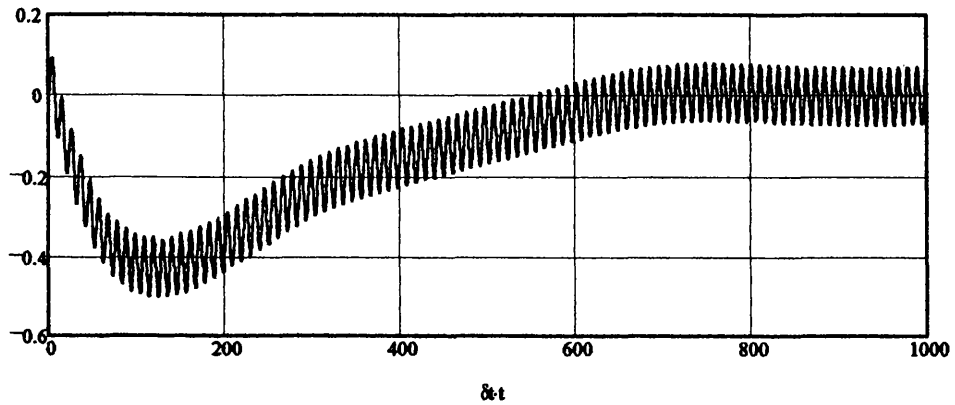

(m)

Figure 6.105

Sway

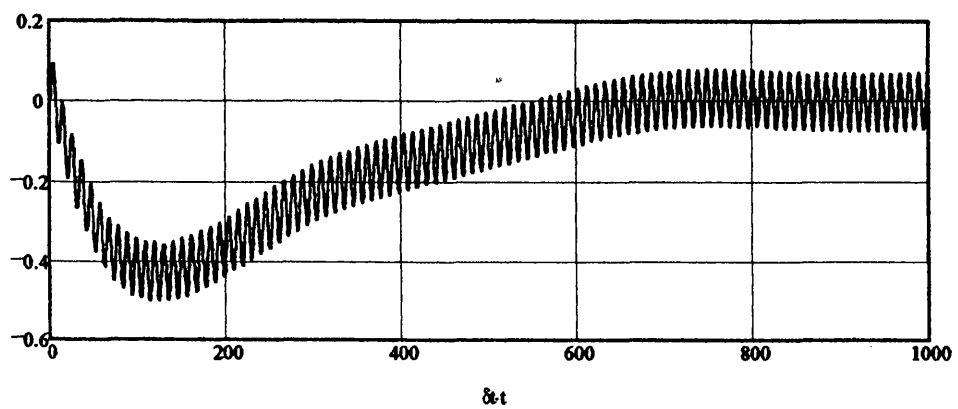

(m)

Figure 6.106

Heave

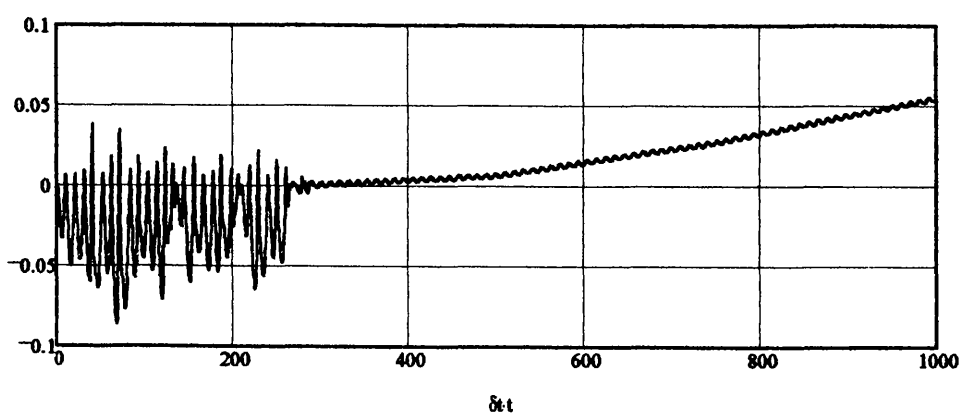

(m)

Figure 6.107

Roll

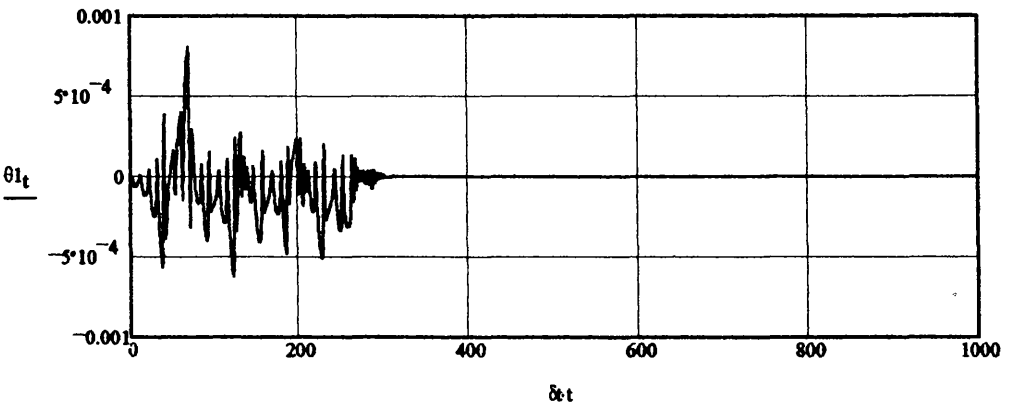

(rad)

Figure 6..108

Pitch

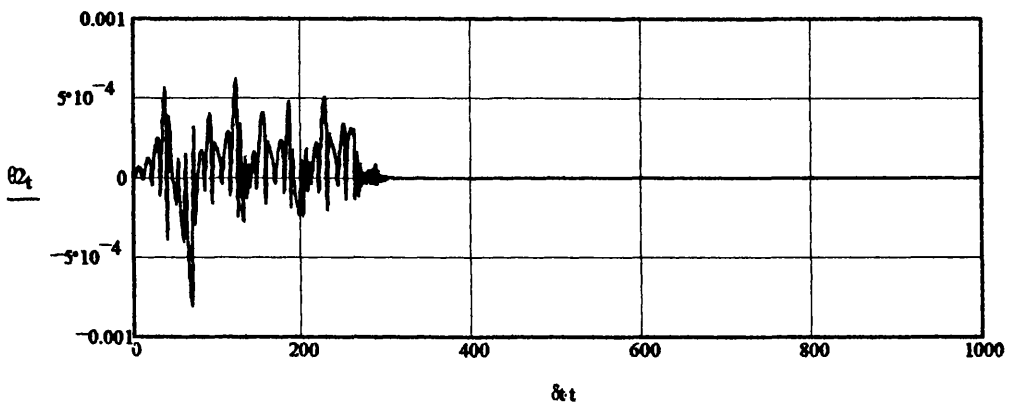

(rad)

Figure 6..109

Yaw

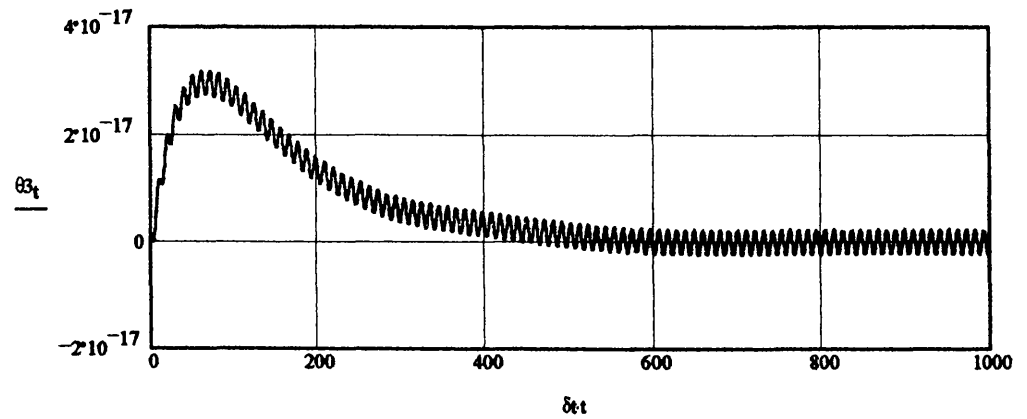

(rad)

Figure 6. 110

Tether Force Time-series

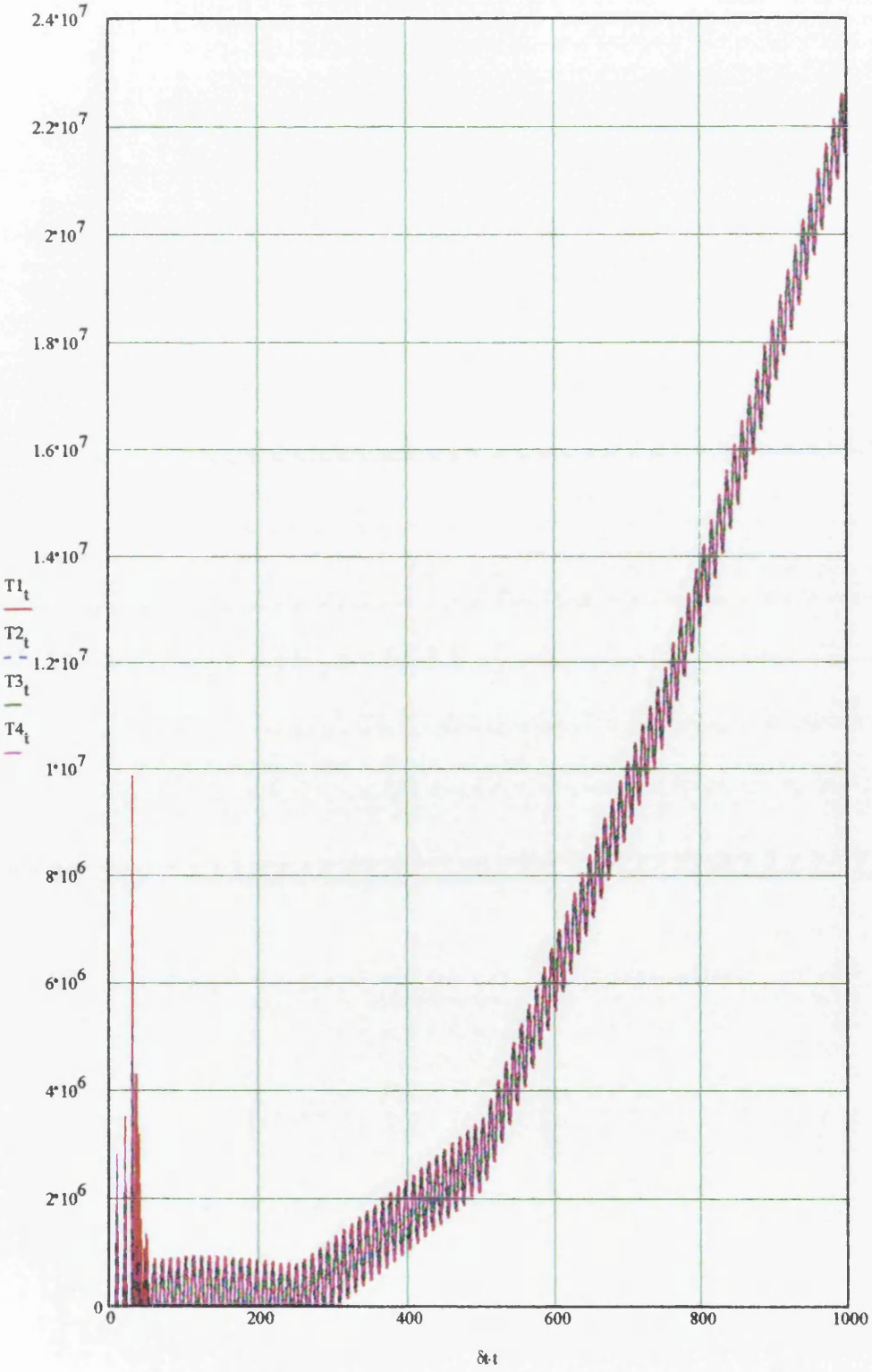

(N)

(s)

Figure 6.111

2D *TLP* c.g. Motion Response (Heave v Surge)

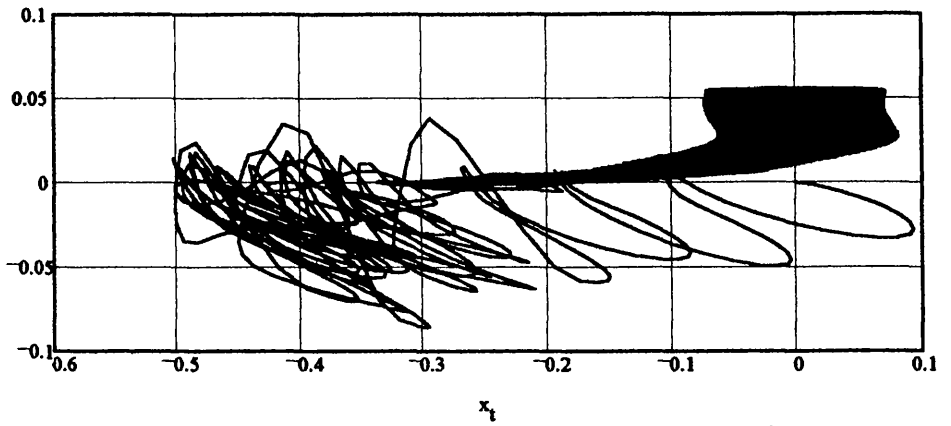

(m)

(m)

Figure 6.113

2D *TLP* c.g. Motion Response (Heave v Sway)

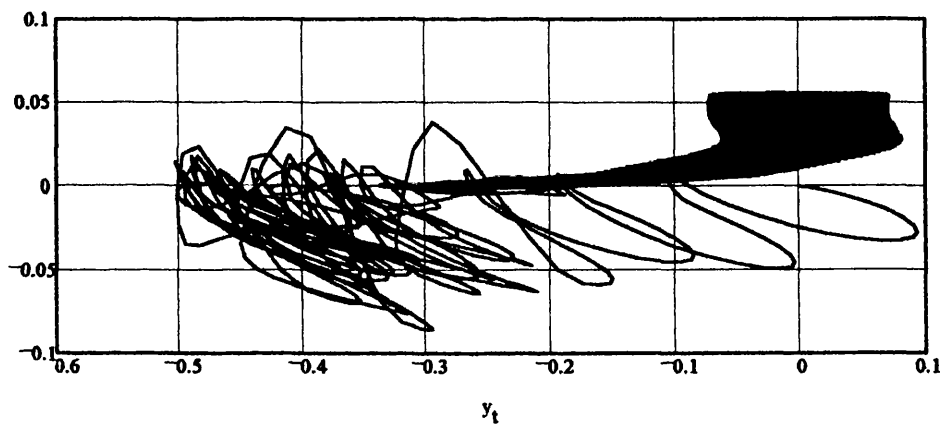

(m)

(m)

Figure 6.114

2D *TLP* c.g. Motion Response (Heave v Roll)

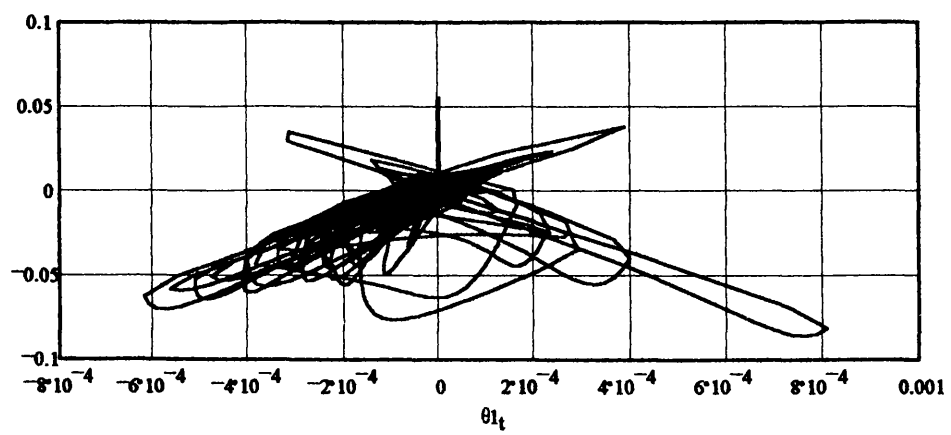

(m)

(rad)

Figure 6.115

2D *TLP* c.g. Motion Response (Heave v Pitch)

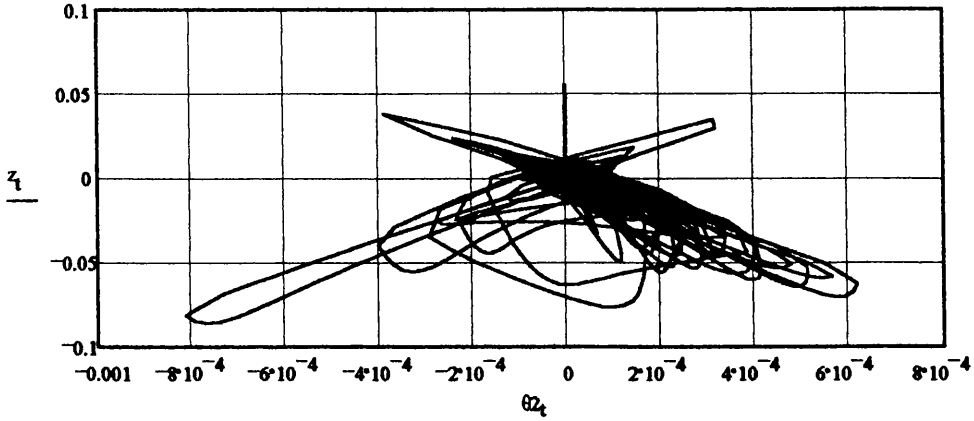

(m)

(rad)

Figure 6.115

2D *TLP* c.g. Motion Response (Heave v Yaw)

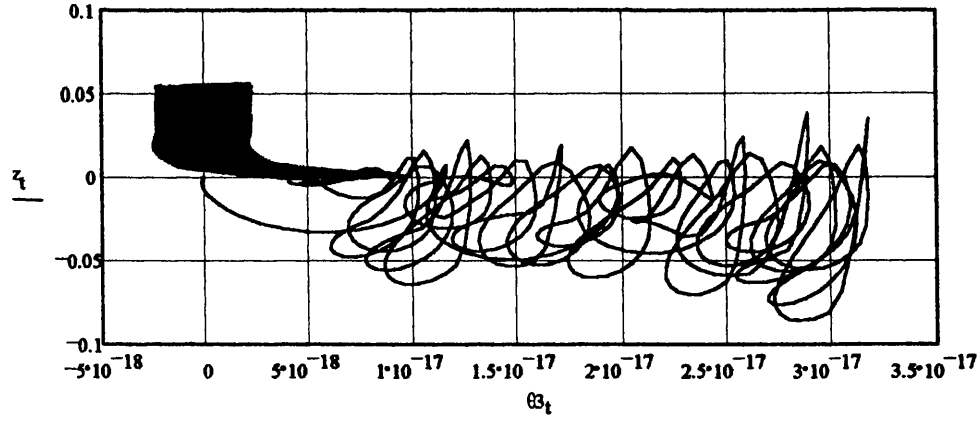

(m)

(rad)

Figure 6.116

2D *TLP* c.g. Motion Response (Surge v Sway)

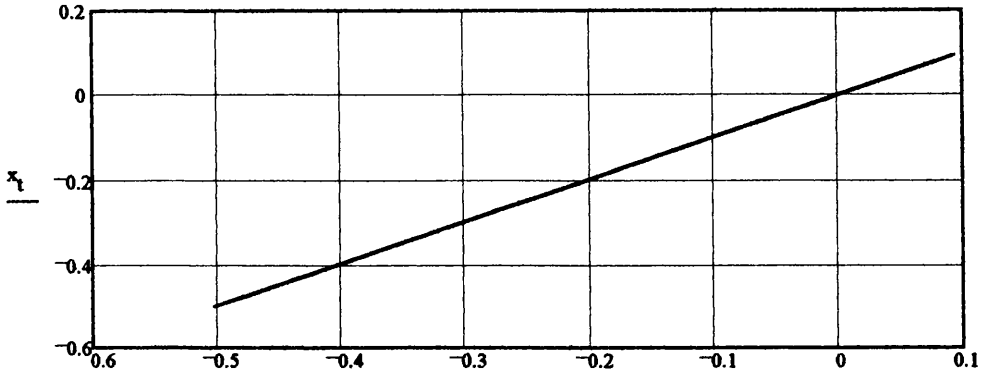

(m)

Figure 6.117

2D *TLP* c.g. Motion Response (Surge v Heave)

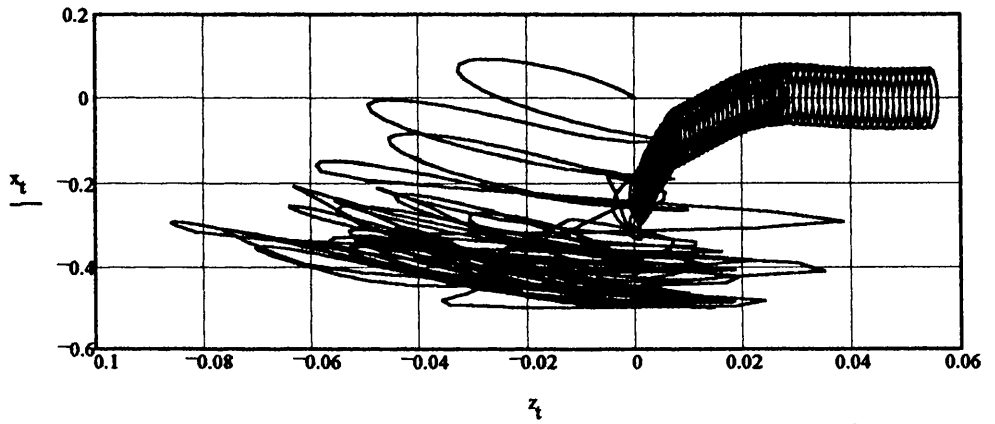

(m)

Figure 6.118

2D *TLP* c.g. Motion Response (Surge v Roll)

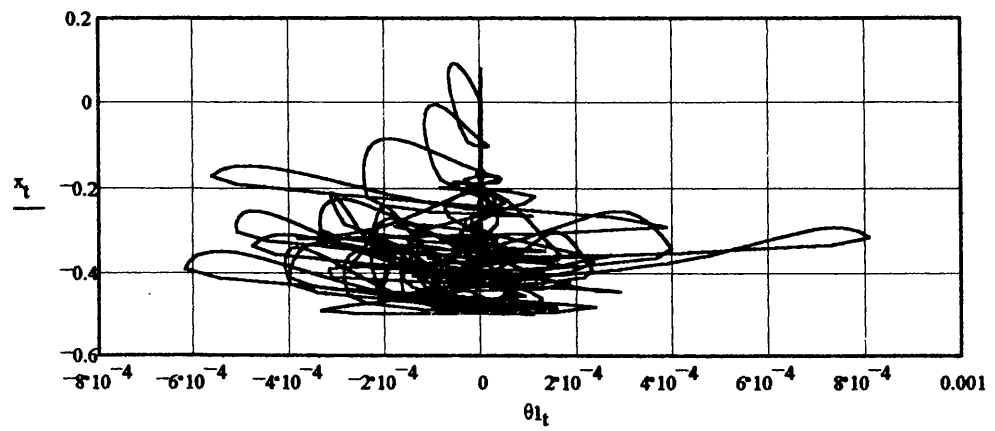

(m)

Figure 6.119

2D *TLP* c.g. Motion Response (Surge v Pitch)

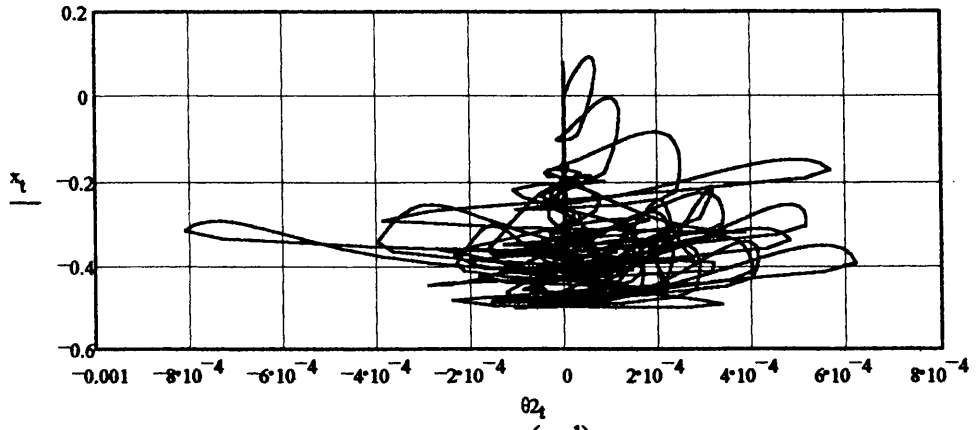

(m)

(rad)

Figure 6.120

2D *TLP* c.g. Motion Response (Surge v Yaw)

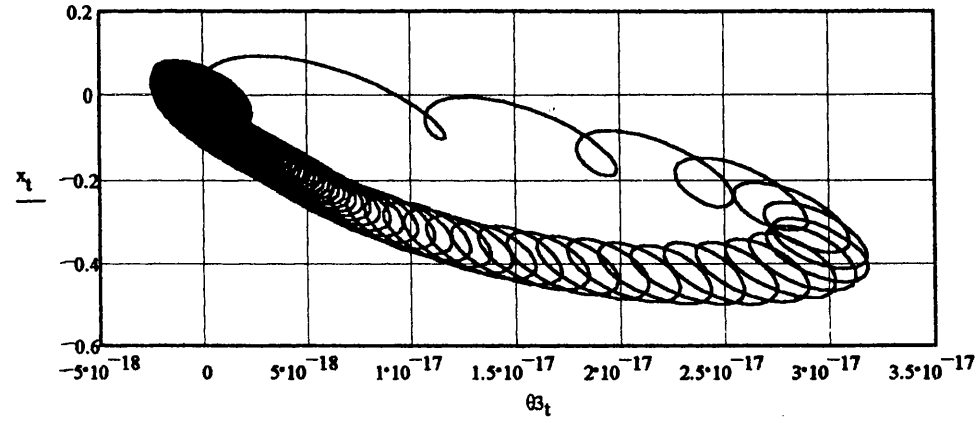

(m)

(rad)

Figure 6.121

Figures 6.122-6.138 detail the time-domain simulation results for the Heidrun Case Study TLP for an incident regular wave of ω =0.6rad/s (ξ_a =9m) with a heading angle of 45^0 (225^0).

Figures 6.122-6.127 detail the surge, sway, heave, roll, pitch and yaw DOF response respectively.

Figure 6.128 details the tether 'bundle' tension time-series response.

Figures 6.129-6.138 detail the platform vertical/horizontal and cross-planer response.

TLP Global Dynamic Response in Time-domain (6*DOF*):

(Space-fixed coordinate system)

DISPLACEMENT

Surge

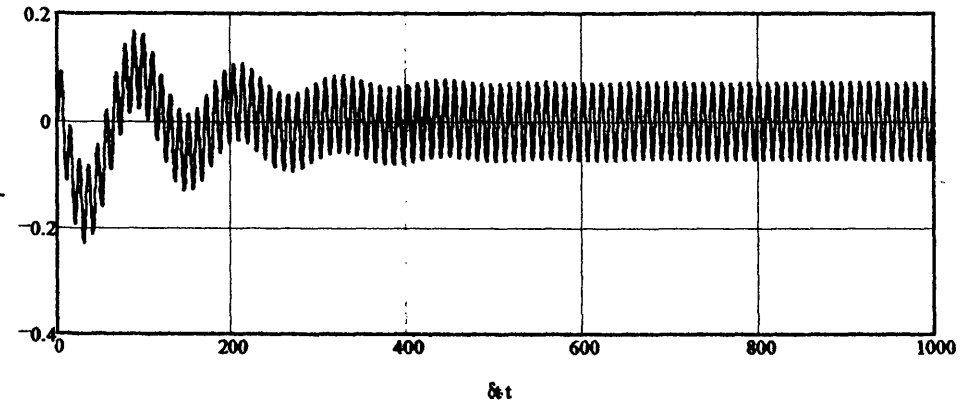

(m)

Figure 6.122

Sway

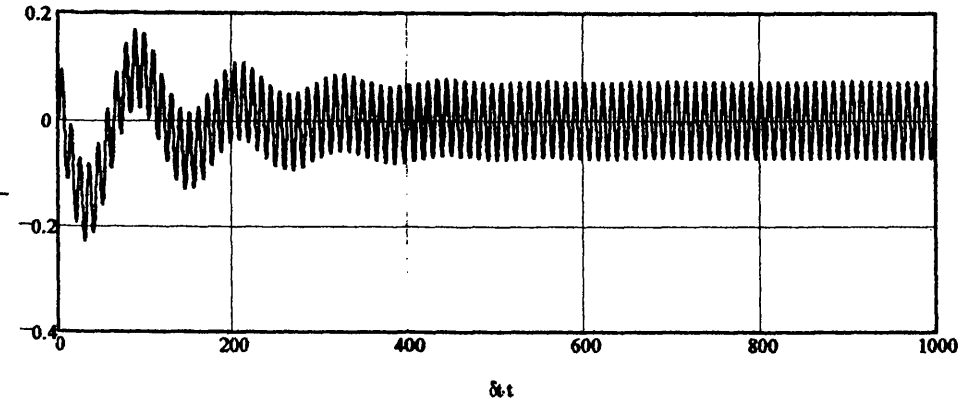

(m)

Figure 6.123

Heave

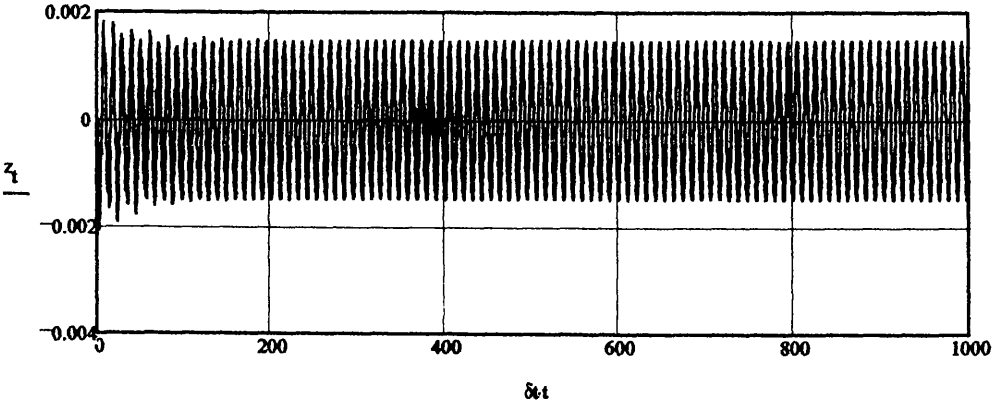

(m)

Figure 6.124

Roll

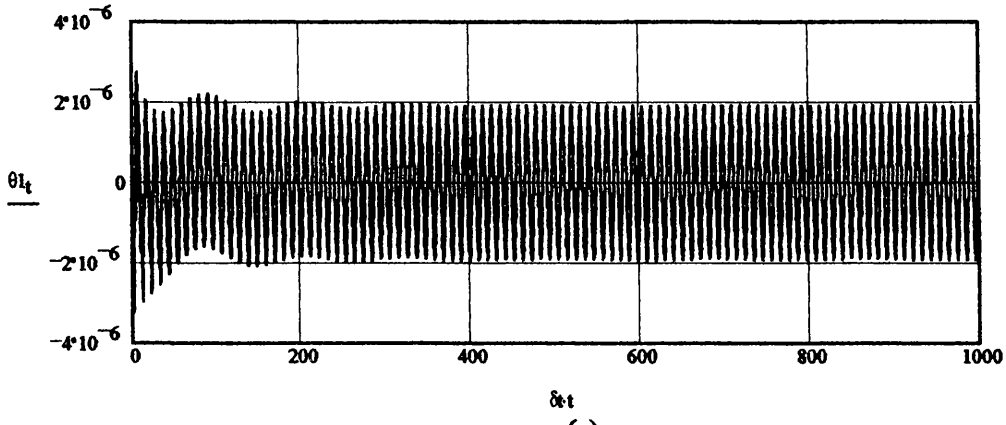

(rad)

Figure 6.125

Pitch

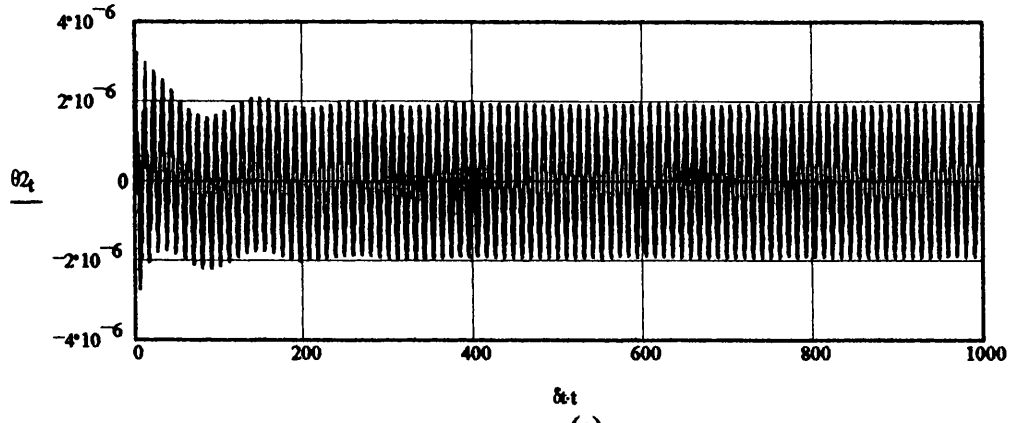

(rad)

Figure 6.126

Yaw

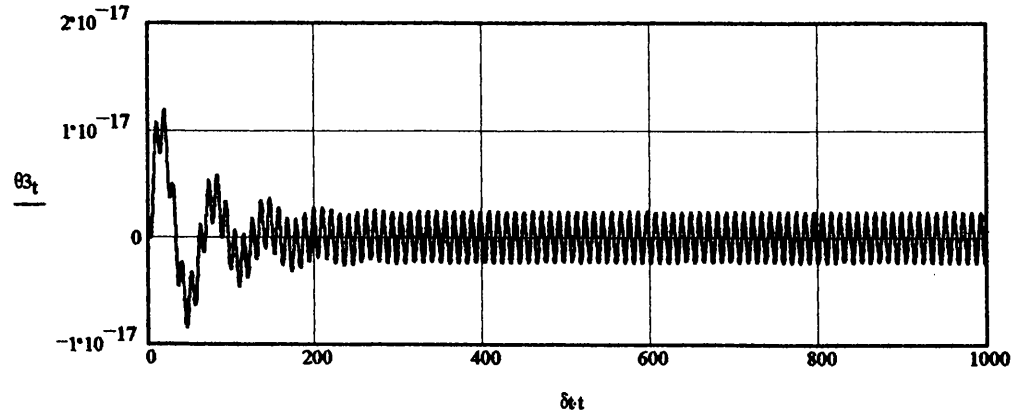

(rad)

Figure 6.127

Tether Force Time-series

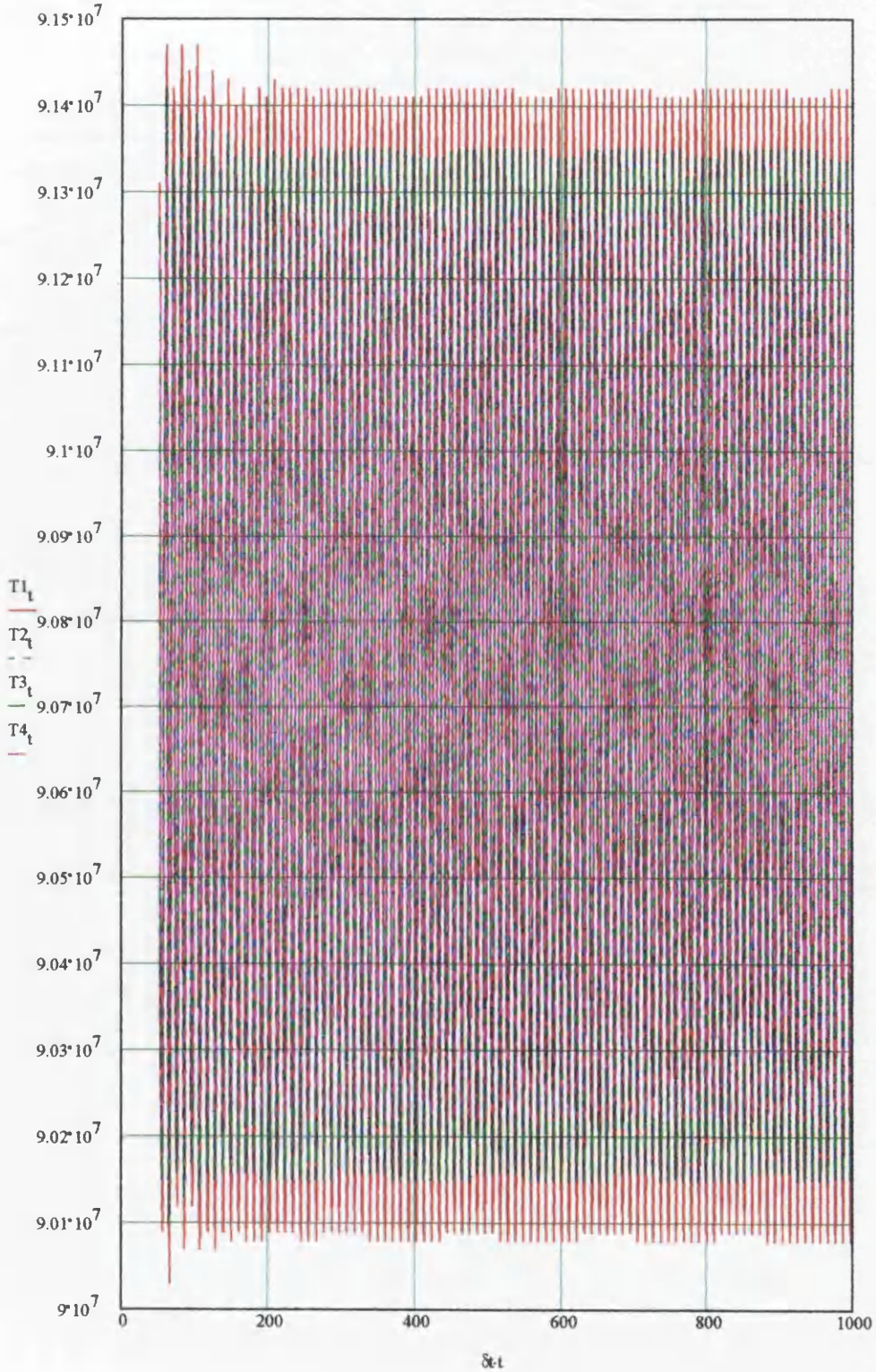

(N)

Figure 6.128

2D *TLP* c.g. Motion Response (Heave v Surge)

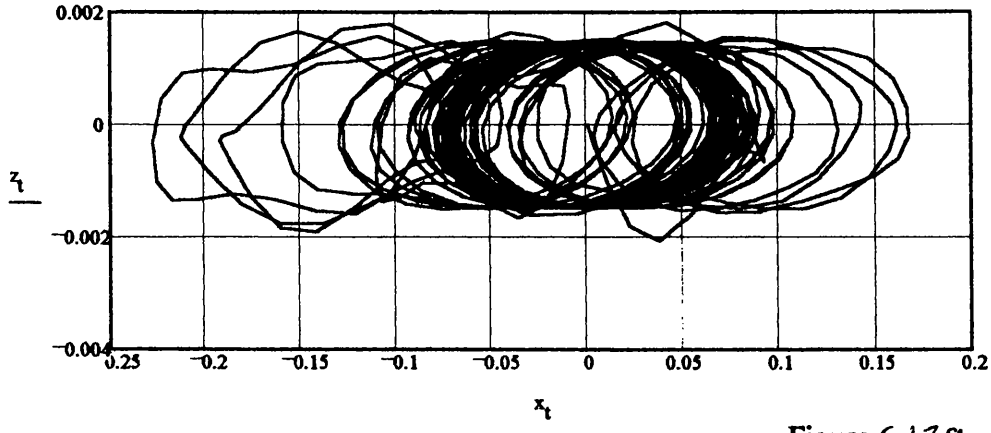

(m)

(m)

Figure 6.129

2D *TLP* c.g. Motion Response (Heave v Sway)

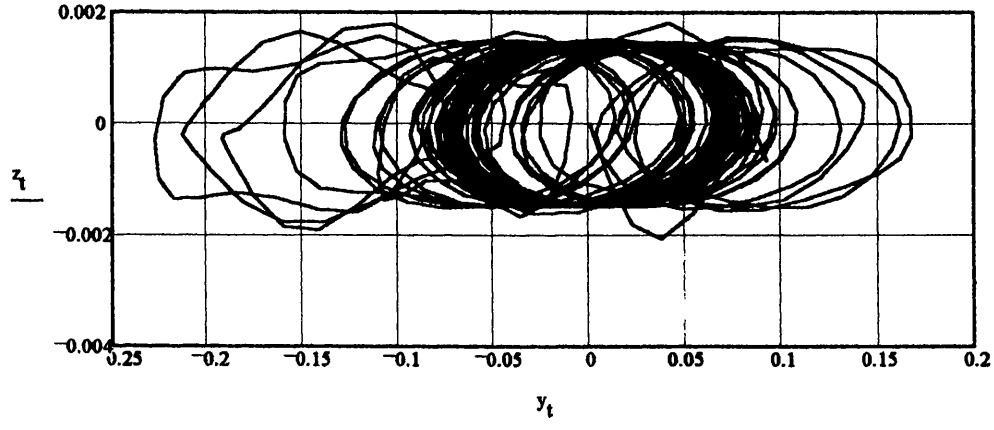

(m)

(m)

Figure 6.130

2D *TLP* c.g. Motion Response (Heave v Roll)

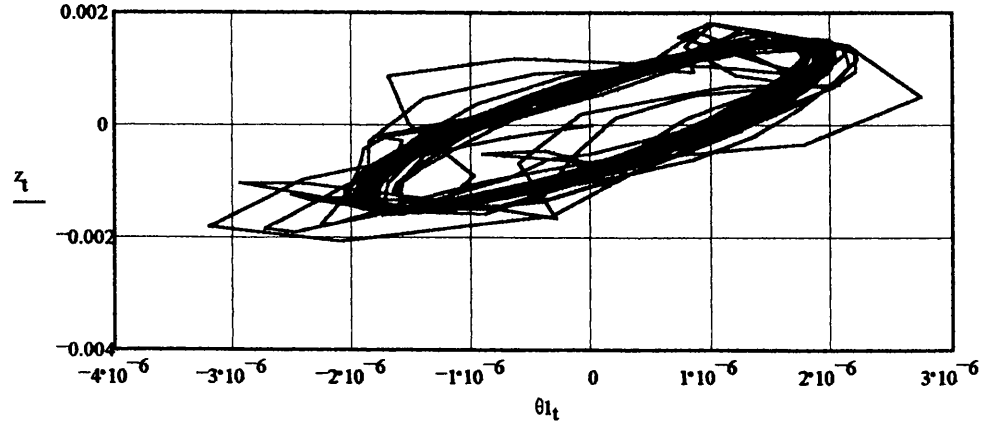

(m)

(rad)

Figure 6.131

2D *TLP* c.g. Motion Response (Heave v Pitch)

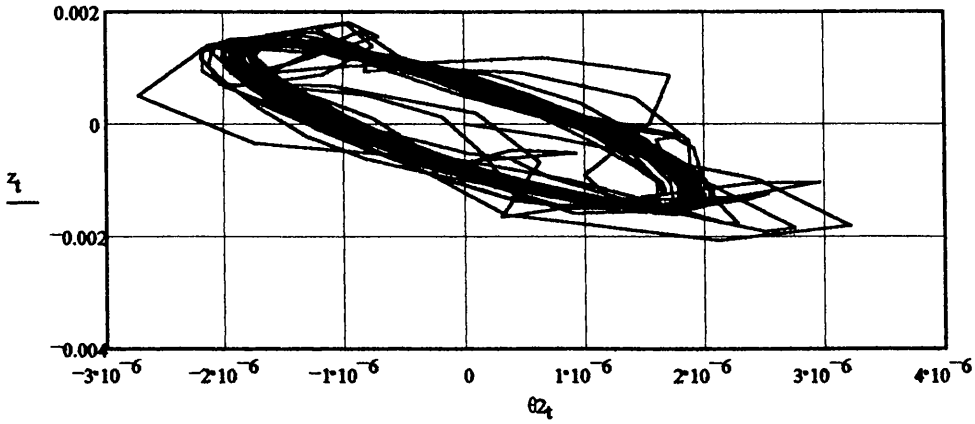

(m)

(rad)

Figure 6.132

2D *TLP* c.g. Motion Response (Heave v Yaw)

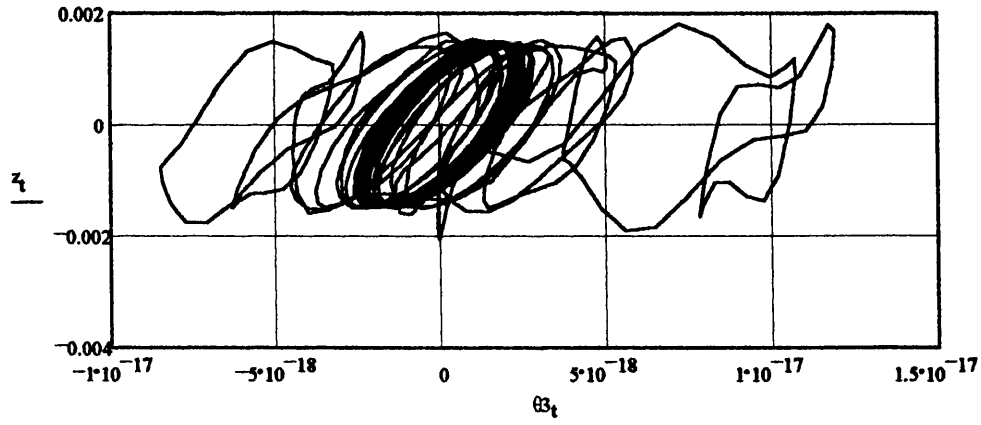

(m)

(rad)

Figure 6.133

2D *TLP* c.g. Motion Response (Surge v Sway)

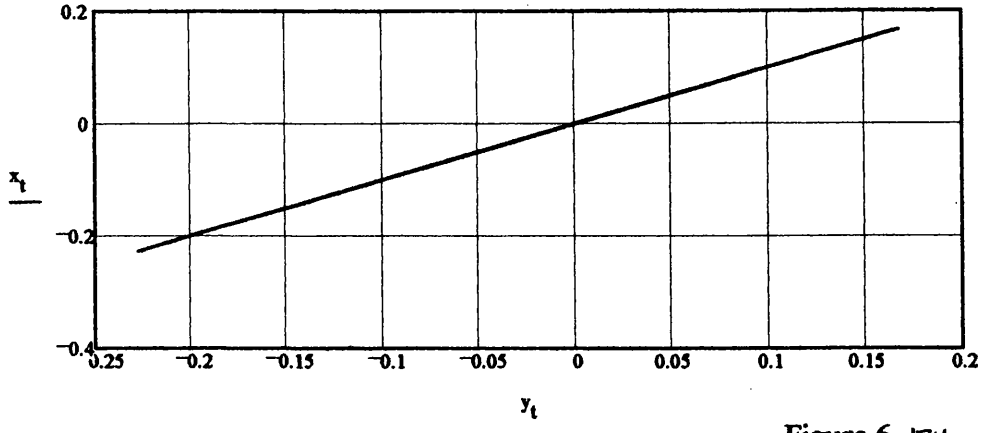

Figure 6..134

2D *TLP* c.g. Motion Response (Surge v Heave)

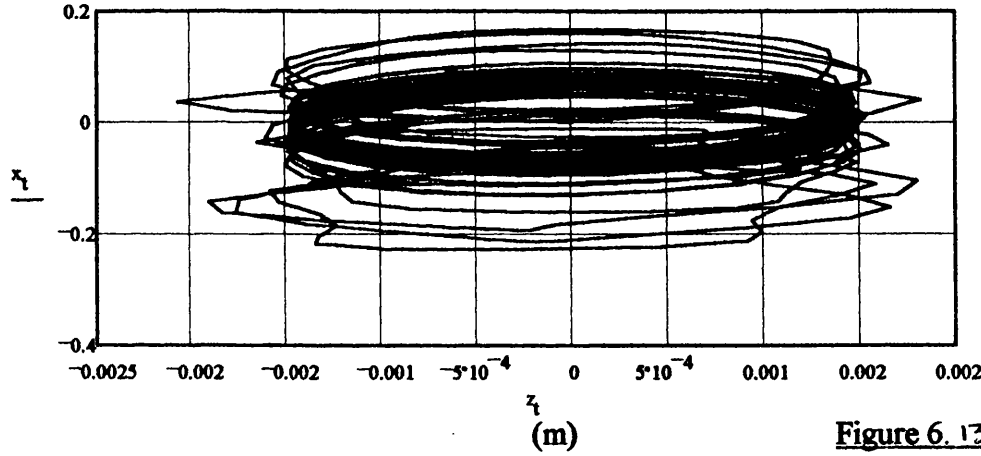

Figure 6. 135

2D *TLP* c.g. Motion Response (Surge v Roll)

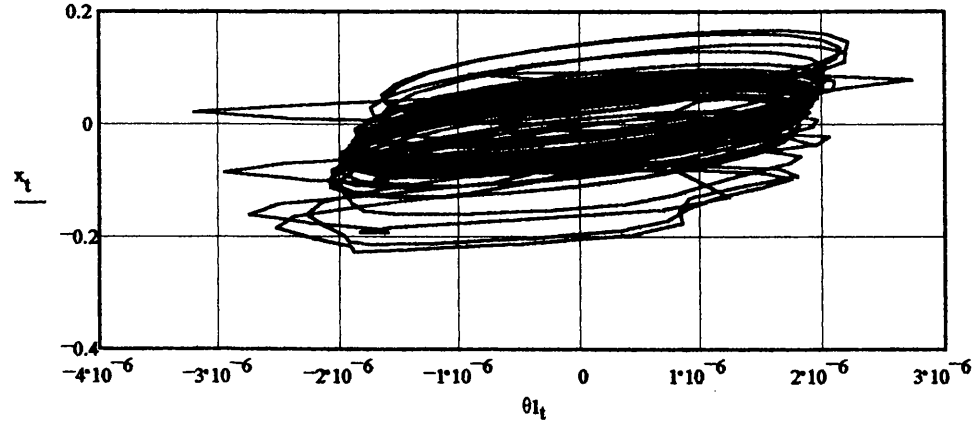

Figure 6. 136

2D *TLP* c.g. Motion Response (Surge v Pitch)

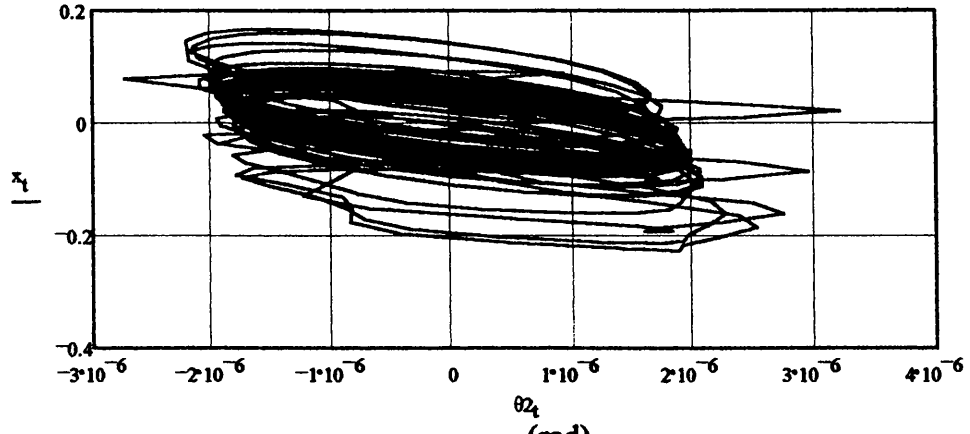

(m)

(rad)

Figure 6.137

2D *TLP* c.g. Motion Response (Surge v Yaw)

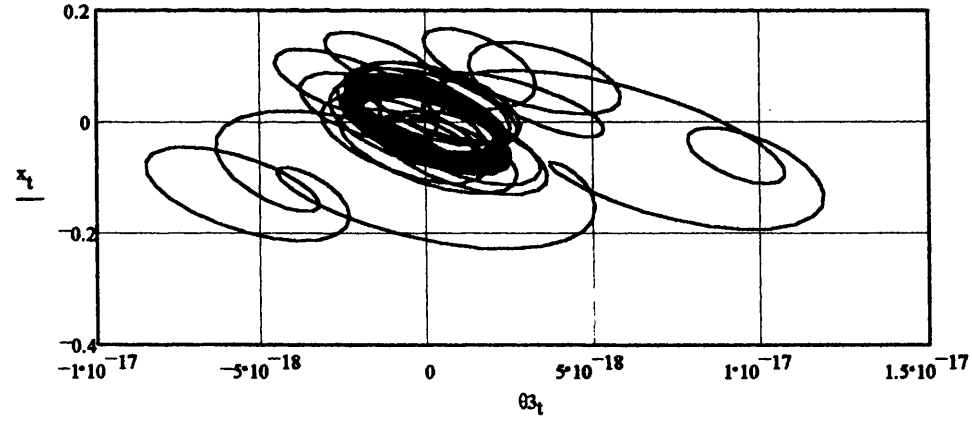

(m)

(rad)

Figure 6.138

6.3.1.4 Snorre TLP

Figures 6.139-6.155 detail the time-domain simulation results for the Snorre Case Study TLP for an incident regular wave of ω=0.6rad/s (ξ_a=1.25m) with a heading angle of 45^0 (225^0) (without motion compensation).

Figures 6.139-6.144 detail the surge, sway, heave, roll, pitch and yaw DOF response respectively.

Figure 6.145 details the tether 'bundle' tension time-series response.

Figures 6.146-6.155 detail the platform vertical/horizontal and cross-planer response.

TLP Global Dynamic Response in Time-domain (*6DOF*):

(Space-fixed coordinate system)

DISPLACEMENT

Surge

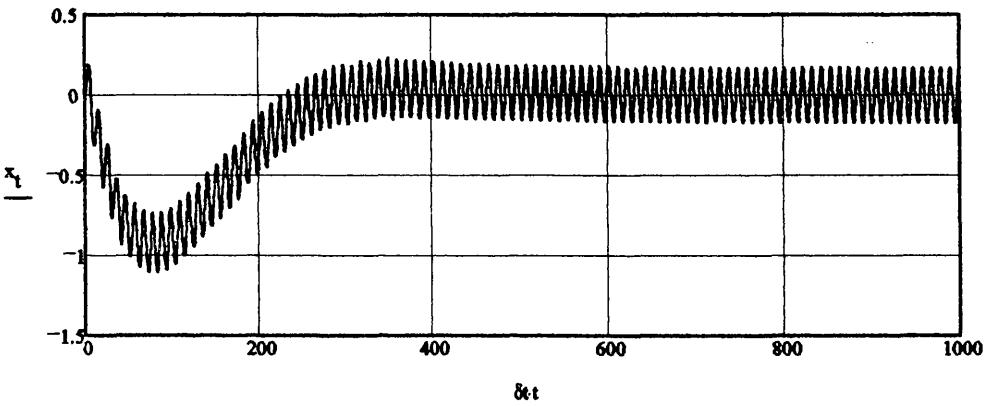

(m)

Figure 6.139

Sway

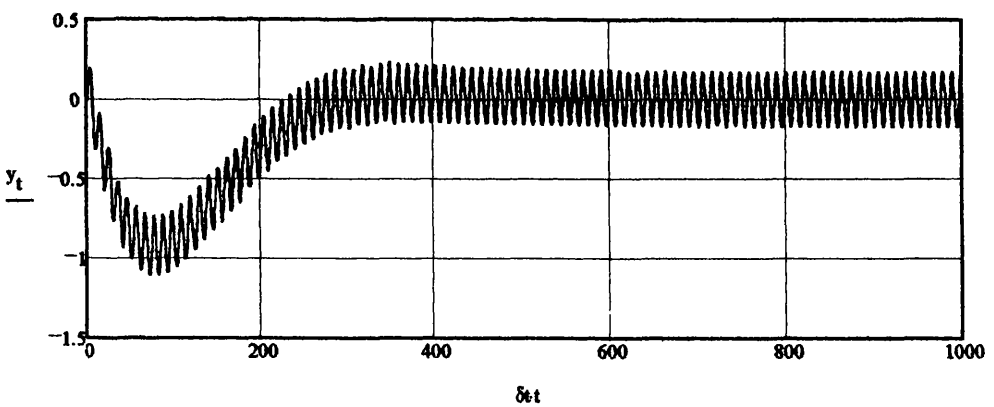

(m)

Figure 6.140

Heave

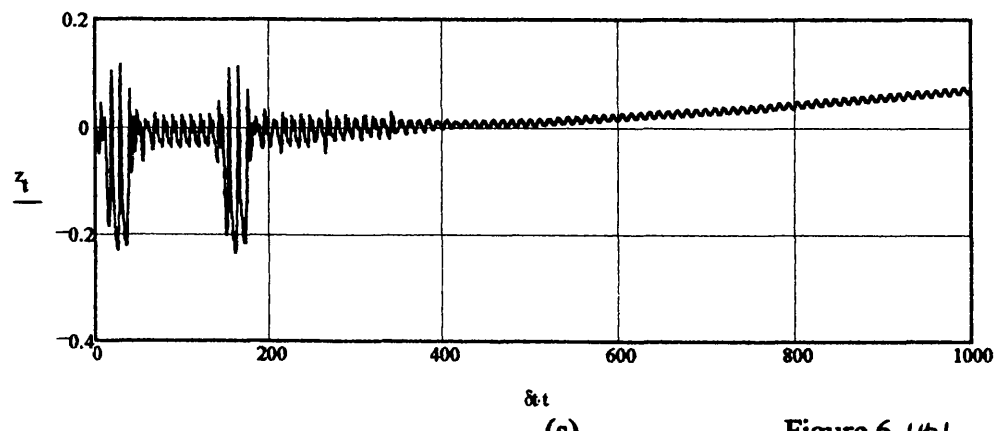

(m)

Figure 6.141

Roll

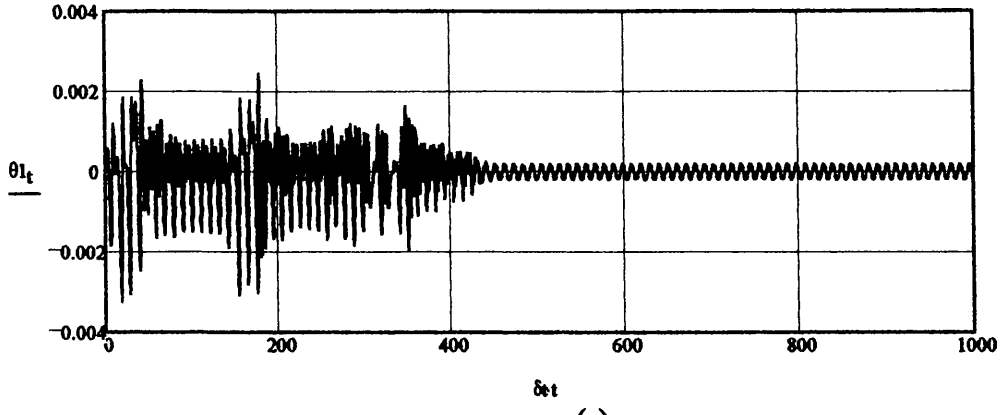

(rad)

Figure 6.142

Pitch

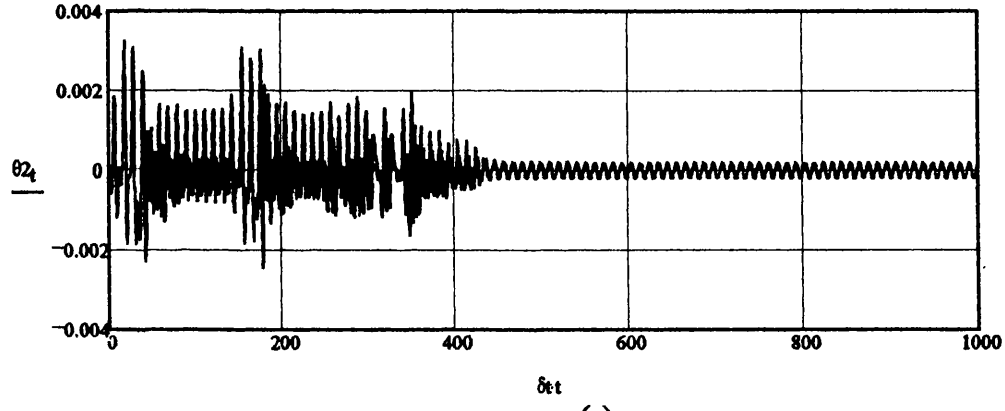

(rad)

Figure 6.143

Yaw

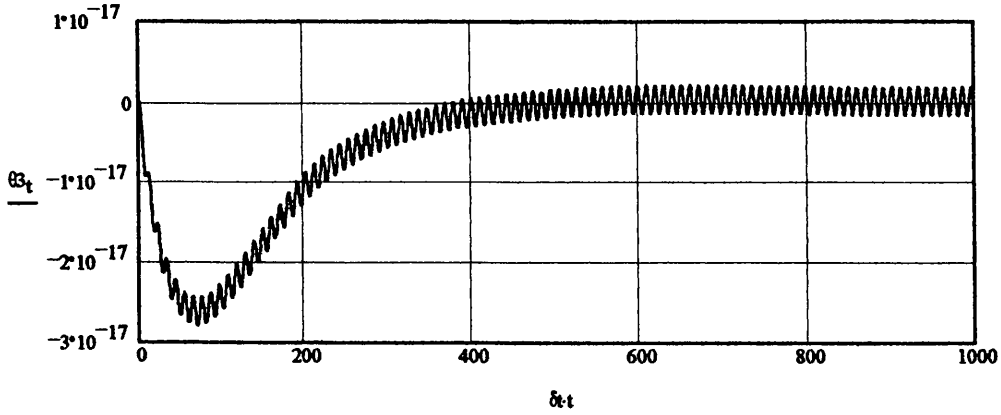

(rad)

Figure 6.144

Tether Force Time-series

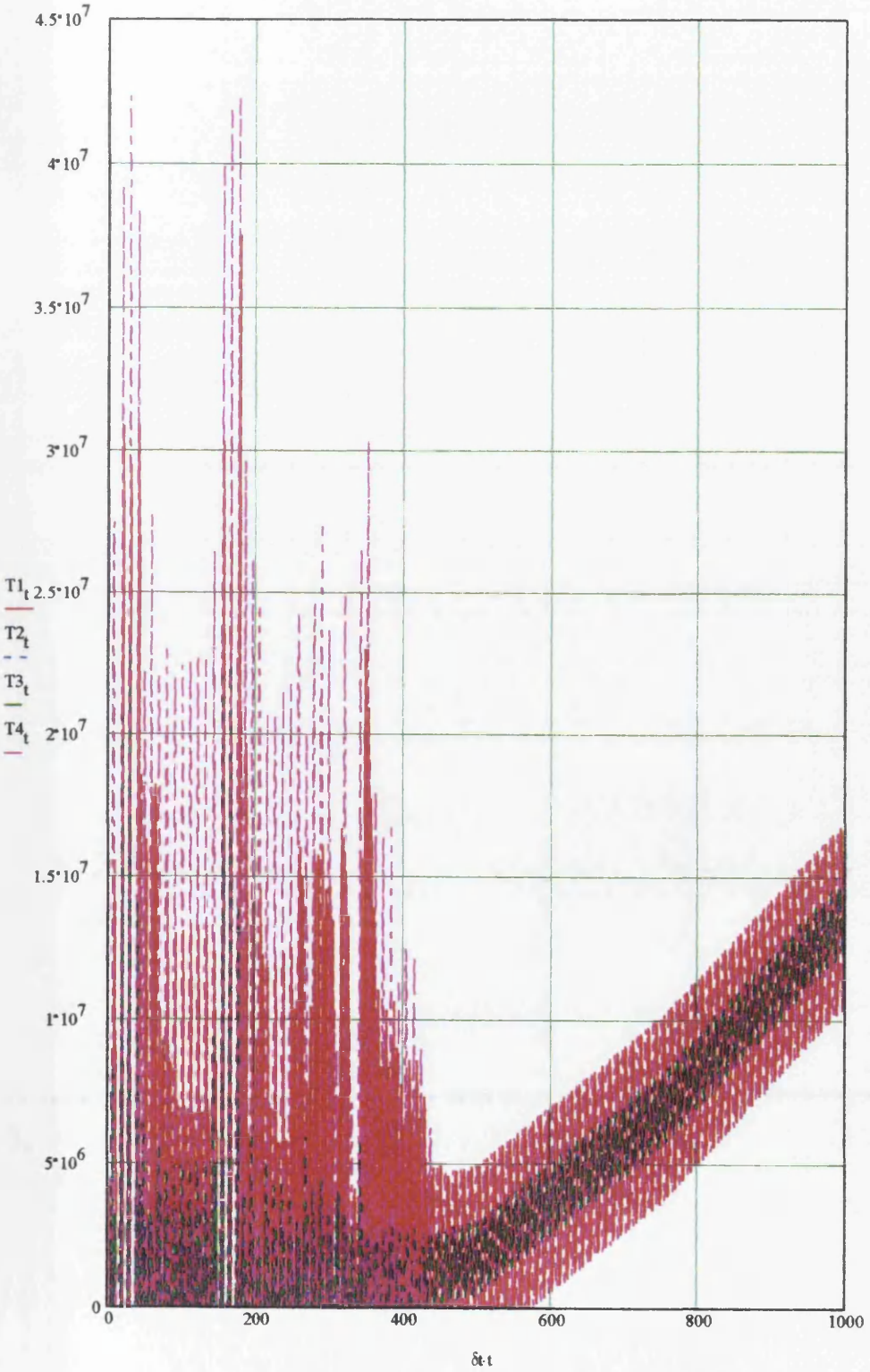

(N)

(s)

Figure 6.145

2D *TLP* c.g. Motion Response (Heave v Surge)

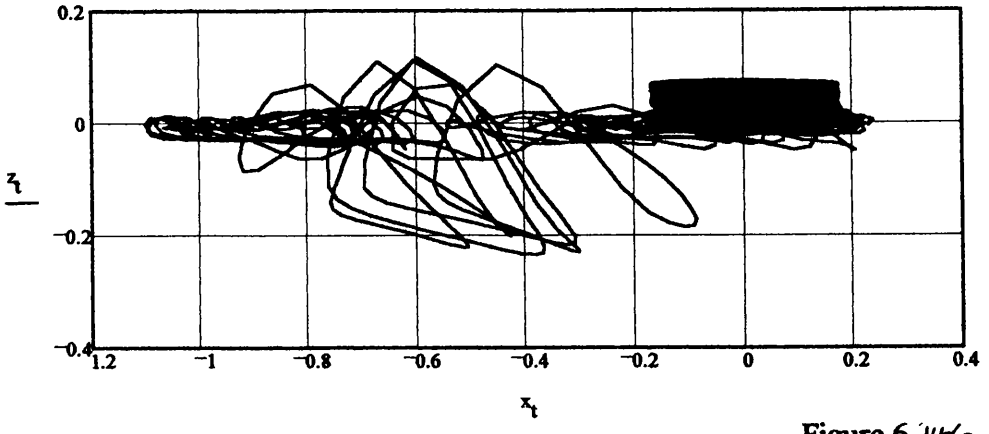

(m)

(m)

Figure 6.146

2D *TLP* c.g. Motion Response (Heave v Sway)

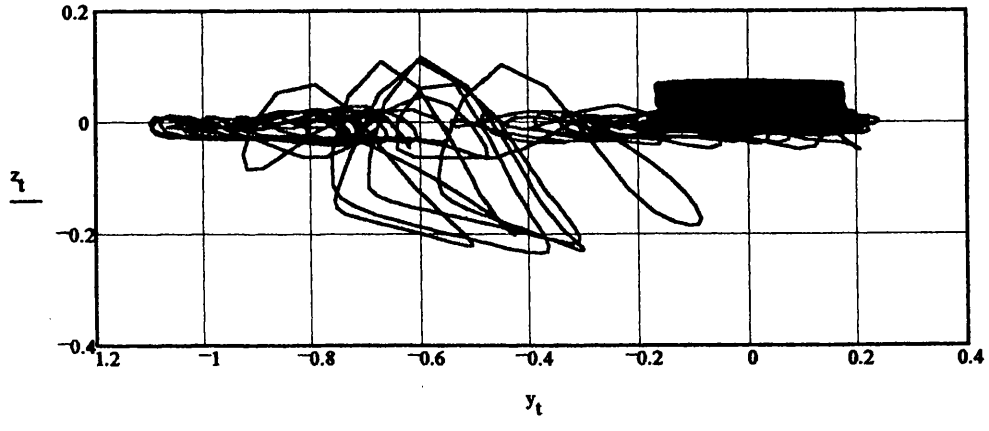

(m)

(m)

Figure 6. 147

2D *TLP* c.g. Motion Response (Heave v Roll)

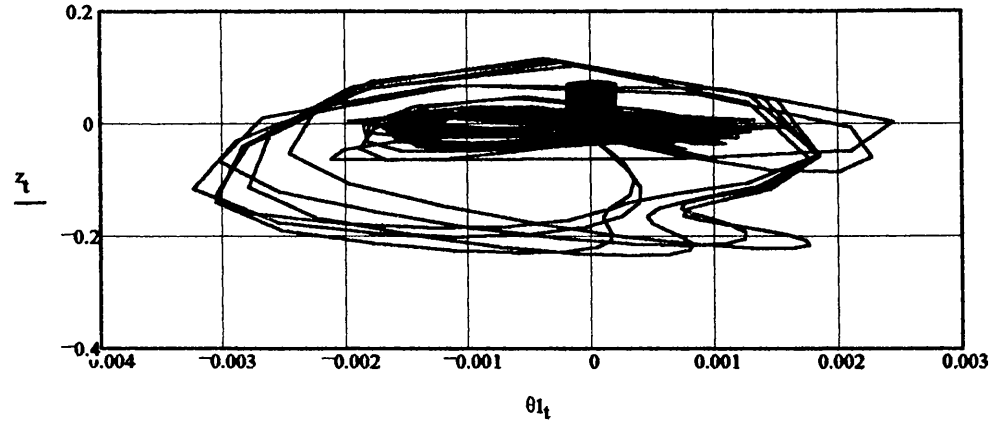

(m)

(rad)

Figure 6. 148

2D *TLP* c.g. Motion Response (Heave v Pitch)

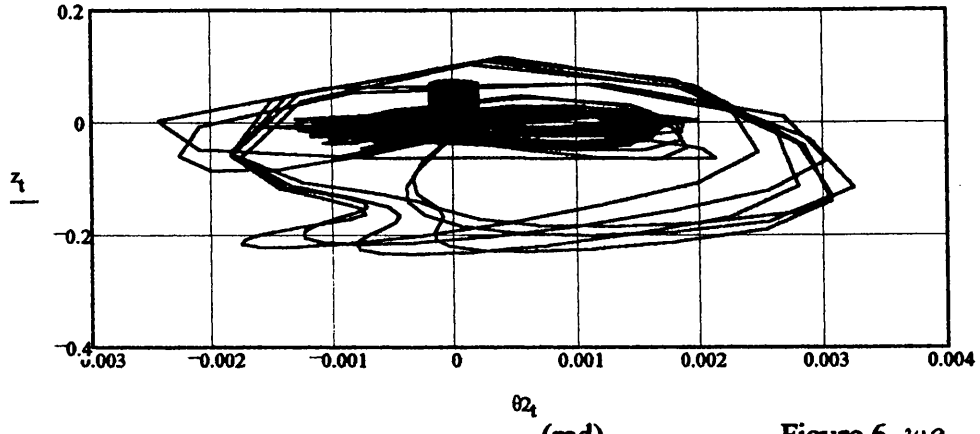

(m)

(rad)

Figure 6.149

2D *TLP* c.g. Motion Response (Heave v Yaw)

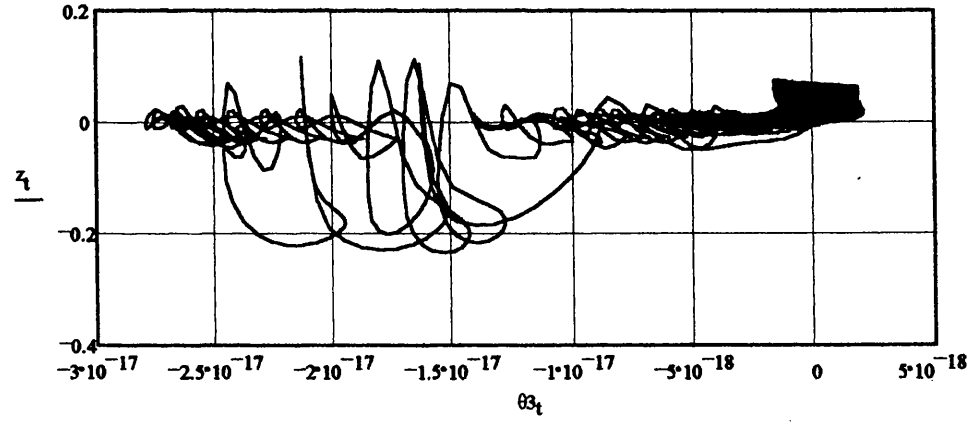

(m)

(rad)

Figure 6.150

2D *TLP* c.g. Motion Response (Surge v Sway)

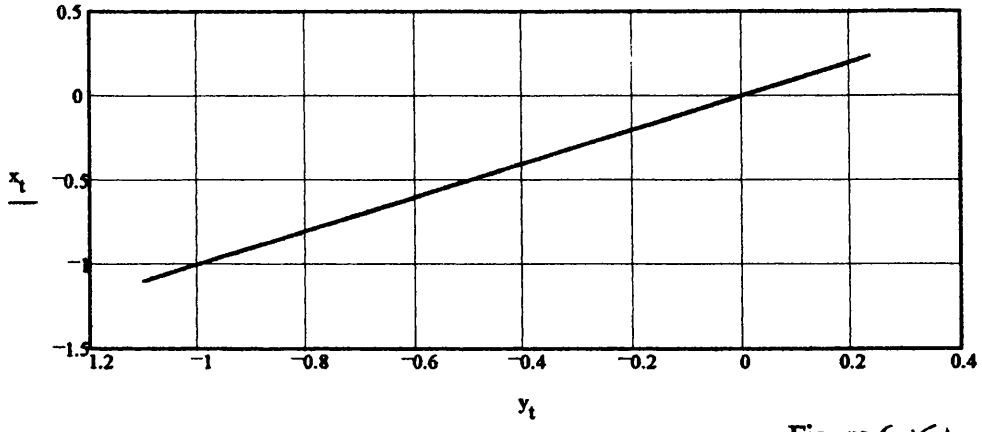

(m)

(m)

Figure 6.151

2D *TLP* c.g. Motion Response (Surge v Heave)

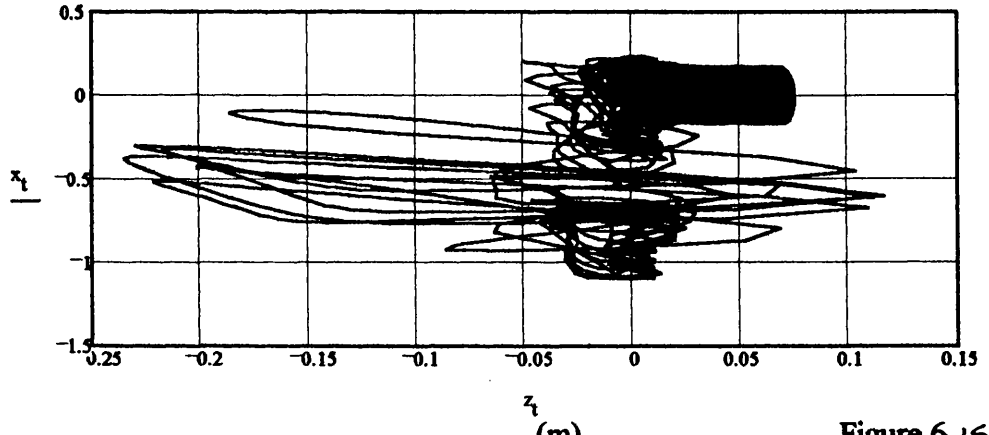

(m)

(m)

Figure 6.152

2D *TLP* c.g. Motion Response (Surge v Roll)

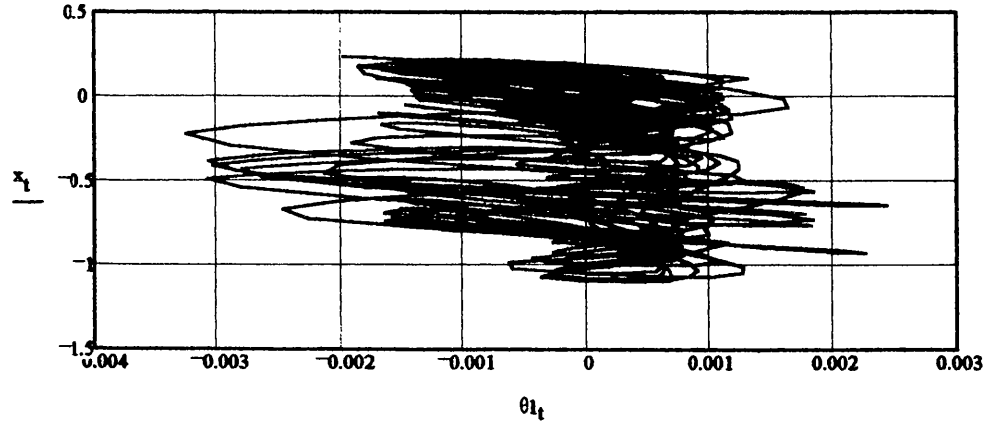

(m)

(rad)

Figure 6.153

2D *TLP* c.g. Motion Response (Surge v Pitch)

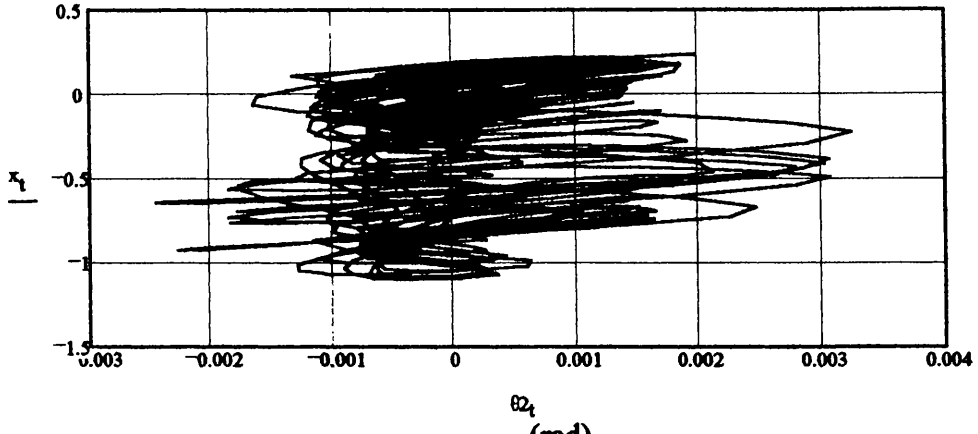

(m)

(rad)

Figure 6.154

2D *TLP* c.g. Motion Response (Surge v Yaw)

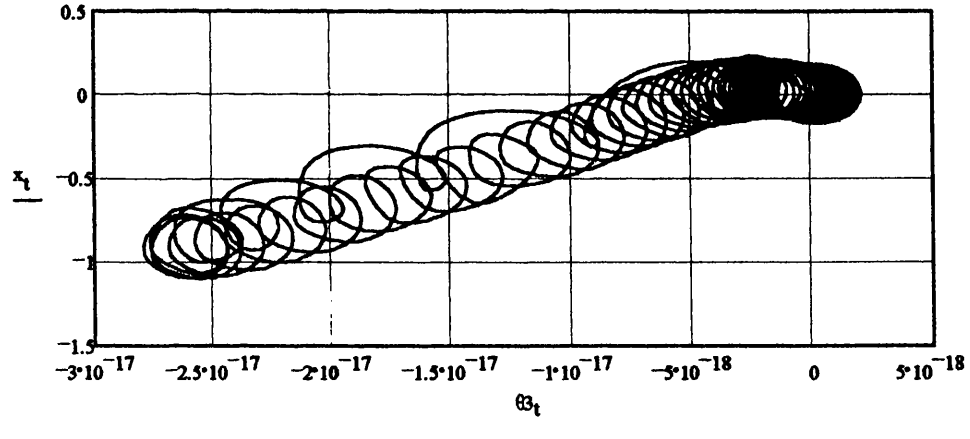

(m)

(rad)

Figure 6.155

Figures 6.156-6.172 detail the time-domain simulation results for the Snorre Case Study TLP for an incident regular wave of ω =0.6rad/s (ξ_a =1.25m) with a heading angle of 45^0 (225^0) (with motion compensation).

Figures 6.156-6.161 detail the surge, sway, heave, roll, pitch and yaw DOF response respectively.

Figure 6.162 details the tether 'bundle' tension time-series response.

Figures 6.163-6.172 detail the platform vertical/horizontal and cross-planer response.

TLP Global Dynamic Response in Time-domain (*6DOF*):

(Space-fixed coordinate system)

DISPLACEMENT

Surge

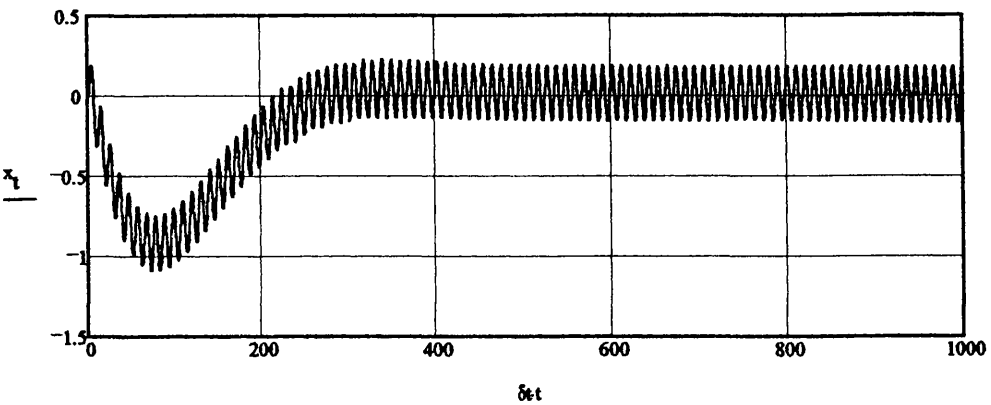

(m)

Figure 6.156

Sway

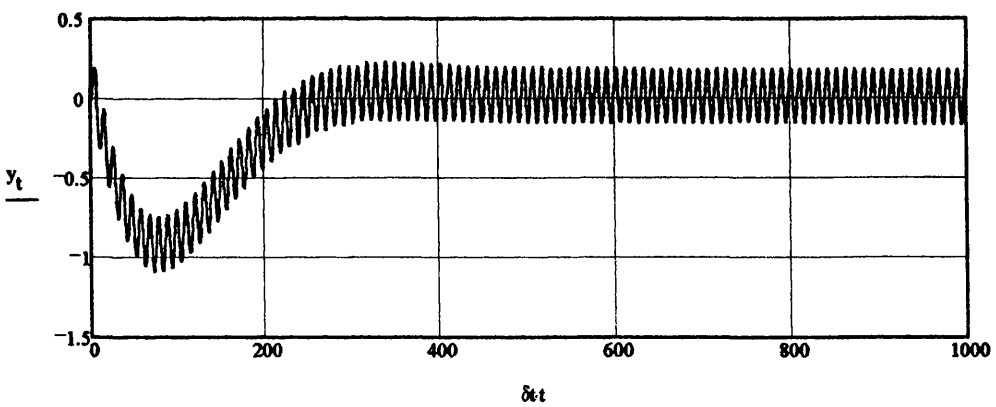

(m)

Figure 6.157

Heave

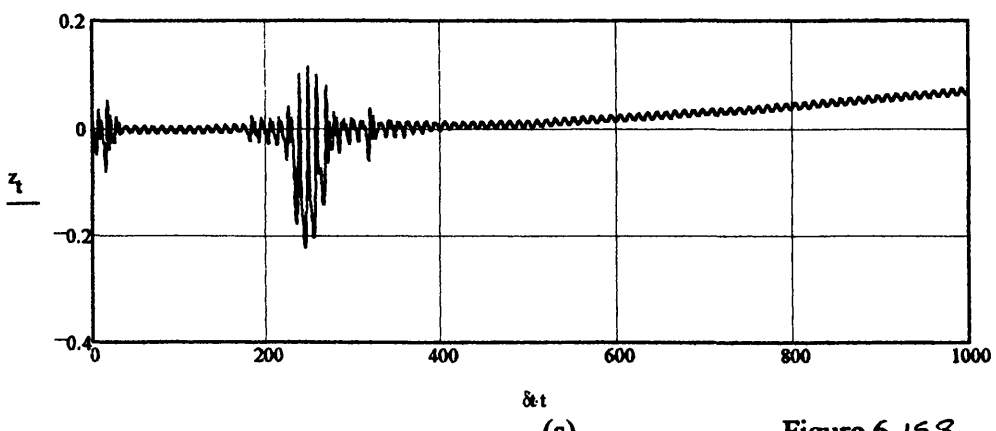

(m)

Figure 6.158

Roll

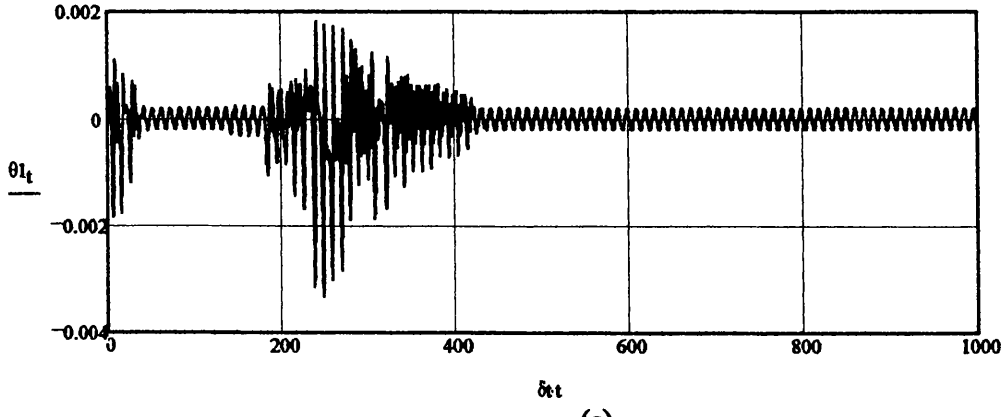

(rad)

Figure 6.159

Pitch

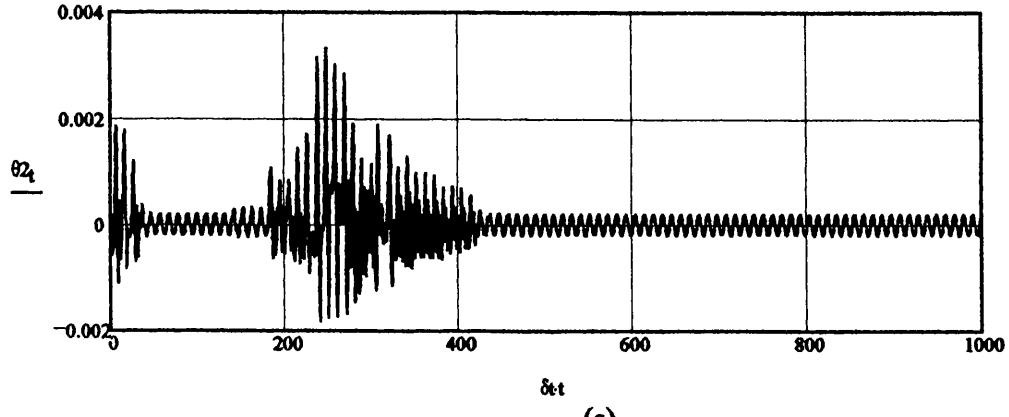

(rad)

Figure 6.160

Yaw

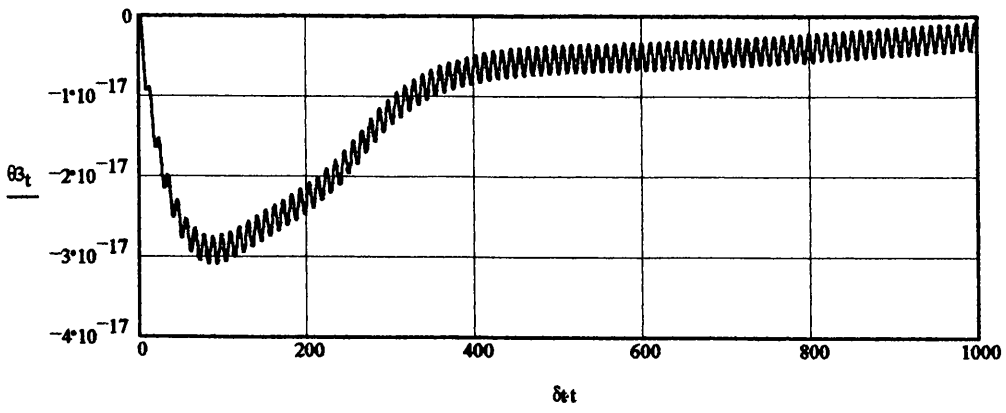

(rad)

Figure 6.161

Tether Force Time-series

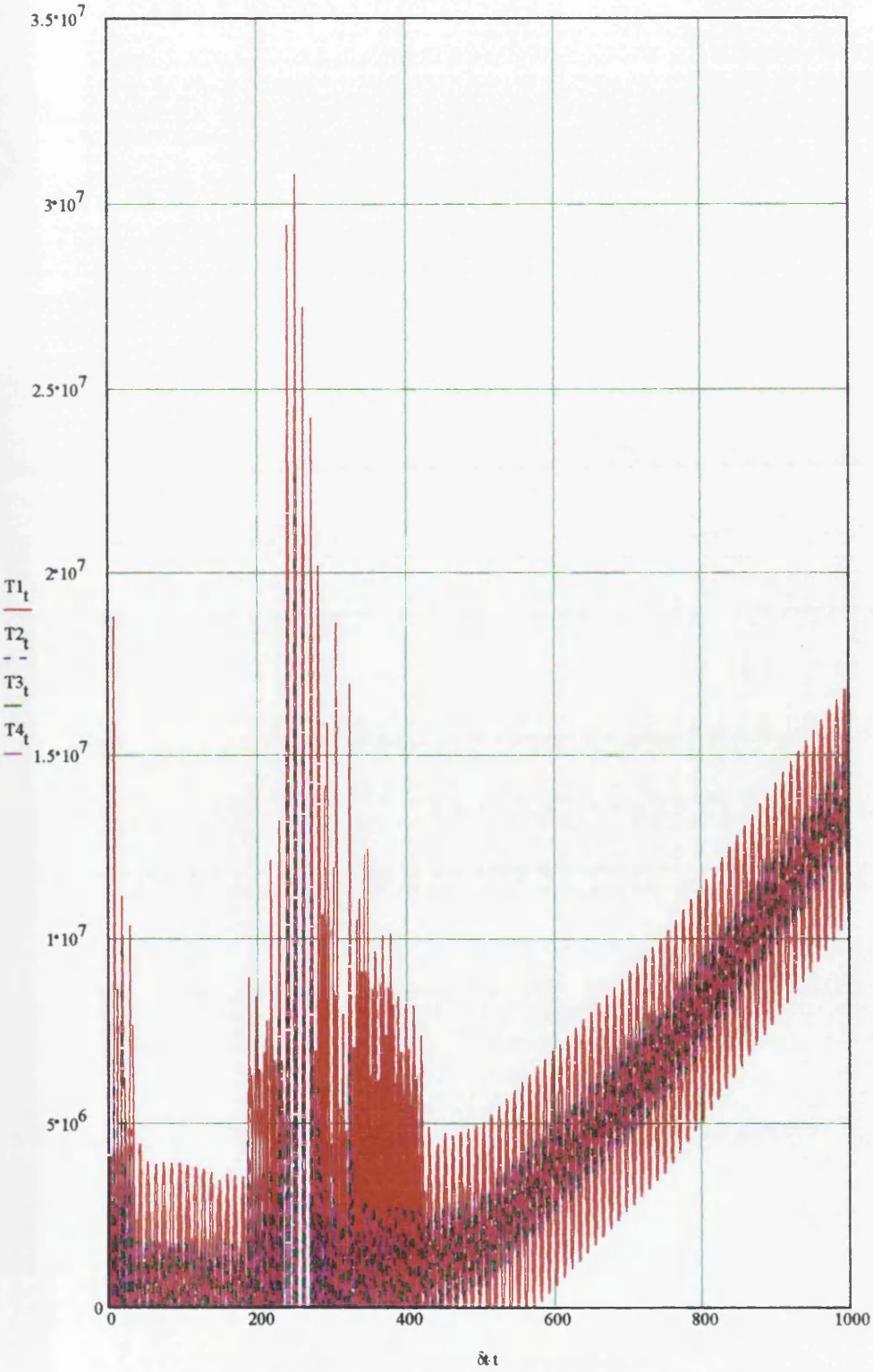

(N)

(s)

Figure 6. 16 入

2D *TLP* c.g. Motion Response (Heave v Surge)

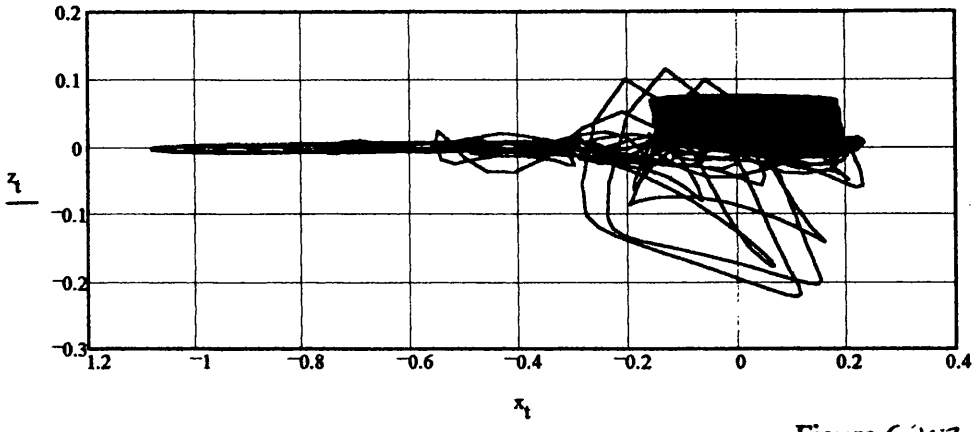

(m)

(m)

Figure 6.163

2D *TLP* c.g. Motion Response (Heave v Sway)

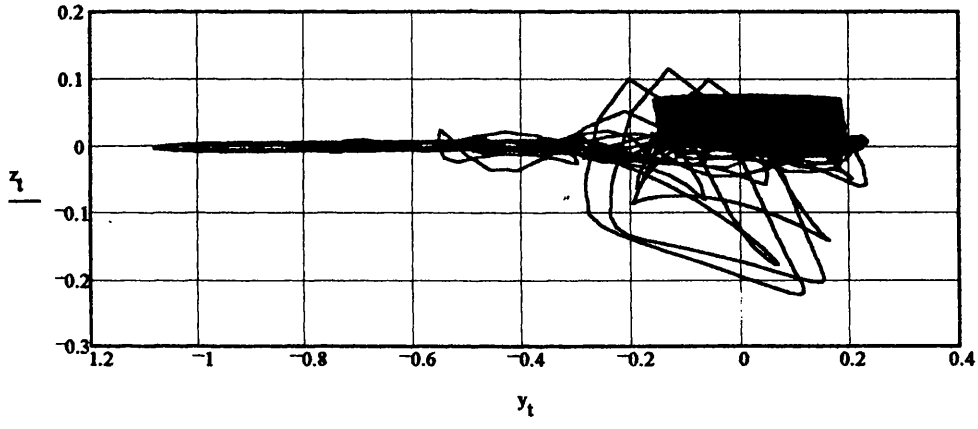

(m)

(m)

Figure 6.164

2D *TLP* c.g. Motion Response (Heave v Roll)

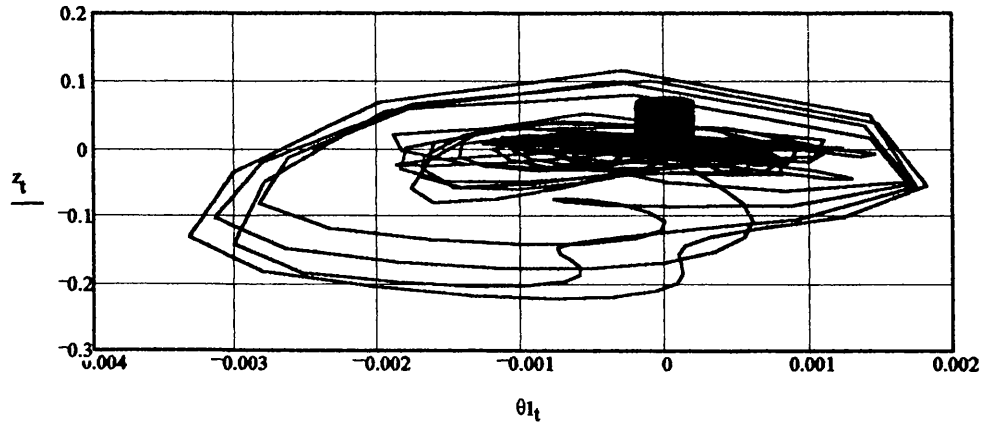

(m)

(rad)

Figure 6.165

2D *TLP* c.g. Motion Response (Heave v Pitch)

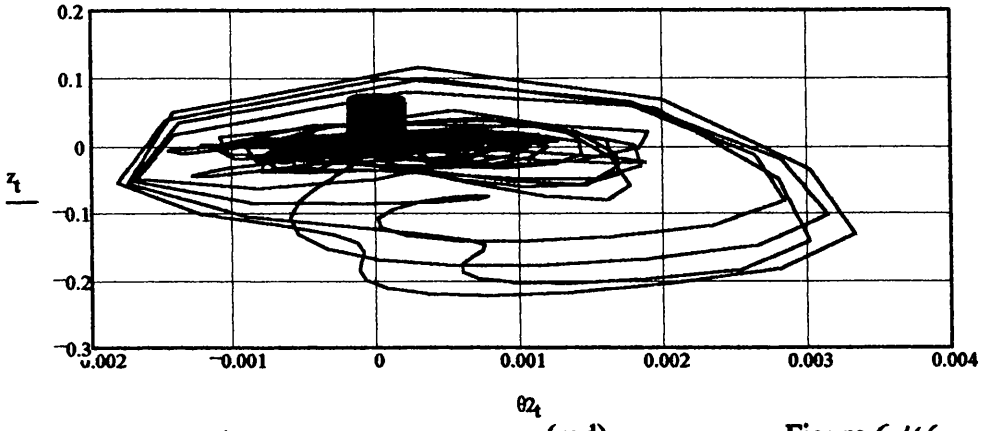

(m)

Figure 6.166

2D *TLP* c.g. Motion Response (Heave v Yaw)

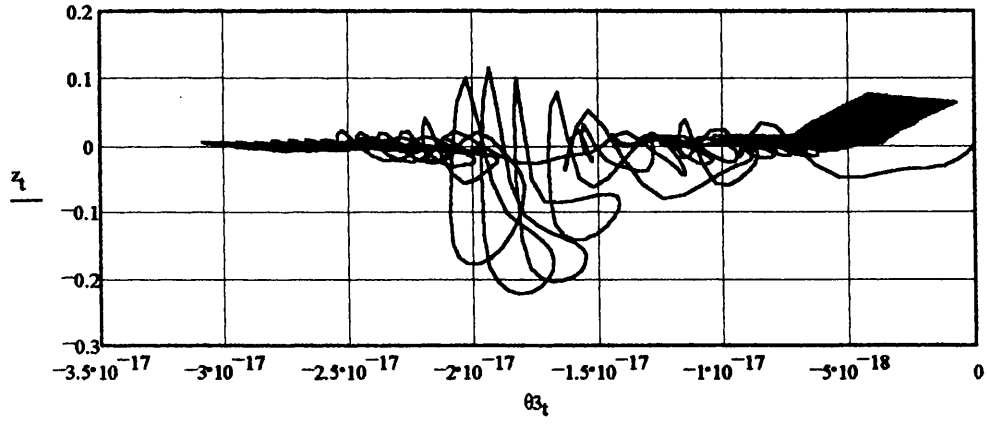

(m)

Figure 6.167

2D *TLP* c.g. Motion Response (Surge v Sway)

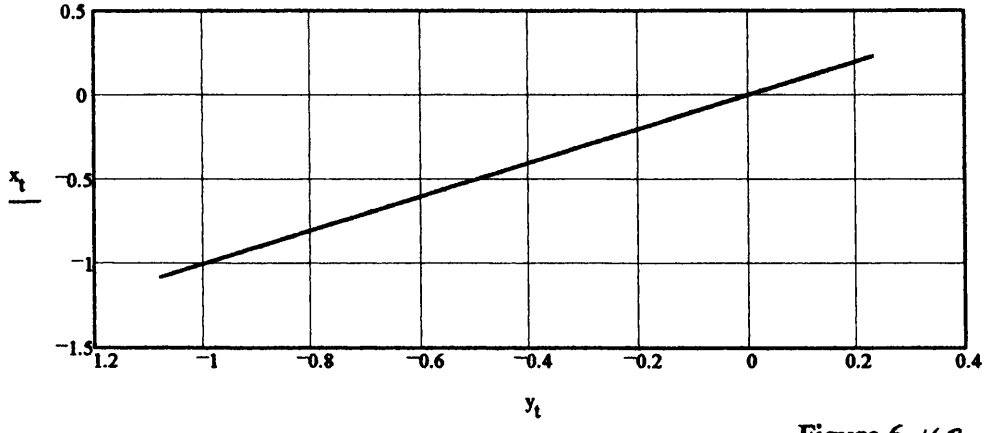

(m)

(m)

Figure 6.168

2D *TLP* c.g. Motion Response (Surge v Heave)

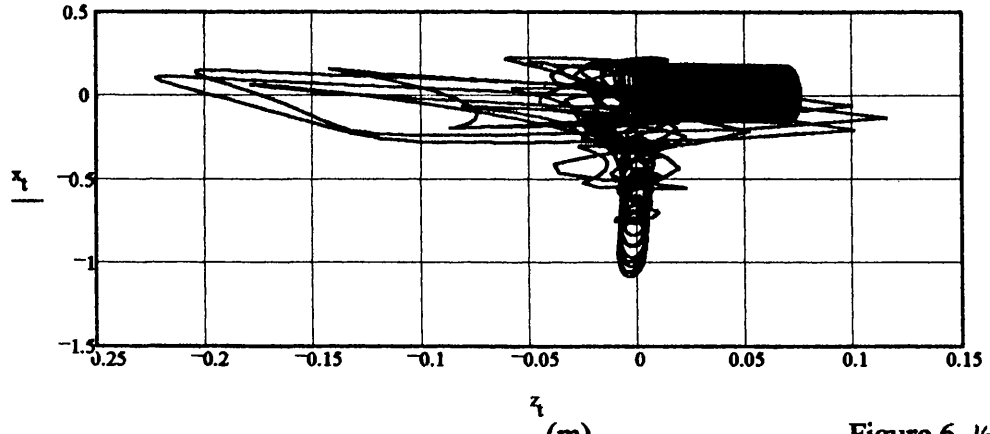

(m)

(m)

Figure 6.169

2D *TLP* c.g. Motion Response (Surge v Roll)

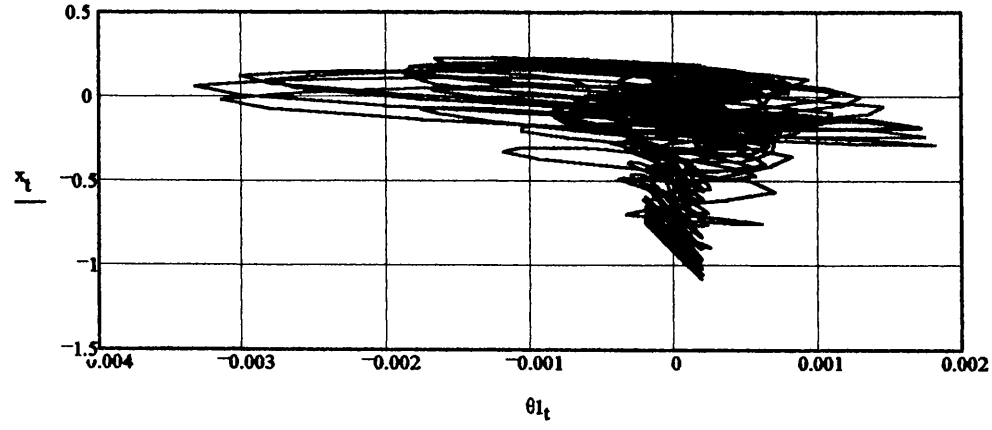

(m)

(rad)

Figure 6.170

2D *TLP* c.g. Motion Response (Surge v Pitch)

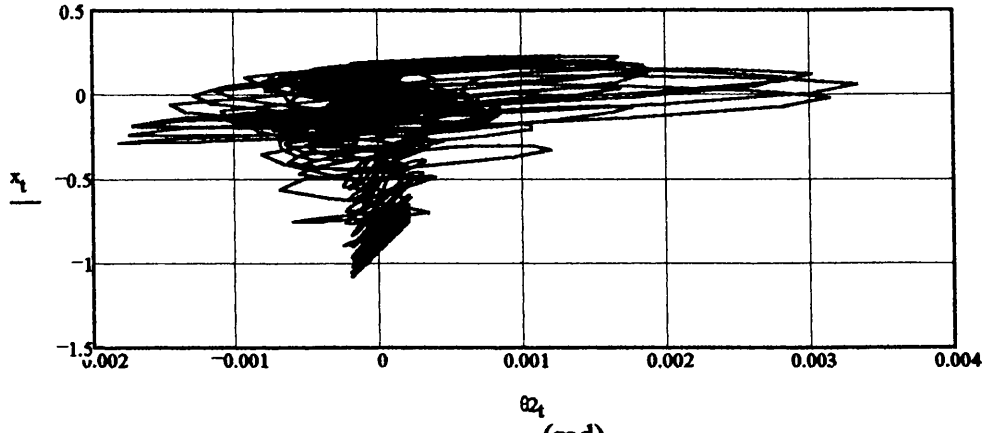

(m)

Figure 6.171

2D *TLP* c.g. Motion Response (Surge v Yaw)

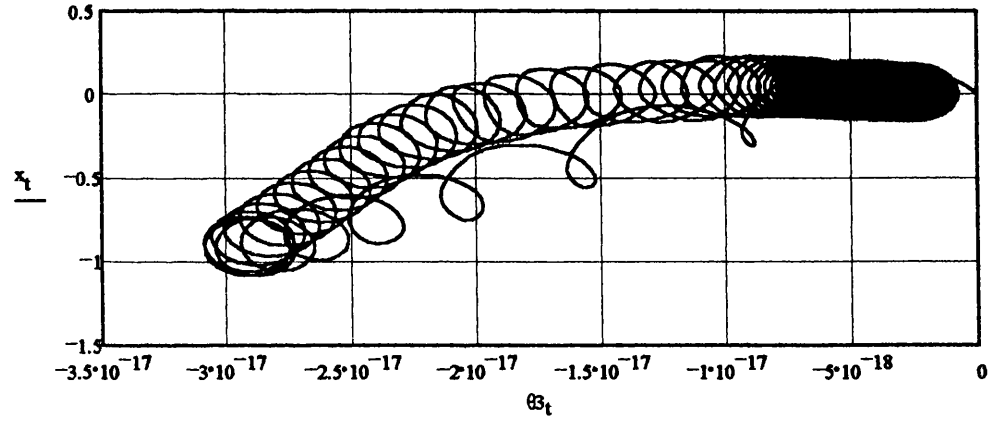

(m)

Figure 6.172

Figures 6.173-6.189 detail the time-domain simulation results for the Snorre Case Study TLP for an incident regular wave of ω =0.6rad/s (ξ_a=9m) with a heading angle of 60^0.

Figures 6.173-6.178 detail the surge, sway, heave, roll, pitch and yaw DOF response respectively.

Figure 6.179 details the tether 'bundle' tension time-series response.

Figures 6.180-6.189 detail the platform vertical/horizontal and cross-planer response.

TLP Global Dynamic Response in Time-domain (*6DOF*):

(Space-fixed coordinate system)

DISPLACEMENT

Surge

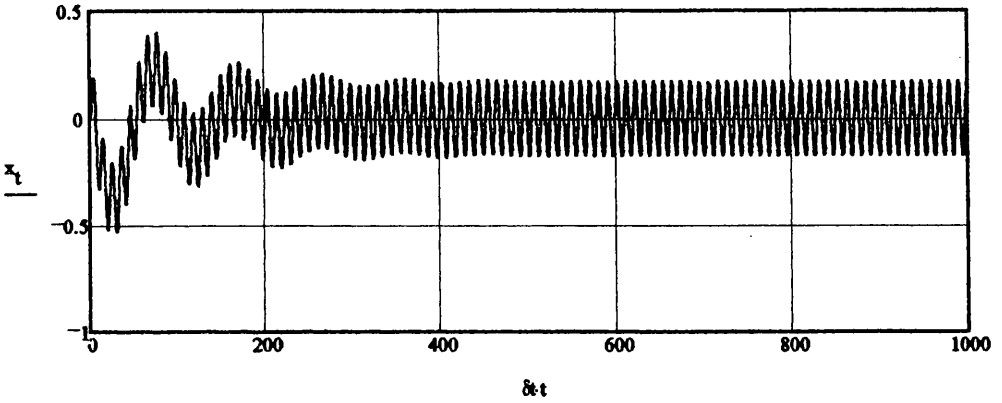

(m)

Figure 6..173

Sway

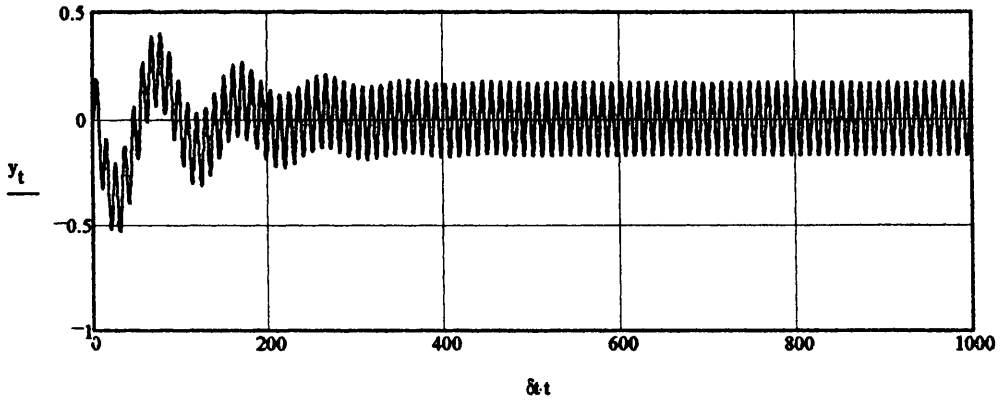

(m)

Figure 6..174

Heave

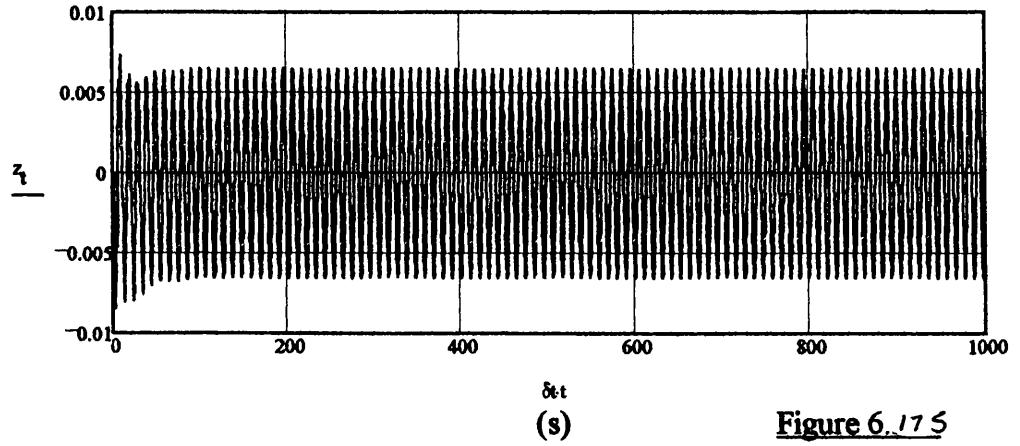

(m)

Figure 6..175

Roll

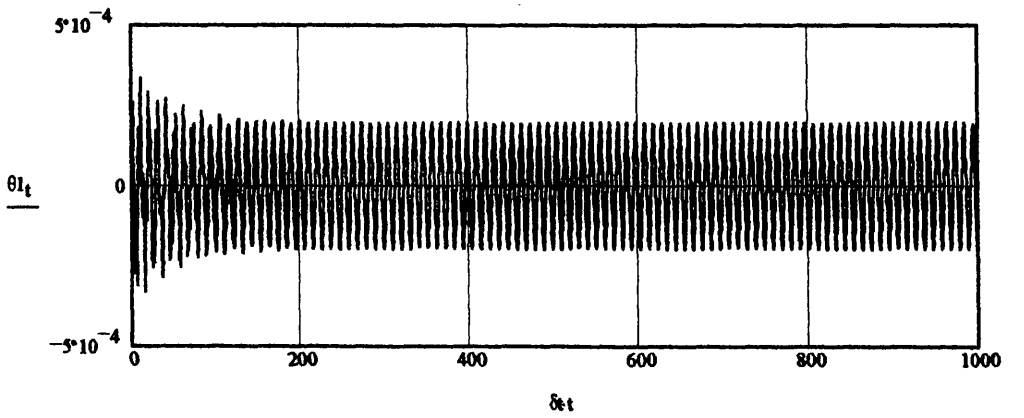

(rad)

Figure 6.176

Pitch

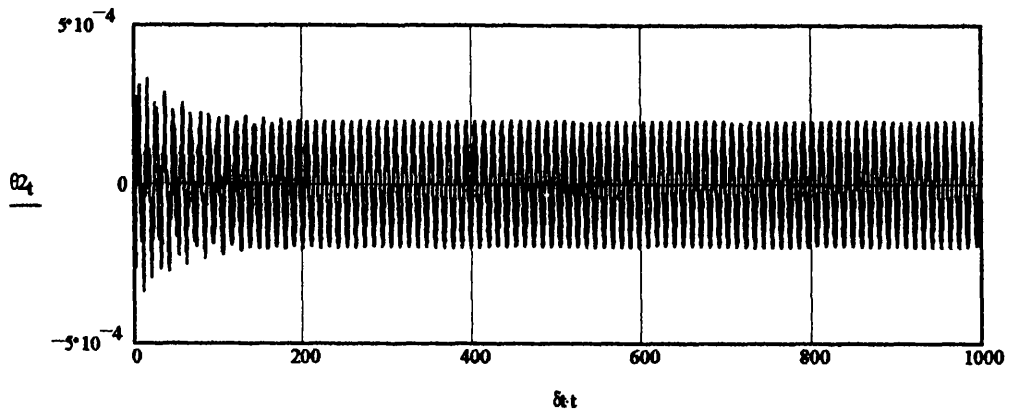

(rad)

Figure 6.177

Yaw

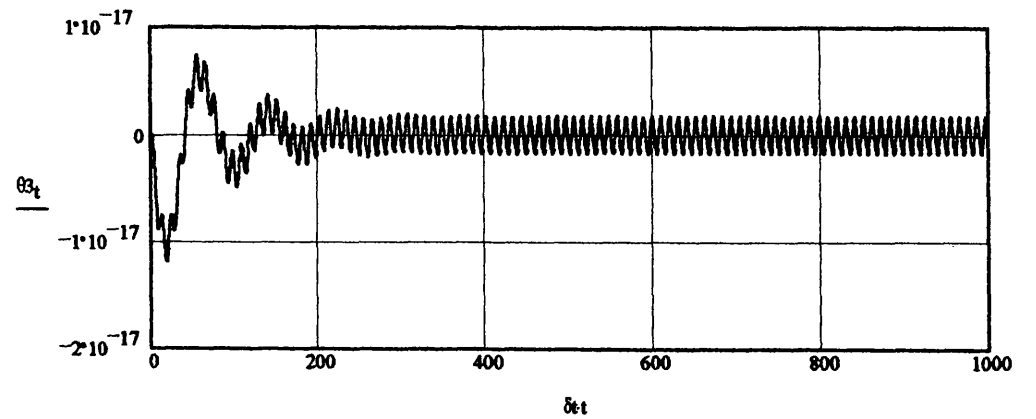

(rad)

Figure 6.178

Tether Force Time-series

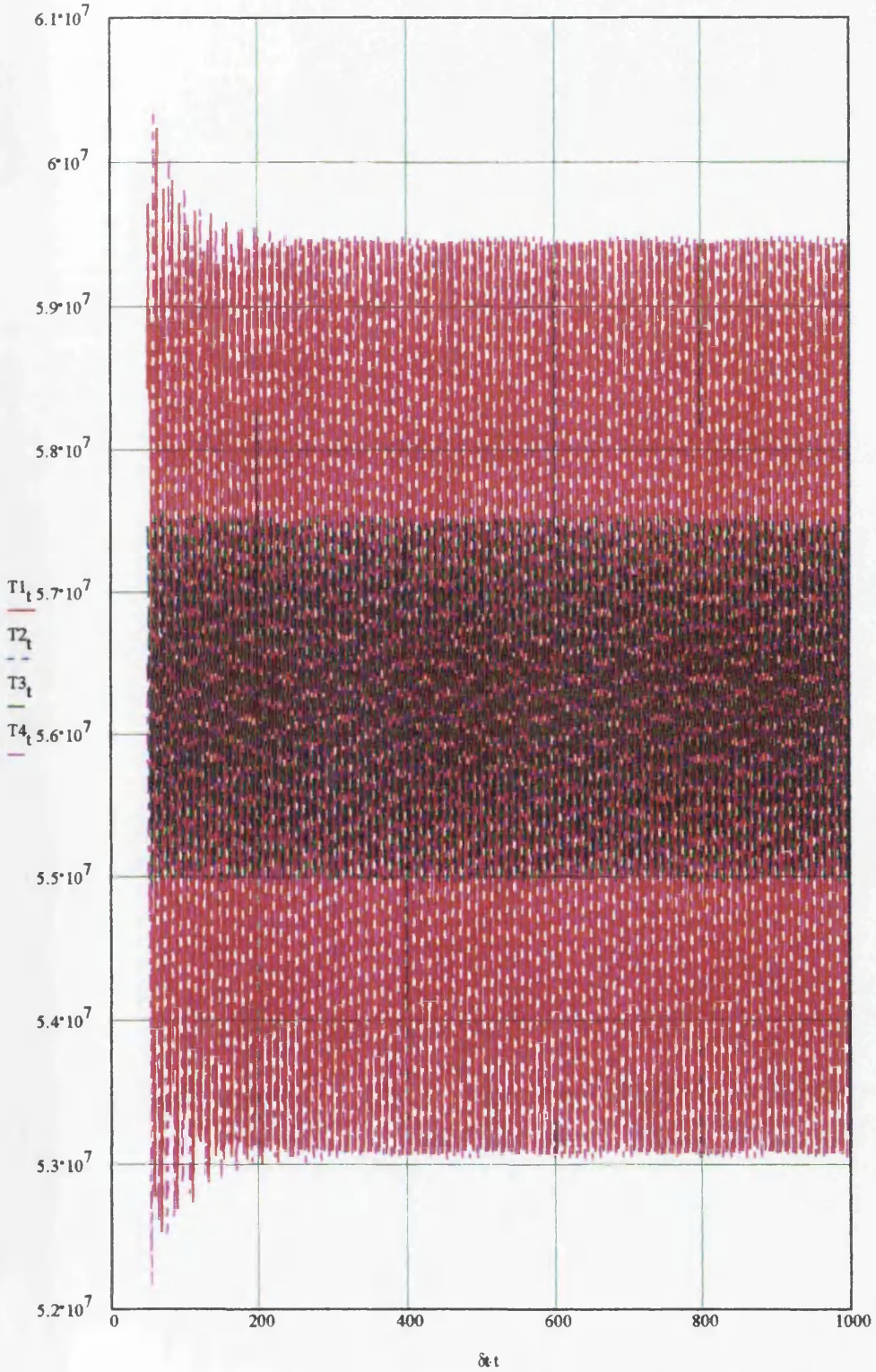

Figure 6.17 9

2D *TLP* c.g. Motion Response (Heave v Surge)

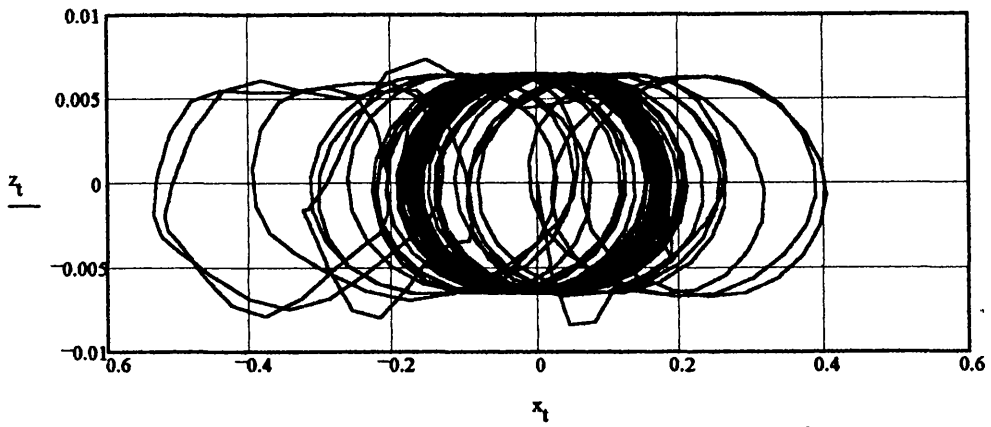

Figure 6.181

2D *TLP* c.g. Motion Response (Heave v Sway)

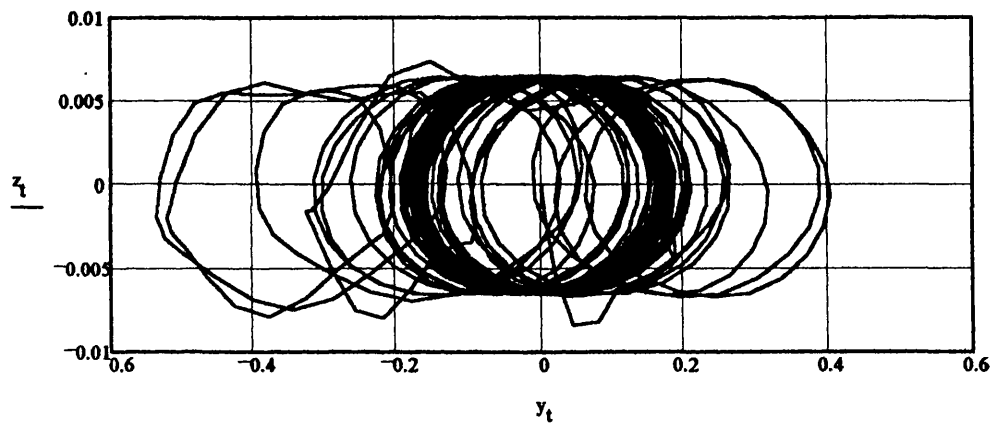

Figure 6.182

2D *TLP* c.g. Motion Response (Heave v Roll)

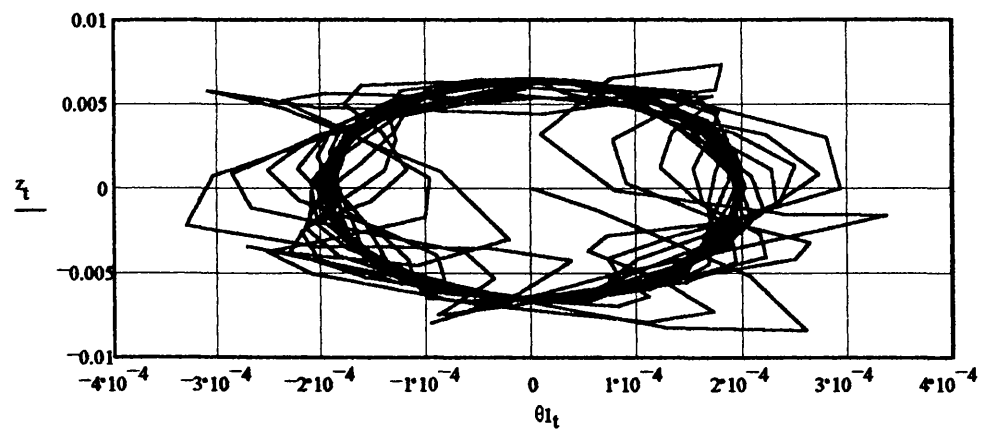

Figure 6.183

2D *TLP* c.g. Motion Response (Heave v Pitch)

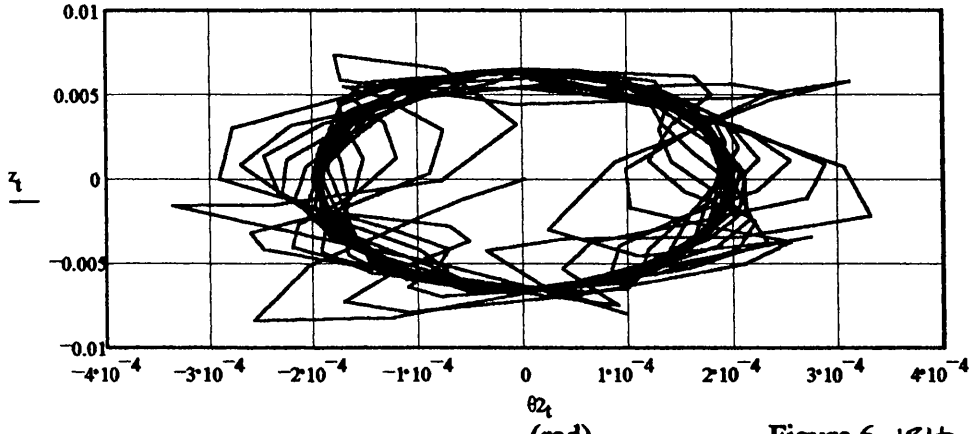

Figure 6. 184

2D *TLP* c.g. Motion Response (Heave v Yaw)

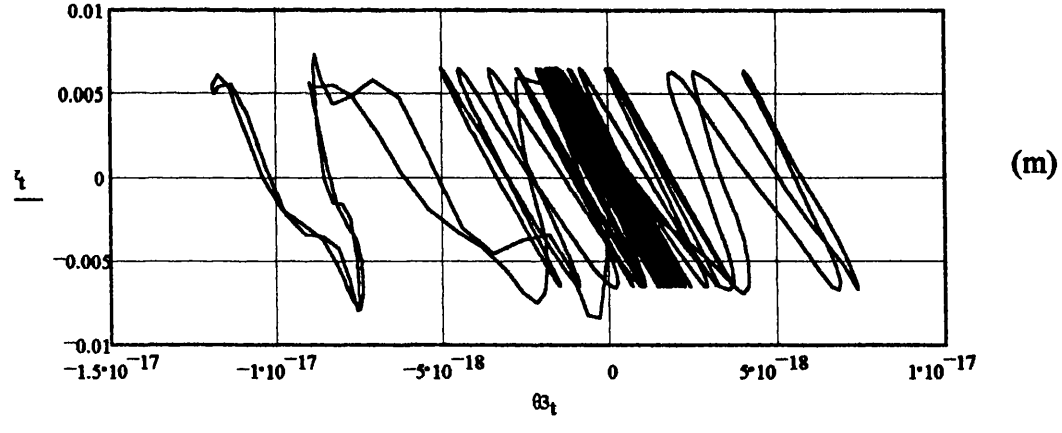

Figure 6.185

2D *TLP* c.g. Motion Response (Surge v Sway)

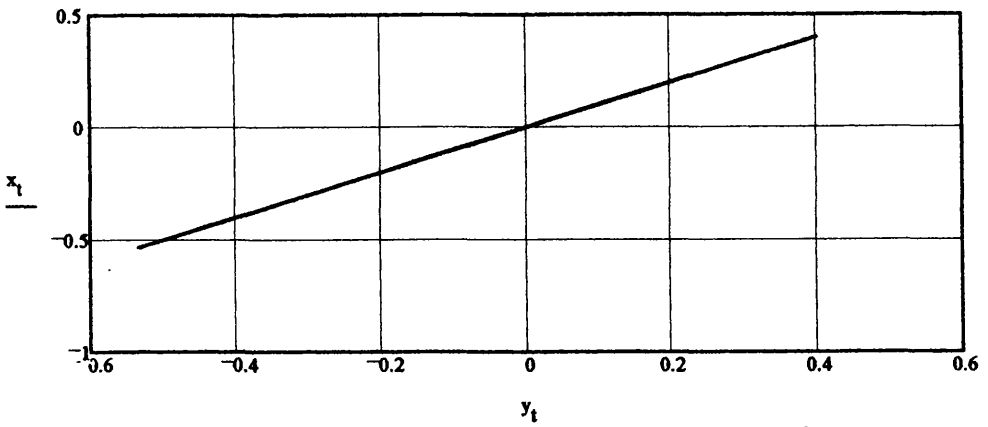

Figure 6.186

2D *TLP* c.g. Motion Response (Surge v Heave)

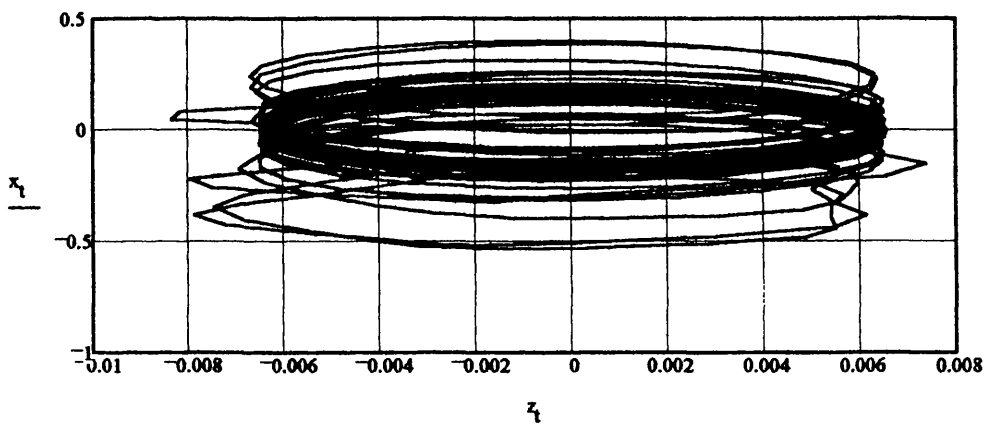

Figure 6.187

2D *TLP* c.g. Motion Response (Surge v Roll)

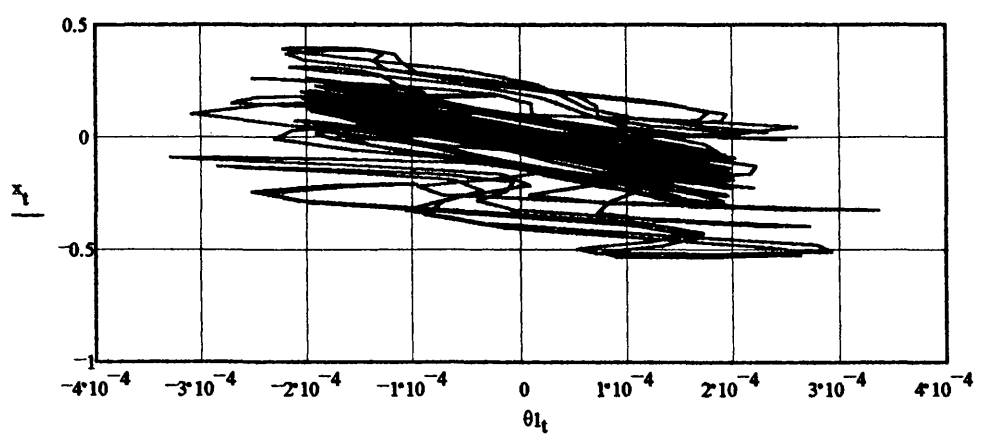

Figure 6.188

2D *TLP* c.g. Motion Response (Surge v Pitch)

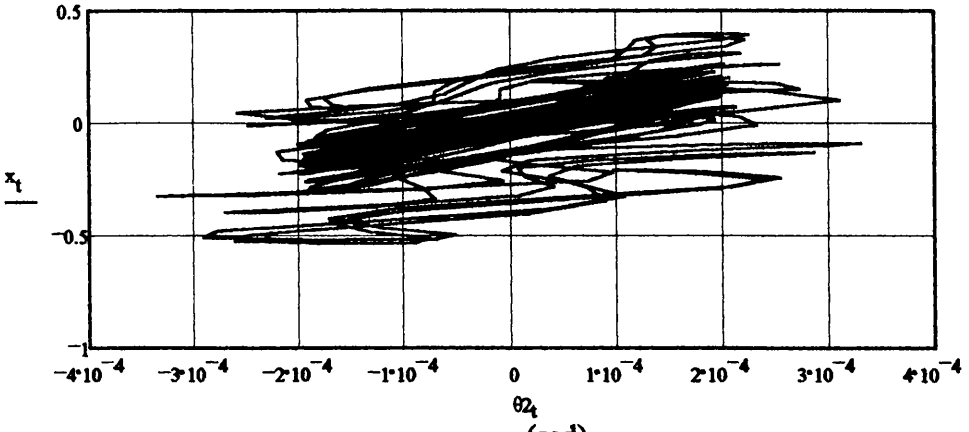

(m)

(rad)

Figure 6.189

2D *TLP* c.g. Motion Response (Surge v Yaw)

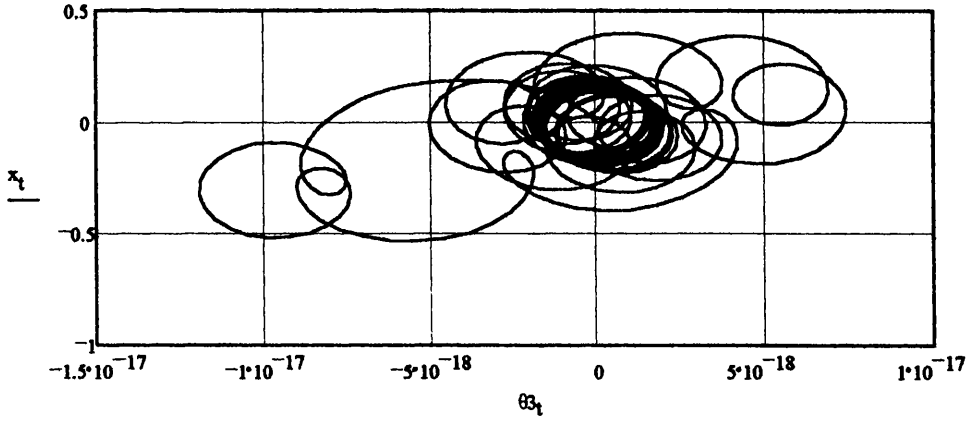

(m)

(rad)

Figure 6.190

6.3.2 Phase 2

6.3.2.1 Introduction

Results generated take the form of time-domain data detailing the Case Study TLP motion response (surge, heave and pitch DOF) and the corresponding tether 'bundle' node displacement and element tension time-series.

The Case Study geometry investigated was that of Heidrun TLP for a head sea (180^0) incident regular waves.

Comparisons and discussion of numerical (Phase 1 and Phase2) and experimental results are detailed in Chapter 7.

6.3.2.2 Heidrun TLP Phase 2 Results

Results for the Phase 2 (TIREE) analysis performed on the Heidrun Case Study TLP system are detailed in Figures 6.190-6.196.

Figure 6.190 details a comparison between the Global surge displacement of the Heidrun TLP system with/without the tether hydrodynamic excitation/reaction force components modeled. The results are for a regular wave installed analysis for a ω =0.7rad/s and ξ_a =1.0m incident wave.

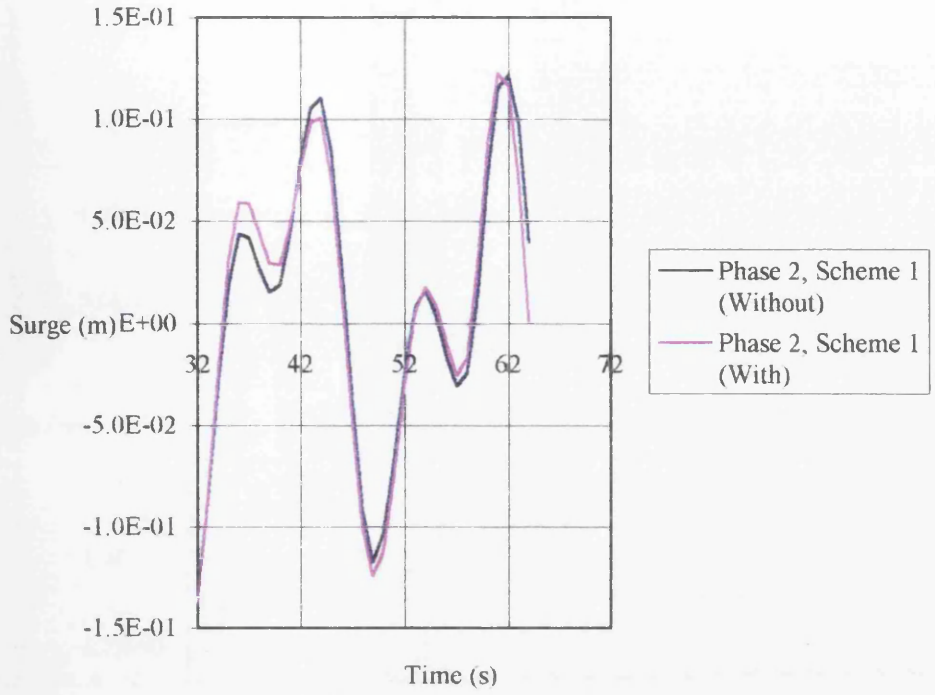

Figure 6.190: Heidrun TLP Global Surge Displacement

(ω =0.7rad/s and ξ_a=1.0m)

Figure 6.191 details the Global Heave displacement for the same simulation details.

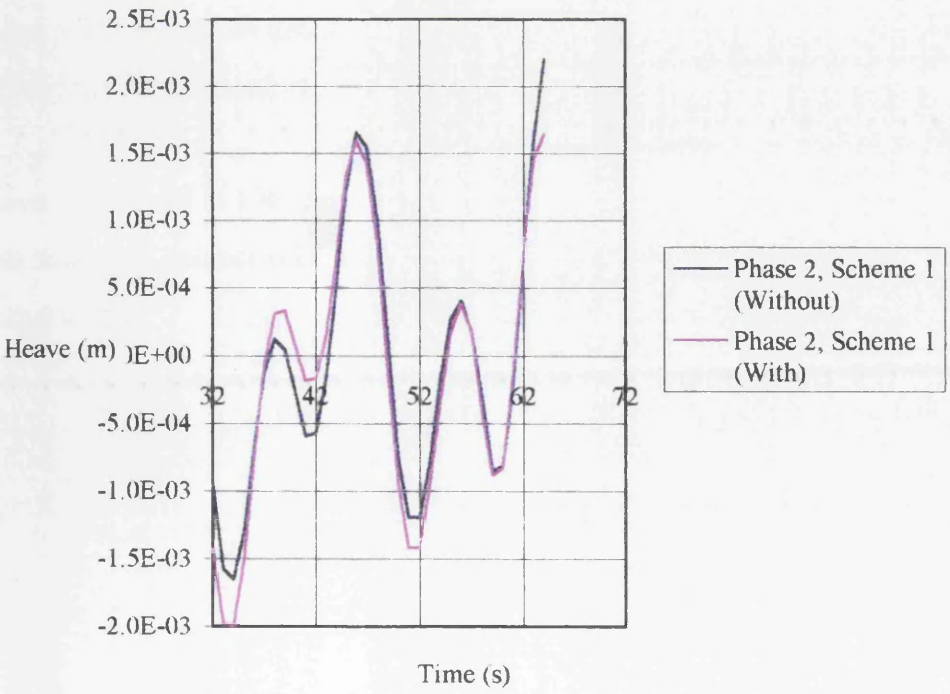

Figure 6.191: Heidrun TLP Global Heave Displacement

(ω =0.7rad/s and ξ_a=1.0m)

Figure 6.192 details the Global Pitch displacement for the same simulation details.

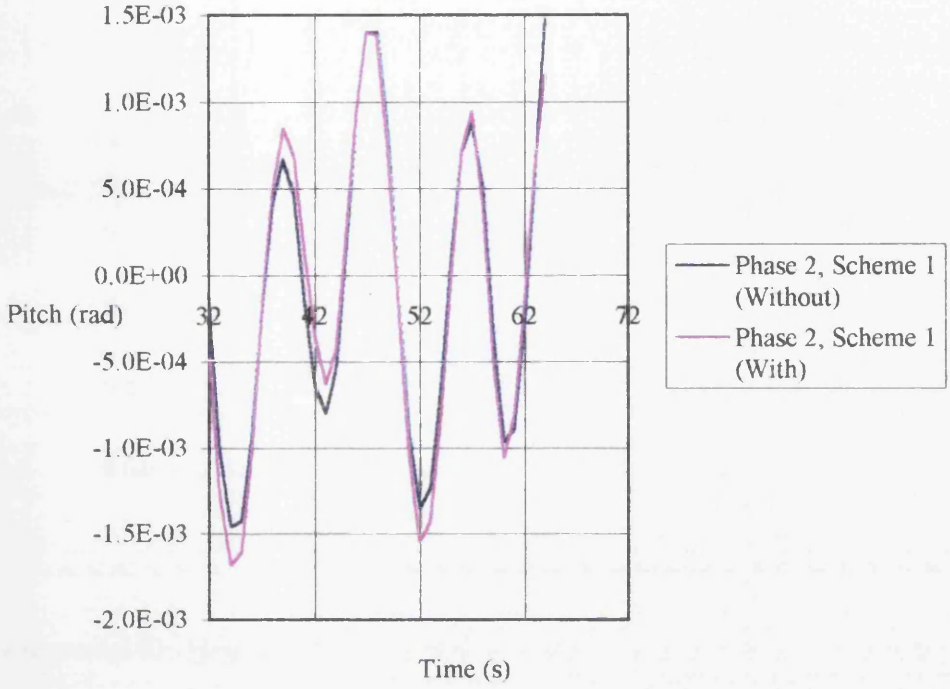

Figure 6.192: Heidrun TLP Global Pitch Displacement

(ω =0.7rad/s and ξ_a =1.0m)

Figures 6.193 and 6.194 detail the tether "bundle" Finite-element tensions without/with hydrodynamic excitation/reaction forces respectively.

Figures 6.195 and 6.196 detail the tether "bundle" Finite-element X and Z mode displacements respectively without hydrodynamic excitation/reaction forces incorporated.

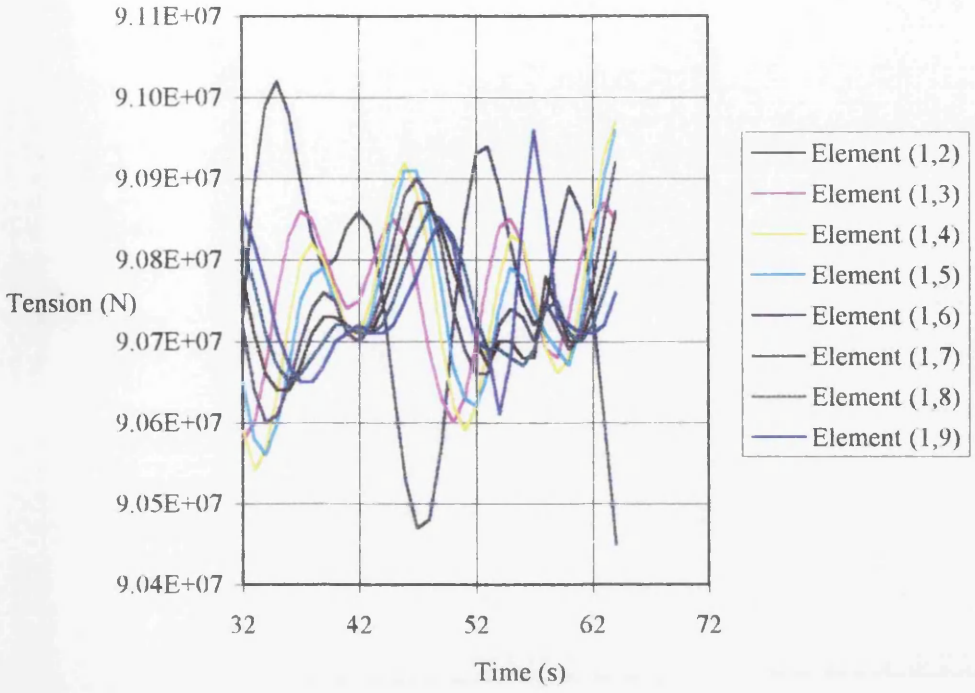

Figure 6.193: Heidrun TLP FWD Port Tether "Bundle" Finite-element Tensions

(Without Tether Fluid Effects, ω =0.7rad/s and ξ_a =1.0m)

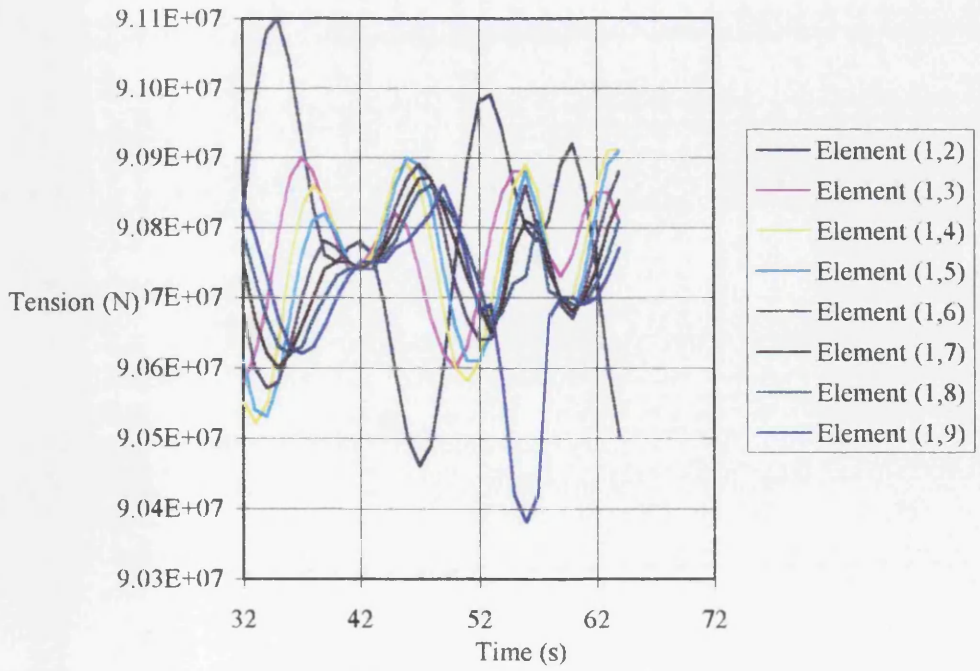

Figure 6.194: Heidrun TLP FWD Port Tether "Bundle" Finite-element Tensions

(With Tether Fluid Effects, ω =0.7rad/s and ξ_a =1.0m)

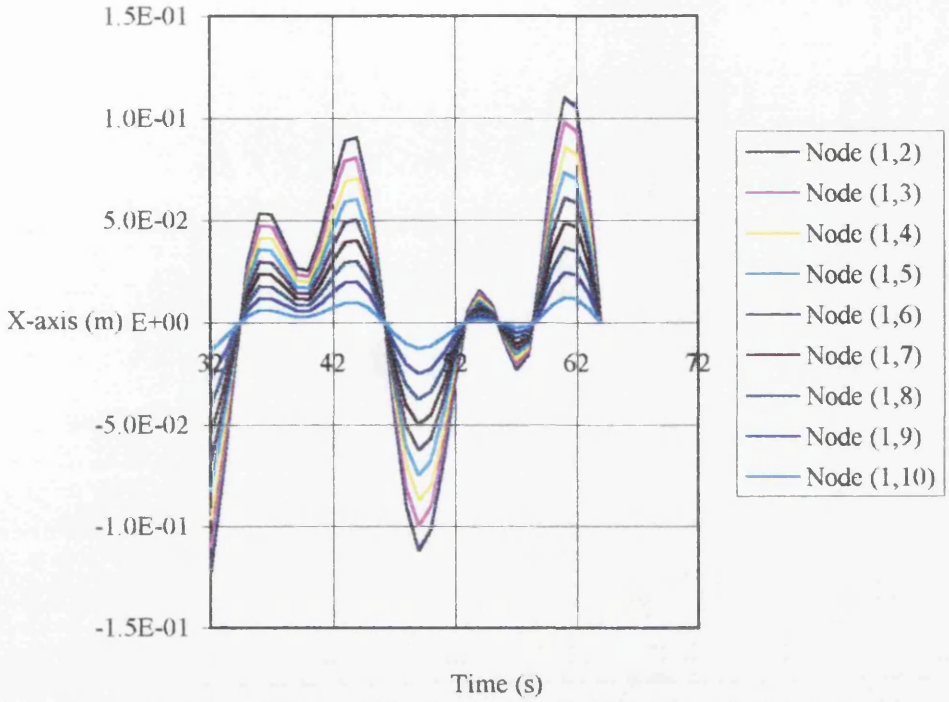

Figure 6.195: Heidrun TLP FWD Port Tether "Bundle" Finite-element Node X-displacement

(Without Tether Fluid Effects, ω =0.7rad/s and ξ_a =1.0m)

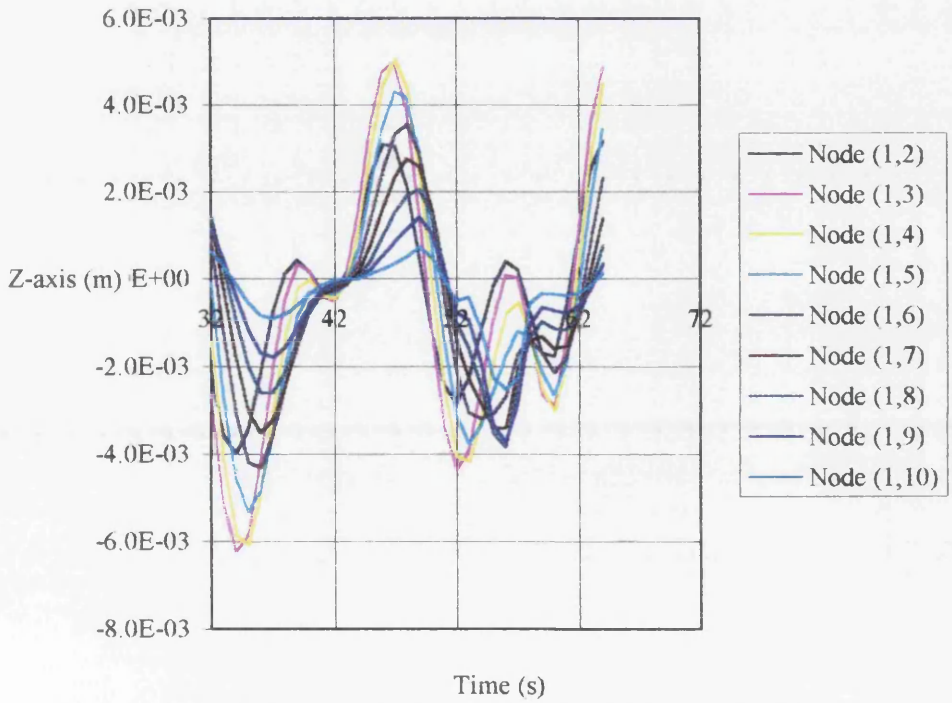

Figure 6.196: Heidrun TLP FWD Port Tether "Bundle" Finite-element Node Z-displacement

(Without Tether Fluid Effects, ω =0.7rad/s and ξ_a =1.0m)

6.4 Case Study Results Discussion

6.4.1 Introduction

The peak responses and trends of the Case Study results for the AA, Heidrun and Snorre TLPs are detailed with comparisons presented in Chapter 7.

6.4.2 AA TLP

The maximum tether transient tension predicted during the Case Study investigation for an installation representative sea-state of ω=0.6rad/s and ξ_a=1.25m was 5.183×10^7N for a 60^0 incident wave heading.

The installed pretension for the AA TLP is 6.53×10^7N.

For the installed mode simulations for a ω=0.36rad/s and ξ_a=9m regular wave the maximum tether tension predicted was 9.25×10^7N with the minimum of 4.708×10^7N.

This indicates that for the sea-states considered the tether transient tension response did not exceed that of the installed pretension level for the AA TLP system.

6.4.3 Heidrun TLP

The maximum tether transient tension predicted during the Case Study investigation for an installation representative sea-state of ω=0.6rad/s and ξ_a=1.25m was 3.224×10^7N for a 135^0 (quartering) incident wave heading.

The installed pretension for the AA TLP is 9.075×10^7N.

For the installed mode simulations for a ω=0.36rad/s and ξ_a=9m regular wave the maximum tether tension predicted was 9.142×10^7N with the minimum of 9.008×10^7N.

This indicates that for the sea-states considered the tether transient tension response did not exceed that of the installed pretension level for the Heidrun TLP system.

6.4.4 Snorre TLP

The maximum tether transient tension predicted during the Case Study investigation for an installation representative sea-state of ω=0.6rad/s and ξ_a=1.25m was 4.237×10^7N for a 135^0 (quartering) incident wave heading.

The installed pretension for the AA TLP is 5.625×10^7N.

For the installed mode simulations for a ω=0.36rad/s and ξ_a=9m regular wave the maximum tether tension predicted was 5.945×10^7N with the minimum of 5.309×10^7N.

This indicates that for the sea-states considered the tether transient tension response did not exceed that of the installed pretension level for the Snorre TLP system.

CHAPTER 7

CONCLUSIONS

7.1 Chapter 2

7.1.1 Introduction

Chapter 2 details a numerical investigation of the wave excitation and hydrodynamic reaction forces acting on a column based TLP geometry.

Wave excitation forces have been predicted utilising an analytical solution to the diffraction problem for an array of circular cylinders developed by Linton and Evans (1990) and by a numerical diffraction/radiation code analyser (AQWA, Atkins Qualitative Wave Analysis). Hydrodynamic reaction forces were predicted by use of the diffraction/radiation code.

7.1.2 Discussion of Loading Prediction Techniques

The analytical solution to the diffraction problem leads to efficient predictions of the diffraction forces acting on an array of circular cylinders. The pontoons must be modeled separately and in this study a Morison approach was utilised. As the cylinders are modeled analytically there is no mesh generated and therefore setting up the model is not computationally demanding.

The numerical diffraction/radiation code yields solutions for both columns and pontoons, but requires a CPU of $\sim 10^3$ greater than the analytical method. As the hull is modeled by a 3D mesh the model requires considerable computation effort, in this study the mesh was generated manually.

7.1.3 Discussion of Loading Comparisons

Comparisons between analytical and numerical diffraction methods as well as the experimental data for the wave excitation forces/moments for head sea (180^0) incident regular waves for surge and heave modes are detailed in Figures 3.25-3.26 (Chapter 3), and Figures 7.1-7.3 for pitch, surge drift force and surge radiation damping.

Results of the diffraction/radiation comparison for the columns only and complete models are detailed in Chapter 2 and are summarised as follows: **(excitation forces)** in the surge, heave and pitch modes for incident regular head sea waves pontoon effects were observed to be significant for low frequency/long waves (maximum ~10% for surge and ~50% for heave and pitch). No pontoon effects were observed for wave drift force calculations. Similar trends to those for head sea incident waves were observed for quartering sea incident regular waves with the pontoons contributing ~10% and 50% in sway and roll respectively. For all comparisons the predicted forces/moment with and without pontoons modeled converge as the wave frequency increases, Ref. Chapter 2, Figures 2.11-2.18 (wave lenght decreases). This is consistent with the rapid decay of fluid kinematics w.r.t. water depth for short wave lengths (depth to top of pontoons for the Case Study TLP geometry (Heidrun) investigated=64.3m); **(radiation solution)** for the TLP geometry modeled (radiation solutions are independent of incident wave direction) the pontoons contribute ~10% of the total surge added mass and ~10% of the sway added mass. In heave, the pontoons contribute a maximum of ~50% at the low frequencies reducing to ~20% at the higher frequencies. In roll and pitch the pontoons contribute ~60% of the total added inertia. In yaw the pontoon effects are small, ~5% contribution to added inertia. The pontoons contribute a maximum of ~20% to the total radiation damping in surge and sway, with negligible contribution elsewhere. In heave the pontoon effects dominate, contributing a maximum of ~90% of the total radiation damping. In roll and pitch the pontoon contribution to the radiation damping was a maximum of ~80%. In yaw the pontoon contribution to the radiation damping is negligible. It was observed (Ref. Chapter 2, Figures 2.27-2.31) that the radiation damping for the model with/without pontoons in surge, sway, heave, roll and pitch converged for the higher frequencies.

It should be noted that the above trends are applicable to the Case Study TLP investigated (Heidrun) and are not generic TLP results. The nature of the TLP geometry utilised is such that pontoon effects may be lower than those that may be relevant to other geomteries due to the deep position of the pontoons (-64.3m from SWL to top of pontoons for Heidrun TLP).

Figure 7.1 details the comparison of the wave excitation force in pitch. The curves are as those detailed above with an additional AQWA-Line diffraction/radiation model of columns only without column bases (AQWA-Line (WCB)) and with experimental data.

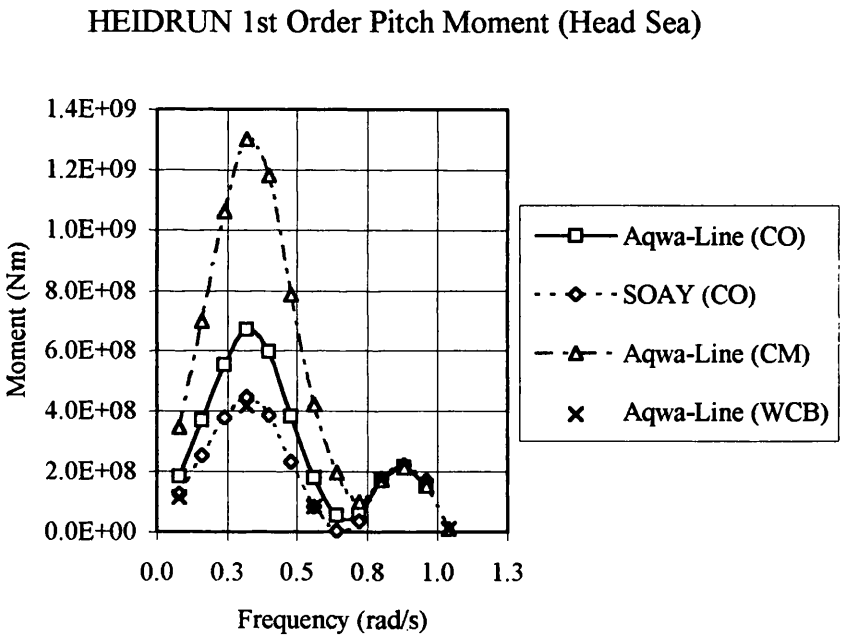

Figure 7.1: Pitch Wave Moment Comparison

The AQWA-Line (CO) and SOAY (CO) results show poor agreement which is explained by the AQWA-Line (WCB) data. This illustrates the column base effects (which are not present in the AQWA-Line (WCB, without column base) data). The comparison between the AQWA-Line (CM) and AQWA-Line (CO) data illustrates the pontoon contribution to the wave pitch moment of ~50%.

For the higher frequencies all curves converge indicating the reduction in significance of the column base/pontoon effects as the incident wave lengths reduce.

Figure 7.2 details the wave drift force in surge for head sea incident regular waves. By comparison of the AQWA-Line (CO) and AQWA-Line (CM) data the negligible effect of the pontoons on the surge wave drift forces is clearly indicted. This is consist with the wave drift forces dependence on the wave making properties of a body in a fluid, in surge the pontoon contribution to this will be low.

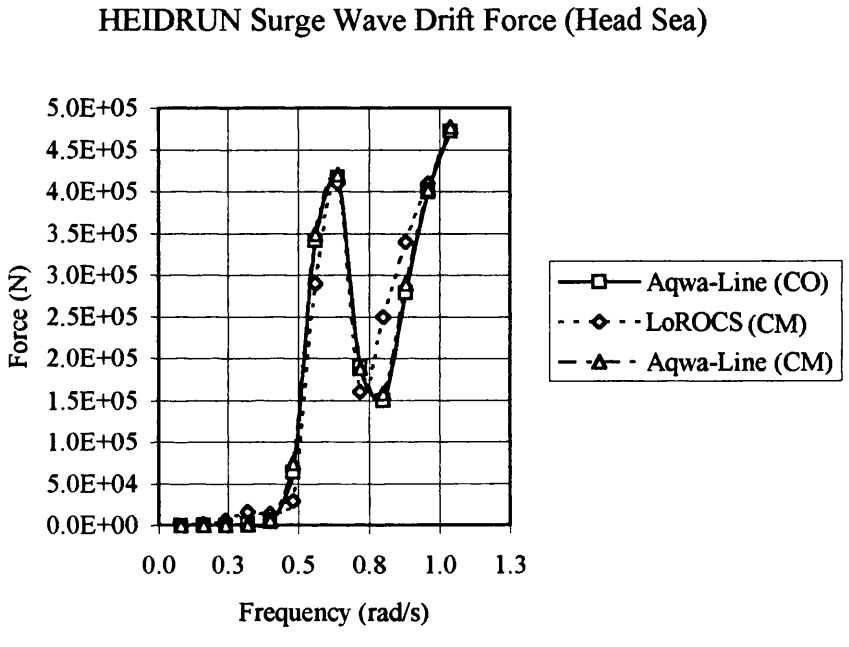

Figure 7.2: Surge Wave Drift Force Comparison

The LoROCS (CO) data was supplied by BP (CASE sponsors) and utilised during the time-domain motion response predictions (Ref. Chapter 6). This data was calculated utilising the LoROCS software (Cornut, 1995) based on analytical solutions to the diffraction/radiation problem. By inspection the comparison is acceptable with an isolated peak discrepancy of ~30% at ~0.85rad/s.

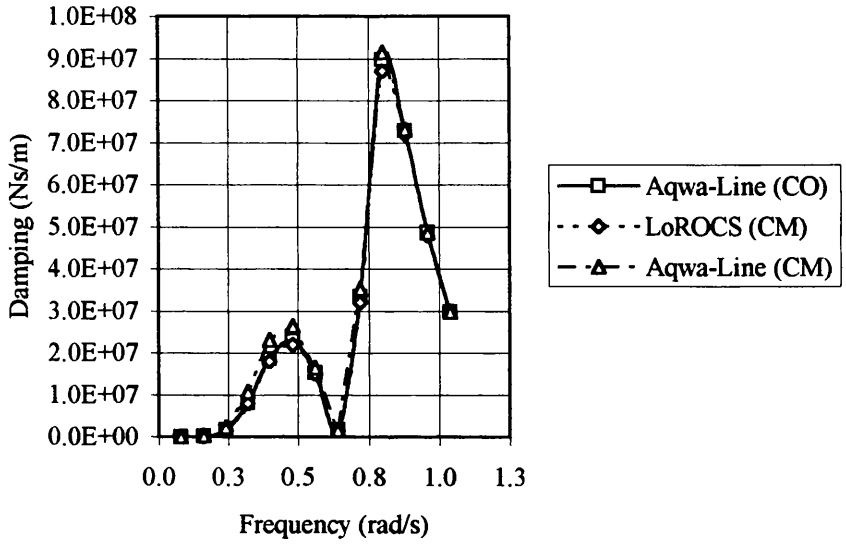

Figure 7.3: Surge Radiation Damping Comparison

Figure 7.3 details the surge radiation damping comparisons. By comparison between the AQWA-Line (CO) and AQWA-Line (CM) data the negligible effect of the pontoons is illustrated. The BP supplied (LoROCS) data is also detailed showing good agreement with numerical diffraction/radiation data.

A comparison between the experimentally sampled surge added mass data and the data utilised during the Case Study simulations is detailed in Figure 3.27, Chapter 3.

7.2 Chapter 3

7.2.1 Introduction

To validate prediction methodologies utilised during the numerical prediction of wave excitation forces/moments (Ref. Chapter 2) and investigate the origins/mechanisms of higher order forces/responses an experimental investigation of wave forces and hydrodynamic reaction forces acting on a Case Study TLP geometry in extreme waves and currents was undertaken.

The approach followed was one of design/construction and testing of an ~1:100 (1:98.4) model of the Heidrun TLP geometry. To measure wave excitation forces the model was mounted fixed in the Glasgow University towing/wave tank and extreme regular waves generated/sampled. To obtain the hydrodynamic reaction forces the model was mounted to an oscillating system and forced oscillation tests were conducted.

7.2.2 Discussion of Experimental Setup (Loading)

The experimental setup developed to investigate the dynamic response characteristics of the Case Study TLP in the Glasgow University towing/wave tank consisted of the following components:

- Data acquisition system
- Instrumentation system
- Case Study TLP Model
- Oscillator Driving System

Full details of the experimental setup are given in Chapter 3.

When designing the experimental setup care must be taken to ensure sufficient rigidity of fixed connections to minimise unwanted flexing and possible resonance. The instrumentation system must be designed with consideration of the form and magnitude of the response to be sampled and the data acquisition system resolution.

7.2.3 Discussion of Higher Order Force Measurements

During the FFT analysis of the global wave excitation force time-series data, force components at multiples of the incident wave frequencies were obtained.

Figures 7.4-7.7 detail these higher order forces for surge and heave (2nd and 3rd order).

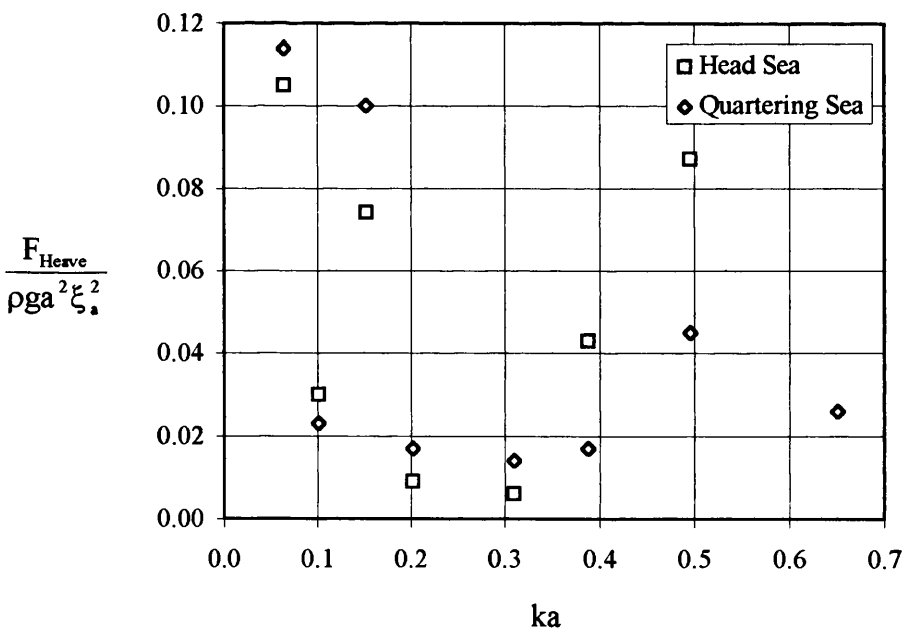

Figure 7.4: Experimental Global Heave Force
(2nd order)

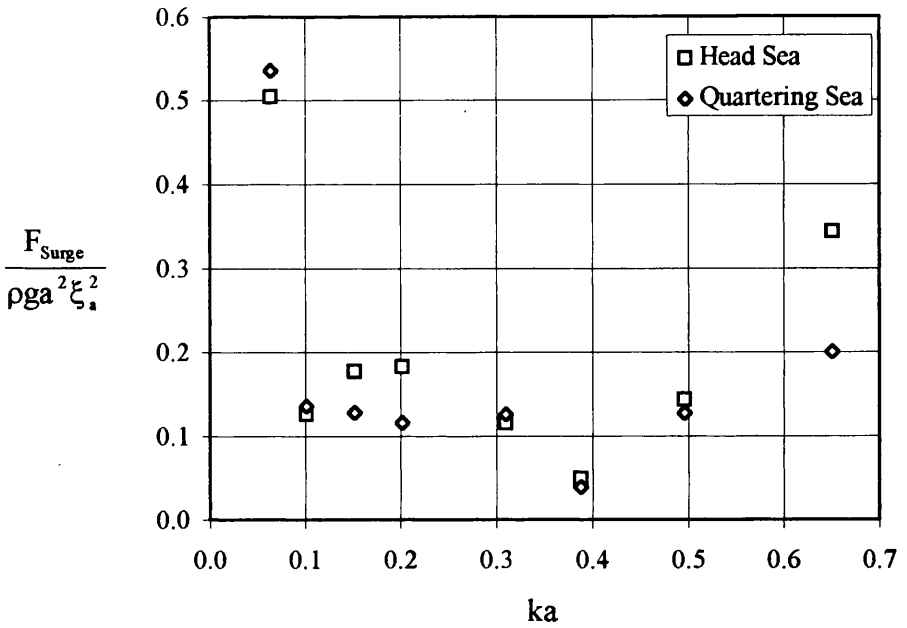

Figure 7.5: Experimental Global Surge Force

(2^{nd} order)

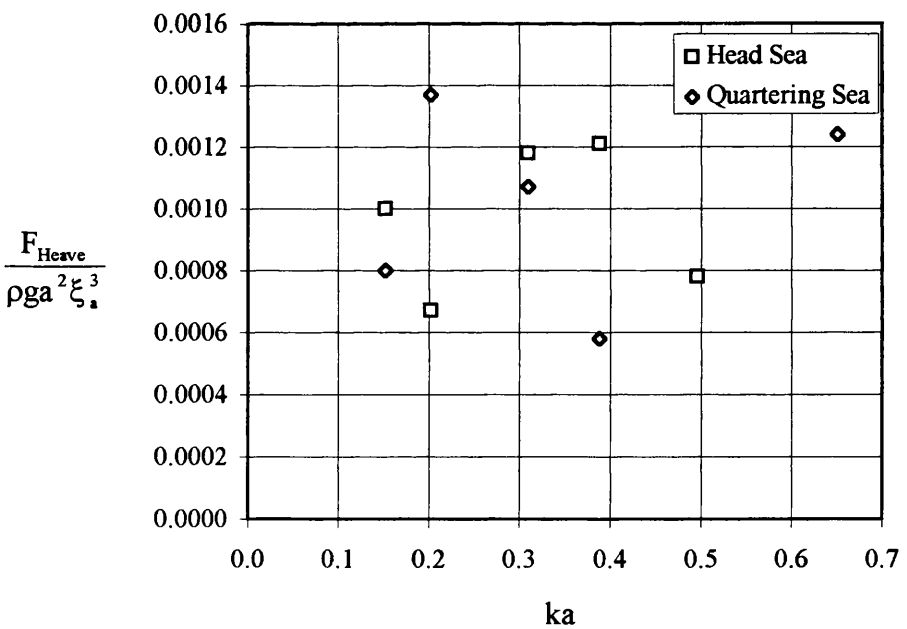

Figure 7.6: Experimental Global Heave Force

(3^{rd} order)

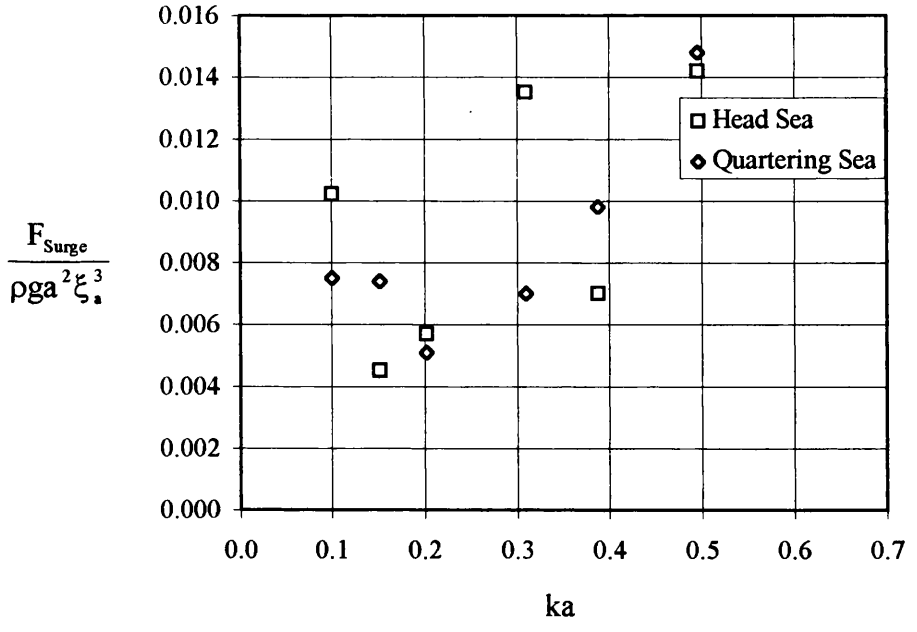

Figure 7.7: Experimental Global Surge Force

(3^{rd} order)

As a simple qualitative comparison; the 1^{st} order surge and heave forces for the Case TLP geometry tested are in the order of 10000tonne and 1000tonne respectively; the 2^{nd} order surge and heave forces are in the order of 100tonne and 10tonne respectively with the 3^{rd} order surge and heave forces in the order of 1tonne and 0.1tonne respectively.

The origins of these forces are considered to be associated with wave elevation harmonics occurring between FWD and AFT columns of a TLP geometry in extreme waves. This hypothesis is supported by research undertaken at the University of Edinburgh were wave surface elevations were measured during experiments with a TLP model in extreme waves. The model utilised for that experimental study was the one utilised during the force measurements detailed above. Results of that research (Arnott *et al*, 1997) detailed wave reflection between the FWD and AFT columns generating waves at multiples of the incident regular wave frequencies. Such waves were noted during the author's experimental work.

Although from an installation perspective the above higher order forces are of low relevance (installation sea-states are typically of a significant wave height of 3.5m), w.r.t. the origins/mechanisms of the ringing phenomenon observed in tether tension time-series these higher forces may be of significance.

7.2.5 Discussion of Current Effects

To investigate the effects of current on the hydrodynamic reaction force components forced oscillation tests were undertaken in the presence of forward speed. It is acknowledged that this will lead to a different radiated wave field to that of incident waves in the presence of current (Faltinsen, 1990).

Figures 7.8 an 7.9 detail global surge added mass and viscous damping for the Case Study TLP hull.

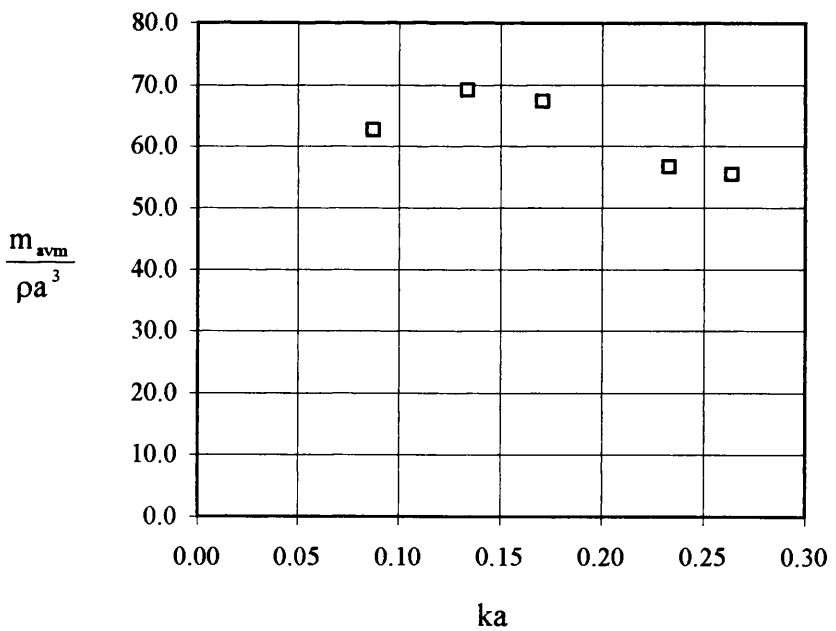

Figure 7.8: Global Surge Added Mass

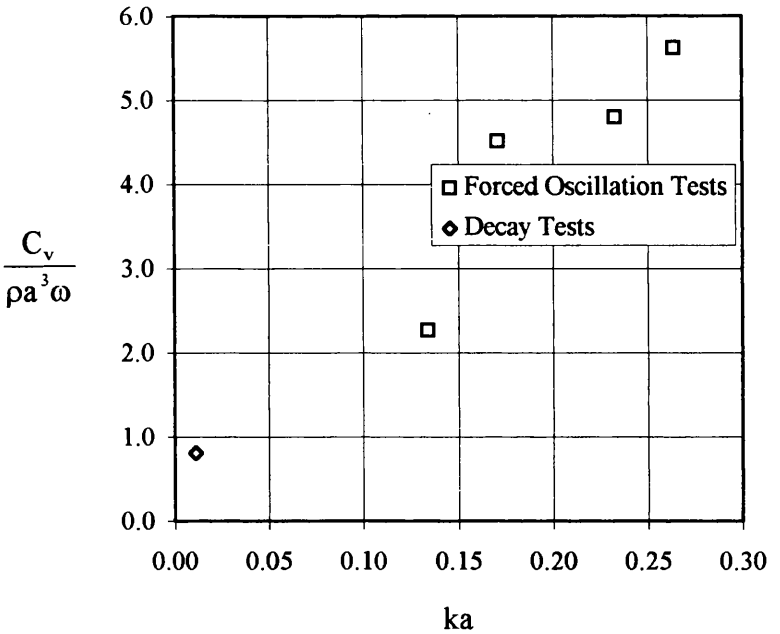

Figure 7.9: Global Surge Viscous Damping

Figures 7.10 and 7.11 detail the surge added mass and damping measured in the presence of current.

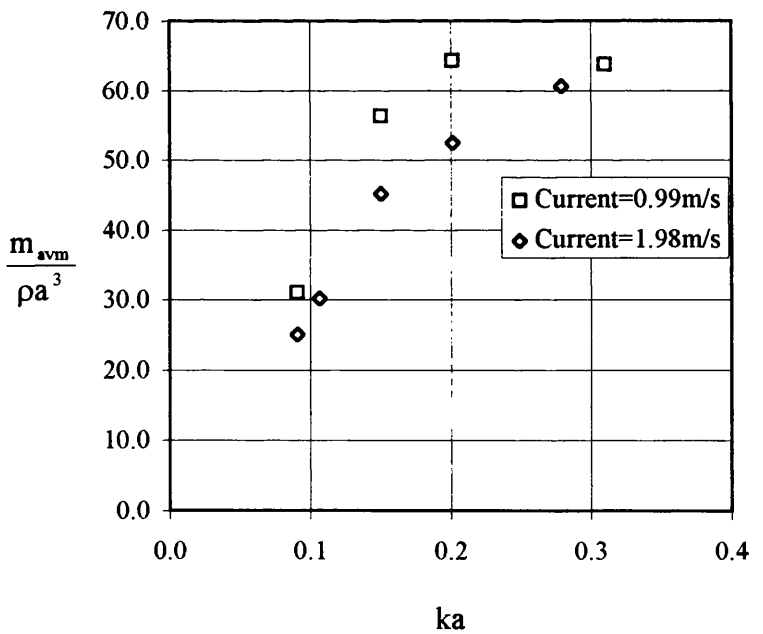

Figure 7.10: Global Surge Added Mass
(With Current Effects)

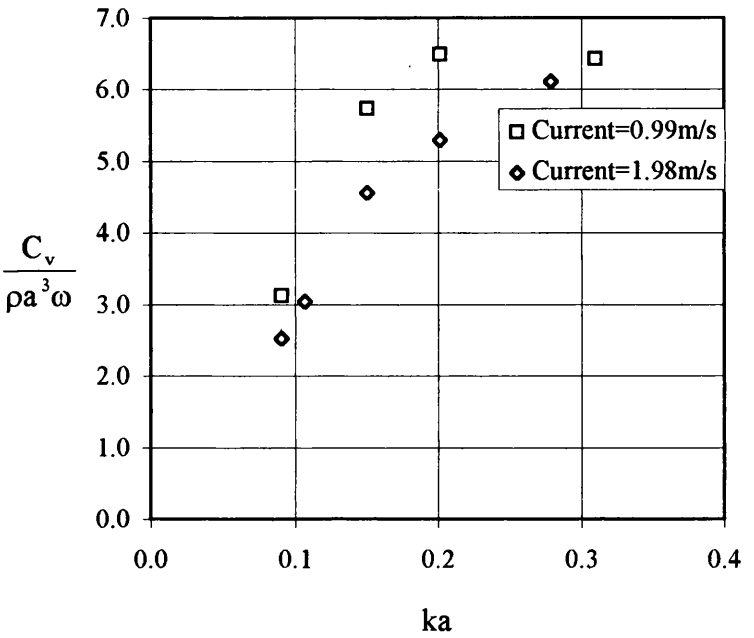

Figure 7.11: Global Surge Viscous Damping
(With Current Effects)

By inspection of Figures 7.8-7.11 in the presence of (and with increasing) current the surge added mass and damping reduces. This indicates a current/hydrodynamic reaction force interaction which leads to a reduction of the reaction forces.

7.3 Chapter 4

7.3.1 Introduction

Chapter 4 details a numerical time-domain investigation of TLP system response during tether installation and installed conditions.

2No. models were utilised:

Phase 1 (JURA): To model the TLP system response during pretension operations a 6DOF rigid-body model was developed.

The coupled time-dependent characteristics of the tether mooring system are incorporated by the derivation of a (6DOF) tether mooring stiffness matrix $[K_m]$ which includes the hull hydrostatic components.

This mooring stiffness $[K_m]$ is based on modeling the tether system as a group of rotating axial springs and incorporating hull hydrostatic stiffness by assuming small angle stability theory.

Phase 2 (TIREE) (Scheme 1): Coupled tether/TLP finite-element model consisting of global system matrices representing the finite-element model of the tether bundle system and the TLP rigid-body system.

Phase 2 (TIREE) (Scheme 2): Finite-element tether bundle model incorporating an External Applied Force vector. The External Applied Force vector can consist of translation force components derived by a coupled tether/TLP analysis or representative installation loads (due to tow-out, upending, etc).

7.3.2 Discussion of Time-domain Prediction Techniques

The time-domain technique is a widely used method employed for the prediction of response characteristics of dynamic systems. Paulling (1977) details a comprehensive discussion of the application of time-domain modeling techniques to TLP systems.

The fundamental computation underlying time-domain simulations is the solving of a system of 2^{nd} order differential equations. There exist many published techniques to achieve this.

During the course of this research study the well known Runge-Kutta (Ref. Thomson, 1988), Newmark-β (Newmark, 1959) and Gear Backward Differentiation techniques (Gear's Stiff Method, Gear, 1971) were utilised.

The Runge-Kutta (explicit) and Newmark-β (implicit) method were utilised during the Phase 1 activities. It was found that for installed simulations the Newmark-β method was more efficient allowing longer time-steps. For the pretensioning simulations the Runge-Kutta method proved to be more reliable. This is consistent with the nature of each solving algorithm; the Newmark-β is an implicit method that achieves solution at time $t + \delta t$ based on equilibrium at time t, therefore for the installed system which behaves linearly longer time-steps can be utilised without numerical failure; the Runge-Kutta is an explicit method where the solution is predicted at time $t + \delta t$ based on equilibrium at time t, therefore during the pretensioning sequence where the response is nonlinear this method proved more reliable. It is acknowledged that by application of a $\beta = 0.25$ the Newmark-β method is rendered unconditionally stable.

This was adopted during the early stages of the pretensioning simulations, however, intuitively erroneous results were computed for some simulation runs and therefore the Runge-Kutta method was then adopted.

To investigate the sensitivity of the simulation results to the differential equation solving routine used a run was made utilising a form of the Phase 1 software, JURA(STAGE5)initial, incorporating the Newmark-β Implicit algorithm. The run examined was the $\omega = 0.32$rad/s, $\xi_a = 3.523$m, PT=0N, yielding a comparison as follows: maximum transient axial tension; Runge-Kutta=4.015×10^7N and Newmark-$\beta = 4.185 \times 10^7$N. This indicates the results are insensitive to the d.e solving routine employed for this frequency. However this is not considered to demonstrate frequency-independence for all runs.

7.3.3 Comparison of Phase 1 and Phase 2 Tether System Models

Comparisons between the TLP system response predicted by the Phase 1 and Phase 2 models are detailed in Figures 7.12-7.22.

Results for the Phase 2 (TIREE) analysis performed on the Heidrun TLP system are detailed in Figures 7.12-7.14.

Figure 7.12 details a comparison between the global surge displacement of the Heidrun TLP system with/without the tether hydrodynamic excitation/reaction force components modeled. The results are for a regular wave installed analysis for a ω =0.7rad/s and ξ_a =1.0m incident wave.

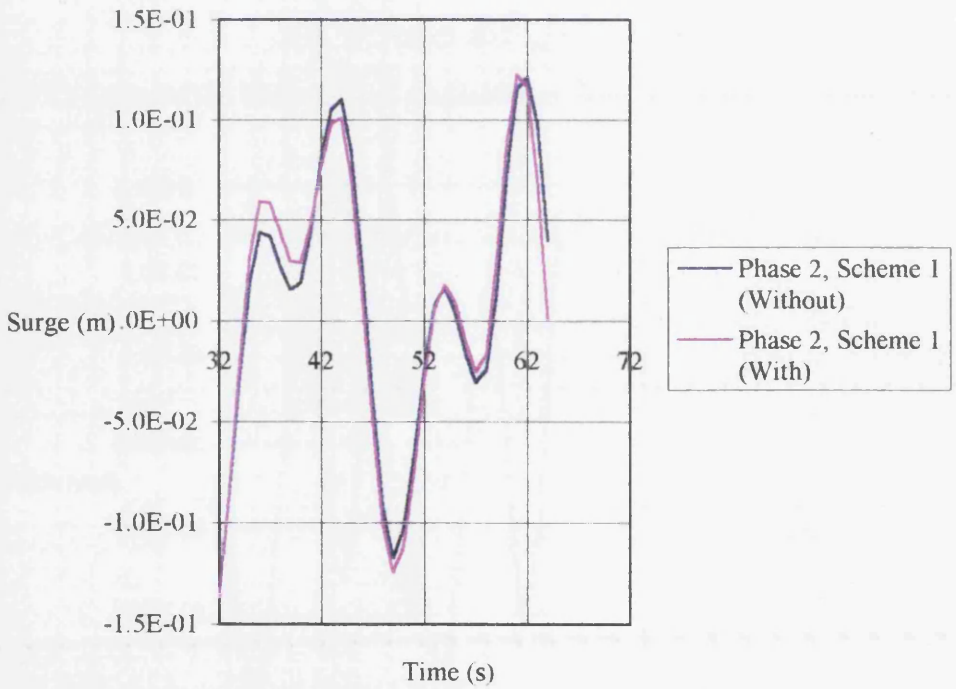

Figure 7.12: Heidrun TLP Global Surge Displacement

(ω =0.7rad/s and ξ_a =1.0m, TIREE)

Figure 7.13 details the Global Heave displacement for the same simulation details.

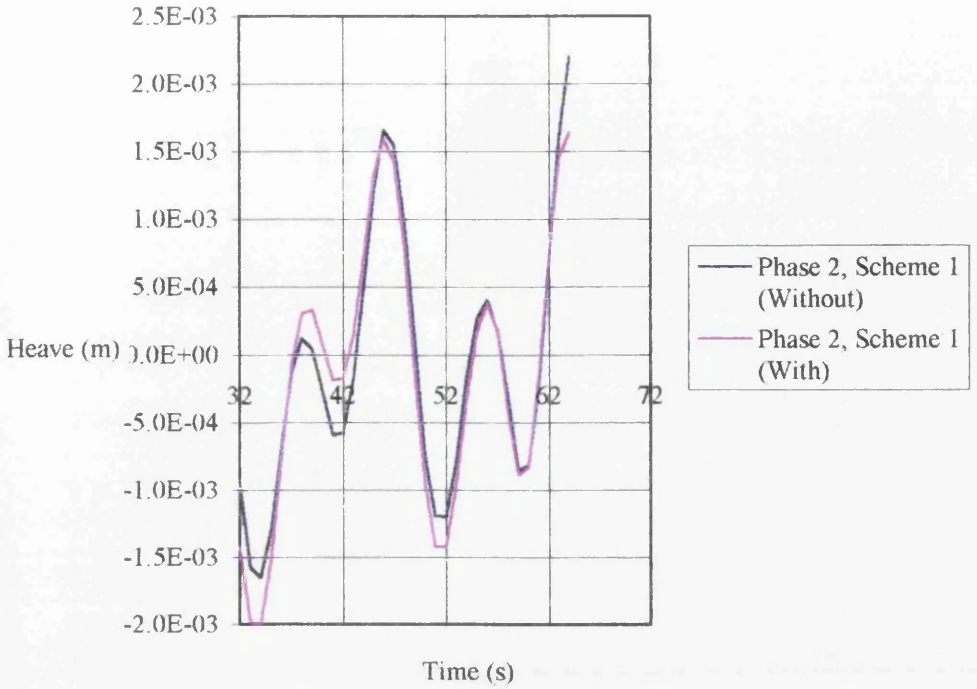

Figure 7.13: Heidrun TLP Global Heave Displacement

(ω =0.7rad/s and ξ_a=1.0m, TIREE)

Figure 7.14 details the Global Pitch displacement for the same simulation details.

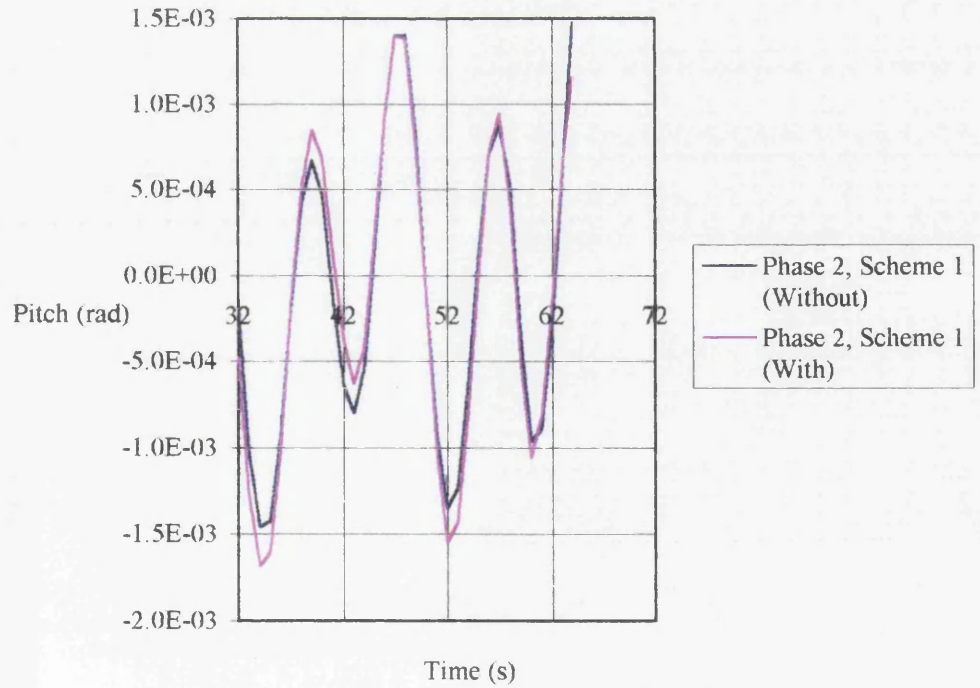

Figure 7.14: Heidrun TLP Global Pitch Displacement

(ω =0.7rad/s and ξ_a=1.0m, TIREE)

For comparison results for same simulation parameters generated utilising the Phase 1 program (JURA) are given in Figures 7.15-7.17 respectively.

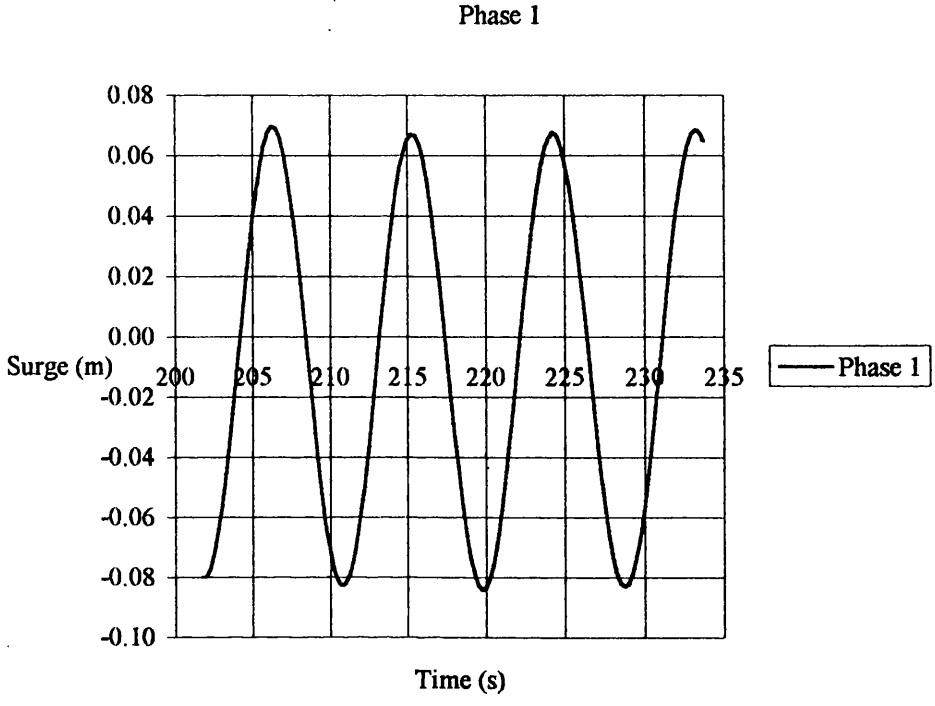

Figure 7.15: Heidrun TLP Global Surge Displacement

(ω =0.7rad/s and ξ_a =1.0m, JURA)

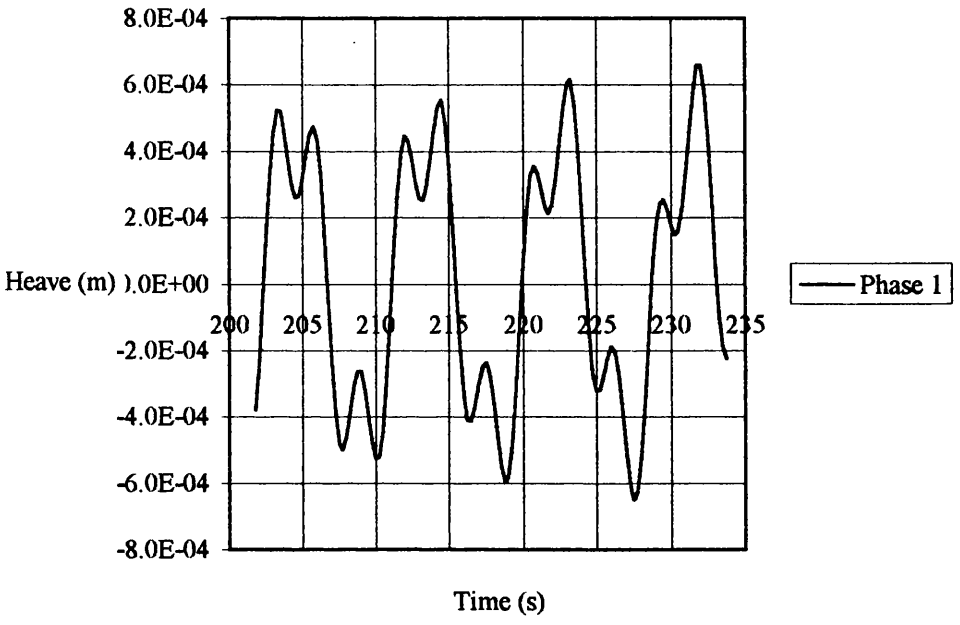

Figure 7.16: Heidrun TLP Global Heave Displacement

(ω =0.7rad/s and ξ_a=1.0m, JURA)

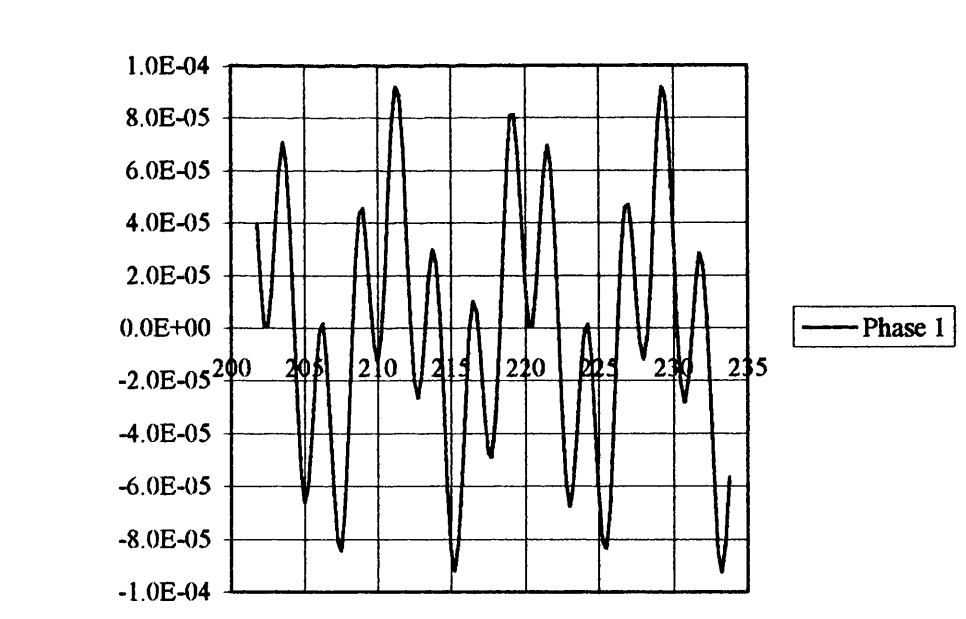

Figure 7.17: Heidrun TLP Global Pitch Displacement

(ω =0.7rad/s and ξ_a=1.0m, JURA)

Figure 7.18 details the tether "bundle" Finite-element tensions without hydrodynamic excitation/reaction forces incorporated.

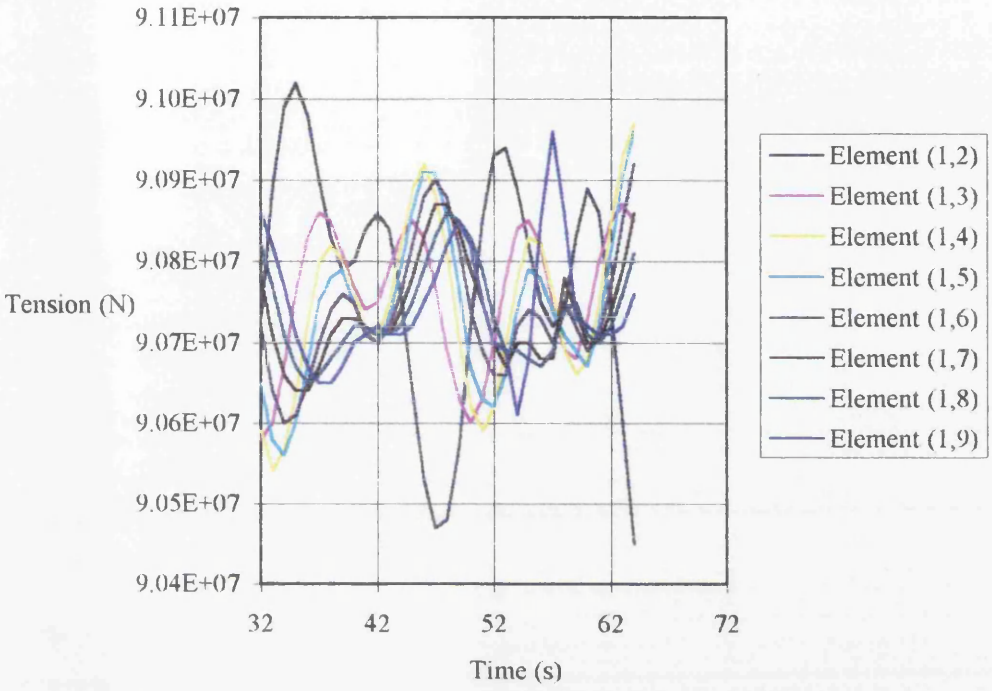

Figure 7.18: Heidrun TLP FWD Port Tether "Bundle" Finite-element Tensions

(Without Tether Fluid Effects, ω =0.7rad/s and ξ_a =1.0m, TIREE)

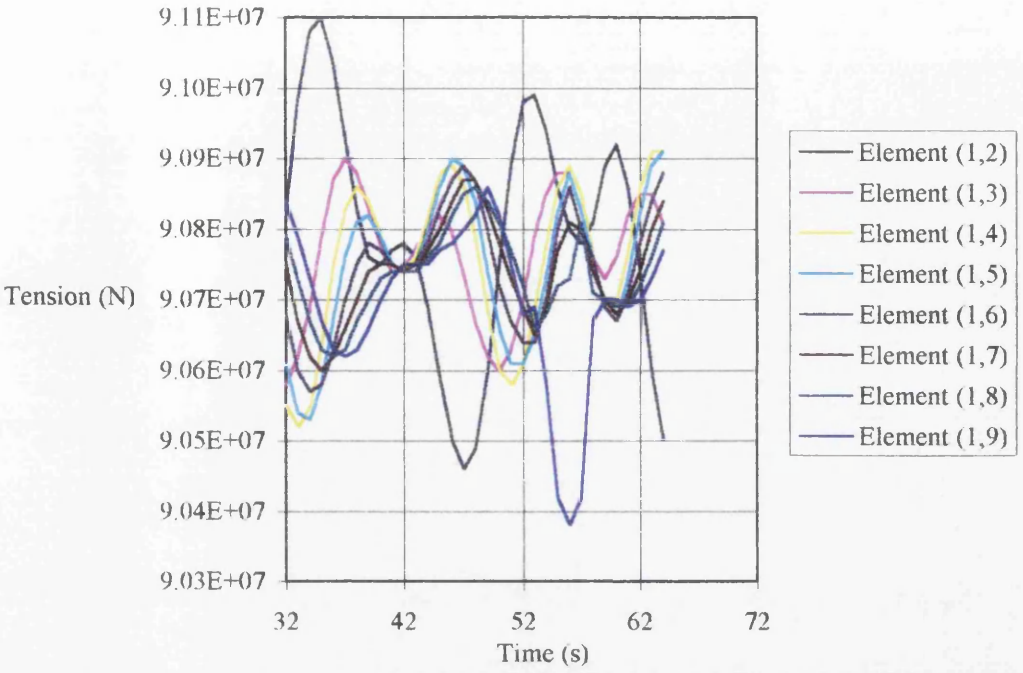

Figure 7.19: Heidrun TLP FWD Port Tether "Bundle" Finite-element Tensions

(With Tether Fluid Effects, ω =0.7rad/s and ξ_a =1.0m, TIREE)

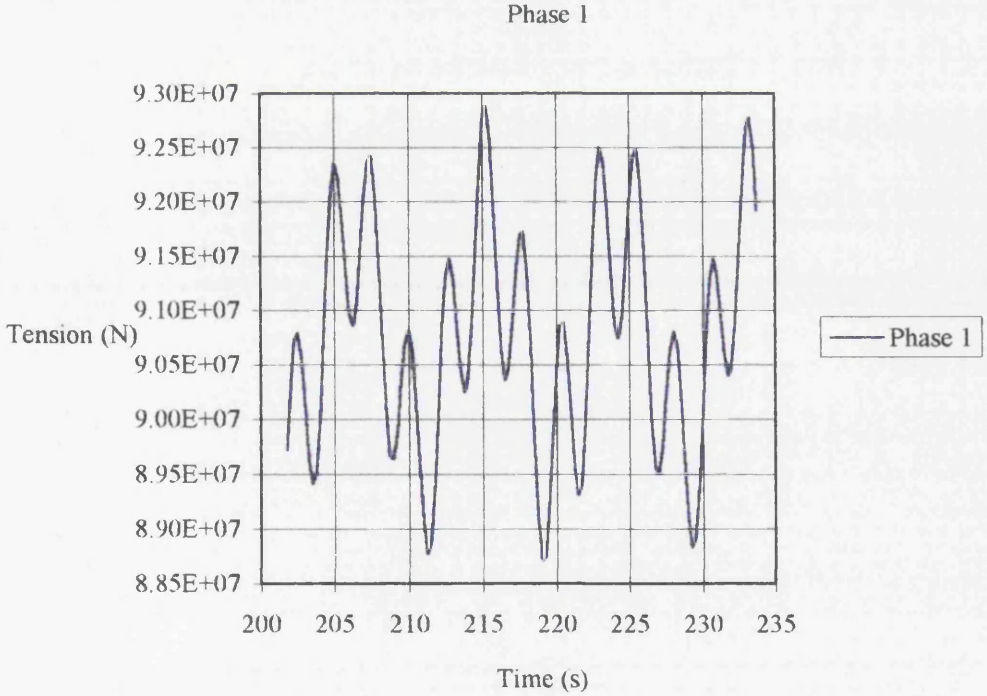

Figure 7.20: Heidrun TLP FWD Port Tether "Bundle" Tension

(ω =0.7rad/s and ξ_a =1.0m, JURA-Stage 6)

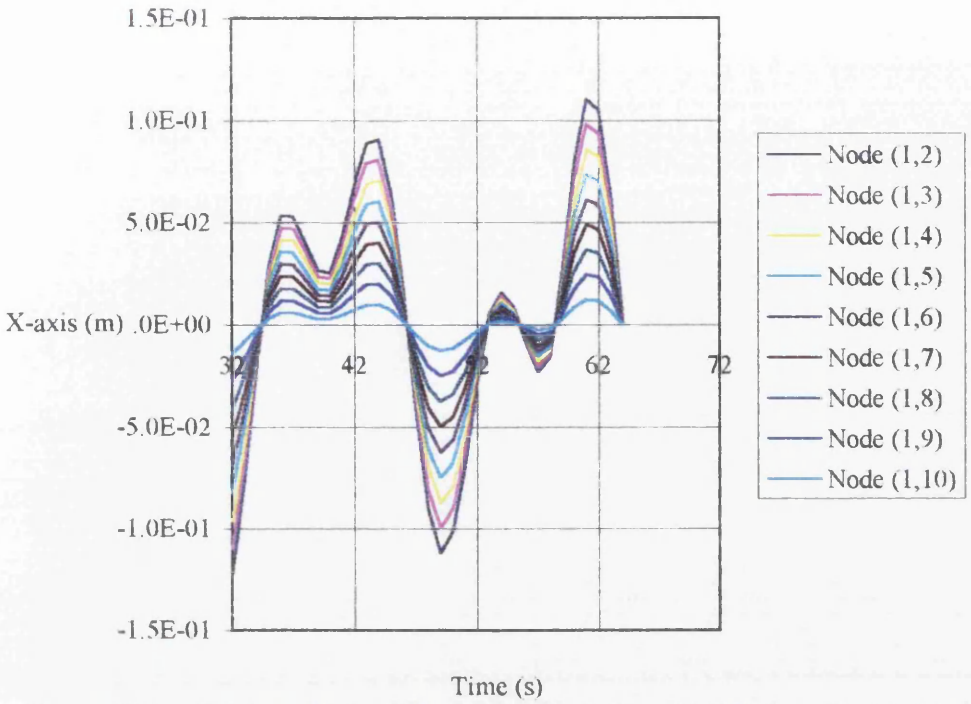

Figure 7.21: Heidrun TLP FWD Port Tether "Bundle" Finite-element Node X-displacement

(Without Tether Fluid Effects, ω =0.7rad/s and ξ_a =1.0m, TIREE)

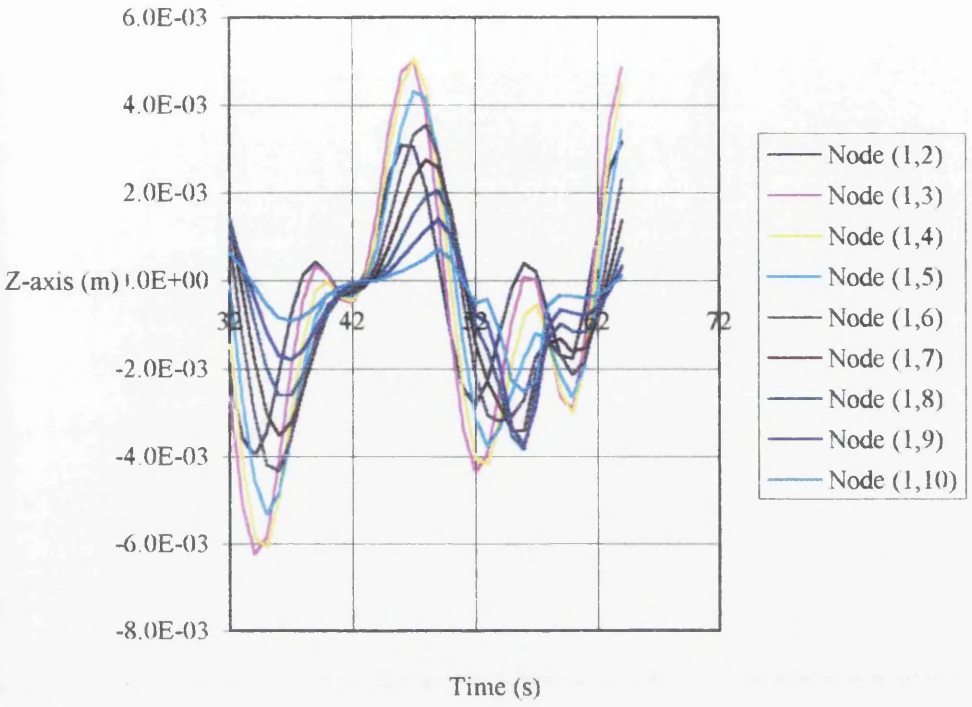

Figure 7.22: Heidrun TLP FWD Port Tether "Bundle" Finite-element Node Z-displacement

(Without Tether Fluid Effects, ω =0.7rad/s and ξ_a =1.0m, TIREE)

Discussion

Inspection of Figures 7.12-7.14 details the effect of local tether fluid loading on the global TLP system response in regular waves.

Good comparison was found between the Phase 2 (TIREE, Figures 7.12-7.14) and Phase 1 (JURA, Figures 7.15-7.17) results which in turn showed good agreement with the selected experimental data. This continuity of agreement serves to partially validate the Phase 2 model against the Phase 1 model (for the exemplary case) which in turn has been validated against the experimental work

Figures 7.18 and 7.19 detail the tether finite-element tensions for the Heidrun TLP system with and without tether fluid effects modeled for a regular incident wave of ω =0.7rad/s and ξ_a =1.0m. By comparison of these curves a slight reduction in the tether tension is observed with the tether fluid effects incorporated for selected elements of the tether assembly. This result is consistent with general overprediction using the Phase 1 software (without tether fluid interaction effects) of the tether tensions compared to the experimentally measured values.

Figures 7.20 and 7.21 detail the tether finite-element node displacement response in the X and Z-axis. These curves are without tether "bundle" fluid effects modeled. Figure 7.22 illustrates the tether response being driven by the TLP response in the absence of tether fluid effects.

Due to the stiff nature of the finite-element system there was poor robustness to the solution of the system of governing 2nd order d.e.s and as a result of this long run times resulted with ultimate solution failure.

These numerical difficulties prevented a large database of Phase 2 prediction data from being generated. Possible mechanisms governing the encountered numerical difficulties are discussed in sections 7.3.4, 7.3.5.

7.3.4 Discussion of Tether Resonance

Tether resonance was not considered as part of this study, but is discussed briefly. The 2No. tether resonance modes excited in the offshore environment are: transverse and longitudinal.

The transverse resonance mode may be excited by vortex induced vibration in regions of high current (possible West of Shetland environment).

Longitudinal resonance could occur during severe storm conditions where steep wave events occur (ringing type response) and also during the pretensioning operations when snatch type response may be induced during the alternating slacking and tensioning of the tethers.

In practice both resonance modes will lead to the development of high tether tensions.

A quantitative measure of the resonance frequencies can be made by the application of equations (7-1), (7-2) and (7-3) derived by Nowacki (1963).

$$\omega_{n(i)} = \frac{\beta_i^2}{L^2}\sqrt{\frac{EI}{\rho}} \qquad \text{(Transverse, without pretension)} \qquad (7\text{-}1)$$

Where,

β_i=roots of the governing differential equation

With for the first 5 modes are:

β_1=3.927, β_2=7.069, β_3=10.210, β_4=13.352 and β_5=16.493

And,

L=lenght of tether

With,

$\sqrt{\frac{E}{\rho}}$ =speed of vibration through the tether

Where,

E =Young's modulus of the tether material

I =Inertia of the tether section

ρ =density of the tether material

With pretension present,

$$\omega_{n(i)} = \sqrt{\frac{i^4\pi^4}{L^4}\frac{EI}{\rho}\left(1-\frac{PT}{\frac{EIi^2\pi^2}{L^2}}\right)} \qquad \text{(Transverse, with pretension)} \quad (7\text{-}2)$$

Where,

PT =pretension (appropriate to tether)

For longitudinal resonance the natural frequency is given by:

$$\omega_{n(i)} = \frac{(2i-1)}{2L}\sqrt{\frac{GL}{2I}} \qquad \text{(Longitudinal)} \quad (7\text{-}3)$$

Where,

G =platform mass (appropriate to tether)

By application of the above equations the 1st natural periods in the transverse and longitudinal modes for the Heidrun Case Study TLP system are: ~41s, ~10s and 0.0001s respectively for the transverse resonance without and with pretension and the longitudinal resonance respectively. The velocity of vibration through the tether material is ~5400m/s.

With reference to the numerical difficulties encountered during the time-domain simulations of the coupled tether/TLP finite-element system (Phase 2, Scheme 1); the time-step was typically of the order of 0.001s, therefore as this is longer than the 1st longitudinal natural period, longitudinal resonance may have contributed to these difficulties.

7.3.5 Numerical Discussion (w.r.t. Solving d.e.s)

The **Phase 1** model behaved well with the d.e. solving algorithm (Runge-Kutta) being fairly robust. Time-steps of the order of 0.1s were used. A form of the program Phase 1 model incorporating the Newmark-β solver algorithm was also developed. This code is unconditionally stable when a β=0.25 is used. Therefore care should be exercised when this code is used as a solution is always returned but may be erroneous.

The **Phase 2** global system consisting of NDOF 2nd order d.e.s was solved at each time-step utilising the ISML solving routine DIVPAG (Microsoft FORTRAN Power Station, ISML Library). Due to the magnitude of the difference between the lateral and vertical/rotation DOF and the foundation translational DOF the problem is inherently a Stiff one. The solver routine DIVPAG is based on the Gear BDF method and is considered to be a robust stiff solver algorithm. The solver behaved reasonably well, however, it was not 'bullet proof' and as such had to be 'tuned'. This 'tuning' took the form of varying the solution tolerance. In addition, the model was very sensitive to the level of damping present. As detailed in Section 7.3.4, longitudinal resonance of the tether system may have contributed to the numerical difficulties associated with the solution of the tether/TLP coupled finite-element system.

7.4 Chapter 5

7.4.1 Introduction

Experimental validation work was conducted in the University of Newcastle Towing Tank. This experimental investigation consisted of testing a 1:281.8 scale model of a Case Study TLP system (Heidrun TLP) at zero/low pretension conditions sampling tether "bundle" force time-series as well as the platform translational displacement time-series (3DOF).

7.4.2 Discussion of Experimental Setup (Response)

A brief review of the experimental setup developed to investigate the tether/TLP response is given below (Ref. Chapter 5 for further details):

Towing Tank

The experimental programme was conducted in the University of Newcastle Towing Tank (40x3.75x1.25m). The Towing Tank is equipped with a *Seasim* Rolling Seal Absorbing Wavemaker at one end with a passive beach at the other.

Model

The geometry tested was a scale model of Heidrun TLP (1:281.8) constructed from PVC.

Prior to the experimental runs the natural periods of the model setup were established for the installed[1] case. These were determined by decay tests performed on the installed model setup in all 6DOF and are as follows:

[1] Model installed pretension was greater than Heidrun installed (96.593×10^6N compared to 90.75×10^6N).

DOF	Model (Prototype Scale)	Heidrun[2]
Surge	107.1s	131s
Sway	112.5s	131s
Heave	1s	2.97s
Roll	2.1s	3.38s
Pitch	1.7s	3.28s
Yaw	31.9s	-

Table 7.1: Natural Period Data

Instrumentation

Quantitative experimental data was sampled at 50 samples/second for 20 seconds via:

1) 2No. *Novatech* F225 25Kg submersible loadcells (tether "bundle" force time-series).

2) *Selspot* optical/electronic displacement measuring system (TLP translational displacement time-series, 3DOF).

3) 2No. "resistance type" wave probes (Incident and Dynamic (encounter) wave elevation time-series).

The sampled data was transferred via a radio link to the data acquisition PC.

Qualitative experimental data consisting of underwater video footage of the tether/tether-hull node behaviour was recorded with the aid of a submersible *Elmo* CCD camera and VCR.

[2] Source: Norwegian Contractors.

Discussion of Response Measurements

An experimental investigation into the coupled tether/TLP response at low pretension has been successfully completed. The experimental data was been utilised to perform validation studies on the Phase 1 simulation software developed under the BP-EPSRC Case Studentship. Comparisons have been made between the experimental and simulation data for installed and zero pretension conditions (Ref. Chapter 5).

For the head sea condition (installed) the Phase 1 software simulation yields a maximum FWD Port Tether "Bundle" axial tension of 6.18×10^7N and a minimum of 1.799×10^6N for an incident regular wave of $\omega = 0.32$rad/s and $\xi_a = 14.09$m. These wave parameters were considered to represent an extreme wave event and would include considerable nonlinear effects. The experimentally sampled time-series for the same extreme wave event yield a maximum FWD Port Tether "Bundle" axial tension of 5.652×10^7N and a minimum of 4.541×10^6N. It is considered that this overprediction of the maximum and underprediction of the minimum tensions are a function of tether dynamic effects due to fluid excitation and reaction forces acting on the tether system. During the course of the experimental programme considerable tether dynamics were observed via the CCD underwater video camera; especially at low pretension levels. At low pretension (during a wave cycle) the tether system developed a fluid loading/self weight induced sagging which maintained positive pretension prevented the tethers slacking.

To investigate the sensitivity of the simulation results to the percentage of $C_{cr(Heave)}$ applied a brief parametric study was performed. The results of this indicate that for certain incident wave frequencies the maximum transient axial tensions are dependent of the percentage of $C_{cr(Heave)}$ applied.

Uncertainties, present in the experimental/simulation data comparisons include: scaling effects; damping present and input excitation force/moment phase angle accuracy. The scaling effects will be significant and can only be accurately quantified by further experimental investigation work performed at a larger scale.

An associated difficulty with small scale testing is the effect on the data sampling resolution and repeatability. The data sampling resolution can be adjusted (within limits) to be compatible with the magnitude of the data to be measured, however, this can lead to resolutions smaller than the specification repeatability of the instrumentation components. There are 2No. components of the damping uncertainty: lack of Reynolds Number (R_n) scaling (and associated viscous effects) and structural damping.

The accuracy of the input excitation force/moment phase angle predictions will be important when comparing the maximum tether transient axial tensions (the maximum tension would vary depending on the in-phase and out-of-phase relationship of the excitation heave force and roll/pitch moments).

In summary, an initial validation study has been undertaken for selected simulation/experimental results.

In general, acceptable agreement has been demonstrated between the experimental and simulation data.

7.4.4 Discussion of Model to Prototype Scaling

Model to prototype scaling of the measured data will lead to uncertainties in the following areas:

- Viscous effects
- Sampling resolution errors

The motions and therefore the velocities were not high so it was considered that the lack of Reynold's number scaling was not detrimental to the reliability of experimental data sampled.

Due to the relatively small scale of the TLP system model tested the sampling resolution errors may be significant. Unfortunately there is no reliable method of quantifying this effect other than repeating the testing program at a larger scale.

In addition to the above, it was not possible to scale match the heave, roll and pitch natural periods. This constraint was due to the physical/practical limitations of suitable and manageable tether material (this in turn was due to the Young's modulus of material being constant from prototype to model scale in Froude scaling law). Consideration was given to using low modulus materials, e.g. PVC, etc., however to ensure linearity steel was chosen. With reference to Table 7.1 the heave, roll and pitch natural periods were ~33% of the prototype values.

This was considered acceptable as the objective of the experimental investigation was to validate the numerical prediction made with the prediction tools developed. Therefore, as the appropriate tether system properties were utilised during the numerical prediction simulations, the resulting comparisons would be valid.

The principal effect of this with respect to the model tests conducted will have been to shift the resonance frequencies in heave, roll and pitch further away from the wave frequencies tested. This will have had a beneficial effect on the reliability of the sampled data, as any transient tensions sampled would occur at the tether system natural modes due to the installation transient motion response and not due to incident wave/TLP system resonance.

7.5 Chapter 6

7.5.1 Introduction

The dynamic response of coupled tether/TLP systems during pretensioning operations was investigated in the time-domain (6DOF). Attention focused on determining the maximum tether "bundle" loads during the transient mode between free-floating and under pretension steady-states. 3No. platform geometries (Ref. Chapter 6 for full details) were investigated for industry accepted installation metocean parameters both with and without motion compensation.

AA	
Water Depth	375m
Number of Columns	3
Column Diameter	28m
Column Spacing	85m
Draft	45m
Tether Length	322m
Pretension	196MN
Total Section	$1.55m^2$

Heidrun	
Water Depth	345m
Number of Columns	4
Column Diameter	31m
Column Spacing	80m
Draft	77.3m
Tether Length	268.6m
Pretension	363MN
Total Section	$2.063m^2$

Snorre	
Water Depth	347.5m
Number of Columns	4
Column Diameter	25m
Column Spacing	76m
Draft	37.5m
Tether Length	310m
Pretension	225MN
Total Section	$1.157m^2$

7.5.2 Discussion of Platform Specific Installation Case Study Results

Results generated take the form of time-domain data detailing the TLP motion response (6DOF) and the corresponding tether "bundle" force time-series.

Platform c.g. response in both vertical and horizontal planes have also be generated.

Full time-domain results are detailed in Chapter 6 and Appendix A.

AA

The tether "bundle" force RAOs are given in Figure 7.23. These RAOs are derived for the pretensioning operation up to $\frac{1}{4}$ of full pretension (16.333MN). These results are calculated with 2% C_c (installed) applied in the heave, roll and pitch modes.

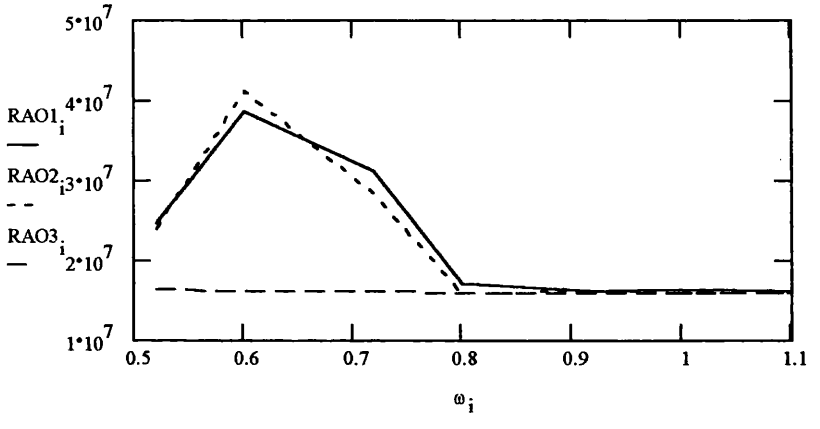

Figure 7.23: AA TLP Tether "Bundle" RAOs (N/m)

It is acknowledged that the tether "bundle" installation transient response is nonlinear and therefore the above spectra approach is not strictly valid, however as the installation sea-states are low, with wave amplitudes rarely above 1-1.5m, it is considered that the above approach will yield acceptable accuracy.

Figures 7.24 and 7.25 detail an example tether "bundle" force time-series without and with motion compensation respectively:

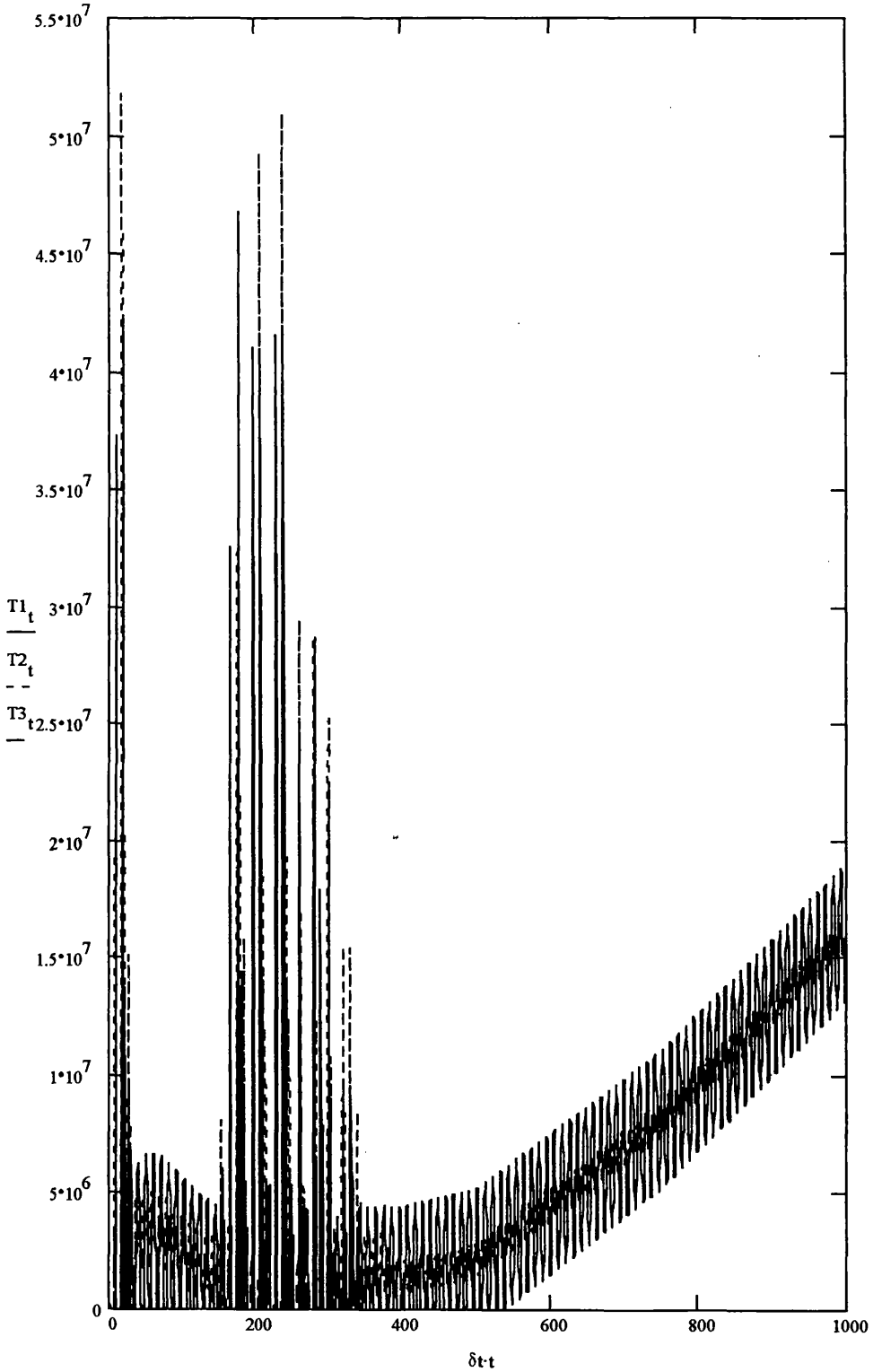

Figure 7.24: AA TLP Tether "Bundle" Force Time-series (N), ξ_a =1.25m, ω =0.6rad/s

(Without Motion Compensation)

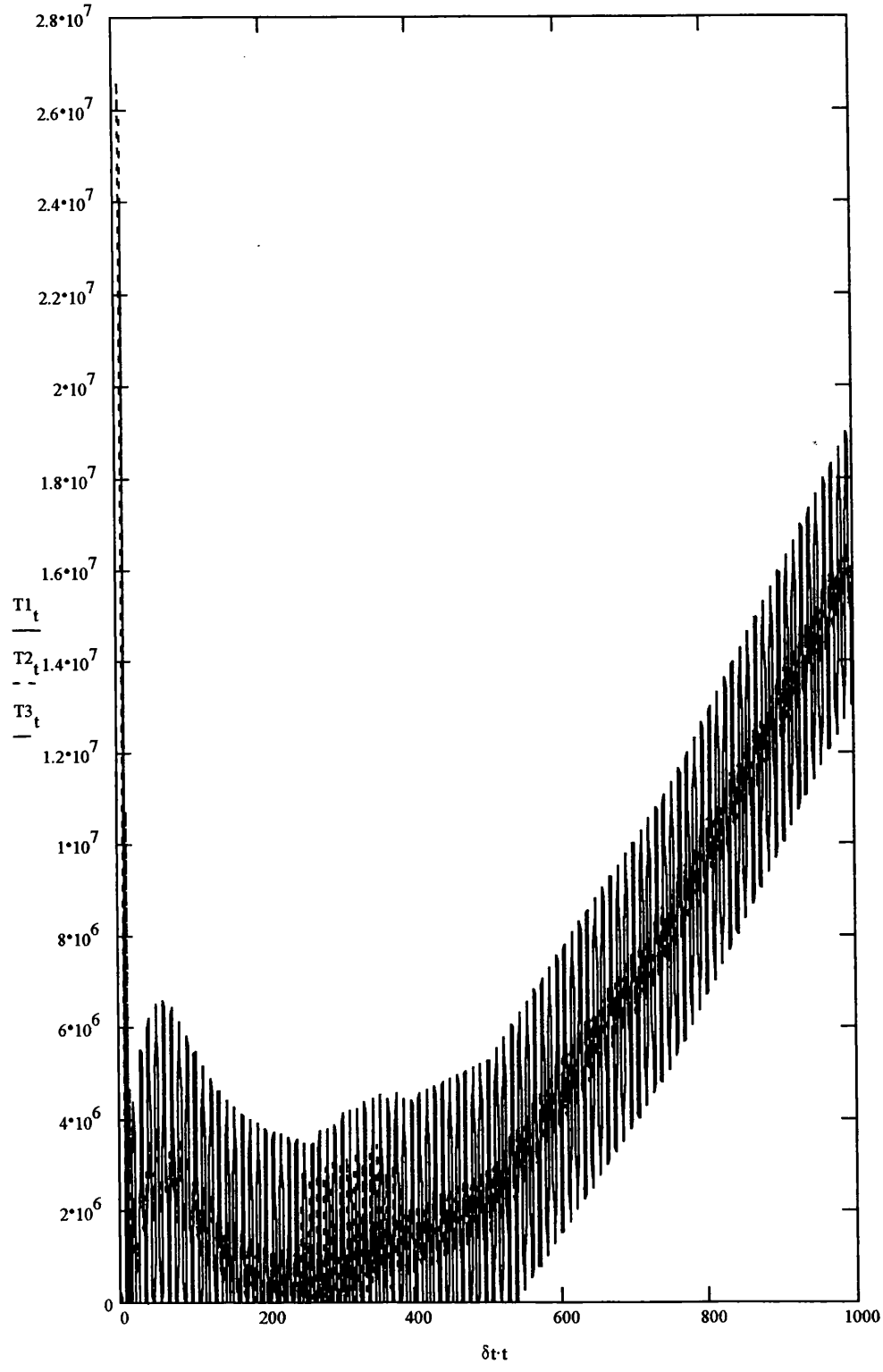

Figure 7.25: AA TLP Tether "Bundle" Force Time-series (N), ξ_a =1.25m, ω =0.6rad/s

(With Motion Compensation)

Figure 7.26 shows the tether "bundle" force time-series with 1% C_c applied to the Heave, Roll and Pitch modes:

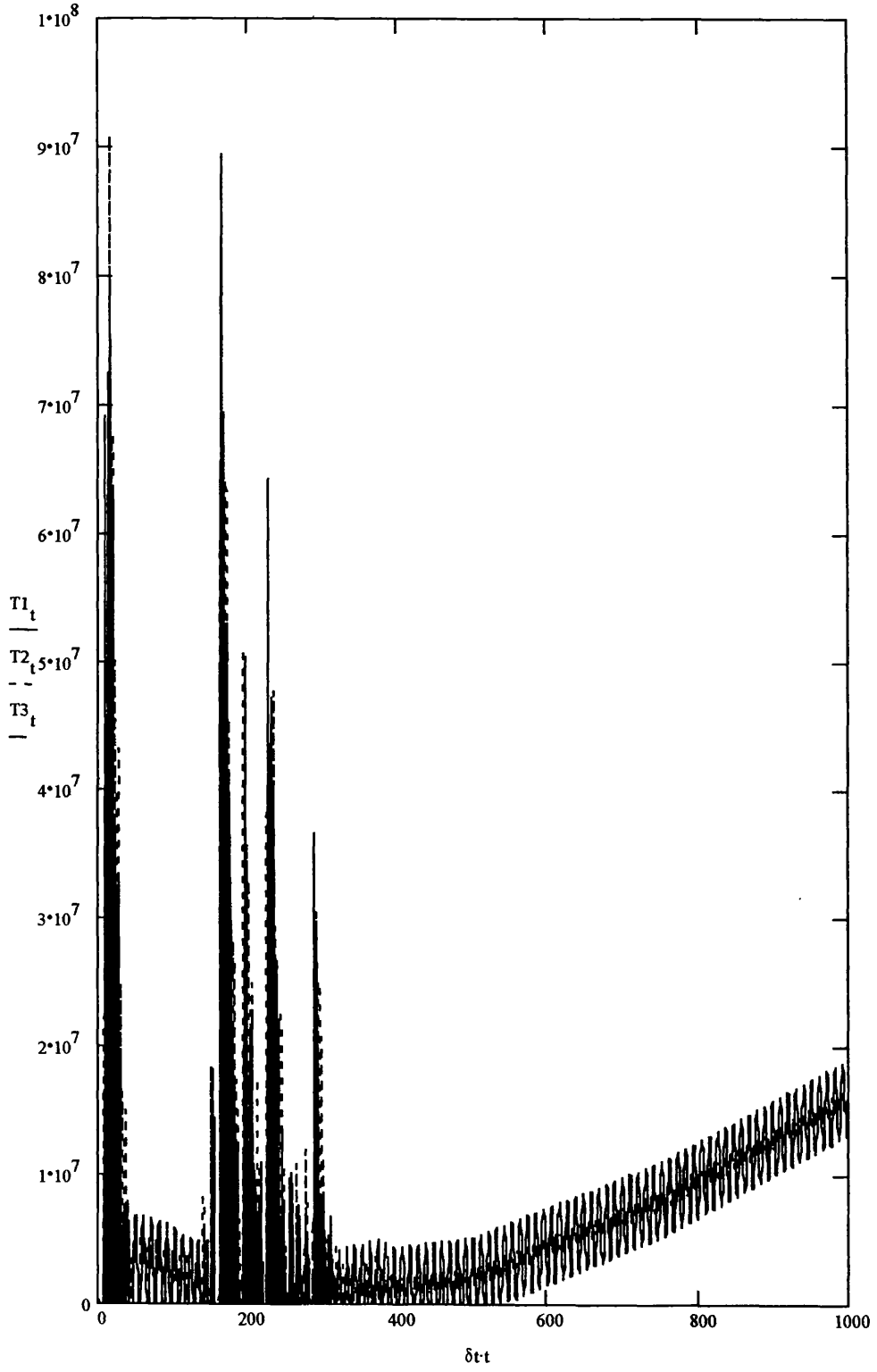

Figure 7.26: AA TLP Tether "Bundle" Force Time-series (N), ξ_a =1.25m, ω =0.6rad/s

(1% C_c Heave, Roll and Pitch, Without Motion Compensation)

The tether "bundle" force time-series for the installed extreme event case are given in Figure 7.27. For the installed simulations the only damping modeled is potential damping. This is considered slightly conservative but due to low platform motions will yield a result of sufficient accuracy (viscous effects being low):

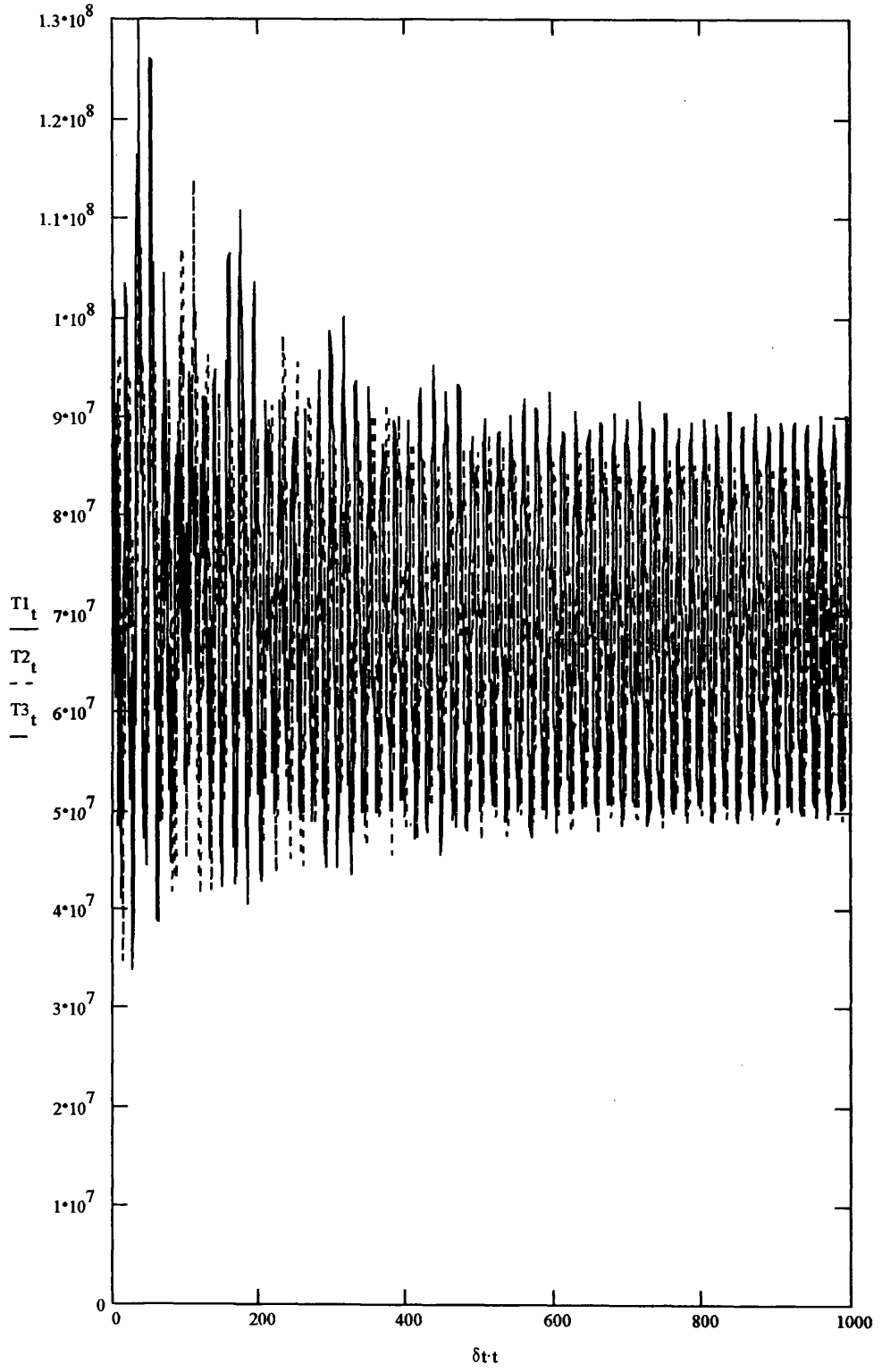

Figure 7.27: AA TLP Tether "Bundle" Force Time-series (N), ξ_a=9m, ω=0.36rad/s

(Installed)

All time-domain results exhibit initial startup numerical transients due to the nature of the initial-value problem. These should be ignored as they do not represent any physical process. This can be illustrated by considering the Pitch displacement time-series corresponding to Figure 7.28:

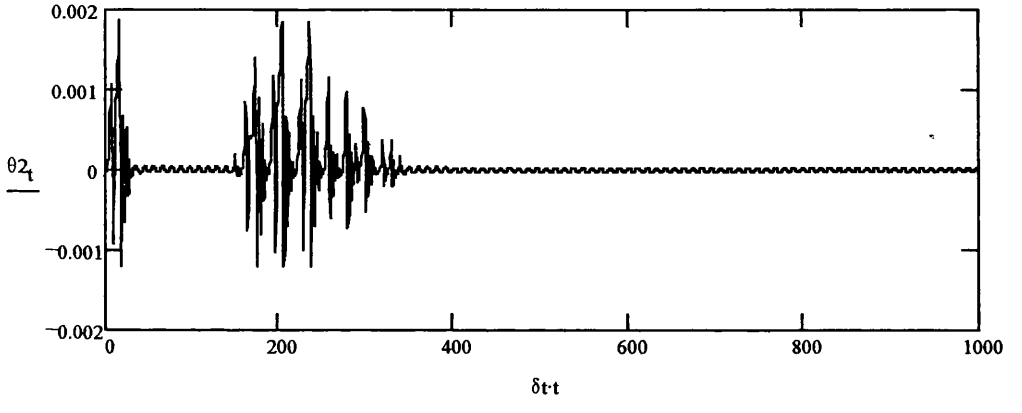

Figure 7.28: AA TLP Pitch Displacement Time-series (rad), ξ_a=1.25m, ω=0.6rad/s

(Without Motion Compensation)

By inspection between 0s and 20s there exists Pitch displacements which are due to numerical startup transients, after this the TLP response is a steady-state wave frequency response. The next period of transient response represents a physical process occurring as the deballasting process takes place. During this stage the tether "bundles" undergo an alternating tensioning and slacking process as the TLP responds in the 6DOF to the time dependent deballasting heave force.

To investigate the sensitivity of the tether "bundle" loading to initial TLP hydrostatic stability, simulations were generated for an initial $\overline{GML}$ and $\overline{GMT}$ of 1m. Figure 7.29 details the tether "bundle" force time-series for this simulation:

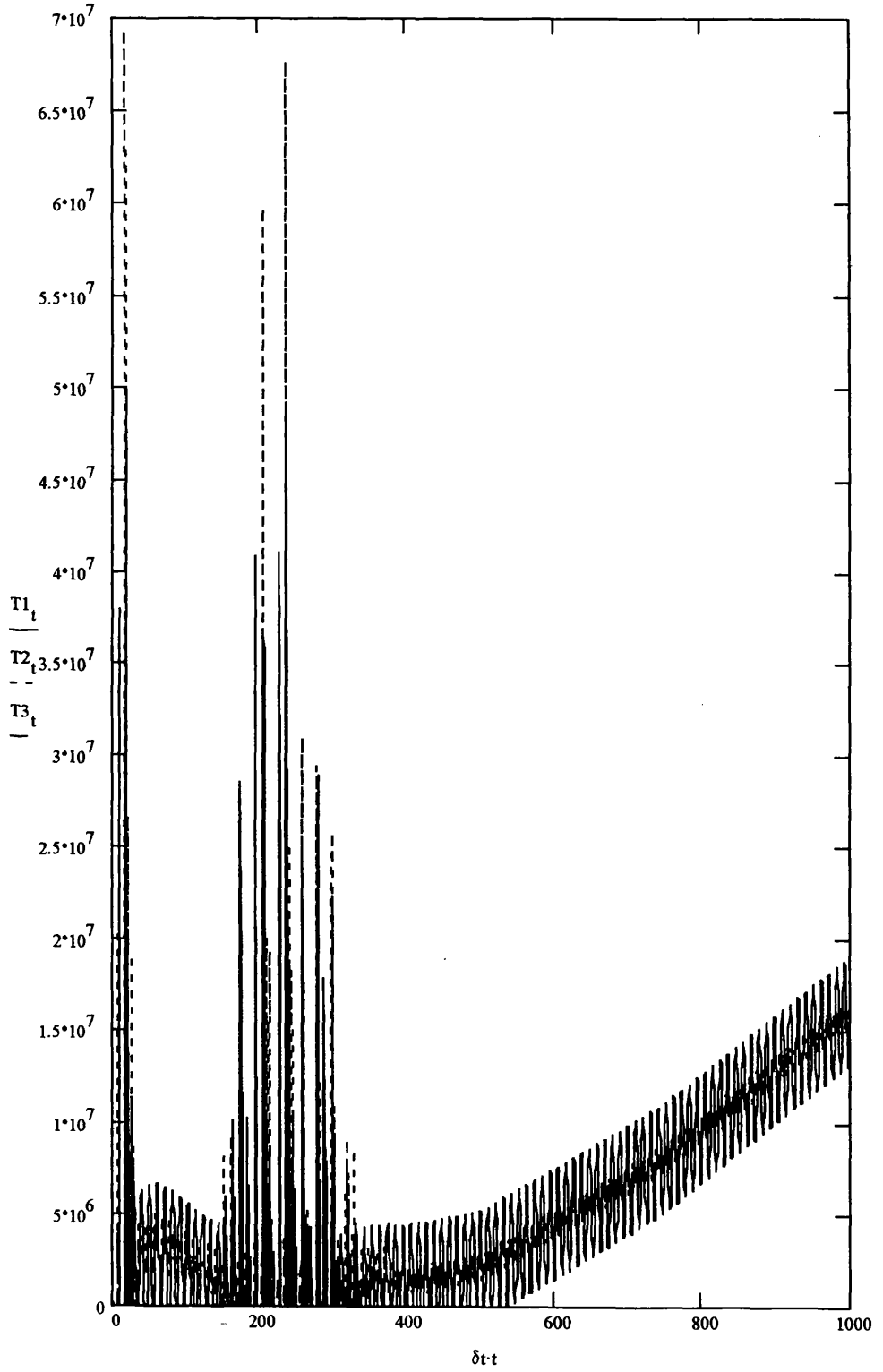

Figure 7.29: AA TLP Tether "Bundle" Force Time-series (N), ξ_a =1.25m, ω =0.6rad/s

(Without Motion Compensation, $\overline{GML}$ and $\overline{GMT}$=1m)

Heidrun

Results were derived for Heidrun for installation with/without motion compensation and the installed case.

Figure 7.30 details the tether "bundle" time-series without motion compensation:

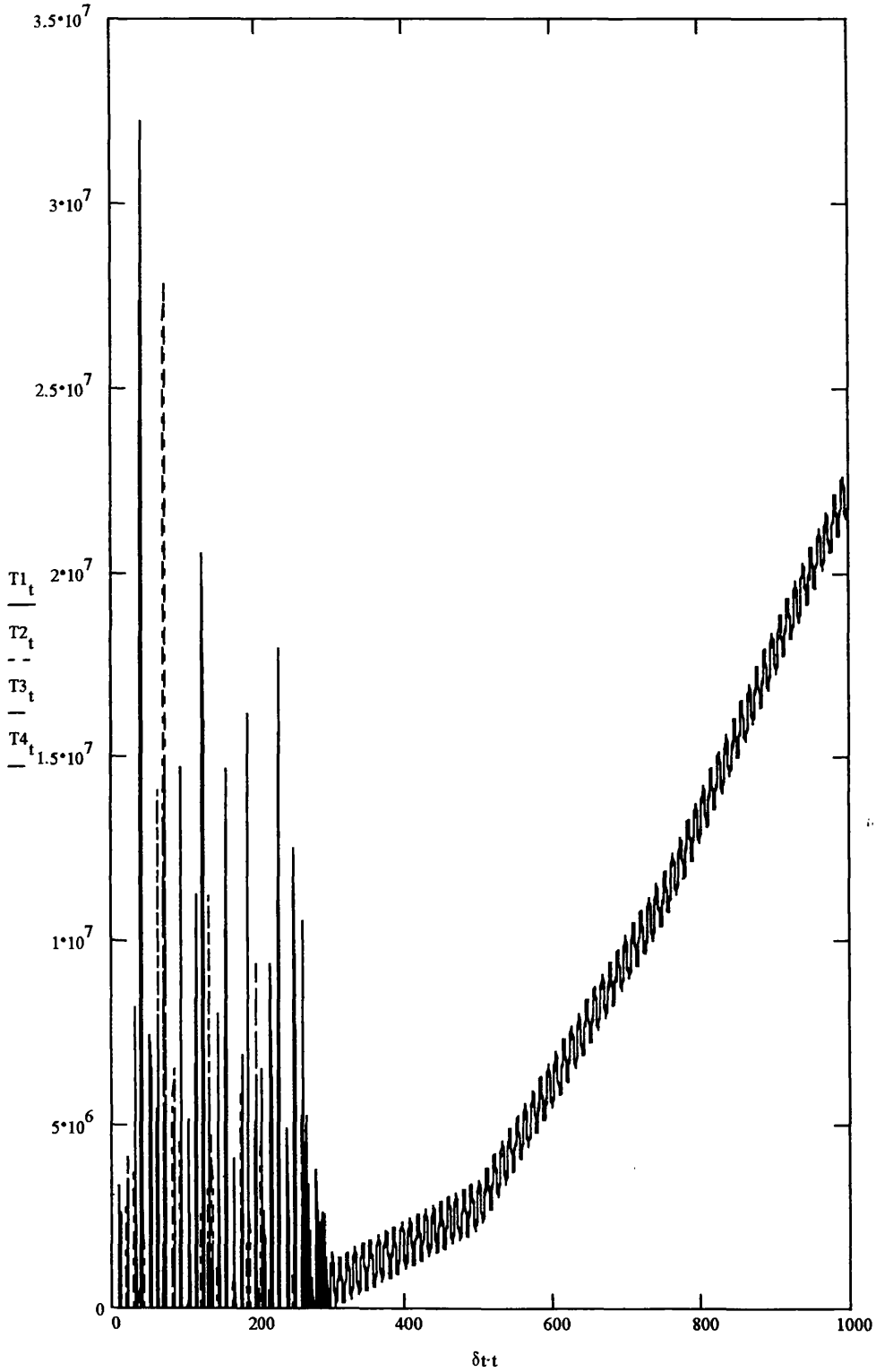

Figure 7.30: Heidrun TLP Tether "Bundle" Force Time-series (N)

(ξ_a=1.25m, ω=0.6rad/s)

(Without Motion Compensation)

Figure 7.31 details the tether "bundle" force time-series with motion compensation:

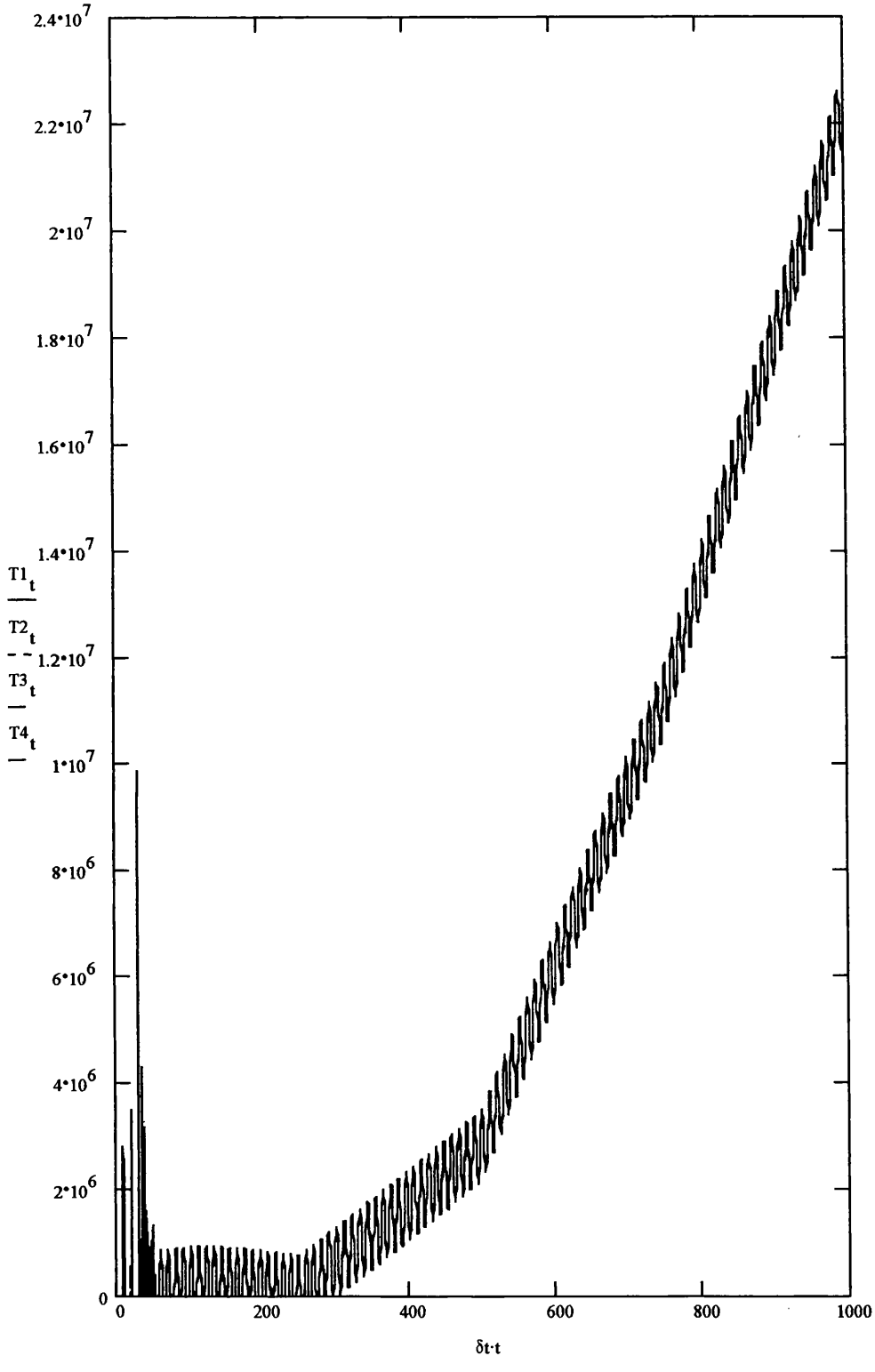

Figure 7.31: Heidrun TLP Tether "Bundle" Force Time-series (N),

(ξ_a =1.25m, ω =0.6rad/s)

(With Motion Compensation)

Snorre

Results were derived for Snorre for installation with/without motion compensation and the installed case.

For installation simulations 1% C_c was applied in Heave, Roll and Pitch modes.

Figures 7.32 and 7.33 detail tether "bundle" force time-series for installation without and with motion compensation respectively.

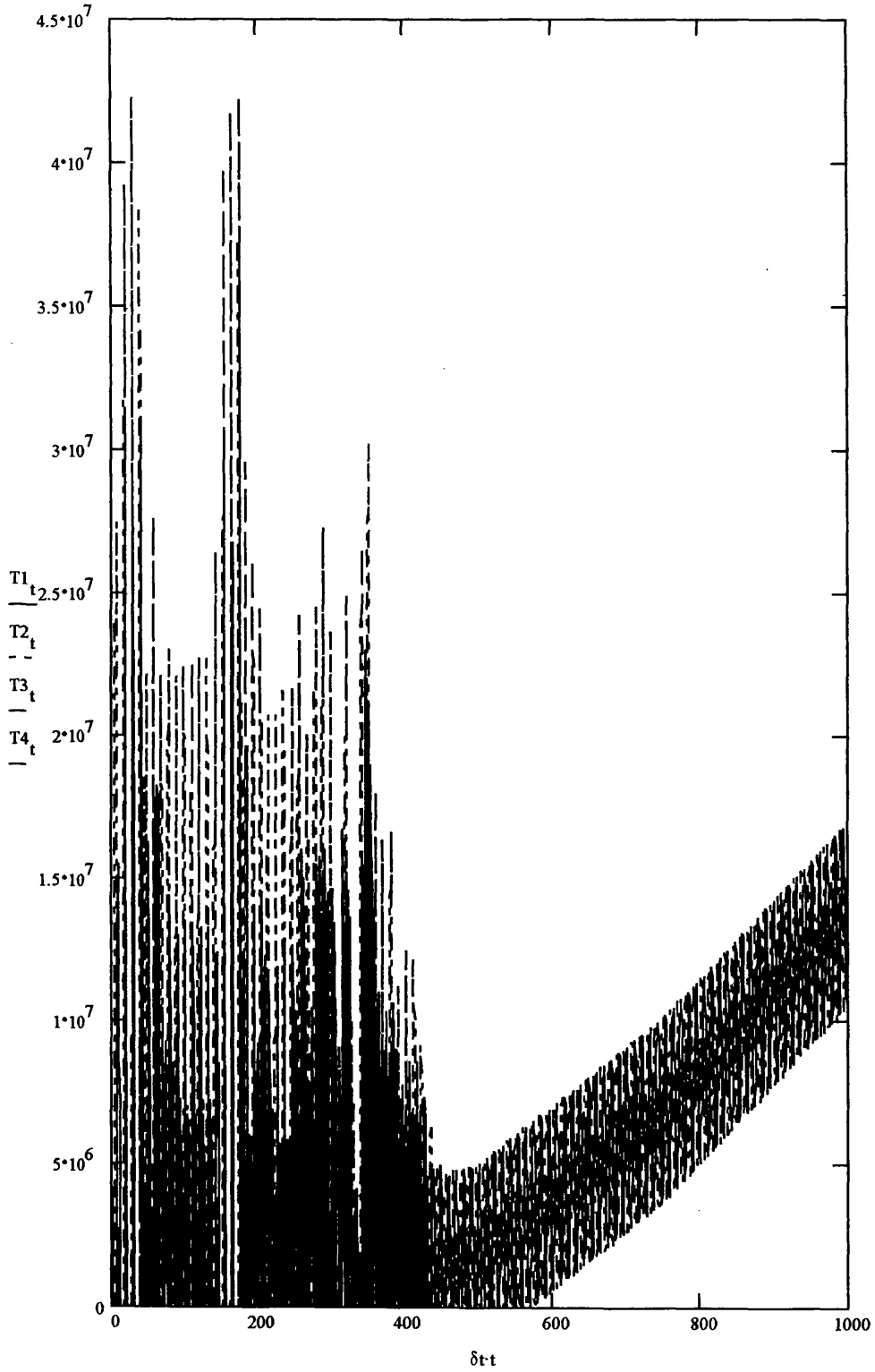

Figure 7.32: Snorre TLP Tether "Bundle" Force Time-series (N), ξ_a =1.25m, ω =0.6rad/s

(Without Motion Compensation)

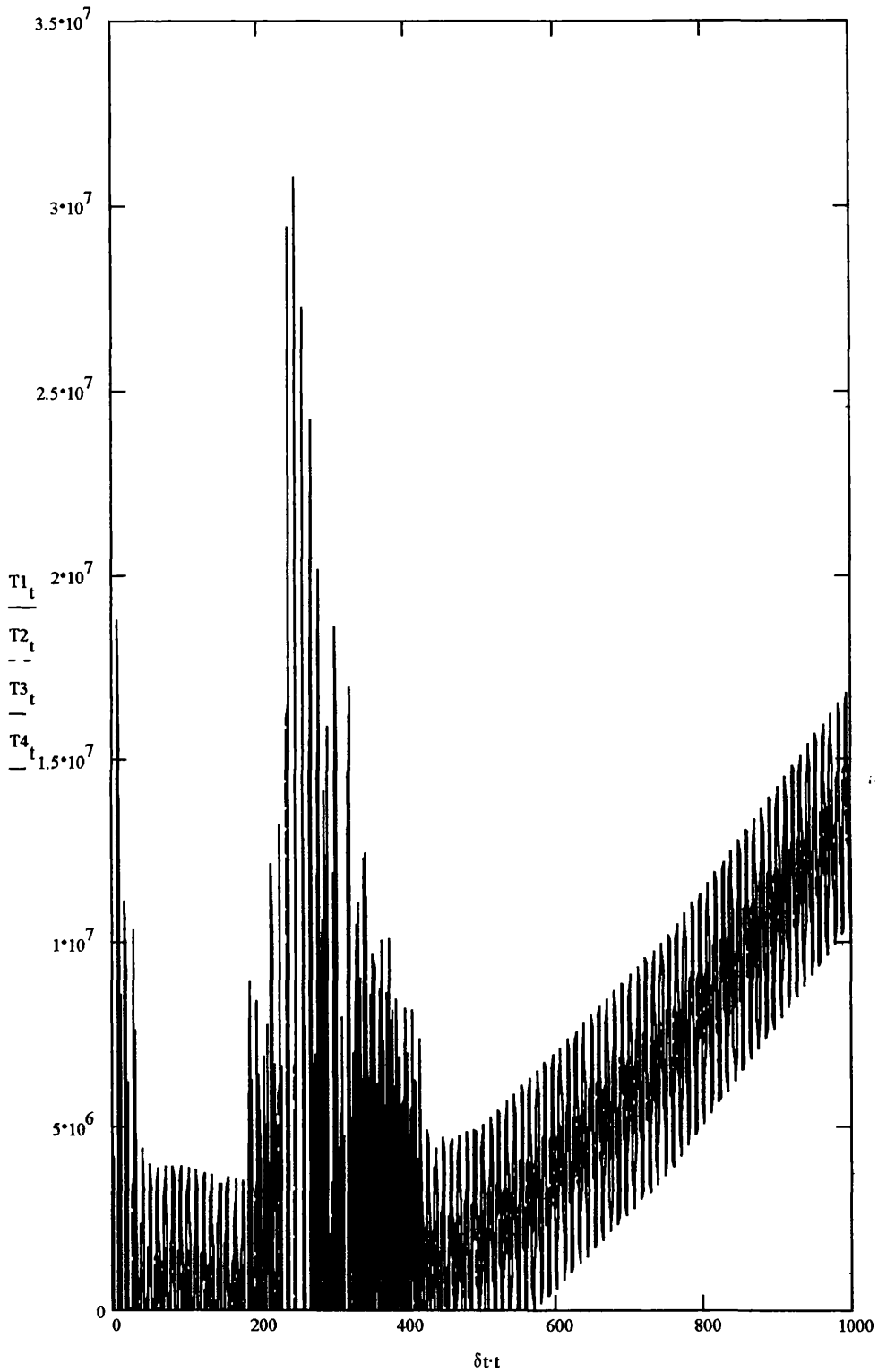

Figure 7.33: Snorre TLP Tether "Bundle" Force Time-series (N), ξ_a =1.25m, ω =0.6rad/s

(With Motion Compensation)

Conclusions

A time-domain simulation method has been developed to investigate the transient response of TLPs during tether pretensioning operations.

Figure 7.23 details the tether "bundle" force RAOs for the AA TLP. Clear incident wave frequency sensitivity can be seen, with peak response occurring around 0.6rad/s for "bundles" (1) and (2).

Comparison of Figures 7.24 and 7.25, demonstrate the peak force reduction due to motion compensation systems for the AA TLP configuration.

Comparing Figures 7.24 and 7.26 the significance of the level of damping present can be clearly seen. Peak tether "bundle" forces present during the transient stage increase from 51.3MN to 91MN with a reduction of C_c applied in the heave, roll and pitch modes from 2% to 1%.

Figure 7.27 details the installed AA TLP tether "bundle" response for the extreme wave event. Peak tether loads are max.=92.5MN, min.=47.8MN. With the maximum load occurring in tether "bundle" (1) and the minimum in (2).

Comparison of Figure 7.24 and Figure 7.29 reveals the metacentric height sensitivity with peak transient tether "bundle" loads of 51.3MN and 68.4MN.

For Heidrun TLP (Figure 7.30) the peak tether "bundle" forces during the transient stage occur in "bundles" (1) and (4), i.e. the "bundles' parallel to the incident wave direction and therefore providing the pitch restoring. These forces are 32.2MN and 22.5MN respectively. With motion compensation these forces are reduced considerably. The

Heidrun analysis was conducted for a single wave condition of ξ_a =1.25m and ω =0.6rad/s (due to time constraints).

Snorre TLP (Figure 7.32) peak tether "bundle' forces during the transient stage occur in "bundles" (1) and (2) corresponding to 37.5MN and 42.4MN.

At no time during the simulations conducted did the tether "bundle" forces exceeded the assumed ULS value of 200MN for a tether "bundle" consisting of 4No. 1118mm diameter pipes of 38mm wall thickness.

One areas of possible cost savings identified is therefore the reduction/omission of motion compensation systems during TLP pretensioning operations.

7.6 Global Conclusions

A research study was undertaken and successfully completed investigating the dynamic response of TLPs during tether installation.

The research programme consisted of numerical simulation work and experimental validation of prediction methodologies/tools developed.

The main conclusions to be drawn from this research are as follows:

- Snatch type transient loads during lock-off simulations, for the metocean parameters considered, did not exceed static pretension levels.

Tether tensions estimated during time-domain simulations conducted for a range of industry accepted installation wave parameters did not exceed static pretension levels.

These simulation were conducted utilising a rotating axial springs tether system stiffness model.

- Under low pretension wave drift forces result in offset induced pretension which reduces the occurrence of tether snatch loads considerably.

During the experiential investigation significant mean wave drift force induced offset developed in low pretension conditions. This offset created pretension in the tether system and thus reduced the transient tensions measured.

- Under low pretension tether sag develops leading to a softening of the restoring stiffness and an increase in damping.

Via the underwater CCD camera video footage it was observed that the tethers developed a catenary form of sagging at low pretensions. This sagging led to a reduction in the tether transient tensions. The mechanisms underlying this reduction are considered to be:

I. Softening of the longitudinal stiffness due to bowed geometry

II. Increase in damping due to viscous tether damping

It is anticipated that this effect will increase with increasing water depth (i.e. tether lenght)

- Fully coupled tether/TLP system finite-element model produces significant numerical instabilities w.r.t. the differential equation solving algorithm employed. Even with the aid of a Gear stiff solving routine excessive run times and convergence failures were encountered.

A fully coupled tether/TLP system finite-element model was developed. Considerable numerical difficulties were encountered in the solution of the system of 2^{nd} order d.e.s governing the response model in the time-domain. It is considered that these difficulties consisted of:

I. The inherent stiff nature of the system, this being due to the large relative differences between the individual DOF, especially those dependent on the longitudinal stiffness of the tether elements.

II. High frequency resonance responses occurring at the longitudinal natural frequencies of the tether elements. These response would be of the period 0.0001s and lower, which in general would be lower than the integration time-step.

- Numerical simulations utilising a tether restoring stiffness model based on rotating axial springs showed acceptable agreement with experimentally derived data.

A time-domain prediction model was developed which demonstrated acceptable agreement with the experimentally measured data. This methodology consisted of a rotating axial springs representation of the tether system.

- As a design tool the tether restoring stiffness model based on rotating axial springs proved more robust than a fully coupled finite-element model.

During the numerical simulations the Phase 1 (rotating axial springs model of the tether system) proved more robust than the Phase 2 (coupled tether/TLP system finite-element model). This robustness led to lower CPU requirements.

- Higher order forces in the presence of steep waves

Higher order forces were measured during experiments with a TLP model in steep waves. It has been reported (Arnott *et al*, 1997) that wave harmonics develop between the columns of a TLP geometry when tested in steep waves. It is therefore considered that these wave harmonics contribute to these higher order forces. These higher order forces where measured up to 4x the incident wave frequency and may be a component of the mechanism driving ringing type responses in TLP systems.

- Measured hydrodynamic reaction force components were lower in presence of current than those in calm water.

By successive forced oscillation test in calm water and then in current (FWD speed), experimentally derived hydrodynamic reaction forces were found to be lower in presence of current than in calm water. This reduction in the oscillatory loads was accompanied by an increase in the mean values.

7.7 Future Research

During the course of this research study the significance of tether system dynamics on the maximum and minimum tether tensions emerged. With the general increase in water depth of new oil field these effects may prove very significant. Future research should focus on the refinement of a fully coupled tether system/TLP finite element model, allowing tether system dynamics to modeled accurately. This could lead to possible field development savings by: omission of expensive motion compensation system during tether installation/pretensioning operations; reduction of static pretension requirements due to the increased understanding of tether behaviour at low pretension level.

In addition to the above, the underlying mechanisms governing the higher forces measured in steep waves could be further investigated to establish a possible link with TLP ringing response.

7.8 Closure

A research investigation into the dynamic response of TLPs during tether installation has been successfully completed and reported. It is hoped that the research detailed will prove useful to design engineers when selecting methodologies to be utilised when conducting analyses of TLP installation response.

7.9 References

Atkins Quantitative Wave Analysis (AQWA), AQWA (LINE) Users Manual (1997), **WS Atkins**.

Arnott A.D., Greated C.A., Incecik A. and M^{c}Leary A. (1997) An Investigation of Extreme Wave Behaviour Around a Model TLP, **Proceedings of the 7th International Offshore and Polar Engineering Conference OMAE'97**, Vol. 1, pp. 185-192.

Faltinsen O.M. (1990) **Sea Loads on Ships and Offshore Structures**, Cambridge University Press.

Linton C.M. and Evans D.V. (1990) The Interaction of Waves with Arrays of Vertical Circular Cylinders, **Journal of Fluid Mechanics**, Vol. 215, pp. 549-569.

Gear C.W. (1971) The Automatic Integration of Ordinary Differential Equations, **Numerical Mathematics**, Vol. 14, pp. 176-190.

Newmark N.M. (1959) A Method of Computation for Structural Dynamics, **Journal of the Proceedings of the American Society for Structural Dynamics** (Engineering Mechanics Division), Vol. EM3, pp. 67-94.

Nowacki W. (1963) **Dynamics of Elastic Systems**, translated from polish by H. Zorski, Chapman and Hall Ltd..

Paulling J.R. (1977) Time Domain Simulation of Semisubmersible Platform Motion with Application to the Tension-Leg Platform, **The Society of Naval Architects and Marine Engineers**, Proceedings of the Spring Meeting/Star Symposium, pp. 303-314.

Thomson W.T. (1988) **Theory of Vibration**, Unwin Hyman.

APPENDIX A

Figures A.1 - A.17 detail the time-domain simulation results for the AA Case Study TLP for an incident regular wave of ω =0.6rad/s (ξ_a =1m) with a heading angle of 60^0.

Figures A.1 - A.6 detail the surge, sway, heave, roll, pitch and yaw DOF response respectively.

Figure A.7 details the tether 'bundle' tension time-series response.

Figures A.8 - A.17 detail the platform vertical/horizontal and cross-planer response.

TLP Global Dynamic Response in Time-domain (*6DOF*):

(Space-fixed coordinate system)

DISPLACEMENT

Surge

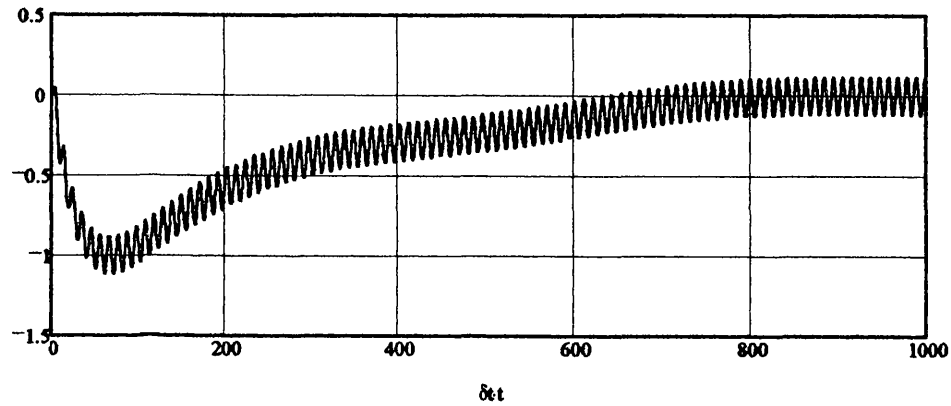

(m)

(s) Figure A.1

Sway

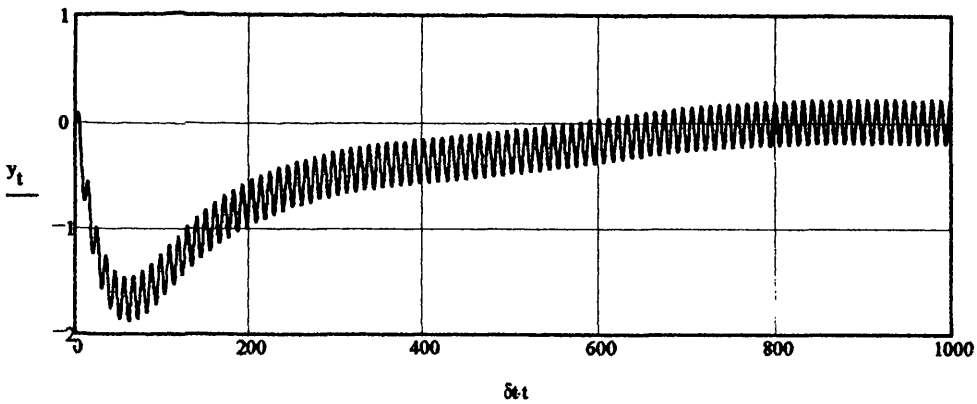

(m)

(s) Figure A.2

Heave

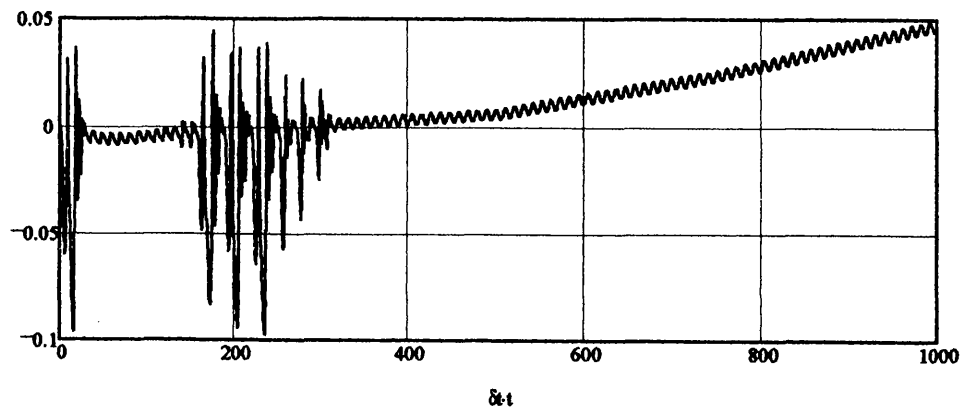

(m)

(s) Figure A.3

Roll

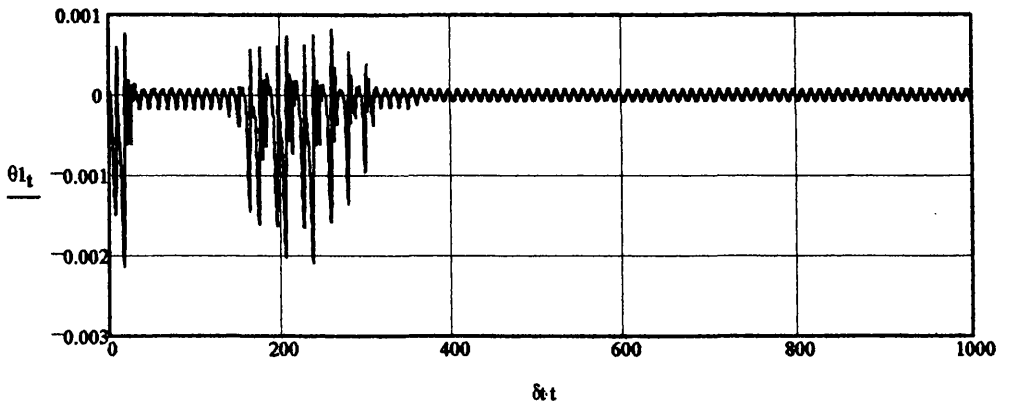

(rad)

Figure A.4

Pitch

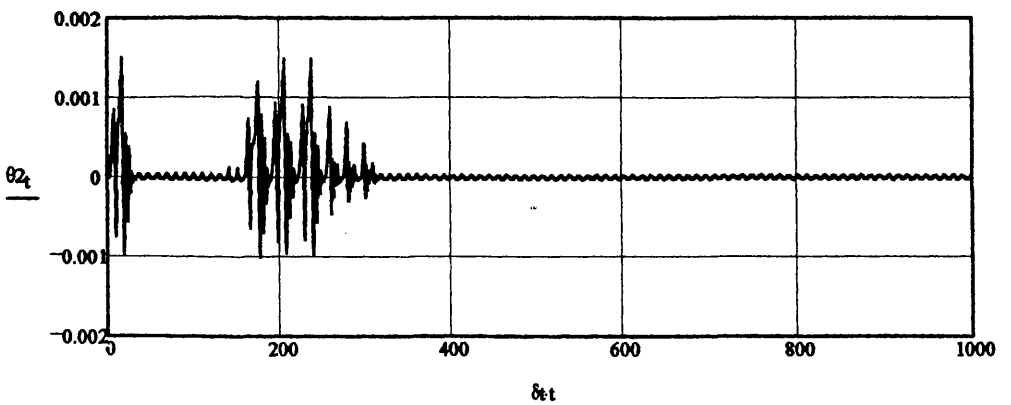

(rad)

Figure A.5

Yaw

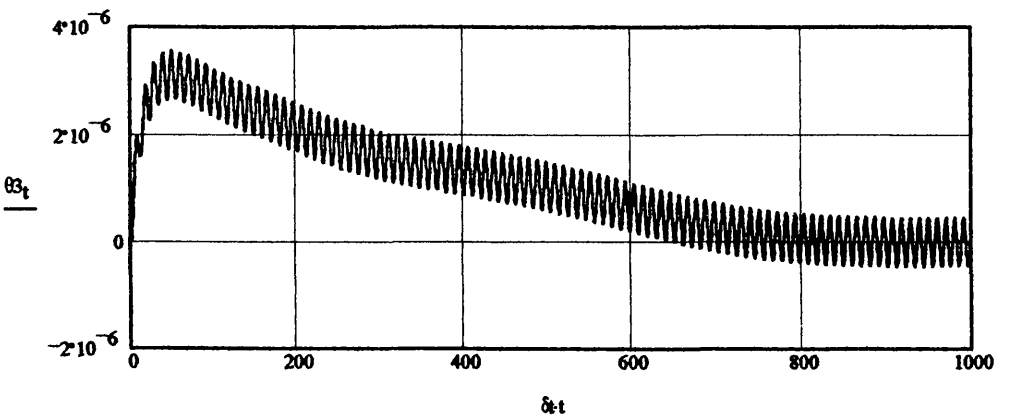

(rad)

Figure A.6

Tether Force Time-series

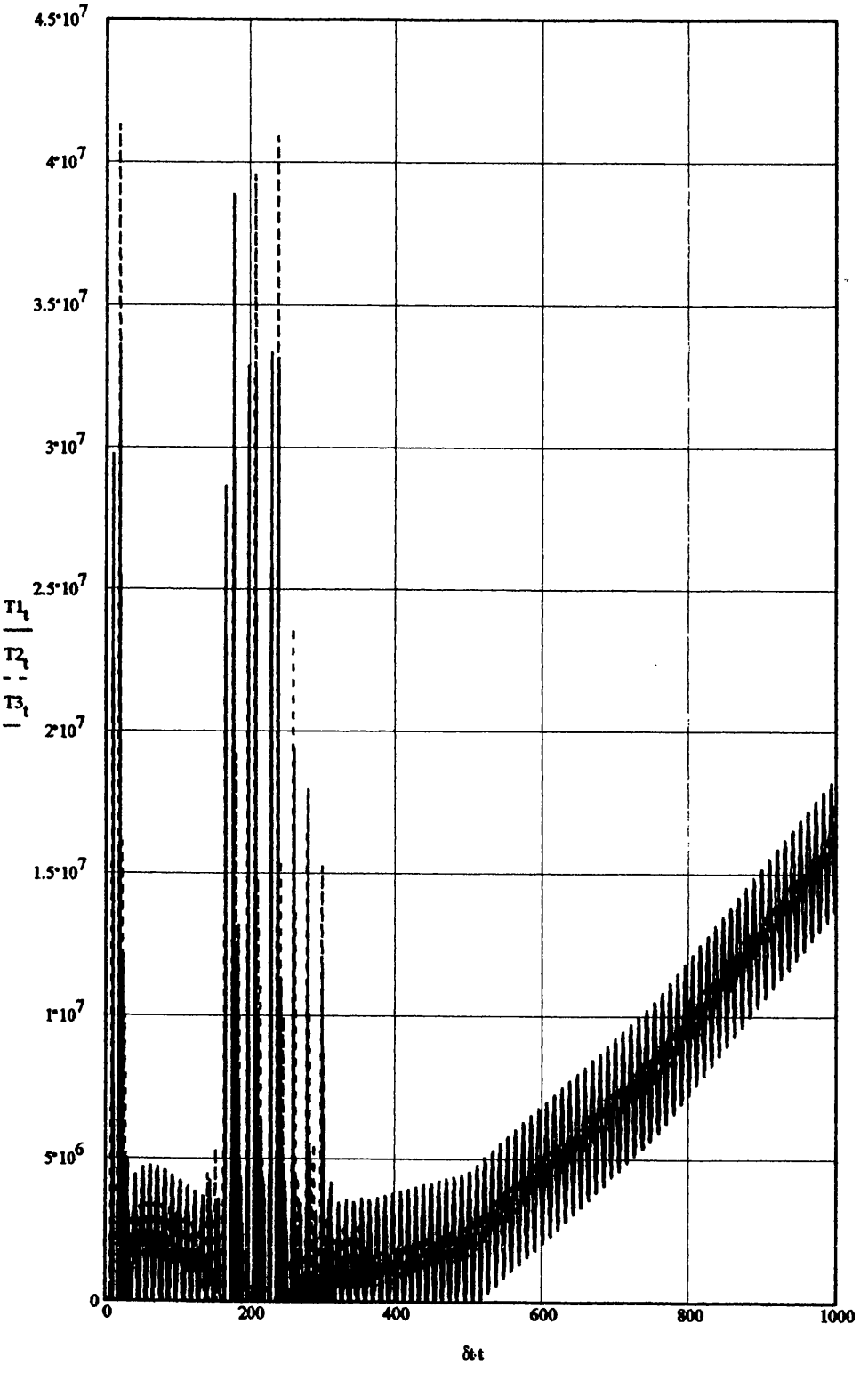

(N)

Figure A-7

2D *TLP* c.g. Motion Response (Heave v Surge)

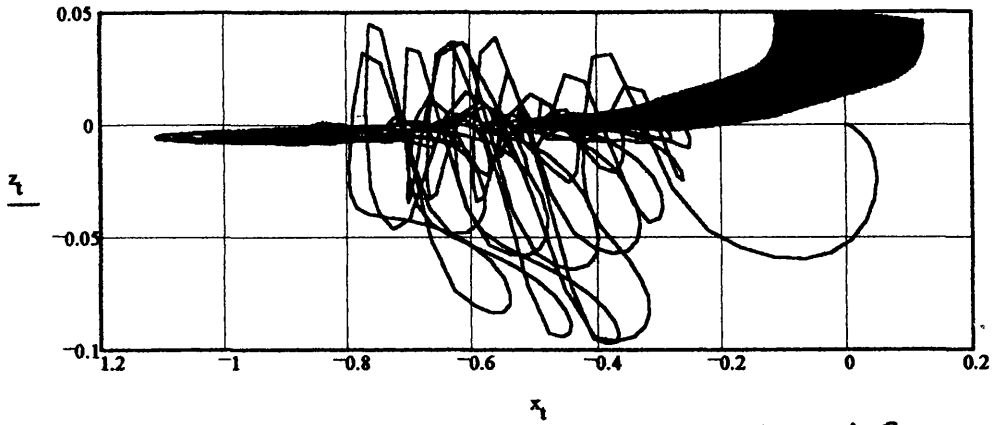

(m)

(m)

Figure A·8

2D *TLP* c.g. Motion Response (Heave v Sway)

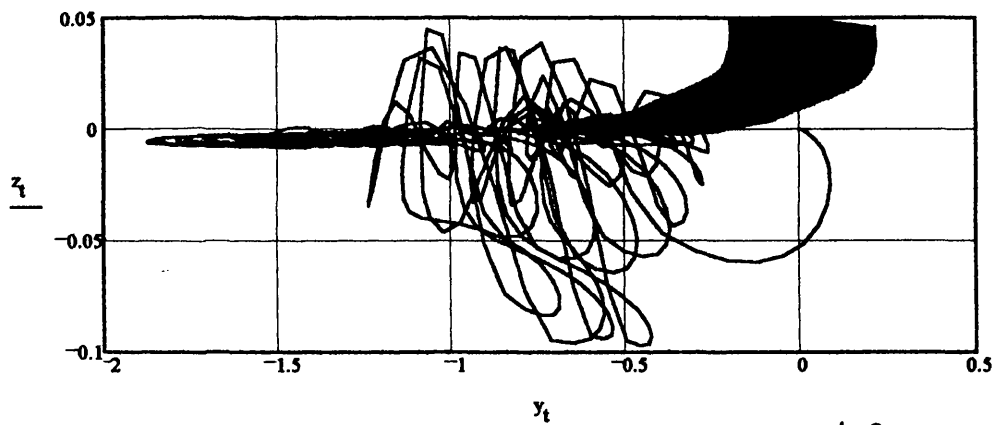

(m)

(m)

Figure A·9

2D *TLP* c.g. Motion Response (Heave v Roll)

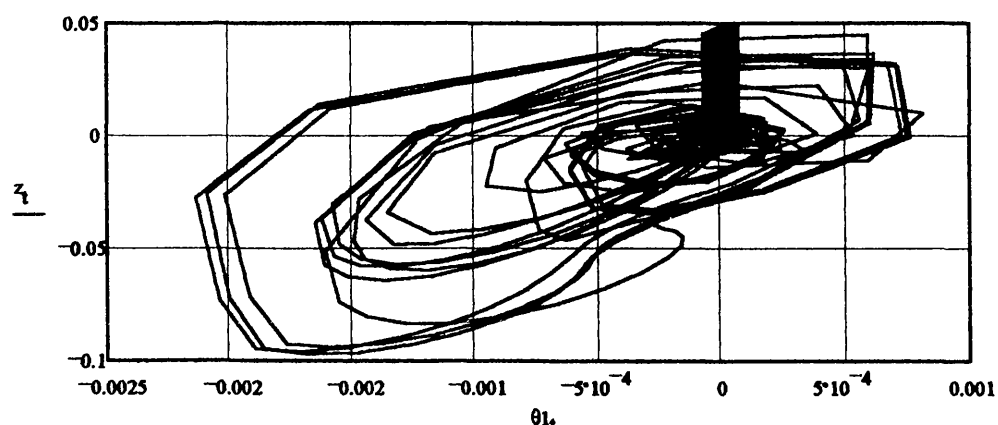

(m)

(rad)

Figure A·10

2D *TLP* c.g. Motion Response (Heave v Pitch)

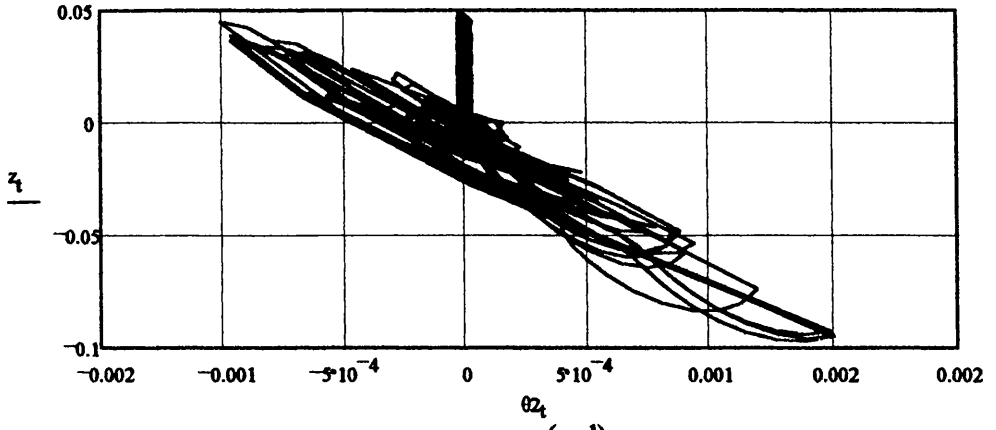

(m)

(rad)

Figure A-11

2D *TLP* c.g. Motion Response (Heave v Yaw)

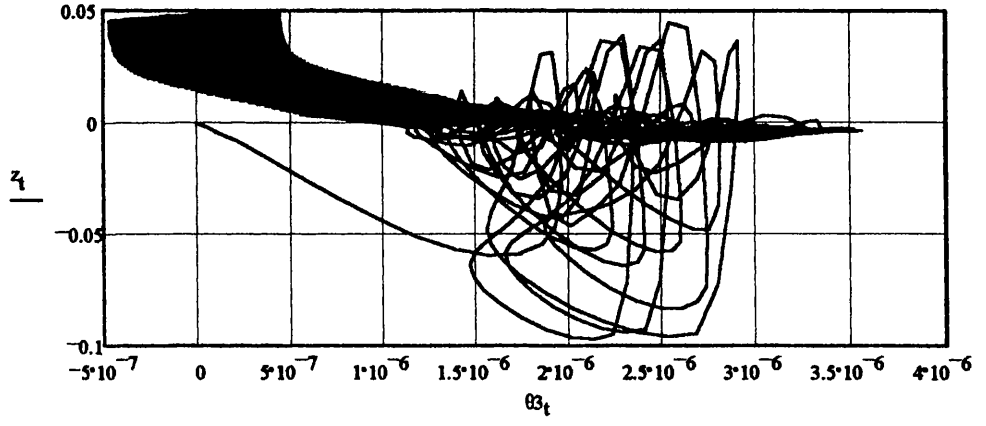

(m)

(rad)

Figure A-12

2D *TLP* c.g. Motion Response (Surge v Sway)

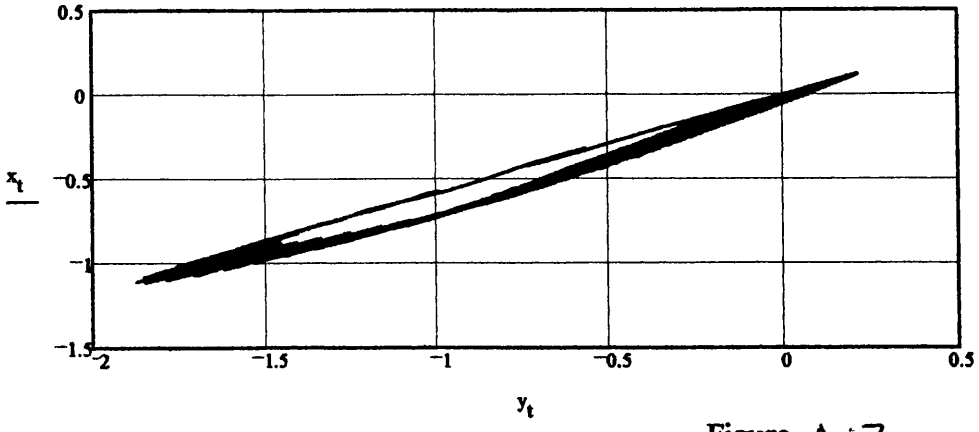

(m)

(m)

Figure A.13

2D *TLP* c.g. Motion Response (Surge v Heave)

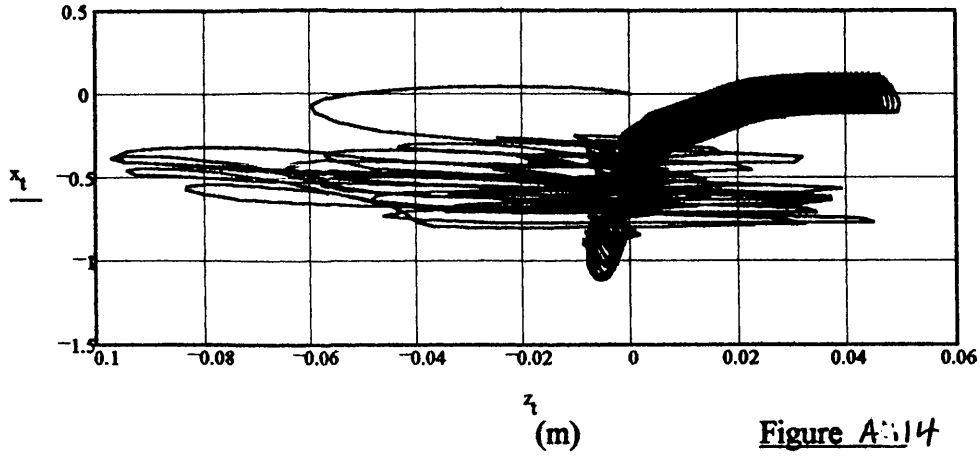

(m)

(m)

Figure A.14

2D *TLP* c.g. Motion Response (Surge v Roll)

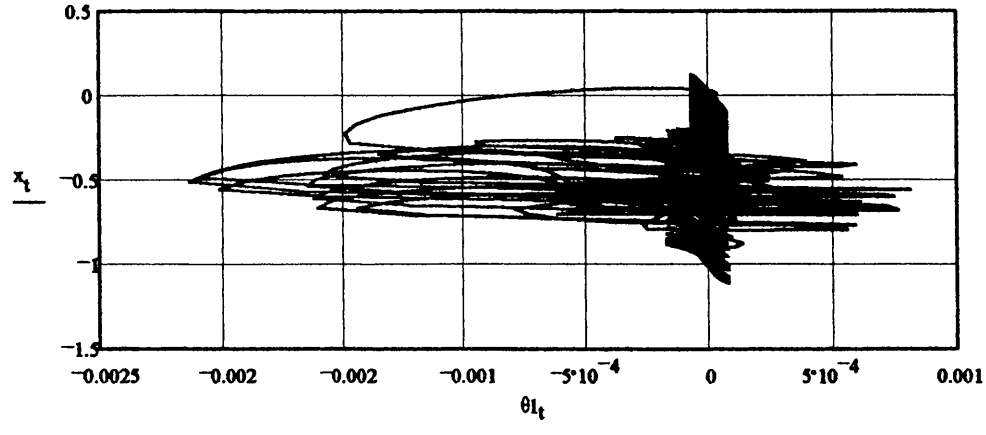

(m)

(rad)

Figure A.15

2D *TLP* c.g. Motion Response (Surge v Pitch)

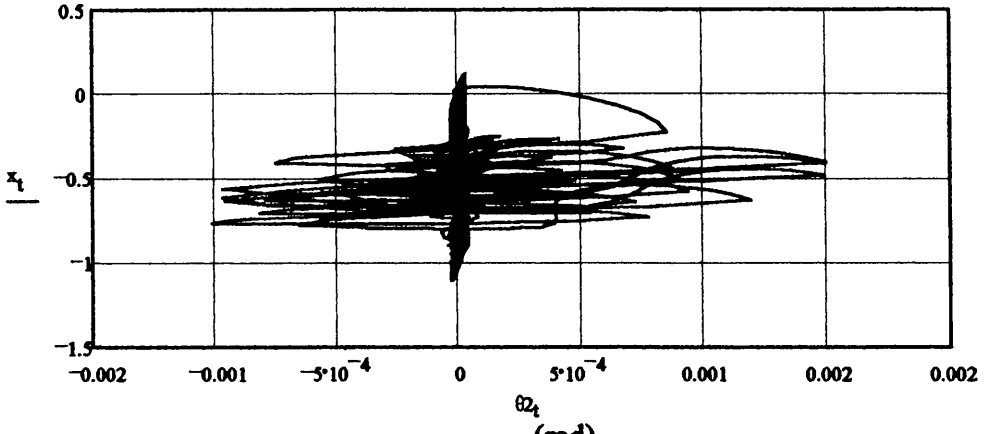

(m)

Figure A.16

2D *TLP* c.g. Motion Response (Surge v Yaw)

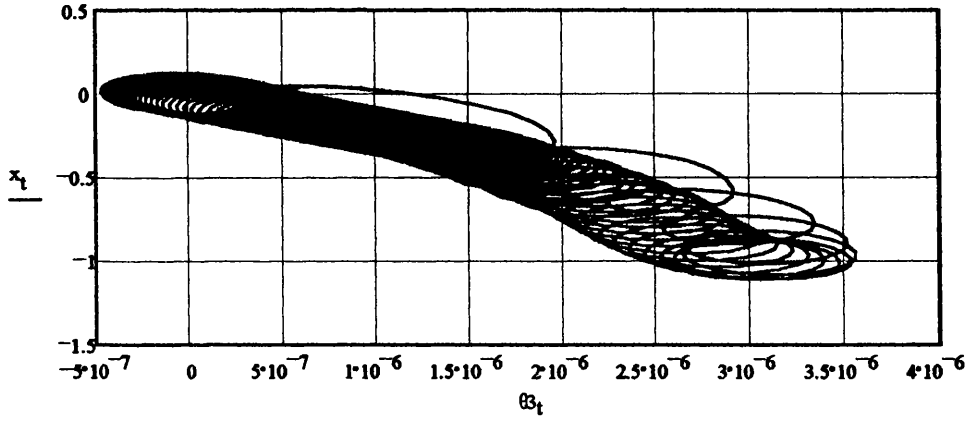

(m)

Figure A.17

Figures A.18-A.34 detail the time-domain simulation results for the AA Case Study TLP for an incident regular wave of ω =0.72rad/s (ξ_a =1m) with a heading angle of 60^0.

Figures A.18-A.23 detail the surge, sway, heave, roll, pitch and yaw DOF response respectively.

Figure A.24 details the tether 'bundle' tension time-series response.

Figures A.25-A.34 detail the platform vertical/horizontal and cross-planer response.

TLP Global Dynamic Response in Time-domain (*6DOF*):

(Space-fixed coordinate system)

DISPLACEMENT

Surge

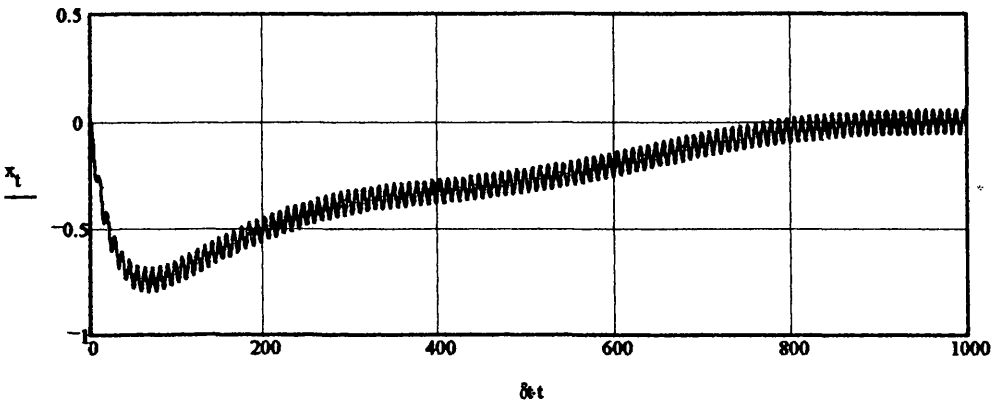

(m)

Figure A.18

Sway

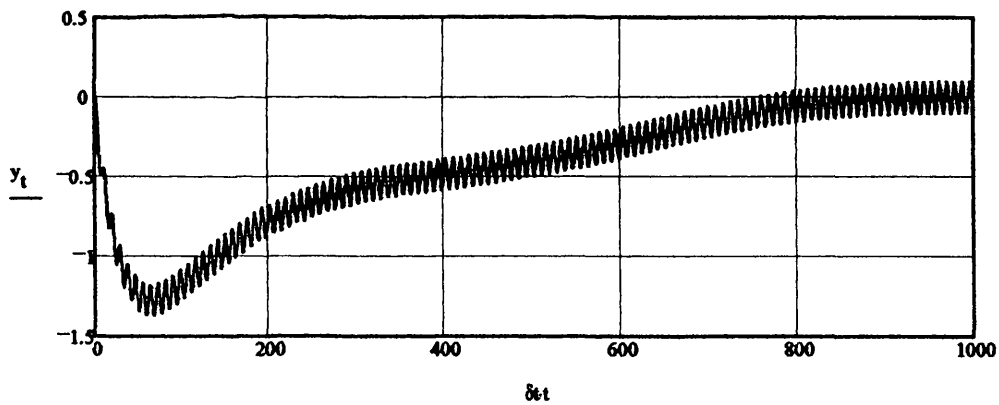

(m)

Figure A.19

Heave

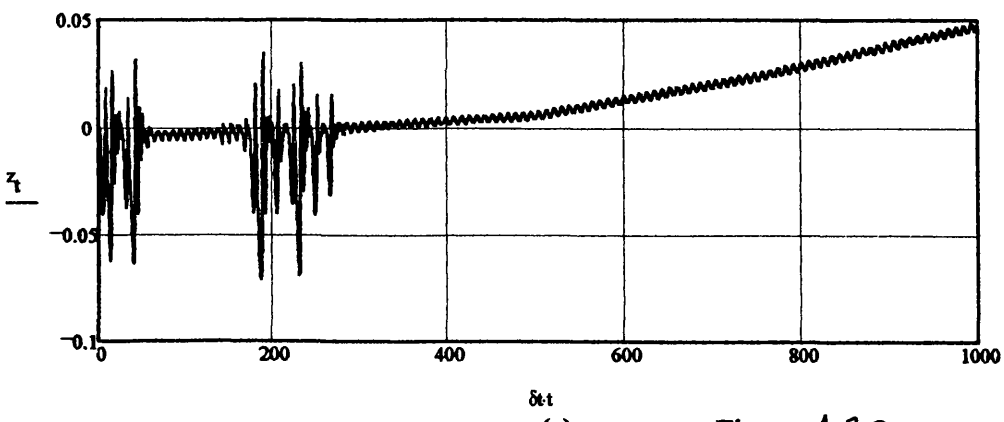

(m)

Figure A.20

Roll

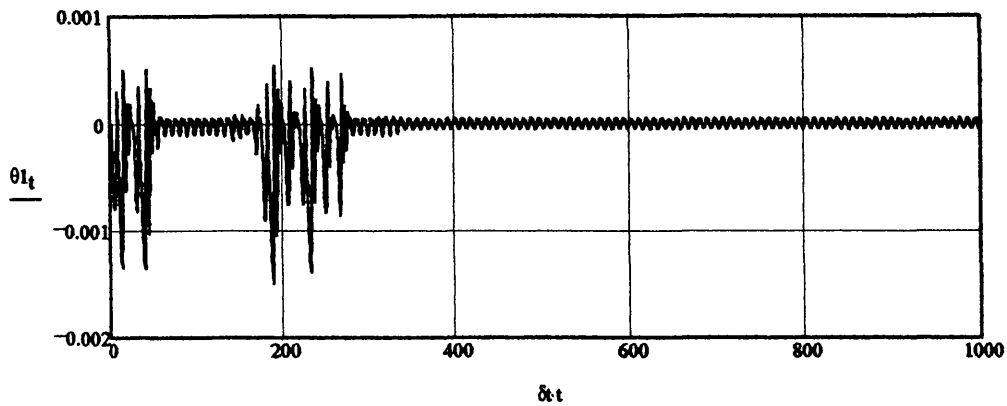

(rad)

(s)

Figure A-21

Pitch

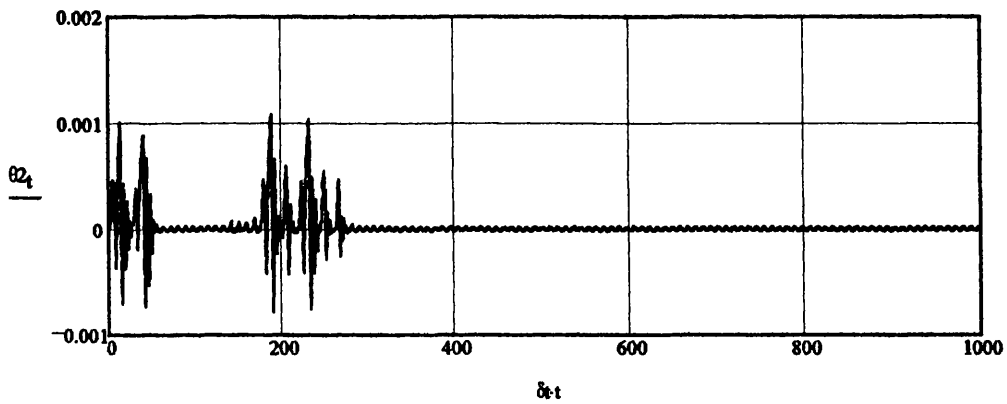

(rad)

(s)

Figure A-22

Yaw

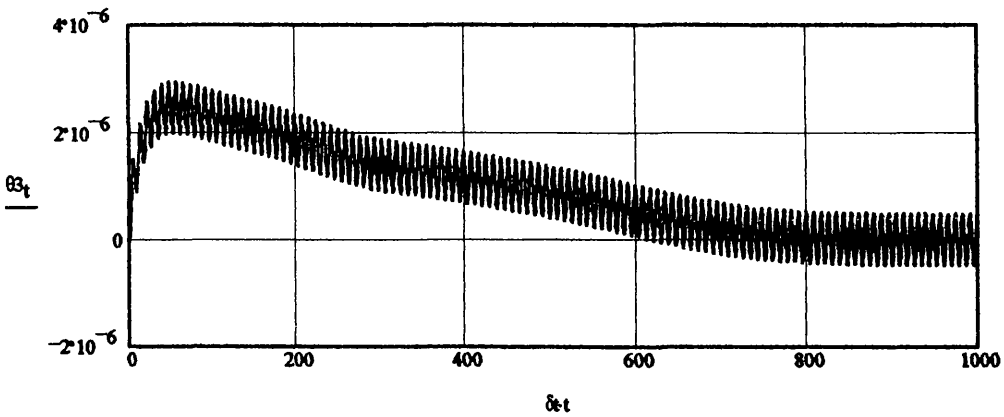

(rad)

(s)

Figure A-23

Tether Force Time-series

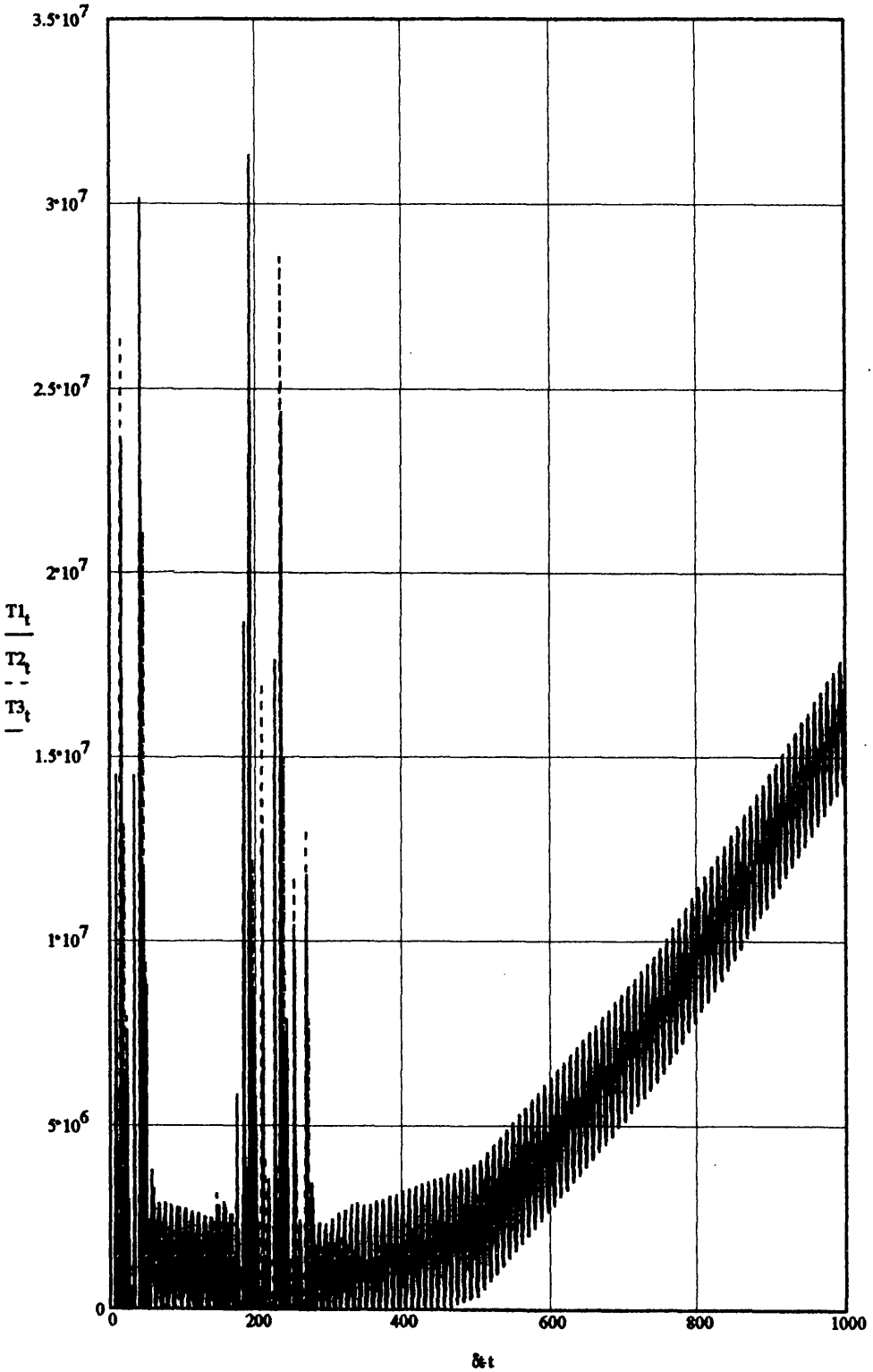

Figure A-24

2D *TLP* c.g. Motion Response (Heave v Surge)

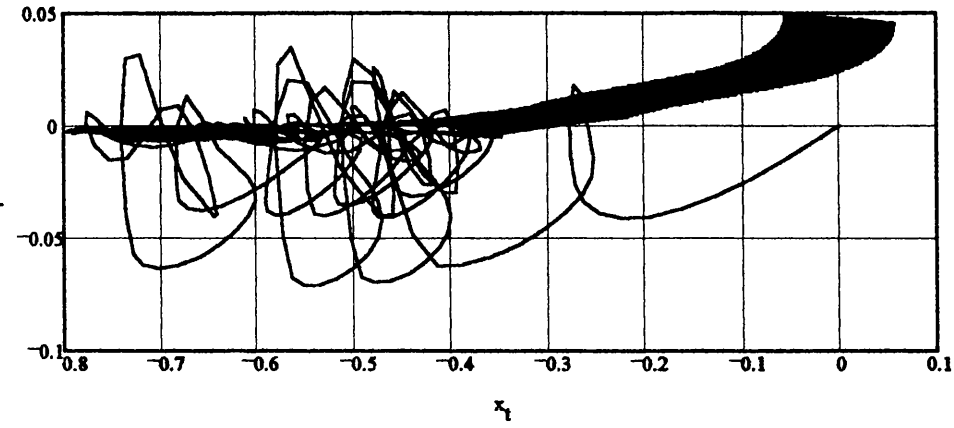

(m)

(m)

Figure A·15

2D *TLP* c.g. Motion Response (Heave v Sway)

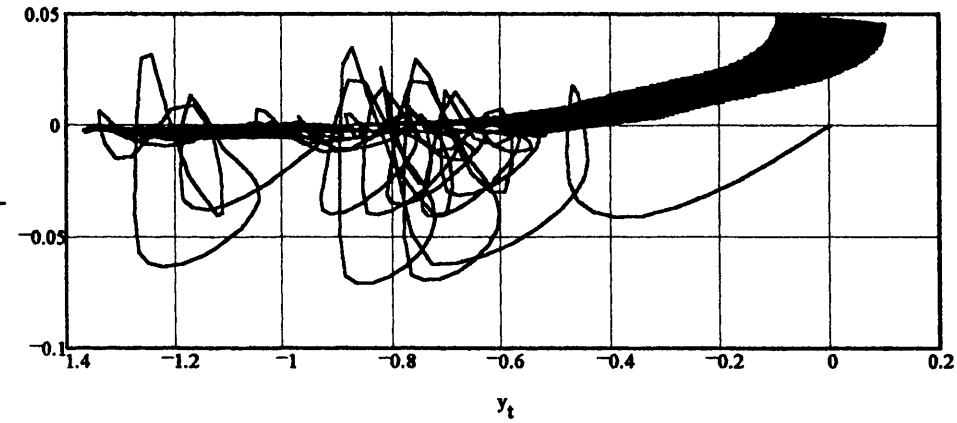

(m)

(m)

Figure A·16

2D *TLP* c.g. Motion Response (Heave v Roll)

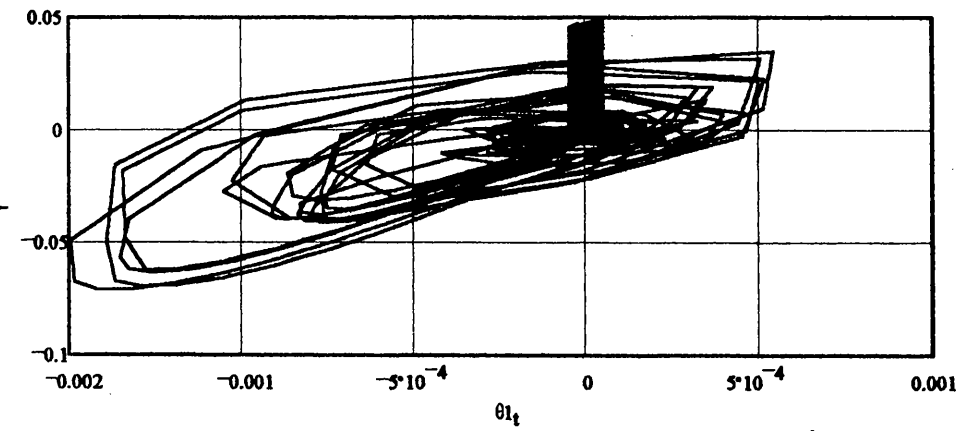

(m)

(rad)

Figure A·17

2D *TLP* c.g. Motion Response (Heave v Pitch)

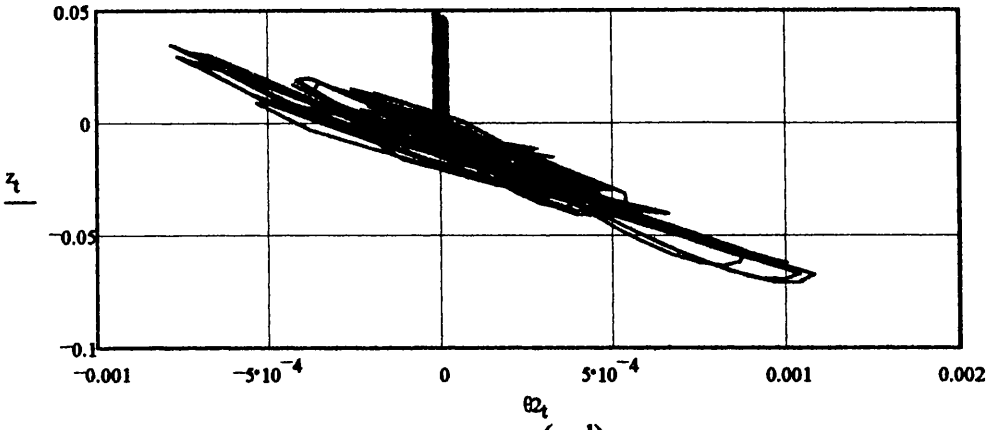

(m)

(rad)

Figure A-28

2D *TLP* c.g. Motion Response (Heave v Yaw)

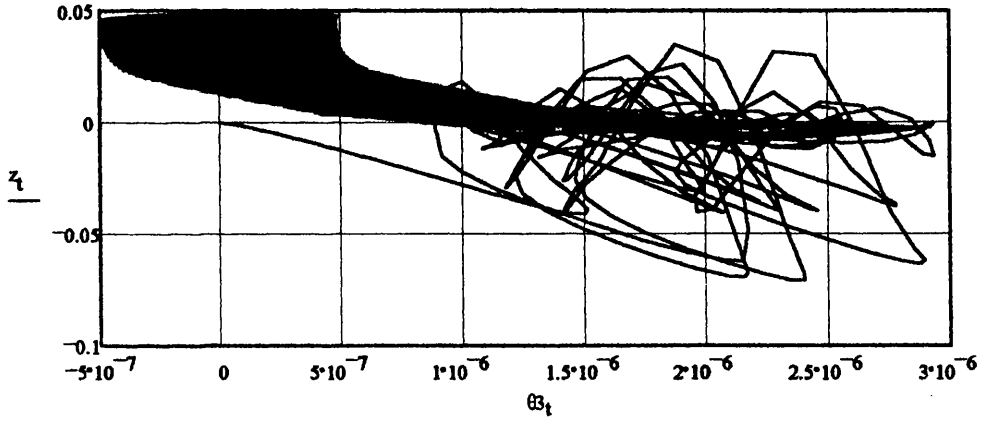

(m)

(rad)

Figure A-29

2D *TLP* c.g. Motion Response (Surge v Sway)

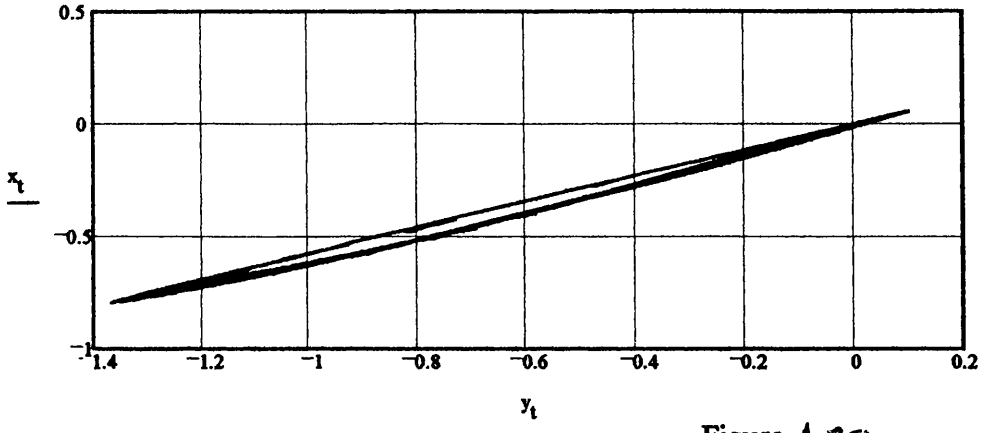

(m)

(m)

Figure A-30

2D *TLP* c.g. Motion Response (Surge v Heave)

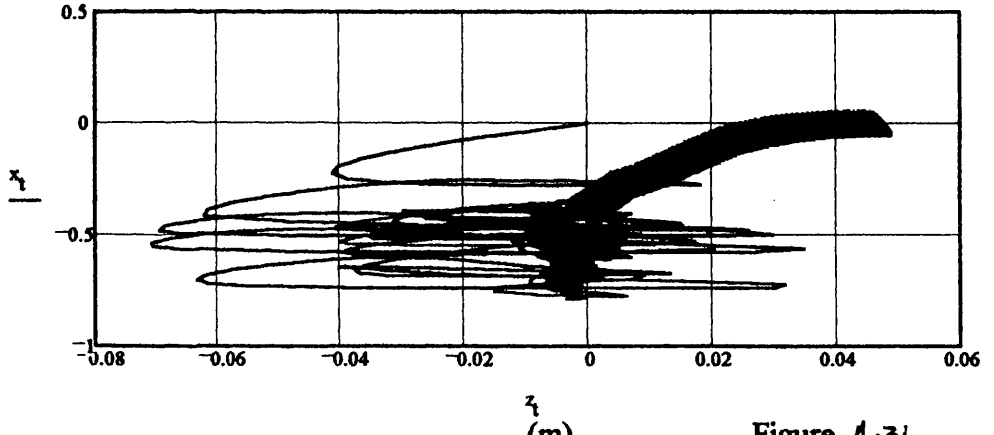

(m)

(m)

Figure A-31

2D *TLP* c.g. Motion Response (Surge v Roll)

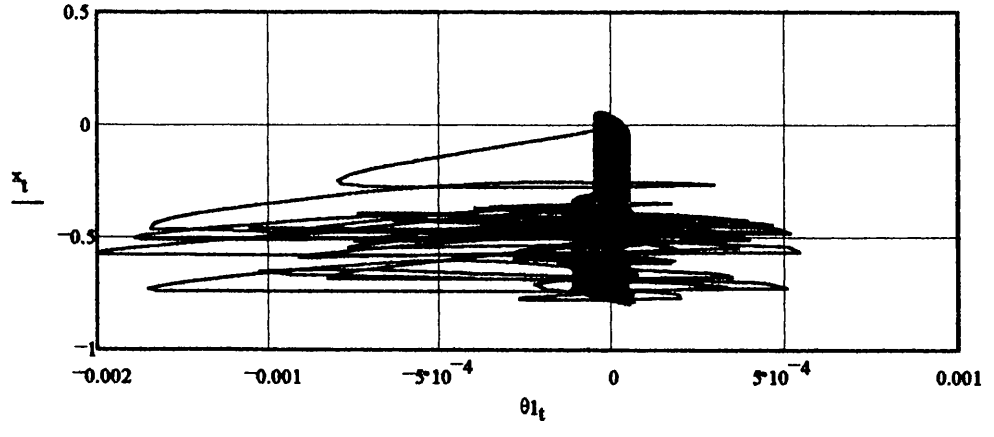

(m)

(rad)

Figure A-32

2D *TLP* c.g. Motion Response (Surge v Pitch)

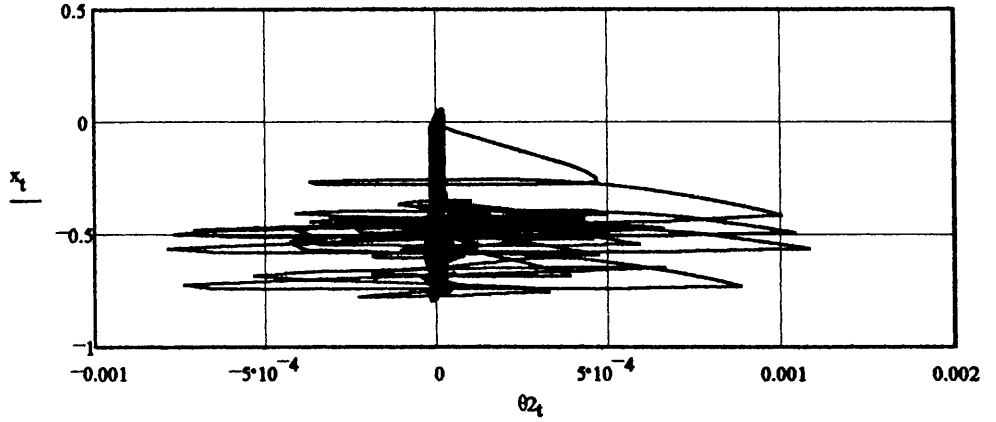

(m)

Figure A.33

2D *TLP* c.g. Motion Response (Surge v Yaw)

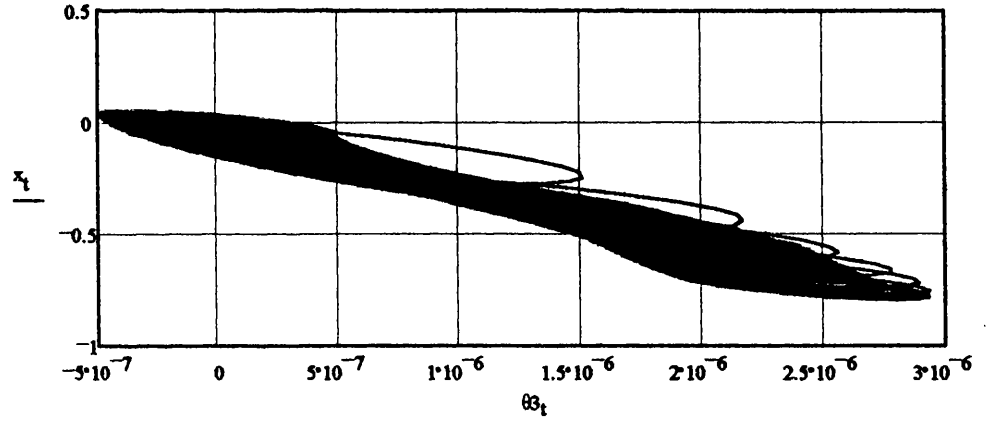

(m)

Figure A.34

Figures A.35- A.51 detail the time-domain simulation results for the AA Case Study TLP for an incident regular wave of ω =0.8rad/s (ξ_a =1m) with a heading angle of 60^0.

Figures A.35- A.40 detail the surge, sway, heave, roll, pitch and yaw DOF response respectively.

Figure A.41 details the tether 'bundle' tension time-series response.

Figures A.42- A.51 detail the platform vertical/horizontal and cross-planer response.

TLP Global Dynamic Response in Time-domain (6*DOF*):

(Space-fixed coordinate system)

DISPLACEMENT

Surge

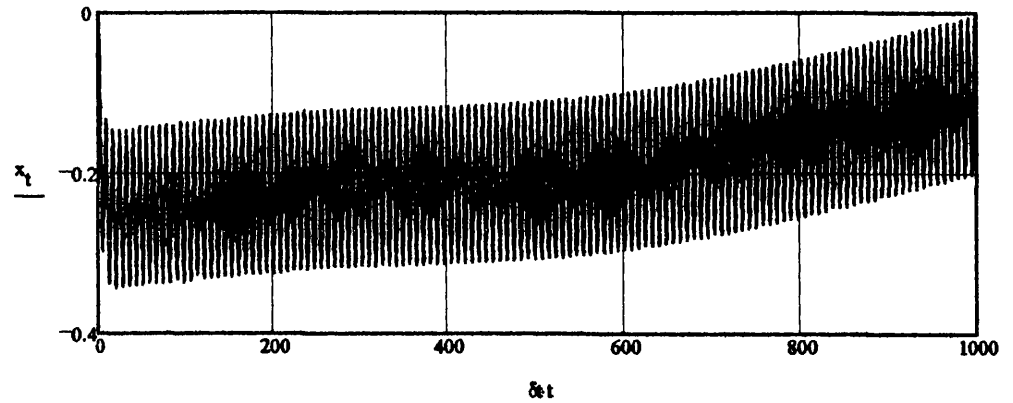

(m)

Figure A.35

Sway

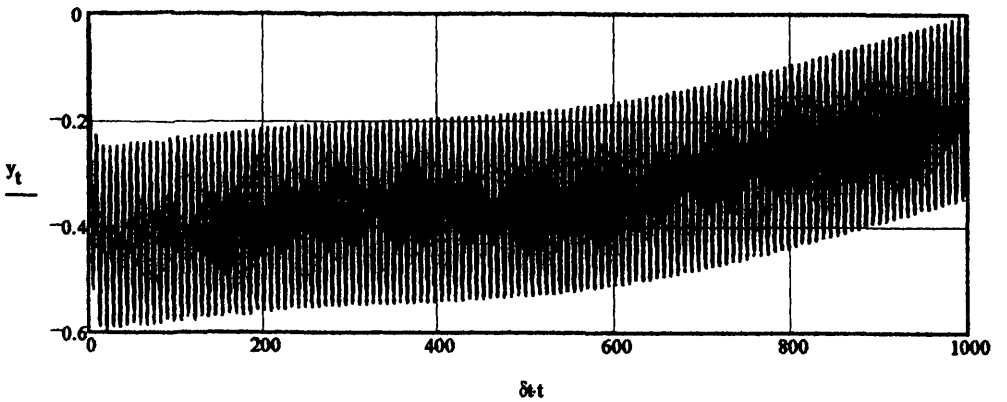

(m)

Figure A.36

Heave

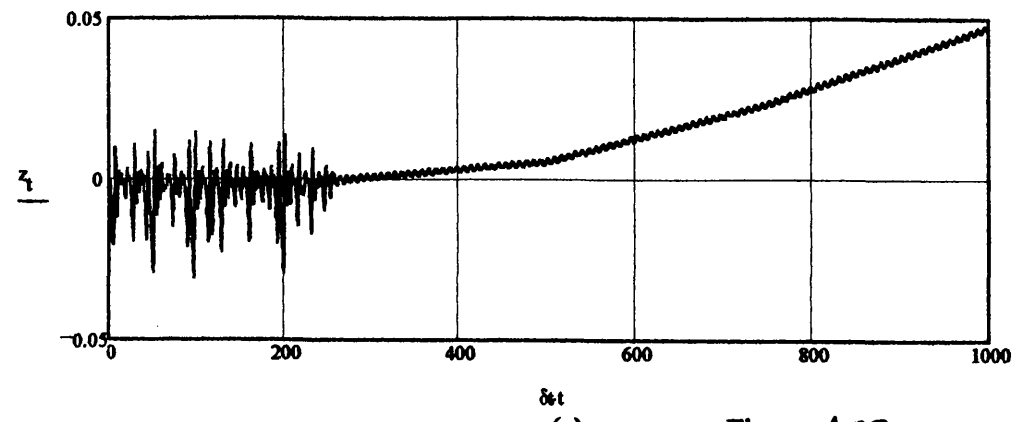

(m)

Figure A.37

Roll

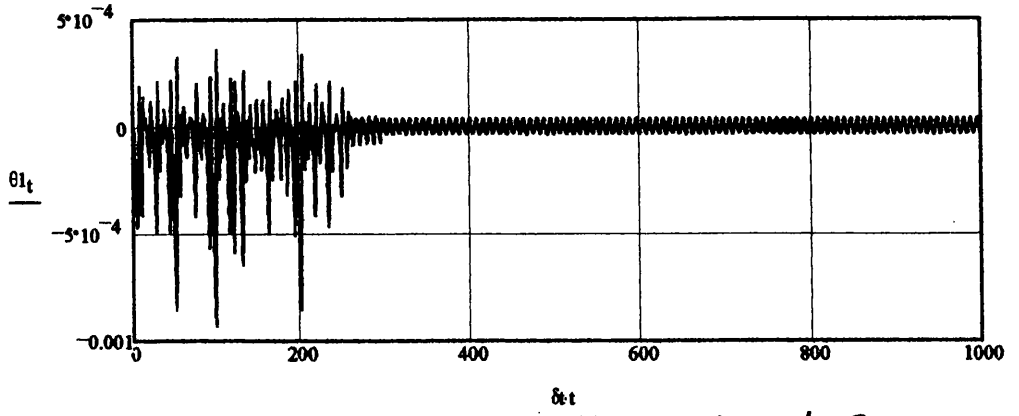

(rad)

Figure A.38

Pitch

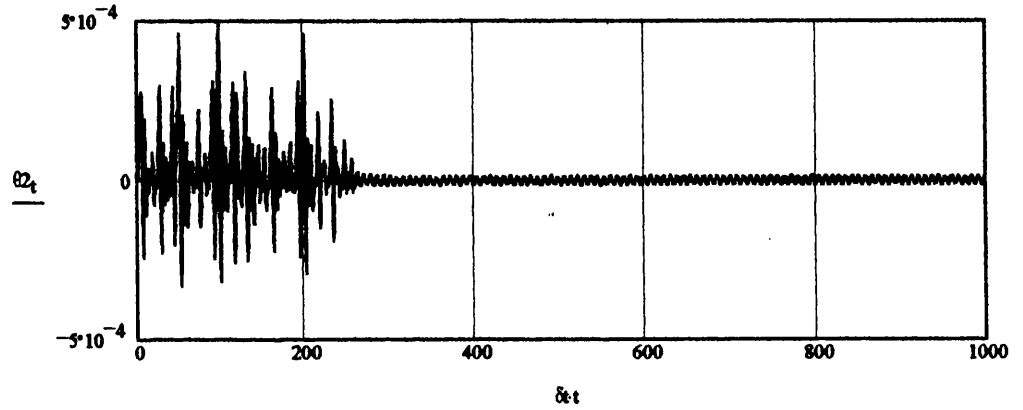

(rad)

Figure A.39

Yaw

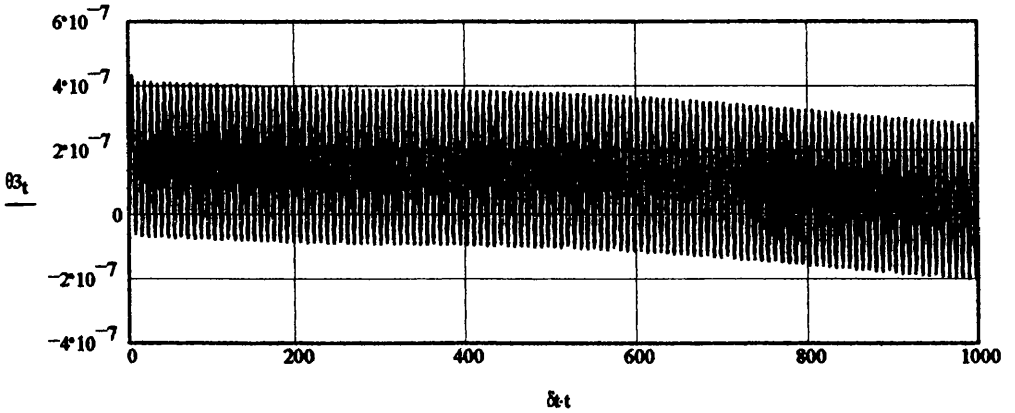

(rad)

Figure A.40

Tether Force Time-series

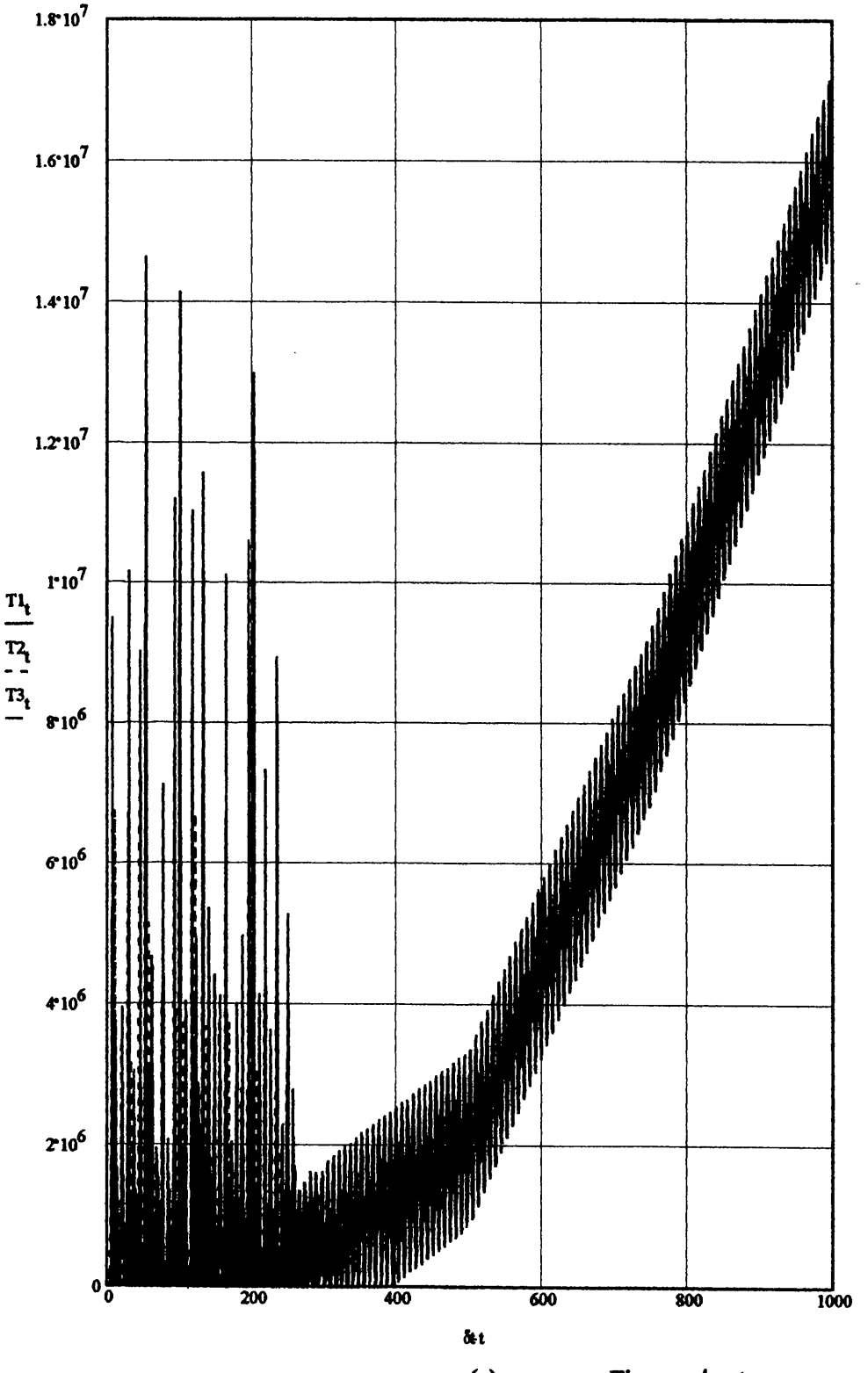

(N)

(s)

Figure A.41

2D *TLP* c.g. Motion Response (Heave v Surge)

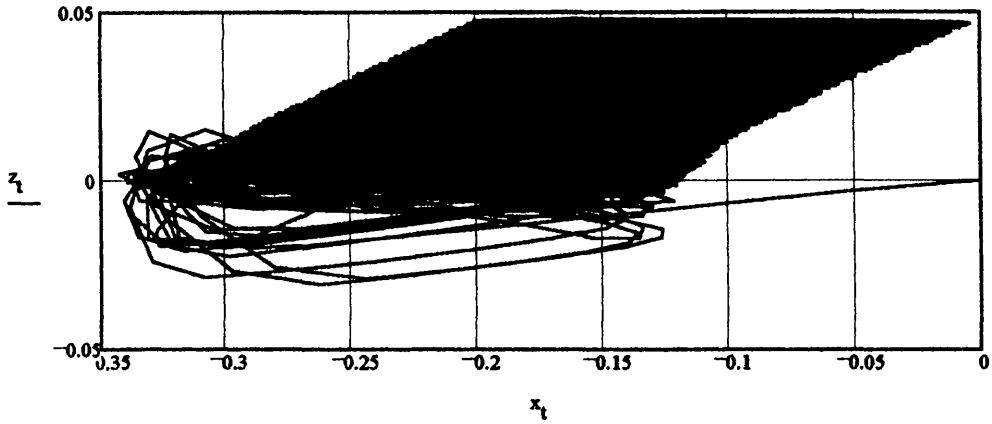

(m)

(m)

Figure A-42

2D *TLP* c.g. Motion Response (Heave v Sway)

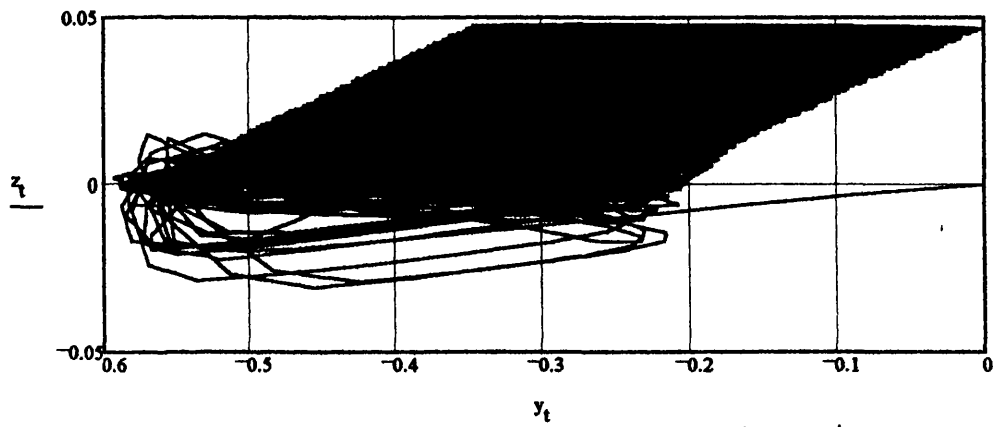

(m)

(m)

Figure A-43

2D *TLP* c.g. Motion Response (Heave v Roll)

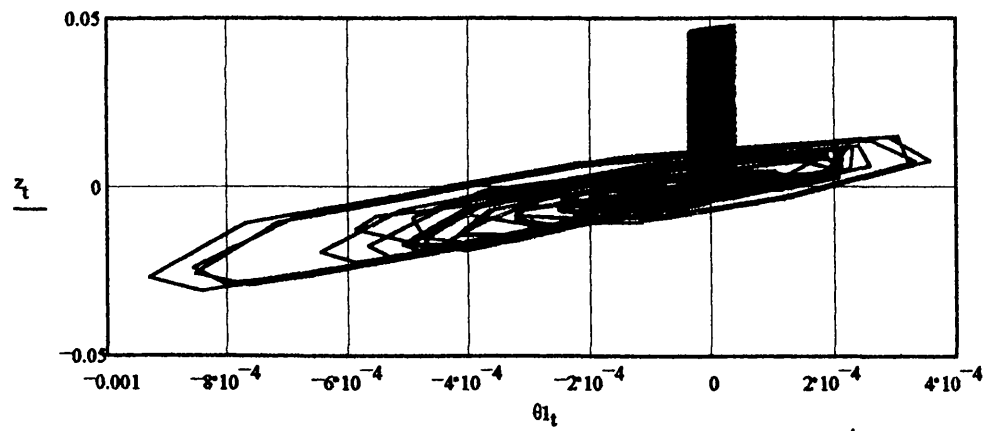

(m)

(rad)

Figure A-44

2D *TLP* c.g. Motion Response (Heave v Pitch)

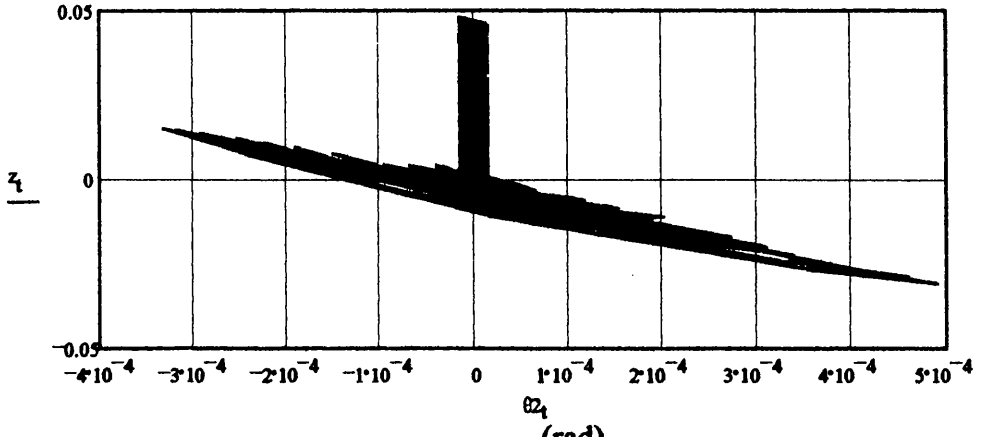

(m)

(rad)

Figure A·45

2D *TLP* c.g. Motion Response (Heave v Yaw)

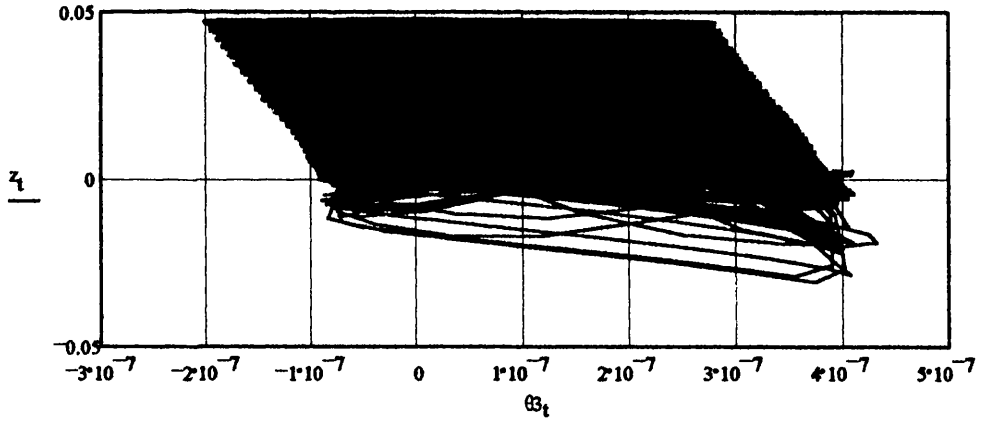

(m)

(rad)

Figure A·46

2D *TLP* c.g. Motion Response (Surge v Sway)

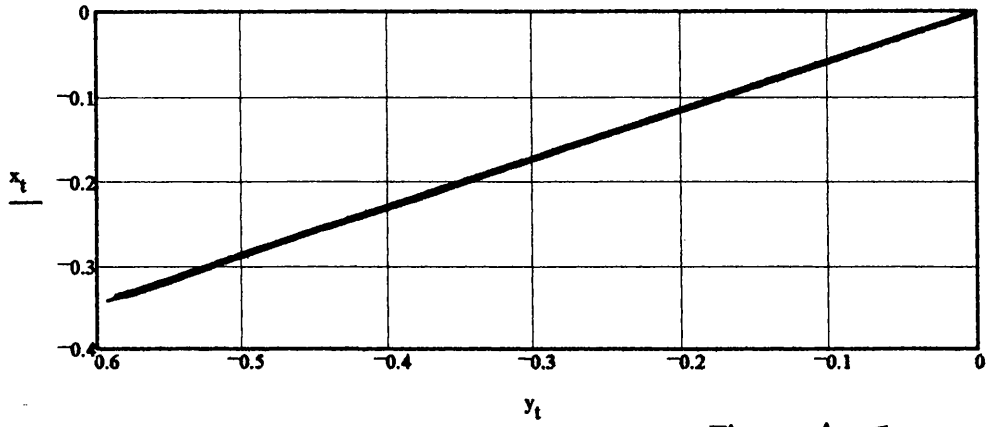

(m)

(m)

Figure A.4-7

2D *TLP* c.g. Motion Response (Surge v Heave)

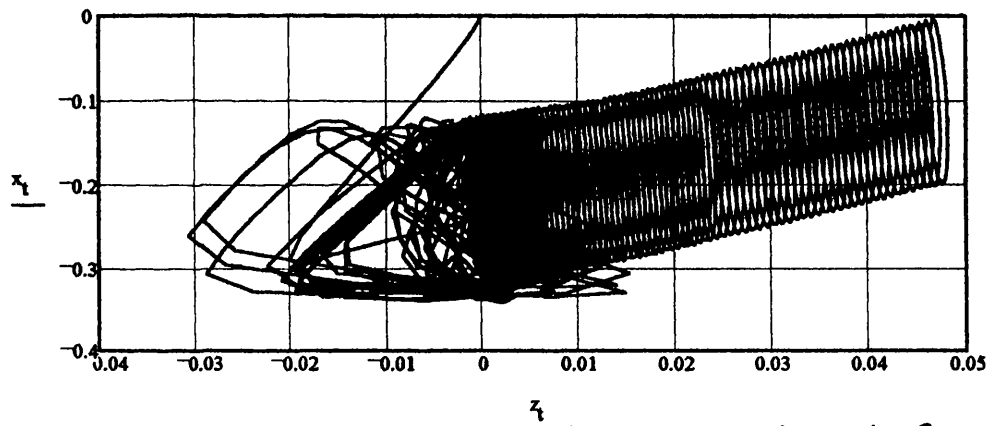

(m)

(m)

Figure A.4-8

2D *TLP* c.g. Motion Response (Surge v Roll)

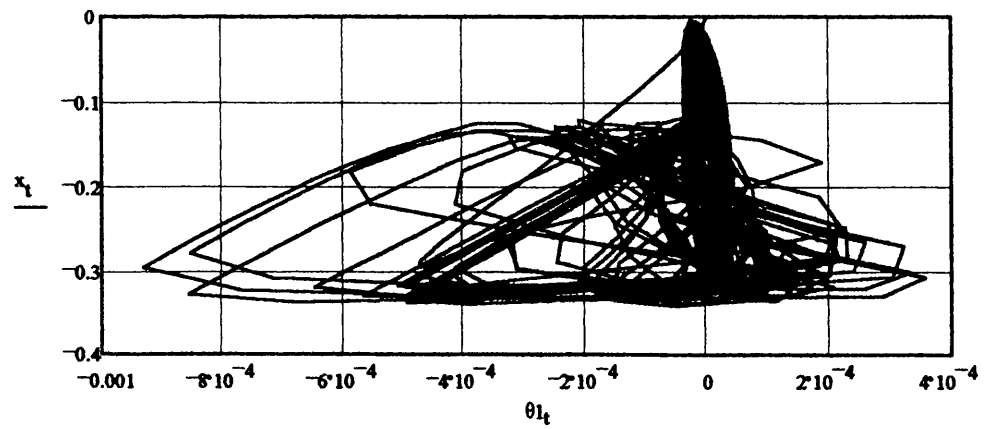

(m)

(rad)

Figure A.4-9

2D *TLP* c.g. Motion Response (Surge v Pitch)

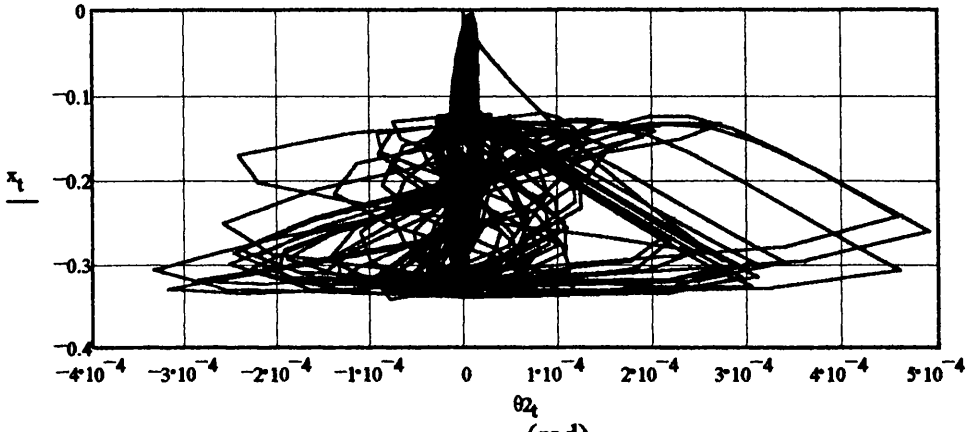

(m)

(rad)

Figure A-50

2D *TLP* c.g. Motion Response (Surge v Yaw)

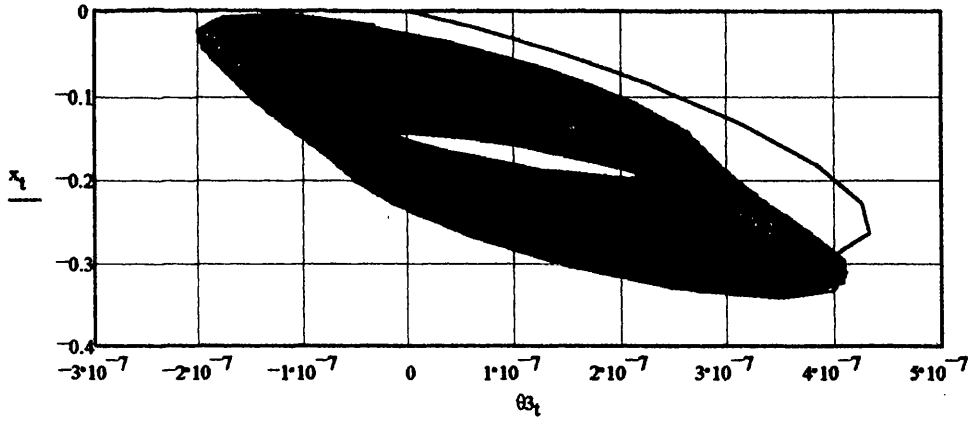

(m)

Figure A-51

(rad)

Figures A.52-6.68 detail the time-domain simulation results for the AA Case Study TLP for an incident regular wave of ω=0.92rad/s (ξ_a=1m) with a heading angle of 60^0.

Figures A.52- A.57 detail the surge, sway, heave, roll, pitch and yaw DOF response respectively.

Figure A.58 details the tether 'bundle' tension time-series response.

Figures A.59- A.68detail the platform vertical/horizontal and cross-planer response.

TLP Global Dynamic Response in Time-domain (*6DOF*):

(Space-fixed coordinate system)

DISPLACEMENT

Surge

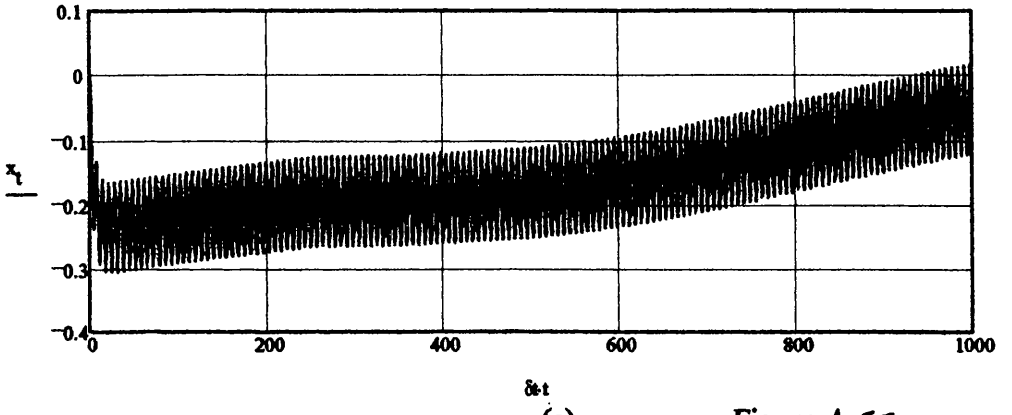

(m)

Figure A·52

Sway

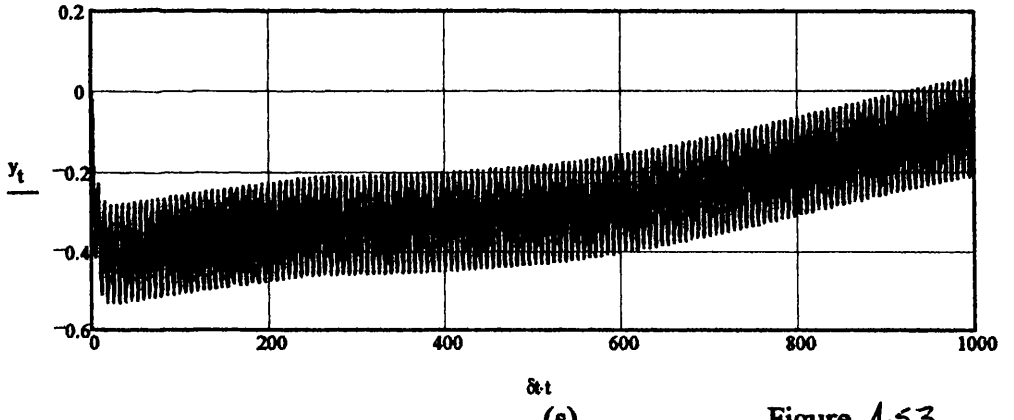

(m)

Figure A·53

Heave

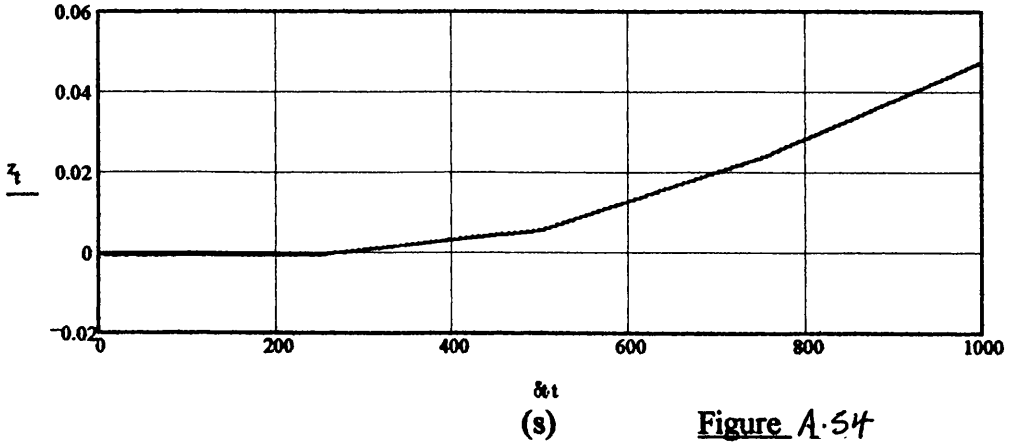

(m)

Figure A·54

Roll

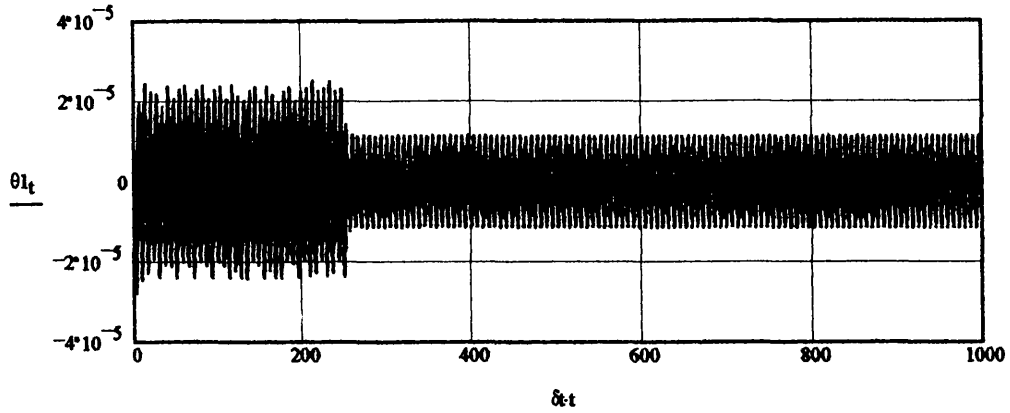

(rad)

Figure A-55

Pitch

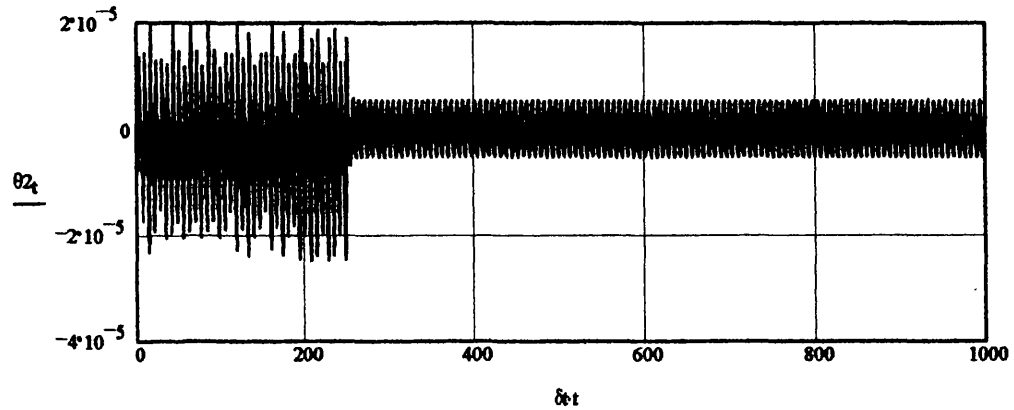

(rad)

Figure A-56

Yaw

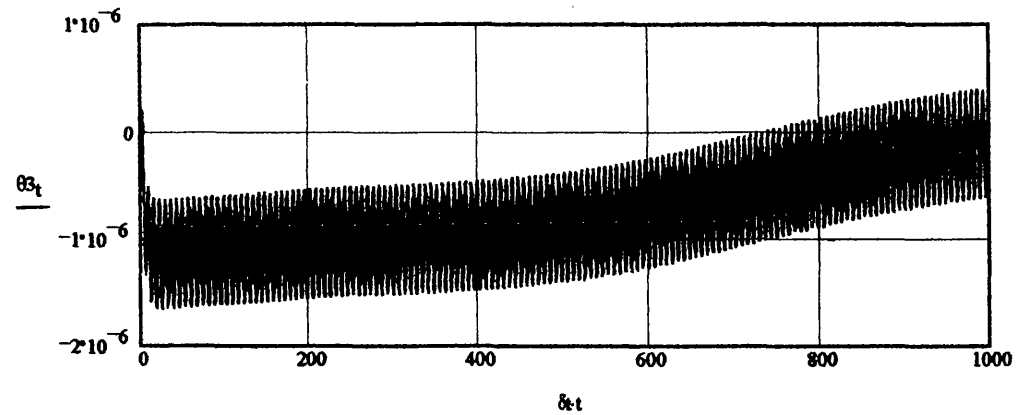

(rad)

Figure A-57

Tether Force Time-series

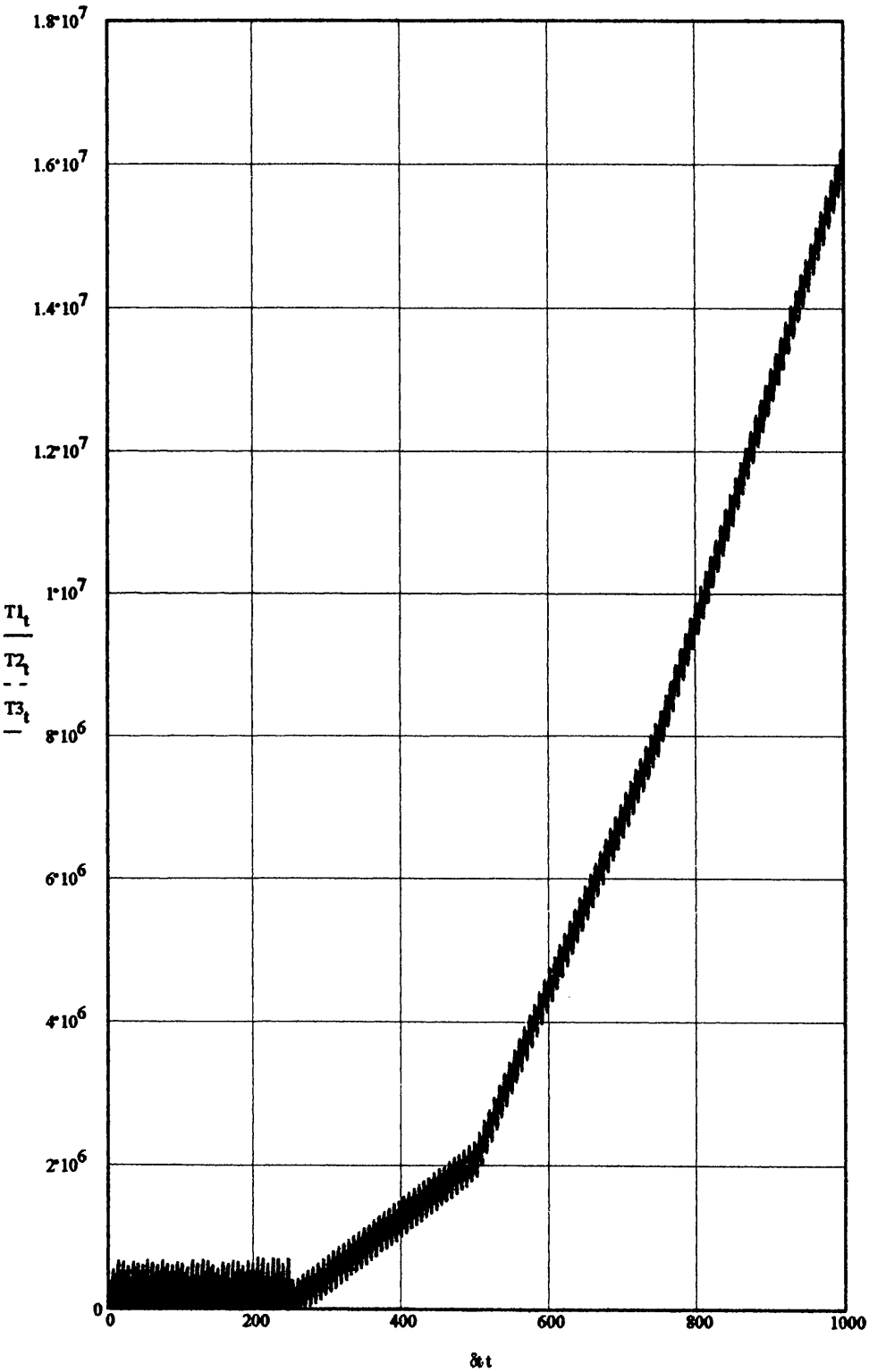

Figure A.58

2D *TLP* c.g. Motion Response (Heave v Surge)

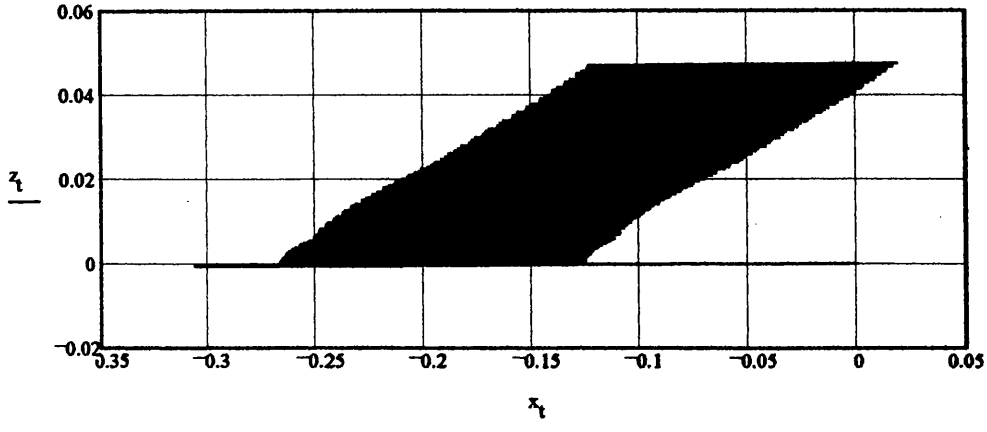

Figure A·59

2D *TLP* c.g. Motion Response (Heave v Sway)

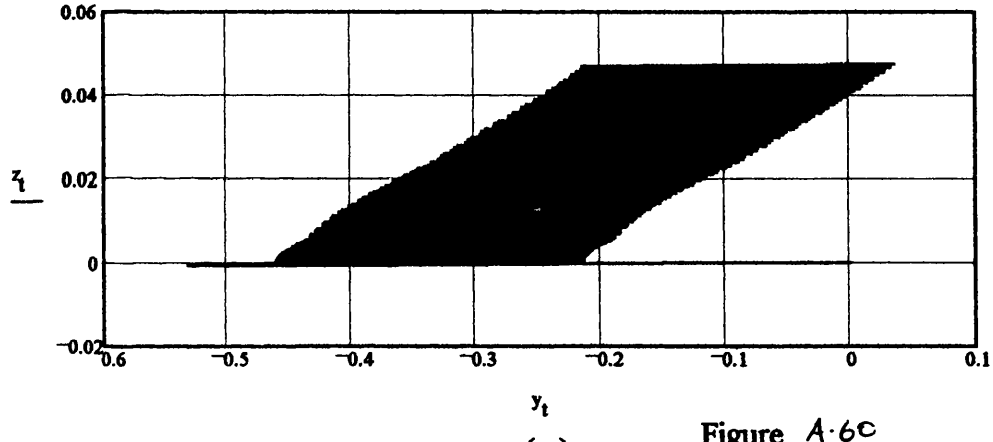

Figure A·60

2D *TLP* c.g. Motion Response (Heave v Roll)

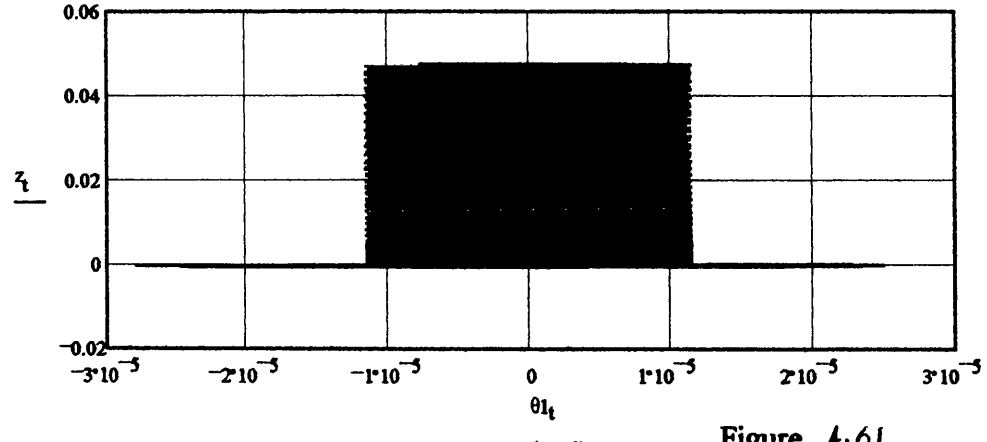

Figure A·61

2D *TLP* c.g. Motion Response (Heave v Pitch)

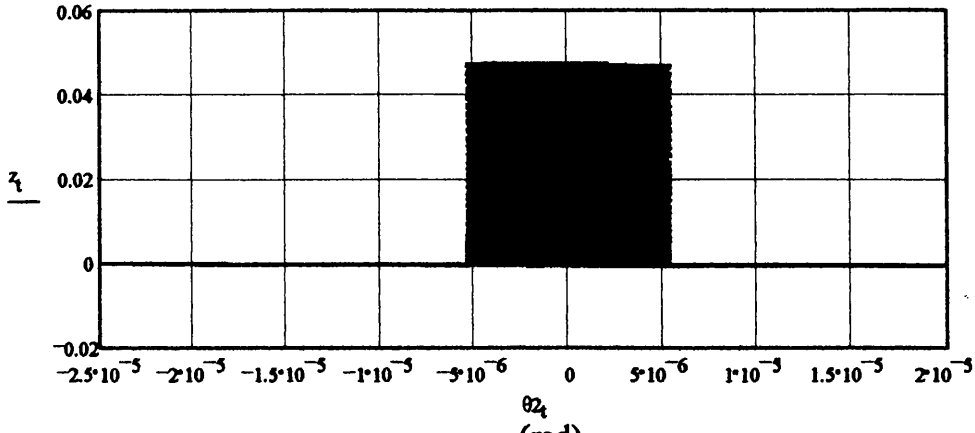

(m)

(rad)

Figure A·62

2D *TLP* c.g. Motion Response (Heave v Yaw)

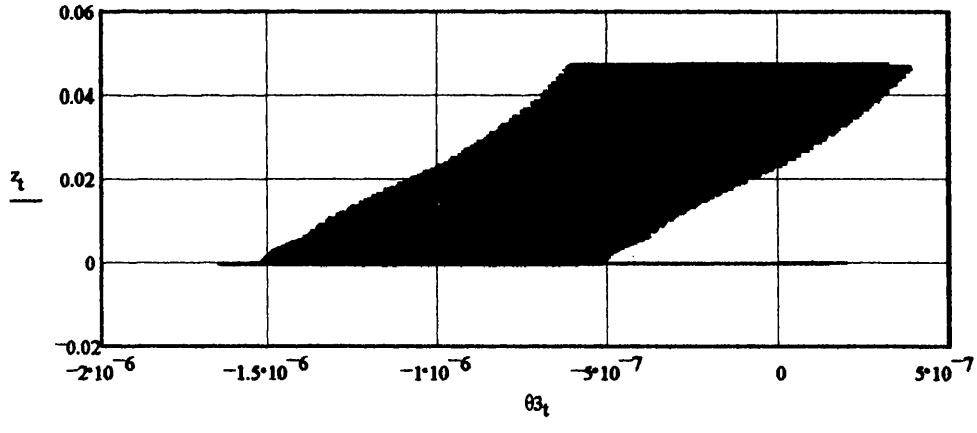

(m)

(rad)

Figure A·63

2D *TLP* c.g. Motion Response (Surge v Sway)

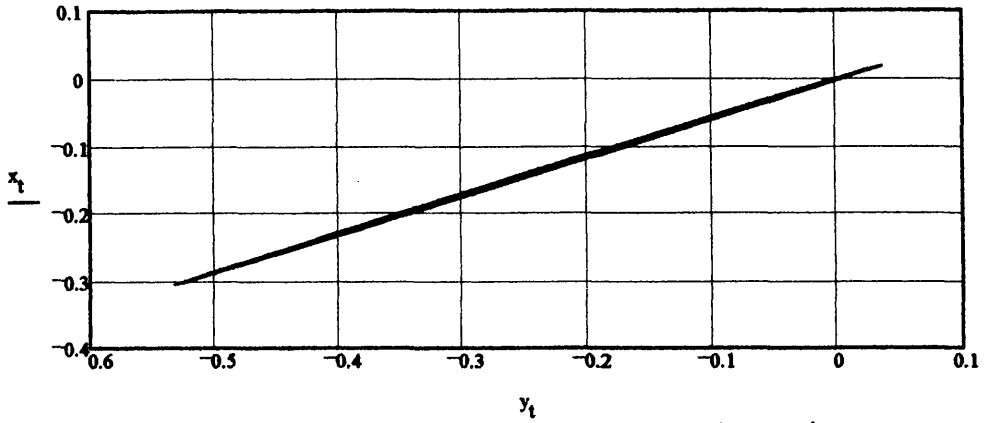

(m)

(m)

Figure A·64

2D *TLP* c.g. Motion Response (Surge v Heave)

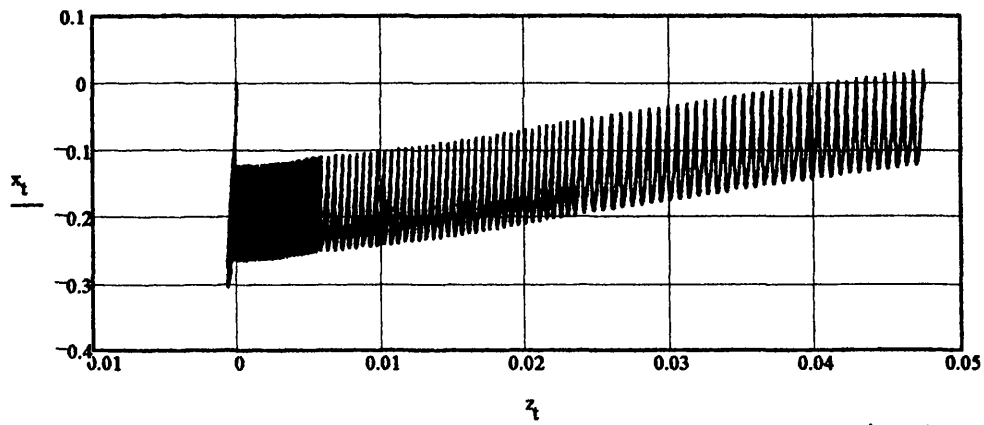

(m)

(m)

Figure A·65

2D *TLP* c.g. Motion Response (Surge v Roll)

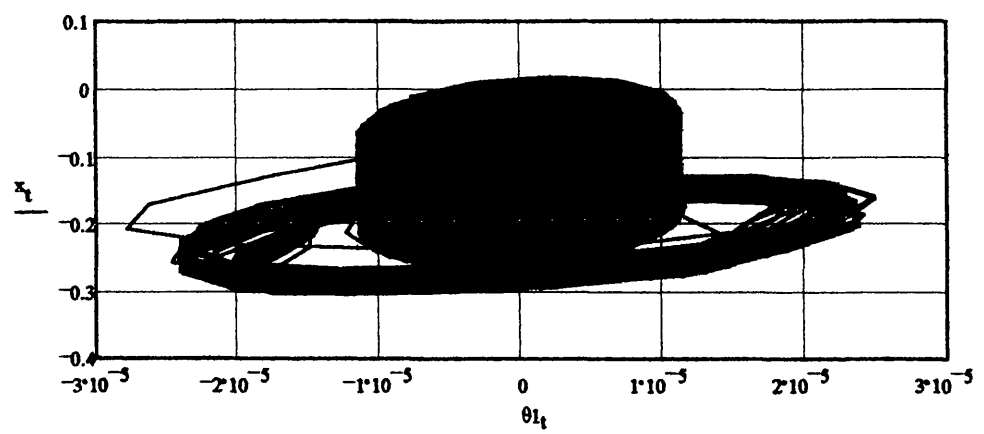

(m)

(rad)

Figure A·66

2D *TLP* c.g. Motion Response (Surge v Pitch)

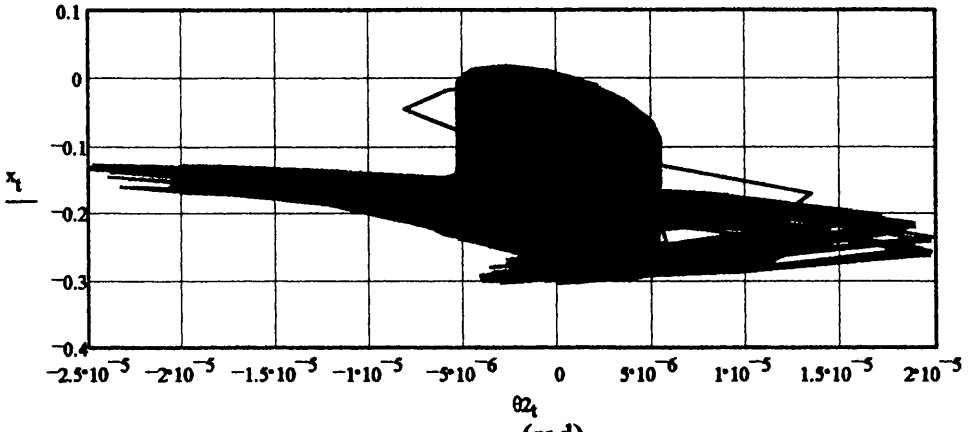

(m)

(rad)

Figure A-67

2D *TLP* c.g. Motion Response (Surge v Yaw)

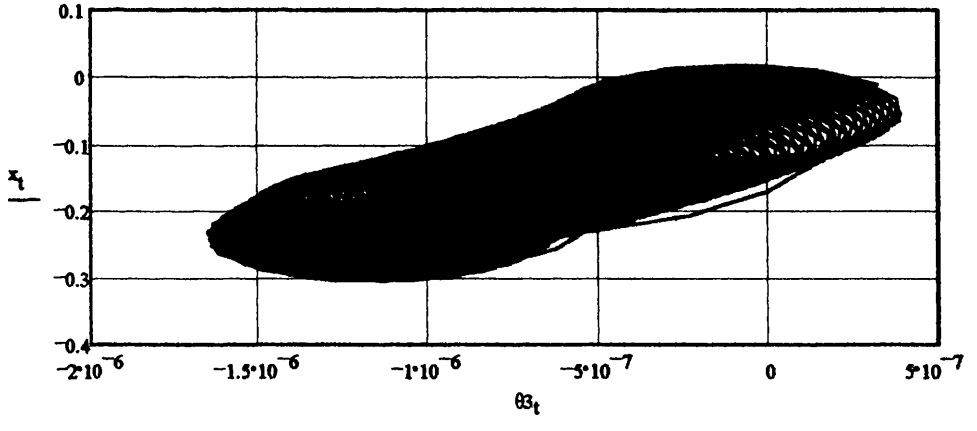

(m)

(rad)

Figure A-68

Figures A.69- A.75 detail the time-domain simulation results for the AA Case Study TLP for an incident regular wave of ω =0.1rad/s (ξ_a =1m) with a heading angle of 60^0.

Figures A.69- A.74 detail the surge, sway, heave, roll, pitch and yaw DOF response respectively.

Figure A.75 details the tether 'bundle' tension time-series response.

Figures A.76- A.85 detail the platform vertical/horizontal and cross-planer response.

TLP Global Dynamic Response in Time-domain (6*DOF*):

(Space-fixed coordinate system)

DISPLACEMENT

Surge

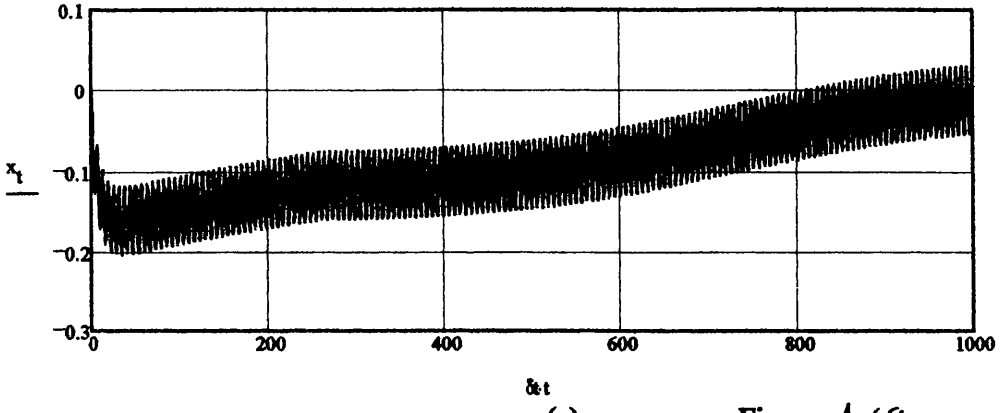

(m)

Figure A.69

Sway

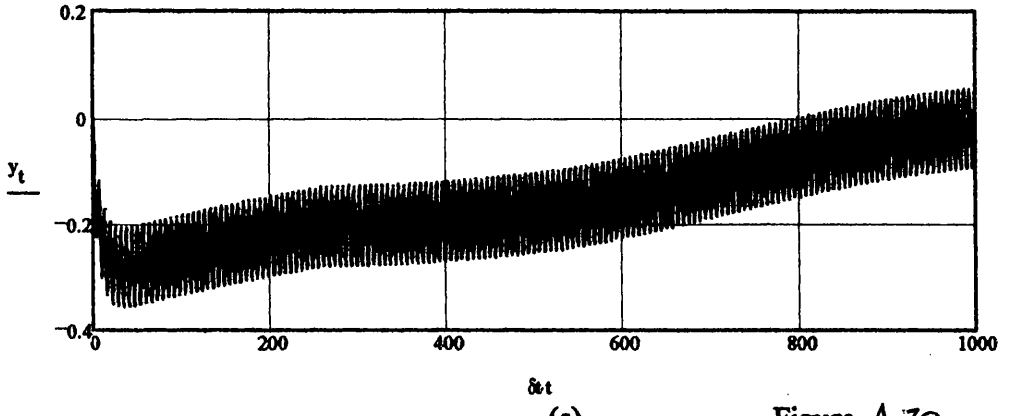

(m)

Figure A.70

Heave

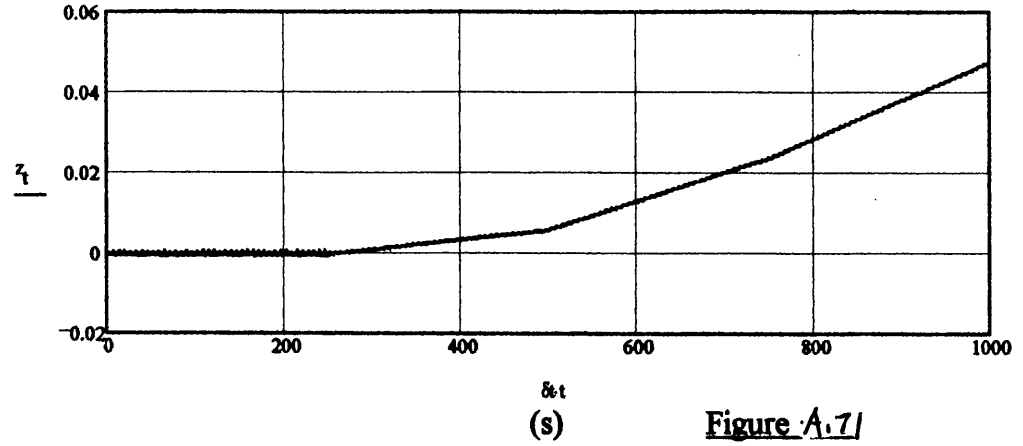

(m)

Figure A.71

Roll

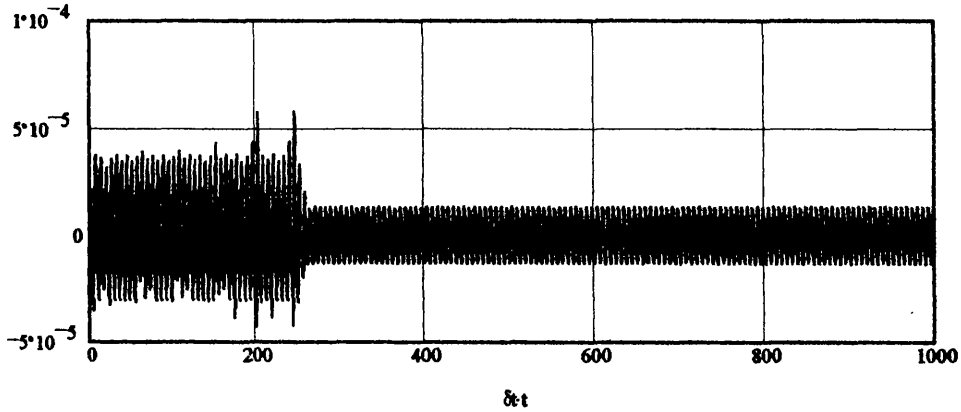

(rad)

Figure A.72

Pitch

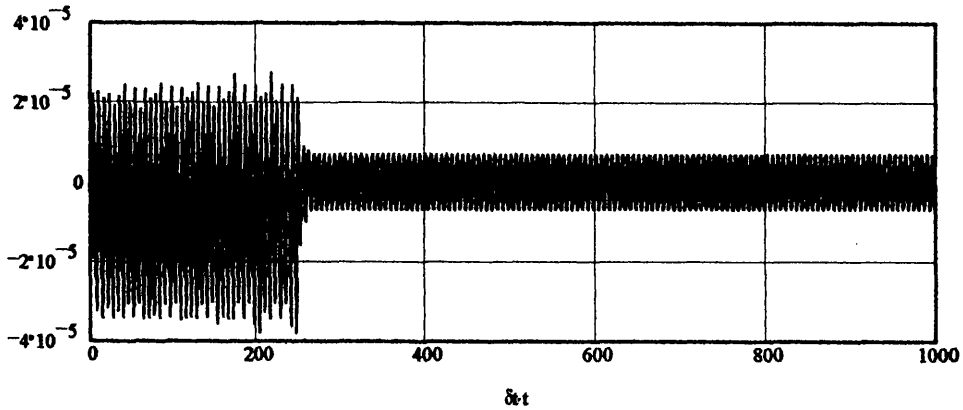

(rad)

Figure A.73

Yaw

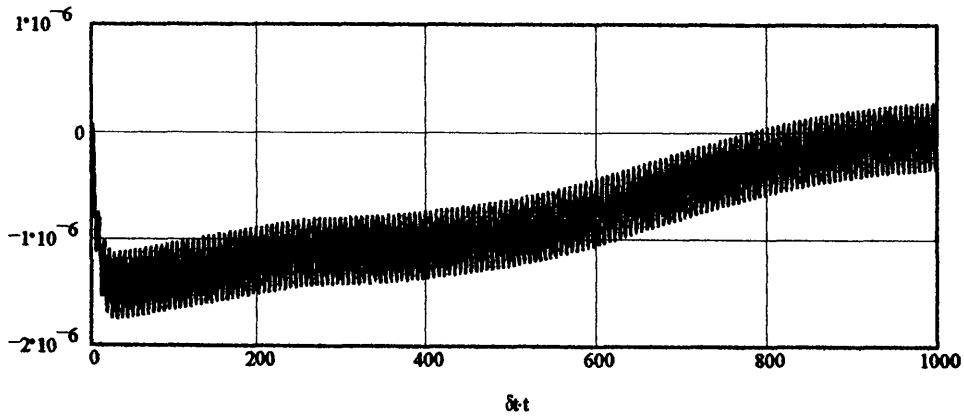

(rad)

Figure A.74

Tether Force Time-series

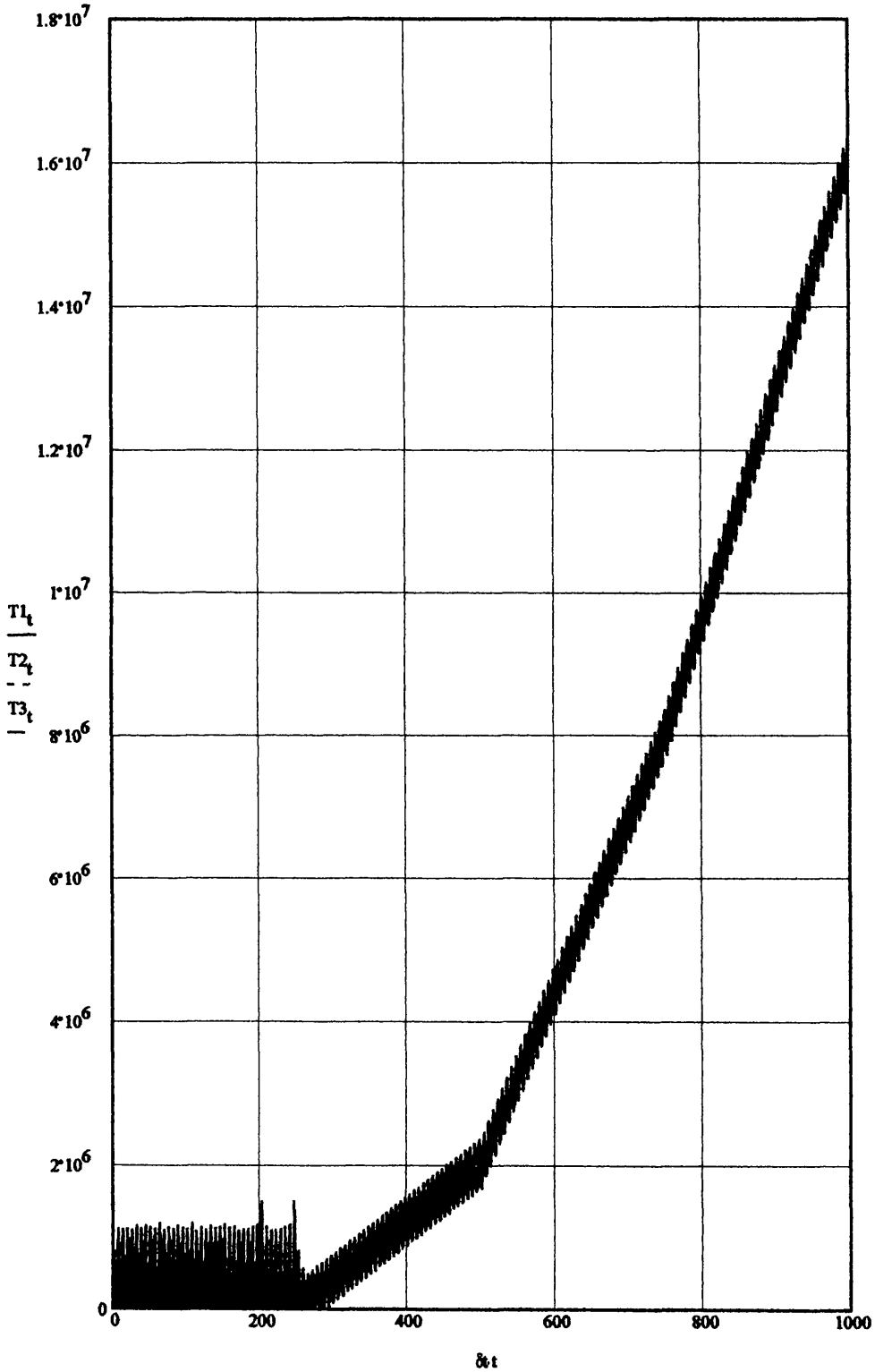

Figure A-75

2D *TLP* c.g. Motion Response (Heave v Surge)

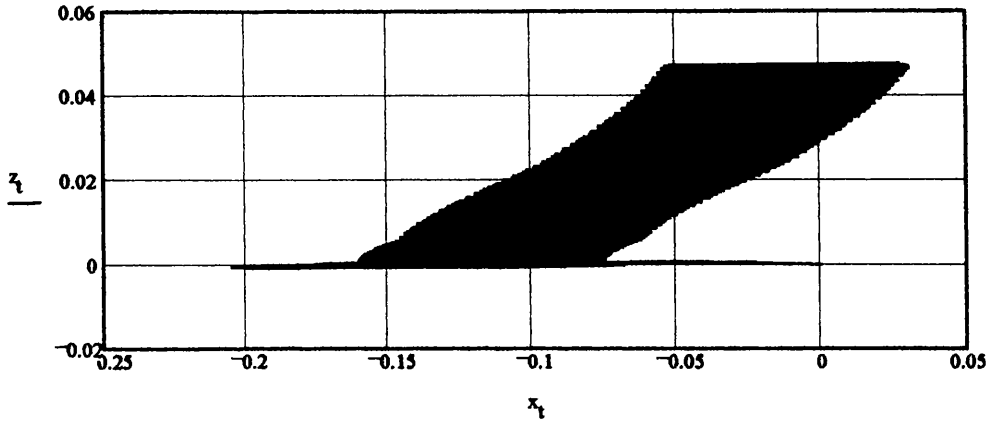

Figure A-76

2D *TLP* c.g. Motion Response (Heave v Sway)

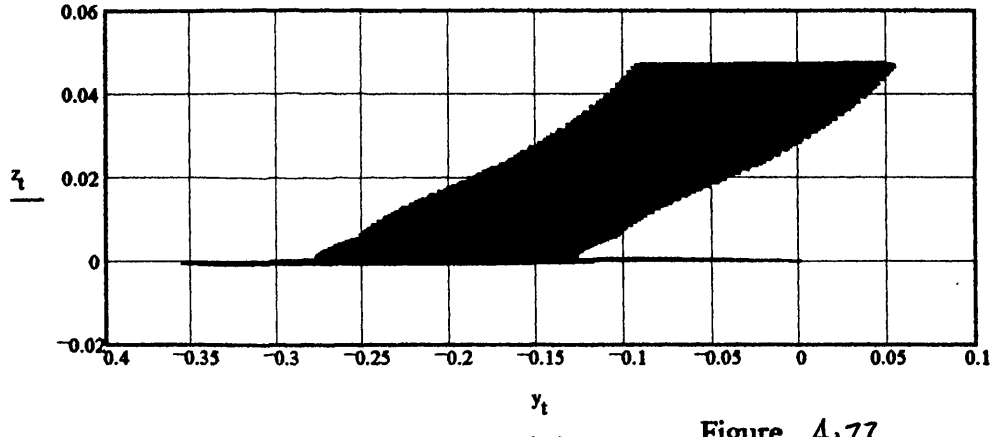

Figure A-77

2D *TLP* c.g. Motion Response (Heave v Roll)

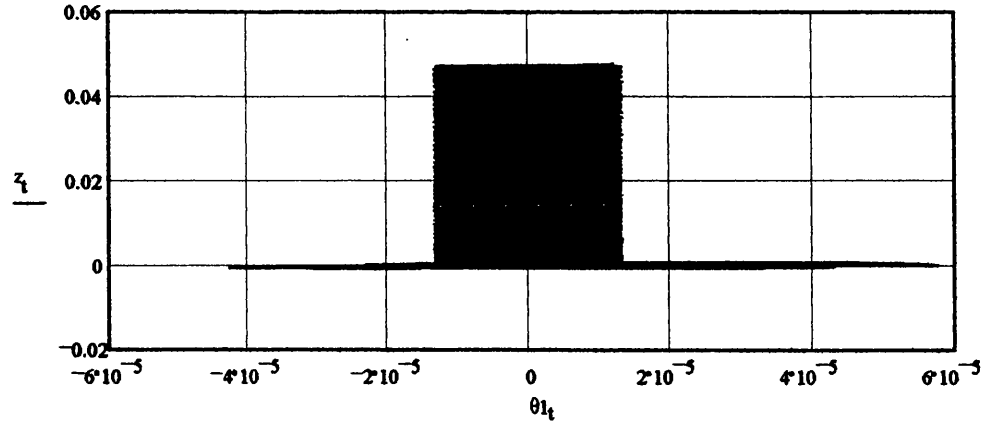

Figure A-78

2D *TLP* c.g. Motion Response (Heave v Pitch)

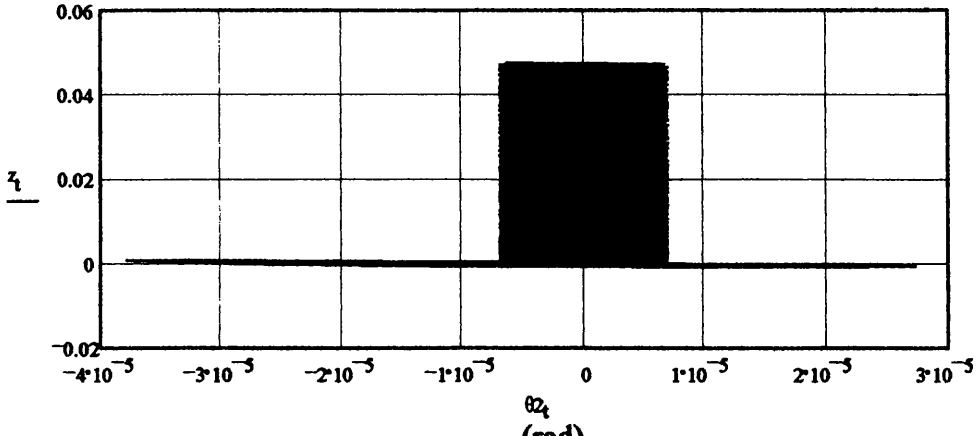

(m)

(rad)

Figure A.79

2D *TLP* c.g. Motion Response (Heave v Yaw)

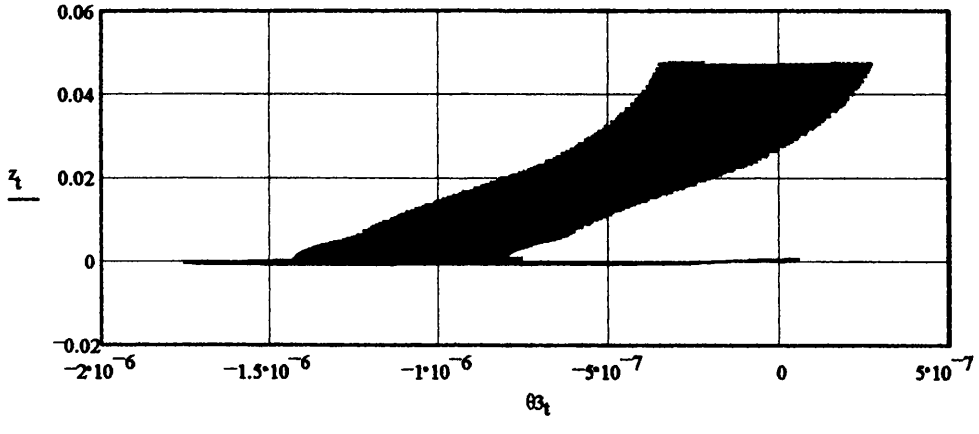

(m)

(rad)

Figure A.80

2D *TLP* c.g. Motion Response (Surge v Sway)

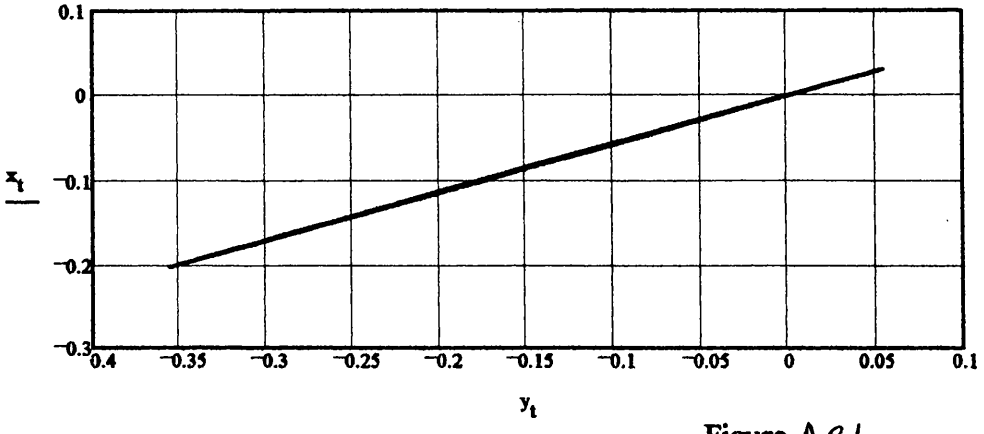

(m)

(m)

Figure A·81

2D *TLP* c.g. Motion Response (Surge v Heave)

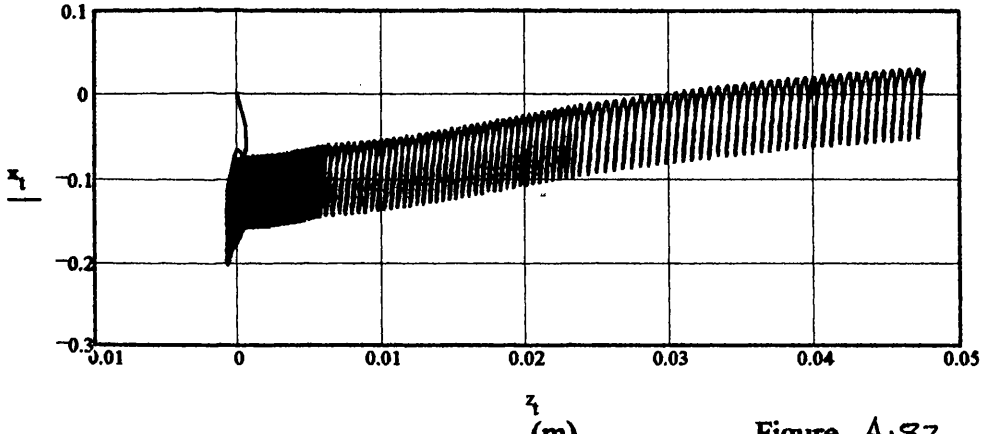

(m)

(m)

Figure A·82

2D *TLP* c.g. Motion Response (Surge v Roll)

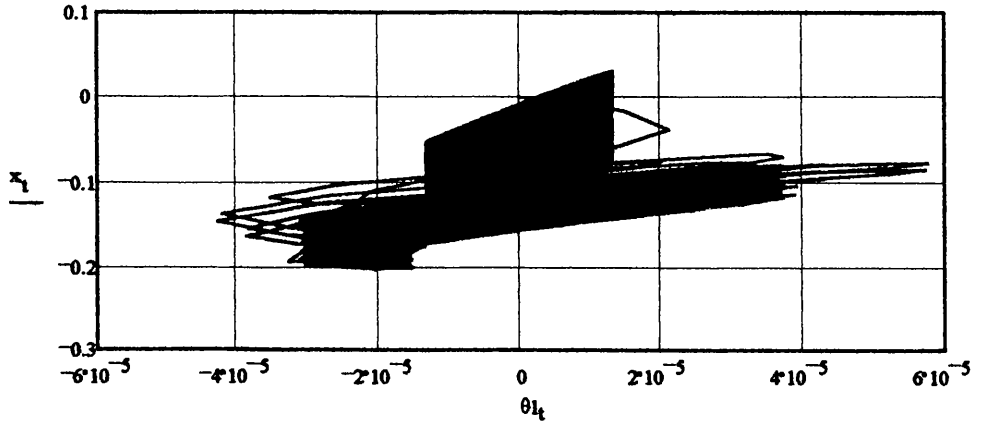

(m)

(rad)

Figure A·83

2D *TLP* c.g. Motion Response (Surge v Pitch)

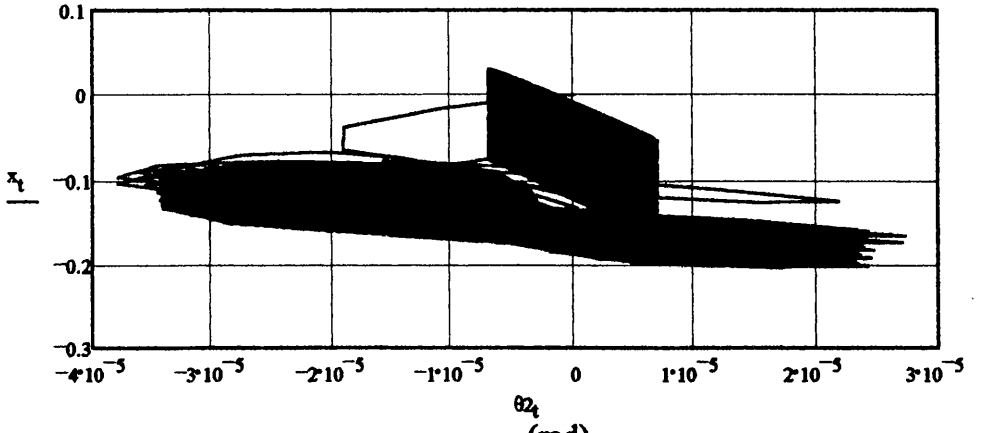

(m)

(rad)

Figure A.84

2D *TLP* c.g. Motion Response (Surge v Yaw)

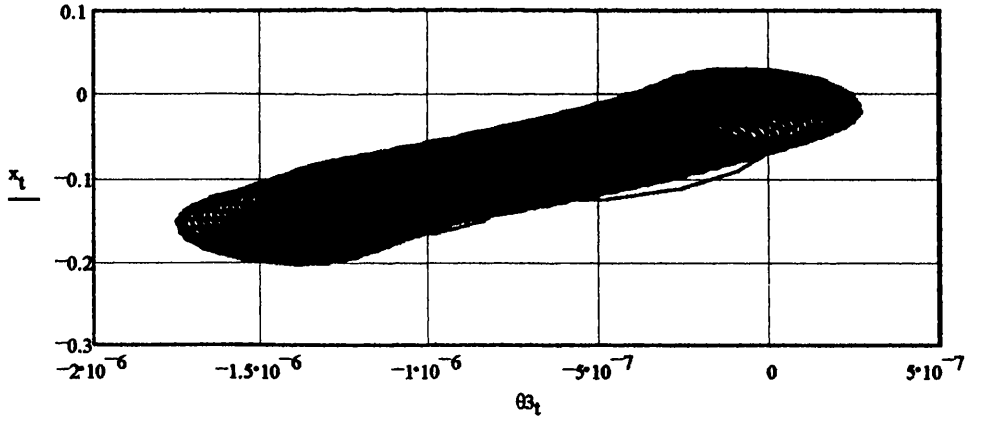

(m)

Figure A.85

(rad)

Figures A.86 - A.102 detail the time-domain simulation results for the AA Case Study TLP for an incident regular wave of ω =1.12rad/s (ξ_a =1m) with a heading angle of 60^0.

Figures A.86 - A.91 detail the surge, sway, heave, roll, pitch and yaw DOF response respectively.

Figure A.92 details the tether 'bundle' tension time-series response.

Figures A.93 - A.102 detail the platform vertical/horizontal and cross-planer response.

TLP Global Dynamic Response in Time-domain (*6DOF*):

(Space-fixed coordinate system)

DISPLACEMENT

Surge

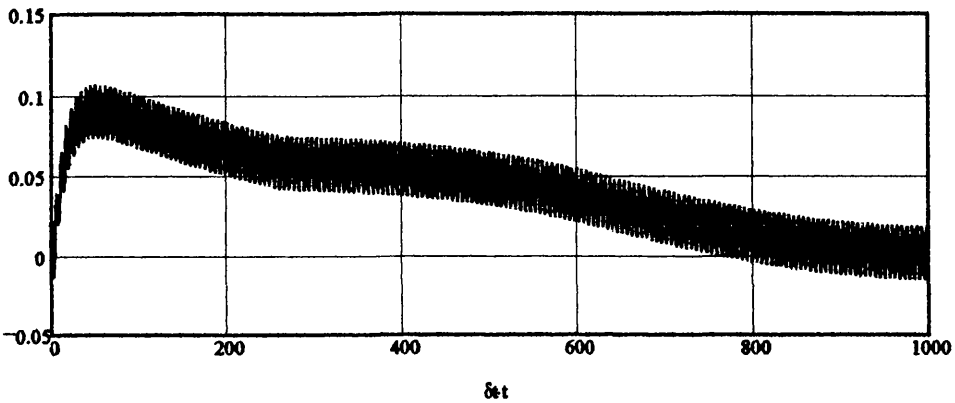

(m)

Figure A·86

Sway

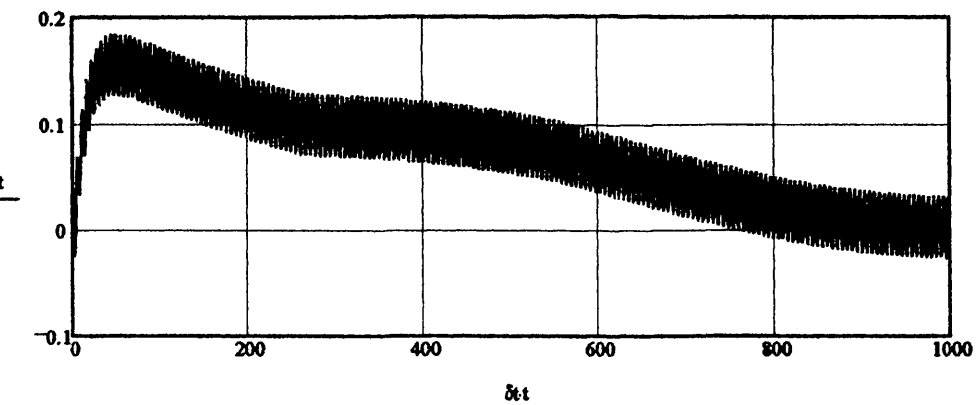

(m)

Figure A·87

Heave

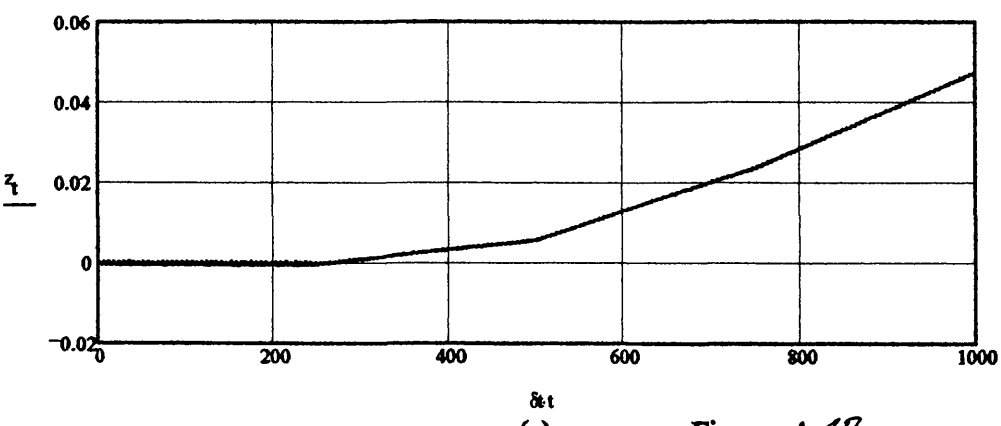

(m)

Figure A·88

Roll

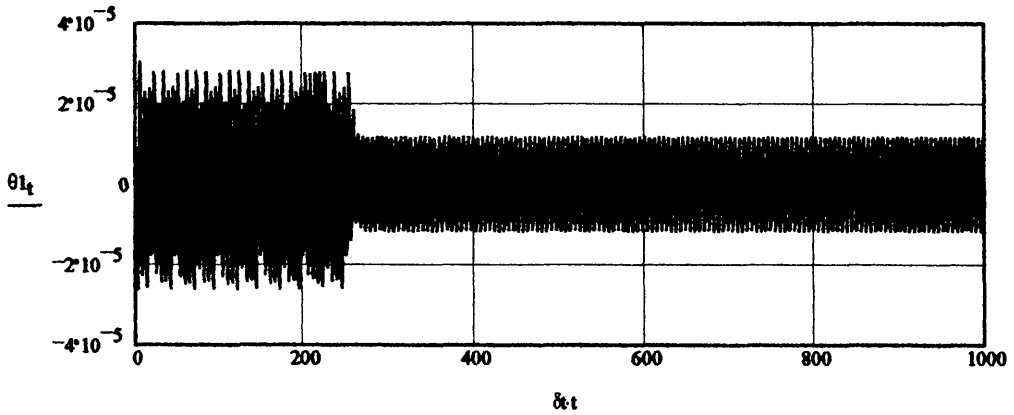

(rad)

Figure A-89

Pitch

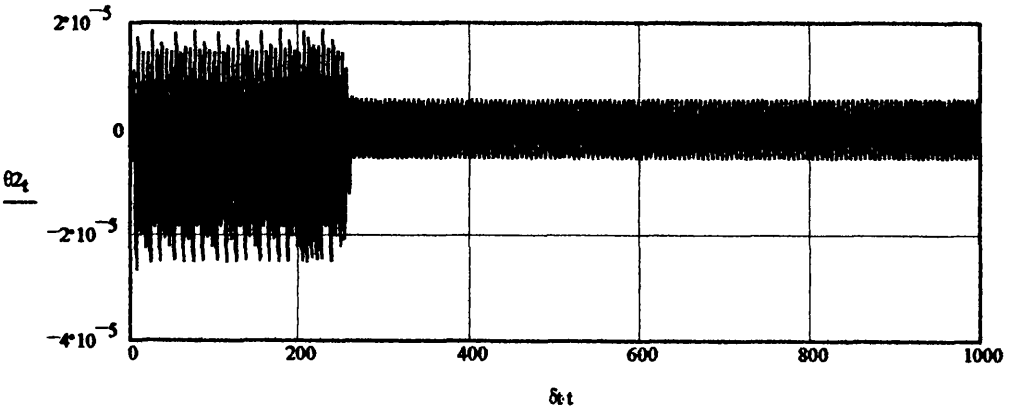

(rad)

Figure A-90

Yaw

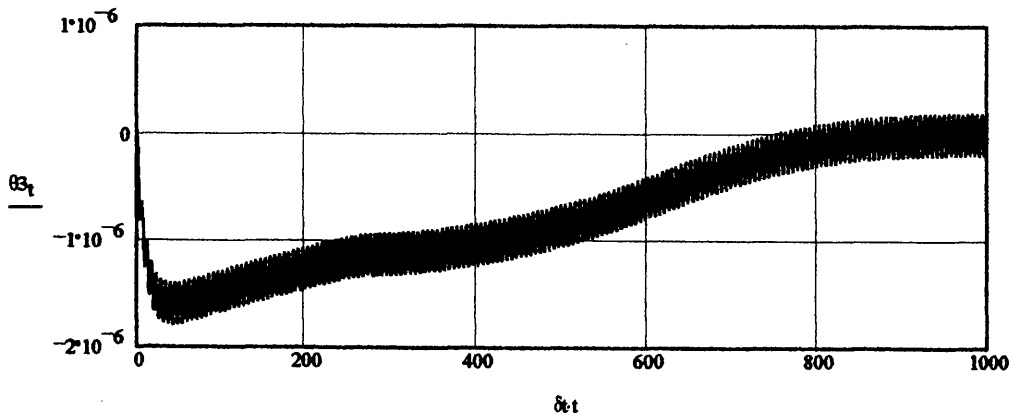

(rad)

Figure A-91

Tether Force Time-series

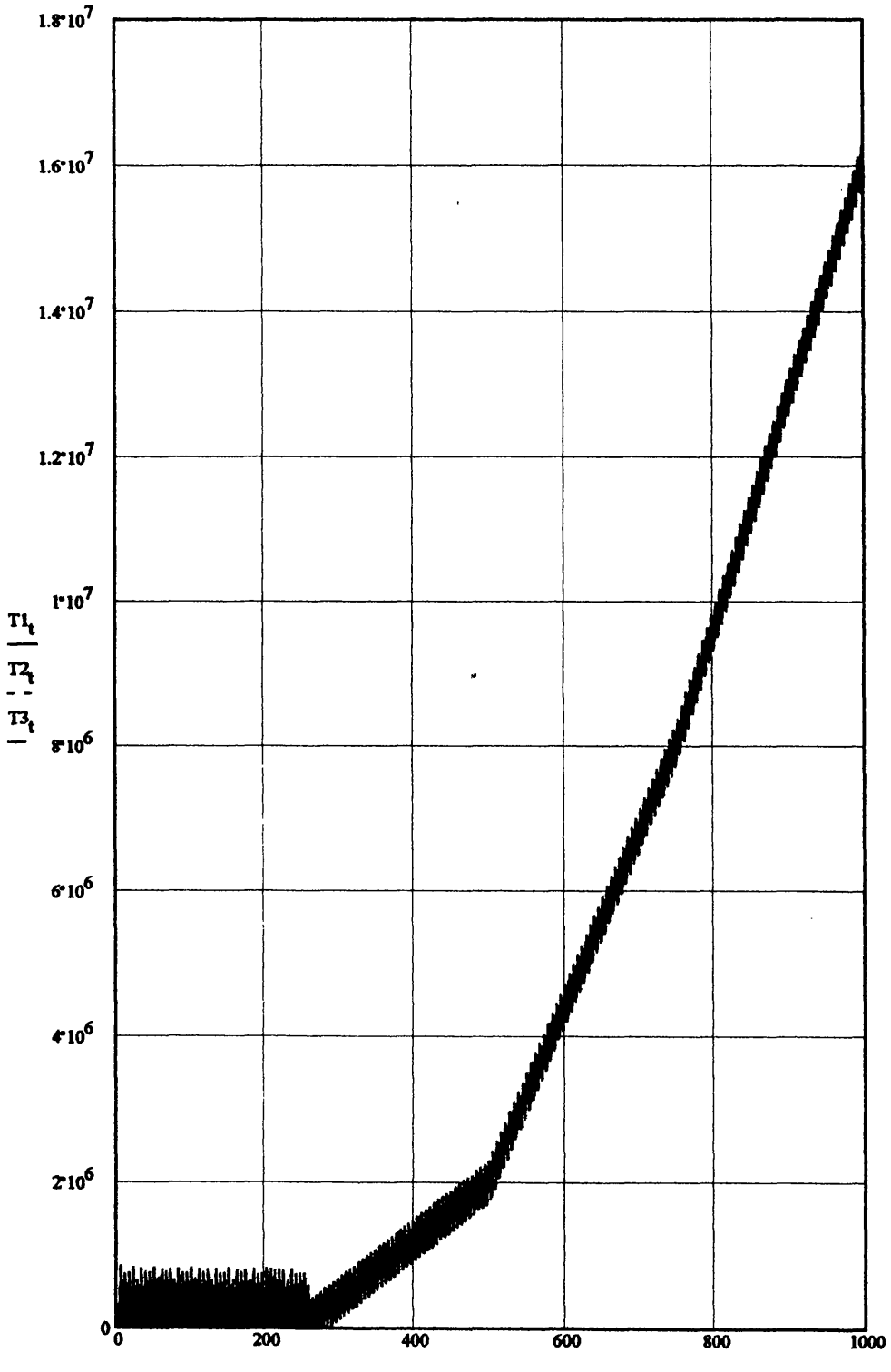

(N)

(s)

Figure A.9λ

2D *TLP* c.g. Motion Response (Heave v Surge)

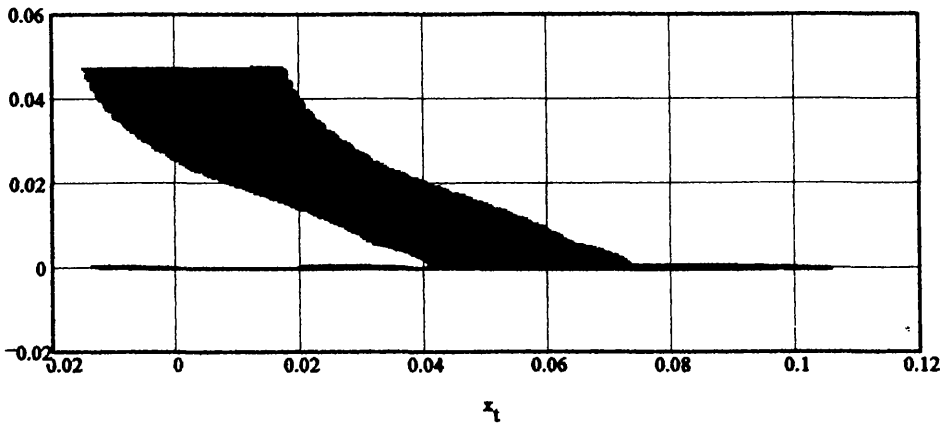

(m)

(m)

Figure A-93

2D *TLP* c.g. Motion Response (Heave v Sway)

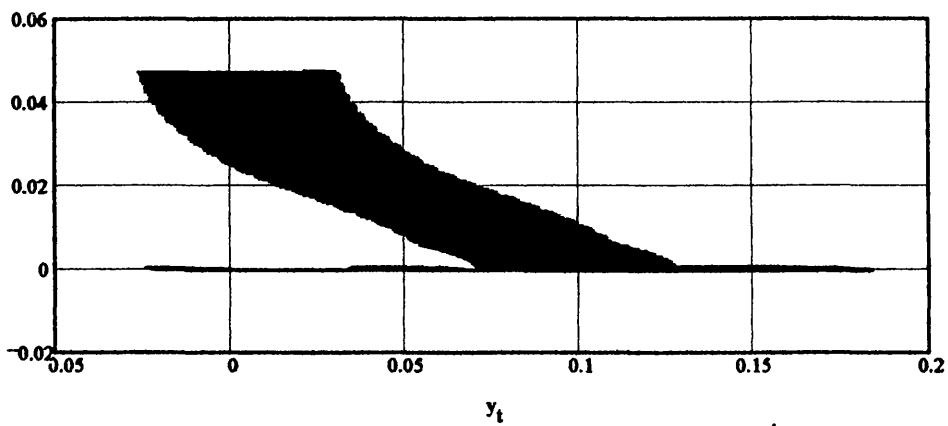

(m)

(m)

Figure A-94

2D *TLP* c.g. Motion Response (Heave v Roll)

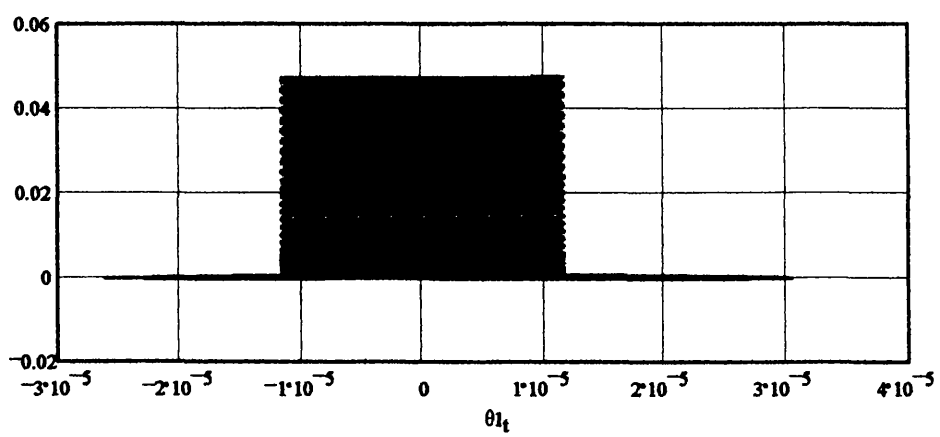

(m)

(rad)

Figure A-95

2D *TLP* c.g. Motion Response (Heave v Pitch)

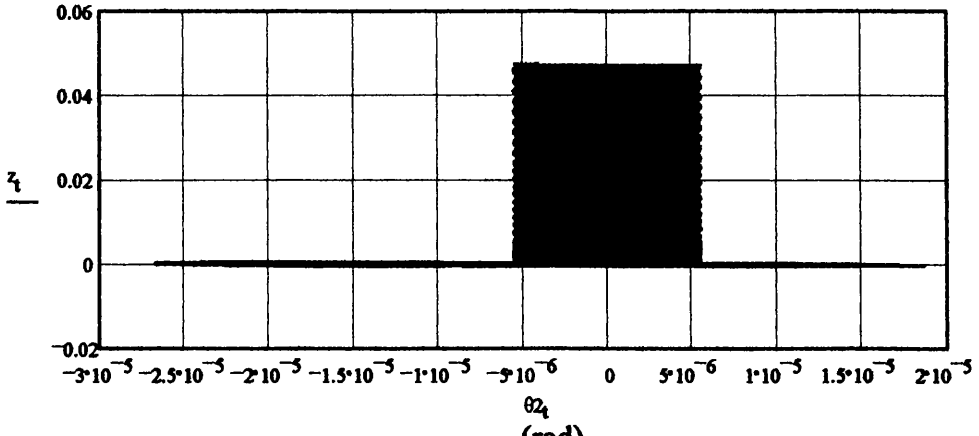

(m)

Figure A·96

2D *TLP* c.g. Motion Response (Heave v Yaw)

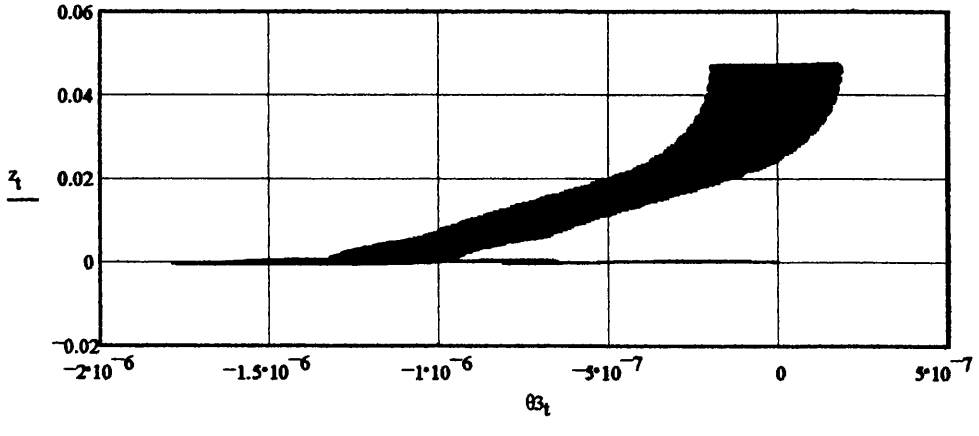

(m)

Figure A·97

2D *TLP* c.g. Motion Response (Surge v Sway)

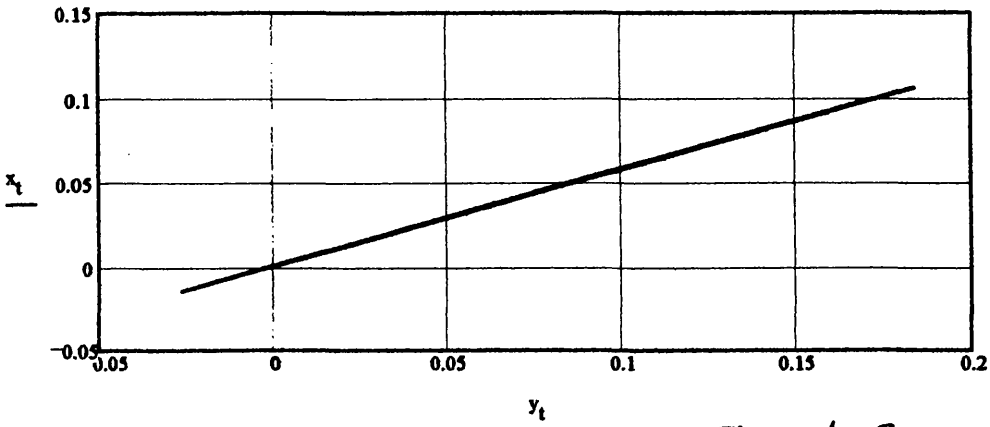

(m)

(m)

Figure A.98

2D *TLP* c.g. Motion Response (Surge v Heave)

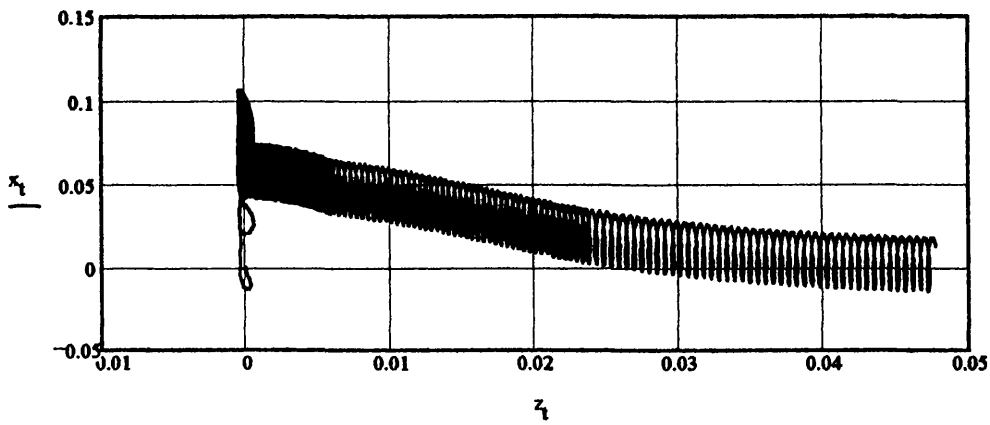

(m)

(m)

Figure A.99

2D *TLP* c.g. Motion Response (Surge v Roll)

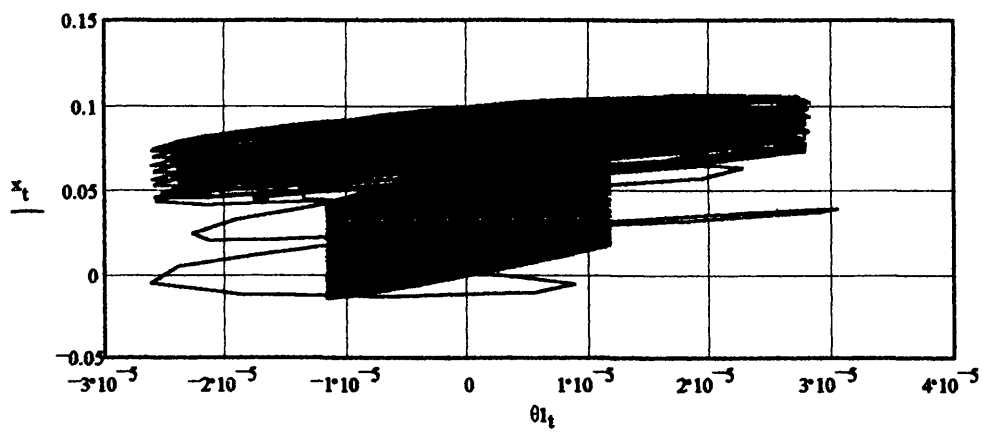

(m)

(rad)

Figure A.100

2D *TLP* c.g. Motion Response (Surge v Pitch)

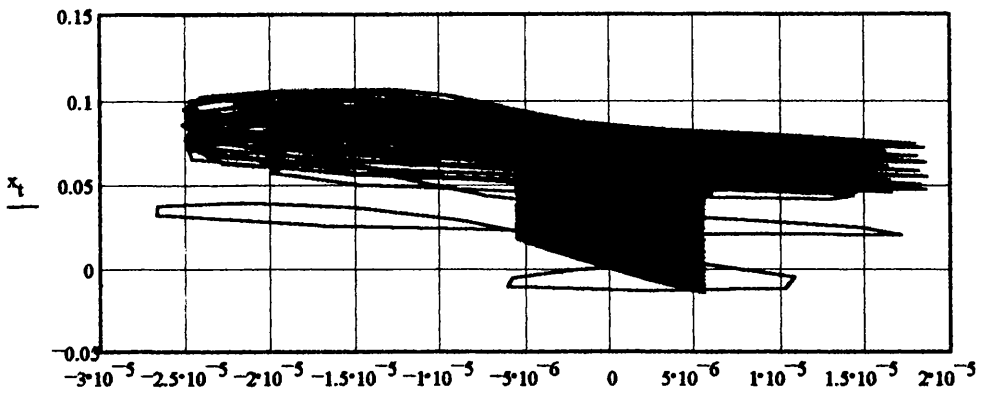

(m)

(rad)

Figure A-101

2D *TLP* c.g. Motion Response (Surge v Yaw)

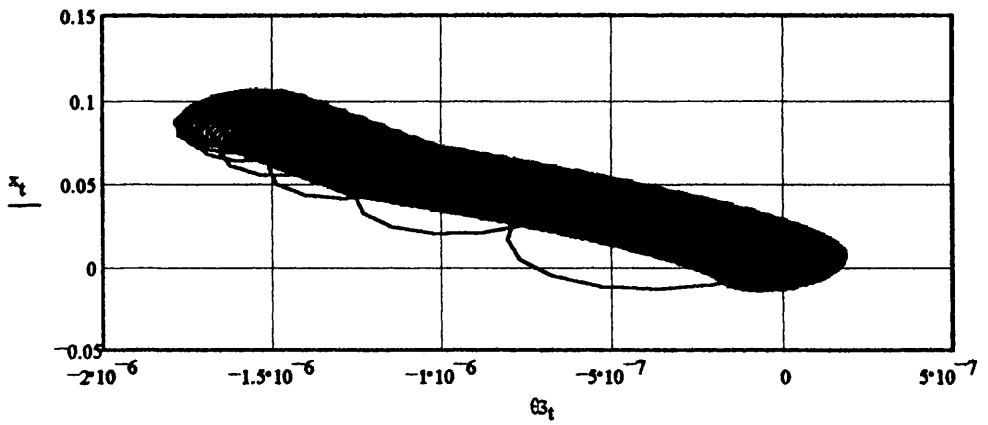

(m)

(rad)

Figure A-102